# UNITED STATES AIR FORCE

SUMMER FACULTY RESEARCH PROGRAM
1990
PROGRAM TECHNICAL REPORT
UNIVERSAL ENERGY SYSTEMS, INC.
VOLUME 1 OF 4

PROGRAM DIRECTOR, U. E. S.
RODNEY C. DARRAH
PROGRAM ADMINISTRATOR, U. E. S.
SUSAN K. ESPY

PROGRAM MANAGER, A. F. O. S. R.
LT. COL. CLAUDE CAVENDER

AIR FORCE OFFICE OF SCIENTIFIC RESEARCH

BOLLING AIR FORCE BASE

WASHINGTON, DC

DECEMBER 1990

REPORT DOCUMENTATION PAGE

Form Approved
OMB No. 0704-0188

Public reporting burden for this collection of information is estimated to average 1 hour per response, including the time for reviewing instructions, searching existing data sources, gathering and maintaining the data needed, and completing and reviewing the collection of information. Send comments regarding this burden estimate or any other aspect of this collection of information, including suggestions for reducing this burden, to Washington Headquarters Services, Directorate for Information Operations and Reports, 1215 Jefferson Davis Highway, Suite 1204, Arlington, VA 22202-4302, and to the Office of Management and Budget, Paperwork Reduction Project (0704-0188), Washington, DC 20503.

1. AGENCY USE ONLY (Leave blank)	2. REPORT DATE	3. REPORT TYPE AND DATES COVERED
	5 June 1991	Annual/Final 1 Sep 89-31 Aug 90

4. TITLE AND SUBTITLE
United States Air Force Summer Faculty Research Program
1990
Program Technical Report (w/atch 1 & 2)   Volume 1 of 4.

5. FUNDING NUMBERS

F49620-88-C-0053

6. AUTHOR(S)

Mr Rodney Darrah

7. PERFORMING ORGANIZATION NAME(S) AND ADDRESS(ES)

Universal Energy Systems (UES)
4401 Dayton -Xenia
Dayton OH 45432

8. PERFORMING ORGANIZATION REPORT NUMBER

AFOSR-TR·   91 0908

9. SPONSORING/MONITORING AGENCY NAME(S) AND ADDRESS(ES)

AFOSR/NI
Bldg 410
Bolling AFB DC 20332-6448

Lt Col V. Claude Cavender

10. SPONSORING/MONITORING AGENCY REPORT NUMBER

11. SUPPLEMENTARY NOTES

12a. DISTRIBUTION/AVAILABILITY STATEMENT

UNLIMITED

12b. DISTRIBUTION CODE

13. ABSTRACT (Maximum 200 words)

The United States Air Force Summer Faculty Research Program
(USAF-SFRP) is designed to introduce university, college, and
technical institute faculty members to Air Force research.
This is accomplished by the faculty members being selected on
a nationally advertised competitive basis for a ten-week
assignment during the summer intersession period to perform
research at Air Force laboratories/centers. Each assignment
is in a subject area and at an Air Force facility mutually
agreed upon by the faculty members and the Air Force. In
addition to compensation, travel and cost of living
allowances are also paid. The USAF-SFRP is sponsored by the
Air Force Office of Scientific Research.

91-18965

14. SUBJECT TERMS

91 1223 177

15. NUMBER OF PAGES

16. PRICE CODE

17. SECURITY CLASSIFICATION OF REPORT	18. SECURITY CLASSIFICATION OF THIS PAGE	19. SECURITY CLASSIFICATION OF ABSTRACT	20. LIMITATION OF ABSTRACT
UNCLASSIFIED	UNCLASSIFIED	UNCLASSIFIED	UL
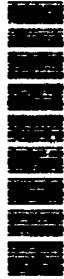
AFOSR-TR· 91 0958

UNITED STATES AIR FORCE

SUMMER FACULTY RESEARCH PROGRAM

1990

PROGRAM TECHNICAL REPORT

UNIVERSAL ENERGY SYSTEMS, INC.

VOLUME I of IV

Program Director, UES
Rodney C. Darrah

Program Manager, AFOSR
Lt. Col. Claude Cavender

Program Administrator, UES
Susan K. Espy

DTIC
COPY
ISPECTED
6

Submitted to

Air Force Office of Scientific Research

Bolling Air Force Base

Washington, DC

December 1990

TABLE OF CONTENTS

PREFACE

The United States Air Force Summer Faculty Resarch Program (USAF-SFRP) is designed to introduce university, college, and technical institute faculty members to Air Force research. This is accomplished by the faculty members being selected on a nationally advertised competitive basis for a ten-week assignment during the summer intersession period to perform research at Air Force laboratories/centers. Each assignment is in a subject area and at an Air Force facility mutually agreed upon by the faculty members and the Air Force. In addition to compensation, travel and cost of living allowances are also paid. The USAF-SFRP is sponsored by the Air Force Office of Scientific Research, Air Force Systems Command, United States Air Force, and is conducted by Universal Energy Systems, Inc.

The specific objectives of the 1990 USAF-SFRP are:

(1) To provide a productive means for U.S. faculty members to participate in research at Air Force Laboratories/Centers;

(2) To stimulate continuing professional association among the faculty and their professional peers in the Air Force;

(3) To further the research objectives of the United States Air Force;

(4) To enhance the research productivity and capabilities of the faculty especially as these relate to Air Force technical interests.

During the summer of 1990, 165-faculty members participated. These researchers were assigned to 23 USAF laboratories/centers across the country. This four volume document is a compilation of the final reports written by the assigned faculty members about their summer research efforts.

NAME / ADDRESS	DEGREE, SPECIALTY, LABORATORY ASSIGNED	
Thomas Abraham Instructor Saint Paul's College Dept. of Science and Math Lawrenceville, VA 23868 (804) 848-3111	Degree: Specialty: Assigned:	MS Mathematics Avionics Laboratory
Charles Alajajian Assistant Professor West Virginia University PO Box 6101 Morgantown, WV 26506 (304) 293-6371	Degree: Specialty: Assigned:	PhD Electrical Engineering Rome Air Development Center
Theodore Aufdemberge Professor Concordia College 4090 Geddes Road Ann Arbor, MI 48105 (313) 985-7349	Degree: Specialty: Assigned:	PhD Physical Chemistry Geophysics Laboratory
Richard Backs Assistant Professor Wright State University Dept. of Psychology Dayton, OH 45435 (513) 873-2656	Degree: Specialty: Assigned:	PhD Psychology Aerospace Medical Research Lab.
William Bannister Professor Lowell, University of Dept. of Chemistry Lowell, MA 01854 (508) 934-3682	Degree: Specialty: Assigned:	PhD Organic Chemistry Engineering & Services Center

NAME / ADDRESS	DEGREE, SPECIALTY, LABORATORY ASSIGNED		

Margaret Batschelet
Assistant Professor
Texas-San Antonio, Univ. of
Division of English
San Antonio, TX 78285
(513) 691-5357

Degree: PhD
Specialty: English
Assigned: Human Resources Laboratory
Training Systems

Frank Battles
Professor
Massachusetts Maritime Acad.
Basic Science Dept.
Buzzards Bay, MA 02532
(508) 759-5761

Degree: PhD
Specialty: Physics
Assigned: Geophysics Laboratory

John Bay
Assistant Professor
Virginia Polytech Institute
Dept. of Electrical Eng.
Blacksburg, VA 24061
(703) 231-5114

Degree: PhD
Specialty: Electrical Engineering
Assigned: Flight Dynamics Laboratory

Reuben Benumof
Professor
Staten Island, College of
130 Stuyvesant Pl.
Staten Island, NY 10301
(718) 390-7973

Degree: PhD
Specialty: Physics
Assigned: Geophysics Laboratory

Phillip Bishop
Assistant Professor
Alabama, University of
PO Box 870312
Tuscaloosa, AL 35487
(205) 348-8370

Degree: PhD
Specialty: Exercise Physiology
Assigned: School of Aerospace Medicine

NAME / ADDRESS	DEGREE, SPECIALTY, LABORATORY ASSIGNED	

Robert Blystone
Professor
Trinity University
715 Stadium Dr.
San Antonio, TX 78212
(512) 736-7243

Degree: PhD
Specialty: Zoology
Assigned: School of Aerospace Medicine

Michael Breen
Assistant Professor
Alfred University
Myers Hall
Alfred, NY 14802
(607) 871-2258

Degree: PhD
Specialty: Mathematics
Assigned: Avionics Laboratory

Bruno Breitmeyer
Professor
Houston, University of
Dept. of Psychology
Houston, TX 77204
(713) 749-6108

Degree: PhD
Specialty: Experimental Psychology
Assigned: School of Aerospace Medicine

Mark Brusseau
Assistant Professor
Arizona, University of
429 Shantz Bldg. #38
Tucson, AZ 85721
(602) 621-3244

Degree: PhD
Specialty: Environmental Chemistry
Assigned: Engineering & Services Center

David Buckalew
Assistant Professor
Xavier University
7325 Palmetto St.
New Orleans, LA 70125
(504) 483-7527

Degree: PhD
Specialty: Biology
Assigned: Occupational & Environmental
Health Laboratory

NAME / ADDRESS	DEGREE, SPECIALTY, LABORATORY ASSIGNED	

Theodore Burkey
Assistant Professor
Memphis State University
Chemistry Dept.
Memphis, TN 38152
(901) 678-2634

Degree: PhD
Specialty: Chemistry
Assigned: Frank J. Seiler Research Lab.

Larry Byrd
Assistant Professor
Arkansas State University
PO Box 1740
State University, AR 72467
(501) 972-2088

Degree: PhD
Specialty: Mechanical Engineering
Assigned: Aerospace Medical Research Lab.

Charles Camp
Assistant Professor
Memphis State University
Civil Engineering Dept.
Memphis, TN 38152
(901) 678-3169

Degree: PhD
Specialty: Civil Engineering
Assigned: Armament Laboratory

William Campbell
Associate Professor
Talladega College
Math Dept.
Talladega, AL 35160
(205) 362-0206

Degree: PhD
Specialty: Mathematics
Assigned: Weapons Laboratory

Arnold Carden
Professor
Alabama, University of
PO Box 870278
Tuscaloosa, AL 35487
(205) 348-1619

Degree: PhD
Specialty: Metallurgy
Assigned: Armament Laboratory

NAME / ADDRESS	DEGREE, SPECIALTY, LABORATORY ASSIGNED		

Richard Carlin
Assistant Professor
Alabama, University of
Dept. of Chemistry
Tuscaloosa, AL 35487
(205) 348-8443

Degree: PhD
Specialty: Chemistry
Assigned: Frank J. Seiler Research Lab.

Gene Carlisle
Professor
West Texas State University
Dept. of Chemistry & Physics
Canyon, TX 79016
(806) 656-2282

Degree: PhD
Specialty: Inorganic Chemistry
Assigned: Weapons Laboratory

Chia-Bo Chang
Associate Professor
Texas Tech. Univ.
PO Box 4320
Lubbock, TX 79409
(806) 742-3143

Degree: PhD
Specialty: Meteorology
Assigned: Geophysics Laboratory

Wayne Charlie
Associate Professor
Colorado State University
Dept. of Civil Engineering
Fort Collins, CO 80523
(303) 491-5048

Degree: PhD
Specialty: Civil Engineering
Assigned: Engineering & Services Center

Chih-Fan Chen
Professor
Boston University
755 Commonwealth Ave.
Boston, MA 02215
(617) 353-2566

Degree: PhD
Specialty: Engineering
Assigned: Electronic Systems Division

NAME / ADDRESS	DEGREE, SPECIALTY, LABORATORY ASSIGNED	

Pinyuen Chen
Associate Professor
Syracuse University
Dept. of Mathematics
Syracuse, NY 13244
(315) 443-1573

Degree: PhD
Specialty: Statistics
Assigned: Human Resources Laboratory
Manpower and Personnel

Muhammad Choudhry
Associate Professor
West Virginia University
PO Box 6101
Morgantown, WV 26506
(304) 293-6375

Degree: PhD
Specialty: Electrical Engineering
Assigned: Aero Propulsion Laboratory

Donald Chung
Associate Professor
San Jose State University
Dept. of Materials Eng.
San Jose, CA 95192
(408) 924-3873

Degree: PhD
Specialty: Materials Science
Assigned: Materials Laboratory

Mingking Chyu
Assistant Professor
Carnegie Mellon University
Dept. of Mechanical Eng.
Pittsburgh, PA 15213
(412) 268-3658

Degree: PhD
Specialty: Mechanical Engineering
Assigned: Aero Propulsion Laboratory

R. H. Cofer
Associate Professor
Florida Instit. of Tech.
150 W. University Blvd.
Melbourne, FL 32901
(407) 768-8000

Degree: PhD
Specialty: Electrical Engineering
Assigned: Avionics Laboratory

NAME / ADDRESS	DEGREE, SPECIALTY, LABORATORY ASSIGNED		

William Cofer
Assistant Professor
Washington State University
Dept. of Civil & Environ. Eng.
Pullman, WA 99164
(509) 335-3232

Degree: PhD
Specialty: Civil Engineering
Assigned: Weapons Laboratory

John Connolly
Professor
Missouri-Kansas City, Univ. of
Dept. of Chemistry
Kansas City, MO 64110
(816) 276-2286

Degree: PhD
Specialty: Chemistry
Assigned: Materials Laboratory

Gary Craig
Assistant Professor
Syracuse University
Link Hall
Syracuse, NY 13244
(315) 443-4389

Degree: PhD
Specialty: Electrical Engineering
Assigned: Rome Air Development Center

Donald Dareing
Professor
Florida, University of
237 MEB
Gainesville, FL 32611
(904) 392-0827

Degree: PhD
Specialty: Mechanical Engineering
Assigned: Aero Propulsion Laboratory

Vito DelVecchio
Professor
Scranton, University of
Dept. of Biology
Scranton, PA 18510
(717) 961-6117

Degree: PhD
Specialty: Biochemistry
Assigned: School of Aerospace Medicine

NAME / ADDRESS	DEGREE, SPECIALTY, LABORATORY ASSIGNED	

Paul Dellenback
Assistant Professor
Southern Methodist Univ.
Civil & Mech. Engineering Dept.
Dallas, TX 75275
(214) 692-4172

Degree: PhD
Specialty: Mechanical Engineering
Assigned: Aero Propulsion Laboratory

Eustace Dereniak
Associate Professor
Arizona, University of
McKale Ave.
Tucson, AZ 85721
(602) 621-1019

Degree: PhD
Specialty: Optics
Assigned: Armament Laboratory

Janet Dizinno
Assistant Professor
St. Mary's University
One Camino Santa Maria
San Antonio, TX 78284
(512) 436-3314

Degree: PhD
Specialty: Psychology
Assigned: Wilford Hall Medical Center

Daniel Dolata
Assistant Professor
Arizona, University of
Dept. of Chemistry
Tucson, AZ 85721
(602) 621-6337

Degree: PhD
Specialty: Chemistry
Assigned: Frank J. Seiler Research Lab.

Joseph Dreisbach
Professor
Scranton, University of
Chemistry Dept.
Scranton, PA 18510
(717) 961-7519

Degree: PhD
Specialty: Chemistry
Assigned: Engineering & Services Center

NAME / ADDRESS	DEGREE, SPECIALTY, LABORATORY ASSIGNED		

John Duncan
Assistant Professor
Kent State University
212 E. Van Deusen
Kent, OH 44242
(216) 672-2892

Degree: MS
Specialty: Technology
Assigned: Aerospace Medical Research Lab.

Randall Dupre
Assistant Professor
Nevada-Las Vegas, Univ. of
4505 S. Maryland Pkwy.
Las Vegas, NV 89154
(702) 739-3399

Degree: PhD
Specialty: Biology
Assigned: School of Aerospace Medicine

James Dykes
Associate Professor
Texas-San Antonio, Univ. of
Div. of Behavioral & Cultural Sci.
San Antonio, TX 78285
(512) 691-5706

Degree: PhD
Specialty: Psychology
Assigned: Human Resources Laboratory
Training Systems

Franklin Eastep
Professor
Dayton, Univ. of
Aerospace Engineering KL304
Dayton, OH 45469
(513) 229-2678

Degree: PhD
Specialty: Aerospace Engineering
Assigned: Flight Dynamics Laboratory

Sherif Elwakil
Professor
Southeastern Massachusetts Univ.
Mechanical Engineering Dept.
N. Dartmouth, MA 02747
(508) 999-8492

Degree: PhD
Specialty: Mechanical Engineering
Assigned: Materials Laboratory

NAME / ADDRESS	DEGREE, SPECIALTY, LABORATORY ASSIGNED		

Dennis Flentge
Associate Professor
Cedarville College
Box 601
Cedarville, OH 45314
(513) 766-2211

Degree: PhD
Specialty: Physical Chemistry
Assigned: Aero Propulsion Laboratory

Charles Fosha
Associate Professor
Colorado, Univ. of
1867 Austin Bluffs Parkway
Colorado Springs, CO 80918
(719) 548-0602

Degree: PhD
Specialty: Electrical Engineering
Assigned: Armament Laboratory

Lionel Friedman
Professor
Worcester Polytechnic Instit.
100 Institute Rd.
Worcester, MA 01609
(508) 831-5303

Degree: PhD
Specialty: Physics
Assigned: Rome Air Development Center

Daniel Fuller
Department Head
Nicholls State University
Highway 1
Thibodaux, LA 70310
(504) 448-4504

Degree: PhD
Specialty: Chemistry
Assigned: Astronautics Laboratory

Ephrahim Garcia
Assistant Professor
New York-Buffalo, State Univ. of
1012 Furnas Hall
Buffalo, NY 14260
(716) 636-3058

Degree: PhD
Specialty: Aerospace Engineering
Assigned: Frank J. Seiler Research Lab.

NAME / ADDRESS	DEGREE, SPECIALTY, LABORATORY ASSIGNED

Daniel Garland
Assistant Professor
Embry-Riddle Aeronautical Univ.
Humanities/Social Sci.
Daytona Beach, FL 32114
(904) 239-6641

<u>Degree:</u> PhD
<u>Specialty:</u> Psychology
<u>Assigned:</u> Human Resources Laboratory
Operations Training Division

Thomas Gearhart
Associate Professor
Captial University
Science Hall E. Main St.
Columbus, OH .43209
(614) 236-6800

<u>Degree:</u> PhD
<u>Specialty:</u> Mathematics
<u>Assigned:</u> Avionics Laboratory

John George
Professor
Wyoming, University of
Box 3036
Laramie, WY 82071
(307) 766-2383

<u>Degree:</u> PhD
<u>Specialty:</u> Applied Mathematics
<u>Assigned:</u> Armament Laboratory

Frederick Gibson
Instructor
Morehouse College
830 Westview Dr. SW
Atlanta, GA 30312
(404) 681-2800

<u>Degree:</u> MS
<u>Specialty:</u> Applied Mathematics
<u>Assigned:</u> Armament Laboratory

Ashok Goel
Assistant Professor
Michigan Tech. University
Dept. of Electrical Engineering
Houghton, MI 49931
(906) 487-2868

<u>Degree:</u> PhD
<u>Specialty:</u> Electrical Engineering
<u>Assigned:</u> Electronic Technology Laboratory

NAME / ADDRESS	DEGREE, SPECIALTY, LABORATORY ASSIGNED	

Harold Goldstein
Associate Professor
District of Columbia, Univ. of
4200 Connecticut Ave. N.W.
Washington, DC 20008
(202) 282-7349

Degree: MS
Specialty: Transportation Engineering
Assigned: Human Resources Laboratory
Training Systems

Reinhard Graetzer
Associate Professor
Penn State University
104 Davey Lab.
University Park, PA 16802
(814) 863-0705

Degree: PhD
Specialty: Physics
Assigned: School of Aerospace Medicine

Paul Griffin
Assistant Professor
Georgia Tech.
School of ISYE
Atlanta, GA 30332
(404) 894-2431

Degree: PhD
Specialty: Industrial Engineering
Assigned: School of Aerospace Medicine

William Grissom
Assistant Professor
Morehouse College
830 Westview Dr.
Atlanta, GA 30314
(404) 681-2800

Degree: MS
Specialty: Mechanical Engineering
Assigned: Arnold Engineering Development
Center

David Grossie
Assistant Professor
Wright State University
Dept. of Chemistry
Dayton, OH 45435
(513) 873-2210

Degree: PhD
Specialty: Chemistry
Assigned: Materials Laboratory

NAME / ADDRESS	DEGREE, SPECIALTY, LABORATORY ASSIGNED	

Pushpa Gupta
Professor
Maine, University of
321 Neville
Orono, ME 04469
(207) 581-3914

Degree: PhD
Specialty: Mathematics
Assigned: School of Aerospace Medicine

Ramesh Gupta
Professor
Maine, University of
Dept. of Mathematics
Orono, ME 04469
(207) 581-3913

Degree: PhD
Specialty: Mathematical Statistics
Assigned: School of Aerospace Medicine

Martin Hagan
Associate Professor
Oklahoma State University
School of Elec. & Comp. Sci.
Stillwater, OK 74078
(405) 744-7340

Degree: PhD
Specialty: Electrical Engineering
Assigned: Aerospace Medical Research Lab.

Lawrence Hall
Assistant Professor
South Florida, Univ. of
Dept. of Computer Sci.
Tampa, FL 33620
(813) 974-4195

Degree: PhD
Specialty: Computer Science
Assigned: Avionics Laboratory

Kevin Hallinan
Assistant Professor
Dayton, Univ. of
Mech. & Aero. Engineering
Dayton, OH 45469
(513) 229-2875

Degree: PhD
Specialty: Mechanical Engineering
Assigned: Aero Propulsion Laboratory

NAME / ADDRESS	DEGREE, SPECIALTY, LABORATORY ASSIGNED		
Marvin Hamstad Professor Denver, Univ. of Dept. of Engineering Denver, CO 80208 (303) 871-3191	Degree: Specialty: Assigned:	PhD Solid Mechanics Flight Dynamics Laboratory	
Frances Harackiewicz Assistant Professor Southern Illinois Univ. Technology Bldg. A Carbondale, IL 62901 (618) 453-7031	Degree: Specialty: Assigned:	PhD Electrical Engineering Rome Air Development Center	
Paul Hedman Professor Brigham Young University Chemical Engineering Dept. Provo, UT 84602 (801) 378-6238	Degree: Specialty: Assigned:	PhD Chemical Engineering Aero Propulsion Laboratory	
Verlin Hinsz Assistant Professor North Dakota State Univ. 115 Minard Hall Fargo, ND 58105 (701) 237-7082	Degree: Specialty: Assigned:	PhD Psychology Human Resources Laboratory Logistics & Human Factors	
Chin Hsu Associate Professor Washington State Univ. Dept. of Elec. and Comp. Eng. Pullman, WA 99164 (509) 335-2342	Degree: Specialty: Assigned:	PhD Electrical Engineering Flight Dynamics Laboratory	

NAME / ADDRESS	DEGREE, SPECIALTY, LABORATORY ASSIGNED		

Ming-Shu Hsu
Associate Professor
Portland, Univ. of
5000 N. Willamette Blvd.
Portland, OR 97203
(503) 283-7436

Degree: PhD
Specialty: Mechanical Engineering
Assigned: Flight Dynamics Laboratory

Delayne Hudspeth
Associate Professor
Texas-Austin, Univ. of
College of Education
Austin, TX 78712
(512) 471-5211

Degree: PhD
Specialty: Education
Assigned: Human Resources Laboratory
Manpower & Personnel Div.

Manuel Huerta
Professor
Miami, Univ. of
PO Box 248046
Coral Gables, FL 33124
(305) 284-2323

Degree: PhD
Specialty: Physics
Assigned: Armament Laboratory

David Hui
Associate Professor
New Orleans, Univ. of
Dept. of Mech. Engineering
New Orleans, LA 70148
(504) 286-6192

Degree: PhD
Specialty: Aerospace Engineering
Assigned: Flight Dynamics Laboratory

George Jumper
Associate Professor
Worcester Poly. Instit.
100 Institute Rd.
Worcester, MA 01609
(508) 831-5368

Degree: PhD
Specialty: Mechanical Engineering
Assigned: Geophysics Laboratory

NAME / ADDRESS	DEGREE, SPECIALTY, LABORATORY ASSIGNED	
Prasad Kadaba Professor Kentucky, Univ. of Rm. 453 Anderson Hall Lexington, KY 40506 (606) 257-2943	Degree: Specialty: Assigned:	PhD Physics Materials Laboratory
Ngozi Kamalu Lecturer California Poly. Univ. Mechancial Engineering Dept. San Luis Obispo, CA 93407 (805) 756-1336	Degree: Specialty: Assigned:	PhD Mechanical Engineering Frank J. Seiler Research Lab.
Gillray Kandel Professor Rensselaer Poly. Instit. 8th St. Troy, NY 12180 (518) 276-8269	Degree: Specialty: Assigned:	PhD Experimental Psychology Human Resources Laboratory Operations Training Division
Mohammad Karim Associate Professor Dayton, University of 300 College Park Dayton, OH 45469 (513) 229-3611	Degree: Specialty: Assigned:	PhD Electrical Engineering Avionics Laboratory
Siavash Kassemi Assistant Professor Colorado, University of 1867 Austin Bluffs Parkway Colorado Springs, CO 80918 (719) 593-3326	Degree: Specialty: Assigned:	PhD Aerospace Engineering Frank J. Seiler Research Lab.

NAME / ADDRESS	DEGREE, SPECIALTY, LABORATORY ASSIGNED	

Yulian Kin
Associate Professor
Purdue Calumet
Engineering Dept.
Hammond, IN 46323
(219) 989-2684

Degree: PhD
Specialty: Mechanical Engineering
Assigned: Flight Dynamics Laboratory

Kevin Kirby
Assistant Professor
Wright State University
3171 Research Blvd.
Kettering, OH 45420
(513) 259-1373

Degree: PhD
Specialty: Computer Science
Assigned: Avionics Laboratory

David Kirkner
Associate Professor
Notre Dame, Univ. of
Dept. of Civil Engineering
Notre Dame, IN 46556
(219) 239-6518

Degree: PhD
Specialty: Solid Mechanics
Assigned: Engineering & Services Center

Ashok Krishnamurthy
Assistant Professor
Ohio State University
2015 Neil Ave.
Columbus, OH 43210
(614) 292-5604

Degree: PhD
Specialty: Electrical Engineering
Assigned: Aerospace Medical Research Lab.

Paul Kromann
Associate Professor
Fort Valley State College
Campus Box 4821
Fort Valley, GA 31030
(912) 825-6245

Degree: PhD
Specialty: Chemistry
Assigned: Engineering & Services Center

NAME / ADDRESS	DEGREE, SPECIALTY, LABORATORY ASSIGNED

Jeffrey Kuhn
Associate Professor
Michigan State University
309 Physics-Astronomy Bldg.
East Lansing, MI 48824
(517) 353-2986

Degree: PhD
Specialty: Physics
Assigned: Geophysics Laboratory

Kyung Kwon
Associate Professor
Tuskege University
Chemistry Dept.
Tuskegee, AL 36088
(205) 727-8089

Degree: PhD
Specialty: Chemical Engineering
Assigned: Engineering & Services Center

Joseph Lambert
Professor
Northwestern University
2145 Sheridan Rd.
Evanston, IL 60208
(708) 491-5437

Degree: PhD
Specialty: Chemistry
Assigned: Materials Laboratory

Gary Leatherman
Assistant Professor
Worcester Polytechnic Instit.
100 Institute Rd.
Worcester, MA 01609
(508) 831-5229

Degree: PhD
Specialty: Materials Science
Assigned: Materials Laboratory

Byung-Lip Lee
Associate Professor
Pennsylvania State University
227 Hammond Bldg.
University Park, PA 16802
(814) 865-7829

Degree: PhD
Specialty: Materials Science
Assigned: Flight Dynamics Laboratory

NAME / ADDRESS	DEGREE, SPECIALTY, LABORATORY ASSIGNED		

Tzesan Lee
Associate Professor
Western Illinois Univ.
900 W. Adams St.
Macomb, IL 61455
(309) 298-1485

Degree: PhD
Specialty: Applied Mathematics
Assigned: Aerospace Medical Research Lab.

Won-Kyoo Lee
Associate Professor
Ohio State University
140 W. 19th Ave.
Columbus, OH 43211
(614) 292-6605

Degree: PhD
Specialty: Chemical Engineering
Assigned: Materials Laboratory

Paul Lemke
Professor
Auburn University
131 Funchess Hall
Auburn University, AL 36849
(205) 844-1662

Degree: PhD
Specialty: Molecular Biology
Assigned: School of Aerospace Medicine

Sigmund Lephart
Lecturer
Melbourne Univ. Australia
Parkville 3052
Victoria Australia,
(03) 344-5158

Degree: PhD
Specialty: Biomechanics
Assigned: Aerospace Medical Research Lab.

Shannon Lieb
Associate Professor
Butler University
4600 Sunset Ave.
Indianapolis, IN 46208
(317) 283-9410

Degree: PhD
Specialty: Physical Chemistry
Assigned: Astronautics Laboratory

NAME / ADDRESS	DEGREE, SPECIALTY, LABORATORY ASSIGNED		

Hao Ling
Assistant Professor
Texas-Austin, Univ. of
Dept. of Elec. & Comp. Eng.
Austin, TX 78712
(512) 471-1710

Degree: PhD
Specialty: Electrical Engineering
Assigned: Rome Air Development Center

C. Randal Lishawa
Assistant Professor
Utica College
Burrstone Rd.
Utica, NY 13502
(315) 792-3139

Degree: PhD
Specialty: Physical Chemistry
Assigned: Geophysics Laboratory

Vernon Matzen
Associate Professor
North Carolina State Univ.
Box 7908
Raleigh, NC 27695
(919) 737-2331

Degree: PhD
Specialty: Structural Mechanics
Assigned: Flight Dynamics Laboratory

Michael McFarland
Assistant Professor
Utah State Univ.
Utah Water Research Lab.
Logan, UT 84322
(801) 750-3196

Degree: PhD
Specialty: Biological Engineering
Assigned: Engineering & Services Center

Perry McNeill
Professor
North Texas, Univ. of
PO Box 13198
Denton, TX 76203
(817) 565-2846

Degree: PhD
Specialty: Education
Assigned: Engineering & Services Center

NAME / ADDRESS	DEGREE, SPECIALTY, LABORATORY ASSIGNED	
Miguel Medina Associate Professor Duke University Dept. of Civil Engineering Durham, NC 27706 (919) 660-5195	Degree: Specialty: Assigned:	PhD Water Resources Occupational & Environmental Health Laboratory
Richard Miers Associate Professor Indiana Univ. - Purdue Univ. 2101 Coliseum Blvd. E. Fort Wayne, IN 46805 (219) 481-6154	Degree: Specialty: Assigned:	PhD Physics Avionics Laboratory
William Moor Associate Professor Arizona State Univ. College of Engineering Tempe, AZ 85287 (602) 965-4022	Degree: Specialty: Assigned:	PhD Industrial Engineering Human Resources Laboratory Operations Training Division
Carlyle Moore Associate Professor Morehouse College 830 Westview Dr. Atlanta, GA 30314 (404) 681-2800	Degree: Specialty: Assigned:	PhD Physics Arnold Engineering Development Center
Kevin Moore Assistant Professor Idaho State Univ. Box 8060 Pocatello, ID 83209 (208) 236-4188	Degree: Specialty: Assigned:	PhD Electrical Engineering Armament Laboratory

NAME / ADDRESS	DEGREE, SPECIALTY, LABORATORY ASSIGNED	
Rex Moyer Professor Trinity University 715 Stadium Dr. San Antonio, TX 78212 (512) 736-7242	Degree: Specialty: Assigned:	PhD Microbiology School of Aerospace Medicine
Arnold Nelson Assistant Professor Louisiana State Univ. 112 Long Field House Baton Rouge, LA 70803 (504) 388-3114	Degree: Specialty: Assigned:	MS Physical Education School of Aerospace Medicine
Kirk Nordyke Instructor Xavier University Dept. of Biology New Orleans, LA 70125 (504) 483-7527	Degree: Specialty: Assigned:	MS Zoology Occupational & Environmental Health Laboratory
Olin Norton Researcher Mississippi State Univ. PO Drawer MM Miss' :sippi State, MS 39762 (601) 325-2105	Degree: Specialty: Assigned:	PhD Mechanical Engineering Arnold Engineering Development Center
Muhammad Numan Assistant Professor Indiana Univ. of Pennsylvania 45 Weyandt Hall Indiana, PA 15705 (412) 357-2318	Degree: Specialty: Assigned:	PhD Physics Electronic Technology Laboratory

NAME / ADDRESS	DEGREE, SPECIALTY, LABORATORY ASSIGNED	

Amit Patra
Associate Professor
Puerto Rico, Univ. of
PO Box 5000
Mayaguez, PR 00709
(809) 832-4040

Degree: PhD
Specialty: Mechanical Engineering
Assigned: Aerospace Medical Research Lab.

Shietung Peng
Assistant Professor
Maryland-Baltimore, Univ. of
5401 Wilkens Ave.
Baltimore, MD 21228
(301) 455-3540

Degree: PhD
Specialty: Computer Science
Assigned: Rome Air Development Center

Richard Peters
Assistant Professor
Vanderbilt University
Box 6091 Station B
Nashville, TN 37235
(615) 322-7924

Degree: PhD
Specialty: Electrical Engineering
Assigned: Arnold Engineering Development Center

Bernard Piersma
Professor
Houghton College
Dept. of Chemistry
Houghton, NY 14744
(716) 567-9301

Degree: PhD
Specialty: Physical Chemistry
Assigned: Frank J. Seiler Research Lab.

Thomas Pollock
Associate Professor
Texas A&M University
Dept. of Aerospace Engineering
College Station, TX 77843
(409) 845-1686

Degree: PhD
Specialty: Materials Science
Assigned: Astronautics Laboratory

NAME / ADDRESS	DEGREE, SPECIALTY, LABORATORY ASSIGNED	

Thomas Posbergh
Assistant Professor
Minnesota, Univ. of
107 Akerman Hall
Minneapolis, MN 55455
(612) 625-2871

Degree: PhD
Specialty: Electrical Engineering
Assigned: Frank J. Seiler Research Lab.

James Price
Professor
Iowa, University of
W140 Seashore Hall
Iowa City, IA 52242
(319) 335-2497

Degree: PhD
Specialty: Sociology
Assigned: Human Resources Laboratory
Manpower & Personnel Div.

Gandikota Rao
Professor
St. Louis University
3507 Laclede Ave.
St. Louis, MO 63103
(314) 658-3115

Degree: PhD
Specialty: Meteorology
Assigned: Geophysics Laboratory

K. Sankara Rao
Professor
North Dakota State Univ.
Dept. of Electrical Engineering
Fargo, ND 58105
(701) 237-7217

Degree: PhD
Specialty: Electrical Engineering
Assigned: Aero Propulsion Laboratory

Craig Rasmussen
Assistant Professor
Utah State University
CASS UMC 4405
Logan, UT 84322
(801) 750-2967

Degree: PhD
Specialty: Physics
Assigned: Geophysics Laboratory

NAME / ADDRESS	DEGREE, SPECIALTY, LABORATORY ASSIGNED

Joan Rentsch
Assistant Professor
Wright State University
Dept. of Psychology
Dayton, OH 45435
(513) 873-2218

Degree: PhD
Specialty: Industrial Psychology
Assigned: Human Resources Laboratory
Logistics & Human Factors

Michael Resch
Assistant Professor
Nebraska-Lincoln, Univ. of
212 Bancroft Hall
Lincoln, NE 68588
(402) 472-2354

Degree: PhD
Specialty: Materials Science
Assigned: Materials Laboratory

Donald Robinson
Assistant Professor
Xavier University
7325 Palmetto St.
New Orleans, LA 70125
(504) 483-7371

Degree: PhD
Specialty: Chemistry
Assigned: School of Aerospace Medicine

Larry Roe
Assistant Professor
Virginia Poly. Instit. State Univ.
Mechanical Engineering Dept.
Blacksburg, VA 24061
(703) 231-7295

Degree: PhD
Specialty: Mechanical Engineering
Assigned: Aero Propulsion Laboratory

John Russell
Associate Professor
Florida Inst. of Tech.
150 W. University Blvd.
Melbourne, FL 32901
(407) 768-8000

Degree: PhD
Specialty: Aerospace Engineering
Assigned: Arnold Engineering Development
Center

NAME / ADDRESS	DEGREE, SPECIALTY, LABORATORY ASSIGNED

Daniel Ryder
Assistant Professor
Tufts University
Chemical Engineering Dept.
Medford, MA 02155
(617) 381-3446

Degree: PhD
Specialty: Chemical Engineering
Assigned: Rome Air Development Center

John Scharf
Chairman
Carroll College
Dept. of Math.
Helena, MT 59625
(406) 442-3450

Degree: MS
Specialty: Civil Engineering
Assigned: Engineering & Services Center

Johanna Schruben
Associate Professor
Houston-Victoria, Univ. of
2302C Red River
Victoria, TX 77901
(512) 576-3151

Degree: PhD
Specialty: Mathematics
Assigned: Weapons Laboratory

Martin Schwartz
Professor
North Texas, Univ. of
PO Box 5068
Denton, TX 76203
(817) 565-3524

Degree: PhD
Specialty: Physical Chemistry
Assigned: Materials Laboratory

David Senseman
Professor
Texas-San Antonio, Univ. of
Div. of Life Sciences
San Antonio, TX 78285
(512) 691-5485

Degree: PhD
Specialty: Biology
Assigned: School of Aerospace Medicine

NAME / ADDRESS	DEGREE, SPECIALTY, LABORATORY ASSIGNED	

Brian Shelburne
Associate Professor
Wittenberg University
Box 720
Springfield, OH 45501
(513) 327-7862

Degree: PhD
Specialty: Mathematics
Assigned: Avionics Laboratory

Behrooz Shirazi
Assistant Professor
Southern Methodist University
Dept. of Comp. Sci. & Engineering
Dallas, TX 75275
(214) 692-2874

Degree: PhD
Specialty: Computer Science
Assigned: Rome Air Development Center

Leonard Shyles
Associate Professor
Villanova University
Dept. of Communication Arts
Villanova, PA 19085
(215) 645-7923

Degree: PhD
Specialty: Communication
Assigned: Aerospace Medical Research Lab.

William Siuru
Associate Professor
Colorado, Univ. of
1867 Austin Bluffs Parkway
Colorado Springs, CO 80918
(719) 548-0602

Degree: PhD
Specialty: Mechanical Engineering
Assigned: Armament Laboratory

Eleanor Smith
Assistant Professor
Florida A&M University
406 Perry-Paige
Tallahassee, FL 32307
(904) 599-3821

Degree: PhD
Specialty: Sociology
Assigned: Human Resources Laboratory
Training Systems Division

NAME / ADDRESS	DEGREE, SPECIALTY, LABORATORY ASSIGNED	

Wayne Smith
Associate Professor
Mississippi State University
Drawer CS
Mississippi State, MS 39762
(601) 325-2642

<u>Degree:</u> PhD
<u>Specialty:</u> Computer Science
<u>Assigned:</u> Rome Air Development Center

Kenneth Sobel
Associate Professor
New York, City College of
Dept. of Electrical Engineering
New York, NY 10031
(212) 690-4241

<u>Degree:</u> PhD
<u>Specialty:</u> Electrical Engineering
<u>Assigned:</u> Armament Laboratory

Glenn Stark
Assistant Professor
Wellesley College
Dept. of Physics
Wellesley, MA 02181
(617) 235-0320

<u>Degree:</u> PhD
<u>Specialty:</u> Physics
<u>Assigned:</u> Geophysics Laboratory

Stanley Stephenson
Associate Professor
Southwest Texas State Univ.
CIS/ADS
San Marcos, TX 78666
(512) 245-2291

<u>Degree:</u> PhD
<u>Specialty:</u> Psychology
<u>Assigned:</u> Human Resources Laboratory
Training Systems Division

Chun Su
Assistant Professor
Mississippi State Univ.
Dept. of Physics
Mississippi State, MS 39762
(601) 325-2931

<u>Degree:</u> PhD
<u>Specialty:</u> Physics
<u>Assigned:</u> Arnold Engineering Development
Center

NAME / ADDRESS	DEGREE, SPECIALTY, LABORATORY ASSIGNED		

Richard Swope
Professor
Trinity University
715 Stadium Dr.
San Antonio, TX 78212
(512) 736-7514

Degree: PhD
Specialty: Mechanical Engineering
Assigned: School of Aerospace Medicine

John Szarek
Assistant Professor
Marshall University
1542 Spring Valley Dr.
Huntington, WV 25755
(304) 696-7314

Degree: PhD
Specialty: Pharmaceutical
Assigned: School of Aerospace Medicine

Kaveh Tagavi
Associate Professor
Kentucky, Univ. of
242 Anderson Hall
Lexington, KY 40506
(606) 257-2739

Degree: PhD
Specialty: Mechanical Engineering
Assigned: Aero Propulsion Laboratory

Devki Talwar
Assistant Professor
Indiana Univ. of Pennsylvania
Dept. of Physics
Indiana, PA 15705
(412) 357-4589

Degree: PhD
Specialty: Physics
Assigned: Electronic Technology Laboratory

Richard Tankin
Professor
Northwestern University
Dept. of Mechanical Engineering
Evanston, IL 60208
(708) 491-3532

Degree: PhD
Specialty: Engineering
Assigned: Aero Propulsion Laboratory

NAME / ADDRESS	DEGREE, SPECIALTY, LABORATORY ASSIGNED

Roger Thompson
Assistant Professor
Pennsylvania State Univ.
233 Hammond Bldg.
University Park, PA 16802
(814) 863-0968

Degree: PhD
Specialty: Mechanical Engineering
Assigned: Astronautics Laboratory

Steven Trogdon
Associate Professor
Minnesota, Univ. of
108 Heller Hall
Duluth, MN 55812
(218) 726-6173

Degree: PhD
Specialty: Mechanics
Assigned: Armament Laboratory

Hai-Lung Tsai
Assistant Professor
Missouri-Rolla, Univ. of
Dept. of Mech. & Aero.
Rolla, MO 65401
(314) 341-4945

Degree: PhD
Specialty: Mechanical Engineering
Assigned: Materials Laboratory

Pamela Tsang
Assistant Professor
Wright State University
309 Oelman
Dayton, OH 45435
(513) 258-2687

Degree: PhD
Specialty: Engineering Psychology
Assigned: Human Resources Laboratory
            Logistics & Human Factors

Ronald VanEtten
Associate Professor
Illinois State University
500 W. Gregory
Normal, IL 61761
(309) 438-8346

Degree: MS
Specialty: Computer Science
Assigned: Rome Air Development Center

NAME / ADDRESS	DEGREE, SPECIALTY, LABORATORY ASSIGNED		

George Veyera
Assistant Professor
Rhode Island, Univ. of
Dept. of Civil Engineering
Kingston, RI 02881
(401) 792-2684

Degree: PhD
Specialty: Civil Engineering
Assigned: Engineering & Services Center

Hung Vu
Assistant Professor
California State Univ.
1250 Bellflower Blvd.
Long Beach, CA 90840
(213) 985-1524

Degree: PhD
Specialty: Applied Mechanics
Assigned: Astronautics Laboratory

Bonnie Walker
Assistant Professor
Central State University
Psychology Dept.
Wilberforce, OH 45384
(513) 376-6516

Degree: PhD
Specialty: Experimental Psychology
Assigned: Aerospace Medical Research Lab.

Steven Waller
Associate Professor
South Dakota, Univ. of
Dept. of Physiol. & Pharmacol.
Vermillion, SD 57069
(605) 677-5157

Degree: PhD
Specialty: Pharmacology
Assigned: School of Aerospace Medicine

Peter Walsh
Professor
Fairleigh Dickinson Univ.
Dept. of Electrical Engineering
Teaneck, NJ 07666
(201) 692-2493

Degree: PhD
Specialty: Physics
Assigned: Weapons Laboratory

NAME / ADDRESS	DEGREE, SPECIALTY, LABORATORY ASSIGNED	

Lorin Weber
Professor
Ricks College
Physics Dept.
Rexburg, ID 83460
(208) 356-1907

Degree: MS
Specialty: Science Education
Assigned: Occupational & Environmental Health Laboratory

Kevin Whitaker
Assistant Professor
Alabama, University of
Box 870280
Tuscaloosa, AL 35487
(205) 348-7366

Degree: PhD
Specialty: Aerospace Engineering
Assigned: Arnold Engineering Development Center

Trevor Williams
Assistant Professor
Cincinnati, University of
ML 70
Cincinnati, OH 45221
(513) 556-3221

Degree: PhD
Specialty: Control Theory
Assigned: Astronautics Laboratory

John Wills
Professor
Indiana University
Physics Dept.
Bloomington, IN 47405
(812) 855-1479

Degree: PhD
Specialty: Physics
Assigned: Geophysics Laboratory

Martin Wilner
Professor
Lowell, University of
1 University Ave.
Lowell, MA 01854
(508) 934-3786

Degree: PhD
Specialty: Physics
Assigned: Rome Air Development Center

NAME / ADDRESS	DEGREE, SPECIALTY, LABORATORY ASSIGNED	
William Wolfe Associate Professor Ohio State University 470 Hitchcock Hall Columbus, OH 43210 (614) 292-0790	Degree: Specialty: Assigned:	PhD Engineering Flight Dynamics Laboratory
James Wolper Assistant Professor Hamilton College Dept. of Math & Comp. Sci. Clinton, NY 13323 (315) 859-4417	Degree: Specialty: Assigned:	PhD Mathematics Rome Air Development Center
Hsien-Yang Yeh Associate Professor California State Univ. 1250 Bellflower Blvd. Long Beach, CA 90840 (213) 985-4611	Degree: Specialty: Assigned:	PhD Structural Mechanics Astronautics Laboratory
Lawrence Zavodney Assistant Professor Ohio State Univ. 209 Boyd Laboratory Columbus, OH 43210 (614) 292-2209	Degree: Specialty: Assigned:	PhD Mechanical Engineering Flight Dynamics Laboratory
Wayne Zimmermann Associate Professor Texas Woman's University PO Box 22865 Denton, TX 76204 (817) 898-2166	Degree: Specialty: Assigned:	PhD Applied Mathematics Weapons Laboratory

PARTICIPANT LABORATORY ASSIGNMENT

1990 USAF/UES SUMMER FACULTY RESEARCH PROGRAM

AERO PROPULSION LABORATORY (WRDC/APL)
(Wright-Patterson Air Force Base)

1.	Muhammad Choudhry	7.	Paul Hedman
2.	Mingking Chyu	8.	K. Sankara Rao
3.	Donald Dareing	9.	Larry Roe
4.	Paul Dellenback	10.	Kaven Tagavi
5.	Dennis Flentge	11.	Richard Tankin
6.	Kevin Hallinan		

ARMAMENT LABORATORY (ATL)
(Eglin Air Force Base)

1.	Charles Camp	7.	Manuel Huerta
2.	Arnold Carden	8.	Kevin Moore
3.	Eustace Dereniak	9.	William Siuru
4.	Charles Fosha	10.	Kenneth Sobel
5.	John George	11.	Steven Trogdon
6.	Frederick Gibson		

HARRY G. ARMSTRONG AEROSPACE MEDICAL RESEARCH LABORATORY (AAMRL)
(Wright-Patterson AFB)

1.	Richard Backs	6.	Tzesan Lee
2.	Larry Byru	7.	Sigmund Lephart
3.	John Duncan	8.	Amit Patra
4.	Martin Hagan	9.	Leonard Shyles
5.	Ashok Krishnamurthy	10.	Bonnie Walker

ARNOLD ENGINEERING DEVELOPMENT CENTER (AEDC)
(Arnold Air Force Base)

1.	William Grissom	5.	John Russell
2.	Carlyle Moore	6.	Chun Su
3.	Olin Norton	7.	Kevin Whitaker
4.	Richard Peters		

ASTRONAUTICS LABORATORY (AL)
Edwards Air Force Base)

1.	Daniel Fuller	5.	Hung Vu
2.	Shannon Lieb	6.	Trevor Williams
3.	Thomas Pollock	7.	Hsien-Yang Yeh
4.	Roger Thompson		

AVIONICS LABORATORY (WRDC/AL)
(Wright-Patterson Air Force Base)

1.	Thomas Abraham	6.	Mohammad Karim
2.	Michael Breen	7.	Kevin Kirby
3.	R. H. Cofer	8.	Richard Miers
4.	Thomas Gearhart	9.	Brian Shelburne
5.	Lawrence Hall		

ELECTRONIC SYSTEMS DIVISION (ESD)
(Hanscom Air Force Base)
1. Chih-Fan Chen

ELECTRONIC TECHNOLOGY LABORATORY (WRDC/ETL)
(Wright-Patterson Air Force Base)
1. Ashok Goel
2. Muhammad Numan
3. Devki Talwar

ENGINEERING AND SERVICES CENTER (ESC)
(Tyndall Air Force Base)

1.	William Bannister	7.	Kyung Kwon
2.	Mark Brusseau	8.	Michael McFarland
3.	Wayne Charlie	9.	Perry McNeill
4.	Joseph Dreisbach	10.	John Scharf
5.	David Kirkner	11.	George Veyera
6.	Paul Kromann		

FLIGHT DYNAMICS LABORATORY (WRDC/FDL)
(Wright-Patterson Air Force Base)

1.	John Bay	7.	Yulian Kin
2.	Franklin Eastep	8.	Byung-Lip Lee
3.	Marvin Hamstad	9.	Vernon Matzen
4.	Chin Hsu	10.	William Wolfe
5.	Ming-Shu Hsu	11.	Lawrence Zavodney
6.	David Hui		

FRANK J. SEILER RESEARCH LABORATORY (FJSRL)
(USAF Academy)

1.	Theodore Burkey	5.	Ngozi Kamalu
2.	Richard Carlin	6.	Siavash Kassemi
3.	Daniel Dolata	7.	Bernard Piersma
4.	Ephrahim Garcia	8.	Thomas Posbergh

GEOPHYSICS LABORATORY (AFGL)
(Hanscom Air Force Base)

1.	Theodore Aufdemberge	7.	C. Randal Lishawa
2.	Frank Battles	8.	Gandikota Rao
3.	Reuben Benumof	9.	Craig Rasmussen
4.	Chia-Bo Chang	10.	Glenn Stark
5.	George Jumper	11.	John Wills
6.	Jeffrey Kuhn		

HUMAN RESOURCES LABORATORY (HRL)
(Brooks, Williams, and Wright-Patterson Air Force Bases)

1.	Margaret Batschelet	8.	Gillray Kandel
2.	Pinyuen Chen	9.	William Moor
3.	James Dykes	10.	James Price
4.	Daniel Garland	11.	Joan Rentsch
5.	Harold Goldstein	12.	Eleanor Smith
6.	Verlin Hinsz	13.	Stanley Stephenson
7.	Delayne Hudspeth	14.	Pamela Tsang

MATERIALS LABORATORY (ML)
(Wright-Patterson Air Force Base)

1.	Donald Chung	7.	Gary Leatherman
2.	John Connolly	8.	Won-Kyoo Lee
3.	Sherif Elwakil	9.	Michael Resch
4.	David Grossie	10.	Martin Schwartz
5.	Prasad Kadaba	11.	Hai-Lung Tsai
6.	Joseph Lambert		

OCCUPATIONAL AND ENVIRONMENTAL HEALTH LABORATORY (OEHL)
(Brooks Air Force Base)

1.	David Buckalew	3.	Kirk Nordyke
2.	Miguel Medina	4.	Lorin Weber

ROME AIR DEVELOPMENT CENTER (RADC)
(Griffiss Air Force Base)

1.	Charles Alajajian	7.	Daniel Ryder
2.	Gary Craig	8.	Behrooz Shirazi
3.	Lionel Friedman	9.	Wayne Smith
4.	Frances Harackiewicz	10.	Ronald VanEtten
5.	Hao Ling	11.	Martin Wilner
6.	Shietung Peng	12.	James Wolper

C. PARTICIPANT LABORATORY ASSIGNMENT (Page 4)

SCHOOL OF AEROSPACE MEDICINE (SAM)
(Brooks Air Force Base)

1. Phillip Bishop
2. Robert Blystone
3. Bruno Breitmeyer
4. Vito DelVecchio
5. Randall Dupre
6. Reinhard Graetzer
7. Paul Griffin
8. Pushpa Gupta
9. Ramesh Gupta
10. Paul Lemke
11. Rex Moyer
12. Arnold Nelson
13. Donald Robinson
14. David Senseman
15. Richard Swope
16. John Szarek
17. Steven Waller

WEAPONS LABORATORY (WL)
(Kirtland Air Force Base)

1. William Campbell
2. Ggene Carlisle
3. William Cofer
4. Johanna Schruben
5. Peter Walsh
6. Wayne Zimmerman

WILFORD HALL MEDICAL CENTER (WHMC)
(Lackland Air Force Base)

1. Janet Dizinno

RESEARCH REPORTS

RESEARCH REPORTS

1990 SUMMER FACULTY RESEARCH PROGRAM

Technical Report Number	Title	Professor
Volume I		
Armament Laboratory		
1	Simple Models for Predicting Runway Failure Due to Blast Loading	Dr. Charles Camp
2	Physical Aspects of the Penetration of Reinforced Concrete Slabs	Dr. Arnold Carden
3	Solid-State Imager Replacement for a High-Speed Film Camera	Dr. Eustace Dereniak
4	Evaluation of Weapon Target Allocation Algorithms	Dr. Charles Fosha
5	Methods Which Accelerate Convergence in Iterative CFD Solvers	Dr. John George
6	Designing a Binary Phase Only Filter Via the Genetic Algorithm	Mr. Frederick Gibson
7	Two-Dimensional Simulation of Railgun Plasma Armatures	Dr. Manuel Huerta
8	Neural Networks for Guidance, Navigation, and Control of Exoatmospheric Interceptors *** Not Publishable at this Time ***	Dr. Kevin Moore
9	Gunner Performance in the BSTING Fire Control System	Dr. William Siuru
10	Robust Eigenstructure Assignment with Application to Missile Control	Dr. Kenneth Sobel
11	Multiple Point Detonation Modeling	Dr. Steven Trogdon

Volume I
Arnold Engineering Development Center

Astronautics Laboratory

Volume I

Volume II
Frank J. Seiler Research Laboratory

Volume II

Rome Air Development Center

Volume II

Volume III
(Wright Research Development Center)
Aero Propulsion Laboratory

Avionics Laboratory

Volume III

Volume III

Volume IV
Human Systems Division Laboratories
Harry G. Armstrong Aerospace Medical Research Laboratory

Human Resources Laboratory

Volume IV

Volume IV

School of Aerospace Medicine

Volume IV

1990 USAF-UES SUMMER FACULTY RESEARCH PROGRAM/

GRADUATE STUDENT RESEARCH PROGRAM

Sponsored by the

AIR FORCE OFFICE OF SCIENTIFIC RESEARCH

Conducted by the

Universal Energy Systems, Inc.

<u>FINAL REPORT</u>

SIMPLE MODELS FOR PREDICTING RUNWAY FAILURE
DUE TO BLAST LOADING

Prepared by:	Dr. Charles V. Camp
Academic Rank:	Assistant Professor
Department and	Department of Civil Engineering
University	Memphis State University
Research Location:	Air Force Armament Laboratory AFATL/MNW Warheads Branch Eglin AFB, FL 32542
USAF Research:	Albert L. Weimorts, Jr.
Dates:	5/14/90 - 7/20/90
Contract No.	F4960-88-C-0053

SIMPLE MODELS FOR PREDICTING RUNWAY FAILURE
DUE TO BLAST LOADING

by

Charles V. Camp

ABSTRACT

Analysis and prediction of runway damage due to buried explosives placed by penetrating weapons is a complicated and difficult problem. A survey of simple models that approximate the character of the structural response of the runway slab subjected to a blast pressure loading is presented. The structural response of the runway is approximated as a single-degree-of-freedom dynamic system, which may include soil/structure interface damping effects with a shear breach failure criterion. The unreinforced concrete is approximated as a rigid, perfectly-plastic material with limited flexural capability. In many cases, formulations originally developed for reinforced concrete structures are adapted for use with plain concrete runways. Conclusions and recommendations on the simple model approach to runway damage are presented.

Acknowledgements

I. INTRODUCTION:

Accurate analysis and prediction of damage to runway pavements due to blast load-ings from buried explosives is a complicated and difficult problem. A reliable model capable of accurately evaluating runway damage has to account for three distinct but interacting phenomena. First, at detonation of the explosive, suitable estimates of physical characteristics of the blast, such as the magnitude, the velocity, and the shape of the initial pressure wave, need to be evaluated. Information on the pressure wave is in turn applied to the underlying pavement subgrade. The reaction of the subgrade to the blast pressure is the second problem considered in the runway damage system. As the blast wave propagates through the soil underlying the pavement, the subgrade responds by transmitting a pressure to the underside of the runway pavement. The resulting transmitted pressure acts like a distributed load on the pavement. The pressure loading is of a highly transient impulsive nature and results in a complex dynamic response from the pavement. The structural response of the pavement is the third mechanism considered in the damage predictions. Although not listed as one of the three mechanisms in the damage model, the interaction between the soil subgrade and the structure is a critical component in the dynamic response of the pavement and probably the least understood.

In this study, the primary emphasis is on reviewing techniques which model the structural response of the concrete pavement including soil/structure interaction. However, since the dynamic motion of the pavement is a result of a blast pressure transmitted through the soil subgrade, some attention is given to methods which represent the spatial and temporal variation of the distributed loading. Concepts developed in simple single-degree-of-freedom (SDOF) dynamic response models, originally intended for reinforced concrete structures, are adapted for use in the analysis of unreinforced concrete pavements. Several different breach shear or punching shear models are reviewed in an effort to improve the prediction of the formation and characteristics of a crater. Both the SDOF response model and shear failure criterion are based on static yield-line theory applied to dynamic analysis. A simple SDOF model developed from yield-line analysis for slabs utilizing an estimate for the dynamic

moment resistance for unreinforced concrete combined with a shear breach failure criterion has the potential for providing a first order assessment of the pavement damage from blast loading.

II. OBJECTIVES OF THE RESEARCH EFFORT:

Prediction of concrete runway failure from cratering due to blast loading is investigated. The problem of determining the response of concrete pavements to localized underground explosives is complicated, especially when considering the dynamic nature of both the structural behavior and the loading function. Although several simple mathematical models exist for estimating the damage of pavements, they are generally not reliable when compared with existing experimental data. Recent advances in experimental instrumentation and test methods have the potential of providing new insights to the problem. The objectives of this study are to review existing modelling procedures and suggest improvements which may result in a more accurate predictive model.

III. SIMPLE STRUCTURAL RESPONSE MODELS:

a. **Introduction.** Dynamic models using a single degree of freedom (SDOF) involve one coordinate or one dependent variable. This type of analysis can be simple or complex depending on the situation. The general equation of motion is:

$$Mx'' + Cx' + kx = F(t) \tag{1}$$

where M is the mass, C is the damping coefficient, k is the stiffness, F(t) is the applied load, and x is the displacement. For many simple systems where the mass, damping, and stiffness characteristics are known, analytical solutions exist. In more complex systems, such as the dynamic behavior of concrete slabs, the solution procedure is more complicated. In many cases, a dynamic system is approximated using an effective form of the mass, damping, stiffness, and loading functions.

When considering the structural response of a concrete plate or slab to the effects of a blast loading, the damping component of the behavior is neglected. Since both

flexural failure, associated with the maximum stress and maximum displacement, and breach failure, related to direct shear, usually accompany the peak of the first cycle, there is relatively little damping in the structural response. Therefore, the basic equation of motion for the equivalent system is:

$$M_e y'' + k_e y = F_e(t) \tag{2}$$

where M_e is the effective mass, k_e is the effective stiffness, $F_e(t)$ is the effective loading function, and y is the center point displacement. More details on how to determine the effective mass, M_e, the effective stiffness, k_e, and the effective loading function, F_e, may be found in any comprehensive structural dynamics test.

   b. **Blast Pressure Model.** After the detonation of an explosive in a soil, a pressure wave moves radially away from the center of the explosion causing soil displacement, velocity, and acceleration. If the response is elastic, then the soil particles move outward normal to the pressure wave and return to their original position after the wave has past.

   In the "free-field" soil environment, the pressure from the explosive source is denoted as the incident pressure. When the incident pressure wave encounters an interface between two different materials, a reflected pressure and a transmitted pressure are produced. Based upon properties of the two materials forming the interface, a set of stress ratios, in terms of the stresses associated with incident, reflected, and transmitted pressures, may be written:

$$\frac{\sigma_R}{\sigma_I} = \frac{\rho_2 c_2 - \rho_1 c_1}{\rho_2 c_2 + \rho_1 c_1} \tag{3}$$

$$\frac{\sigma_T}{\sigma_I} = \frac{2\rho_2 c_2}{\rho_2 c_2 + \rho_1 c_1} \tag{4}$$

where σ_R is the radial stress, σ_T is the transmitted stress, σ_I is the incident stress, ρ is the density, c is the wave speed, the product ρc is the characteristic impedance, and the subscripts, 1 and 2, denote the different materials. Values of the transmitted stress

ratio for soil/structure interfaces vary from 1.4 for saturated clay to 1.9 for dry sandy soils [Ross, et al 1985].

Based on available data, an expression for the free-field pressure is given as [Higgins, 1983, and Drake, et al, 1983]:

$$P_{ff} = 160 \ f\rho c(R/W^{1/3})^{-n} \qquad (5)$$

where P_{ff} is the free-field pressure (psi), f is a dimensionless coupling factor (0.0 - 1.0), n is a dimensionless soil attenuation coefficient, R is the range or standoff distance (ft), and W is the equivalent explosive weight of TNT (lbf). The coupling factor, f, is defined as the ratio of the free-field pressure of a shallow buried explosive to the free-field pressure of a fully buried explosive. Values for the coupling factor in air, concrete, and soil have been determined from experimental data [Drake, et al, 1983]. Estimates for the attenuation coefficient and the characteristic impedance, ρc, depend on the medium in which the explosion takes place. Values for several soil types have been determined from experimental data [Drake, et al, 1983].

A model for the spatial variation of the pressure produced from a spherical-shaped charge is based on the maximum free-field pressure [Ross, et al, 1985]. The maximum pressure is given as:

$$P_{max} = 160 \ f\rho c(R_o/W^{1/3})^{-n} \qquad (6)$$

where R_o is the minimum standoff distance (measured along a line perpendicular to the slab intersecting the center of the explosion). The variation of the pressure at any other point in the free-field, located by R_θ, along the flat slab is based on the maximum pressure and is expressed as a ratio:

$$P_{ff}/P_{max} = (R_\theta/R_o)^{-n} = (\cos \theta)^n \qquad (7)$$

where the coefficient n is a characteristic of the soil. The expression for the free-field pressure, given by Equation (5), may be rewritten as:

$$P_{ff} = P_{max}(\cos \theta)^n \qquad (8)$$

The fluctuation of the free-field pressure as a function of position and time is modelled by a separated-variable approach where the spatial effects are described by Equation (8) and the time variation by a time function F(t).

$$P(R,t) = P_{ff}F(t) \tag{9}$$

The time function, F(t), may be written as:

$$F(t) = \left(1 - \frac{t - t_{or}}{\Delta t} \right) \exp\left(-\alpha \frac{t - t_{or}}{\Delta t} \right) \tag{10}$$

$$\text{for} \quad \frac{R_0}{c_s} \leq t \leq \frac{2R_0}{c_s}$$

$$F(t) = 0 \tag{11}$$

$$\text{for} \quad \frac{R_0}{c_s} > t > \frac{2R_0}{c_s}$$

where t_{or} is the arrival time at point R_0, Δt is the pulse time, and α is a time attenuation coefficient. The minimum arrival time, t_0, is calculated from R_s/c_s, where c_s is the wave speed of the soil. In general, the arrival time of the pressure wave at any point on the slab, t_{or}, is determined by R_0/c_s. The pulse time is assumed to be a function of the distance from the explosive charge and is approximately 1.0 to 1.5 times the propagation time from the explosive source.

c. **Soil/Structure Interaction.** The previous discussion of the free-field pressure did not consider any effects due to the interaction of the structure and the soil. For conventional explosions at close range, a reduction in the loading will occur as the structure moves away form the pressure source. The general approach to this problem is to reduce the applied pressure at a point on the slab by the quantity ρcV. This term is composed of ρc, the characteristic impedance of the soil, and V, the velocity of the slab at the point in question. A model for the stress transmitted to a slab from an explosive at close range, including soil/structure interaction, may be given as:

$$\sigma_T = (\sigma_T/\sigma_L) P_{ff} - \rho cV \tag{12}$$

Research has shown that the interaction phenomena between soil and structural elements for blast or impulse loadings is very complex. The interaction is controlled

by the velocity of the structure relative to the velocity of the soil particles [Wong, et al, 1983]. A generalized soil/structure interaction model including soil velocity is given as:

$$\sigma_T = (\sigma_T/\sigma_L) \, P_\pi + \rho c (V_\pi - V) \qquad (13)$$

where V_π is the free-field soil particle velocity.

d. Yield-Line Analysis of Plates. In square slabs, there are two basic types of yield-line formations, depending on the loading. When a distributed load acts over a large section of the slab, yield-lines form along both diagonals of the square. As the area on which the load acts becomes smaller, as with a concentrated load, a circular yield-line fan forms with the point load at its center. In this case, the determination of the yield-line fan radius is of interest. Understanding the time and spatial variation of the blast loading is critical to determining the yield line pattern.

To analyze the failure mechanism of a square concrete plate subjected to a blast load, an upper-bound solution based on the conservation of energy and the principle of virtual work will be used. First, consider the failure surface defined by a circular fan of yield lines. At failure, the circumferential moment will reach the ultimate moment, M_u, of the material creating positive yield lines which run radially from the center of the plate. At some radius, the radial moment will also reach its ultimate value, M_u'. The work done by the internal forces over this circular wedge may be obtained from:

$$W_i^n = \int_{\phi_0}^{\phi_1} (M_u + M_u') \, \frac{\delta}{r} \, r \, dr \, d\phi \qquad W_i = \Sigma \, W_i^n = 2\pi(1 + \mu)M_u \, \delta \qquad (14)$$

where δ is the virtual displacement at the center of the plate, μ is a positive multiplier, and n is the number of plate segments. The work done by the external forces due to a virtual displacement field $w(r)$ is:

$$W_e^n = \int^{A_n} P \, w(r) \, dA_n \qquad\qquad W_e = \Sigma \, W_e^n \qquad (15)$$

1-9

Since the deflections along yield lines are large in comparison with the elastic deformations, each plate segment is considered to be rigid. In this calculation, the weight of the plate will be considered negligible in order to simpify the results. By equating the internal work to the external work, $W_i = W_e$, the critical load may be estimated as:

$$P = 2\pi(1 + \mu)M_u \tag{16}$$

It is of interest to note that the internal work of a circular fan is independent of the radius, provided the load is a real point load.

An estimation of the critical load for a wedge shaped plate section may be obtained from virtual work. The internal work is:

$$W_i^* = (1 + \mu)M_u \frac{\delta}{a} 2a = 8(1 + \mu)M_u \delta \tag{17}$$

where a is the dimension of the square plate. In this case, since the boundary of the wedge is at the intersection of two slabs, the multiplier μ is a measure of the moment capacity of the construction joint. Some judgement must be used in establishing a value for the multiplier μ which will best represent the actual moment response of the joint. Equating the internal work to the external work results in the following expression for the critical load:

$$P = 8(1 + \mu)M_u \tag{18}$$

By comparing the internal work for both types of yield line failures. Equations (16) and (18), for equal values of μ, the load required to cause a fan-type failure is found to be less than the load which will cause a diagonal-type failure. A study of high-speed films portraying the complete slab failure event indicate an initial failure response similar to the diagonal-type yield mechanism.

e. **Equations of Motion - Yield Theory.** In the next two sections, two different approaches for developing equations of motion for concrete slabs subjected to blast loading will be briefly presented. The first approximation describes the motion of rigid plate segments defined by yield-line theory. The second method uses the equations of motion developed in plate theory and a moment-curvature failure criterion. While the second tactic provides a more sophisticated representation of the failure mechanism, it

is significantly more complicated and may require considerable numerical effort to obtain a solution.

The equation of motion for a square slab segment defined by diagonal yield-lines may be written as a SDOF system in terms of the rotation at the support:

$$I\ddot{\theta} = \int^{A_n} [P(x,t) - \gamma_c h] \times dA_n - a(1 + \mu)M_u \qquad (19)$$

where I is the mass moment of inertia, θ is the rotation at the support, γ_c is the unit weight of the slab, h is the slab thickness, and a is the dimension of the square slab. An expression for the rotation of the rigid plate segment as a function of time may be found by integrating Equation (19).

$$\theta = \frac{6}{ma^3} \left(\int^t \int^\tau F\, T(\xi)\, d\xi\, d\tau - \frac{\gamma_c ha^3 t}{3} - aM_u(1 + \mu)t^2 \right) \qquad (20)$$

$$F = \int P_{ff}(r) \left(\frac{\pi}{2} - \frac{\sqrt{2}r}{a} \right) r\, dr \qquad (21)$$

A simple strain failure criterion may be applied to the rigid slab segment to determine onset of tensile cracking. If the strain is assumed to be due to axial elongation, a simple ultimate tensile strain failure criterion may be developed as:

$$\varepsilon_t = \frac{\theta^2}{2} \leq \varepsilon_u \qquad 0.002 \leq \varepsilon_u \leq 0.003 \qquad (22)$$

Some type of shear criterion should be incorporated into this type of analysis to determine if a breach failure will occur. Several shear failure models will be discussed in the next section. If a shear failure is predicted, the equations of motion would be modified to neglect the material removed in forming the breach crater.

f. **Equations of Motion - Plate Theory.** In general, it is difficult to determine the response of a structural plate to a blast loading large enough to cause significant structural failure. The stress-strain relationships are complicated by the nonlinear and biaxial nature of the reaction. In order to develop a simple SDOF model, the stress-strain relationship of plain concrete is idealized as an elastic perfectly-plastic material.

1-11

Equations of motion derived for a circular plate element may be applied to large rectilinear plate systems. The construction joints between adjacent concrete slabs provide continuity of displacements and some moment capacity. The resulting pavement structure may be idealized as a circular plate with a moment resistance capability at its supports. Determining the response of the circular plate to a dynamic loading is difficult. However, the resulting model should be a more accurate representation of the failure of the runways. The classical equations of equilibrium or motion for a circular plate element are:

$$\frac{\partial}{\partial r} [Q r] + [P - m \frac{\partial^2 w}{\partial t^2}] r = 0 \tag{23}$$

$$\frac{\partial}{\partial r} [M_r r] - M_\phi - Qr = 0 \tag{24}$$

where Q is the shear force, M_r is the radial moment per unit length, M_ϕ is the circumferential moment, w is the plate deflection, P is the applied load, and m is the mass per area of the plate. Equation (23) may be integrated with respect to r and substituted into Equation (24). The resulting expression has the form:

$$\frac{\partial}{\partial r} [M_r r] - M_\phi = - \int^r [P - m \frac{\partial^2 w}{\partial t^2}] r \, dr \tag{25}$$

The motion of the plate may be obtained by solving Equation (25) using an ultimate moment yield criterion. In addition to the ultimate moment criterion, the plate is assumed to respond as a rigid perfectly-plastic material. For plain concrete, the moment capacity is restricted by the low tensile strength of the material. The moment-curvature response of plain concrete may be modelled as a perfectly plastic material if some level axial compression is present. Experimental observations have shown that plastic-limit analysis is an appropriate model for predicting the structural response of plain concrete pavements [Chen, 1982].

In terms of the radial and circumferential moments, a Tresca yield condition may be established as:

$$\text{MAX} \left[|M_r|, \ |M_\theta|, \ |M_r - M_\theta| \right] = M_o \tag{26}$$

where M_o is the fully plastic moment per unit length.

The equations of motion for a circular slab element derived using plate theory and a moment-curvature Tresca yield criterion, subjected to a blast loading, are difficult to formulate. The resulting equations, for even simple variations of the pressure load, are complex and generally require numerical solution techniques. In the absence of thrust forces, the perfectly-plastic material response model over-estimates the resistance capacity of the structure. In addition, when considering the failure of plain concrete elements, some mechanism for modelling the rupture and ejection of the debris should be included. However, even with these difficulties, the perfectly-plastic theory may provide a good first-order approximation.

IV. SHEAR FAILURE CRITERIA:

a. Shear or Breach Failure. As the location of an explosive is moved closer to the structure, slab failure by a flexural response is diminished by the possibility of a shear failure resulting in a breach of the concrete. A direct shear model similar to methods for metal beams, proposed by Jones [1976], may be adapted for unreinforced concrete. Jones' model states that for edge shear to occur, the structure will have to reach a critical velocity from an impulsive load. The critical velocity is given as:

$$V_{cr} = \frac{2\sqrt{2}}{3} \ (\sigma_u/\rho)^{1/2} \tag{27}$$

where σ_u is the ultimate tensile strength of the material and ρ is the density of the material. By relating the critical velocity, V_{cr}, to a specific impulse, a critical impulse may be defined as:

$$I_{cr} = \rho h V_{cr} \tag{28}$$

where h is the slab thickness. The dynamic tensile strength of concrete is assumed to be $0.13f'_c$, where f'_c is the static uniaxial compressive strength of concrete. The factor 0.13 relates the f'_c to the uniaxial tensile strength, f'_t, and includes an increase in strength due to the dynamic application of the loading. Equation (28) becomes:

1-13

$$I_{cr} = \frac{2\sqrt{2}}{3} (\rho(0.13)f'_c)^{1/2} \tag{29}$$

If the applied specific impulse over a given area is equal to or larger than the critical impulse, then a direct shear failure is assumed to occur. The initial applied specific impulse for a square plate is given as:

$$I_{sp} = \frac{4}{\pi h^2} \int_0^{\tau_{cr}} \int_{a-h}^{a} \int_{a-[h^2 - (a-y)^2]^{1/2}}^{a} P_{ff}(x,y) \, dx \, dy \, T(t) \, dt \tag{30}$$

where τ_{cr} is the critical time required for direct shear. If the applied impulse, I_{sp}, does not exceed the critical impulse, I_{cr}, then a direct shear failure is assumed not to occur. However, if I_{sp} is greater than I_{cr}, then the initial guess of the radius is incremented to h + Δh and the value for the applied impulse is recalculated. This procedure is repeated until the applied impulse does not exceed the critical impulse. The radius of the direct shear breach is assumed to be the value of the radius used in the final iteration, h + nΔh. There are no guidelines for selecting values of the critical time, τ_{cr}. However, values equal to a quarter of the period of the 2nd or the 3rd flexural mode have been used.

Based upon experimental and theoretical work, a model for breaching of unreinforced concrete slabs may be given as:

$$P_{max} = \frac{A \, W^{1/3}}{R^n} \tag{31}$$

$$I_{sp} = 0.001 \, P_{max} \tag{32}$$

where n and A are parameters based on the explosive medium. Once the maximum pressure is determined, the applied specific impulse is obtained from Equation (32).

b. Punching Shear Failure. Punching shear failure in structural plate elements is similar to shear failure in beams or one-way slabs. The response is considered to be a sudden rupture-type failure where the main reinforcing does not affect the shear response. Since the effect of the reinforcement is neglected, this type of punching

shear failure is valid for unreinforced concrete slabs. The critical load that will produce a punching shear failure is less than that which will cause flexural failure. However, a punching shear failure is a localized response and occurs under high concentrated loads acting over a relatively small area.

A punching shear mechanism may provide a more accurate representation of the initial response of plain concrete plates to impulse or blast-type loads. The dynamic punching shear response due to a blast load may be estimated by using the static criterion with dynamic load increase factors.

A brief description of the punching shear failure mechanism is presented. For a more detailed discussion, see Chen [1982]. A punching shear failure surface may be derived by considering the response of a plain concrete slab loaded over a small circular area. The slab is assumed to be reinforced in a way that prohibits flexural failure. The punching shear mechanism describes the displacement of a solid of revolution which is detached form the surrounding rigid plate. The resulting axisymmetric failure surface is a function of depth, $r = r(x)$, the initial punching shear radius r_0, and the plate thickness h. The relative vertical displacement, v, makes an angle α with the failure surface. Since the problem is axisymmetric, the failure surface is considered a plane-strain yield line. The resulting failure surface is valid for an annular support radius of:

$$r_1 \geq r_0 + h \tan \phi \tag{33}$$

where ϕ is the angle of internal friction from the Mohr-Coulomb failure criterion.

An upper-bound solution for the failure surface, $r(x)$, may be obtained by considering the conservation of energy of the assumed failure mechanism. The work relationship is given as:

$$Pv = \int^h D_A \frac{2\pi r}{\cos \alpha} dx \tag{34}$$

where P is the ultimate concentrated load and D_A is the internal energy dissipation function. For a Mohr-Coulomb material the internal energy is given as:

$$D_A = v \left(\frac{1 - \sin \alpha}{2} f'_c + \frac{\sin \alpha - \sin \phi}{1 - \sin \alpha} f'_t \right) \tag{35}$$

A functional relationship may be developed from Equation (35) by introducing the relationship $\tan \alpha = dr/dx = r'$. An upper-bound solution for the critical load P may be obtained by solving the following functional using variational calculus:

$$Pv = \int^h r([1 + (r')^2]^{1/2} + r')dx \tag{36}$$

The solution of Equation (36) is given as:

$$r = \begin{cases} r_0 + x \tan \phi \\ \\ a \cosh \dfrac{x - h_0}{c} + b \sinh \dfrac{x - h_0}{c} \end{cases} \tag{37}$$

where the constant c, defined as $(a^2 - b^2)^{1/2}$, and h_0 are determined by two continuity conditions at $x = h_0$ and the boundary condition at $x = h$:

$$a = r_0 + h_0 \tan \phi \tag{38}$$

$$\tan \phi = b/c \tag{39}$$

$$r_1 = a \cosh \frac{x - h_0}{c} + b \sinh \frac{x - h_0}{c} \tag{40}$$

Using the conditions in Equations (38) - (40), the resulting least upper-bound ultimate load is given as:

$$P = 0.5\pi f'_t \left[0.5h_0(d_0 + h_0 \tan \phi) \frac{1 - \sin \phi}{\cos \phi} (f'_c/f'_t) + c(h - h_0) \right.$$
$$\left. + r_1 (r_1^2 - a^2 + b^2)^{1/2} - ab + r_1^2 - a^2 \right] \tag{41}$$

The solution is not sensitive to changes in the angle of friction, ϕ; however, the calculation is sensitive to the ratio f'_t/f'_c. In predicting the damage of runways to buried explosives, the ratio of tensile to compressive strength is usually assumed to be

1/10 (based on static strength tests). Equation (41) may be used to predicte the load required for a punching shear failure and the shape of the failure surface. For different values of r_0 and h_0, a least upper-bound for the ultimate load may be calculated. An approximation for the initial punching radius, r_0, may be estimated from the contact area of the pressure load at some increment of time.

Application of the punching shear failure mechanism may be more difficult to implement than other simple breaching models; however, this formulation may provide a more realistic prediction of the failure surface. A punching shear failure criterion is valid over the early stages of the pressure loading. As the maximum pressure attenuates and the shape of the pressure distribution changes, a punching shear failure becomes less likely.

V. CAVITY PRESSURE MODEL:

A cavity pressure model is a simple model for predicting damage of concrete runways due to a blast loading originating in the adjacent subgrade soil [Everhart, et al, 1989]. In this representation, the breach radius of the concrete slab is generally chosen as the measure of the damage criteria. The model incorporates characteristics of the soil (density, wave speed, and seismic wave speed), the concrete slab (density, structural dimensions, compressive strength), the properties of the detonation (cavity pressure) and the distance the explosive is located beneath the slab.

The simple breach model may be described as follows. An estimate of the free-field environment in the soil, at a given time, is determined from the explosive properties. From the free-field analysis, an approximation of the stress in the soil, at a given time, is derived in terms of the velocity and the acceleration of the pressure wave, the cavity pressure of the explosive, and distance. The resulting stress field is used to calculate a distributed load on the concrete slab. A shear response model is developed to determine if the applied load, at a given time, is sufficient to breach the concrete slab.

In order to calculate the free-field conditions of the soil as they vary with distance, two important assumptions are made. First, the behavior of the soil environment may

be described in one-dimensional spherical coordinates. The interaction of the concrete slab with the soil is considered to be negligible. Second, the soil is assumed to be incompressible at some stress and recover little to no strain after unloading. Most common soils and rocks display this type of behavior at some stress level.

The distribution of stress in the free-field soil environment is calculated in terms of the variation of the velocity and acceleration of the wave front with time and distance and the initial cavity pressure. The distribution of velocity is derived using the principle of conservation of momentum. The density of soil is assumed to be constant due to the nature of a locking soil. The stress in the soil as a function of range, velocity, and acceleration is given as:

$$\sigma = \sigma_A + \rho \left[(-a_A R_A^2 - 2U_A^2 R_A)(\frac{1}{R} - \frac{1}{R_A}) + U_A U R_A^2 (\frac{1}{R^2} - \frac{1}{R_A^2}) \right] \qquad (42)$$

Equation (42) may be used to calculate the stress as it varies with range for a given time. The stress in the soil is used to determine the size and magnitude of the distributed load applied to the concrete slab by the explosive. The stress acting on the slab, at a given time, is the component of the radial soil stress distribution normal to the concrete surface.

In this analysis, the determination of the breach radius is the main objective. Breach is assumed to occur when the normal load on the slab exceeds the shear capacity of the concrete. The total normal load on the slab is the integral of the normal stress distribution over the loading area. The concrete slab is assumed to resist the applied load only in shear. No type of flexural response is considered. The shear capacity of the slab is simply the shear strength of concrete multiplied by the shear area. The resisting shear force is calculated using a model based on the deviatoric stress:

$$Q = A_s \sqrt{J_2'} \qquad (43)$$

where A_s is the shear area and J_2' is the second invariant of the deviatoric stress. The shear area is assumed to be:

$$A_s = 2\pi R_B h \qquad (44)$$

where R_s is the radius of the shock front and h is the thickness of the slab.

The simple cavity model was also compared to calculations performed using EPIC-II (Elastic Plastic Impact Calculations). EPIC-II is a two-dimensional Lagrangian finite element program formulated for impact and detonation problems. A comparison of the free-field soil velocity determined from the cavity pressure model and the numerical results from the EPIC-II program indicate that the simple model has the ability to represent the basic nature of the EPIC-II calculations.

VI. RECOMMENDATIONS:

There are several directions in which research into the structural response of concrete runways can advance. While each course has advantages and disadvantages, they all share a common obstacle in the inability to accurately model the dynamic response of concrete.

The following is a list of recommended areas for continued research:

1. Development of more sophisticated SDOF response model for concrete.

2. Application of multiple-degree-of-freedom (MDOF) dynamic response analysis to concrete.

3. Development of simple flexural and crater heave models to compliment breach model.

4. Numerical modelling of the runway as a concrete plate subjected to a mathematical approximation of the blast load.

5. Application and modification, if necessary, of existing non-linear dynamic FEM or FDM computer programs to simulate the complete runway damage phenomena (detonation, soil, and concrete analysis).

REFERENCES

Abrahamson, G.R., Florence, A.L., and Lindberg, H.E., "Radiation Damage Study (RADS) Volume XIII -- Dynamic Response of Beams, Plates, and Shells to Pulse Loads," Ballistic Systems Division, BSD-TR-66-372, Vol. XIII, September, 1966.

Chen, W.F., "Plasticity in Reinforced Concrete," McGraw-Hill, New York, New York, 1982.

Cole, R.H., Underwater Explosives, Princeton University Press, 1948.

Drake, J.L., and Little, C.D., Jr., "Ground Shock from Penetrating Conventional Weapons," Proceedings of the Symposium on the Interaction of Non-Nuclear Munitions with Structures, USAFA, Colorado Springs, CO, May, 1983.

Everhart, R.D., Maestas, F.A., Galloway, J.C., and Partch J.C., "Parametric Analysis of Explosive Effectiveness," Applied Research Associates, Inc., Final Report Contract No. F08635-89-C-0057 for the Air Force Armament Laboratory (AFATL/MNW), Eglin AFB, 1989.

Higgins, C.J., "Some Considerations in the Analysis and Prediction of Ground Shock from Buried Conventional Explosives," Proceedings of the Symposium on the Interaction of Non-Nuclear Munitions with Structures, USAFA, Colorado Springs, CO, May, 1983.

Jones, N., "Plastic Failure of Ductile Beams Loaded Dynamically," Trans ASME, Vol 98, Series B, No 1, February 1976, pp. 131-136.

Ross, C.A., Sierakowski, R.L., and Schauble, C.C., "Concrete Breaching Analysis," USAF Armament Laboratory, Eglin AFB, Florida, AFATL-TR-81-105, December, 1981.

Ross, C.A., and Sierakowski, R.L., " Vulnerability Analysis of Underground Structures to Buried Explosives and Impactors," USAF Armament Laboratory, Eglin AFB, Florida, AFATL-TR-85-64, September, 1985.

Wong, F.S., and Weidlinger, P., "Design of Underground Shelters Including Soil-Structure Interaction Effects," Proceedings of the Symposium on the Interaction of Non-Nuclear Munitions with Structures, USAFA, Colorado Springs, CO, May, 1983.

1990 USAF-UES SUMMER FACULTY RESEARCH PROGRAM

GRADUATE STUDENT RESEARCH PROGRAM

Sponsored by the

AIR FORCE OFFICE OF SCIENTIFIC RESEARCH

Conducted by the

Universal Energy Systems, Inc.

FINAL REPORT

Physical Aspects of the Penetration of Reinforced Concrete Slabs

Prepared by: A. Eugene Carden, Ph.D.
                      C. R. Wanstall, B.S.

Academic Rank: Professor and Graduate Student

Department: Engineering Mechanics

University: The University of Alabama

Research Location: USAF/AFATL/SAA
                      Eglin AFB FL 32542-5434

USAF Researcher: John Collins

Date: 13 July 1990

Contract Number: F49620-88-C-0053, Project #210

Physical Aspects of the Penetration of Reinforced Concrete Plates

by

A. Eugene Carden

and

C. R. Wanstall

ABSTRACT

The process of dynamic penetration of concrete plates proceeds by several processes. On impact a wave of high pressure and particle velocity proceeds from the penetrator into the concrete. This wave expands more or less spherically. A hemispherical volume of high pressure (and high density) preceed the penetrator into the material At the edges of this pressure hemisphere, above the corner of the penetrator, regions of large pressure gradient and large shearing stress accompany the penetration. Failure of the material is accomplished by shear. Some material may be ejected backwards. Complete failure of the plate does not occur until the penetrator approaches the back side and the pressurized zone pushes a cone of material ahead of the penetrator.

Steel reinforcement mesh parallel to and near the front and back surfaces of the plate can modify the process in four ways which increase the plate's resistance to penetration. The first is to provide a high impedance surface to reflect the energy of impinging waves. The second is to provide containment and allow build-up of the pressurized volume. The third is to provide a lateral membrane (to sustain tensile stress) that limits scabbing and failure of the concrete. Finally, if the rebar is of sufficient size and strength, the penetrator does work (and looses kinetic energy) to deform and break the steel. Too, eccentric contact can change the direction of the penetrator.

Acknowledgements

I. INTRODUCTION.

Concrete is a composite material consisting of three materials. First, a hard elastic, brittle aggregate; second, a hard elastic sand, and third, concrete is held together by a softer, nonlinear matrix containing a significant amount of voids. This matrix joins the first two elements together. Concrete will not tolerate a significant tensile stress without fracture. It is used primarially in structures whose stress state is compressive. If tensile loads are to be sustained by the structure, steel bars are placed in the concrete slab when cast. These reinforcing bars (rebar) are stiffer than the matrix by a factor of 6 to 8. Consequently the presence of rebar changes the load-deflection characteristics of a structure. Numerous tests and journal references describe the behavior, analysis or design of reinforced concrete structures that sustain static or nearly static loads.

Some concrete structures must be designed to resist dynamic loads. In armaments, these dynamic analyses involve penetration by missiles. The missiles can be of the form of bombs, artillery shells, or any shape that has sufficient kinetic energy to penetrate the slab. The analysis of such structures and their behavior depends, in part, on the impact velocity of the missile. For velocities of about 50 m/s the concrete sustains a shock pressure of about 2 kbar (29 ksi). For impact velocities of 300 m/s the shock pressure is about 13.5 kbar (196 ksi) and the time period for penetration of a one foot thick slab is about one ms. For large slabs this time period is generally less than the period of its natural frequency. For these impacts only the geometry local to the penetrator and local material properties are of primary importance. Concrete is not able to sustain these kinds of pressures without serious damage and alteration of the ambient density.

Concrete is not a homogeneous, linear-elastic or elastic-plastic material. The strength is strain rate dependent. Any analysis of concrete behavior which requires constitutive equations and failure criteria will contain the uncertainties and approximations based on the uncertainty of the material properties. As shock pressures go up, the thermodynamic relationship (equation of state) show that density and temperature also go up. That being so, there is a condition of impact so severe that the temperature could convert the hydrated water in the matrix to steam. The current hydrocodes do not account for phase changes.

Of further importance in the penetration of concrete is the propagation of elastic, plastic or shock waves and of the zone of high pressure and density in the vicinity of the penetrator. Failure of unreinforced concrete proceeds as the punching out of a cone of damaged material in front of the penetrator and, possibly, some scabbing of the exit side of the slab. Scabbing is a tensile failure of a chin surface layer that results from the impingement of a nonuniform compressive wave on a free surface.

Purpose of this work. For reinforced concrete slabs, that is, slabs with a rectangular mesh of reinforcing steel on both the entrance and exit planes of the slab, the penetration process is modified. The purpose of this research was to study the physical aspects of the effect of reinforcement on the penetration of concrete slabs. The scope was to limit velocities to about 300 m/s and study slabs of a fixed thickness. The Hull hydrocode was the analytical tool used to perform this study.

II. Physical Aspects of the Penetration of Reinforced Concrete

The Hull hydrocode has been effectively used in evaluating many impact phenomena over a wide range of impact conditions. Neither of the two

2-5

authors of this report had used any hydrocode prior to this work. Several weeks were spent in learning the hardware, operating system and the procedures for using Hull to perform an analysis of the mechanics of penetration.

The problem was set up as an axisymmetric problem. The penetrator was modeled as a rigid rod. The material was treated as isotropic and homogeneous. This simplification has consequences. The concrete slab was given a velocity against the penetrator. An Eulerian grid was used to set up the mesh for the problem generator. This grid was fixed relative to the penetrator. The material moved through the grid. Stations were fixed relative to the penetrator in the grid. Numerous physical parameters were calculated for each station location as a function of time. The grid size was initially picked as 0.5 cm. Later, it was refined to 0.1 cm. The calculations for each cell were saved at every 10 microsec interval. We had to learn how far to take the calculations to obtain meaningful results. We finally settled on 300 microsec. This time period is not long enough for complete penetration but does allow sufficient time to see the differences in the behavior of unreinforced vs. reinforced concrete slabs. For a small (0.1 cm) mesh size, and tracking the calculations to 300 microsec, and using a Microvax, the CPU time was over 200 hours. Consequently, we did not get many runs. Too, power outages cause the loss of several runs.

The version of Hull that we used contained a Hugoniot for concrete but did not contain an Equation of State. Consequently no temperatures were available from the analysis. Too, the failure criteria was a technique for limiting the peak tensile stress (or negative pressure) to one-tenth the value of the compressive strength. A Von Mises criterion of yielding was used to limit the stresses in the inelastic case. No interfaces were

generated if fracture occurred. The strains were calculated from the velocity gradients. Consequently the strains could continue to increase while the stresses were held constant by either a failure or a yield criteria.

Color graphics of the pressure, density, stresses, velocities, etc., were obtained and plotted on a Tektronix color graphics monitor/printer. These, combined with the station data, were used to judge the process of penetration and to assess the differences between the response of reinforced and plain concrete slabs.

After the summer work period, one of the authors returned to Eglin to attend a course on CTH, another hydrocode. One of the previous Hull runs was rerun on the same machine using CTH. The graphics indicates that there are some differences. No station data were obtained from the CTH run, and the reasons for and the degree of the differences are not documented.

The Hugoniot, Equation of State, Constitutive Equation and Failure Criteria for many metals are well known and used widely in the Hydrocode analysis of penetration. Such data for Concrete are not well established.

A Hugoniot and a Von Mises Yield condition based on unconfined compressive strength of concrete was in the material Library of Hull and these were used in our analyses. However, some significant differences in the behavior of concrete and that of metal require some modification in the analysis of penetration of concrete. The Hugoniot for concrete is nonlinear and large pressures cause permanent density changes and do significant internal damage. The cement is more like a powdered matrix, rather than a bonding material after exposure to, say, 50 kbar.

During the course of the summer, two visits were made to a test range to examine failed (penetrated) three foot thick, 16 ft square reinforced concrete slabs. Three significant observations were made. The reinforcing

2-7

mesh on both the entrance and exit surfaces were stretched and pushed out beyond the normal exterior surface of the slab. The radial area of spalled concrete was larger on the exit surface than on the entrance surface. Thirdly, the central hole was just that, a smooth circular hole. We judge that the hole was not much larger than the diameter of the penetrator. Usually only one, though sometimes, two, rebars were broken by the penetrator. In all cases the rebars had sustained significant tensile strains in being pushed outward from the flat surface of the slab. If the rebar mesh on the entrance side protrudes in the backward direction of the penetrator velocity, then there must be a large region of high pressure to "push" the mesh outward. From the limited Hull analyses that we performed, we believe that the pressure results from the multiple reflection of the pressure wave between these two planes of reinforcing steel. The steel mesh cover about 45 % of the surface area. The acoustic impedance of steel (Rho x C or the square root of(E x rho)) is much greater than that of concrete. A significant portion of a propagating pressure (and particle velocity) wave is reflected from the rebar. While there is spherical expansion of the pressure wave from the penetrator and the attendant inverse square root attenuation of the wave, there is an intensification of the wave every time it impinges on the front surface of the projectile. Too, the steel rebar mesh acts like a strong membrane and confines the concrete. This allows the pressures to build significantly greater that in the unconfined (unreinforced) case. Confinement and reflection of the waves from an acoustically hard material allows the build up of pressure in concrete much greater than would occur without the rebar. This pressure on the front end of the penetrator is responsible for the retarding force. This force integrated over time is in impulse which extracts momentum (velocity) from the penetrator. Thus, reinforced concrete should extract considerably more

kinetic energy from a penetrator that just that energy required to break the reinforcement ligaments. This, we believe, is the physical explanation of why a penetrator looses so much more of its kinetic energy in reinforced slabs as compared to unreinforced than can be accounted for by rebar breakage.

Another observation by others and coroborated by our analysis is this. Penetrators have been observed to penetrate thick concrete and the paint on the back surface of the cylinder has not been scraped off. Our analysis shows a space which forms in the region behind the penetrator corner. Material is expelled out this region (given a backward velocity) and the location of the ejecta is radially further out than the outer surface of the penetrator.

In the last run that we made we put a steel disc inmmediately in front of the penetrator and a circular ring in the region between the disc and the penetrator. The pressure built up in this confined zone and caused severe bulging of the disc and radial expansion of the ring. The graphics also showed reflection of the wave off of the disc and a build up of pressure from this reflection.

Some of the mistakes that we made would have been obvious to analysts who have used hydrocodes. We document a few to aid those who follow in our train. If the lateral edges of the concrete disc are too close to the penetrator a release wave reflects back and erases the pressure from the front of the penetrator. We tried to use boundaries without placing air around the boundary. These boundaries and the reflections from these boundaries confuse the results. We recommend that the lateral boundaries be surrounded by air and that they be at least twice the thickness away from the centerline. The station locations need to be placed in regions of interest. The zone just in front of the edge of the penetrator is a region

of extremely high shearing stress (and fracture). Eulerian stations need to be located in several regions aroung the penetrator nose. Lagrangian stations need to be located in front of and near the inserted steel and at locations where failure is likely to occur to determine the history of the material; that is, at fixed positions in the slab. Failure in the concrete seems to follow the penetrator and the failure mechanism is by shear of the material along the edge of the penetrator corner. A region of high pressure and density is attached to the front plane of the penetrator. This wedge is pushed through the material as a wedge. When the pressure bulge reaches the exit side free surface, the concrete will fail by tensile stress along a cone attached to the penetrator. Though the hydrocode does not allow the concrete to sustain any significant tensile stress, no fracture surface is created. That is, the material is still continuous and the particle velocity gradients continue to generate strains. The analyst must render a judgment about when and where fracture occurs by a careful review of the stress and strain data.

III CONCLUSIONS

We believe that the presence of significant amounts of reinforcing bar on the entrance and exit planes of a concrete slab alter the penetration process. For the reinforced case the penetrator looses more kinetic energy due to the increased pressure on the penetrator during the penetration period and due to the energy required to break the rebar as the projectile penetrates the entrance and exit planes. This loss of kinetic energy in the reinforced slab case can be rationalized as confinement of pressure caused by the planes or sheets of rebar mesh. In some of the field tests the pressure in the concrete was sufficiently high enough to push the rebar

outward on both the exit and entrance surfaces. Some of this may have been be due to the density change in the concrete caused by the volume of concrete displaced by the penetrator. We believe that the penetration of concrete proceeds by mode II shear failure of the concrete on the corners of the penetrator and eventually by cone tensile failure on the exit side when the penetrator nears the exit surface.

IV. RECOMMENDATIONS

We recommend that the 2D axisymmetric modelling of concrete slab be continued. Specifically, the rebar analogue in the axisymmetric case be done as circular rings on both entrance and exit planes. Further, we recommend that the station data be changed to Lagrangian stations imbedded in the concrete on the interior sides of the steel rebar and the pressure time history be compared to a similar run without the reinforcing rings. We also recommend that CTH be implemented and the results from Hull and CTH hydrocode analyses be compared.

1990 USAF-UES SUMMER FACULTY RESEARCH PROGRAM

GRADUATE STUDENT RESEARCH PROGRAM

Sponsored by the

AIR FORCE OFFICE OF SCIENTIFIC RESEARCH

Conducted by the

Universal Energy Systems, Inc.

FINAL REPORT

Solid-State Imager Replacement for a High-Speed Film Camera

Prepared by:	Eustace L. Dereniak, Ph.D.
Academic Rank:	Associate Professor
Department and	Optical Sciences Center
University:	University of Arizona
Research Location:	AFATL/AGI Eglin AFB, FL 32542-5434
USAF Researcher:	Donald Snyder
Date:	28 Sep 90
Contract No:	F49620-88-C-0009

Solid-State Imager Replacement for a High-Speed Film Camera

by

Eustace L. Dereniak

ABSTRACT

We discuss our investigation of the replacement of high-speed film cameras used by the Air Force with high-speed, high-definition solid-state cameras. Development of specifications for such an imager, and the analysis of the associated radiometry are discussed. In addition, we represent an experiment to determine the signal levels expected for this imager. Analysis of the experimental data indicates that light levels sufficient to achieve a reasonable signal-to-noise ratio are available.

ACKNOWLEDGEMENTS

My appointment this summer afforded me the unique opportunity to learn first hand the Air Force requirements for solid-state imagers. The experience was both rewarding and enlightening. Not only did I learn about new technology, I made new friends. I would like to thank the friendly people from Sverdrup: Jeff Rowe and Gene Chenette, who helped me greatly; Dennis Goldstein, Air Force Focal Point, who gave me the opportunity to be at Eglin AFB, Florida; and Rod Powell, for his reassurance. Thanks to Bob Webb of the Air Force Armament Laboratory for taking me into his group, special thanks to Don Synder, for making me feel part of the team laboratory. In addition to challenging me, Don provided an enjoyable work atmospheres, and made special housing arrangements for my visit. Finally, I would like to thank the Air Force Office of Scientific Research and Air Force Armament Laboratory (AFATL) for awarding me this faculty research position.

Solid-State Imager Replacement for a High-Speed Film Camera

I. INTRODUCTION:

Until recently, the realization of a solid-state sensor focal plane array (FPA) that is both large and fast was an impossibility. That limitation is being overcome, and solid-state sensor FPAs, with high frame rates and high resolution, may soon replace high-speed film cameras. High-speed FPA cameras with low resolution have already been developed and implemented (Bixby, 1981). Examples are the Eastman Kodak 40,000 frames per second (FPS) 64 x 64 element array, and the reticon 64 x 64 (E-K 1990/Tanner, 1989). Their small number of pixels limit the resolution of these systems to small fields of view, or render their picture quality coarse. Higher resolution imagery has been possible only with image-intensifier tubes (I^2T) for short integration times. Image-intensified versions of these systems are capable of short data integration times (about 10 ns) but are not capable of high frame rates, so continuous video frames are not possible.

At the present time, the best choice for an array is the Ford Aerospace 1024 x 1024 pixel array, which has 64 outputs and which, at least in theory, meets our goals (Bredthauer, 1989/Sauer, et al, 1990). Some reservations about this array's performance remain, however, and these are currently under examination in the laboratory. In the course of these studies we have measured the radiometric signature of an aircraft in direct sunlight, to determine whether or not sufficient energy exists for high frame rates (i.e., for short integration times). Intuitively, we should obtain a sufficient signal, since a camcorder recording at a 1/1000 sec rate produces a good quality image.

II. OBJECTIVES OF THE RESEARCH EFFORT:

Our objective is to determine whether or not, using current technologies in solid-state sensor FPA, we can produce a high-speed (1000 FPS), high-definition (10^6 pixels) camera to replace the film cameras used by the Air Force (Snyder and Rowe, 1990). This objective encompasses many technologies, and requires the investigation of basic physics problems (Kriss, et al, 1989). No existing system can produce a 1000^3 system (defined as 1000 x 1000 pixel elements operating at 1000 frames per sec). There are some 1000 x 1000 pixel FPAs but, because of limitations inherent in their architectures, they can't be read out beyond 20 frames per second. On the other hand, some small (128 x 128) arrays can be read out at high rates (10,000 frames per second in some cases) (McNeill and Raanes, 1990). If a 1000^3 system is to be realized, its focal-plane architecture and data acquisition scheme must be integrated into the overall system. They are not separate problems to be addressed independently. The type of FPA architecture influences the design as well as the overall system configuration; for example as in the relationship between readout time, integration time (Appendix B). The key problems that must be addressed are:

- the array's electrical driver requirements for moving the charge efficiently, in terms of current load and power requirements.
- dissipation of power within the FPA. This heating effect causes thermal runaway.
- meeting the optical resolution of the existing film camera systems.
- optical resolution versus pixel size. As the pixel grows larger, the manufacturing yield diminishes.
- noise introduced by electrical crosstalk at high video clocking rates.
- Data handling and storage of 10^9 pixels/sec with a 12 bit A/D converter resolution.

III. AIR FORCE MISSION REQUIREMENTS:

To better understand how well solid-state optical sensors must perform, we must evaluate film camera systems currently in use. Film cameras are being challenged by solid-state cameras because of several technological breakthroughs in the silicon foundries (i.e. submicron photolithography capability). While current film camera systems meet Air Force mission objectives, they hold two major shortcomings:

- they don't allow real-time viewing of the scene under evaluation during a mission; the operator can't tell what he is recording; and
- data collection with a film camera can produce only latent images; the film must be developed and processed after flight.

Both shortcomings are overcome through solid-state camera technology. If image quality (resolution and sensitivity) can be maintained, the solid-state camera is far superior to the film camera.

A. FILM CAMERA/IDAP CAPABILITIES:

A 16-mm film camera scenario from a sensor point of view is shown in Fig. 1. The field of view is about 57° (1 radian), with a resolution requirement of 1 mr. The equivalent film camera hangs from the wing of an aircraft and monitors the lowering and engagement of the landing gear. The camera's frame rate is about 200 FPS, with exposure times as fast as 1/1800 second. The film is developed and processed after the flight, and frames are digitized through an IDAP system. The IDAP system consists of a film-illumination plane, relay optics and a CCD Videk camera. The Videk camera has 1035 x 1320 pixels. The overall resolution is about 260 line pairs across each frame after the entire procedure using the IDAP system based on film size of 10.26 x 7.49 mm (horizontal F.O.V. with 10 mm f.l. lens is 57°).

B. FORD AEROSPACE 1024 X x 1024 ARRAY:

The 1024 x 1024 pixel array produced by Ford Aerospace has a full-frame readout structure. This device has 64 parallel video outputs, dividing the array into 64 subsections of

32 x 512 pixels each. It is a three-phase device, with 15 μm x 15 μm pixels (3 gates of 5 x 15).

We use this array as a baseline for this program of high-speed video. A top view of the array is shown in Fig. 2.

To operate this array at 1000 frames per second, each video output runs at a 16.7-MHz output rate, giving a rate of 10^9 pixels/sec (1000^3). Present-day analog-to-digital (A/D) converters operate in this frequency range with up to 12 bits of digital resolution. 12 bits (4096 ADU) are sufficient to cover the dynamic range of the array. It is expected that the full well capacity of the array is about 120,000 electrons (e⁻), with a read noise of approximately 150 e⁻. This corresponds to a dynamic range of about 800 to 1000 at best-- about 60 db of dynamic range.
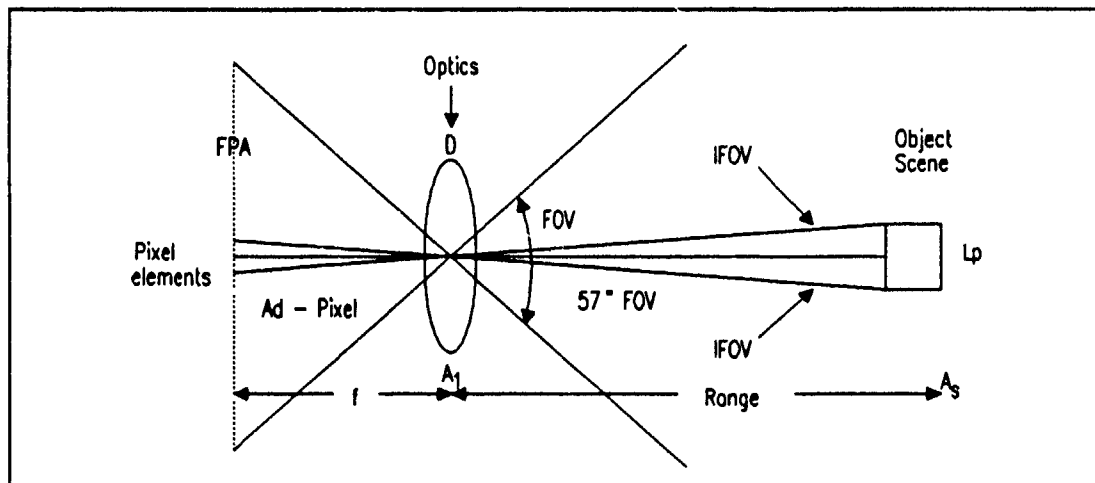
Figure 1
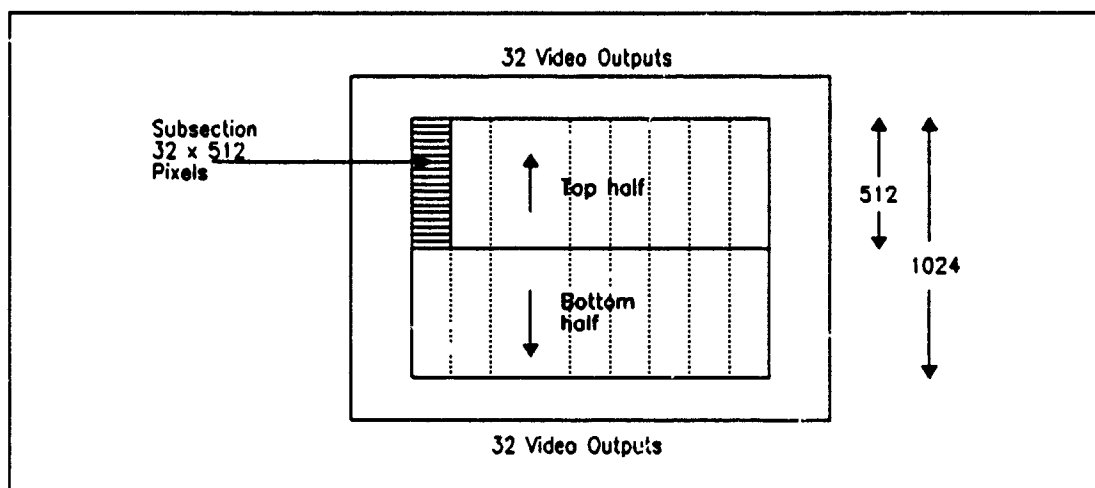
Figure 2. Ford's 1024 x 1024 Array

C. RADIOMETRIC CALCULATIONS.

We will base our analysis of the system's sensitivity on the assumption that a signal-to-noise (S/N) ratio of 10 is necessary to detect and identify a target correctly. We will also assume that the integration time will be 100 μsec for a 1000-FPS solid-state imager. These are conservative estimates; a longer integration time (1 ms) will improve the S/N ratio.

Specifications and operating parameters for the solid-state imager (see Fig.1) are shown in Table 1.

Table 1. Solid State Image Specifications

Field of View	~ 57°
IFOV	~ 1 mr
$\lambda_1 - \lambda_2$	.45 - .95 μm
Quantum Efficiency (η)	~ 40%
Integration Time	~ 100 μs
Optical Transmission (T_o)	~ 70%
F/No. (C mount)	1.4
Read Noise (σ_r)	150 e$^-$

The photon flux (ϕ_p - photon/sec) collected from a target, as shown in Fig. 1, is

$$\phi_p = \frac{L_p A_s A_l}{R^2} T_o \quad , \qquad (1)$$

where L_p = Target source radiance (source luminance)

A_s = Source area

A_l = Lens area

T_o = Optical Transmission

R = Sensor to target distance.

From the geometry of Fig. 1, this equation can be rearranged:

$$\phi_p = \frac{L_p A_d A_l}{f^2} T_o$$

where A_d = Pixel area, and

f = Focal length of sensor optics.

Recalling the F-number for a rotational symmetrical optical system (F/No. = $\frac{f}{D}$), and

rearranging terms:

$$\phi_p = \frac{\pi L_p A_d T_o}{4(f/No.)^2} \text{ (photon/sec)} \quad .$$ (2)

The signal-to-noise ratio detected from this radiometric signal flux is

$$\frac{S}{N} = \frac{\eta \phi_p T_i}{\left[\sigma_r^2 + \eta \phi_p T_i\right]^{1/2}} \quad ,$$ (3)

where η =   Quantum efficiency
        T_i =   Integration time
        σ_r =   Read noise.

Rearranging terms, and assuming a S/N of 10 is sufficient for identification, the photon flux, ϕ_p, is the only unknown in Eq. (3).

$$\phi_p = \frac{\left(\frac{S}{N}\right)\left[\sigma_r^2 + \eta \phi_p T_i\right]^{1/2}}{\eta T_i}$$ (4)

Because Eq. (4) is a quadratic in ϕ_p, direct substitution of Eq. (2) is not easily performed. Conceptually, we desire in this analysis the value of the source radiance (L_p) in Eq. (2), which is necessary for a S/N of 10.

Solving Eq. (4) for ϕ_p: $\phi_p = 3.9(10^7) \frac{\text{photon}}{\text{sec}} \quad ,$ (5)

then using Eq. (2), we can determine the necessary source radiance (luminance). From Eq. (2), and solving for the radiance (luminance), L_p:

$$L_p = \frac{\phi_p 4(f/No.)^2}{\pi A_d T_o} \quad .$$ (6)

Substitution of Eq. (5) into Eq. (6), and using other parameters below,

$$A_d \quad = \quad 15 \ \mu m \ x \ 15 \ \mu m \ (\text{active detector area})$$

$$T_o \quad = \quad 70\%$$

$$f/No. \quad = \quad 1.4$$

L_p is calculated to be

$$L_p = 6.2(10^{13}) \ \frac{\text{photon}}{\text{sec-cm}^2\text{-sr}} \ . \tag{7}$$

The value in Eq.(7) is the photon radiance from the source necessary to give a S/N of 10, with a 100-μs integration time.

This source radiance (luminance) is the number of photons/sec-cm^2-sr that are within the spectral sensitive region of the detector (λ_1 - λ_2). Appendix C relates the photon radiance (Luminance) within various spectral regions to photometric units and radiometric units for sunlight. Photometric units are used here because the aircraft data was recorded with photometric instruments. We know the aircraft signature in photometric units (lumen/cm^2, Lux, Cd/M^2) (Meyer-Arendt, 1968).

Two spectral regions are of interest: 0.45 to 0.67 μm (photopic response); and 0.45 to 0.95 μm (radiometric response). For the 0.45 - 0.95 μm spectral region, the relationship between candelas and photon/sec-cm^2 for sunlight is 1.83 (10^{12}) photon/sec-cm^2-Sr = 1 $\frac{Cd}{m^2}$ (from Appendix C). The source luminance, therefore, must be

$$L_s = \frac{6.2 \, (10^{13})}{1.8 \, (10^{12})} = 34 \, \frac{Cd}{m^2} \ .$$

This luminance (34 $\frac{Cd}{m^2}$) provides a S/N of 10 in a spectral response over the 0.45 - 0.95 μm region. This spectral response is used because the solid-state camera spectral sensitivity extends beyond the response of the human eye.

How does this data compare to data taken on an aircraft? As shown in Appendix A, the measured values of luminance are higher than 34 $\frac{Cd}{m^2}$ even for the most shaded area of the craft (its wheel wells). This data was taken in a worst case scenario, since the craft is on

the flightline where no reflected light from the ground is illuminating its underside.

When the craft is airborne, as shown in Fig. 3, the earth reflects the solar radiation with about 18% reflectivity. Assuming a sunlit day, the earth is irradiated by solar flux (E_p^{Sun}) of about 80 kLux. This radiation is reflected toward the airplane, and acts as an extended source. The illuminance on the belly of the airplane, therefore, is

$$E_p^{plane} = \rho E_p^{sun}$$
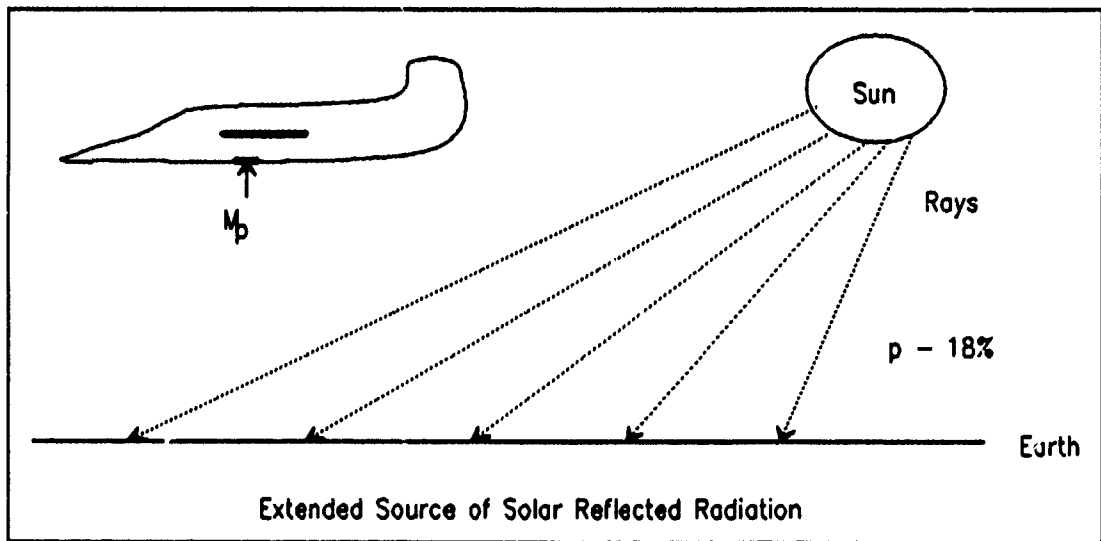
Figure 3. In-Flight Scenario

The illuminance of the airplane in flight, then, will be greater than that measured for the craft on the ground (see Appendix A).

D.   PIXEL SIZE TRADEOFF:

We based our radiometric study on the Ford Aerospace 1024 x 1024 array. We have to examine the effects of pixel size on other performance parameters, since pixel size influences the dynamic range, minimum detectable source flux, resolution, and dissipation of power over the focal plane.

The table below relates pixel area to various parameters, and shows the parameter values for the Ford Aerospace array.

Parameter	Relationship	Ford Array
Dynamic Range	$\dfrac{32}{9}$ A_d (μm^2)	800
Resolution (max spatial frequency Lp/mm)	$\dfrac{500}{\sqrt{A_d\ (\mu m^2)}}$	33
Power Dissipation (watt)	$8.9\ (10^{-3})\ A(\mu m^2)$	2
Source Luminance Level for $T_i = 100\ \mu s$, S/N $= 10$, $\sigma_r \approx 150\ e^-$ (photon/sec-cm²-Sr)	$\dfrac{1.4\ (10^{16})}{A_d\ (\mu m^2)}$	$\dfrac{6.2\ (10^{13})}{1.8\ (10^{12})} \approx 34\ \dfrac{Cd}{M^2}$

IV.   CONCLUSIONS/RECOMMENDATIONS:

The technology exists to develop a solid-state camera that would challenge the film camera. The sensitivity of a solid-state camera is greater than that of the film camera; resolution, however, is less. From the point of view of the overall system, the resolution currently achievable is great enough to meet the requirements.

Areas of risk are the dissipation of power in the focal plane array, video data-handling rates, and electrical crosstalk in the drive electronics.

The increased read noise arising from the high clock'ng frequencies will also degrade the performance of the imagers. The extent of that effect will be known only after the array is operational.

Radiometry calculations indicate that there is sufficient flux to produce a good signal-to-noise ratio. If illumination is insufficient, a laser diode illumination technique could be incorporated into the instrumentation.

V   REFERENCES

1   Bixby, James A , "High-speed television camera and video tape recording system for motion analysis," SPIE 301, 28 Aug 1981

2   Bredthauer, Richard A , "64-output 1024 x 1024 pixel imager for high-frame-rate applications," SPIE   1155, pp 89-92, 1989

3   Eastman-Kodak, KHS-0016, Ultrahigh Frame Rate Interline CCD Imager, Data Sheet, Mar 1990

4   Kriss, M , K Parulsk, and D Lewis, "Critical technologies for electronic still-imaging systems," SPIE 108,   1989

5   McNeill, John A and Chris A Raanes, "Fast framing detector systems for sensor applications," SPIE   1155, pp 80-88, 1990

6   Meyer-Arendt, Jurgen R , "Radiometry and photometry units and conversion factors," Applied Optics, Vol 7, pp 2081-2084, 1968

7   Sauer, D J et al , "High fill-factor CCD imager with high-frame-rate readout," David Sarnoff Research Center Booklet, 1990

8   Snyder, Donald R   W Jeffrey Rowe "System analysis and design for next-generation high-speed video systems," SPIE Vol 1346, Ultahigh and High-Speed Photography Videography, Photonics and Velocimetry, July, 1990

9   Tanner John E , "A high-speed video camera and recorder " SPIE 1155 1989

APPENDIX A

Luminance of Plane at Various Locations in Sunlight.

We evaluated reflected sunlight in various locations around and under a plane on the flight line. These measurements were performed on a clear, sunlit day. The plane was pointing west on a concrete flight line.

I. **OBJECTIVES**:

The objectives of these tests were to determine the radiometric signals expected from stores payloads for various geometrical configurations in sunlight conditions. These radiometric signal levels would determine if video imagery could be obtained at high frame rates (short integration times), using solid state cameras in an airborne application. There are two questions, one of signal-to-noise ratio expected and on the resolution needed. The resolution question is whether we can resolve a 1-in target at 500" (~ 1 milliradian) with a contrast greater than 5:1. This leads to questions of reflectance of various surfaces and background (sky or ground) radiance levels.

II. **APPROACH**:

The description of the data collection and experiments performed follows. The airplane was parked on a cement area isolated from any structures or other planes by at least 300 ft. The data in this report are primarily concerned with radiance levels on the under side of the aircraft, however, other view angles were taken and recorded.

The radiometric measuring instruments used during this data collection were:

Photometers	-	Luminance Meter - Minolta LS 110
Illuminance Meter	-	' Minolta Model T1H
Radiometer	-	UDT S370

In addition to the test equipment, we videotaped the procedures and equipment location relative to the plane's area of interest. The voice channel was used to record data, and hard copy data sheets were also used. The data were collected from sunrise to midday to evaluate various levels of sunlight reflected from the appendages of the plane.

The measurement sequence followed a similar pattern for each location relative to the aircraft. The sequence was:

1. Define target or region of interest on the airplane.
2. Measure and record sky illuminance at zenith angle with radiometer (UDT) - both photometric (Lux) and radiometric ($mwatt/cm^2$).
3. Measure and record the illuminance incident (Lux) on the surface or area of interest with a Minolta illuminance meter (Minolta T1H).
4. Measure and record the luminance from the surface with photometer - luminance meter (cd/M^2) (Minolta - LS 110).

5. Position standard sources on surface of interest (reflectance standards were 16% and 45% reflectance).

6. Measure and record luminance from reflectance standards.

During the data collection, a camcorder monitored the location and recorded the data. This additional data was critical in case of anomalies or misinterpretation of data during the analysis. Only minimal data analysis was performed in real time because the temperatures and conditions on the flight line were not conducive to real-time data analysis.

III. DATA ANALYSIS:

The analysis gives quantitative values of reflectance for various appendages located on the plane. The luminance expected from these surfaces will be used in predicting signal-to-noise ratios for the solid state cameras.

The relationship between the incident solar sunlight on a surface and the luminance is

$$ L = \frac{\rho E}{\pi} , $$

where

L - luminance

E - incident illuminance

ρ - reflectance

This relationship assumes a Lambertian surface, which means it is diffuse and uniformly redistributes the incident radiation into a hemisphere. This Lambertian assumption is a worst-case analysis for the radiometric analysis. If the surface is more specular, the contrast will go up, yielding a large signal-to-noise signature for the camera.

Table A.1 shows a summary of the location of data collection. The X on the airplane sketches in the legend locates the surface of interest; the dot (•) and arrow (→) indicate the location of the radiometric instrumentation and the direction of observation. All data taken was for the underside of the aircraft.

Table A.1 - Legend

Test Point 1
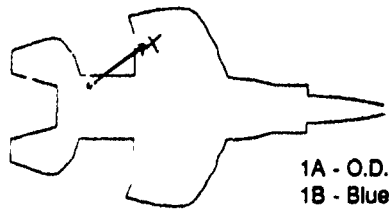
1A - O.D.
1B - Blue
1C - Pylon
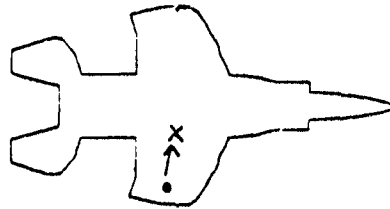
Test Point 2

Missile Rail

Test Point 3

Fuel Tank

Test Point 4

4A - O.D.
4B - Light Blue
4C - Dark Blue

Test Point 5

5A - Light Paint
5B - Dark Paint
5C - Bare AL
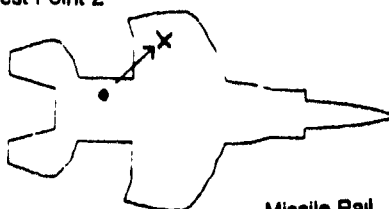
Test Point 6
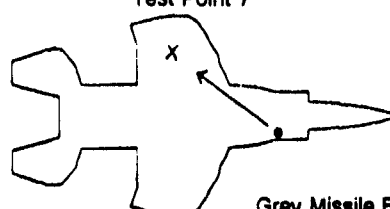
Test Point 7

Grey Missile Body
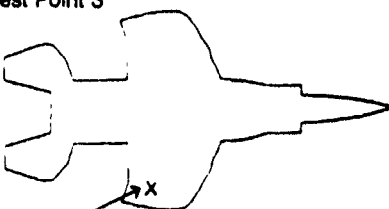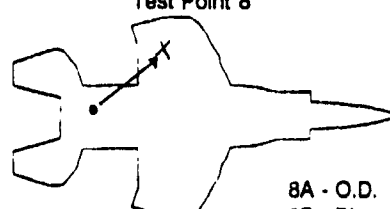
Test Point 8

8A - O.D.
8B - Blue
8C - Pylon

Test Point 9

Missile Rail

Test Point 10
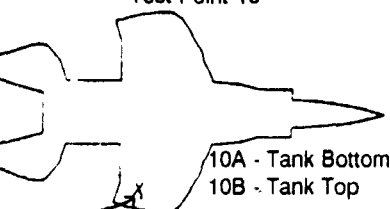
10A - Tank Bottom
10B - Tank Top

Photometric to Radiometric Flux from Sunlight

The experiments used photometric instrumentation while evaluating the various flux levels off an airplane that result from incident sunlight. The solid state sensors that will be used in an airborne camera will have a much broader spectral coverage ($0.45 - 0.95$ μm) so a conversion factor must be determined. This conversion factor (F_F) relates lux in the eye's spectral response to watts/cm^2 in a $0.45 - 0.95$ μm spectral response for sunlight (blackbody temperature $\sim 5900°$K). (See Appendix C.)

$$F_F = 1.8 \, (10^3) \, \frac{\text{Lux}}{\text{m watt/cm}^2} \, .$$

This conversion factor (F_F) for sunlight was measured with a radiometer/photometer. The data taken for various times of the day are shown in Table A.2. The average value of F_F measured is $5.54 \, (10^3)$. The difference between the measured value and the calculated value of $1.8 \, (10^3)$ is approximately a factor of π due to the measurement instrument not having a cosine diffuser on the radiometric measurements.

Table A.2. Measured Skylight in Photometric and Radiometric Units

Time (a.m.)	Lux	mw/cm^2	Lux/mw Ratio (10^3) F_F
6:35	1.85 kLx	0.532	3.48
6:50	5.2	0.834	6.24
6:59	5.2	1.135	4.58
7:04	7.1	1.37	5.18
7:10	8.2	1.6	5.13
7:17	10.2	1.78	5.73
7:25	11.2	2.1	5.33
7:34	15.46	2.63	5.89
8:06	26.6	3.9	6.82
8:15	29.5	4.2	7.02
			$\overline{F_F}$ = 5.54

See Figure A.1 for the configuration of the detector housing using a photometric filter and radiometric filter

IV. CONCLUSION.

The average surface luminance measured in the experiment is on the order of 1000

Cd/m^2. Using a conversion factor of $\frac{1}{\pi}$ • 1.83 (10^{12}) photons/sec-cm^2 per Lux, this value

corresponds to a target photon flux radiance of 5.8 (10^{14}) photons/sec-cm^2-sr over the 450 nm to 950 nm band. For a camera with an F/2 lens and 95% lens transmission, using

$$E_4 = \frac{\pi}{4} \cdot t_1 \cdot (FN)^{-2} \cdot L \quad ,$$

the resulting photon flux at the focal plane comes to 1.1 (10^{14}) photons/sec-cm^2. Assuming a detector with 25% quantum efficiency, 1 ms integration time and a 100 μm^2 active area, we get a signal of approximately 25,000 electrons per pixel. This signal can be scaled according to the actual surface luminance present. Since most detectors today have full well capacities of only a few 100,000 electrons, this signal is well within the detection capabilities of today's technology.

For a plane flying in the air, the signal should be slightly improved since the light reflected from the ground onto the underside of the plane is not reduced by the plane's own shadow. Some rough calculations indicate that the surface illuminance on the underside of a plane flying in the air is about one third of the sky illuminance on the ground (assuming the earth to be an infinite Lambertian surface of 18% reflectivity). This is somewhat better than the values measured in the experiment, thus improving the expected signal by approximately another 50%.
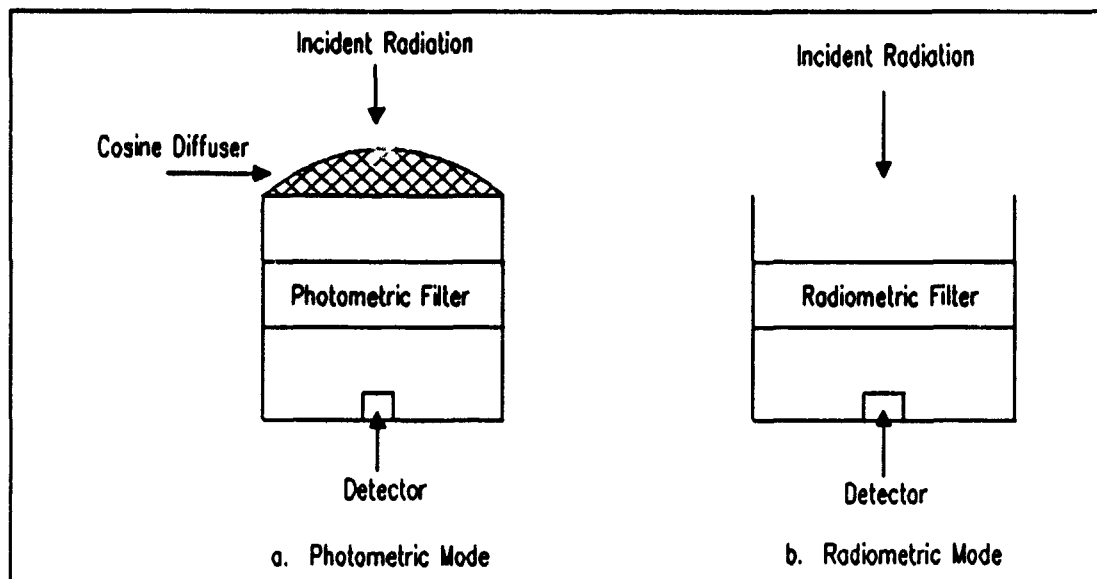
Figure A.1. Radiometer Sensor Head

APPENDIX B

Contrast Degradation due to Integration/Readout Time Ratio

(T. Graeve)

Let the ratio of integration time to readout time be R (i.e. R:1). For a given array size and frame rate, a full frame architecture has the lowest R, a frame transfer device has a higher R, and an interline device has the highest R. However, for the latter there is no degradation in contrast due to charge readout. The following analysis is therefore valid only for full frame and frame transfer devices.

For a normal scene, we define the maximum and minimum irradiance incident on the devices E_{max} and E_{min}, respectively. The maximum contrast for this scene then becomes

$$C_{max} = \frac{\eta A_d t_i (E_{max} - E_{min})}{\eta A_d t_i (E_{max} + E_{min}) + 2 t_i n} \quad ,$$

where η is the quantum efficiency and A_d the area of the device. During readout, each pixel collects an additional charge proportional to the average irradiance on the column that it is transferred through. If this average irradiance is given by $\alpha \cdot E_{max}$, where α is a factor between zero and one, and the readout time is t_i/R, the minimum and maximum signal levels are

$$S_{min} = \eta A_d t_i E_{min} + t_i (1 + \frac{1}{R})n + \eta A_d \frac{t_i}{R} \alpha E_{max}$$

$$S_{max} = \eta A_d t_i E_{max} + t_i (1 + \frac{1}{R})n + \eta A_d \frac{t_i}{R} \alpha E_{max}$$

The actual contrast then becomes

$$C_{act} = \frac{\eta A_d [E_{max} - E_{min}]}{\eta A_d \left[\left(1 + \frac{2\alpha}{R}\right)E_{max} + E_{min}\right] + 2\left(1 + \frac{1}{R}\right)n} \quad ,$$

For an E_{min} of zero and no dark current, this equation reduces to

$$C_{act} = \frac{1}{1 + \frac{2\alpha}{R}} \quad .$$

In general, the reduced formula can be applied as long as the dynamic range of the incurrent radiation is greater than 20 dB and the dark current in the device is less than 100 nA/cm².

Note that this analysis assumes that all random noise sources have been averaged to zero. The remaining noise sources that average to a DC level are included in the dark current term. The resulting contrast degradation is superimresed onto the MTF response of the device (i.e. it scales down the MTF curve).

Example: Under the following conditions (either equation applies) the contrast becomes:

$$E_{max} = 5 \cdot 10^{14} \text{ photons/sec-cm}^2 \qquad \eta = 25\%$$

$$E_{min} = 1 \cdot 10^{12} \text{ photons/sec-cm}^2 \qquad A_d = (15 \ \mu m)^2$$

$$n = J_d A_d / q = 1.4 \cdot 10^4 \text{ electrons/sec}$$

(for a dark current of 1 nA/cm^2)

$\alpha = 1$ and $R = 17$ $\quad \rightarrow \quad$ $C = 89\%$

$\alpha = 1$ and $R = 3$ $\quad \rightarrow \quad$ $C = 60\%$

$\alpha = \frac{1}{2}$ and $R = 17$ $\quad \rightarrow \quad$ $C = 94\%$

$\alpha = \frac{1}{2}$ and $R = 3$ $\quad \rightarrow \quad$ $C = 75\%$
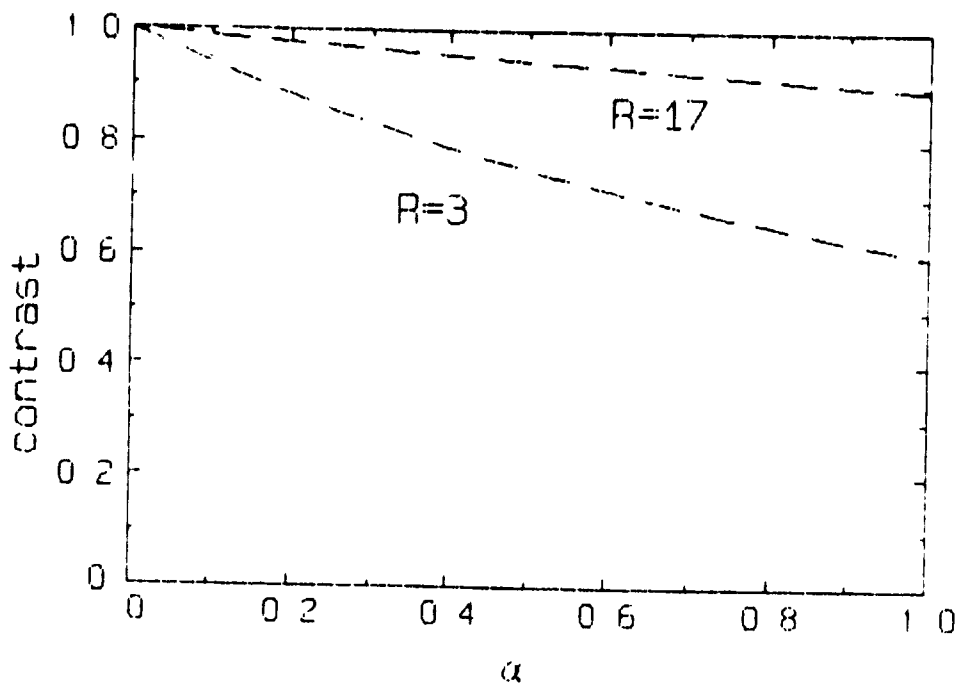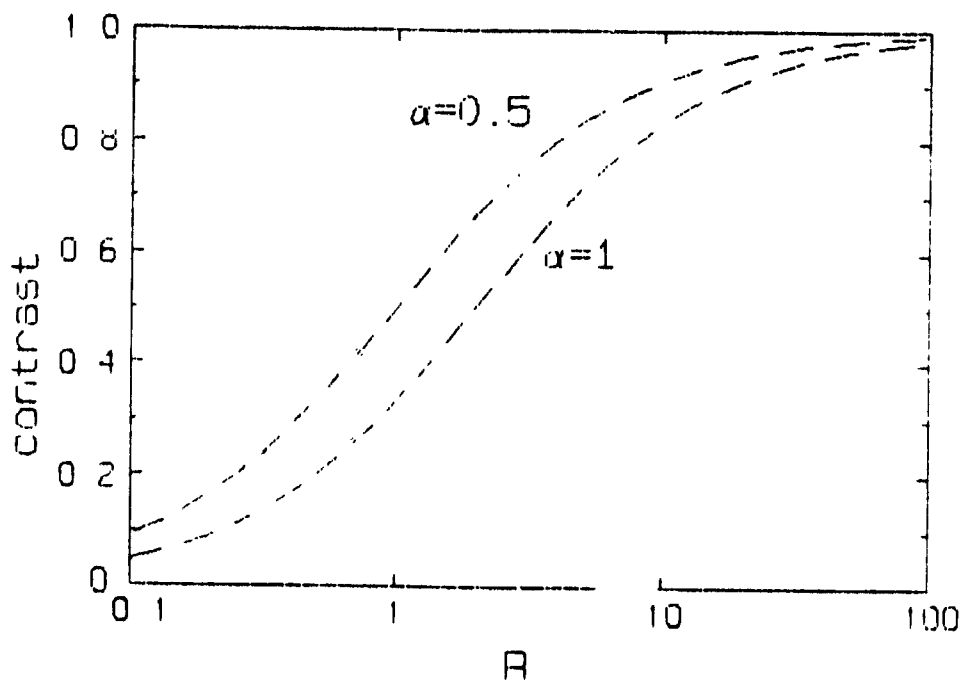
APPENDIX C

Conversion Factors Between Photometric Unit and Radiometric Units with Sunlight as Source

$\Delta \lambda$			C_F		
.45 - .67	$\dfrac{Cd}{m^2}$ †	*	$3.00\,(10^{-7})$	=	$\dfrac{watt}{cm^2 - Sr}$
.45 - .95	$\dfrac{Cd}{m^2}$ †	*	$5.47\,(10^{-7})$	=	$\dfrac{watt}{cm^2 - Sr}$
.45 - .67	$\dfrac{Cd}{m^2}$ †	*	$8.41\,(10^{11})$	=	$\dfrac{photon}{sec - cm^2 - Sr}$
.45 - .95	$\dfrac{Cd}{m^2}$ †	*	$1.83\,(10^{12})$	=	$\dfrac{photon}{sec - cm^2 - Sr}$

$$\dagger \quad 1\,\frac{Cd}{m^2} \;=\; \frac{Lumen}{m^2 - Sr} \;=\; 10^{-4}\,\frac{Lumen}{cm^2 - Sr}$$

Evaluation of Weapon Target Allocation Algorithms

1990 USAF-UES SUMMER FACULTY RESEARCH PROGRAM

GRADUATE STUDENT RESEARCH PROGRAM

Sponsored by:

AIR FORCE OFFICE OF SCIENTIFIC RESEARCH

Conducted by:

Universal Energy Systems, Inc.

Evaluation of Weapon Target Allocation Algorithms

by

Charles E. Fosha, Jr.

Abstract

The SDI offers extraordinary challenges in the battle management area. Battle management here is defined as the process of allocating and assigning weapons to targets in an engagement to optimize the result. To optimize means to allocate interceptors in such a way that a Measure of Effectiveness (MOE) function representing probability of miss or probability of leakage is minimized. The MOE could also be a function of intercept time, projected miss distance, importance of target or other measures. The battle management process may include real time decisions by the battle manager, as well as autonomous decisions based on a predetermined criteria in situations where human decision making is not possible due to time or other limitations. Decisions may be made on the lowest level (autonomous) or on a higher level (coordinated). This study deals with the coordinated decision of allocating interceptors to targets.

The objective of this research is to evaluate specific target allocation algorithms and from them attempt to gain insight into more general underlying principles. The scope of this effort encompasses defense against ICBMs during the boost phase using high velocity kinetic kill weapons. A specific battle scenario is used to conduct the research. This scenario is the launching of 54 missiles from three missile fields. The interceptors are in orbits whose planes pass nearby the missile fields. This allows for all aspects of shots and a wide range of closing velocities. This is a taxing scenario on a boost phase defensive system. Targets must be identified early during the boost phase, and

interceptors allocated to those boosters so that the intercept will occur before the booster burns out. Many complex decisions must be made in a very short period of time. Taking out boosters prior to bus deployment is a parato-superior decision. Thus a kill prior to bus deployment yields the destruction of 2 to 20 re-entry vehicles (RV). This requires high speed optimization solvers.

Different algorithms are evaluated from a rather straight forward minimum cost approach to advanced linear network configuration algorithms. Since the decision process of allocation of interceptors to targets is not precise, the role of fuzzy logic in the decision process is considered.

Two cases are analyzed, the static and dynamic case. For the static case, for each interceptor, a cost to intercept each missile is assigned arbitrarily. For the dynamic case, the Interceptor Manager (IM) engagement simulation being evaluated by Science Applications International Corporation (SAIC), generated a cost matrix that was evaluated. Execution time and allocation cost are the evaluation criteria. Since the algorithms were not incorporated into the IM, no consideration was given to the cost in time to load the data for the algorithm or the core memory required to run these algorithms.

Acknowledgments

I. INTRODUCTION

The general problem investigated here is the allocation of scarce resources. This problem has been worked in many different ways by operations research analysts, so a wealth of algorithms exist. The particular problem being considered is the weapon allocation problem. The aspect of this problem that makes it unique, is that the objective function is dynamic. As weapons are allocated or targets are destroyed, and the geometry changes, a new objective function must be computed. New objective functions are computed for every weapon allocation cycle (WAC). This research paper will only address the allocation of interceptors (IVs - Interceptor Vehicles) to targets at one WAC. The objective function could be to minimize cost, where the cost elements represent probability of miss, or could be to maximize cost, where the cost represents the probability of kill. These are equivalent problems and either case can be solved by the algorithms discussed in this report. While there may be an excess of interceptors over targets or vise versa, only one interceptor is allocated to one target. The allocation of several interceptors to a single target, in proportion to a probabilistic measure of hit for example, is not considered in this report.

II. THE PROBLEM AND ALGORITHMS CONSIDERED

A. PROBLEM DEFINITION

The weapon allocation problem can be considered as a directed graph with a set of nodes N (interceptors and targets) and a set of arcs A connecting the nodes. Each arc has a flow (1 if that interceptor is allocated to that target, or 0 if that interceptor is not allocated to that target) denoted by x_{ij}, and a cost c_{ij} of the flow on that arc. Given that, the problem is to minimize a scalar function subject to linear equality constraints.

Minimize $\sum\limits_{(i,j)\mathcal{E}A} c_{ij}\, x_{ij}$

subject to $\sum\limits_{\substack{m \\ (m,i)\mathcal{E}A}} (g_{mi}x_{mi} - \sum\limits_{\substack{m \\ (n,i)\mathcal{E}A}} x_{im}) = 0$

for all i $\mathcal{E}$ N (conservation of flow)

$$l_{ij} \leq x_{ij} \leq u_{ij}$$

for all (i,j)$\mathcal{E}$A (capacity constraint)

The computation of the cost elements is discussed below in Section II, C. The arc gain elements are $g_{ij} = 1$ for all (i,j)$\mathcal{E}$A.

The dual of this problem (formulated in [6]) is now stated. A new variable called the Lagrange multiplier p_i, is associated with the ith flow constraint. The corresponding Lagrangian function is:

$$L(x,p) = \sum\limits_{(i,j)\mathcal{E}A} c_{ij}\, x_{ij} + \sum\limits_{i\mathcal{E}N} p_i\, (\sum\limits_{\substack{m \\ (m,i)\mathcal{E}A}} g_{mi}\, x_i - \sum\limits_{\substack{m \\ (i,m)\mathcal{E}A}} x_{im})$$

The dual problem is then to maximize q(p) subject to no constraint on p, where:

q(p) = min L(x, p)

$$l_{ij} \leq x_{ij} \leq u_{ij}$$

$$= \sum\limits_{(i,j)\mathcal{E}A} q_{ij}\, (\, p_i - g_{ij}\, p_j\,)$$

where:

$$q_{ij} (p_i - g_{ij} p_j) = \min \left\{ (c_{ij} + g_{ij} p_j - p_i) x_{ij} \right\}$$

$$= (c_{ij} - t_{ij}) u_{ij} \qquad \text{if } t_{ij} > c_{ij}$$

$$= 0 \qquad \text{if } t_{ij} < c_{ij}$$

and,

$$t_{ij} = p_i - g_{ij} p_j \text{ for all } (i,j) \in A$$

B. THE INTERCEPTOR MANAGER

The IM originated with Coleman Research Corporation and has recently been modified by SAIC. The program was originally a part of a larger simulation called SDISEM, for simulation of an SDI type engagement. The IM starts with interceptors in orbit and target locations read from a target tape. It then simulates a battle engagement. For this report, the important procedures are the existence algorithm, the refinement algorithm and the allocation algorithm (see Figure 1).

The existence algorithm computes the interceptor time-of-launch, time-of-flight, time-of-intercept, and AIM vector for each IV-target pair. The algorithm works by computing all possible solutions to the pointing problem uniformly spaced over a legal time of intercept. The cost element for each IV-target pair is then computed. These elements are generated by computing the probability of kill. The probability of kill is computed as a product of the probability that the IV will be close enough to the target to intercept it and the conditional probability that it will intercept the target given that it is close enough. The cost is then computed as one minus this probability or a negative exponential of this probability. Then one of seven Rules-of-Engagement (ROE) criteria, earliest or latest launch, earliest or

latest time of intercept, shortest or longest time of flight, or lowest cost is computed for each IV-target. These initial IV-target pairs are refined in the refinement algorithm. The refinement algorithm predicts the interceptor and target trajectories to check for intercept. Some of the IV-target pairs can be rejected by the refinement algorithm where the cost matrix is set to 1 (probability of kill = 0). For the IV-target pairs that pass the refinement check, a new cost element is computed.
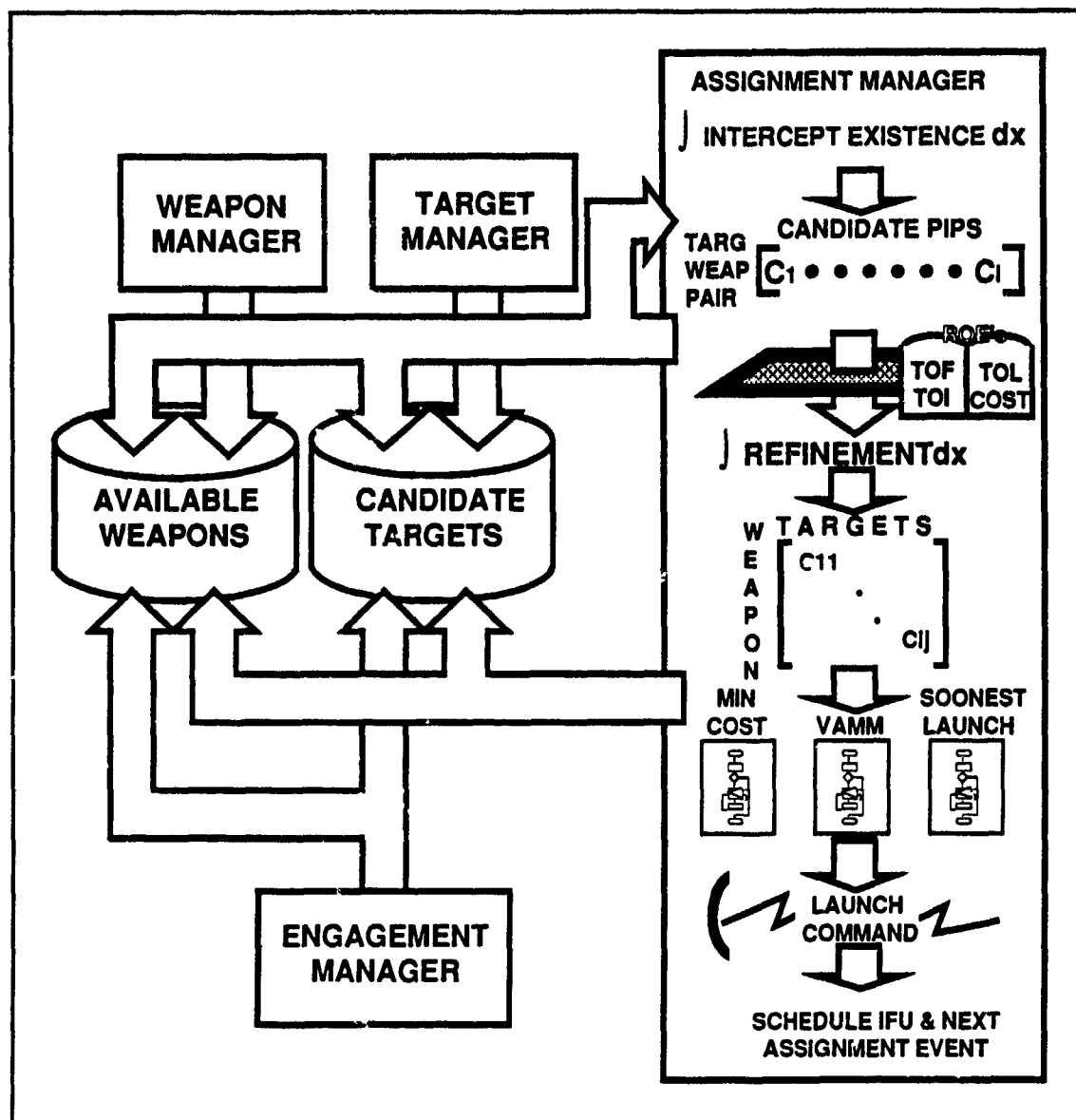
Figure 1 Assignment Manager

Figure 2 gives a time line of the target launch, detect action, selection and interceptor launch process and shows some of the parameters which affect the assignment/selection process. The user inputs which affect the events are included in the shaded box. The numbers indicate the nominal times which have been used in most of the scenarios. The time interval indicated in the cloud break parameter is given in kilometers. The translation to time is a function of the booster type and trajectory. The time line is not to scale; for instance, the launch cycle window is 40 seconds long when subtracting the message and IV prep intervals from the look ahead time for the assignment interval. The look ahead time for assignment is a parameter which the IM uses to set aside assignments for subsequent consideration which are too far in the future.

The weapon allocation algorithm then takes the interceptor target pairs and by one of three selection criteria, earliest launch, lowest cost, or a near optimal solution using the modified Vogel Approximation Method assigns interceptors to targets. The IM then simulates the flyout and provides statistics of the engagement. It is the purpose of this research to compare the approach used in the IM to assign IVs to targets with other assignment algorithms, using the time to compute the allocation and resulting cost as figures of merit. Since the new algorithms considered in the report were not incorporated into the IM directly, no consideration was given to the cost in time to load the data for these algorithms or the core memory required to run the algorithms.
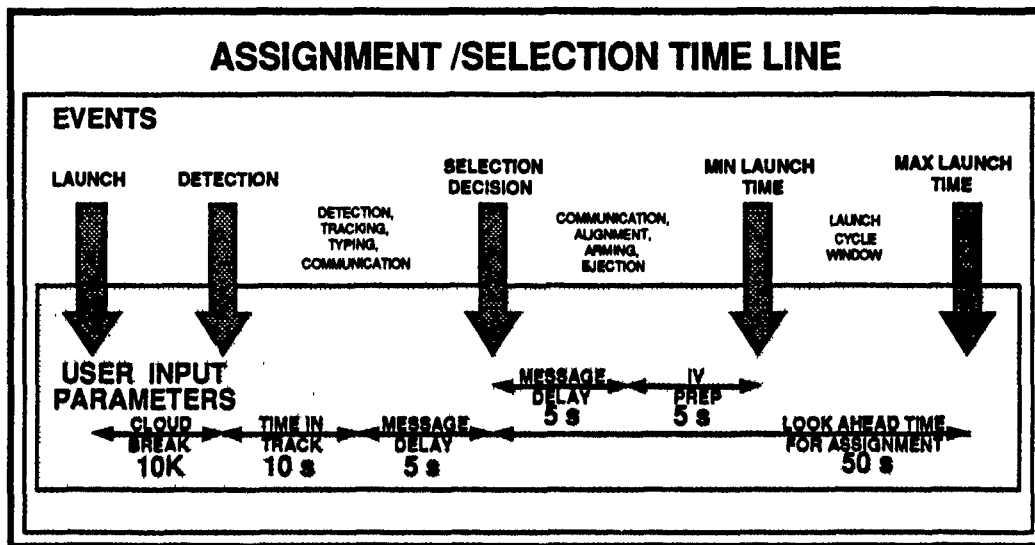
Figure 2 Assignment/Selection Time Line

C. THE COST MATRIX

The cost is a function of the probability of miss and the value of the target. The probability of miss is one minus the probability of kill. One of two cost functions may be selected; a function that is a power (**) or exponent function, i.e.,

$$cost = (1 - P_k)**VAL$$

or,

$$cost = exp(-K*P_k*VAL), \quad (k = 1.386, \text{ makes cost} = .5$$
$$\text{for } P_{ky} = .5 \text{ and val} = 1)$$

where:

$$P_k = PNear * PKill | PNear$$

an estimate of P_k is

4-10

$$P_k = \exp(-.5*Err/Divert^2) * IVP_k \text{(for a given target,IV type)}$$

where IVP_k is a predefined number for an IV target pair and Err is a function of the estimated uncertainty in predicted position at intercept and the error perpendicular to the closing velocity at intercept. Divert is the divert capability of the IV in meters.

D. ALLOCATION ALGORITHMS

1. Soonest Launch or Minimum Cost (SL/MC)

This algorithm finds the soonest launch time or lowest cost for every IV target pair and then allocates that IV target pair that has either the soonest launch time or the lowest cost. Then that IV and target are deleted from further consideration. The process is then repeated until all targets are allocated an IV. While this is a fast, simple algorithm, the latter selections tend to be higher cost, since less costly shots have been deleted. This is not an optimal selection or in some cases even a good approximation to an optimal solution.

2. VAMM

The modified Vogel Approximation Method (VAMM) [1] is not an optimization method, but an heuristic, with the initial solution often close enough to the optimal that the heuristic from VAMM will suffice. The method is based on determining the row or column which effects the change in cost most significantly, and then allocating resources to the cell that will provide the minimum cost in that row or column.

3. Munkres

The Munkres algorithm [2] is a variant of the (Kuhn's) Hungarian algorithm. This method is based on the fact that adding or subtracting a constant from all the elements of a row or column of the cost matrix does not change the optimality of the solution. A solution that gives a zero cost is an optimal solution. The Munkres algorithm generates an optimal solution as compared to the VAMM method which may not.

4. GNET

This algorithm is a generalized network solver, solving the primal simplex problem, while recognizing efficient data structures [3]. It provides a guaranteed optimal solution to the problem.

5. RSDNET

Restricted Simplicial Decomposition for nonlinear networks [4] is related to the feasible direction methods of nonlinear programming. For the linear problem, RSDNET returns a NETFLO [6] solution, determined by solving the primal simplex algorithm for networks. It provides an optimal solution to the problem. This code was included because of the possibility of switching between linear and nonlinear cost matrices which will be considered in future research.

6. RELAX

This code is based on the iterative ascent of the dual functional discussed above. The main feature of this algorithm that distinguishes it from the the classical primal-dual methods is that the choice of ascent directions is very simple, being based on the lagrange variable. Most of the ascent directions are

single coordinate directions, leading to the interpretation of the algorithms as coordinate ascent or relaxation methods. It provides an optimal solution to the problem. [5]

7. SSPNET

SSPNET stands for successive shortest path assignment algorithm [9]. This algorithm is more restrictive than the others in that it only works the assignment problem. If there are more interceptors than targets, then dummy targets with high cost (= 1) must be set up. Only one interceptor can be allocated to one target. This algorithm yields a guaranteed optimal solution.

III. RESULTS

Static and dynamic cases were considered. Cost matrices for the static cases were generated using a random number generator. The data for a dynamic case was a direct output from the IM.

A. Static case

Two subcases were evaluated here. The first level was a moderate 50 x 50 weapon allocation problem. The second case was a 200 x 200 weapon allocation problem.

B. Dynamic Case

The IM generated a cost matrix from a spike attack of 52 missiles from three separate missile fields. Two-hundred interceptors were available for the attack. Due to geometrical conditions, only 39 or 40 intercepts actually occurred based on the ROE.

Table 1 Simulation Results

Case 1 50 x 50
Optimal Cost = 1.44

Algorithm	Time to Execute	Total
SL/NC	.47	3.07
VAMM	.27	1.78
Munkres	2.10	1.44
GNET	.34	1.44
RSDNET	0.14	1.44
RELAX	0.18	1.44
SSPNET	0.03	1.44

Case 2 200 x 200
Optimal Cost = 1.67

Algorithm	Time to Execute	Total
SL/NC	25.99	4.56
VAMM	4.58	2.06
Munkres	114.73	1.67
GNET	10.09	1.67
RSDNET	2.35	1.67
RELAX	4.39	1.67
SSPNET	1.07	1.67

Dynamic Case 200 x 52
Optimal Cost = 16.97

Algorithm	Time to Execute	Total
SL/NC	2.87	17.88
VAMM	2.83	18.67
Munkres	12.67	16.97
GNET	8.94	16.97
RSDNET	.98	16.97
RELAX	DNC**	DNC**
SSPNET*	14.96	16.97

* Expanded to 200 x 200
**Did not Converge

IV. OTHER CONSIDERATIONS

A. FUZZY LOGIC

The word fuzzy seems out of place in this report on target
allocation techniques. Very precise algorithms for computing the
elements of the cost matrix, the optimization function, the result
cost and the interceptor and target pair leave no room for fuzzy
or vague concepts. A definition of fuzzy logic is appropriate
before continuing.

Fuzzy logic defines a minimum set of operations that deal
with vague or uncertain concepts. While the field of probability
and statistics deals with numbers and uncertainties, probability
and statistics are not equipped to deal with high variance in P_k's
or target valuations. For example, the value placed on a target
drives the target allocation process. But what is meant by the
statement, "that is a high value target, or that is a low value
target?" The analyst uses certain criteria to include number of
contained RVs, hardening, high or slow boost, and perhaps other
factors to assign a number, in the most elementary case, a 1 or 2,
based on his analysis. Then the future target position
uncertainty is also factored in to derive a cost of attacking this
target. The mathematics of fuzzy logic could be used to provide a
more rigorous algorithm to compute the cost of attacking a target
by an interceptor.

The objective of the weapon allocation problem is to allocate
interceptors to targets (call this the set S) to minimize a
function (call this function f). Mathematically, all of the
algorithms considered here generate a set S which a function f
maps on to the real line. The solution is the set S that does not
violate the constraints (1 interceptor to 1 target) and minimizes
the point on the real line. But there are other considerations in

this problem. For example, if there are an excess of interceptors, additional interceptors may be allocated to the high value targets, or to targets where the target position uncertainty is high. Considerations of communication overload, battle management assessment, blinding of sensors of other interceptors during interceptor target impact, and other factors make the concepts of best allocation more vague. In fuzzy optimization, best becomes the subjective evaluation of elements that have degrees of membership in a set, rather than existence in a set.

While the best allocation may be evaluated differently, the best result is still a real number. The computation of that number is based on using fuzzy numbers. While this concept is not pursued in any depth in this report, it should be investigated in a future study.

B. NEURAL NETS

The weapon target allocation problem is the determination of weights (in this case 0 or 1) defining the allocation of an interceptor to a target. The cost of making that assignment is based on a nonlinear cost function, the probability of miss. This problem can be solved using artificial neural networks [8]. An artificial neural network is a set of processing elements called neurons having a specified transfer function with a specific topology of weighted interconnections between neurons and with a learning law for updating the connection weights. In the learning mode, the weights are adjusted to give the neural net the desired property of minimizing the objective function, in this case the probability of miss.

The drawback to applying neural nets is the learning phase. The learning phase places a heavy computational load on the system tasked to train the neural nets.

V. RECOMMENDATIONS

While the objective of this study was to evaluate execution speed of various weapon allocation algorithms, several other related areas should be measured. These are the ROE, cost computation, and soonest launch or minimum cost algorithm.

The IM provides for seven ROEs. These are minimum and maximum time of launch, minimum and maximum time of intercept, and minimum cost. The candidate IV target pairs are selected by one of these criteria. These are predetermined criteria that a battle manager would select before the actual engagement. In this study for the dynamic case run using the IM, no significant differences were observed in the value of cost (see Table 2). The largest variance was in the number of interceptors launched between earliest intercept and minimum cost.

It is recommended that these ROE be investigated so that a more definitive explanation can be given to the operator or battle command as to when or in what situation that ROE should be used. Since all of the ROE parameters are computed, a fuzzy logic algorithm should be considered to provide a balance between launch parameters and launch cost which is a function of future target position uncertainty.

The elements of the cost matrix did not vary significantly. If the IV could not reach the target (determined in the existence and refinement algorithms) the cost matrix was set to 1 ($P_k = 0$). Otherwise, the values of the cost matrix were closely packed around a small number. Given the wide range of intercept conditions (the impact angle and velocity) a wider range of cost elements is expected. The algorithm used to compute cost should be investigated.

Table 2 Allocation Runs from IM

RUN	ROE	ENGAGEMENTS	COST AVERAGE
*VAMM			
1	Earliest Launch	39	0.146
2	Latest Launch	39	0.146
3	Earliest Intercept	40	0.147
4	Latest Intercept	39	0.148
5	Min Time of Flight	40	0.145
6	Max Time of Flight	39	0.150
7	Min Cost	40	0.145
*Soonest Launch			
7	Min Cost	40	0.156
3	Earliest Intercept	38	0.158

*Launch Algorithms

The soonest launch or minimum cost algorithm is a deficiency. When all cost units are about the same, or all shots equally probable, this simple algorithm of selecting the minimum cost IV for each target, then selecting the minimum cost over all minimum targets and then deleting that target and IV from further consideration works satisfactorily. But if cost vary significantly, this algorithm takes the least expensive cost first and then often finishes up by selecting IV target pairs that have very expensive costs or low probability of kill.

This study determined that there are many different network algorithms that can solve the problem considered. The most important result of the study is that there are optimal selections

to the problem that run faster than the approximate methods (see Table 1).

While additional study needs to look at core memory requirements, and data loading time, time-of-execution time is most important. The bottom line is that continual optimization runs stacked between missile warning/space track updates significantly outweighs the selection of higher resolution solvers that would run slowly. Another issue that needs to be addressed is what is the preferred weapon allocation cycle? Another issue to be considered is, does incremental allocation save time. For example, as new targets come into view, should an incremental reallocation be accomplished or should new targets be included in the next WAC with a new allocation.

The conclusions are that NETFLO (USED BY RSDNET) should be incorporated into the IM for additional testing and possible replacement of VAMM. SSPNET is also a viable candidate if the assignment problem restriction can be relaxed. The soonest launch or minimum cost algorithm has serious deficiencies and should be deleted. Fuzzy logic should be considered in the ROE selection algorithm.

REFERENCES

1. Linear Programming, Llewellyn, R. W., Holt, Rinehart and Winston, 1964

2. "Algorithms For The Assignment And Transportation Problems", Munkres, J, Journal Society of Industrial Applied Mathematics", Vol 5. No 1, March 1957

3. "Design and Implementation of Large Scale Primal Transshipment Algorithms", Bradley, G. H., Brown, G. G., Graves, G. W., Management Science, Vol. 24, No. 1, September 1977

4. "RSDNET USER MANUAL", Hearn, D. W., et al, Research Report No. 87-17, Department of Industrial and Systems Engineering, University of Florida, Gainesville, Fl, December 4, 1987

5. "Relaxation Methods for Minimum Cost Ordinary and Generalized Network Flow Problems", Bertseka, D. P., and Tseng, P., Operations Research, Vol 36, No 1, Feb 1988

6. Algorithms for Network Programming, Kennington, J. L., and Helgason, R. V., John Wiley and Sons, New York, (1980)

7. Expert Systems and Fuzzy Systems, Negcita, C. V., Benjamin/; Publishing Co, Inc., 1985

8. "A Neural Network-Based Optimization Algorithm for the Static Weapon-Target Assignment Problem", Wacholder, E., ORSA Journal on Computing, Vol. 1, No. 4, Fall 1989.

9. "Successive Shortest Path Assignment Algorithm", Rosenthal R., Oroept, Naval Postgraduate School, Monterey, CA (408/646-2795)

USAF-UES SUMMER FACULTY RESEARCH PROGRAM

GRADUATE STUDENT RESEARCH PROGRAM

Sponsored by the

AIR FORCE OFFICE OF SCIENTIFIC RESEARCH

Conducted by the

Universal Energy Systems, Inc.

<u>FINAL REPORT</u>

<u>Methods Which Accelerate Convergence in
Iterative CFD Solvers</u>

Prepared by: John H. George

Academic Rank: Professor of Mathematics

Department and   Mathematics Department

 University: University of Wyoming

Research Location: AFATL/FXA

                    Eglin AFB, FL   33542-5000

USAF Researcher: Bruce Simpson

Date: 20 Aug 90

Contract No.:   F49620-85-C-0013

Methods Which Accelerate Convergence in Iterative CFD Solvers

by

John H. George

ABSTRACT

Several methods have been investigated to speed up the convergence of vector sequences generated in the solution of the Navier-Stokes equations. These methods include the generalized minimum residual (GMRES), the conjugate gradient squared (CGS), the generalized nonlinear minimal residual (GNLMR) as well as other vector extrapolation schemes. These methods have been coded, and the GNLMR is being included in a flow solver.

In addition, new techniques of unstructured grid generation are being developed based on the generalized Veronoi diagram concept for gridding complex regions. Several pieces of this code are already developed.

Acknowledgements

I. INTRODUCTION:

The numerical solution of the Navier-Stokes equations [1,5] over complex multiple bodies, needs many mathematical tools to obtain a solution. The final optimum solution does not currently exist, and will always need some user input to decide the combination of algorithms.

Often, a steady state solution is sought of the fluid motion around the particular configuration, but in the process, it is desirable to obtain a time accurate solution. The solution involves several complex techniques which will now be described. A transformation from physical space to computational space (rectangular) is introduced. This allows proper application of the correct boundary conditions to the body.

The most common method of grid generation is to solve a Poisson equation for the grid, adjusting the right hand side to avoid "singularities" in the grid, then piecing together the grids for each main component. This procedure is used in the EAGLE code, as well as the GRAPE algorithm.

Any grid generation computation involves a lot of user input, and cannot be used without some expertise. One way to make the generation of a grid more user-friendly is to have the code generate the grid from a given placement of the grid points on the boundaries. This is the idea of the method of unstructured

grids. The use of unstructured triangular grids for grid generation is an attactive alternative to the elliptically generated grid. Unstructured grids are often used in finite element solvers, which are being used by some CFD'ers. The grid generation can be used with a finite volume formulation of the flow, which is similar to the finite difference solution.

Steve Kennon [3] has recently developed a "C" code called Sugar2D which is based on a generalization of the Voronoi diagram and Delaunay triangulation. Sugar2D does not permit a violation of the solid boundary in the gridding process, by introducing the concept of a 'generalized boundary node'. The incremental point insertion method used by Bowyer and later by Jameson is used to generate the unstructured grids.

II. OBJECTIVES OF THIS RESEARCH EFFORT:

The problem of speeding the convergence of the flow solver is a complex problem due to the strong nonlinearities and the large dimensionality of this class of problems.

One method for improving convergence is to start with a 'good' grid. In this option, we are exploring the use of the unstructured grid solvers, such as the generalization by Kennon, and to incorporate the concept of domain decomposition into the grid construction.

On another level, the solutions can be calculated in less
iterations if a more efficient use can be made of the residual
which is calculated at each step. Here, the objective is to use
the methods of conjugate gradient and minimum residual to obtain
a new improvement to the solution that converges in fewer
iterations.

III. ORGANIZATION:

We are investigating the possibility of moving the grid via a
moving grid scheme such as the moving finite element method.
Another possibility is to use a 'Monte Carlo' scheme to add
random points into the original region, along with a
partitioning scheme to block the problem into regions that can be
treated relatively independent (domain decomposition) [4] which
would permit a vectorization of Kennon's gridding concept.

While the unstructured grid has great promise in automating the
gridding of complicated structures, the resulting flow solver
has trouble when using the conventional LU splitting, because of
the irregular matrix structure. The use of solvers such as the
conjugate gradient method involves only the multiplication of
the resulting Jacobian by an arbitrary vector. This a promising
alternative to LU solution methods for unstructured grids.
This technique has had good success in complex oil reservoir
simulations.

Any improvement in the computional efficency of a typical flow
code should have immediate impact on the entire class of CFD
numerical methods, so the next step in this research is to apply
the conjugate gradient class solvers to a typical problem. It
is hoped this research will continue with funding from the Mini
Grant Program.

The basic premise is that if the equations can be solved with more
accuracy at each step, then the resulting trek to steady state
will be much faster. The same premise should yield better
solutions to unsteady problems by obtaining a more accurate
solution at each step than the LU factorization.

The use of methods to improve convergence of sequences has a long
history and goes back to improving the convergence of power
series and convergence of sequences. For example, the Shanks
transformation transforms a slowly convergent sequence into a
sequence which converges faster. (See Smith, Ford and Sidi SIAM
review '87' for a comprehensive review) [9]. The Shanks
transformation was the first evidence that methods could be
devised to improve the convergence of sequences.

The application to CFD problems is complicated by the fact that
the highly nonlinear interactions cause many problems. The
main class of methods we are looking at involve using the
conjugate gradient method to accelerate an existing code. The
idea is that oscillations caused by complex eigenvalues can

greatly slow the convergence history. As the problem complex
eigenvalue propagates through the system of nonlinear
equations, by minimizing the new residual using a fixed set of
residuals from past iterations, the determination of the
parameter k is critical as it determines the number of
eigenvalues that will be 'filtered' out of the iteration. The
generalized minimum residual idea is due to Saad and Schultz [7].
A nonlinear version of the generalized minimum residual [2],
with a carefully chosen residual that permits a solution, will be
used on an actual CFD code such as Redcoon.

This summer research has produced several research codes,
1. The GMRES code with an arbitrary fixed number of vectors
needed to "filter" the frequencies that are retarding
convergence.
2. The CGS code converges very rapidly given a good
approximation to the solution.
3. A code to evaluate various preconditioners using the
singular valued decomposition.

IV. RECOMMENDATIONS:

The application of the conjugate gradient class of solution to a
real flow solver is the highest priority. To validate the
concept, the use on a actual problem is essential. The
nonlinear generalized residual scheme [2] is the most promising
possibility for speeding convergence.

The conjugate gradient solvers will be tried on an actual nonlinear solver to improve the LU splitting accuracy. The CGS [6] method is an ideal candidate for a quick improvement in the accuracy of the solution.

A carefully designated unstructured grid generation scheme using the generalized Voronoi concept will be investigated for possible use of the concept of domain decomposition to produce a grid on an arbitrary multiply connected region.

REFERENCES

[1] Anderson, D.A., Tannehill, J.C., and Pletcher, Richard H., _Computational Fluid Mechanics and Heat Transfer,_ Hemisphere Publishing Corporation, New York, 1984.

[2] Huang, C-Y., Kennon, S.R. and Dulikravich, G.S., "Generalized nonlinear minimum residual (GNLMR) method for iterative algorithms", _J. Comp. and Appl. Math._ 16 pp. 215-232 (1986).

[3] Kennon, S.R. "A new look at finite-volume methods", SBIR Contract F08635-89-C-0211, Final Report MDA Engineering Inc., Arlington, Texas, July 1989.

[4] Meurant, G., "Domain decomposition methods for partial differential equations on parallel computers", _Int. J. of Supercomput._ Appl. 2 No. 4 pp. 5-12 (1988).

[5] MacCormack, R.W., "Current status of numerical solutions of the Navier- Stokes equations", _AIAA-85-0032._

[6] Sonneveld, P., "CGS, a fast Lanczos-type solver for nonsymmetric linear systems", _SIAM J. SCI. STAT. COMPUT._ 10 pp.36-52 (1989).

[7] Saad, Y., and Shultz, M.H., "GMRES: A generalized minimum residual algorithm for solving nonsymmetric linear systems", _SIAM J. SCI. STAT. COMPUT._ 7 pp. 856-869 (1986).

[8] Smith D., Ford, W.F., and Sidi, A., "Extrapolation methods for vector sequences", _SIAM Review_ 29 pp 199-232 (1987).

1990 USAF-UES SUMMER FACULTY RESEARCH PROGRAM

GRADUATE STUDENT RESEARCH PROGRAM

Sponsored by the

AIR FORCE OFFICE OF SCIENTIFIC RESEARCH

Conducted by the

Universal Energy Systems, Inc.

<u>FINAL REPORT</u>

<u>Designing A Binary Phase Only Filter
Via The Genetic Algorithm</u>

Prepared by: Frederick W. Gibson

Academic Rank: Instructor

Department and   Mathematics Department

 University: Morehouse College

Research Location: AFATL/AGA
                      Eglin AFB
                      Ft. Walton FL 32542

USAF Researcher: Tom Davis

Date: 24 Aug 90

Contract No: F49620-88-C-0053

Designing A Binary Phase Only Filter
Via the Genetic Algorithm
by
Frederick W. Gibson

ABSTRACT

The design of a binary phase only filter for three different binarized test targets (re-entry vehicle, booster and decoy) is obtained using the Genetic Algorithm (GA). The GA is a search procedure based upon the mechanics of natural genetics, blending a Darwinian survival-of-the fittest principle with a random yet structured information exchange among a population of artificial chromosomes. Our results show that GAs are able to design binary phase only filters for each of the three binarized test targets by searching over a 256 total pixel search space. The filter designed for each binarized test target is compared against the other two binarized test targets to determine how well that particular binary phase only filter rejects the other binarized test targets. Because of its ease in operation and simple requirements as compared to many other optimization methods, the GA may find wide application within the field of applied optics.

Acknowledgements

I wish to thank the Air Force Systems Command and the Air Force Office of Scientific Research for sponsorship of this research. I also wish to acknowledge Universal Energy Systems for their concern and help to me in all administrative and directional aspects of this program.

My experience was rewarding and enriching because of my many different influences. Dr. Dennis Goldstein is greatly appreciated for providing a truly enjoyable working atmosphere and the optimization problem to be researched. The concern and encouragement of Tom Davis in every phase of this project served as a valuable source of stimulation. Capt David Calloway provided me with programming support, encouragement and a stimulating relationship. The help of Capt Jeff Barnes and Mr. and Mrs. Otto Martinez was invaluable in overcoming many computer software roadblocks.

I.   INTRODUCTION:

The Genetic Algorithm has been established as a valid approach to problems requiring efficient and effective search. This search algorithm offers potentially good convergence behavior which we apply to the design of a binary phase only filter.

The Air To Air Guidance section of the Advanced Guidance Division of the USAF Armament Laboratory at Eglin Air Force base is particularly concerned with detecting and classifing various types of military targets. The design of the binary phase only filter via the Genetic Algorithm is a vast improvement over the Simulated Annealing stochastic search technique[6] that has previously been applied to this optimization problem. Due to the slow convergence behavior of the Simulated Annealing Algorithm we feel that the search capabilities of the genetic algorithm make the GA a valid alternative approach.

My research interests have been in the area of applied mathematics and computer investigation to real life applications. My work as a research assistant in performing analysis on picture signal processing and educational software as well as my background in operations research has contributed to my investigation of the design of binary phase only filters via the Genetic Algorithm.

II. OJECTIVE OF THE RESEARCH EFFORT:

Currently, there is no evidence of the design of a binary phase only filter via the Genetic Algorithm. This algorithm, which offers potentially improved convergence behavior, has been established as a valid approach to solving optimization problems. Another search technique, the Simulated Annealing Algorithm, has been applied to the design of the matched filter optimization problem and offers a high potential payoff for targeting weapons applications. It involves computer generation of scale and filter designed to detect and classify various types of military targets. However, this search algorithm offers very slow convergence behavior which we hope to improve.

My assignment as a participant in the 1990 Summer Faculty Research Program (SFRP) was to determine if the Genetic Algorithm is adaptable to the design of a binary phase only filter. It was determined that the Genetic Algorithm designed binary phase only filters capable of distinguishing between each of the three test targets (re-entry vehicle, booster and decoy). Thus the Genetic Algorithms was specific enough to be of use in designing filters for military applications.

Since the Genetic Algorithm was able to design filters for images of size 16x16, investigation into the development of filters for larger images (say 128x128 and 256x256) should be undertaken through continued research.

III.   Binary Phase-Only Filters

A common technique in pattern recognition is to perform a cross-correlation between an unknown image and a pattern that is to be recognized. If the image contains the pattern, then the cross-correlation results in a peak with optimal signal-to-noise ratio. If the image does not contain the pattern, then this operation typically results in a low correlation peak. The correlation operation is efficiently performed in the frequency domain by Fourier transforming the image and the pattern and then inverse Fourier transforming their mutual power spectrum. This approach is known as the Classical Matched Filter.

In a paper by Oppenheim and Lim[7], they demostrated the importance of phase information in visual images. They showed that while many images could be reconstructed from phase-only information, magnitude-only information was typically not sufficient to reconstruct most visual images. Gianino and Horner[3] used this information to produce a modified matched filter in which all magnitude information was set to unity. The resulting filter contained only phase information and was thus called a phase-only filter.

Surprisingly, the phase-only filter produced by normalizing all magnitude information is superior (in terms of producing higher SNR correlations) then the matched filter on which it is based. In addition, phase filters are especially useful in optical image recognition systems since they pass 100% of the incident energy while matched filters attenuate much of the input signal.

Most real-world images have very little high frequency energy. However, the features that we use to differentiate one image from another are often contained in the "edge" information represented by this small amount of high frequency data. The phase-only filter effectively performs a high-pass filter since setting all frequency magnitudes to unity emphasizes the high frequencies more than the corresponding matched filter. This explains, in part, why the phase-only filter outperforms the matched filter in typical pattern recognition tasks.

A Binary Phase-Only Filter (BPOF) is a phase-only filter in which the phase information is binarized to contain only two phase values. This is typically accomplished by setting all positive phases to π radians and all negative phases to 0 radians. The resulting filter preserves little of the original information: The magnitude information is set to unity at all frequencies and the phase information is represented by only a single bit at each

frequency. Nevertheless, BPOF filters are generally as proficient as the classical matched filter in correlating unknown images with stored patterns. They are especially useful in optical systems using a binary Spatial Light Modulator (SLM).

IV. The Genetic Algorithm

Genetic Algorithms (GAs) according to Goldberg[8], are search algorithms based on the mechanics of natural selection and natural genetics. They combine an artificial survival of the fittest among string structures with genetic operators abstracted from nature to form a surprisingly robust search mechanism that is suitable to a variety of search problems.

Genetic Algorithms use finite-length codings of problem parameters (artificial chromosomes) rather than the parameters themselves. By refusing to adopt a particular problem structure and by exploiting similarities in codings, GAs can achieve greater breadth of applicablity than would otherwise be possible. GAs use a population-by-population approach rather than the point-by-point technique adopted by more traditional schemes. By working from a population, GAs are less likely to be fooled by false optima.

A simple GA consist of three operators: Reproduction, Crossover and Mutation.

Reproduction incorporates the survival of the fittest within the GA. There are many ways to achieve effective reproduction. Ranking, tournament, and proportionate reproduction methods have all been used with success. One simple proportionate scheme selects individual strings for reproduction according to their fitness, where fitness is defined as the nonnegative figure of merit being maximized. When this is done, individuals with higher fitness values have a higher probability of being selected for mating and subsequent genetic action.

Crossover is a randomized yet structured recombination operator. Simple crossover proceeds in three steps. Two individual strings are picked using the reproduction operator. In single-point crossover a cross site along the string length is selected at random, and positions are swapped among the two strings following the cross site. For example, starting with two strings A= 11111 and B= 00000, if the random selection of a cross site turns up a 3, we would obtain the two new strings A'= 11100 and B'= 00011 following crossover, and these strings would be placed in the new population.

In a binary-coded GA, Mutation is the occasional (with low probability) alteration of a bit position (the changing of a 1 to a 0 and vice versa). By itself mutation is a simple random walk through the string space. When used sparingly in combination with reproduction and crossover, mutation

is an insurance policy against the loss of important genetic material at

a particular position. The low level of mutation used in most artificial

genetic search is evidence of secondary importance of the operator when

compared to reproduction and crossover.

The images for which we would like to design a binary phase only filter

are two dimensional. Thus, we felt that a two dimensional crossover was

necessary for implementation in the Genetic Algorithm program. Currently

there are no published articles on the two dimensional crossover we are

utilizing in this GAs.

PARENT 1   PARENT 2

	vert. & hori.			vert. & hori
	cross site			cross site
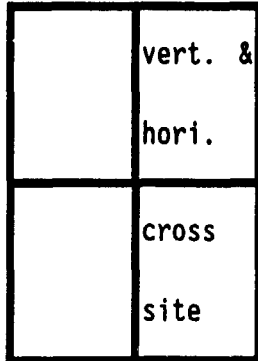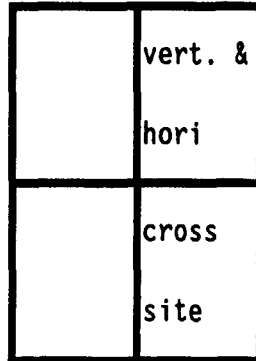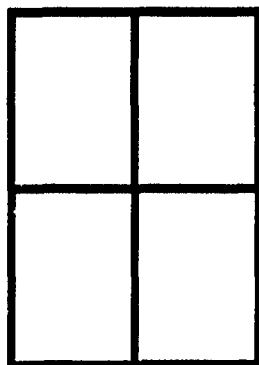
Child 1   Child 2
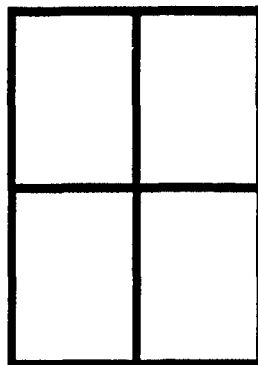
Our two dimensional crossover produces four quadrants. The crossover sites

are the same in each individual parent (as indicated in the above diagram).

Two   children are produced from their parents.   The outcome of four

independent coin tosses determines whether the alleles in each quadrant

pass from parent1 to child1 and parent2 to child2 (no crossover) or from

parent1 to child2 and parent2 to child1 (crossover). Rather than keeping

the offspring as the new population, we check to see who has the higher

fitness values of the two parents and two offsprings. The two individuals

with the best fitness value are assigned to the new population. This

process is continued until the new population is filled.

The fitness function used in our implementation of the genetic algorithm

is based on the signal-to-noise ratio[4] (SNR) resulting from the cross-

correlation between the reference image and the BPOF represented by an

individual's GA chrosmosome. The SNR was defined as the ratio of the correlation peak maximum amplitude to the rms noise response elsewhere in the correlation plane. The correlation peak is assumed to contain all pixels at or above 50% of the m: :imum amplitude in the plane.

$$SNR = \frac{[R(x_i)]^2_{max}}{N_{rms}}$$ (1)

$$N_{rms} = \left(\sum_{A=A'} \frac{|R(x_i)|^2}{(N_A - N_A')} \right)^{.5}$$ (2)

Where N_A is the total number of pixels in the correlation plane and N_A' is the number of pixels considered to be in the correlation peak region.

The sequence of steps in evaluating the fitness of each individual in the population starts with a Fourier transform of the image to be recoynized and the chromosome for the member of the population to be evaluated. Each gene in the chromosome represents one element of a BPOF. The BPOF is produced from the chromosome by setting the corresponding phase to Π radians if the allele is a one and setting the phase to zero if the allele is zero. All magnitude information in the filter is set to unity. The reference image is then filtered using this BPOF and the resulting spectrum is inverse Fourier transformed (using a two-dinensional FFT) to produce a correlation in the spatial domain. The SNR in the correlation plane is evaluated as described above, and this signal-to-noise ratio is used as the fitness

6-12

value for the individual.

V.   Analysis of Results

In general, we would expect a filter designed to detect a particular image to produce a high SNR if a cross-correlation between that binarized image and the filter is performed. Conversely, appling the filter to an image that it was not designed to detect should result in a low correlation peak. This is exactly the type of analysis we performed. That is, we used the GA to design a binary phase only filter for the re-entry vehicle (see test data) and performed a cross-correlation between the resulting filter and this pattern. The binary phase only filter was able to recongnize this pattern as indicated by the high SNR in the correlation plane (see RV vs. RV illustration).

The filter designed for the re-entry vehicle was then applied to the image of the decoy (see test data). Just as we expected this operation resulted in a peak with a low signal-to-noise ratio (see RV vs. Decoy illustration).

Finally the filter designed for the RV was applied to the booster (see test data) and again this operation yielded a very low SNR (see RV vs. booster illustration).

Binary phase only filters were designed for the the decoy and booster images as well. As we expected, applying these filters to the targets themselves as well as the other binarized targets supported the previous finding. That is, the decoy and booster BPOF when applied to the decoy and booster images, respectively yielded correlation peaks with high SNRs. However, when cross-correlated between the other binarized targets the end result was low correlation peaks.

In our bar charts we show the comparison of the SNRs of the test data. The first chart shows the SNR resulting from appling the RV RPOF to the RV, booster, and decoy images. Notice that the RV BPOF vs RV image produces a higher BPOF SNR than that of the booster or the decoy. This indicates that the BPOF produced by the GA can indeed distinguish between an image of an RV and a decoy or booster.

We also illustrate in the other bar chart the SNR performance of the GA binary phase only filter, the classical matched filter, the continous phase only filter (CPOF), and the conventional BPOF. The CPOF has the highest SNR. However, there is no binarization in this filter. Clearly the GA BPOF has better performance than the classical matched filter or the conventional BPOF. Notice that the classical matched filter and the BPOF perform about the same.

VI. Recommendations

This preliminary investigation of the design of the binary phase only filter via the genetic algorithm has shown to be promising and may be the key to improved convergence for this type of optimization problem. Continued research for upscale images of size 128x128 and 256x256 should be investigated using the GAs. Also the presence of noise should be introduced to determine how well the binary phase only filter designed via the GAs will perform under this added condition.

Other routines for enhancement of the genetic algorithm should be implemented.   That is, scaling of the fitness values (to avoid premature convergence), selecting three or more crossover sites at random to yield more offspring for the new population, and inducement of niche and species[8] (sharing among individuals) to help GAs search.

The computer time for generating a population of 100 individuals for 250 generations took approximately 12 hours on a zenith 286 AT system. For bigger images (128x128 or 256x256) we suggest a larger computer possibly a VAX system to handle these runs successfully.

VII.   TEST DATA

Below are three images with an embedded pattern centered in the middle.
These 16x16 images are composed of binary alphebets (zeros(.) and ones(#)).
The ones represents the on position of the pattern and the zeros the off
position. These images are without noise.

fig.1   Re-entry vehicle - the return of a missile or spacecraft
                            to the earth's atmosphere.

```
. . . . . . . . . . . . . . . .
. . . . . . . . . . . . . . . .
. . . . . . . . . . . . . . . .
. . . . . . . . . . . . . . . .
. . . . . . . . . . . # # # . .
. . . . . . # # # # # # # # . .
. . . . # # # # # # # # # # # .
. # # # # # # # # # # # # # # .
. . . # # # # # # # # # # # # .
. . . . . . # # # # # # # # # .
. . . . . . . . . # # # # . .
. . . . . . . . . . . . . . . .
. . . . . . . . . . . . . . . .
. . . . . . . . . . . . . . . .
. . . . . . . . . . . . . . . .
. . . . . . . . . . . . . . . .
```

fig.2 Booster - Initial stages of an ICBM.

```
. . . . . . . . . . . . . . . .
. . . . . . . . . . . . . . . .
. . . . . . . . . . . . . . . .
. . . . . . . . . . . . . . . .
. # # # # # # # # # # # # # . .
. # # # # # # # # # # # # # # .
. # # # # # # # # # # # # # # .
. # # # # # # # # # # # # # # .
. # # # # # # # # # # # # # # .
. # # # # # # # # # # # # # # .
. # # # # # # # # # # # # # # .
. . . . . . . . . . . . . . . .
. . . . . . . . . . . . . . . .
. . . . . . . . . . . . . . . .
. . . . . . . . . . . . . . . .
. . . . . . . . . . . . . . . .
```

fig.3 Decoy - a spherically shaped object with the
                same radar cross-section as the RV.

```
. . . . . . . . . . . . . . . .
. . . . . . . . . . . . . . . .
. . . . . . # # # . . . . . . .
. . . . . # # # # # # . . . . .
. . . . . # # # # # # # . . . .
. . . . . # # # # # # # # . . .
. . . . # # # # # # # # # . . .
. . . . # # # # # # # # # . . .
. . . . # # # # # # # # # . . .
. . . . . # # # # # # # # . . .
. . . . . # # # # # # # # . . .
. . . . . . # # # # # # # . . .
. . . . . . . # # # . . . . . .
. . . . . . . . . . . . . . . .
. . . . . . . . . . . . . . . .
. . . . . . . . . . . . . . . .
```

VIII.   Figures and Bar chart

The following figure illustrates the correlation between the BPOF produced

by the GA using the RV as a scoring image when applied to this image.
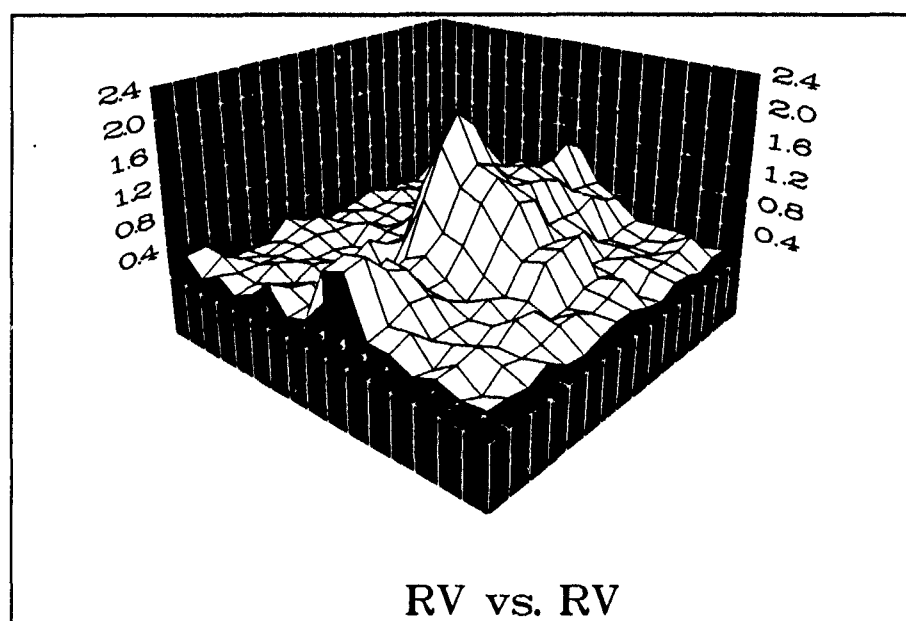
RV vs. RV

The next two figures illustrate the result of applying this same filter

to the other two images. Notice that the correlation peak is not as sharp

as the RV vs RV case and the noise floor is higher.
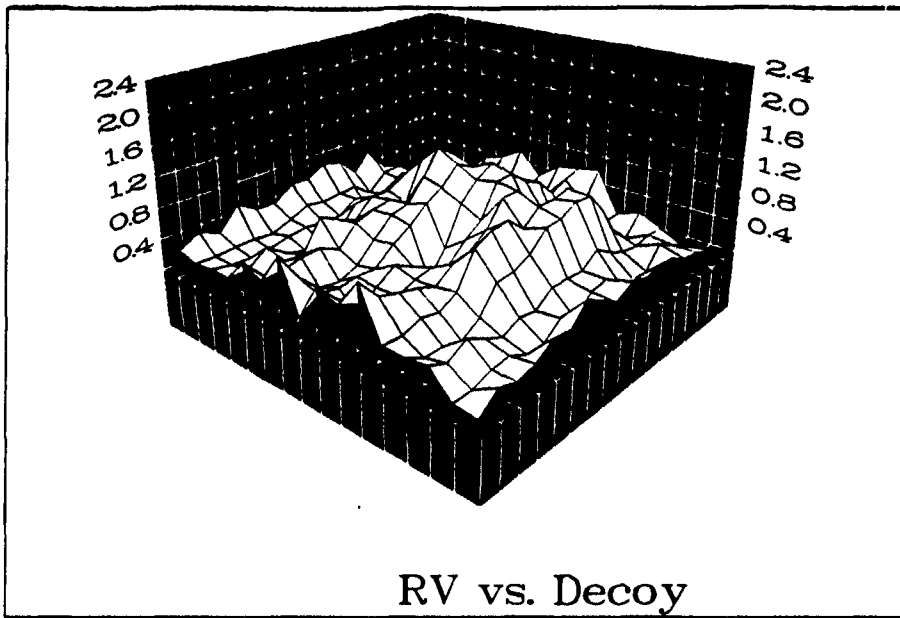
RV vs. Decoy

RV vs. Booster

Signal to Noise Ratio
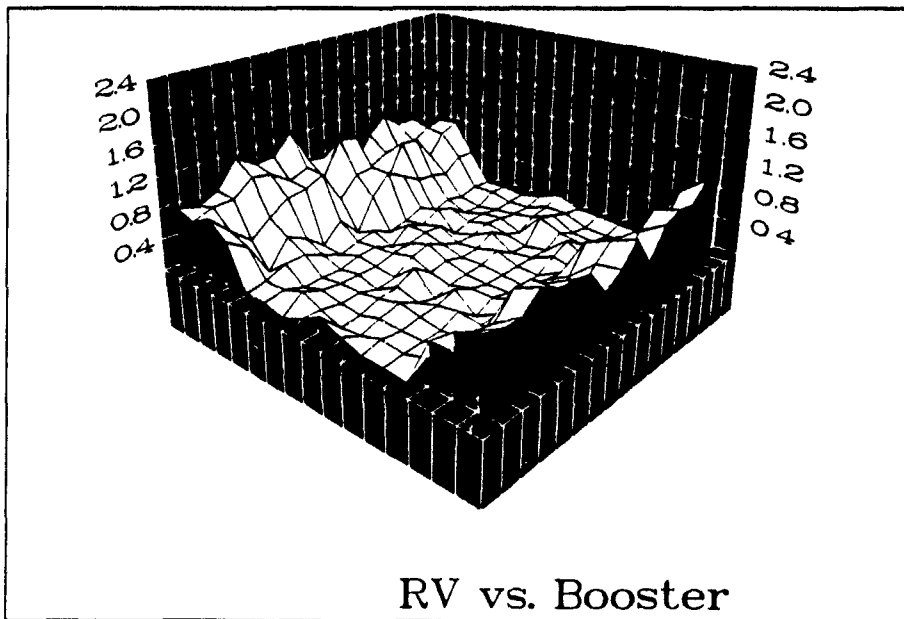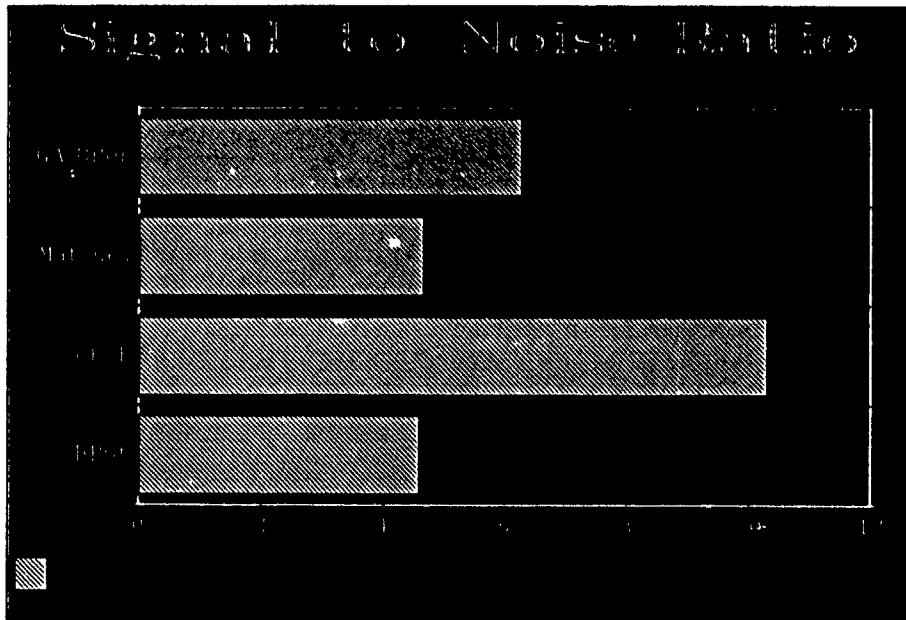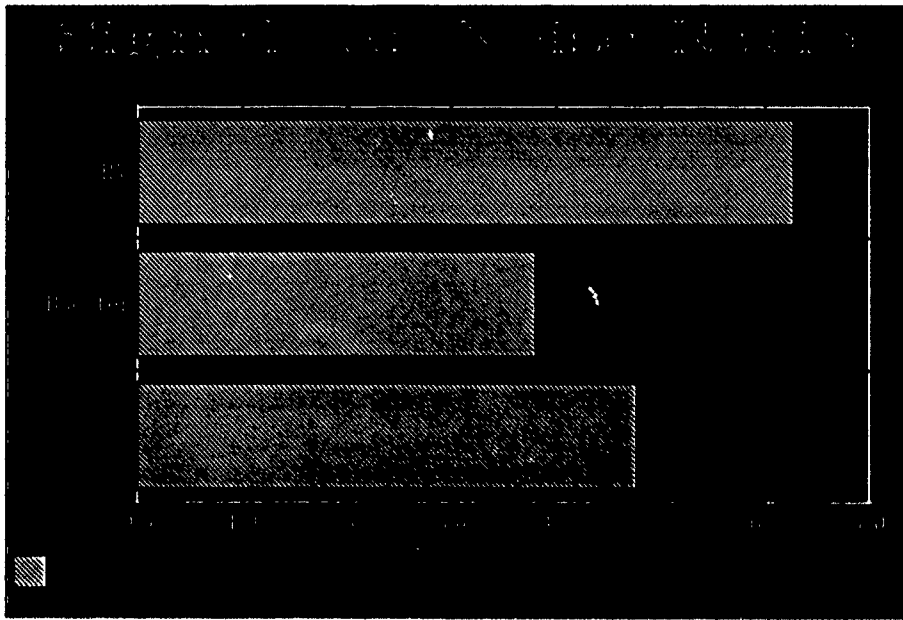
REFERNCES

Conference and journal publications:

1. Bartelt, H., Horner, J. Improving binary phase correlation filters using iterative techniques. <u>Applied Optics</u>. 1985,Vol.24,pp2894-7.

2. Davis, J.A., D.M. Cottrell, G.W. Bach and R.A. Lilly. Phase-Encoded Binary Filter for Optical Pattern Recognition. <u>Applied Optics</u>. 1989,Vol.28,pp.258-61.

3. Horner, J.L., P.D. Gianino. Phase-Only Match Filtering. <u>Applied Optics</u>. 1984, Vol.23,pp.812-6.

4. Horner, J.L., H.O. Bartelt. Two-Bit Correlation. <u>Applied Optics</u>. 1985, Vol.28,pp.258-61.

5. Horner,J.L., P.D. Gianino. Applying the Phase-Only Filter Concept to the Synthetic Discriminant Function Correlation Filter. <u>Applied Optics</u>. 1985,Vol.24,pp.851-5.

6. Kim,M.S., C.C. Guest. Simulated Annealing Algorithm for Binary Phase Only Filters in Pattern Classification. <u>Applied Optics</u>. 1990,Vol.29,pp1203-8.

7. Oppenheim A.V., Lim,J.S. The Importance of phase in Signals, <u>Proc. IEEE Internatiol Pulse Power Conference</u>, Vol.69, No.5,May 1981.

Texbooks:

8. Goldberg, David E., <u>Genetic Algorithms in Search, Optimization and Machine Learning</u>, New York: Addison-Wesley Publishing Company, Inc

1990 USAF - UES SUMMER FACULTY RESEARCH PROGRAM

Sponsored by the

AIR FORCE OFFICE OF SCIENTIFIC RESEARCH

Conducted by the

Universal Energy Systems, Inc.

<u>FINAL REPORT</u>

Two-Dimensional Simulation of Railgun Plasma Armatures

Prepared by: Manuel A. Huerta, Ph. D.   and G. Christopher Boynton

Academic Rank: Professor   Graduate Student

Department and   Physics Department

University: University of Miami

Research Location: AFATL/SAH

                    Eglin AFB, FL 32542-5000

Effort Focal Point: Mr. Kenneth K. Cobb

Address: AFATL/SAH

                  Eglin AFB, FL 32542-5434

Date: 22 August 1990

Contract No: F49620-88-C-0053

Two Dimensional Simulation of

Railgun Plasma Armatures

by

Manuel A. Huerta
G. Christopher Boynton

ABSTRACT

We report on our work in incorporating a more realistic initial state and rail ablation into our two dimensional MHD code to simulate the internal dynamics of a railgun plasma armature. Our code uses the equations of resistive MHD, with Ohmic heating, and radiation heat transport. All quantities are advanced in time using an explicit Flux Corrected Transport scheme. Careful examination of our output has revealed very short lived weak secondary arcs that grow and move very rapidly to the rear and contribute to heating the rear region. Preliminary runs with a new initial state show an interesting accumulation of current toward the rear of the armature. Most of our work was spent in developing and coding our model for the ablation. The problem of heat transport in the rail was considered in detail in calculating the rise of rail temperature at the surface, and in calculating the amount of ablation. The rate of heat flux into the rail is basically σT_e^4, where T_e is the effective radiation temperature that the rail sees. This temperature is calculated in the two dimensional simulation using various approximations that remain to be tested. We also include the heat due to the anode and cathode drops. The time required for the rail to reach the vaporization temperature depends on T_e^8. This is an extraordinarily high sensitivity to any variations in the temperature.

Acknowledgements

I would like to thank the Air Force Systems Command and the Air Force Office of Scientific Research for sponsorship of this research. I would also like to thank Universal Energy Systems for the efficient way in which they administered the USAF - UES Summer Faculty and Graduate Student Research Programs.

I spent the summer at AFATL together with my graduate student, Mr. G. C. Boynton. Our experience was productive and enjoyable thanks to the cooperation we received from many people at AFATL. We would specially like to thank Mr. Kenneth K. Cobb who helped us so much in getting access to the computer resources that we needed. We also thank him for useful discussions of work in rail guns. We had fruitful discussions with several people, specially Dr. Glen Rolader of SAIC, and Dr. Chia Thio, newly of the University of Miami, who was at site A15 collaborating with Dr. Eugene Clothiaux of Auburn University. We thank Mr. Andy Marino for setting us up with abundant disk space and other resources on the VAX 8650 at site A15, and for his system assistance.

I. INTRODUCTION

I have spent the summer working at AFATL/SAH, site A15, together with my graduate student Mr. G. C. Boynton who was supported under the 1990 USAF Graduate Student Research Program. Mr. Boynton and I have been working on a two dimensional simulation of armature plasmas. Our main objective this summer was to improve our model by incorporating rail ablation. One of our principal needs is access to computing power to run our programs. Even though our code should be run on a supercomputer we benefited from abundant access to the VAX 8650 available at site A15 for debugging purposes.

An impressive railgun facility has been built on Okaloosa Island at site A15 and there is quite a bit of experimental activity on diagnostics of the arc plasma armature. We found it very useful to interact with people involved with the experiments in deciding on specific details of our simulation. Our conversations with Mr. Kenneth Cobb were important in motivating us to look carefully at the heat diffusion in the rails in formulating an ablation model. Our discussions with Dr. Chia Thio were specially useful in clarifying the radiation heat transport to the rails. We also profited from discussions with Dr. Glen Rolader of SAIC who has a lot of experience with one dimensional simulations.

We model the plasma with the equations of resistive MHD and we use a two dimensional fully explicit FCT code to advance all quantities in time. Our model includes the Spitzer conductivity and heat conductivity in the radiation diffusion approximation. The physical effects that we include in our model are the same as in the steady, one dimensional model of Powell and Batteh[1]. Therefore we leave out viscosity, and other effects that can be important in a boundary layer. A good deal of effort has also been expended on developing graphical methods that

allow convenient display of the results. We have published two papers[2,3] on this work. A third one was presented at the 5th Symposium on Electromagnetic Launch Technology in Sandestin, Florida last April. It should appear in the January 1991 issue of the IEEE Transactions on Magnetics dedicated to EML's. This last paper shows that our simulation describes the formation of a secondary arc far to the rear of the armature. This sort of arc is considered by many people to be of importance in degrading the performance of railguns.

II. OBJECTIVES OF THE RESEARCH EFFORT

In our previous simulations we took the initial state of the plasma to be closely related to the equlibrium calculated by Powell and Batteh[1]. Our intention was to show that the rear region of the equilibrium would be disturbed by instabilities so material would be left behind the arc. We believe this has been shown satisfactorily. One of our objectives this summer was to develop a simulation with an initial state more closely related to the experimental situation to use in future simulations.

Rail and insulator ablation are considered to be among the most important effects in degrading the performance of railguns. The two main issues are to get the right amount of ablation, and to describe how the ablated material is entrained into the main plasma arc. If the ablated material were left behind the plasma arc, as it tends to be, it would do little to slow down the velocities reached. The ablated material seems to be entrained by the formation of secondary arcs far behind the main arc. Our simulations already produce secondary arcs without ablation. Therefore our main objective this summer was to incorporate rail ablation into our simulation. This should produce larger secondary arcs, and produce them at an earlier time, than our previous models. This would make the simulations agree more closely with experimental observations.

III. WORK ACCOMPLISHED

The availabilty of the VAX 8650 enabled us to do several runs of our original code and to examine the output carefully. Fig. 1 is a plot of the projectile acceleration vs. time. The oscillations are due to a longitudinal pressure wave. Near 0.00026 sec the acceleration dropped to a new average value. This seemed to indicate that we had lost some curent out the rear of our computational region. Fig. 2 shows the electrical conductivity σ at t=0.0002527 sec. The rear of the plasma is nonconducting, except that a small increase of σ can be seen on the 19th and 20th cells from the rear. Fig. 3 shows σ in the rear region in a greatly expanded scale after 160300 time steps, or t=0.00025269 sec., Fig. 4 after 160500, and Fig. 5 after 160600 time steps. These figures show how σ is growing in the rear region. This is caused by a small secondary arc moving very rapidly toward the rear. Figs. 6 and 7 show the rail to rail component J_y of the current density vector in the rear region in a very enlarged scale after 160400 and 160500 time steps. A truer picture of the current distribution in the entire plasma is shown in Fig. 8 where the current spike of Fig. 7 is hardly visible 12 cells from the rear. Fig. 9 shows the small secondary arc reaching the end of our computational region after 160600 time steps. The secondary arc grows as it moves back. This happens because the secondary arc produces local heating a bit to the rear. As the current commutes toward the newly conducting region it must grow due to the conservation of flux in this very fast time scale. We believe these results are encouraging for our code to describe the larger secondary arcs seen in experiments.

Our main effort was spent in putting ablation into our code. We divide each rail into R cells of length Δx_r. We calculate the heat flux into the rth cell $q(r, t)$ from

two sources. We take

$$q(r,t) = (1 - \alpha)q_{rad} + q_{sh}.$$

Here α is the reflectivity of the rail. q_{rad} is the radiation diffusion heat flux into the rail, calculated in the same way as in Ref. 1, evaluated 1/4 of a cell inward from the boundary of our computational region.

$$q_{rad} = \frac{16}{3}\sigma_{SB}\lambda T^3 \frac{\partial T}{\partial y_n},$$

where y_n is the coordinate normal to the rail and λ is the Roseland mean free path for radiation. We can also take

$$q_{rad} = \sigma_{SB}T_e^4$$

where T_e is the temperature at depth λ from the boundary of the computational region. q_{sh} represents the heat flux due the contact potential that exists at the plasma sheath next to the rail. We take $q_{s}h$ to be

$$q_{s}h = \frac{1}{2}J_y V_s$$

where V_s is the sheath voltage. Of course one must be careful that each rail cell gets heat from the plasma cell that is in front of it.

The rails need to be heated from their initial temperature T_0 to the ablation temperature T_v, which we take equal to the vaporization temperature of tha rail material. We need the solution for the rail temperature at a depth y given the heat flux $q(r,t)$ at the $y = 0$ surface. Neglecting heat diffusion along the rails, the solution for the temperature at a depth y from the surface of the rth cell is

$$T(y,r,t) = T_0 + \frac{2}{\pi c \rho}\int_0^t dt' q(r,t')\sqrt{\frac{\pi}{4\nu(t-t')}}exp[\frac{-y^2}{4\nu(t-t')}].$$

7-7

where c is the specific heat, ρ the density, $\nu = \kappa/c\rho$ is the heat diffusivity, and κ is the heat conductivity. At the $y = 0$ rail surface this is

$$T(r,t) = T_0 + \frac{2}{\pi c\rho} \int_0^t dt' q(r,t') \sqrt{\frac{\pi}{4\nu(t - t')}}.$$

Unfortunately this quantity is a convolution integral that at each time step requires us to do an integral that goes back to the beginning of time. This is too burdensome in terms of CPU time. Therefore we deviced an approximation based on the result

$$T(r,t) = T_0 + \frac{q(r,av)}{\kappa} \sqrt{\frac{4\nu t}{\pi}},$$

where $q(r,av)$ is the average heat flux into the rail, that is exact if $q(r,t)$ is constant in time. We define

$$q(r,av) = \frac{1}{t} \int_0^t q(r,t') dt' \equiv \frac{1}{t} E(r,t), \tag{1}$$

where $E(r,t)$ is the total heat input into the rail element.

New cells appear as the projectile passes and others disappear as they reach the end of our computational region. They are managed in such a way that the heat deposited in each cell is properly accounted for. We do this by defining an integer that counts how many cells have been passed by the projectile

$$I_c(t) = INT(\frac{d(t)}{\Delta x_r})$$

where $d(t)$ is the distance traveled by the projectile and INT is the Fortran integer function. If $I_c(t + \Delta t) = I_c(t)$ then we take

$$E(r, t + \Delta t) = E(r, t) + q(r, t)\Delta t$$

to increment the heat into the rth cell. If $I_c(t + \Delta t) = I_c(t) + 1$ then we take

$$E(r, t + \Delta t) = E(r - 1, t) + q(r, t)\Delta t.$$

We decide ablation begins when the rail surface reaches the vapor temperature. Based on the approximation of Eq. (1) we test when

$$E(r,t) \geq [c_s\rho_s(T_m - T_0) + L_m\rho_m + c_m\rho(T_v - T_m)](\sqrt{\frac{\pi\nu t_{ex}(r)}{4}} \qquad (2)$$

where $t_{ex}(r)$ is the time that cell r has been exposed, and the subscripts s, m, and v refer to solid, molten , and vapor. We do not treat the change in the heat conductivity of solid to liquid. After Eq. (2) is satisfied at time $t = t_v$ we take it that ablation begins. Not all the heat flux $q(r,t)$ goes to ablate material because some heat flux $q_l(r,t)$ is lost by diffusion into the rail. The temperature at the rail surface stays at T_v and the solution in the interior is

$$T(y,r,t) = \frac{2T_v}{\sqrt{\pi}} \int_s^\infty du\, e^{-u^2}, \quad \text{where} \quad s = \frac{y}{\sqrt{4\nu(t - t_v)}}. \qquad (3)$$

From Eq. (3) we calculate that

$$q_l(r,t) = -\kappa\frac{\partial T}{\partial y}|_{y=0} = \kappa\frac{T_v - T_0}{\sqrt{\pi\nu(t - t_v)}}.$$

TYhis is an approximation that overestimates the $q_l(r,t)$ at early times. Then we calculate than an element of rail of area A ablates mass at the rate

$$\frac{\Delta m}{\Delta t} = A\frac{q(r,t) - q_l(r,t)}{L_v} \equiv s_a A\Delta y, \qquad (4)$$

where L_v is the latent heat to vaporize, and s_a is the ablated mass density which is to be added as a source of mass to the plasma cell of thickness Δy adjacent to the wall.

The fluid equations are the usual ones. First the equation of mass conservation, with ablation,

$$\frac{\partial\rho}{\partial t} + \nabla \cdot (\rho\mathbf{v}) = s_a, \qquad (5)$$

is used to advance ρ in time. The fluid velocities v_x and v_y in the frame of the projectile are advanced by the equations for the x and y components of momentum,

$$\frac{\partial(\rho v_x)}{\partial t} + \nabla \cdot (\rho v_x \mathbf{v}) = -\frac{\partial}{\partial x}(p + \frac{1}{2\mu_0}B_z^2) + \rho\frac{dv_p}{dt} + s_a v_p, \tag{6}$$

where the ablated mass is added at rest relative to the rails with a velocity v_p toward the rear in the frame of the projectile, and

$$\frac{\partial(\rho v_y)}{\partial t} + \nabla \cdot (\rho v_y \mathbf{v}) = -\frac{\partial}{\partial y}(p + \frac{1}{2\mu_0}B_z^2) + s_a v_a y. \tag{7}$$

The pressure p is advanced from the equation for the energy e per unit mass,

$$\frac{\partial(\rho e)}{\partial t} + \nabla \cdot (\rho e \mathbf{v}) + p\nabla \cdot \mathbf{v} = -\nabla \cdot \mathbf{q} + \frac{J_x^2}{\sigma} + \frac{J_y^2}{\sigma} + s_a e_a, \tag{8}$$

and relating p to e using an energy equation. The simplest energy equation is for the monoatomic ideal gas with $\gamma = 5/3$,

$$e = \frac{p}{(\gamma - 1)\rho}. \tag{9}$$

IV. RECOMMENDATIONS

Our code has shown the potential to describe the main experimental facts. Now that we have put ablation into it we should be able to get a good description of secondary arcs. This should give valuable insights into the workings of plasma armatures. We recommend that this work be supported in the future.

REFERENCES

1. Powell, J. D., and Batteh, J. H., "Plasma Dynamics of an Arc-Driven Electromagnetic Projectile Accelerator," J. Appl. Phys., vol. 52, 2717 (1981)

[2] M. A. Huerta and G. C. Boynton, " Two-dimensional time dependent MHD simulation of plasma armatures", IEEE Trans. MAG., vol. 25, pp.238–242, Jan. 1989.

[3] G. C. Boynton and M. A. Huerta, " Two–dimensional MHD simulation of isothermal plasma armatures", IEEE Trans. Plasma Sci., vol. 17, pp. 468–475, June 1989.

ACCELERATION VS TIME

Figure 1

7-12
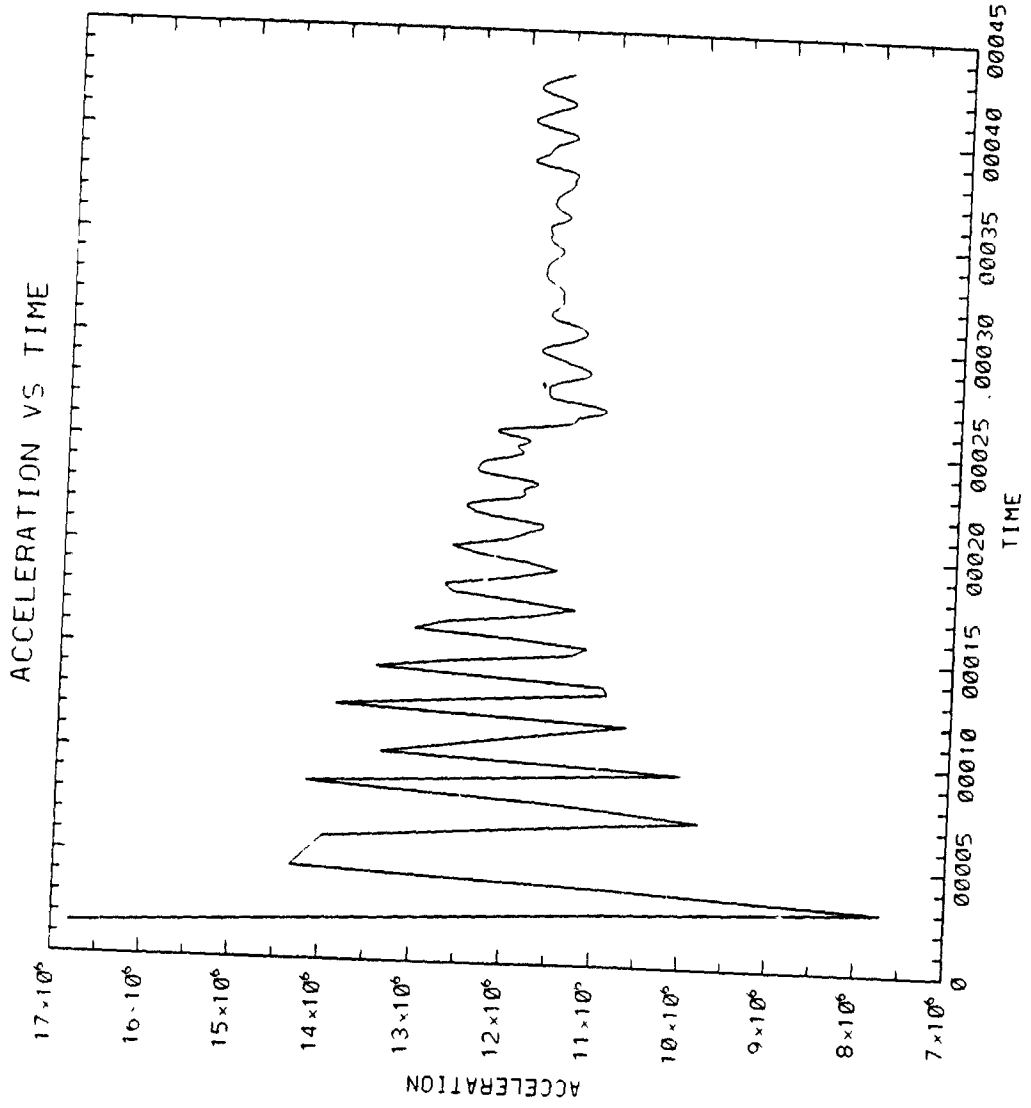
Figure 2

ETIME = 2.527377E-04s
GFRM = 1.19E+07m/s^2
VFRM = 4.1E+03m/s
SFRM = 6.4E-01m
Max = 6.68E+04
Min = 0.00E+00
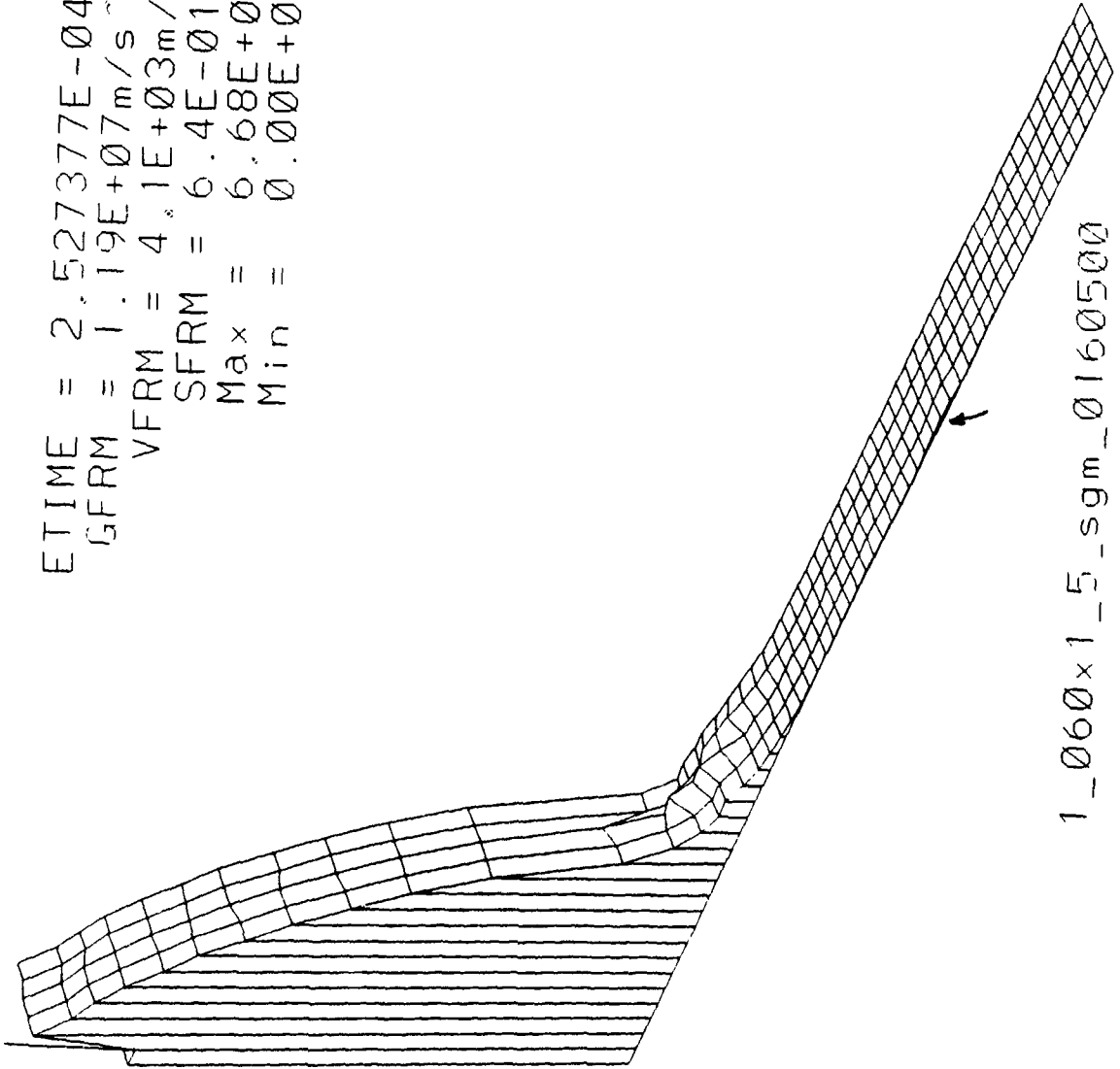
1_060x1_5_sgm_016050Ø

Figure 3

ETIME = 2.526911E-04s
GFRM = 1.19E+07m/s^2
VFRM = 4.1E+03m/s
SFRM = 6.4E-01m
Max = 3.04E+02
Min = 0.00E+00
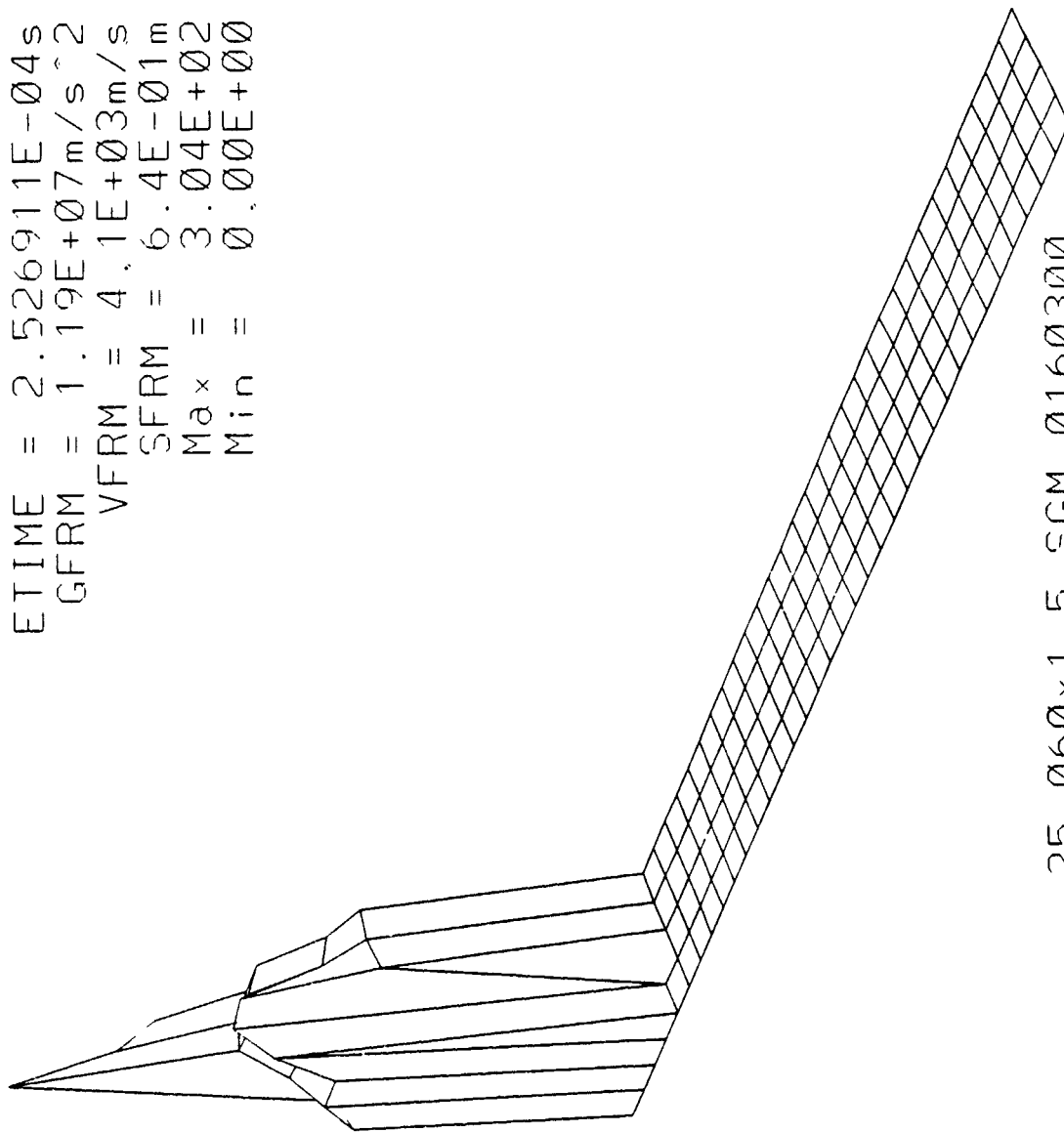
25_060×1_5_SGM_0160300

Figure 4

ETIME = 2.5273777E-04s
GFRM = 1.19E+07m/s^2
VFRM = 4.1E+03m/s
SFRM = 6.4E-01m
Max = 3.84E+02
Min = 0.00E+00
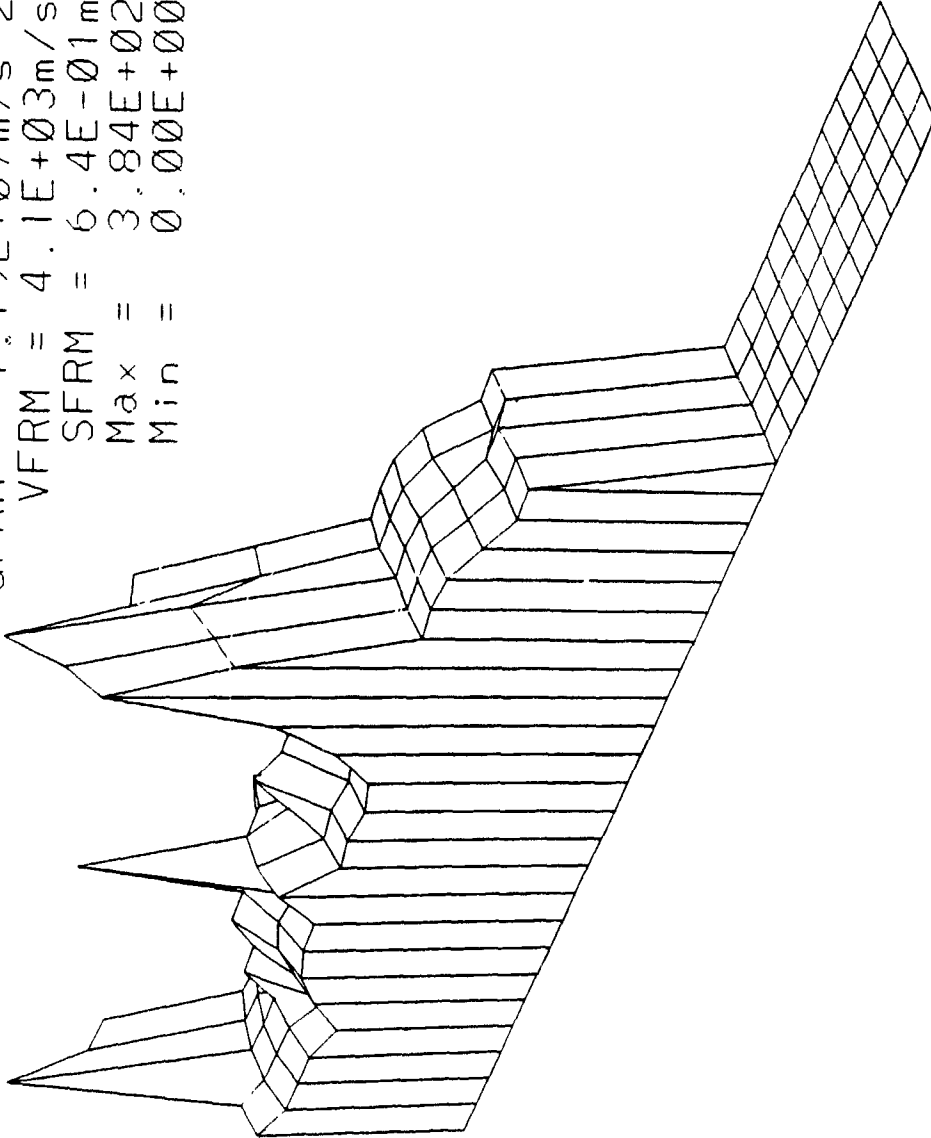
25_060x1_5_SGM_016Ø500

Figure 5

ETIME = 2.527609E-04s
GFRM = 1.19E+07m/s^2
VFRM = 4.1E+03m/s
SFRM = 6.4E-01m
Max = 2.56E+02
Min = 0.00E+00
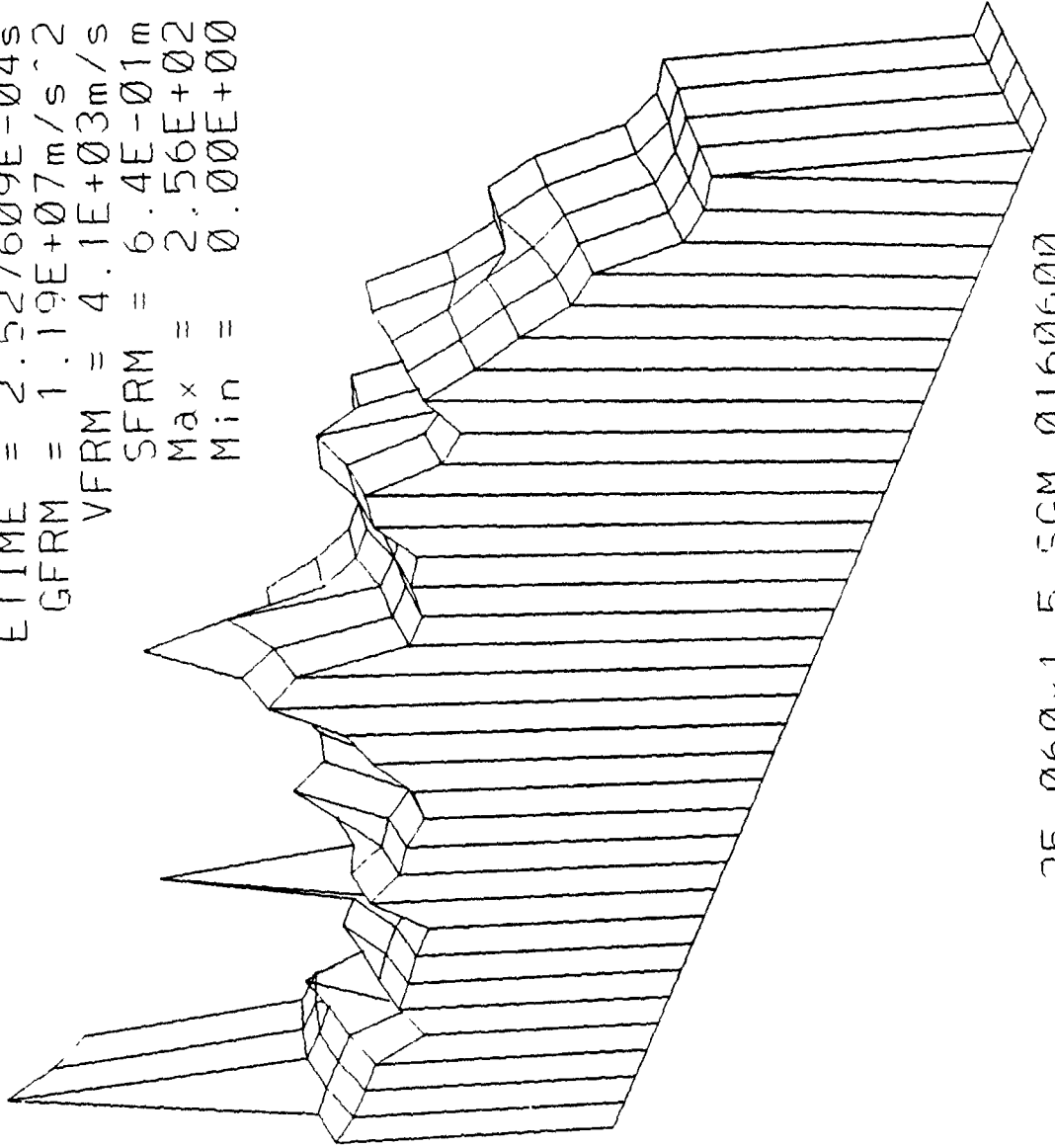
25_060×1_5_SGM_016@6.00

ETIME = 2.527144E-04s
GFRM = 1.19E+07m/s^2
VFRM = 4.1E+03m/s
SFRM = 6.4E-01m
Max = 2.23E+06
Min = -3.37E+05
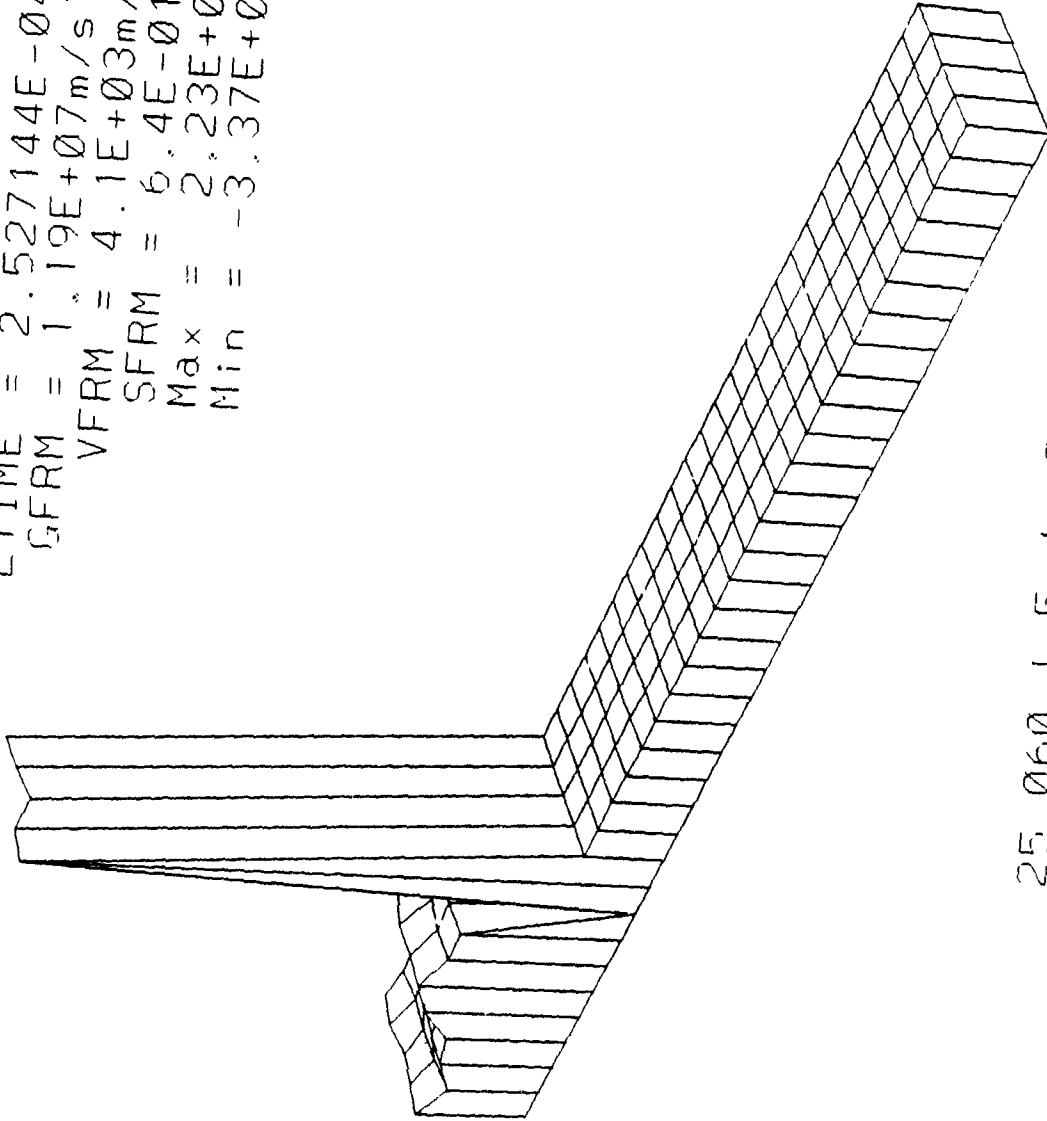
25_060.1_5_JY_0160400

Figure 6

figure 7

ETIME = 2.527377E-04s
GFRM = 1.19E+07m/s^2
VFRM = 4.1E+03m/s
SFRM = 6.4E-01m
Max = 2.10E+06
Min = -6.72E+04
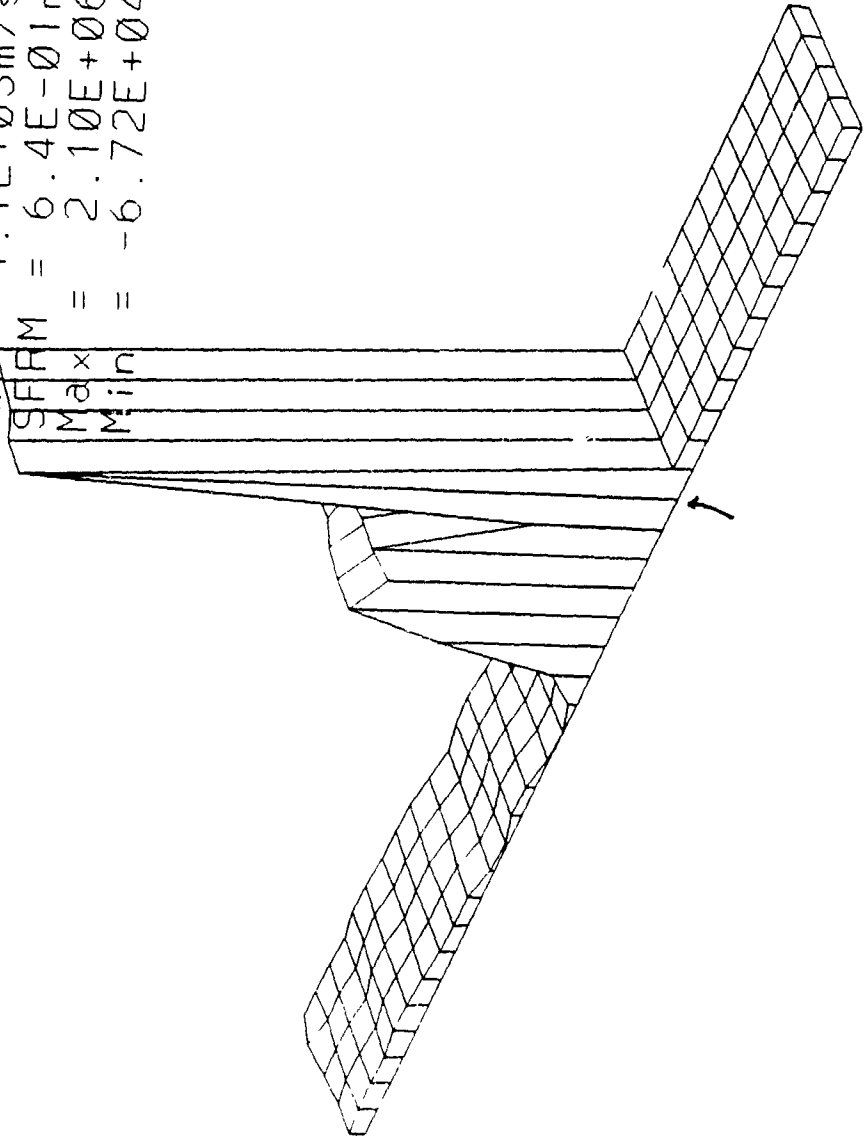
25_060x1_5_JY_0160500

Figure 8

ETIME = 2.527377E-04s
GFRM = 1.19E+07m/s^2
VFRM = 4.1E+03m/s
SFRM = 6.4E-01m
Max = 9.89E+08
Min = -2.14E+05

1_060x1_5_jy_016050Ø
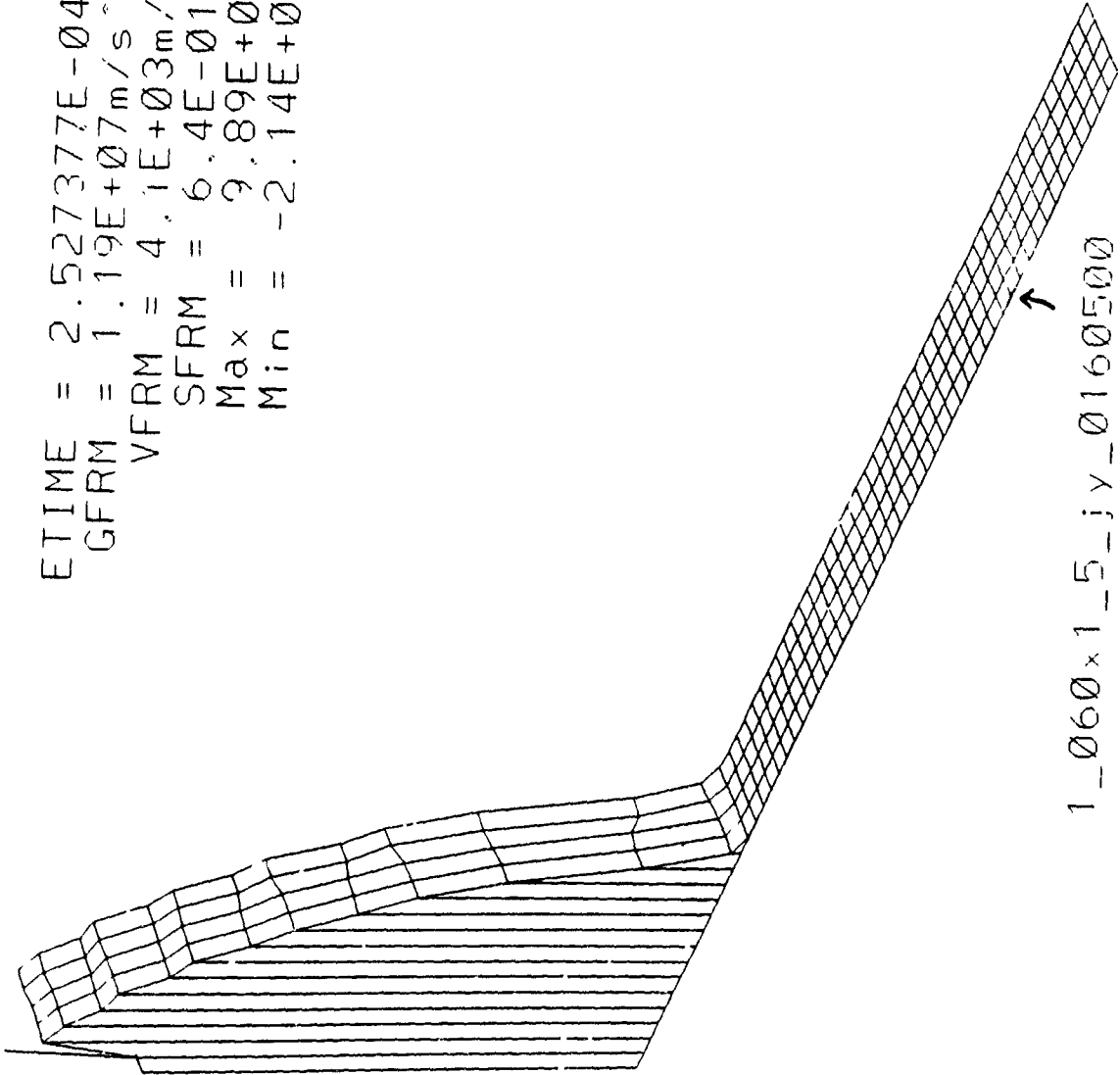
Figure 9

ETIME = 2.527609E-04s
GFRM = 1.19E+07m/s^2
VFRM = 4.1E+03m/s
SFRM = 6.4E-01m
Max = 2.55E+06
Min = -1.0E+05

25_060×1_5_JY_0160600
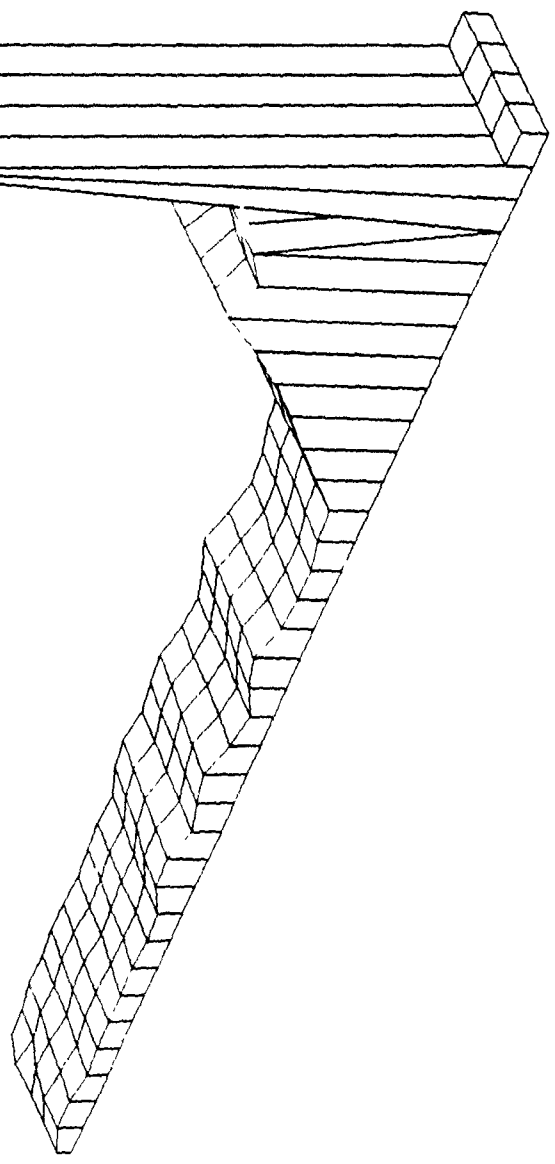
Dr. Kevin Moore

Report Not Publishable

At This Time

1990 USAF-UES SUMMER FACULTY RESEARCH PROGRAM/

GRADUATE STUDENT RESEARCH PROGRAM

Sponsored by the

AIR FORCE OFFICE OF SCIENTIFIC RESEARCH

Conducted by the

Universal Energy Systems, Inc.

FINAL REPORT

Gunner Performance in the BSTING Fire Control System

Prepared by: William D. Siuru,. PhD, PE

Academic Rank: Senior Research Associate

Department and   Space and Flight Systems Laboratory

 University   University of Colorado
                    at Colorado Springs

Research Location: WL/MNMF
                    Eglin AFB, Florida   32542-5434

USAF Researcher: Don Cunard

Date: 17 January 1991

Contract No: F49620-88-0053

Gunner Performance in the BSTING Fire Control System

by

William D. Siuru,. PhD, PE

ABSTRACT

A major portion of the results from the flight tests of the
Beam Sight Technology Incorporating Night Vision Goggles
(BSTING) system conducted in September and October 1990 were
reduced and analyzed. A theoretical model of the aiming system
was developed and used as a standard of the comparison for
measurements and calculations performed by the BSTING system.
The ability of the gunner to keep the laser spot on the target
was evaluated from the location of the laser spot recorded by
the Low Light Video system. The ability of the system to
accurately place bullets on target was scored using information
obtained from both Infrared and Low Light Video imagery.
Recommendations are made on how the accuracy of the BSTING can
be improved.

Acknowledgements

I wish to thank the Air Force Systems Command and the Air
Force Office of Scientific Research for sponsorship of this
research. Universal Energy Systems' efficient
administration of the program was greatly appreciated.

Technical guidance provided by Don Cunard was most
helpful. I especially appreciate the many discussions I
had with Sandy Eldering (Baird Optical Systems Division,
Imo Industries, Inc.) that allowed me to understand the
detailed working of the BSTING system and the procedures
used during the flight test program. Bob Hall's (Space and
Aeronautical Sciences, Inc.) help in reducing data is also
greatly appreciated.

I.   INTRODUCTION

The Air Force Armament Laboratory at Elgin AFB has sponsored
the exploratory development of the BSTING fire control system
as a low cost, stand-alone device to improve the aiming
accuracy of a machine gun mounted on a moving platform. The
BSTING system, developed by the Baird Optical Systems Division
of Imo Industries, was flight tested at the Naval Weapons
Center, Chinalake, California during August and September 1990.

BSTING replaces the tracer rounds with a infrared
laser/range finder mounted on the gun. The gunner wearing night
vision goggles to see the laser beam aims the spot on the
target. A simple fire control system allows the gunner to keep
the laser beam on the target by aiming the gun. A computer
calculates the necessary corrections for the bullet's
trajectory and the motion of the helicopter. The motion of the
helicopter is sensed through a pair of simple rate sensors also
mounted on the gun. The computed corrections drive servos which
positions the laser beam/range finder relative to the gun.

II.   OBJECTIVES OF THE RESEARCH EFFORT

My research consisted of analyzing the data obtained during the
flight tests to determine the accuracy of the BSTING system
and the performance of the gunners using the system. Evaluation
of the BSTING system consisted of determining how well the

system computed the azimuth and elevation corrections using measurements obtained by the stand-alone system. Evaluation of gunner performance consisted of scoring the "hits on target" and the gunner's ability to keep the laser beam aimed at the target.

III. METHODOLOGY

A "truth" model was needed to assess the performance of the BSTING system and the performance of the gunner using it. The model was based on the radar data provided by the Range Control Center Integration and Processing Center (RIPS) at the Naval Weapons Center.

By using a parabolic fit to the RIPS slant range data, the time-dependent range to target can be expressed by:

$$R_{sl} = At^2 + Bt + C \qquad (1)$$

Referring to the figure below, the azimuth rate can be determined. Incidently, in the BSTING system the azimuth plane is described by the swept of the line-of-sight of the laser beam between the gun and target.

TARGET

Az

R_{sl}

R_{min}

Az

V

$_{ac}$

$$\dot{Az} = V_{ac} \cos Az / R_{sl}$$
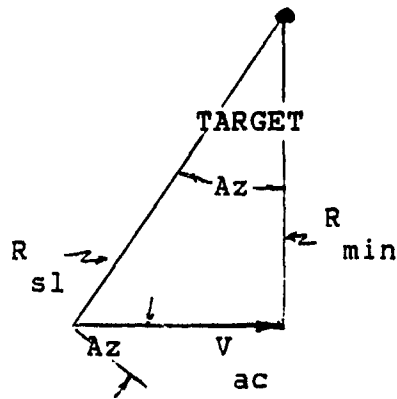
Since $\cos Az = R_{min} / R_{sl}$ where $R_{sl} = C - B^2/4A$

$$\dot{Az} = - V_{ac} R_{min} / R_{sl}^2 \tag{2}$$

The negative sign is consistent with the BSTING sign convention.

The range rate is simply

$$\dot{R}_{sl} = 2At + B \tag{3}$$

The elevation rate can be determined by referring to the following figure.

R_{sl}

ALT

El
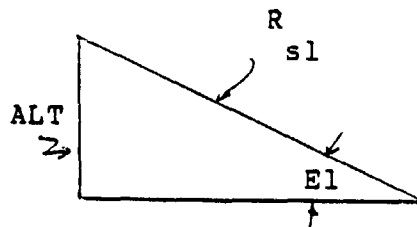
$$El = \text{Arcsin} (ALT/R_{sl})$$

and thus

$$\dot{El} = - \frac{ALT \times (2At + B)}{R_{sl} \times SQR(R_{sl}^2 - ALT^2)} \tag{4}$$

The "theoretical" values of R_{sl}, $\dot{R}_{sl}$, $\dot{Az}$ and $\dot{El}$ determined by equations 1 through 4 correspond to values measured by the BSTING rangefinder and rate sensors. Thus, the theoretical values of AIMX and AIMY, the aiming corrections in the azimuth and elevation planes respectively, were determined using the BSTING algorithms with the "theoretical" values.

IV.   SAMPLE RESULTS

An example of the results comparing the "theoretical" computed range (curve fit to radar data), azimuth and elevation rates and aiming corrections against the BSTING measurements are shown in figures 1 to 3.

The plot of the slant range shows the sequence of events during the BSTING operation. The aiming corrections, AIMX and AIMY, are calculated over a two or three second period. After this, the system servos move the laser beam to implement the corrections taking about a second. In the BSTING system, the gunner aims the gun rather than laser beam itself. The BSTING algorithm determines the relationship between the beam and gun bore. During the period the servos are implementing the corrections, the gunner is also repositioning the spot on the target since the "reticle" has been disturbed by the repositioning of the laser beam. After the servos have

SLANT RANGE

- CALCULATED   □ BSTING

AZIMUTH RATE

- CALCULATED   □ BSTING

Figure 1

ELEVATION RATE

milliradians/second

100
40
-20
-80
-140
-200

TIME - seconds

30   33   36   39   42   45

- CALCULATED   □ BSTING

ACCELERATION

Gs

1.5
1.1
0.7
0.3
-0.1
-0.5

2 FIRE

TIME - seconds

30   33   36   39   42   45

□ X   ▽ Y   ✳ X

Figure 2

AZIMUTH CORRECTION

CALCULATE

- CALCULATED   □ BSTING

ELEVATION CORRECTION

CALCULATE

- CALCULATED   □ BSTING

Figure 3

9-10
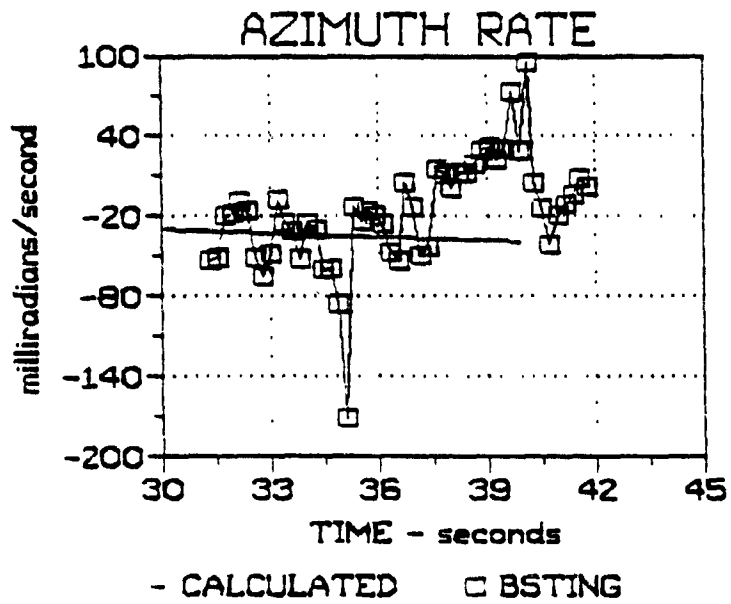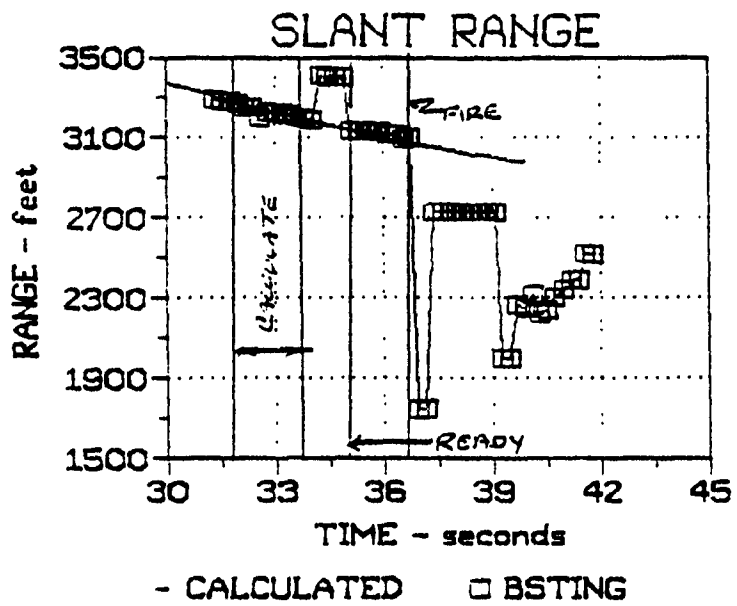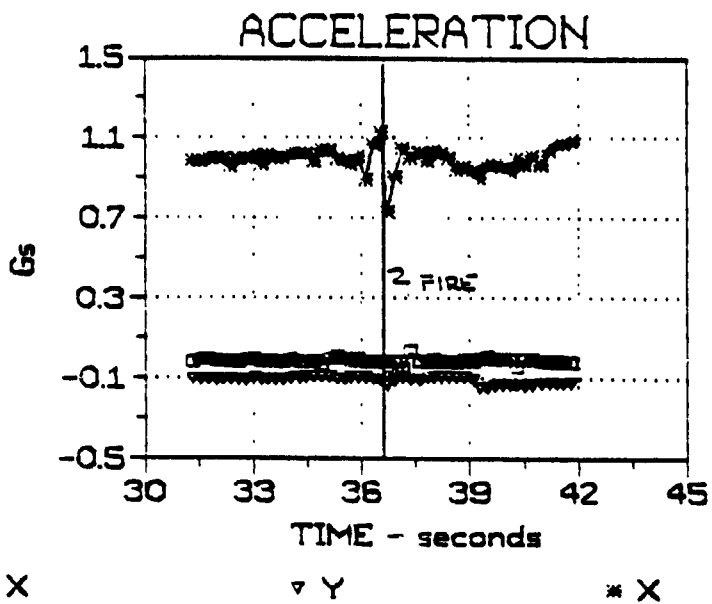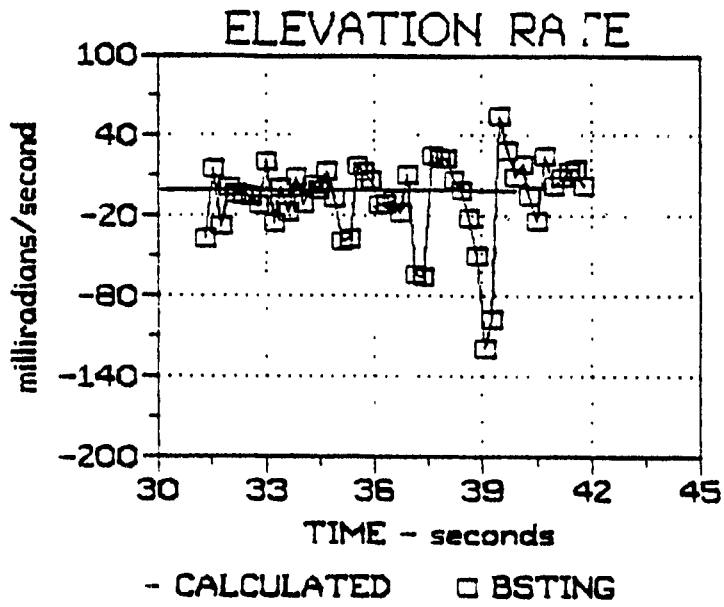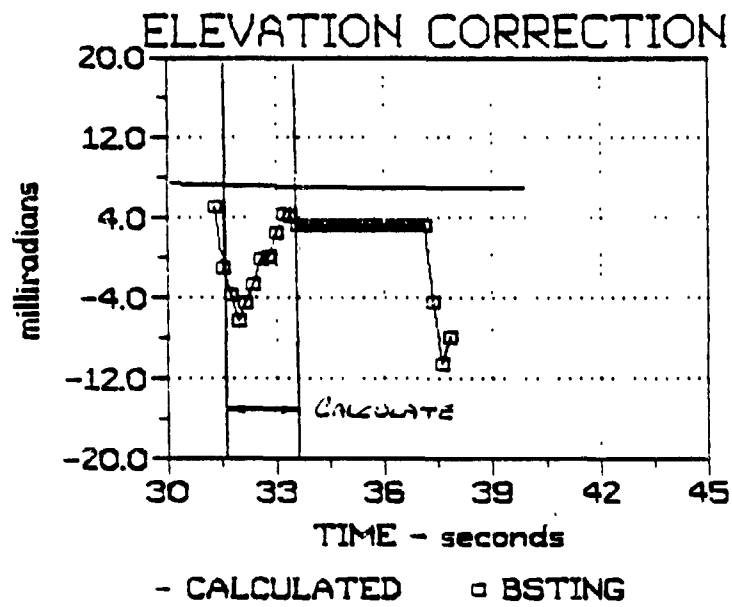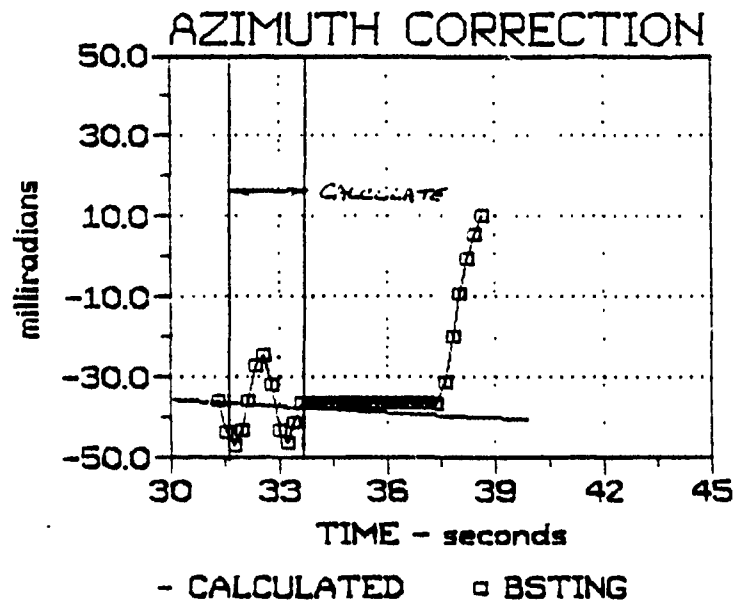
completed their task, the gunner is provided a ready signal and can fire at will. As seen in figure 3, the aiming corrections are frozen at their values at the completion of calculations. From the plot of accelerations measured by three accelerometers mounted on the gun, shown in figure 3, it is usually quite easy to establish when the gun was fired.

V. GUNNER AND SYSTEM PERFORMANCE

The performance of the gunner was measured by the gunner's ability to keep the laser spot on the target. BSTING system performance was measured by the accuracy of the azimuth and elevation corrections, AIMX and AIMY respectively, computed by the BSTING algorithms using measurements obtained by the laser rangefinder and rate sensors compared to the AIMX and AIMY values computed by these algorithm using "theoretical" measurements based on radar data.

A four milliradian circular error criteria was used. That is the laser spot was considered "on target" if it fell within a circle with a radius of 4 milliradians and centered at the center of the target. Two periods during each pass of the helicopter were considered. These were (1) while the BSTING algorithms were performing their computations and (2) after the "ready" signal was given and the gunner was aiming at the

2

target in preparation to fire. During these two periods it was assumed that the gunner was using the greatest concentration in maintaining the laser spot on the target. Two ranges were used in computing the milliradian values, the ranges midway during the computation period and between the ready signal and firing, respectively.

The laser spot location was determined from the low light video data as reduced by the Naval Weapon Center in terms of x and y coordinates with respect to the center of the target. Since the laser beam was not observed continuously, scoring was only done when the light spot was seen. Since the laser spot is more likely to be entirely off the target than just not seen, the resulting gunner performance is on the optimistic side.

The results of the laser spot "scoring" is summarized in Table I. The first number in the pass code is the month of the test, the next two are the day and P"X" identifies the individual pass. The nominal range is the slant range to the target at the point of closest approach. The velocity and altitude are an average during the computation period. Range, velocity and altitude were determined from radar data. The laser spot scoring percentage represents the ratio of the time the spot is within the 4 milliradian radius criteria out of the total time the spot is actually seen.

TABLE I

GUNNER AND BSTING PERFORMANCE

PASS CODE	NOMINAL PARAMETERS RANGE (feet)	VELOCITY (ft/sec)	ALTITUDE (feet)	4 MIL CRITERIA (calc/fire)	SCORING LASER SPOT ON TARGET (%) (calc/fire)		AIM ERROR AZ/EL (mils)
Note: + aim error means more than calculated							
807P3	1700	127	445	11/9.6	71.3	51.6	-4.3/0.7
807P4	1700	128	490	11/9.6	n/a	63.3	-5.2/2.1
807P5	1830	127	510	12/10.5	72.8	54.0	0.4/-3.2
807P6	1750	162	455	11/10	n/a	83.0	7.9/1.2
807P8	1750	125	281	12.5/11	n/a	24.2	-4.5/-2.2
807P17	2900	131	520	17/16.5	81.2	59.2	-1.8/-4.2
807P21	2750	185	512	16/15.5	70.6	55.0	-5.2/5.3
					AVERAGE		-1.8/0.0
					AVERAGE (absolute)		4.2/2.7
808P3	2500	135	535	17/14.7	72.2	n/a	-4.7/-2.6
808P4	2550	190	565	17/14.5	n/a	n/a	-1.5/-0.8
808P7	2500	172	584	17/14.1	73.3	54.3	4.5/5.4
808P9	2550	126	260	16/14.5	53.3	35.5	0.0/-3.4
					AVERAGE		-0.4/-0.4
					AVERAGE (absolute)		2.7/3.1

Note Radar Data Not Available for 904P3, 904P4, 904P5, 904P9, 904P16, 904P18, 904P19. Slant range determined from curve fit to BSTING range data and velocity/altitude are nominal values - therefore results only approximate.

PASS CODE	RANGE	VELOCITY	ALTITUDE	4 MIL CRITERIA	LASER SPOT		AIM ERROR
904P3	1350	70 kts	250	10.5/7.6	n/a	n/a	1.2/2.8
90494	1450	100 kts	200	11/8.2	36.8	22.0	7.0/10.3
904P5	1400	70 kts	100	9/8	n/a	n/a	-2.6/13.5
904P9	1500	100 kts	100	9/7.9	27.6	41.9	4.7/8.0
904P16	2400	100 kts	100	18/13.6	n/a	n/a	7.9/13.3
904P18	2300	150	100	14/13	n/a	n/a	0.4/-0.4
904P19	2400	70 kts	100	14.1/13.3	n/a	n/a	-3.1/-0.1
					AVERAGE		2.2/6.8
					AVERAGE (absolute)		3.8/7.0

TABLE I (Con't)

PASS CODE	NOMINAL PARAMETERS			4 MIL CRITERIA (calc/fire)	SCORING LASER SPOT ON TARGET (%) (calc/fire)		AIM ERROR AZ/EL (mils)
	RANGE (feet)	VELOCITY (ft/sec)	ALTITUDE (feet)				

Note: + aim error means more than calculated

PASS CODE	RANGE	VELOCITY	ALTITUDE	4 MIL	LASER	SPOT	AIM ERROR
904P21	2650	30	425	15.0	75.0	66.7	-1.5/-1.4
904P22	2600	10	580	14.7	79.8	73.9	-4.9/-0.6
904P23	2700	5	450	15.0	33.3	62.5	6.2/1.0
					84.3	94.1	8.5/-6.9
904P24	2625	0	640	15.0	Never Completed Computations		
				AVERAGE			2.1/2.0
				AVERAGE (absolute)			5.3/2.5

PASS CODE	RANGE	VELOCITY	ALTITUDE	4 MIL	LASER	SPOT	AIM ERROR
905P2	3100	120	280	18.7/17.5	62.3	70.0	-1.1/-3.9
905P3	3200	110	200	18.7/18.1	80.6	78.9	-2.4/-3.7
905P4	3050	120	275	18.0/17.5	63.0	37.5	3.5/-6.9
905P5	3200	170	190	18.7/18.1	64.7	71.4	-0.5/-7.2
905P11	3800	120	90	22.6/22.6	(1)	--	(2) ---
905P19	3400	170	90	19.2/19.2	(1)		-7.6/0.8
905P27	4900	125	270	30.0/--	(1)	--	(2) ---

(1) Criteria greater than target size
(2) Calculations did not terminate

AVERAGE		1.7/4.2
AVERAGE (Absolute)		3.0/4.5

OVERALL

AVERAGE	0.1/-1.5
AVERAGE (Absolute)	3.8/3.2

The last column of data is the aiming error which is the
difference between the AIMX and AIMY corrections based on BSTING
measurements and corrections determined using radar obtained
measurements. Two average values are presented, the "true" and
"absolute" where signs are not considered.

Radar data was not available for the first seven passes on
4 September 1990 so the calculated corrections are based on a
curve fit to the BSTING range measurements (widely varying
ranges omitted). The results from these passes were not
included in the overall averages. The last four passes were
hovering cases. On a couple of passes on 5 August 1990, the
gunner did not activate the "calculation" button so
computations of AIMX and AIMY were not completed. Also when the
range exceeded about 1500 meters, the 4 milliradian criteria
encompassed the entire target so everytime the spot was seen it
was within the criteria.

For the overall averages, it can be seen that the BSTING system
is providing aiming accuracy corrections within the 4
milliradian accuracy tolerance. The gunner is able to keep the
laser spot on the target usually on an average of 65 percent
of the time during the calculations and 59 percent during the
aim-to-fire period. Again remember these are optimistic values.
When the aiming errors were plotted as a function of slant

range or helicopter velocity (see figure 4), there did not seem to be either a velocity or range dependency. Also there is no obvious variation between dates that would indicate any dependence on a particular gunner's proficiency with the system.

VI. HIT SCORING

Both the Infrared Video and Low Light TV data as reduced by the Naval Weapons Center were used to score the ability of the overall BSTING system plus gunner to put bullets on the target. Because of the uncertainty in insuring that both video systems were observing the same bullet, results from the two systems were scored independently. As can be seen in Table II, more bullets were seen by the LLTV system. Again a 4 milliradian radius circle was used as the scoring criteria with the range being the slant range at the time the first bullet was fired ("streaking starts" in the NWC reports). Because only bullets "seen" were scored, the scoring is on the optimistic side. This was necessitated by the fact that some of the bullets that impacted the target were not seen by either video system. Between 35 and 50 percent of the bullets seen were scored as hits.

While tracer rounds were fired during the test program, these passes are not included here. In the tracer firing tests, the

RANGE VS AIM ERROR

VELOCITY VS AIM ERROR
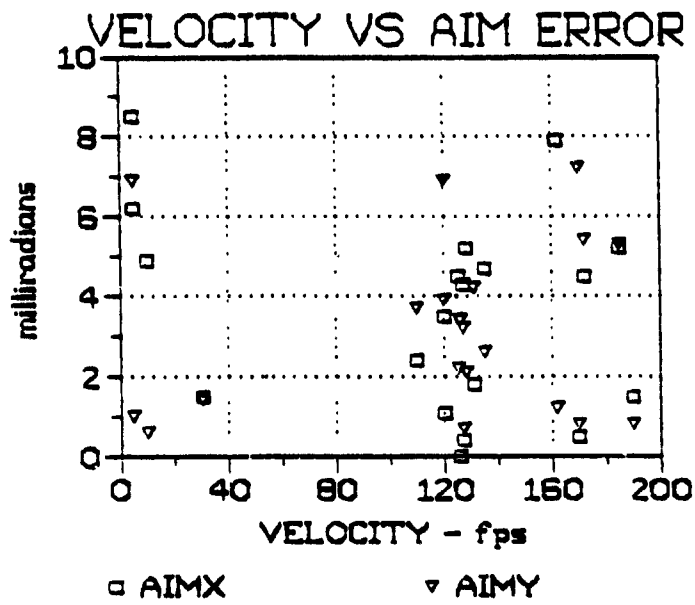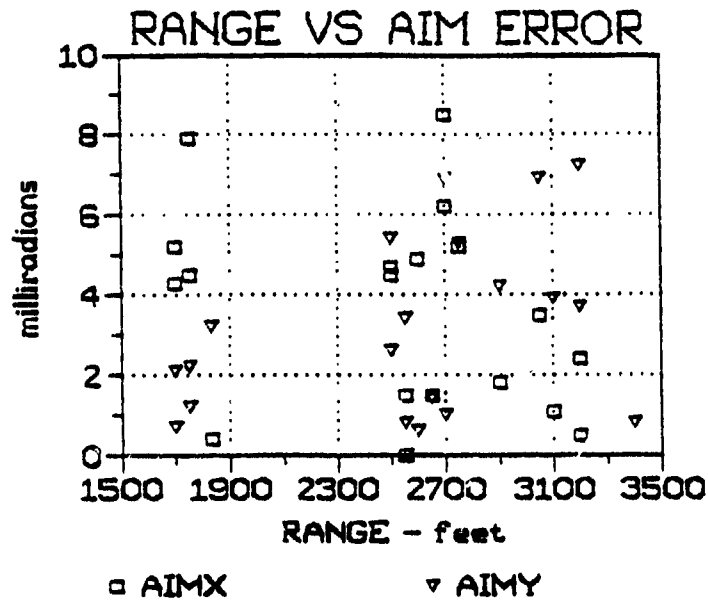
Figure 4

TABLE II

HIT SCORING

PASS CODE	NOMINAL PARAMETERS			4 MIL CRITERIA (feet)	NUMBER OF HITS		SCORING (%)
	RANGE (feet)	VELOCITY (ft/sec)	ALTITUDE (feet)		SEEN	WITHIN CRITERIA (LLTV/IR)	
807P3	1700	127	445	9.6	4/2	1/1	25/50
807P4	1700	128	490	9.6	5/3	0/0	0/0
807P5	1830	127	510	10.5	8/3	4/3	50/100
807P6	1750	162	455	10.0	10/5	6/4	60/80
807P8	1750	125	281	10.0	9/4	5/2	56/50
807P17	2900	131	520	16.5	3/3	2/2	67/67
807P21	2750	185	512	15.5	8/4	3/3	37.5/75
					47/24	21/15	
						AVERAGE	45/63
808P3	2500	135	535	14.0	8/2	3/2	37.5/100
808P4	2550	190	565	14.5	6/2	0/1	0/50
808P7	2500	172	584	14.0	5/4	0/0	0/0
808P9	2550	126	260	14.5	8/7	3/4	0/57
					27/15	6/7	
						AVERAGE	22/47

Note Radar Data Not Available for 904P3, 904P4, 904P5, 904P9, 904P16, 904P18, 904P19

PASS CODE	RANGE (feet)	VELOCITY	ALTITUDE (feet)	4 MIL CRITERIA (feet)	SEEN	WITHIN CRITERIA (LLTV/IR)	SCORING (%)
904P3	1350	70 kts	250	7.6	9/7	2/2	22/29
90494	1450	70 kts	200	8.2	10/9	3/2	30/22
904P5	1400	70 kts	100	8.0	6/2	0/0	0/0
904P9	1500	100 kts	100	8.5	8/3	1/0	12.5/0
904P16	2400	70 kts	100	13.5	2/2	0/0	0/0
904P18	2300	70 kts	100	13.0	3/1	0/0	0/0
904P19	2400	70 kts	100	13.5	9/3	2/1	22/33
					47/27	8/5	
						AVERAGE	26/19

TABLE II (Con't)

| PASS CODE | NOMINAL PARAMETERS | | | 4 MIL CRITERIA (feet) | NUMBER OF HITS | | SCORING (%) |
	RANGE (feet)	VELOCITY (ft/sec)	ALTITUDE (feet)		SEEN	WITHIN CRITERIA (LLTV/IR)	
904P21	2650	30	425	15.0	3/1	0/1	0/100
904P22	2600	10	580	15.0	3/0	1/0	33/0
904P23	2700	5	450	15.0	3/1	0/0	0/0
904P24	2625	0	640	15.0	4/2	4/2	100/100
					13/4	5/3	
					HOVER AVERAGE		38/75

905P2	3100	120	280	17.5	1/0	0/0	0/0
905P3	3200	110	200	18.0	2/1	1/1	50/100
905P4	3050	12	67/100				
905P5	3200	170	190	18.0	1/0	1/0	100/0
905P11	3800	120	90	21.5	2/1	2/1	100/100
905P19	3400	170	90	19.0	0/1	0/0	0/0
905P27	4900	120	270	27.5	1/2	1/2	100/100
					13/9	9/8	
					AVERAGE		69/89
				OVERALL	142/79	49/38	35/48

BSTING aiming light was left on to obtain range data and thus the gunners could not help but use the aiming light while firing the tracer rounds. Therefore the gunner had a definite advantage over normal firing of tracer rounds for aiming and they do not represent a realistic standard for comparison.

VII. CONCLUSIONS AND RECOMMENDATIONS

Under the conditions of this flight test program, the BSTING provides accurate aiming corrections (less than 4 milliradians circular error). The tests were conducted at slant ranges of less than 1500 meters, velocities of hover to 190 ft/sec and from altitudes of 640 feet or less. The rangefinder and rate sensor are providing measurements of sufficient accuracy even when the gunner is on target only 65 percent of the time.

Even though the BSTING system is conceptually good, refinements are still needed. These include:

1. Optimization of the filters mainly for best performance. For instance, currently the range and range rates take too long to reach their proper values.

2. The gravity drop algorithm needs to be "tuned" for long range applications. Other ballistic parameters such as Magnus effect, bullet drift, and jump may have to included for long range, long time-of-flight trajectories.

3. Currently, the aiming corrections are frozen at the end of the computation period. A predictive technique is needed to insure corrections are still accurate when firing is delayed.

4. A method needs to be devised to eliminate the need to realign the laser beam after the servos have implemented the aiming corrections, or at least provide faster response and less perturbation.

5. Research should be done to find the optimum way for gunners to use the system and a training program developed to train gunners. While filters are available during the computation period to smooth out gunner's aiming inaccuracies, during the firing period the bullet travels the trajectory is dependent on where the laser beam is pointed the moment the trigger is pulled.

1990 USAF-UES SUMMER FACULTY RESEARCH PROGRAM

GRADUATE STUDENT RESEARCH PROGRAM

Sponsored by the

AIR FORCE OFFICE OF SCIENTIFIC RESEARCH

Conducted by the

Universal Energy Systems, Inc.

FINAL REPORT

Robust Eigenstructure Assignment with Application to Missile Control

Prepared by: Kenneth M. Sobel, Ph.D.

Academic Rank: Associate Professor

Department and   Electrical Engineering

University: The City College of New York

Research Location: AFATL/FXG
                      Eglin AFB, FL 32542-5434

USAF Researcher: Dr. J. Cloutier

Date: 28 Aug 90

Contract No: F49620-88-C-0053

Robust Eigenstructure Assignment with Application to Missile Control

by

Kenneth M. Sobel

ABSTRACT

Eigenstructure assignment is a method which allows the incorporation of classical specifications on damping, settling time, and mode decoupling into a modern multivariable control framework. However, this method does not consider that the plant parameters are uncertain or that the plant contains dynamics which are not included in the design model. New time domain stability robustness results have been obtained for a non-strictly proper linear time invariant plant which is subject to simultaneous structured state space uncertainty and norm bounded unmodelled dynamics. Sufficient conditions for robust stability are obtained both for a constant gain output feedback controller and an output feedback dynamic compensator. The robustness conditions are explicitly in terms of the closed loop eigenvalues and eigenvectors so that these new results are especially well suited for a robust eigenstructure assignment design method. An example is presented of a robust eigenstructure autopilot design for the yaw/roll dynamics of the enhanced medium range air to air technology (EMRAAT) bank-to-turn missile.

Acknowledgements

I wish to thank the Air Force Systems Command and the Air Force Office of Scientific Research for sponsorship of this research. Universal Energy Systems must be mentioned for their concern and help to me in all administrative and directional aspects of this program.

My experience was rewarding and enriching because of many different influences. Dr. Jim Cloutier provided me with support, encouragement, and a truly enjoyable working atmosphere. I would like to thank Robert Wilson for valuable technical discussions. The concern of Dave Gardner, (Chief, Guidance and Control Branch) was greatly appreciated.

I. INTRODUCTION:

Eigenstructure assignment is a method which allows the incorporation of classical specifications on damping, settling time, and mode decoupling into a modern multivariable control framework. This method has been utilized to design flight control laws for aircraft with uncertainty in the linearized model parameters.

The Flight Control Technology Section of the Guidance and Control Branch of the USAF Armament Laboratory is concerned with the design of robust autopilots for bank-to-turn missiles. The design models for these missiles are characterized by simultaneous uncertainty in the aerodynamic coefficients and by unmodelled dynamics such as neglected high frequency bending modes. The Flight Control Technology Section has been working on the application of eigenstructure assignment to bank-to-turn missile autopilot design by using either state feedback or loop transfer recovery techniques.

My research interests have been in the area of robust eigenstructure assignment and its application to flight control design. My work has included the theory for robust eigenstructure assignment for plants with structured state space uncertainty using constant gain output feedback. I have applied these results to the design of a constant gain output feedback controller for a pitch pointing/vertical translation maneuver of the AFTI F-16 aircraft.

II. OBJECTIVES OF THE RESEARCH EFFORT:

The earlier work which my students and I have published considers the robust eigenstructure design problem for plants with only structured state space uncertainty. The effects on stability of dynamics which are not included in the design model are not considered. Furthermore, the sufficient condition for robust stability assumes that a constant gain output feedback control law is utilized.

My assignment as a participant in the 1990 Summer Faculty Research Program (SFRP) was to extend the sufficient condition for robust stability to include simultaneous structured state space uncertainty and unmodelled dynamics. In contrast to other approaches which utilize the frequency domain, our results should be obtained in the time domain. Time domain results which are explicitly in terms of the closed loop eigenvalues and eigenvectors are especially well suited to the design of robust eigenstructure asssignment controllers.

Our new result indicates that a constant gain output feedback controller for a plant with unmodelled dynamics should be a low authority controller. This result concurs with frequency domain results and is a statement that the gain must be sufficently small at high frequencies to guarantee that the unmodelled high frequency dynamics do not destabilize the plant. Thus, a further objective was to extend the sufficient conditions for robust stability to low order dynamic compensators. This will allow the gain to be frequency dependent so that larger gains may be utilized at low frequencies to achieve the control objectives while a smaller gain is utilized at high frequencies to achieve robustness to unmodelled high frequency dynamics.

The final objective was to develop an algorithm for robust eigenstructure assignment which utilizes the new sufficient conditions for robust stability. This algorithm should be applied to the design of a controller for a bank-to-turn missile autopilot which is characterized by state space uncertainty and unmodelled dynamics. The state space

uncertainty is typically due to uncertainty in the stability derivatives and control derivatives which appear in the linearized design models. The unmodelled dynamics typically result from high frequency bending modes which are not included in the design model. The direct design of low order dynamic compensators using eigenstructure assignment has some advantages over other methods which design a high order dynamic compensator and then utilize model order reduction techniques to obtain a controller with an acceptably low order.

III. PROBLEM FORMULATION

Consider a nominal linear time-invariant multi-input multi-output plant described by

$$\dot{x} = Ax + Bu \qquad (1a)$$

$$y = Cx + Du \qquad (1b)$$

where $x \in R^n$ is the state vector, $u \in R^m$ is the input vector, $y \in R^r$ is the output vector, and A, B, C, and D are constant matrices. We shall refer to Eq.(1) as either the nominal plant or the design model.

Suppose that the nominal system is subject to simultaneous linear time-varying structured state space uncertainty and unmodelled dynamics. The linear time-varying state space uncertainty is described by uncertainties in the entries of A, B, C, and D and is denoted by $\Delta A(t)$, $\Delta B(t)$, $\Delta C(t)$, and $\Delta D(t)$, respectively. The unmodelled dynamics $\Delta H(t)$ satisfy

$$\Delta H(t) = C_\Delta e^{A_\Delta t} B_\Delta + D_\Delta \delta(t) + E_\Delta \dot{\delta}(t) \qquad (2)$$

which affects the output via a convolution with the input. Then, the plant with uncertainty is given by

$$\dot{x} = Ax + Bu + \Delta A(t)x + \Delta B(t)u \qquad (3a)$$

$$y = Cx + Du + \Delta C(t)x + \Delta D(t)u + \Delta H(t)*u(t) \qquad (3b)$$

We shall refer to Eq.(3) as the uncertain plant or the true model. Further, suppose that bounds are available on the absolute values of the maximum variations in the elements of $\Delta A(t)$, $\Delta B(t)$, $\Delta C(t)$, and $\Delta D(t)$. That is,

$$|\Delta a_{ij}(t)| \leq (a_{ij})_{max}; \quad i=1,\ldots,n; \quad j=1,\ldots,n \qquad (4a)$$

$$|\Delta b_{ij}(t)| \le (b_{ij})_{max}; \quad i=1,\ldots,n; \quad j=1,\ldots,m \qquad (4b)$$

$$|\Delta c_{ij}(t)| \le (c_{ij})_{max}; \quad i=1,\ldots,r; \quad j=1,\ldots,n \qquad (4c)$$

$$|\Delta d_{ij}(t)| \le (d_{ij})_{max}; \quad i=1,\ldots,r; \quad j=1,\ldots,m \qquad (4d)$$

Define $\Delta A^+(t)$, $\Delta B^+(t)$, $\Delta C^+(t)$, and $\Delta D^+(t)$ as the matrices obtained by replacing the entries of $\Delta A(t)$, $\Delta B(t)$, $\Delta C(t)$, and $\Delta D(t)$ by their absolute values. Also, define A_{max}, B_{max}, C_{max}, and D_{max} as the matrices with entries $(a_{ij})_{max}$, $(b_{ij})_{max}$, $(c_{ij})_{max}$, and $(d_{ij})_{max}$, respectively. Then,

$$\{\Delta A(t): \Delta A^+(t) \le A_{max}\} \qquad (5a)$$

$$\{\Delta B(t): \Delta B^+(t) \le B_{max}\} \qquad (5b)$$

$$\{\Delta C(t): \Delta C^+(t) \le C_{max}\} \qquad (5c)$$

$$\{\Delta D(t): \Delta D^+(t) \le D_{max}\} \qquad (5d)$$

where "$\le$" is applied element by element by element to matrices and $A_{max} \in R_+^{nxn}$, $B_{max} \in R_+^{nxm}$, $C_{max} \in R_+^{rxn}$, $D_{max} \in R_+^{rxm}$ where R_+ is the set of non-negative real numbers.

Further, suppose that bounds are available on the individual terms in $\Delta H(t)$. That is,

$$\bar{\sigma}(C_\Delta e^{A_\Delta t} B_\Delta) \le r_2 e^{-\beta t} \qquad (6a)$$

$$\bar{\sigma}(D_\Delta) \le r_0 \qquad (6b)$$

$$\bar{\sigma}(E_\Delta) \le r_1 \qquad (6c)$$

Consider the output feedback dynamic compensator described by

$$\dot{x}_c = A_c x_c + B_c y \qquad (7a)$$

$$u = C_c x_c + D_c y \qquad (7b)$$

Stability Robustness Problem: Given a dynamic compensator (A_c, B_c, C_c, D_c) such that the nominal closed loop system exhibits desirable dynamic performance, determine if the uncertain closed loop plant is

asymptotically stable for all $\Delta A(t)$, $\Delta B(t)$, $\Delta C(t)$, and $\Delta D(t)$ described by Eq.(5) and unmodelled dynamics described by Eq.(2) which satisfy the assumptions shown in Eq.(6).

IV. SUFFICIENT CONDITIONS FOR ROBUST STABILITY

Sobel, Banda and Yeh [1] have proposed a sufficient condition for robust stability for the plant described by Eq.(1) when $D = \Delta D(t) = \Delta C(t) = \Delta H(t) = 0$. The contributions of our new work include (1) extending the sufficient condition to include non-strictly proper plants, (2) extending the sufficient condition to include structured state space uncertainty in the measurement matrices C and D, (3) extending the sufficient condition to include simultaneous structured state space uncertainty and unmodelled dynamics, and (4) extending the sufficient condition to include output feedback using dynamic compensators.

Theorem (Main Result):

Consider the linear time-invariant plant with time-varying structured uncertainty and unmodelled dynamics described by

$$\dot{x}(t) = (A+\Delta A(t))x(t) + (B+\Delta B(t))u(t) \tag{8a}$$

$$y(t) = (C+\Delta C(t))x(t) +(D+\Delta D(t))u(t) + \Delta H(t)*u(t) \tag{8b}$$

with dynamic compensator described by

$$\dot{x}_c(t) = A_c x_c(t) + B_c y(t) \tag{9a}$$

$$u(t) = C_c x_c(t) + D_c y(t) \tag{9b}$$

Let the unmodelled dynamics $\Delta H(t)$ satisfy

$$\Delta H(t) = C_\Delta e^{A_\Delta t} B_\Delta + D_\Delta \delta(t) + E_\Delta \dot{\delta}(t) \tag{10}$$

and let the time-varying structured state space uncertainty $\Delta A(t)$, $\Delta B(t)$, $\Delta C(t)$, and $\Delta D(t)$ satisfy

$$\{\Delta A(t): \Delta A^+(t) \leq A_{max}\} \tag{11a}$$

$$\{\Delta B(t): \Delta B^+(t) \leq B_{max}\} \tag{11b}$$

$$\{\Delta C(t): \Delta C^+(t) \leq C_{max}\} \tag{11c}$$

$$\{\Delta D(t): \Delta D^+(t) \leq D_{max}\} \tag{11d}$$

The plant and unmodelled dynamics satisfy the following assumptions:

Assumption (i): $\bar{\sigma}(C_\Delta e^{A_\Delta t} B_\Delta) \leq r_2 e^{-\beta t}$

Assumption (ii): $\bar{\sigma}(D_\Delta) \leq r_0$

Assumption (iii): $\bar{\sigma}(E_\Delta) \leq r_1$

Assumption (iv): $x(t)$ and $y(t)$ are uniformly continuous

Assumption (v): $\bar{\sigma}(\dot{u}(t)) \leq \gamma \cdot \bar{\sigma}(u(t))$

Suppose (A_c, B_c, C_c, D_c) is such that the nominal closed loop system is asymptotically stable with a non-defective modal matrix. Then, the uncertain closed loop system described by Eq.(8) is asymptotically stable for all $\Delta A(t)$, $\Delta B(t)$, $\Delta C(t)$, and $\Delta D(t)$ which satisfy Eq.(11) and $\Delta H(t)$ which satisfies assumptions (i)-(v) if

$$\left(\frac{1}{\alpha \cdot \underline{\sigma}(Q)}\right)\left\{\bar{\sigma}\left[(D_1^{-1}M^{-1})^+ \begin{pmatrix} A_m + B_m(D_cC)^+ + (B^+ + B_m)\Gamma_c^{\dot{}}C_m & B_m C_c^+ \\ B_c C_m & 0 \end{pmatrix}(MD_1Q)^+\right]\right.$$

$$+ \frac{\bar{\sigma}\left[(D_1^{-1}M^{-1})^+ \begin{pmatrix} (B^+ + B_m)D_c^+(D^+ + D_m) \\ B_c^+(D^+ + D_m) \end{pmatrix}\right] \cdot \bar{\sigma}\left[[D_c^+(C^+ + C_m), C_c^+](MD_1Q)^+\right]}{[1 - \bar{\sigma}[D_c^+(D^+ + D_m)] - \bar{\sigma}(D_c) \cdot (r_2/\beta + r_0 + \gamma \cdot r_1)]}$$

$$\bar{\sigma}\left[(D_1^{-1}M^{-1})^+\begin{pmatrix}(B^++B_m)D_C^+\\B_C^+\end{pmatrix}\right]\cdot\bar{\sigma}\left[[D_C^+(C^++C_m),C_C^+](MD_1Q)^+\right]\cdot(r_2/\beta + r_0 + \gamma\cdot r_1)$$

$$+\ \frac{\rule{11cm}{0.4pt}}{[1 - \bar{\sigma}[D_C^+(D^++D_m)] - \bar{\sigma}(D_C)\cdot(r_2/\beta + r_0 + \gamma\cdot r_1)]}\ \Bigg\}\ < 1 \tag{12}$$

and if

$$\bar{\sigma}[D_C^+(D^++D_m)] + \bar{\sigma}(D_C)\cdot(r_2/\beta + r_0 + \gamma\cdot r_1) < 1 \tag{13}$$

where

$$\alpha = -\max_i Re[\lambda_1(\tilde{A}_{c1})]$$

and

$$\tilde{A}_{c1} = \begin{pmatrix}A+BD_CC & BC_C\\B_CC & A_C\end{pmatrix}$$

and M is the modal matrix of $\tilde{A}_{c1}$.

Corollary 1 (Bounded Unmodelled Dynamics): If $E_\Delta = 0$, then assumption (v) is not required.

Corollary 2 (Constant Gain Output Feedback): For constant gain output feedback $u = D_Cy$, the uncertain closed loop system is asymptotically stable if

$$\left(\frac{1}{\alpha\cdot\underline{\sigma}(Q)}\right)\Bigg\{\bar{\sigma}\left[(D_1^{-1}M^{-1})^+[A_m+B_m(D_CC)^++(B^++B_m)D_C^+C_m](MD_1Q)^+\right]$$

$$+\ \frac{\bar{\sigma}\left[(D_1^{-1}M^{-1})^+(B^++B_m)D_C^+(D^++D_m)\right]\ \bar{\sigma}\left[D_C^+(C^++C_m)(MD_1Q)^+\right]}{[1 -\bar{\sigma}[D_C^+(D^++D_m)] - \bar{\sigma}(D_C)\cdot(r_2/\beta + r_0 + \gamma\cdot r_1)]}$$

$$+ \left. \frac{\bar{\sigma}\left[(D_1^{-1}M^{-1})^+(B^++B_m)D_c^+\right]\ \bar{\sigma}\left[D_c^+(C^++C_m)(MD_1Q)^+\right](r_2/\beta + r_0 + \gamma\cdot r_1)}{[1 - \bar{\sigma}[D_c^+(D^++D_m)] - \bar{\sigma}(D_c)\cdot(r_2/\beta + r_0 + \gamma\cdot r_1)]} \right\} < 1 \quad (14)$$

and if

$$\bar{\sigma}[D_c^+(D^++D_m)] + \bar{\sigma}(D_c)\cdot(r_2/\beta + r_0 + \gamma\cdot r_1) < 1 \qquad (15)$$

where

$$\alpha = -\max_1 \text{Re}[\lambda_1(A+BD_cC)]$$

and M is the modal matrix of $(A+BD_cC)$.

<u>Remark 1:</u> For constant gain output feedback, Eq.(15) is an explicit constraint on the norm of the feedback gain matrix D_c. The reason for this constraint is that $\Delta D(t)$ and $\Delta H(t)$ represent high frequency paths which can destabilize the plant unless the feedback gain is sufficiently small. This observation is consistent with the results of O'Reilly [2] who indicates the robustness problem which may result when closing high frequency plant loops with constant gains. Thus, a robust constant gain controller must be a low authority controller such that the gain is small enough at high frequencies so that closing the uncertain high frequency paths does not destabilize the plant. An alternative is to use a proper, but not strictly proper, compensator described by the quadruple (A_c, B_c, C_c, D_c). In this case, Eq.(13) is an explicit constraint on D_c which represents a high frequency path. Thus, although the proper compensator need not be a low authority controller, we require that the gain D_c be small.

<u>Corollary 3 (Strictly Proper Plant with a Strictly Proper Compensator):</u>
Let $D = \Delta D = D_c = 0$. The uncertain plant in Eq.(1) is asymptotically stable if

$$\left(\frac{1}{\alpha\cdot\bar{\sigma}(Q)}\right)\left[\bar{\sigma}\left[(D_1^{-1}M^{-1})^+\begin{pmatrix} A_m & B_mC_c^+ \\ B_c^+C_m & 0 \end{pmatrix}(MD_1Q)^+\right]\right.$$

$$\left. + \bar{\sigma}\left[(D_1^{-1}M^{-1})^+\begin{bmatrix} 0 \\ B_c^+ \end{bmatrix}\right]\ \bar{\sigma}\left[[0,C_c^+](MD_1Q)^+\right]\cdot(r_2/\beta + r_0 + \gamma\cdot r_1)\right] < 1 \quad (16)$$

where

$$\alpha = -\max_i \text{Re}[\lambda_i(\hat{A}_{cl})]$$

and

$$\hat{A}_{cl} = \begin{pmatrix} A & BC_c \\ B_cC & A_c \end{pmatrix}$$

and M is the modal matrix of $\hat{A}_{cl}$.

Remark 2: For the strictly proper compensator described by the triple (A_c, B_c, C_c), there are no explicit constraints on the norms of the gains. However, B_c and C_c are implicitly constrained via the singular values in Eq.(16) and A_c is implicitly constrained via the eigenvalues of $\hat{A}_{cl}$ which must be sufficiently far into the left half of the complex plane. Note that the compensator (A_c, B_c, C_c) has no high frequency paths due to its low pass characteristic. Our results are consistent with O'Reilly [2] who suggests that the designer should avoid closing high frequency plant loops. However, we observe that we can close the high frequency loops and still guarantee robustness if the high frequency gain D_c is sufficiently small as shown by either Eq.(13) or Eq.(15).

Remark 3: When using the compensator represented by the quadruple (A_c, B_c, C_c, D_c), we can use eigenstructure assignment to assign $(r + n_c)$ eigenvalues. Here r is the number of plant outputs and n_c is the number of compensator states. However, when D_c is constrained to be zero we lose some of the degrees of freedom in eigenstructure assignment. Thus, there may be some advantages with regard to eigenvalue and eigenvector assignment in using a non-strictly proper compensator. There appears to be a tradeoff between robustness to high frequency uncertainty and the ability to exactly assign certain eigenvalues and eigenvectors.

Corollary 4 (Norm Bounded Uncertainty; Constant Gain Output Feedback):
Let $\bar{\sigma}(\Delta A(t)) \leq \gamma_1$, $\bar{\sigma}(\Delta B(t)) \leq \gamma_2$, $\bar{\sigma}(\Delta C(t)) \leq \gamma_3$, $\bar{\sigma}(\Delta D(t)) \leq \gamma_4$ and let $u(t) = D_c y(t)$.
Then, the uncertain closed loop plant its asymptotically stable if

$$\left(\frac{x_2(M)}{\alpha}\right)\left[(\gamma_1+\gamma_2\bar{\sigma}(D_c)\bar{\sigma}(C)+[\sigma(\bar{B})+\gamma_2]\sigma(\bar{D}_c)\gamma_3)\right.$$

$$+ \frac{[\bar{\sigma}(D_c)]^2[\bar{\sigma}(B)+\gamma_2][\bar{\sigma}(C)+\gamma_3][\bar{\sigma}(D)+\gamma_4]}{1 - \bar{\sigma}(D_c)\{[\bar{\sigma}(D)+\gamma_4] + (r_2/\beta + r_0 + \gamma \cdot r_1)\}}$$

$$+ \frac{[\bar{\sigma}(D_c)]^2[\bar{\sigma}(B)+\gamma_2][\bar{\sigma}(C)+\gamma_3](r_2/\beta + r_0 + \gamma \cdot r_1)}{1 - \bar{\sigma}(D_c)\{[\bar{\sigma}(D)+\gamma_4] + (r_2/\beta + r_0 + \gamma \cdot r_1)\}}\left.\right] < 1 \qquad (17)$$

and if

$$\bar{\sigma}(D_c) \cdot [\bar{\sigma}(D) + \gamma_4 + r_2/\beta + r_0 + \gamma \cdot r_1] < 1 \qquad (18)$$

where

$$\alpha = -\max_i \text{Re}[\lambda_i(A+BD_cC)]$$

and M is the modal matrix of $(A+BD_cC)$ and $x_2(M)$ is the 2-norm condition number of the matrix M.

Remark 4: We observe from Corollary 4 that robust constant gain output feedback controllers are characterized by (1) well conditioned closed loop modal matrices, (2) low norm feedback gain matrices, and (3) eigenvalues which are far into the left half of the complex plane. This suggests that $x_2(M) \cdot \bar{\sigma}(D_c)/\alpha$ should be small. Design methods which minimize either $x_2(M)$, $x_2(M) \cdot \bar{\sigma}(D_c)$ or $x_2(M)/\alpha$ will not always yield robust designs.

V. ROBUST EIGENSTRUCTURE ASSIGNMENT ALGORITHM

Three Algorithms for Robust Eigenstructure Assignment

The nominal plant or design model is described by Eq.(1) and the compensator is described by Eq.(7). The composite system used for computing A_c, B_c, C_c, and D_c for the plant (A,B,C) is given by [4]

$$\bar{A} = \begin{pmatrix} A & 0 \\ 0 & 0 \end{pmatrix}, \; \bar{B} = \begin{pmatrix} B & 0 \\ 0 & I \end{pmatrix}, \; \bar{C} = \begin{pmatrix} C & 0 \\ 0 & I \end{pmatrix}, \; \bar{F} = \begin{pmatrix} D_c & C_c \\ B_c & A_c \end{pmatrix} \qquad (19)$$

This composite system was used by Sobel and Shapiro [5] to design eigenstructure assignment dynamic compensators. The composite system which is used in Eq.(12) to determine robustness is given by

$$\tilde{A}_{cl} = \begin{pmatrix} A + BD_c C & BC_c \\ B_c C & A_c \end{pmatrix} \qquad (20)$$

The objective function to be minimized, which is denoted by ρ, is the left hand side of Eq.(12).

Algorithm 1 (Optimal Solution)

Minimize $\quad \rho(M, \Lambda, D_1, Q)$
M_s, Λ_s, D_1, Q

subject to
$$\bar{\sigma}[D_c^+ (D^+ + D_m)] + \bar{\sigma}(D_c) \cdot (r_2/\beta + r_0 + \gamma \cdot r_1) < 1 \text{ and } \lambda_i \, \epsilon \, C_i$$
where

M_s is a matrix whose columns are v_i; $i=1,\ldots,s$
Λ_s is a diagonal matrix with entries λ_i; $i=1,\ldots,s$
and C_i is a region of the complex plane.

THe optimization may be over a subset of the eigenvalues and eigenvectors of $\tilde{A}_{cl}$ where $s \le n+n_c$ with dim(A)=n and dim(A_c)=n_c.

Computations Required for Each Function Evaluation in Algorithm 1

Initialize: If D_c is non-zero, then set $\bar{F}$ equal to the orthogonal projection solution using eigenstructure assignment [5]. If D_c equals zero, then use eigenstructure assignment with gain suppression.

For each function evaluation:

1. Obtain the composite matrices $\bar{A}$, $\bar{B}$, $\bar{C}$ which are defined by Eq.(19).

2. If D_c is non-zero, then use eigenstructure assignment to obtain $\bar{F}$. If D_c is zero, then use eigenstructure assignment with gain suppression to compute

$$\bar{F} = \begin{pmatrix} 0 & C_c \\ B_c & A_c \end{pmatrix} \qquad (21)$$

3. If D is non-zero, then compute C_c^D and D_c^D as shown in Ref. 7.

4. Obtain the composite matrix $\tilde{A}_{cl}$ from Eq.(20).

5. Compute the eigenvalues of $\tilde{A}_{cl}$ to obtain α and compute the eigenvectors of $\tilde{A}_{cl}$ to obtain the closed loop modal matrix M.

6. Evaluate ρ.

A suboptimal algorithm (algorithm #2) and an ad hoc algorithm for a first order compensator with $D=D_c=0$ (algorithm #3) are described by Sobel, Yu, Piou, Cloutier, and Wilson [7].

VI. EXAMPLE

Consider the Extended Medium Range Air to Air Technology (EMRAAT) bank-to-turn missile which is described by Bossi and Langehough [6]. A sixth order model of the yaw/roll dynamics is considered with state vector, control vector, and measurement vector given by

$x = [\beta,r,p,p_I,\delta_r,\delta_a]^T$, $u = [\delta_r,\delta_a]^T$, and $y = [\beta,r,p,p_I]^T$, respectively.

Here β is sideslip angle (deg), r is yaw rate (deg/sec), p is roll rate (deg/sec), p_I is integrated roll rate (deg), δ_r is rudder deflection (deg), and δ_a is aileron deflection (deg). The state space matrices A, B, and C are shown in Ref. 7. The design described in Ref. 6 uses a full state feedback linear quadratic regulator design for the 4th order reduced order model which does not include the actuator dynamics. The optimal eigenvalues for the 4th order model are $\lambda_{1,2} = -24\pm j18$, $\lambda_3 = -5.1$, and $\lambda_4 = -14.5$. The closed loop eigenvalues for the 6th order model are shown in Ref. 7 where we observe that the eigenvalues are no longer at their optimal locations. The open and closed loop eigenvectors for the dominant modes of the 6th order model are shown in Ref. 7. We observe that the open loop eigenvectors each have their largest entry in either roll rate or integrated roll rate. Thus, there is no well defined dutch roll mode (composed predominantly of yaw rate and sideslip angle) which is quite different from most other aircraft and missile control designs which have appeared in the literature. We observe that the linear quadratic regulator design has caused the largest entry in each eigenvector to correspond to roll rate. Hence, a small perturbation in sideslip angle will cause large roll rate motion for both the open loop

and the linear quadratic regulator design. We note that the design of Ref. 8 yields a closed loop system which does not exhibit a clearly defined dutch roll mode. The time responses for the closed loop missile for a one degree initial sideslip angle are shown in Figure 1. We observe that the Ref. 6 design exhibits acceptable overshoot and settling time, but the sideslip angle induces an unacceptably large roll rate response with a peak value of -50.1 degrees per second.

Next, we design an eigenstructure assignment autopilot by using the same four measurements which were used in the Ref. 6 design. The desired eigenvalues and desired eigenvectors are shown below where we can specify four closed loop eigenvalues because we have four measurements.

$$
v_{dr}^d = \begin{bmatrix} 1 \\ x \\ 0 \\ 0 \\ x \\ x \end{bmatrix} \pm j \begin{bmatrix} x \\ 1 \\ 0 \\ 0 \\ x \\ x \end{bmatrix} \qquad v_{roll}^d = \begin{bmatrix} 0 \\ 0 \\ 1 \\ x \\ x \\ x \end{bmatrix} \pm j \begin{bmatrix} 0 \\ 0 \\ x \\ 1 \\ x \\ x \end{bmatrix}
$$

$$\lambda_{dr}^d = -24 \pm j18 \qquad\qquad \lambda_{roll}^d = -10 \pm j10$$

Dutch Roll Mode   Roll Mode

We remark that the desired eigenvectors are chosen to create a dutch roll mode which is predominantly yaw rate and sideslip angle together with a roll mode which is predominantly roll rate and integrated roll rate. The zero eigenvector entries are chosen so as to decouple the dutch roll mode and the roll mode. The achievable eigenvectors are shown in Ref. 7 where we observe that we have obtained clearly defined dutch roll and roll modes. The roll mode eigenvector is characterized by its largest entry corresponding to roll rate with very small entries corresponding to sideslip angle and yaw rate. The dutch roll eigenvector is characterized by its largest entry corresponding to yaw rate with a very small entry corresponding to integrated roll rate and a small entry corresponding to roll rate. We would desire that the entry corresponding to roll rate be even smaller. Nevertheless, this new eigenstructure design should exhibit significantly improved decoupling between sideslip angle and roll rate. The time responses for the eigenstructure
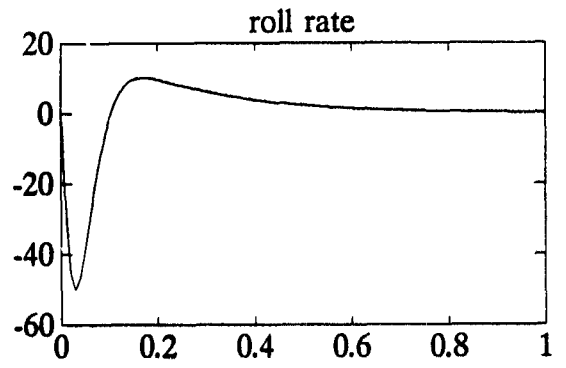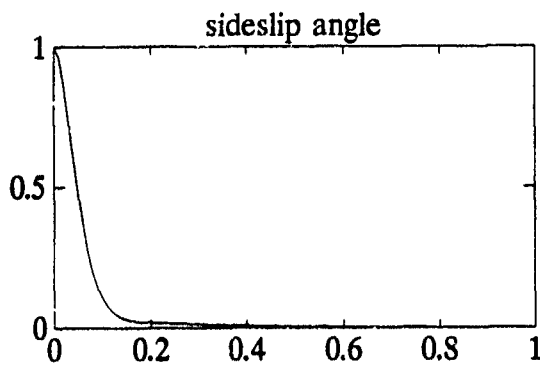
Figure 1. Closed Loop Responses (LQR)
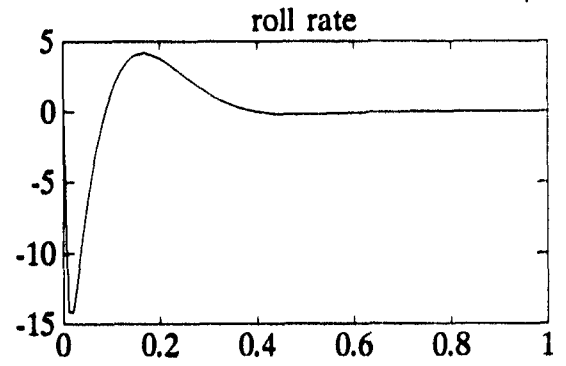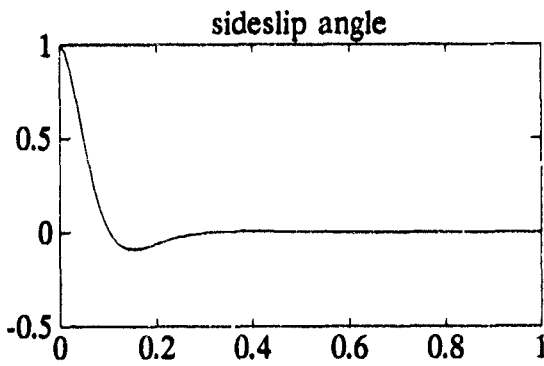
Figure 2. Closed Loop Responses (Eigenstructure)

assignment autopilot to a one degree initial sideslip are shown in Figure 2 where we observe the significant improvement in the decoupling between sideslip angle and roll rate. The peak value of roll rate is now -14.2 deg/sec which compares with -50.1 deg/sec for the linear quadratic regulator design and represents an improvement of approximately 72%. The condition number of the modal matrices, which is a commonly used measure of eigenvalue sensitivity, are compared in Ref. 7. We observe that the linear quadratic regulator design exhibits a modal matrix condition number which is 3.8 times larger than the open loop value while the eigenstructure assignment design has a condition number which is almost half the open loop value. A comparison of the quantity $\text{cond}(M) \cdot \bar{\sigma}(F)/\alpha$ (which was described in Remark 4) indicates that the eigenstructure assignment design has a value which is approximately 7 times smaller than the linear quadratic regulator design. Thus, the eigenstructure assignment design exhibits significantly improved decoupling between sideslip and roll rate together with significantly improved sensitivity and robustness properties.

We now use Corollary 2 to determine if the new sufficient condition for robust stability is satisfied. The choice for the structured state space uncertainty matrices A_m and B_m are shown in the Ref. 7.

We use Eq.(14) to determine the robustness of the design and obtain the following results: (1) If there is only structured state space uncertainty we use an optimal value for D_1 to show that the closed loop system is robust to the uncertainty represented by 1.8 times the chosen A_m; (2) If there is only unmodelled dyanmics, then the closed loop system is robust if $r_0 + r_2/\beta$ is less than 1.0×10^{-5} where D_1 is not used. We note that the sufficient condition exhibits acceptable conservatism for the structured state space uncertainty. However, the conservatism in this example for the unmodelled dynamics is unacceptable. Further research is needed toward the goal of reducing this conservatism in the new sufficient condition for robust stability of simultaneous structured state space uncertainty and unmodelled dynamics.

VII. RECOMMENDATIONS

Eigenstructure assignment has been used to design an autopilot for the

EMRAAT missile which exhibits a significant improvement in mode decoupling when compared to an earlier linear quadratic regulator design described by Bossi and Langehough [6]. However, further research is needed to further improve the mode decoupling. One approach will be to optimize over the eigenvalues in order to find a set of closed loop eigenvalues which will improve the decoupling. Another approach will be to compare the currently used orthogonal projection with a method which minimizes the one norm or infinity norm difference between the desired and achievable eigenvectors. The autopilot design in Ref. 6 considers the yaw/roll dynamics separately from the pitch dynamics. A decoupled eigenstructure assignment autopilot should be designed for the combined yaw/roll/pitch dynamics which has 3 inputs and thus greater freedom in eigenstructure assignment than either the yaw/roll dynamics or the pitch dynamics.

The robustness condition in Eq.(12) appears to yield acceptable results when the model of the missile exhibits only structured state space uncertainty. However, the conservatism is unacceptable when unmodelled dynamics are present. The robust eigenstructure assignment algorithms should be used with a constrained nonlinear optimization to obtain improved results. Another approach might be to obtain an output feedback gain matrix by optimizing the quantity $\{cond(M) \cdot \bar{\sigma}(F)/\alpha\}$. Both constant gain output feedback and dynamic compensation designs should be considered. The designs should be compared with the linear quadratic regulator design from Ref. 6 for mode decoupling, stability robustness, and eigenvalue sensitivity.

The robustness sufficient conditions should be extended to include sampled data control systems. A robust digital autopilot for the EMRAAT missile should be designed by using eigenstructure assignment. The robust stability condition for structured uncertainty should be extended to obtain a performance robustness result. The condition should guarantee that the closed loop eigenvalues remain within chosen settling time and damping regions in the z-plane for all $\Delta A(k)$ and $\Delta B(k)$. If possible, a performance robustness result should be obtained for the

case of simultaneous structured state space uncertainty and unmodelled dynamics.

A sufficient condition for stability robustness should be obtained for an LTI plant with a time delay. Such a time delay might model the time required to obtain angle of attack from pressure measurements. Alternatively, it might represent the delay involved in estimating angle of attack from velocity and angle measurements.

REFERENCES

1. Sobel, K.M., Banda, S.S., and Yeh, H.H., "Robust Control for Linear Systems with Structured State Space Uncertainty", International Journal of Control, 1989, Vol. 50, No. 5, 1991-2004

2. O'Reilly, J., "Robustness of Linear Feedback Control Systems to Unmodelled High Frequency Dynamics", International Journal of Control, 1986, Vol. 44, No. 4, 1077-1088

3. Maciejowski, J. M., Multivariable Feedback Design, Addison-Wesley Publishing Company, Wokingham, England, 1989

4. Johnson, T.L. and Athans, M., "On the Design of Optimal Constrained Dynamic Compensators for Linear Constant Systems", IEEE Transactions on Automatic Control, Vol. AC-15, 1970, 658-660

5. Sobel, K.M. and Shapiro, E.Y., "Application of Eigenstructure Assignment to Flight Control Design: Some Extensions", Journal of Guidance, Control, and Dynamics, Vol. 10, No. 1, Jan.-Feb. 1987, 73-81

6. Bossi, J.A. and Langehough, M.A., "Multivariable Autopilot Designs for a Bank-To- Turn Missile, "Proceedings of the 1988 American Control Conference, Atlanta, Georgia, June 1988, 567-572

7. Sobel, K.M., Yu, W., Piou, J.E., Cloutier, J., and Wilson, R., "Robust Eigenstructure Assignment with Structured State Space Uncertainty and Unmodelled Dynamics," submitted to the 1991 American Control Conference, Boston, MA, June 1991

1990 USAF-UES SUMMER FACULTY RESEARCH PROGRAM/

GRADUATE STUDENT RESEARCH PROGRAM

Sponsored by the

AIR FORCE OFFICE OF SCIENTIFIC RESEARCH

Conducted by the

Universal Energy Systems, Inc.

FINAL REPORT

MULTIPLE POINT DETONATION MODELING

Prepared by:	Steven A. Trogdon, Ph.D.
Academic Rank:	Associate Professor
Department and	Mathematics and Statistics
University:	University of Minnesota - Duluth
Research Location:	AFATL/SAA Eglin AFB Eglin AFB, FL 32542-5434
USAF Researcher:	David M. Jerome
Date:	7 September 1990
Contract No:	F49620-88-C-0053

MULTIPLE POINT DETONATION MODELING

by

Steven A. Trogdon

ABSTRACT

The HULL hydrodynamics code has been modified to accommodate
multiple point detonations or multiple detonations resulting
from a single impact. The modifications have been made relative
to the physics burn option in HULL. A density criteria is used as
the mechanism to trigger a detonation. The resulting detonation
is instantaneous with the propagation of the detonation front
proceeding at a rate determined by the physics burn option in HULL.
The modifications have been documented in a change rile so that
they can be directly incorporated in the HULL hydrocode. The change
file appears in the Appendix. Comparisons of the multiple point
detonation model have been made with a previously developed model
which could handle only single point detonations. The results were
identical when there was only a single detonation. The multiple
point detonation model predicted significantly more damage than did
the single point detonation model when the potential existed for a
second detonation. The multiple point detonation model represents
a contribution to continuing efforts to study the complex problem
of the lethality of kinetic energy weapons.

ACKNOWLEDGMENTS

I wish to thank the Air Force Systems Command, the Air Office
of Scientific Research and the Armament Laboratory/Eglin AFB for
sponsoring the Summer Faculty Research Program (SFRP), thus
giving me the opportunity to become acquainted with research
objectives of the Air Force. I also wish to thank Universal
Energy Systems for the part they played in making the SFRP a
possibility.

My stay at Eglin AFB was extremely rewarding. I wish to give
special thanks to Colonel Donohue, at whose request, my stay at
Eglin was made possible, to Dave Jerome who provided me with a
congenial and stimulating environment in which to work and lastly
to all personnel in the Technology Assessment Branch at the Air
Force Armament Laboratory, Eglin AFB who gave me both friendship
and technical support.

I.   INTRODUCTION:

The equations of continuum mechanics consist of a system of
coupled partial differential equations which represent basic
expressions for conservation of mass, momemtum and energy.
The HULL [1,2] code solves these equations in an Eulerian and/or
Lagrangian framework and as such provides a useful tool for
assessing, from a deterministic point of view, the potential
lethality of given impact scenarios. These impact scenarios
are often contemplated as occurring under conditions which
preclude experimental verification. The impacting of an
explosive material represents one such scenario. If sufficient
energy is transferred to the explosive during the impact process
then the potential exists for the initiation of a sustained
detonation of the explosive.

The Air Force Armament Laboratory has for some time been
engaged in a comprehensive program to study the potential
lethality of kinetic energy weapons under various impact
scenarios with space targets. These space targets generally
have on board multiple warheads. The ultimate goal is to
destroy the space target. Destruction of the space target may
be conceived of as occurring through an impact process in which
a sustained detonation of one of the warheads occurs. The
sustained detonation may then cause subsequent sustained
detonations of the remaining warheads. If at any one step in
this chain of detonations there is insufficient energy present
to spawn a new detonation then the detonation chain will be
broken and the warhead will be incompletely destroyed. Of interest

is a determination of those impact conditions which, if met,
will precipitate in the destruction of the warhead. Before
one can answer the destruction question one must be able to
consistently model multiple point detonations or multiple
detonations resulting from a single impact. The implementation,
within HULL, of a means of modeling these detonations would
therefore serve as a valuable first step in understanding the
effectiveness of kinetic energy weapons.

My research interests have been in the area of partial
differential equations, particularly those differential equations
which arise in various branches of continuum mechanics. My most
recent efforts have been in obtaining an analytical solution to
the unsteady Stokes flow of a fluid issuing from a circular
orifice and usinging symbolic algebra to obtain a solution
to the buoyancy induced motion of a thermally stratified fluid.
My understanding of the origin of the equations of continuum
mechanics, my familiarity with numerical algorithms used to
solve these equations, my background in programming and my
understanding of several computer operating systems proved to
be invaluable resources in enabling me to make a contribution
to understanding the effectiveness of kinetic energy weapons.

II.   OBJECTIVES OF THE RESEARCH EFFORT:

My assignment as a participant in the 1990 Summer Faculty
Research Program (SFRP) was

          (i)   to perform a literature review of the

state-of-the-art in explosive modeling to insure that
the highest levels of explosives understanding was
available for application.

(ii)   to provide an appropriace modification of the
HULL code which would allow its physics burn option to handle
the occurrence of multiple point detonations.

(iii)   to compare the qualitative features of the
multiple point detonation model with a model which had
only a single point detonation.

III.   OVERVIEW OF RESEARCH:
         ----

a.   Pertinent detonation literature was first reviewed to
insure that the highest levels of explosives understanding was
available for application. It was found that there are basically
four popular approaches to modeling detonations. Firstly, there
is the programmed burn approach [1,2]. This approach is one
available option for modeling detonations in the HULL code. This
approach, as the name "programmed" implies, must be completely
programmed. That is, the initiation point of the detonation, the
detonation velocity and the time at which the detonation should
occur must all be programmed by the user of the code. Secondly,
there is the physics burn option used in the HULL code [1,2].
This, method essentially assumes that the propagation of the
detonation front is governed by the steady-state conditions as
outlined by Mader [3] and, except for che modification of Trogdon [4]
to this option, the user must specify the initiation point of

11-6

the detonation. Thirdly, there is the approach of Tarver et. al [5]. This approach, unlike the two previously outlined approaches, uses the concept of initiation and growth to model detonations. The two previous approaches, with the exception of the Trogdon modification, are models which require programmed initiation with resulting instantaneous detonation. The Trogdon modification provides a density criteria to trigger initiation with resulting instantaneous detonation. The Tarver approach couples a phenomenological reaction rate equation that governs the rate of change of detonated (i.e. burned) material with a programmed burn to advance the detonation front. Lastly, there is the Forest Fire [6,7] approach. This approach couples a reaction kinetics equation with the flow equations behind a shock via the shock jump conditions. The Forest Fire approach is an initiation and growth model.

b.   A simple impact problem was next formulated to serve as a basis for comparisons to determine if modifications to the HULL code to accommodate multiple point detonations was working properly. The revised HULL code was checked to see if a multiple point detonation was actually occurring in a manner which was physically consistent and meaningful. The modification used the same density trigger that was used in the Trogdon [4] modification of the physics burn option in HULL to accommodate single point detonations. A comparison of results obtained with modifications to the HULL code to accommodate multiple point detonations was made with the Trogdon modification mentioned above.

c.   By making the comparisons indicated above we were able

to incorporate a multiple point detonation model in the HULL code
which seemed to be physically consistent and meaningful. These
changes are given in the Appendix. In section IV we give the
explict comparisons mentioned above.

IV.   COMPARISONS:

We next make comparisons of results obtained with modifications
to the HULL code to accommodate multiple point detonations with
the Trogdon modification which can accommodate single point
detonations. The impact situations are identical except that
the Trogdon modification can only accommodate a single detonation
while the modifications to handle multiple point detonations can
accommodate the potential for multiple detonations. The density
criteria discussed in [4] has been incorporated in the detonation
modeling to trigger a detonation. In Figure 1 we have, by means
of a raster plot of the density in the respective materials,
depicted the physical problem prior to impact. The problem is
axially symmetric and impact occurs along the axis of symmetry.
Physically, we have a cylindrical tungsten penetrator impacting
a cylindrical arrangement of materials at 6 kilometers/second.
The cylindrical arrangement of materials consists of (from bottom
to top) steel with an adjacent explosive (octol). The explosive
is separated by an aluminum plate. The separator plate of aluminum
was included in order to determine if the multiple point detonation
model was working properly. For the single point detonation model,
there should be an initiation point at the interface between the
steel and the explosive and along the axis of symmetry. There

should not be a second detonation at the interface between the
aluminum plate and the explosive above it. The explosive above
the aluminum plate will not detonate until the explosive "burns"
through the aluminum. However, for the multiple point detonation
model there will exist the potential for not only an initiation
point at the interface between the steel and explosive but also
a shock-initiated detonation at the interface between the aluminum
and the explosive above it.

In Figures 2 and 3 we have given raster plots of the density
in the respective materials for a single point detonation. In
the left half of the figures we have depicted the density variations
throughout the entire configuration. In the right half of the
figures we have depicted the density variations throughout only
that portion of the entire configuration which is actually
detonated material. In this way we may make direct comparisons
between the single point detonation model and the multiple point
detonation model. In Figure 2, at 4 microseconds, the detonation
front (i.e. shock wave) has reached the aluminum plate. In Figure
3, at 8 microseconds, the shock wave has been transmitted through
the aluminum plate but not as a detonation front since there can
at most be a single detonation point. There is present at 8
microseconds a portion of the explosive above the aluminum plate
which has been detonated. The presence of this material is not
due to a second detonation, but is due rather to the detonated
material below the aluminum plate "burning" through the plate
and subsequently detonating the explosive above the plate.

In Figures 4 and 5 we have given raster plots when the potential

exists for multiple detonations. Figures 4 and 5 are to be compared respectively with Figures 2 and 3. In Figure 4, at 4 microseconds, the characteristics of the detonated region below the aluminumn separator plate is identical to that in Figure 2. However, as the shock wave passes through the separator plate it does so as a detonation front. That is, there is sufficient energy transmitted to the explosive above the separator plate due to the shock wave below the plate to spawn a second detonation. In Figure 5, at 8 microseconds, the detonation front has propagated into the explosive above the separator plate and has actually burst through the back plane of that explosive. This second detonation is to be contrasted with the results in Figure 3. The damage is much more extensive when there is a second detonation.
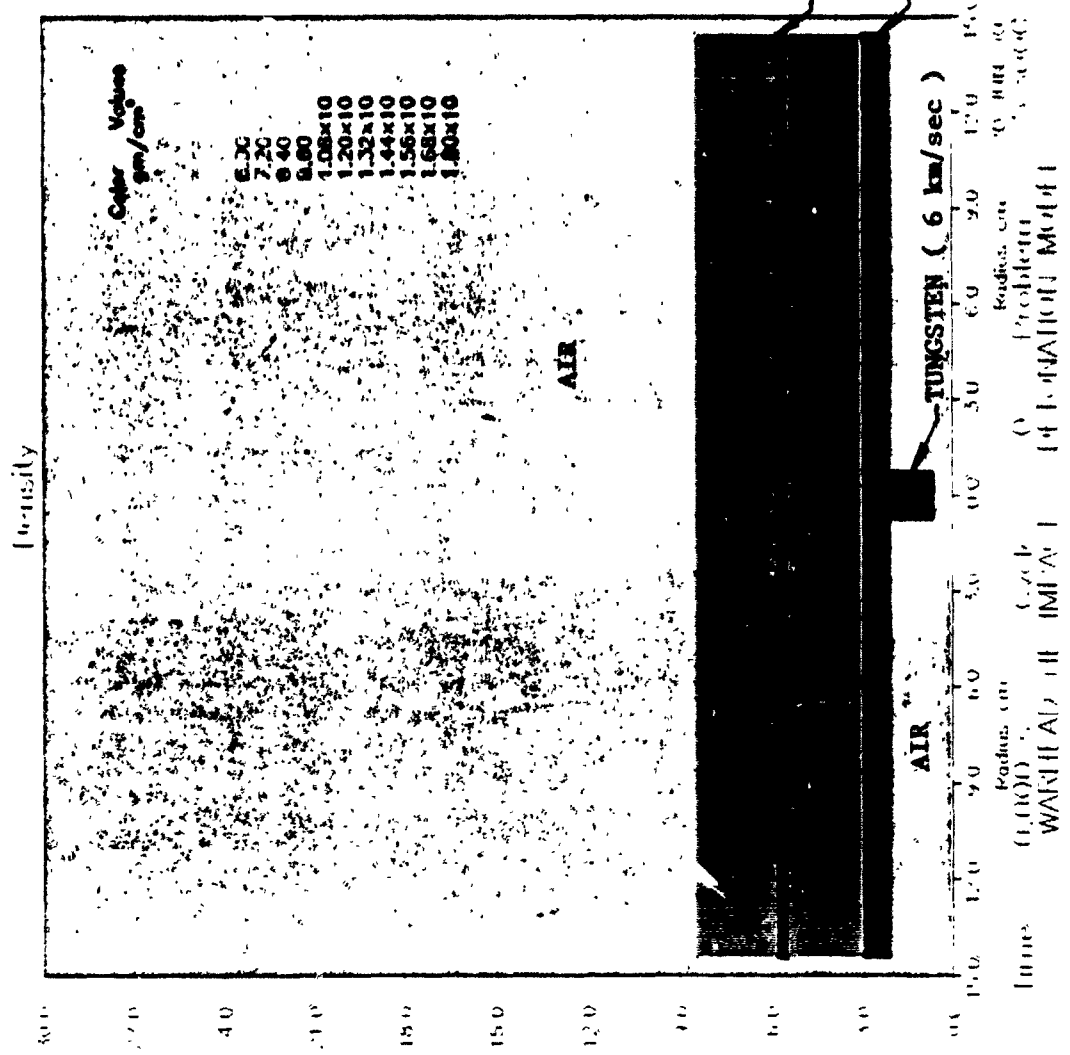
Figure 1. Configuration prior to impact at 6 km/sec.
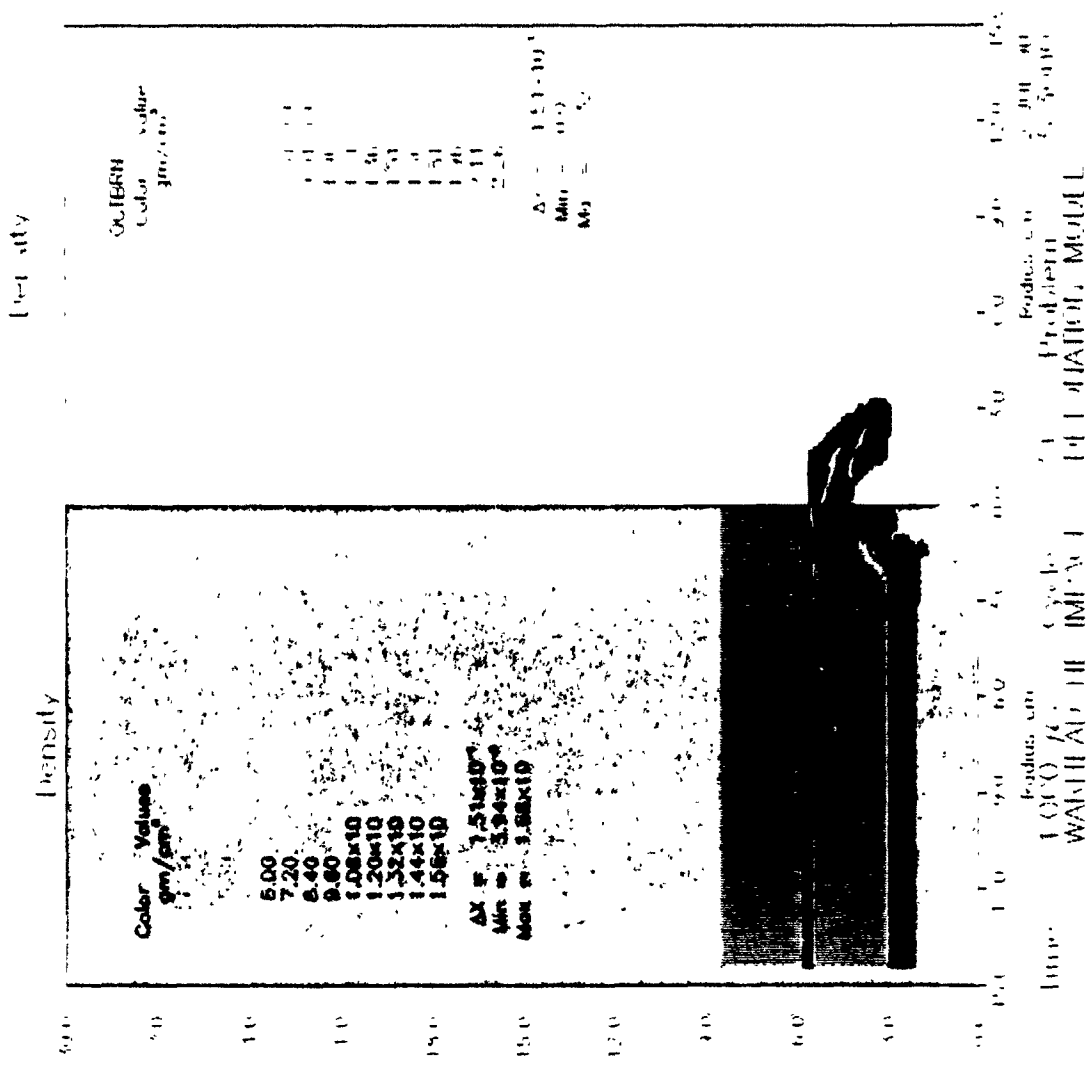
Figure 2. Configuration 4 μsec after impact, single point detonation.

Figure 3. Configuration 8 μ sec after impact, single point detonation.
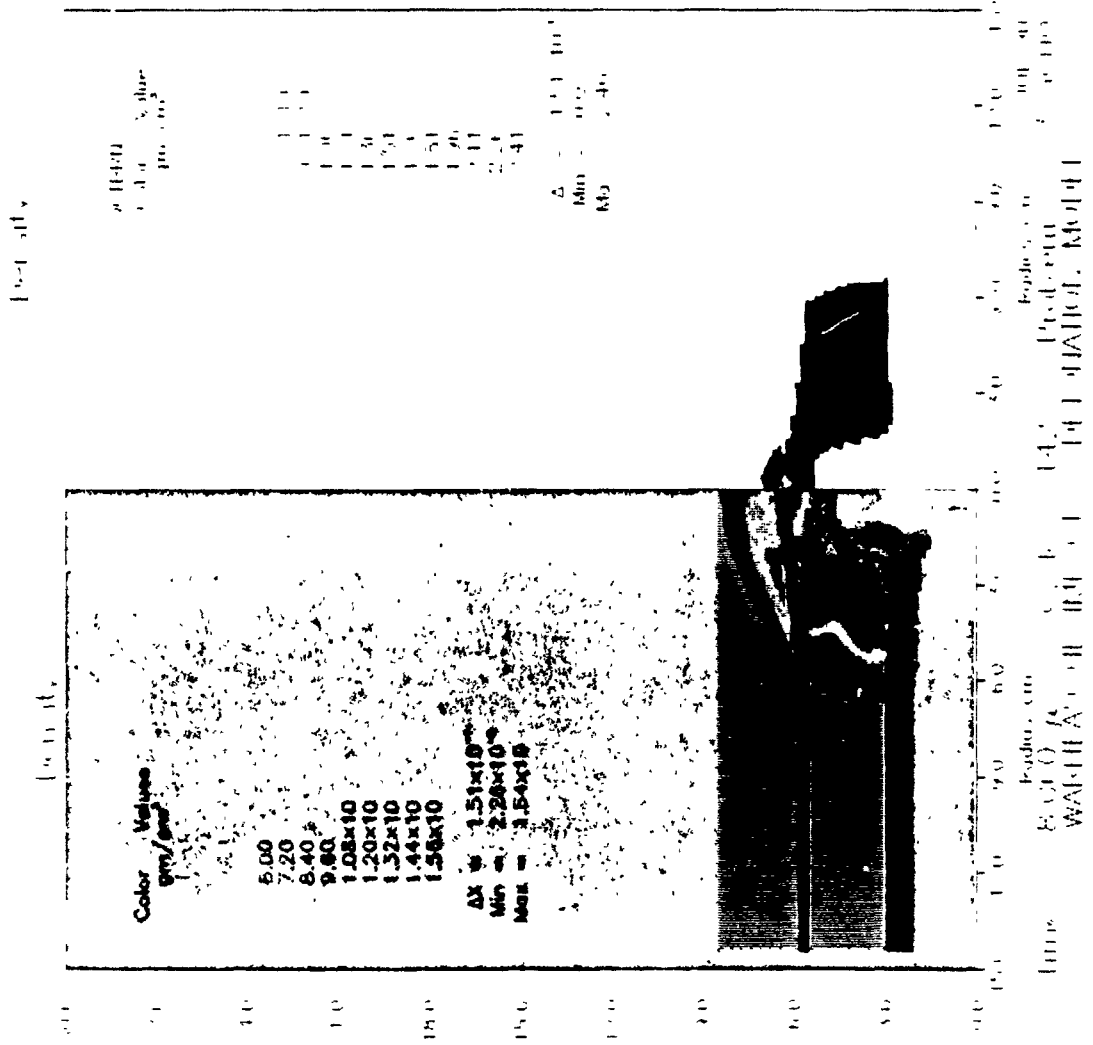
Figure 3. Configuration 8 μsec after impact, single point detonation.
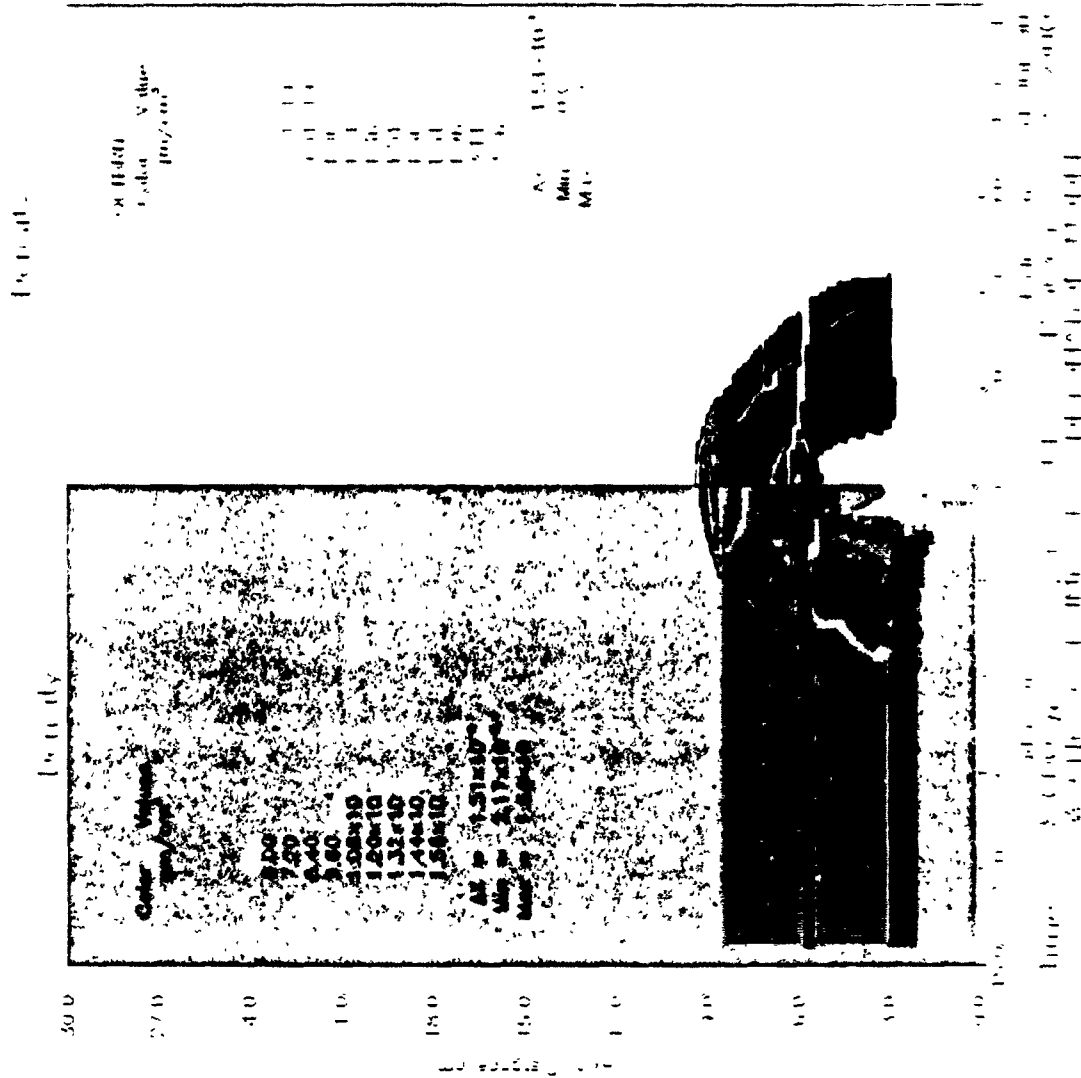
Figure 5. Configuration 8 μsec after impact, multiple point detonation.

V.   RECOMMENDATIONS:
      ----

a.   Modeling multiple point detonations of an explosive has

been implemented using the physics burn option of HULL. A

change file has been provided in the Appendix of this report

which will allow these changes to be implemented with any running

of HULL. The research presented herein represents a continuing

effort to study the more complex problem of the lethality of

kinetic energy weapons. The present modeling possesses several

advantages over previous modeling [4] of shock initiated detonations

using HULL:

        (i)   The present modeling can handle sympathetic

        detonations. These detonations may be initiated by debris

        fragments or they may be initiated by shock wave

        interations resulting from the detonation of some other

        explosive.

        (ii)   The present modeling can handle situations in

        which a penetrator initiates a detonation, outruns the

        detonation front and initiates subsequent detonations.

b.   Several questions arose during the course of the research.

These questions are provided as evidence of the need for future

research:

        (i)   Does the multiple point detonation model that has

        been incorporated in the physics burn model of HULL or

        even the previous [4] shock initiated detonation model

        actually model reality? Perhaps a way to answer this

question is to perform a series of experiments to see how closely results can be matched with reality.

(ii)   What is the effect of considering the shock-to-detonation transition? The modifications to date to the physics burn model of HULL have assumed that this transition is instantaneous. To adequately answer the question of whether or not a space target will be destroyed one must be able to determine, with known initial conditions, if sufficient energy is present to result in spontaneous detonation of the space target's warheads. At present, the best way to obtain information about the potential lethality of given impact conditions is to have at one's disposal codes which utilize initiation and growth mechanisms to model detonations. One possible way to do this is to incorporate the Forest Fire burn model in the physics burn option of HULL.

(iii)   The present modeling needs to be carefully evaluated. The code, at times, appeared to "generate" undetonated material in regions which were completely detonated. Although the impact on the physics of the detonation process could be minimized, this artifact of the modifications to HULL needs to be investigated to see if the modeling has been correctly incorporated in HULL and to see if HULL is correctly advancing the detonation front.

REFERENCES

1.   HULL Documentation, Vol. I, Technical Discussion,
     Orlando Technology, Incorporated, Shalimar, FL., 1987.

2.   HULL Documentation, Vol. II, Users Manual, Orlando
     Technology, Incorporated, Shalimar, FL., 1987.

3.   Charles L. Mader, "Numerical Modeling of Detonations",
     Berkeley and Los Angeles, University Press, 1979.

4.   Steven A. Trogdon, "Shock Wave Initiated Detonation of
     an Explosive", USAF-UES SFRP Final Report, AFATL/SAA,
     Eglin AFB, 1989.

5.   C. M. Tarver, J. O. Hallquist and L. M. Erickson,
     "Modeling Short Pulse Duration Shock Initiation of
     Solid Explosives", 8th Symposium on Detonations,
     pp. 951 - 961, 1985.

6.   C. L. Mader and C. A. Forest, "Two-Dimensional
     Homogeneous and Heterogeneous Detonation Wave Propagation",
     Los Alamos Scientific Laboratory, Pub. LA-6259, 1976.

7.   Eric A. Lundstrom, "Evaluation of Forest Fire Burn
     Model of Reaction Kinetics of Heterogeneous Explosives",
     Naval Weapons Center, China Lake, CA, Pub. NWC TP 6898,
     1988.

APPENDIX - CHANGES TO THE HULL CODE

```
*I 50928
*KEEPTO TROGBURN BURN1
c
c       VARIABLES USED IN TROGDCN-BURN1 RHO-INITIATION
c
        COMMON /BURN/IBURN,irho(193)
c
*LABEL TROGBURN
*I 70474
*KEEPTO TROGBURN BURN1
        IBURN=0
*LABEL TROGBURN
*I 87719
*KEEPTO TROGBURN BURN1
c
c*******************************************************************
c       this is the beginning of trog-burn1 rho-initiated detonation
c*******************************************************************
        if (iburn .eq. 1) goto 110
c
c       dimension irho(imax) in common/burn/iburn,irho(imax)
c       where imax is initialized in the keel input file
c
c
c       this is the density threshold
c
        denc=1.92d0
        nstart=n
        nlsave=nl
        nrsave=nr
        do 100 istep=2,iq
          irho(istep)=0
          n=nstart+(istep-1)*nh
          nl=n-nh
          nr=n+nh
c
c       check to see if cell is a candidate for detonation. do not
c       detonate cell (ie. change mass in cell to burned material)
c       unless:
c               1. cell has no burned material in it
c               2. density threshold has been reached
c               3. all surrounding cells (cells to left, to right, above
c                  and below) have no burned material in them
c
c
c       check to see if cell has burned material in it
c
          if (xm(n+ib) .gt. 0.0 .or. xv(n+iu) .le. epl) goto 100
          den=xm(n+iu)/xv(n+iu)
c
c       check to see if the density threshold has been reached
c
          if (den .ge. denc) then
            tntb=0.
            tntl=0.
            tntr=0.
            tnta=0.
            fact=4.
            if (istep .gt. 1) tntl=xm(nl+iu)+xm(nl+ib)
            if (j .gt. 1) tntb=xm(nb+iu)+xm(nb+ib)
            if (j .lt. jmax) tnta=xm(na+iu)+xm(na+ib)
            if (istep .lt. imaxm1) tntr=xm(nr+iu)+xm(nr+ib)
c
c       calculate mass fractions of burned material in neighboring cells
c
            if (tntl .ge. 0. .and. tntl .lt. epl) then
              thetal=0.
              fact=fact-1.
            else
              thetal=xm(nl+ib)/tntl
            endif
            if (tntr .ge. 0. .and. tntr .lt. epl) then
              thetar=0.
              fact=fact-1.
```

```
            else
              thetar=xm(nr+ib)/tntr
            endif
            if (tntb .ge. 0. .and. tntb .lt. epl) then
              thetab=0.
              fact=fact-1.
            else
              thetab=xm(nb+ib)/tntb
            endif
            if (tnta .ge. 0. .and. tnta .lt. epl) then
              thetaa=0.
              fact=fact-1.
            else
              thetaa=xm(na+ib)/tnta
            endif
c
c        calculate average mass fraction of burned material in
c        neighboring cells
c
            if (fact .eq. 0.) then
              irho(istep)=1
              goto 100
            else
              ave=(thetal+thetar+thetab+thetaa)/fact
            endif
c
c        pick out those cells in the given row which essentially have
c        neighboring cells which are unburned
c
            if (ave .ge. 0.0 .and. ave .le. epl) irho(istep)=1
              endif
100         continue
c
c        detonate those cells in the given row which have satisfied the
c        criteria for detonation
c
            do 105 istep=2,iq
            n=nstart+(istep-1)*nh
            if (irho(istep) .ne. 0) then
              xmu=xm(n+iu)
              xvu=xv(n+iu)
              den=xm(n+iu)/xv(n+iu)
              xm(n+ib)=xm(n+ib)+xm(n+iu)
              xm(n+iu)=0.d0
              xv(n+ib)=xv(n+ib)+xv(n+iu)
              xv(n+iu)=0.d0
            write(*,1) istep, j, t, den
1           format(1x,'i = ',i3,3x,'j = ',i3,3x,'time = ',e14.6,3x,'density'
     1' = ',f5.3)
            write(*,2) xmu,xmv
2           format(10x,'mass = ',e14.6,3x,'volume = ',e14.6/)
            endif
105         continue
            n=nstart
            nl=nlsave
            nr=nrsave
110         continue
c*******************************************************************************
c        this is the end of trog-burnl rho-initiated detonation
c*******************************************************************************
c
*LABEL TROGBURN
*KEEPTO TROGBURN BURN1
*I 88264
        IF (XM(NB+IU) .LE. 0.) GO TO 6010
*LABEL TROGBURN
```

1990 USAF-UES SUMMER FACULTY RESEARCH PROGRAM

GRADUATE STUDENT RESEARCH PROGRAM

Sponsored by the

AIR FORCE OFFICE OF SCIENTIFIC RESEARCH

Conducted by the

Universal Energy Systems, Inc.

FINAL REPORT

DEVELOPMENT OF A COMBUSTION MODEL FOR LIQUID FILM COOLED ROCKET ENGINES

Prepared by:	William M. Grissom
Academic Rank:	Assistant Professor
Department and University:	Physics Department Morehouse College
Research Location:	AEDC, SVT/900 Arnold AFB, Tenn 37389
USAF Researcher:	Chad Limbaugh
Date:	July 27, 1990
Contract No:	F49620-88-C-0053

APPLICATION OF A TURBULENT COMBUSTION
MODEL TO LIQUID FILM COOLED ROCKET ENGINES

by
William M. Grissom

ABSTRACT

A 3-D turbulent spray combustion model developed for internal combustion engines (Los Alamos KIVA) was modified for a liquid film cooled rocket. The transpiration of vapor from the liquid film on the combustion chamber walls required modification of the boundary conditions.

A previous model of liquid film cooling by the author was modified to include transient heat conduction into the wall. The heat conduction was modeled by a 2-D finite difference formulation of the diffusion equation. For an epoxy combustion chamber, transient wall conduction is insignificant after the first second of a rocket firing. However, for a metal combustion chamber the times are significant and transient wall conduction should be modelled.

ACKNOWLEDGEMENTS

I. INTRODUCTION

I spent the summer of 1987 at AEDC developing a model of liquid film cooling in rocket engines. Hand calculations gave good comparison with the data in existing test reports. During the summer of 1988 I returned to AEDC and developed a computer code which eliminated many of the approximations used in the hand calculations. The code was thoroughly tested against existing data and found to predict liquid film lengths and wall temperatures downstream of the liquid film within about 20% (Reference 1).

I have a background in heat transfer and fluid flow, with academic training in mechanical and aerospace engineering. My Master's thesis dealt with spray cooling of heated surfaces (Reference 2). My Doctoral research used Rayleigh and Raman scattering for combustion diagnostics. Presently I am working on droplet sizing in rocket injectors, begun as a minigrant following my summer 1988 tenure at AEDC. This experience contributed to my being assigned to the current task.

Since my last work at AEDC two summers ago, tests on a liquid film cooled rocket engine were completed. No detailed temperature data was taken, so that a direct comparison with my liquid film model was not possible. However, extensive plume spectroscopic measurements were made.

To analytically predict the plume radiation requires that the temperatures and species at the nozzle exit plane be determined by a flow model. While 1-D kinetics codes such as JANNAF's TDK are routinely used at AEDC, these fail to consider radial variations. Most rocket engines have multi-element injectors which distribute the propellants evenly over the combustion chamber. However, the TRW TR-201 rocket tested has a single pintle injector on the axis, giving significant radial variations. This is compounded by the addition of fuel vapor at the walls. Therefore, a 1-D model would not be expected to accurately model this engine.

Los Alamos Lab's KIVA code, developed over the past 10 years, models 3-D turbulent combustion in fuel sprays. It was developed for internal combustion engines. D.W. Lankford of AEDC modified the KIVA code to simulate rocket nozzles and obtained favorable comparison with the simpler TDK code (Reference 3). In his work a uniform flow of combustion products was input to the model. The spray combustion subroutines in the model were not used.

II. OBJECTIVES OF THE RESEARCH EFFORT

Before modifying the KIVA code, it was necessary to explain a change in the plume observed 15 seconds after beginning one test. It was initially thought that the most likely time lag of that magnitude would be transient heating of the combustion chamber walls, which might gradually alter the liquid film length. To give a definitive answer required that I extensively modify my liquid film cooling model to account for conduction into the wall. This modification took half of the 10 week period.

The second half of the research period was spent in continuing Dennis Lankford's work on modifying the KIVA code to simulate the TRW TR-201 rocket. This involved modifying the boundary conditions to include the mass, momentum, and energy of the vapor and activation of the spray combustion subroutines.

III. TRANSIENT WALL HEATING

Initially, a 1-D finite difference model of the wall conduction was developed. Using the nomenclature of Figure 1, the discretized energy equation is:

$$\rho c (A \Delta y) \frac{\Delta T}{\Delta t} = kA \left[\frac{\Delta T}{\Delta y} \bigg|_{in} - \frac{\Delta T}{\Delta y} \bigg|_{out} \right]$$

Using simple Euler differencing for the time derivative:

$$T_i{}^n - T_i{}^{n-1} = R(\Delta T_{in} - \Delta T_{out})$$

$$\text{where:} \quad R = \alpha \Delta t / (\Delta y)^2 \quad \text{"Fourier's Modulus"}$$
$$\alpha = k / (\rho c) \quad \text{"thermal diffusivity"}$$

The superscripts refer to the time step, either n for the present time or n-1 for the value at the last time step.

At first, simple Euler differencing was tried for the spatial derivatives, termed the "classic explicit" method. However, this required excessively small time steps for accuracy. The well known "Crank-Nicolson" differencing was found more efficient. This uses the average of the value at the previous and present time steps (Reference 4):

$$\Delta T_{in} = \tfrac{1}{2}(T^n + T^{n-1})_{i+1} - \tfrac{1}{2}(T^n + T^{n-1})_i$$

Similarly for ΔT_{out}. The energy equation then becomes:

$$(T_{i-1} + bT_i + T_{i+1})^n = d_i$$

$$\text{where:} \quad b = -2(1+1/R)$$
$$d_i = (-T_{i-1} + b_2 T_i - T_{i+1})^{n-1}$$
$$b_2 = 2(1-1/R)$$

Since the temperatures in term d are known from the previous time step, d is a constant. However, the three temperatures on the left side are unknown and must be solved simultaneously, making this is an implicit method.

At the first node ($i=1$) $T_{i-1}=T_0$ is known, giving,

$$bT_1 + cT_2 = d_1 \quad ; \quad \text{where:} \quad d_1 = (-T + b_2 T_1 - T_2)^{n-1} - T_w$$

The outside wall is assumed adiabatic, so the en gy balance at the last node ($i=N$) becomes (after some algebra):

$$T_{N-1} + b_N T_N = d_N$$

where:
$$b_N = -(1+2/R)$$
$$d_N = -T_{N-1} + b_3 T_N$$
$$b_3 = 1-2/R$$

The system of equations is then:

$$bT_1 + T_2 = d_1$$
$$T_1 + bT_2 + T_3 = d_2$$
$$T_2 + bT_3 + T_4 = d_3$$
$$\bullet \qquad \bullet$$
$$T_{N-1} + b_N T_N = d_N$$

The well known "Thomas algorithm" readily solves this "tri-diagonal" system of equations. Similar to Gaussian elimination, the 1st equation is solved for T_1 and substituted into the 2nd, giving:

$$T_1 = a_1 T_2 + c_1 \qquad \text{where:} \quad a_1 = -1/b \quad , \quad c_1 = d_1/b$$

$$T_2 = a_2 T_3 + c_2 \qquad \text{where:} \quad a_2 = -\frac{1}{a_1+b} \quad , \quad c_2 = \frac{d_2 - c_1}{a_1+b}$$

Generalizing, the a and c coefficients are found recursively on the "forward march" as:

$$a_i = -\frac{1}{a_{i-1}+b} \quad \text{and} \quad c_i = \frac{d_i - c_{i-1}}{a_{i-1}+b} \qquad \text{for } i = 2 \text{ to } N-1$$

Substituting into the last equation:

$$(a_{N-1} T_N + c_{N-1}) + b_N T_N = d_N$$
$$\text{or}$$
$$T_N = (d_N - c_{N-1})/(a_{N-1}+b_N)$$

The other temperatures are found recursively on the "backward march" as:

$$T_i = a_i T_{i+1} + c_i \qquad \text{for } i = N-1 \text{ to } 1$$

Note that the a_i coefficients are constants which can be pre-calculated.

12-6

In the present application, the wall temperature is initially uniform at room temperature, T_0. When the engine starts, the wall is covered with liquid coolant at the saturation temperature. The analytical solution for an infinite wall is (Reference 5):

$$\theta = \frac{2}{\sqrt{\pi}} \int_0^{\eta} e^{-\eta^2} d\eta = erf(\eta)$$

$$\text{where:} \quad \theta = \frac{T_w-T}{T_w-T_0} \quad ; \quad \eta = y/(2\sqrt{\alpha\pi t})$$

Initially, the heat does not penetrate far into the wall. If a fixed grid is used, the nodes beyond the penetration depth do not appreciably change. This requires that an inordinate amount of time be spent calculating zeros. A more efficient approach is to concentrate the calculations in the area of steep temperature gradient, ignoring those points beyond the penetration depth. This is done by beginning the simulation with a thin grid zone, a power of 2 factor thinner than the total wall thickness. When the temperature rise at the last node becomes noticeable, the grid is doubled in size. This continues until the grid covers the entire wall thickness.

While the reduced grid is used, a constant temperature condition is maintained at the outer node. In this case the temperature at the last node is calculated as:

$$T_N = (d_N-c_{N-1})/(a_{N-1}+b)$$

$$\text{where:} \quad d_N = (-T_{N-1}+b_2 T_N-2T_0)^{n-1}$$

The 1-D conduction model was written in Microsoft QuickBASIC. The program allows several plotting choices. A time plot gives the temperature profiles versus time. A nondimensional plot gives the temperature profiles in the nondimensional variables θ and η above. This causes the profiles to collapse to the single error function curve until the temperature penetrates to the outer wall. A final option is to plot the total heat flux (per area) into the wall:

$$Q_{tot} = \int_0^t q_{wall} \, dt$$

$$\text{where:} \quad q_{wall} = k_{wall}(T_0-T_1)/\Delta y$$

which asymptotically approaches the heat stored in the wall at steady state:

$$Q_{tot}|_{t \to \infty} = \rho C_p T_{wall}(T_w-T_0)$$

where T_{wall} is the wall thickness. Initially, the heat flux into the wall follows the analytical solution (Reference 6): $q_{wall} = k(T_w-T_0)/\sqrt{\pi\alpha t}$, which is also plotted.

Using 20 nodes and setting the time step such that $R = 1$ gave excellent agreement with the analytical solution. Setting $R > 5$ caused oscillations.

After checkout, the program was ported to FORTRAN and extended to 2 dimensions for coupling with the existing liquid film evaporation code. The grid nomenclature is given in Figure 2.

The axial differencing was done explicitly using values from the last time step. This simply adds a term d_{ax} to the previous d term:

$$d_{ax} = -2(\Delta y/\Delta \ell)^2 (T_{j-1} - 2T_j + T_{j+1})$$

where $\Delta \ell$ is the axial node spacing. The axial boundary conditions are taken as the liquid coolant temperature at the left (due to the coolant manifold), and adiabatic at the right side. The adiabatic condition is forced by using a fictitious column of nodes set equal to the temperatures at the last axial node.

The net heat flux (per area) into the liquid film is: $Q_{tot} = Q_{conv} + Q_{rad} - q_{wall}$ where Q_{conv} and Q_{rad} are the convective and radiative heat fluxes from the combustion chamber and q_{wall} is the heat flux into the wall calculated from the wall temperature profile, as above.

In the author's previous liquid film evaporation model, initial heating of the liquid to the saturation temperature was treated simply by augmenting the latent heat term. A more correct treatment is to calculate the initial temperature rise as: $dT_{liq}/dx = Qtot/(M_{liq}C_p)$, where M_{liq} is the local liquid mass flow rate per circumference. After the liquid film reaches the saturation temperature, T_v, the evaporation rate per area is: $m_v = Q_{tot}/\lambda$. The difference is that initially there is no evaporation, and therefore no transpiration decrease of the convective heat flux, resulting in calculated liquid film lengths about 2% shorter than with the approach of Reference 1. Additionally, the transpiration term in Reference 1, Sec. 2.1.2 should be changed to read:

$$h/h_o = [\ln(1 + H)]/H \; ; \quad \text{where } H = C_p/\lambda [\Delta T + (Q_{rad} - q_{wall})/h]$$

Given q_{wall} at each axial position, the liquid film length is calculated by the previous liquid film code in subroutine "liquid". Where the liquid film exists, the wall temperature equals the saturation temperature. Downstream of the liquid film, the wall temperature is set to the freestream gas temperature. Actually, the wall temperature rises gradually, as given by the gaseous film cooling code of Reference 1, however, axial conduction was found to be negligible, so that this is unimportant.

It was difficult to obtain a stable solution, as coupling between the wall conduction and liquid film evaporation codes was very strong near time = 0. It was

necessary to wait 0.01 sec before allowing interaction. The liquid film length was then updated every 8th time iteration. The resulting solution is shown in Figure 3.

Initially the wall heat flux is infinite, so that the liquid film does not evaporate. However, after 0.2 seconds the wall heat flux becomes negligible and the liquid film length approaches the steady-state value. These results can be qualitatively verified by a simple hand calculation.

When $q_{wall} = 0.091(Q_{conv} + Q_{rad})$, the liquid film will be 10% longer than the steady state value (where $q_{wall} = 0$). Solving the previous analytical expression for the time when this occurs:

$$t = (k\Delta T/q_{wall})^2/(\pi\alpha)$$

For the TRW TR-201 engine this gives a time of 0.44 sec, which is the same order as Figure 3. Changes in the transpiration term were neglected in this analysis.

The property values used above were: $T_v = 419$ K, $T_0 = 300$ K, $k = 0.568$ W/m•K, and $\alpha = 7.0 \ 10^{-8} m^2/s$. k was calculated by assuming equal volumes of phenolic resin ($k = 0.35$ W/m•K) and SiO_2 glass ($k = 1.5$ W/m•K) (Reference 7). Another source (Reference 8) quotes $k = 0.374$ W/m•K at 1200° F.
α was given for a phenolic/glass composite in Reference 7, along with notes stating a density of 1.93 kg/m^3 and an average resin content of 50% (phenolic/asbestos). The heat fluxes in the TR-201 rocket are: $Q_{conv} = 1.67$ MW/m^2 (avg) and $Q_{rad} = 0.71$ MW/m^2.

The comparable time would be 18 sec for a chamber with steel walls ($k = 52$ W/m•K, $\alpha = 1.44 \ 10^{-5} m^2/s$). Of course, the heat would have penetrated to the outer wall by this time, making this simplified analysis invalid, however the computer code would still be valid.

The conclusion is that conduction into the chamber walls is negligible for the present rocket, so that the original steady-state liquid evaporation code is sufficient. However, for other rocket engines the transient wall heating may be significant.

IV. DROPLET VAPORIZATION MODEL

Presently, the KIVA code includes both heat convection to a droplet and mass transfer of vapor away from the droplet. The mass transfer rate depends upon the vapor pressure at the droplet surface. Increasing the surface temperature increases the vapor pressure and resulting mass transfer rate, but decreases the heat convection. Since the heat convection rate must equal that required to vaporize this mass flow, the droplet surface temperature results implicitly.

While this approach is needed for slow evaporation in a cold free stream gas (Reference 9, Problem 21.E), the high heat fluxes in a rocket engine assure that the droplet surface will stay at the saturation temperature. Therefore, the problems of mass transfer and determining the vapor pressure need not be considered. Note that this same assumption was made in the liquid film cooling analysis.

In general, internal heat conduction in the droplet must be considered. The simplest approach is to assume a solid sphere, with conduction defined by the 1-D spherical diffusion equation. This can be solved by reformulating the finite differencing of Section III for spherical coordinates. To account for internal circulation in the droplet, the thermal conductivity is increased by a factor which depends upon the circulation velocity (Reference 10). For large circulation velocities ($Pe_\ell > 200$), as would exist in an injector spray, this factor asymptotes to 2.72 . However, a much simpler approach termed the "infinite conductivity model" is to lump the droplet temperatures to a single temperature, T_d, and is suggested initially.

The heat transfer coefficient to a moving sphere is given by "Frossling's Equation" (Reference 9, Equation 13.3-1):

$$Nu = 2.0 + 0.60 \, Pr^{0.333} \, Re^{\frac{1}{2}}$$

where $Nu = h_o D / k$, k and Pr are the thermal conductivity and Prandtl number of the gas, and Re is the Reynold's number based upon the droplet diameter.

The vapor generated decreases the heat transfer coefficient through transpiration, by a factor:

$$\frac{h}{h_o} = \frac{\ln(1+B)}{B} \quad ; \quad \text{where:} \quad B = \frac{C_p \Delta T}{\lambda}$$

Parameter B is termed the "Spalding Transfer Number". This correction is somewhat obscure when derived from "film theory", as in Reference 9. It is more easily understood when derived from Couette flow theory as in Reference 11.

Time has not permitted implementing these changes in the KIVA code. It is also necessary to modify the KIVA code to handle both fuel and oxidizer droplets. However, it might be noted that some rocket models assume that the oxidizer is instantly vaporized so that only fuel droplets exists.

V. KIVA CODE MODIFICATIONS

The last four weeks were spent working with G.W. Lewis, a Sverdrup programmer, modifying Los Alamos Lab's KIVA code for liquid film cooling in rockets, an effort begun by D.W. Lankford of Sverdrup. This section outlines the code modifications and results to date.

The liquid film length and vaporization rate versus axial position is calculated in subroutine "Cool". Cool requires the free stream gas density, temperature, and axial velocity near the wall, but outside the boundary layer. Since it takes some program logic to define this position, it was decided instead to supply Cool with the bulk gas "mass flow" $G_{ch} = \rho v$, which is the overall mass flow rate per chamber area. The mass flow is readily determined from the flow rates measured during a test. For simplicity, the temperature on the axis was used for the free stream temperature. These assumptions are most appropriate when the free stream flow is fairly uniform across an axial section, which must be verified when the engine simulation is complete.

The liquid film affects the KIVA code through the transpiration of vapor from the surface. The vapor affects both the mass, energy, and momentum balances at the outermost cells in the grid. Only the effect upon the momentum balance was studied here. D.W. Lankford previously modified the mass and energy balances.

Since the liquid surface velocity, Us, is very small, the transpiring vapor carries no appreciable axial momentum. However, it must be accelerated from Us to the axial velocity at the last grid cell, U. The mass flux of vapor from the wall is ρV_w. Applying Newton's 2nd law, this requires a shear stress at the last cell of $\rho U V_w$. In addition, there is a shear stress at the wall, τ_w, which must also be balanced, so that the total shear stress acting upon the last cell is $\tau_{cell} = \tau_w + \rho U V_w$.

Without vapor transpiration, τ_w is calculated from the "law-of-the-wall":

$$\frac{U}{U_*} = 2.5 \ln\left[\frac{y U_*}{\nu}\right] + 5.5$$

where y is the distance from the wall, $U_* = (\tau_w/\rho)^{1/2}$ is termed the "shear velocity", and ν is the kinematic viscosity. U_* is found implicitly and τ_w calculated as $\tau_w = \rho U_*^2$. To avoid an implicit solution, the argument of the logarithm is approximated in the KIVA code, resulting in an explicit expression (Reference 12):

$$\frac{U}{U_*} = 2.19 \ln\left[\frac{y U}{\nu}\right] + 0.79$$

With vapor transpiration, a "modified law-of-the-wall", given by Cebeci and Bradshaw (Reference 13), applies. It can be written as:

$$U = \frac{U_*^2}{V_w} (F^2 - 1)$$

where:

$$F = \frac{V_w}{U_*}\left[1.25\ln\left(\frac{yU_*}{\nu}\right) - 2.65\right] + \left[1 + 10.8\frac{V_w}{U_*}\right]^{\frac{1}{2}}$$

which reduces to the standard "law-of-the-wall" as $V_w \rightarrow 0$.

This "modified law-of-the-wall" must be solved implicitly. While it converges by simple iteration for some values of V_w, the Newton-Raphson method gives stable solutions for all values of V_w. In functional form, the modified law is $U = f(U_*)$. The problem is to find the value of U_* which makes $f(U_*) = U$, where U is the correct axial velocity at the last cell. The projected value of U_* is calculated as:

$$U_*|_{i+1} = U_*|_i + \frac{U - U_i}{f'}$$

where:

$$f' = \frac{2U_*}{V_w}(F^2 - 1) + F\left[8.3 - \frac{10.8}{(1 + 10.8V_w/U_*)^{\frac{1}{2}}} - 2.5\ln\left(\frac{yU_*}{\nu}\right)\right]$$

where U_i is the value of U calculated using $U_*|_i$. This implicit solution is calculated in function "Tauwall".

A simpler approach is to use the value of τ_w calculated in subroutine "Cool". This calculation assumes a developing boundary layer and is less general, however, it is advantageous in that this approach decouples the liquid film calculation from the KIVA code. Both approaches were found to give similar results for the wall shear stress.

A representative simulation result is given in Figure 4 for the temperature contours with and without liquid film cooling. These are tentative results since the program is still under development. Presently, methane replaces the actual vapor constituents and no reactions with this methane are allowed. Still the simulation shows some interesting trends. Notice that the temperatures in the core gas flow are hardly affected by the presence of a liquid film, while the temperatures next to the wall are significantly cooler. This is expected since the velocity plots show smooth streamlines. Another expected result (not shown) is that the boundary layer is much thicker when using film cooling.

VI. RECOMMENDATIONS

Continued development of the KIVA code is needed before realistic simulations are obtained. Presently the simulation is started with the products of combustion, obtained from an equilibrium code. Instead, the spray combustion and chemical kinetics subroutines need to be modified and actuated. Additionally, the actual vapor should replace the methane presently input in place of the vapor.

Long period velocity fluctuations in the downstream direction were observed in the cells adjacent to the wall. This problem arose even without film cooling, using the standard "law-of-the-wall". It may be due to an interaction between shear heat generation and the gas density. Presumably it does not arise when the KIVA code is used to simulate diesel engine combustion chambers, as intended. The much higher wall shear stresses in a rocket engine may drive the code into a region of instability. This problem needs further study.

An important input to the spray combustion subroutine is the droplet size distribution. However, no data exists for the pintle injector used in the TR-201 rocket. Presently the author is continuing work begun on a minigrant from 1989 to obtain such data. However, this work is limited to atmospheric pressure. Since the back pressure is known to significantly affect the drop size distribution, it is suggested that a pressure chamber be built to allow testing with varying back pressure. This is being considered as a follow-on minigrant project.

REFERENCES

1. Grissom, W.M., "Liquid Film Cooling in Rocket Engines", Arnold Engineering Development Center TR-?, December 1989.
2. Grissom, W.M. and F.A. Wierum, "Liquid Spray Cooling of a Heated Surface", Int. Journal of Heat and Mass Transfer", February 1981.
3. Lankford, D.W., "Application of CONCHAS-SPRAY to Rocket Nozzle Analysis". AIAA paper AIAA-87-2129
4. Lapidus, L. and G.F. Pinder, Numerical Solution of Partial Differential Equations in Science and Engineering, J. Wiley, 1982, Sec. 4.3.5.
5. Arpaci, V.S. Conduction Heat Transfer, Addison-Wesley, 1966, Eq. 5-96.
6. Gosman, A.D., Launder, B.E., and Reece, G.J., Computer-Aided Engineering - heat transfer and fluid flow, Ellis Horwood Ltd, 1985, Problem 1, Lesson 1. (note error in their equation).

7. Touloukian, Y.S., Powell, R.W., et al, <u>ThermoPhysical Properties of Matter</u>. IFI/Plenum, 1970.

8. Hines, W.S. et al, "Development of Injector Chamber Compatibility Analysis", AFRPL-TR-70-12, March 1970.

9. Bird,R.B., Stewart, W.E., and Lightfoot, E.N. <u>Transport Phenomena</u>. Wiley (1960)

10. Abramzon, B. and Sirignano, W.A., "Droplet Vaporization Model for Spray Combustion Calculations", <u>International Journal of Heat and Mass Transfer</u>, Vol. 32, no. 9, pp. 1605-1618. (1989)

11. Hartnett, J.P. et. al. <u>Heat and Mass Transfer in Boundary Layers</u>. Vol.1 N. Afgan, editor, Pergamon, 1972.

12. Amsden, A.A., J.D. Ramshaw, et al. "KIVA: A Computer Program for 2 and 3 - Dimensional Fluid Flows with Chemical Reactions and Fuel Sprays", Los Alamos National Laboratory Report LA-10245-MS, February 1985.

13. Cebeci, T. and Bradshaw, P. <u>Momentum Transfer in Boundary Layers</u>, 1977.

<u>NOMENCLATURE</u>

C_p = specific heat per mass

D = diameter of combustion chamber at position x

G = free-stream mass flow per area = $\rho_g U_g$

m_v = total coolant evaporation rate per surface area

Pe_ℓ = Peclet no in liquid = DU_s/α_ℓ

St = Stanton no = $h/(G\ C_p)$

T_v = saturation temperature of coolant

ΔT = T_g-T_v

U_* = "shear velocity" = $(\tau_w / \rho)^{\frac{1}{2}}$

x = axial distance from injector

y = distance from chamber wall

Greek Symbols:.

α = thermal diffusivity = $k/(\rho c)$

λ = latent heat of vaporization of coolant

λ^* = λ + $C_{pl}(T_v$-$T_c)$

Γ = liquid coolant mass flow rate per circumference

ρ = mass density
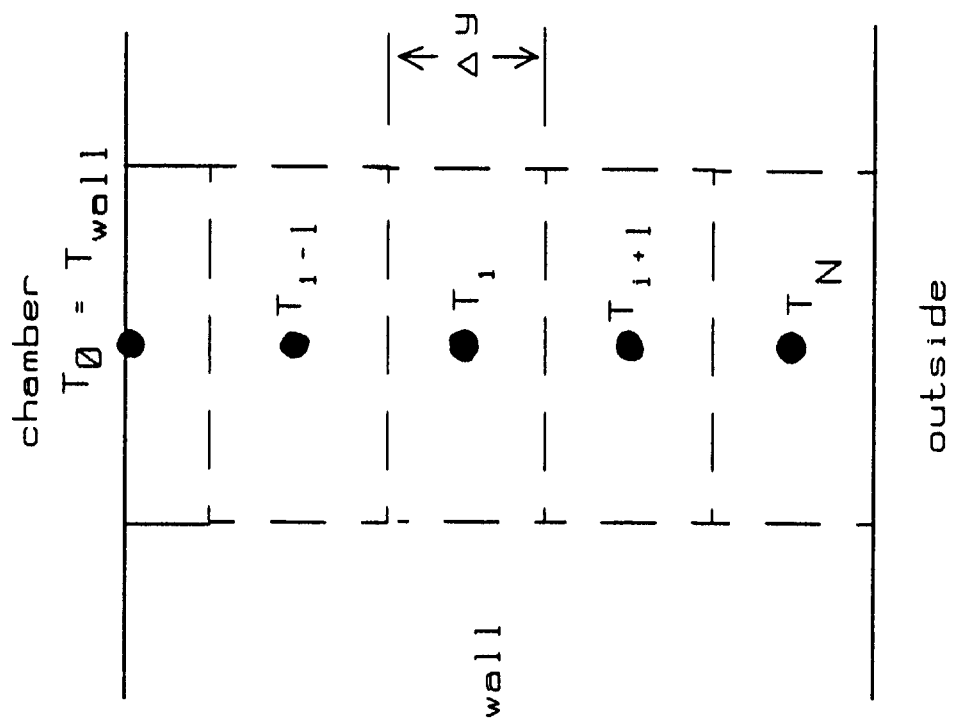
Figure 1. 1-D Conduction Model
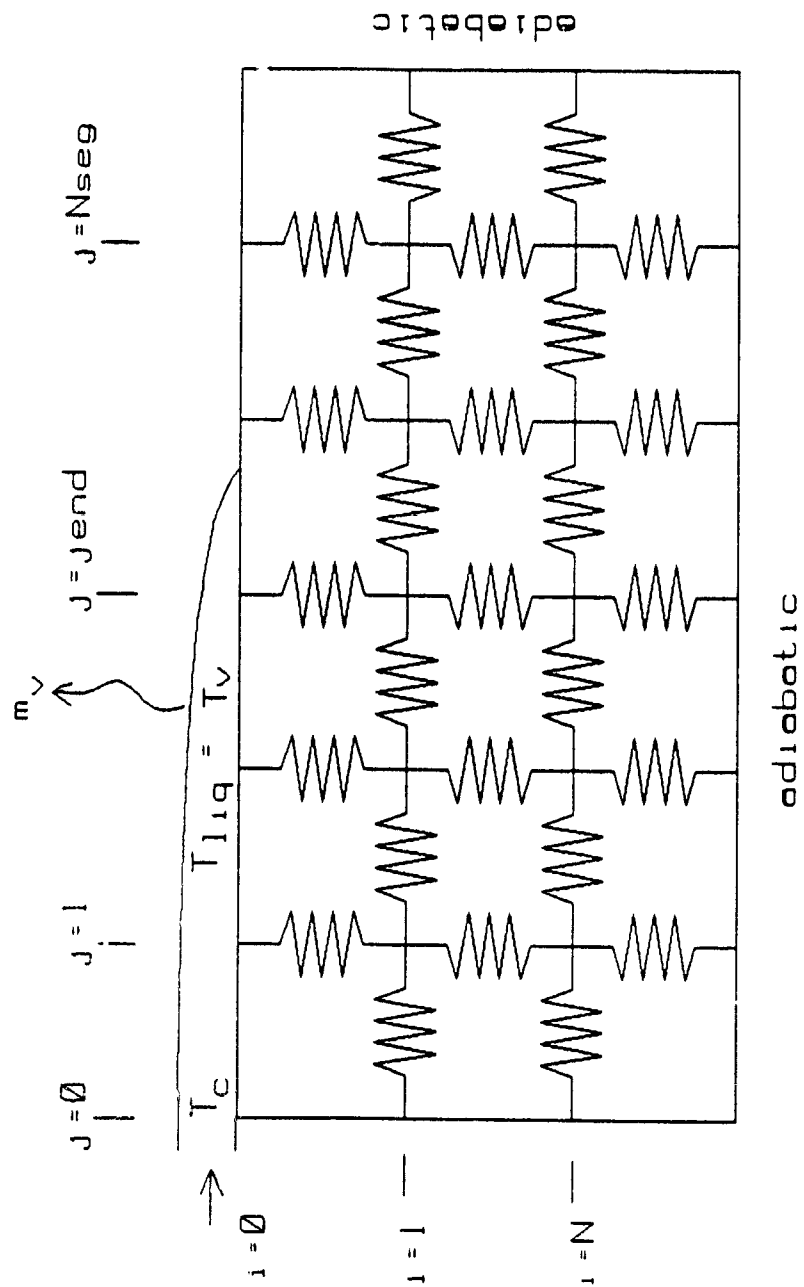
Figure 2. Transient Simulation of Film Cooling

Figure 3. Transient Film Cooling
TRW TR-201 Rocket

TEMP ACROSS J= 1 PLANE, L= 6.42570E+02 H= 2.95913E+03
07/25/90 ?~I?C??? T= 2.60245E-03 CYCLE 2121 CRANK= 0.00
MN= 3.52999E+02 MAX= 3.24870E+03 DQ= 2.89571E+02
LEM FILM COOLING DEMONSTRATION - DIESEL FUEL FILM   9-10

M_{liq} = 0.4 kg/m-s
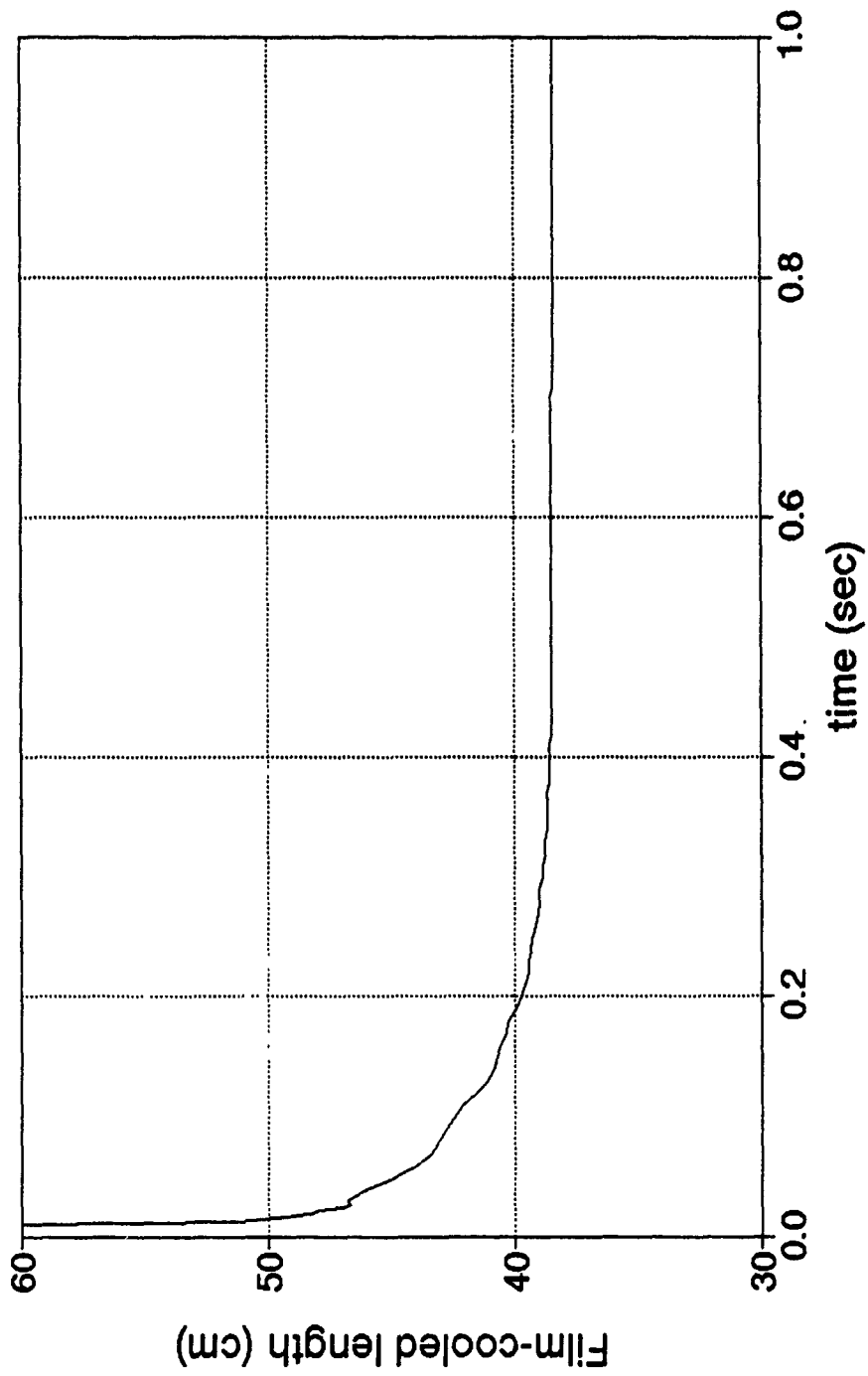
TEMP ACROSS J= 1 PLANE, L= 1.07963E+03 H= 3.16207E+03
07/27/90 ?~I?C??? T= 4.79409E-03 CYCLE 3621 CRANK= 0.00
MN= 8.19213E+02 MAX= 3.42239E+03 DQ= 2.60318E+02
LEM FILM COOLING DEMONSTRATION - DIESEL FUEL FILM   9-10

M_{liq} = C.
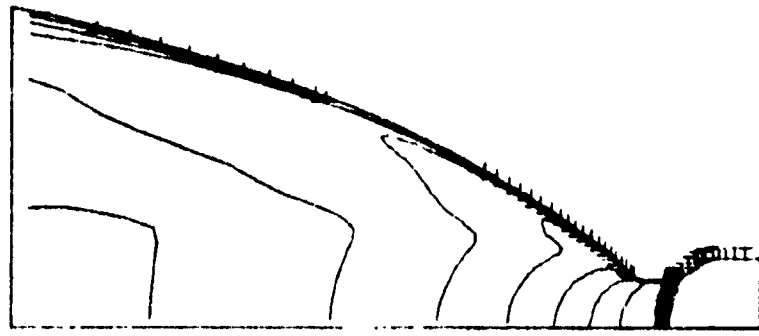
Figure 4.   Temperature contours with and without liquid film cooling

1990 USAF-UES SUMMER FACULTY RESEARCH PROGRAM/

GRADUATE STUDENT RESEARCH PROGRAM

Sponsored by the

AIR FORCE OFFICE OF SCIENTIFIC RESEARCH

Conducted by the

Universal Energy Systems, Inc.

FINAL REPORT

FEASIBILITY OF MEASURING PULSED X-RAY SPECTRA
USING PHOTOACTIVATION OF NUCLEAR ISOMERS

Prepared by: Carlyle E. Moore

Academic Rank: Associate Professor

Department and   Physics Department

 University: Morehouse College, Atlanta, GA

Research Location: Arnold Engineering Development Center

                                Arnold AFB

                                Tullahoma, TN 37389-5000

USAF Researcher: William G. Kirby

Date: July 27, 1990

Contract No: F49620-88-C-0053

FEASIBILITY OF MEASURING PULSED X-RAY SPECTRA
USING PHOTOACTIVATION OF NUCLEAR ISOMERS

by

Carlyle E. Moore

ABSTRACT

The photoactivation of nuclear isomers as a possible method of measuring the spectra of pulsed bremsstrahlung has been examined. Potential target nuclei include ^{77}Se, ^{79}Br, ^{107}Ag, ^{111}Cd and ^{115}In. The method has been found to be suitable, in principle. Its successful implementation hinges on the accurate measurement of the fluorescence yield from each isomer and the availability of complete and reliable data on the nuclear parameters involved. At present, unfortunately, the available data is incomplete and there appears to be a lingering controversy over the dominant gateways in ^{111}Cd and ^{115}In. These difficulties must be removed if the method is to be applied with confidence.

I. INTRODUCTION

Excited nuclear states can be produced by a number of mechanisms (including electromagnetic excitation), the lifetime of the state being generally of the order of 10^{-9} sec or less. The decay rate depends strongly on the angular momentum I and if there is a large difference in I between the excited state and all of the lower states ($\Delta I \geq 3$), transitions to these states are highly forbidden and the lifetime of the excited state turns out to be relatively large[2]. Such long-lived excited nuclear states are called Isomers. They have life-times ranging from a few seconds to several hours.
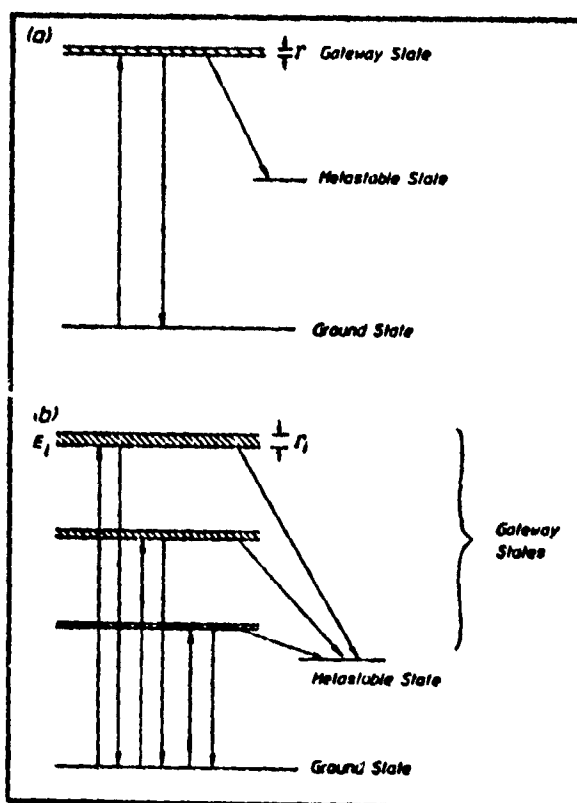
Fig. 1.   Schematic representation of isomer production in (a) single gateway isotope (b) multiple gateway isotope.

Nuclear reactions of the type
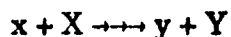
$$x + X \rightarrow y + Y$$

(particle x is incident on the nucleus X, creating the nucleus Y together with particle y) are described compactly by the notation X(x,y)Y or, simply, as (x,y) reactions.

Photoactivation of nuclear isomers proceeds via (γ, γ') reactions, which may be represented schematically as shown in Fig. 1. The nucleus is excited from its ground state to an excited state (also known as an activation or "gateway" state) of width Γ by absorption of a photon γ. It subsequently decays to the metastable state m (isomer) with emission of the photon γ'. The isomer then decays by a process of delayed fluorescence, emitting a signature photon which may be used to identify the isomer.

II. OBJECTIVES

A proposal is under consideration to build a facility at AEDC to test space-bound military equipment in a nuclear-weapons environment, with a view to ensuring its survivability against nuclear attack. The major threat comes from release of X-radiation, which can result in degradation of performance or even permanent damage. Simulation of nuclear- weapons radiation would be achieved by exposing the equipment to intense flash X-ray sources. These are generated by injecting high- energy pulsed electron beams into standard converter configurations, where they produce continuous X-rays (bremsstrahlung) together with characteristic line radiation. In order to implement this testing program, it would be necessary to measure the spectrum of the pulsed bremsstrahlung on a shot-by-shot basis, for end-point energies up to 1.5 Mev.

A new technique,[8,12] based on the photoactivation of nuclear isomers, has recently been reported for the absolute calibration of pulsed X-ray spectra. The purpose of this Report is to examine the feasibility of using this technique to calibrate the spectra of pulsed bremsstrahlung on a shot-by-shot basis. It should be pointed out that it is possible, using a Monte Carlo model,[1] to make predictions of the spectral distribution of the radiation from records of the time-dependent voltage and current. However, the spectra produced by these flash sources suffer from a lack of reproducibility and it is therefore desirable to have a direct, reliable method of extracting the spectrum on a shot-by-shot basis.

III. THEORETICAL DISCUSSION

It is assumed that the excitation of the gateway levels proceeds entirely via resonant absorption. The possibility of non-resonant excitation has been considered by a number of authors[4-6]. These investigations were inspired by large discrepancies between the measured cross-sections and the values calculated on the basis of resonant absorption alone. A number of mechanisms of non-resonant excitation (e.g. an inelastic photoelectric effect, inelastic Raman scattering) were postulated but the cross-sections calculated on the basis of these processes were much too low to account for the discrepancies. More recent investigations[7-12], moreover, have found no evidence for non-resonant activation.

We consider a target of cross-sectional area A which is irradiated with bremsstrahlung radiation of end-point energy E_o. The number N_r of nuclei which are excited to the gateway state r is given by

$$N_r = N \int_0^{E_o} \sigma_r(E) \; d\Phi = N \int_0^{E_o} \sigma_r(E) \; \frac{d\Phi}{dE} \; dE \qquad (3.1)$$

where N is the number of target nuclei, $\sigma_r(E)$ is the cross-section for excitation of the gateway state r by absorption of a photon of energy E and Φ is the photon flux, i.e. the number of photons per unit area. The cross-section $\sigma_r(E)$ is given by the Breit-Wigner formula[3]

$$\sigma_r(E) = \frac{\lambda^2}{8\pi} \left[\frac{g \, \Gamma_0 \, \Gamma}{(E - E_r)^2 + (\Gamma/2)^2} \right] \qquad (3.2)$$

in which it is assumed that the absorption will take place with appreciable probability only if the energy E of the X-ray photon is close to the energy E_r of the gateway state. In equation (3.2) the following symbols are used:

13-5

E Energy of the X-ray photon

λ Wavelength of the X-ray photon

E_r Energy of the gateway level r

g Statistical weight $(2I + 1)/(2I_o + 1)$

I Angular momentum of the gateway state

I_o Angular momentum of the ground state

Γ Total width of the gateway state $(h/2\pi\tau = 6.58 \times 10^{-16} ev/\tau)$

Γ_o Partial width of the gateway state for decay to the ground state

Since the width Γ is very small ($\leq 10^{-3}$ ev) in comparison with the range of energy over which the X-ray intensity is likely to change appreciably, we may assume that $d\Phi/dE = U(E)$ is constant in the vicinity of the gateway energy E_r and replace $U(E)$ by $U(E_r)$. We then obtain from equation (3.1)

$$N_r = N U(E_r) \int_0^{E_o} \sigma_r(E) \, dE \tag{3.3}$$

and using (3.2), we get

$$N_r = N \frac{\lambda^2}{8\pi} g \Gamma_o \Gamma U(E_r) \int_{-\infty}^{+\infty} \frac{dE}{(E - E_r)^2 + (\Gamma/2)^2} \tag{3.4}$$

where the limits of integration have been formally extended to $-\infty$ and $+\infty$, respectively. On evaluating the integral, we get

$$N_r = N\left[\frac{1}{4}\lambda^2 g b_o \Gamma\right]_r U(E_r) \qquad (3.5)$$

where b_o is the branching ratio Γ_o/Γ and $U(E) = d\Phi/dE$ is the spectral photon distribution (measured in photons/kev-cm^2, say). The isomer population N_m is obtained by multiplying N_r by the branching ratio $b_m = \Gamma_m/\Gamma$, where Γ_m is the partial width of the gateway level for decay to the isomer state. We shall now introduce the fluence $F(E) = E \ U(E)$, and write

$$N_m = N \ \xi_r \ F(E_r) \qquad (3.6)$$

$$\xi_r = \frac{\left[\frac{1}{4}\lambda^2 g \ b_o b_m \Gamma\right]_r}{E_r} = \frac{\sigma_r}{E_r} \qquad (3.7)$$

The quantity

$$\sigma_r = \left[\frac{1}{4}\lambda^2 g \ b_o b_m \Gamma\right]_r \qquad (3.8)$$

is the integrated cross-section for the excitation of the isomer state m via the gateway state r. We have tacitly assumed that the isomeric state is pumped by a single gateway state r. For a multiple gateway isotope, we make the generalization

$$P = N \sum_r \xi_r \ F(E_r) = N \sum_r \sigma_r \ U(E_r) \qquad (3.9)$$

where the isomer population is now denoted by P.

We mention, in passing, that while isomeric states can be created by direct resonant excitation (without contribution from higher levels), the absorption cross-section for such processes is negligibly small, in view of the fact that the isomer states have extremely long lifetimes (small line widths Γ) relative to other excited states. As can be seen from equation (3.8), the cross-section is proportional to the width Γ.

IV. EXPERIMENTAL METHOD

Photoactivation of nuclear isomers has been studied experimentally by various authors,[4-6] with widely differing results. For the purpose of examining the feasibility of using this technique to measure the spectrum of pulsed bremsstrahlung, we refer to recent studies by two groups based at the University of Texas at Dallas[8-11] and at Sunol[12], California, respectively. The bremsstrahlung source used in each case was the DNA/PITHON nuclear simulator at PHYSICS INTERNATIONAL, operating at end-point energies in the 0.8 to 1.6 Mev range. The experiments conducted by both groups incorporated the same basic design feautures: (i) a sample holder which allowed several targets to be irradiated simultaneously (ii) a device for rapidly transferring the sample to the counting chamber (iii) the counting system, comprising a detector and its associated electronics. Details of the experimental set-up used by these groups may be found in the References listed.

The number of counts recorded by the detector must be corrected for a number of factors:

t transit time of sample

T actual counting time

q fraction of isomer states which decay with
   emission of a photon

ε efficiency of the detector

Ω fraction of solid angle subtended by detector

When counting begins, the number of isomer states remaining is $Pq e^{-\beta t}$, where β is the decay constant. The number of states which decay after a further time T is $Pq e^{-\beta t}(1 - e^{-\beta T})$. Hence the number of counts C is given by

$$C = Pq\epsilon\Omega e^{-\beta t}(1 - e^{-\beta T}) \qquad (4.1)$$

It is also necessary to take account of self-absorption within the sample. This effect, together with the solid angle Ω, was estimated using Monte Carlo calculations.

V. ANALYSIS

Calibration of the bremsstrahlung spectrum U(E) can, in principle, be achieved by measuring the isomer population P produced by irradiating a number of different targets with the same pulse. The population of the jth target is given by

$$P_j = N_j \sum_{r=1}^{n_j} \sigma_{jr} U(E_{jr}) \quad ; \quad j = 1, 2, \ldots s \qquad (5.1)$$

where s is the total number of targets and there are n_j gateway levels in the jth target. Successful calibration depends on the availability of complete and accurate data on the nuclear parameters describing the target nuclei chosen.

We have already alluded to the fact that experimental determinations of activation cross-sections have produced results covering a wide range. There is also some disagreement regarding the location of the dominant gateways in certain nuclei. For example, Anderson et al[11] have recently proposed that the 396 kev isomer in ^{111}Cd is pumped predominantly by the gateway at 1190 kev, and not by the one at 1330 kev, as other workers have maintained. It might be useful to review the techniques employed, with a view to shedding some light on this tangled situation.

The isomer population of a given nucleus X has been written as

$$P(X) = N(X) \sum_r \xi_r(X) F(E_r) \qquad (5.2)$$

where the summation is taken over all the contributing gateway levels. Equation (5.2) may be rewritten in terms of a relative fluence

$$\eta_E(E_o) = \frac{F(E)}{F_{761}(Br)} \qquad (5.3)$$

i.e. the fluence is normalized by the value at the 761 kev activation level in ^{79}Br. The relative fluence η is clearly a function of the end-point energy E_o, with the X-ray energy E as a parameter. The graphs of $\eta_E(E_o)$ are obtained from the TIGER CODE calculations. The activation probability ratio is given by

$$R(X) = \frac{P(X)}{P(Br)} \frac{N(Br)}{N(X)} = \frac{1}{\xi_{761}(Br)} \sum_r \xi_{E_r}(X)\, \eta_E(E_o) \qquad (5.4)$$

This formulation can be used to examine the onset of certain activation levels as the end-point energy increases. It was applied by Anderson and Collins[9] to the activation of ^{77}Se and, subsequently, by other groups[10,11] to ^{115}In and ^{111}Cd. The approach taken by these groups is typified by the case of ^{111}Cd. The ratio R(Cd) was plotted versus end-point energy E_o, as shown in Fig. 3a. A straight line was fitted to the data and intersected the E_o axis near 1.2 Mev. From this it was concluded that the 396 kev (48.6m) isomer in ^{111}Cd is pumped predominantly by the 1190 kev excitation level and not by the 1330 kev level, as others[5] have maintained. On this assumption, R(Cd) was then plotted against η_{1190} and a straight line through the origin was drawn. From the slope of this line, the quantity $\xi_{1190}(Cd) = \sigma_{1190}(Cd)/1190$ kev was determined, and hence the integrated cross-section $\sigma_{1190}(Cd)$ was estimated to be (9.8 +

$2.5) \times 10^{-29} cm^2$-kev. Ref. 11 quotes measurements by a number of authors, ranging from 5.8 to 35 (in units of $10^{-29} cm^2$-kev), for the activation cross-section "through a level near 1200 kev", though in most cases a gateway of 1330 kev is assumed[5]. An identical procedure was used[10] in the case of [115]In, resulting in an estimate of the cross-section $\sigma_{1078}(In) = (18.27 + 2.7) \times 10^{-29} cm^2$-kev. It should be pointed out that as the end-point energy increases, abrupt changes in the behaviour of the activation probability ratio R should be observed as new activation channels become open. In Fig. 3a there are, unfortunately, no measurements of this ratio below about 1.3 Mev which would indicate the opening of an activation channel at 1190 kev. The analysis hinges, apparently, on the _a priori_ assumption of a monolithic gateway in this vicinity. Earlier measurements by Boivin et al[13], on the other hand, suggest activation levels at 740, 1120 and 1330 kev. the cross-section for excitation of [111]Cd^m through the 1330 kev level being 3 to 4 orders of magnitude higher than the others. The relative fluences $\eta_{740}(E_o), \eta_{1120}(E_o)$ and $\eta_{1330}(E_o)$ must, of course, also be taken into account in deciding whether, and at what end-point energies, the 1330 level may be considered dominant.

By contrast, these same nuclei were examined by Prussin et al[12], using the same DNA/PITHON shots. Their activation probability ratios, both measured and calculated (using their own cross-section data and the TIGER code predictions) are shown in Fig. 3b. This group used a much wider range of end-point energies (0.9 to 1.5 Mev) and their results purport to show the threshold behaviour of the activation probability ratio, especially in the case of [111]Cd, where there is an abrupt increase around 1330 kev. The cross-sections used were calculated from nuclear parameters, where available, or determined by direct measurement, using the results obtained by Boivin, Cauchois and Heno.[13,14] For some nuclei, both calculated and measured data were available for a few levels only; for the remaining levels, "adjusted" cross-sections were computed, using the average ratio of the calculated

and measured values. Available nuclear parameters (and the calculated cross-sections) for ^{77}Se, ^{79}Br, ^{107}Ag, ^{111}Cd and ^{115}In are listed in Table 1.

In order to obtain the X-ray spectrum of a given pulse of radiation, we use the equation

$$P_j = N_j \sum \sigma_{jr} U(E_{jr}) \; ; j = 1, 2, \dots s \tag{5.1}$$

where there are s targets in the sample and the jth target has n_j activation levels. Some assumption must be made about the functional form of the spectral distribution function $U(E)$. We consider first[12] the curve-fitting formula

$$U(E) = c_1 E^{-1} + c_2 + c_3 E + c_4 E^2 + \dots = \sum_{k=1}^{s} c_k E^{k-2} \tag{5.5}$$

Inserting (5.5) into (5.1), we get

$$P_j = \sum_{k=1}^{s} \left(N_j \sum_{r=1}^{n_j} \sigma_{jr} E_{jr}^{k-2} \right) c_k \tag{5.6}$$

or

$$P_j = \sum_{k=1}^{s} a_{jk} c_k \tag{5.7}$$

where

$$a_{jk} = N_j \sum_{r=1}^{n_j} \sigma_{jr} E_{jr}^{k-2} \tag{5.8}$$

13-12

Equation (5.8) may be written in matrix form as

$$P = A \, C \qquad (5.9)$$

and the matrix C (hence the coefficients c_k) may be found by matrix inversion:

$$C = A^{-1} \, P \qquad (5.10)$$

However, Prussin et al[12] have cautioned that if a power series is used, large errors in the experimental values of the isomer populations P_j and in the activation cross-sections can lead to unphysical oscillations in the spectral distribution function. In some cases these problems can be alleviated by using the method of singular value decomposition[18].

Another technique suggested by Prussin et al[12] is based on their observation that the X-ray spectra derived from the TIGER code, when plotted as log U vs. E, consist of a number of connected straight line segments, i.e. the graph of U vs. E may be approximated by a number of connected exponential segments. Each segment of the spectrum may therefore be represented by

$$U(E) = U_1^{\alpha_1} U_2^{\alpha_2} \qquad (5.11)$$

where
$$\alpha_1 = \frac{E_2 - E}{E_2 - E_1} \quad ; \quad \alpha_2 = \frac{E - E_1}{E_2 - E_1} \qquad (5.12)$$

and E_1 and E_2 are the end-points of the segment. The end-point energies are arbitrary, and may be chosen from the gateway energies of the nuclei which have been

activated. We then obtain a set of coupled non-linear equations in which the unknowns are the $U(E_r)$. These eequations may be solved by the Newton-Raphson method[18].

The idea of modelling the X-ray spectrum as a set of connected exponential segments is an interesting one, especially in view of the fact that there are some nuclei which have only a single activation level for end-point energies less than a certain value. For example, ^{79}Br has a single activation level at $E_r = 761$ kev for end-point energies in the 0 - 1.8 Mev range. In such a case, measurement of the isomer population P yields the intensity $U(E_r)$ directly. Thus if two targets are irradiated simultaneously by a pulse of radiation whose end-point energy is such that only the gateways E_1 and E_2, respectively, are excited, then equation (5.12) could be used to obtain $U(E)$ at any intermediate energy E $(E_1 < E < E_2)$. Examples of this technique are shown below:

$$U(E) = U_{250}^{\alpha_1} U_{423}^{\alpha_2} \quad (250 < E < 423)$$

$$\alpha_1 = \frac{423 - E}{173} \; ; \; \alpha_2 = \frac{E - 250}{173}$$

$$U(E) = U_{423}^{\alpha_1} U_{761}^{\alpha_2} \quad (423 < E < 761)$$

$$\alpha_1 = \frac{761 - E}{338} \; ; \; \alpha_2 = \frac{E - 423}{338}$$
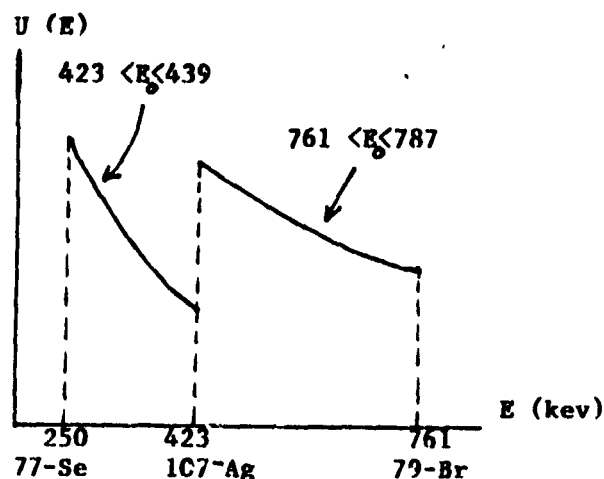
Figure 2. Exponential segmentation of x-ray spectrum.

The function $U(E)$ depends strongly on the end-point energy E_0 and it is apparent that this method is not suitable for finding the intensity at small X-ray energies for large end-point energies. For example, if the end-point energy in Fig. 2 becomes sufficiently greater than 423 kev, the activation channel at 439 kev in ^{77}Se is

opened, thus violating the requirement that each nucleus should have only one gateway. Another drawback is that for a given shot the spectrum can be measured only over a limited range. Nonetheless, the method has the virtue of simplicity and may be particularly useful at low end-point energies (~ 0.5 Mev) where only a few (possibly two) nuclei can be excited and numerical methods of solution are inapplicable.

VI. RECOMMENDATIONS

We have examined the photoactivation of nuclear isomers as a possible method of measuring the spectra of pulsed bremsstrahlung on a shot-by-shot basis. A number of potential targets have been identified and a catalog of available data on the relevant nuclear parameters compiled. Once the fluoresence yield from each nucleus has been measured, all that remains is to choose a suitable model for the functional form of the fluence $F(E)$ and to carry out the required numerical or analytic solution. The main obstacle to the implementation of this procedure is the lack of complete and accurate data on the integrated cross-sections for the production of isomers via the various gateways. A number of direct measurements of these cross-sections have been made over the years but the results obtained span such a wide range as to render them unreliable. Perhaps a special effort should be made to obtain an updated listing of nuclear parameters (mean lifetimes τ, nuclear spins I and I_o, and branching ratios b_o and b_m) on such promising targets as ^{77}Se, ^{87}Sr, ^{107}Ag, ^{111}Cd, ^{115}In. In particular, the controversy surrounding the dominant gateways in ^{111}Cd and ^{115}In must be resolved. If the 1078 kev level in ^{115}In, the 1229 kev level ^{x}in ^{87}Sr and the 1330 kev level in ^{111}Cd are indeed predominant, then together with the 761 kev level in ^{79}Br, they offer a simple and effective way of measuring the fluence directly at these energies. The photoactivation of nuclear isomers can be used successfully to measure the X-ray spectra, but the key to doing so is the availability of complete and reliable data.
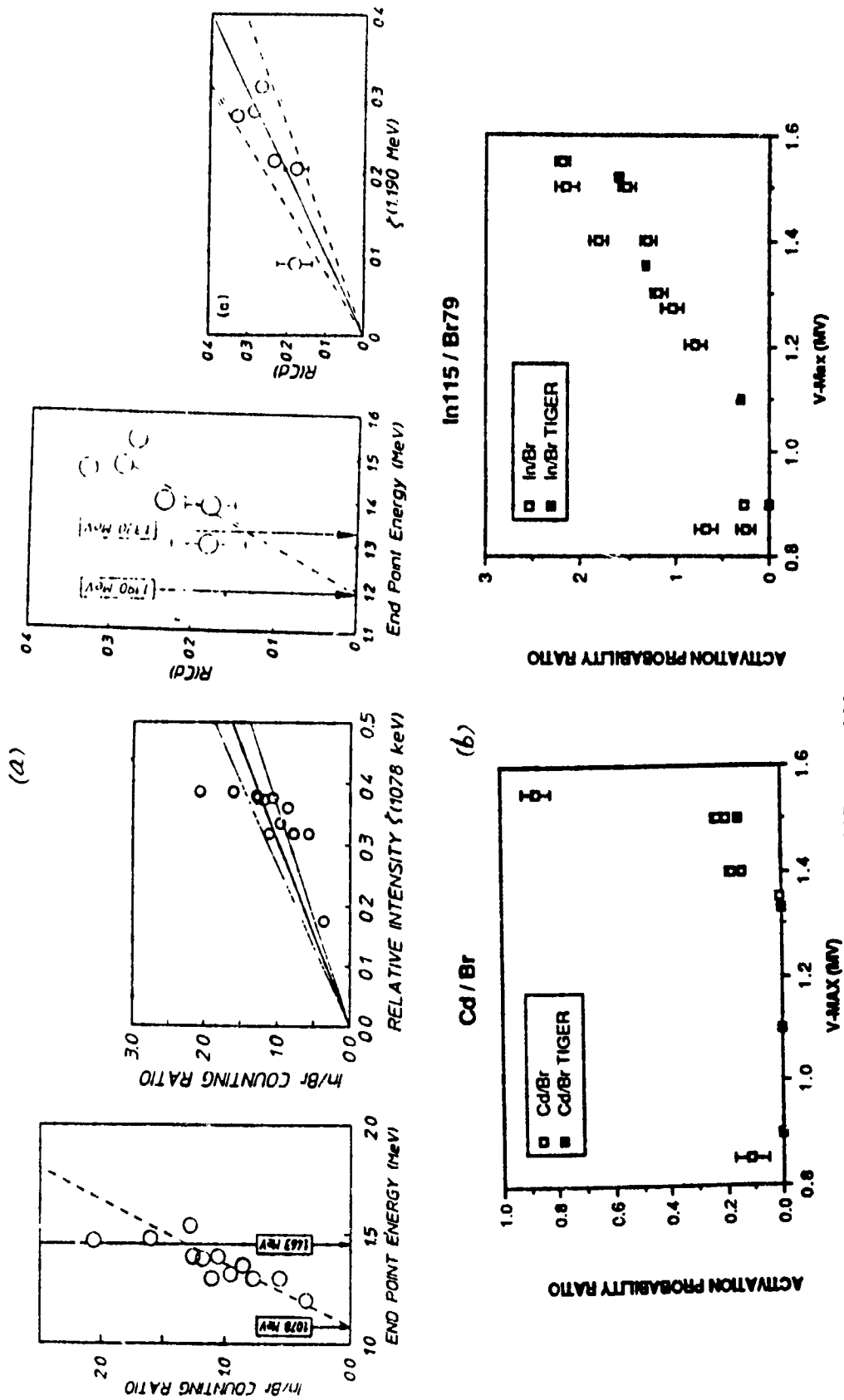
Fig. 3. Ratio R vs E_o in ^{115}In and ^{111}Cd from (a) Refs. 10, 11 (b) Ref. 12.

Table 1. Available Nuclear Parameters on ^{77}Se, ^{79}Br, ^{107}Ag, ^{111}Cd, ^{115}In
(Level energies in kev, half-lives in ps and cross-sections in Mev-μb)

E_r	Source	$\tau_{1/2}$	b_o	b_m	I_o	I_r	σ
77-Se							
250	TOI	9300	6.8E-1	3.2E-1	0.5	2.5	1.97E-3
439	TOI	23	5.6E-1	1.2E-2	0.5	2.5	8.14E-3
521	TOI	?	8.9E-1	4.2E-3	0.5	1.5	?
824							
911							
1005							
1187							
79-Br							
761	NDS	1.2	3.4E-1	3.5E-2	1.5	3.5	6.00E-2
107-Ag							
423	NDS	30	9.5E-1	2.1E-3	0.5	2.5	1.95E-3
787	NDS	0.27	6.4E-1	1.6E-4	0.5	1.5	2.17E-3
950	NDS	1.3	1.2E-1	9.7E-3	0.5	2.5	5.22E-3
1250							
1325							
111-Cd							
740							
1120							
1330							
115-In							
597							
829							
934	NDS	57	9.9E-1	2.4E-3	4.5	3.5	6.70E-5
941	NDS	15	8.5E-1	1.5E-1	4.5	2.5	1.01E-2
1078	NDS	0.86	8.6E-1	1.4E-1	4.5	2.5	1.27E-1
1465							
1495							

NDS: Nuclear Data Sheets; TOI: Table of Isotopes (Taken from Ref. 12).

REFERENCES

1. J. A. Halbleib and T. W. L. Sanford, Sandia Report SAND 83-2572 (1983).

2. J. M. Blatt and V. F. Weisskopf, Theoretical Nuclear Physics (John Wiley and Sons, New York and London, 1952).

3. F. Metzger, Prog. Nucl. Phys., 7, 54 (1959).

4. A. Ljubicic, K. Pisk and B. A. Logan, Phys. Rev. C 33, 2238 (1981).

5. M. Kremar, A. Ljubicic, K. Pisk, B. A. Logan and M. Vrtar, Phys. Rev. C 25, 2097 (1982).

6. M. Kremar, A. Ljubicic, B. A. Logan and M. Bistrovic, Phys. Rev., C 33, 293 (1986).

7. K. Yoshihara, Zs. Nemeth, L. Lakosi, I. Pavlicsek and A Veres, Phys. Rev., C 33, 728 (1986).

8. J. A. Anderson and C. B. Collins, Rev. Sci. Instrum., 58(11), 2157 (1987).

9. J. A. Anderson and C. B. Collins, Rev. Sci. Instrum., 59(3), 414 (1988).

10. C. B. Collins, J. A. Anderson, Y. Paiss, C. D. Eberhard, R. J. Peterson and W. L. Hodge, Phys. Rev. C 38, 1852 (1988).

11. J. A. Anderson, M. J. Byrd and C. B. Collins, Phys. Rev. C 38,2838 (1988).

12. S. G. Prussin, S. M. Lane, D. R. Kania, J. E. Trebes and M. Krishnan, IR&D Project #50020921, conducted at the Physics International Company.

13. M. Boivin, Y. Cauchois and Y. Heno, Nucl. Phys., A 137, 520 (1969).

14. M. Boivin, Y. Cauchois and Y. Heno, Nucl. Phys., A 176, 626 (1971).

15. E. C. Booth and J. Brownson, Nucl. Phys., A 98, 529 (1967).

16. Nuclear Data Sheets (Academic Press).

17. E. U. Condon in Handbook of Physics, edited by E. U. Condon and H. Odishaw (McGraw Hill, New York, 1967).

18. H P. Press, B. P. Flannery, S. A. Teukolsky and W. T. Vetterling, Numerical Recipes (Cambridge University Press, Cambridge, 1987).

ACKNOWLEDGEMENTS

Engineering Development Center, Arnold AFB, TN for its hospitality during the Summer. I particularly want to thank Bill Kirby of CALSPAN for suggesting this project and for providing such a warm and congenial atmosphere in which to work. His friendship and support throughout my stay are greatly appreciated. Several others were helpful in many ways, including Sid Steely, whose geniality, patience and dedication are truly inspiring.

1990 USAF-UES SUMMER FACULTY RESEARCH PROGRAM

Sponsored by the
AIR FORCE OFFICE OF SCIENTIFIC RESEARCH

Conducted by the
Universal Energy Systems, Inc.

FINAL REPORT

Combustion of Carbon Particles in the Plume of a Flare

Prepared by:	Olin Perry Norton
Academic Rank:	Research Engineer II
Department and University:	Diagnostic Instrumentation and Analysis Laboratory, Mississippi State University
Research Location:	AEDC/DOTR Arnold AFB, TN, 37389
USAF Researcher:	H. T. Bentley III
Date:	20 Sep 90
Contract No:	F49620-88-C-0053

Combustion of Carbon Particles in the Plume of a Flare

by

Olin Perry Norton

ABSTRACT

A burning flare produces a plume which contains a substantial quantity of solid carbon particles. As the flare products mix with the surrounding air, these carbon particles will burn. The rate of combustion of these carbon particles is expected to have a significant influence on the infrared emissions of the flare plume.

The gases in the plume contains six species which can attack a solid carbon surface. The list includes the stable molecular species CO_2, H_2O, and O_2 and the radicals OH, O, and H. Based on published reaction rates for these species with solid carbon, the rate of burning of the particle is found as a function of the composition and temperature of the surrounding gas. Also, the increase in temperature of the particle due to these reactions is found.

Acknowledgements

I. INTRODUCTION:

During the summer research period, the author worked with a group of scientists and engineers at Arnold Engineering Development Center whose mission was to develop a computer model of a flare. Such flares are intended to produce infrared radiation and act as decoys, thus the primary purpose of this model is to correctly predict the emission signature of the flare. Existing computer programs, originally written to model rocket plumes, were used as much as possible. The flow field program calculates the mixing and reaction of the plume gases with the surrounding air. The infrared radiation program uses the results of the flow field calculation to calculate the infrared emissions from the plume. The radiation program will include the emission due to particles in the flow, but the flow field program is not able to handle reacting particles in the flow.

Since the author's background is in combustion, it was decided that the summer research effort should focus on the chemical reactions of carbon particles in the plume of the flare. Typically, a flare is made of fine magnesium particles dispersed in a solid fluorocarbon. The NASA chemical equilibrium code by Gordon and McBride (1976) was used to estimate the composition of the flare products. The result is a mixture of magnesium vapor (39% mole fraction), solid carbon (30%), liquid magnesium difluoride (24%), and the remaining 7% or so is composed of an assortment of other species. The flare is clearly fuel rich, so additional exothermic reactions will take place when the flare products mix with the surrounding air. The burning rate of the solid carbon particles will be important in determining the temperature distribution, and thus the infrared emission, within the plume. Further, the solid carbon particles may be the dominant emitting species within the plume, since the other particulate species (magnesium difluoride and magnesium oxide) are poor emitters. Clearly, an accurate flare model should include these reacting carbon particles.

Although no reliable data were available, the author's colleagues at AEDC believed that the carbon particles were less than a micron in diameter and had approximately the same properties as soot.

II. OBJECTIVES OF THE RESEARCH EFFORT:

A number of species in the plume might react with solid carbon. After first identifying these species, the literature was searched to find expressions for the rate of reaction of each species with carbon. Then, using concentrations and temperatures typical of the plume, the rate of carbon loss due to each reactant could be found. This identified the species most important in removing carbon from the surface.

Next, a differential equation was written for the change of radius of a carbon particle as a function of time. The radius diminishes due to the chemical removal of carbon from the surface until eventually the radius reaches zero. Thus, numerically solving this differential equation determined the lifetime of a carbon particle as a function of initial diameter.

The chemical reactions are generally exothermic and thus release heat at the particle surface. Equating this heat generation to the heat lost by conduction to the surrounding gas gives an equation for the temperature of the carbon particle, which will be higher than the surrounding gas. If this temperature difference was significant, it could greatly effect the radiation due to the particles. This temperature rise was estimated for typical plume conditions.

III. GASEOUS REACTIONS WITH SOLID CARBON:

a. A literature survey was performed to identify the gaseous species which oxidize or gasify the carbon surface and to estimate kinetic rates for these reactions. When reading the results of this research, given below, one should keep in mind the many sources of uncertainty which afflict experimentalists in this field. To begin with, the carbon used in these experiments may come from a variety of sources, such as soot particles, carbon black particles, graphite particles, carbonized filaments, or the char particles which remain after a coal particle is pyrolized. The solid may not consist of pure carbon; according to Haynes and Wagner (1981), soot particles may contain up to 10 mole percent of hydrogen. When dealing with gas-solid reactions, the rate often depends on active sites on the surface. Obviously, the number and activity of these sites will be highly variable depending on the crystalline structure of the solid, which crystal plane is exposed at the surface, and impurities. To express the reaction rate per unit surface area, one must know the particle surface area. Soot particles

consist of agglomerates of tiny (10 to 20 nm.) spheres and coal chars contain internal pores, so knowing the actual surface area is not trivial. Finally, particularly when measuring the reaction rate of some radical species with the surface, the gas will contain more than one species which can react with the surface. Thus, there is a problem of identifying which species is responsible for the reaction.

In the course of the literature survey, six species were identified which will be present in the plume and will react with solid carbon. The stable molecules O_2, CO_2, and H_2O meet these criteria, as do the radicals OH, O, and H.

The reactivity of O_2 with a solid carbon surface was calculated using the formula of Nagle and Strickland-Constable. Radcliffe and Appleton (1971) and Park and Appleton (1973) have successfully correlated measurements of soot oxidation rates to the predictions of this formula. The use of this formula is also discussed in a review article by Haynes and Wagner (1981). Alternative rate expressions for this reaction are given by Feugier (1972), Lee, et al. (1962), and by Blyholder, et al. (1958).

The reaction rates of CO_2 and H_2O with solid carbon were computed using expressions given by Kuo (1986). Kuo used his expressions to compute the erosion rate of graphite rocket nozzles. Alternate expressions for the rates of these reactions are used by Bradley, et al. (1984).

The rate of reaction of a carbon surface with the hydroxyl radical OH has been measured by Fenimore and Jones (1967), Neoh, et al. (1981), and others. For the calculations described herein, this rate was estimated by first calculating the collision rate of OH with the surface, using kinetic gas theory, and then assigning a constant collision efficiency of 0.28 (Bradley, et al., 1984). Thus, the reaction rate of OH with the surface was found.

The same procedure was followed for the reactions of O and H. Although some measurements of the collision efficiency are found in Rosner and Allendorf (1965, 1968, 1970) and Wright (1974) for the O radical, and in Rosner and Allendorf (1970) for the H radical, here the approach of Bradley, et al. (1984) is followed. A constant collision efficiency of 0.5 was assumed for O and an efficiency of 0.036 was assumed for H.

b. The expressions discussed above can be used to find the rate of carbon loss from a surface if the concentrations of the reacting species and the temperature were known. To allow the presentation of some preliminary results, the NASA equilibrium code described by Gordon and McBride (1976) was used to estimate these properties in the plume. At any point in the plume, the gas will consist of a mixture of a certain fraction X of flare products and a fraction (1-X) of outside air. Thus, given a value of X, the equilibrium code can be used to find the species concentrations and temperature of the mixture. This calculation was performed for values of X (called the mixture fraction) varying from 0 to 1. Then, for any location in the plume, these results can be used to find the local concentrations and temperature. The answer is only approximate, since chemical equilibrium is assumed.

These concentrations and temperatures were used to find the rate of carbon loss from a surface as function of the mixture fraction X. The results of this calculation are shown in Figure 1. The results indicate that the maximum reactivity occurs when the mixture consists of 30% flare products and 70% outside air. Furthermore, the most important reactants are O, CO_2, and O_2.

IV. PARTICLE LIFETIME CALCULATIONS:

a. When the gas reacts with solid carbon, a carbon particle will decrease in size until its diameter equals zero. This defines the lifetime of the particle, which is a function of the initial particle diameter as well as the composition and temperature of the surrounding gas. If the lifetime of a particle is very short, compared to a characteristic flow time, then the finite time required for the particle to burn is unimportant and thus need not be included in the flare model. On the other hand, if the particle lifetime is comparable to or larger than some appropriate flow time scale, then the finite particle burning rate will have an important effect on the plume. Thus, the reaction rates discussed above will be used to estimate the particle lifetime.

The burning of a particle (or droplet) in an oxidizing atmosphere is treated in a number of texts on combustion, such as Glassman (1977). There are two processes which must occur for the gaseous oxidant to react with the particle. First, the reactant must diffuse to the surface, and then it must react with the surface. Depending on which process is the slower, one can distinguish two limiting cases of particle combustion.

Rate of Reaction with Carbon Surface
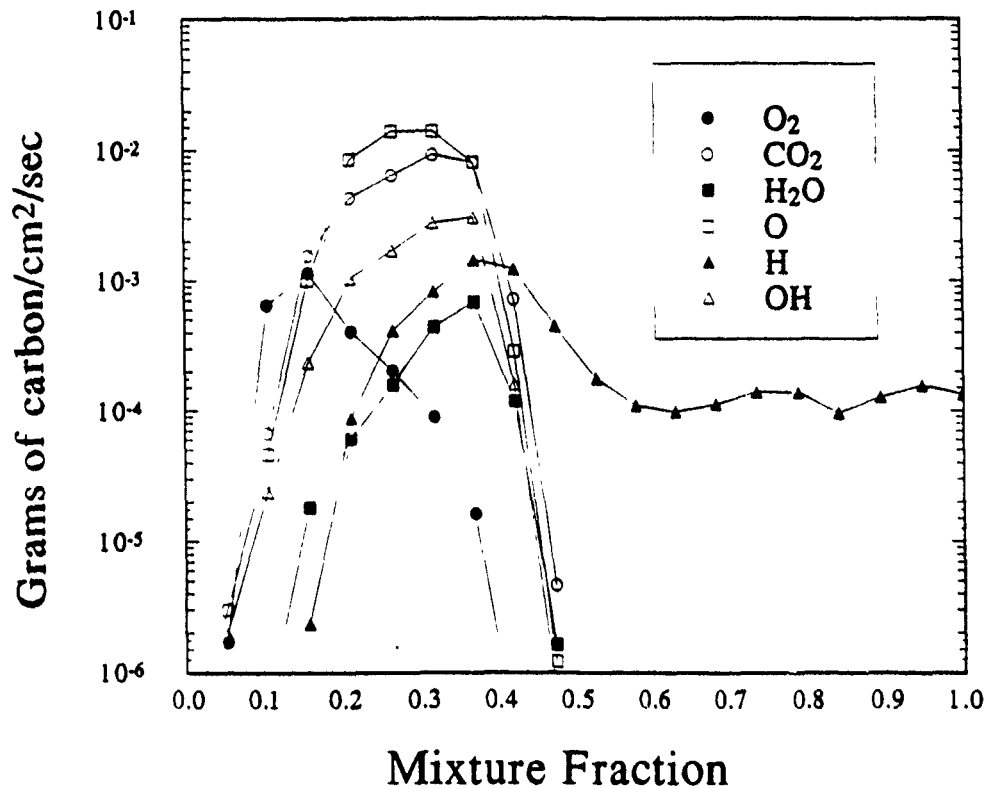
Figure 1

A mixture fraction of 0 corresponds to pure air and a mixture fraction of 1 corresponds to pure flare products. Intermediate values correspond to mixtures of flare products and outside air. The composition and temperature of the gas around a particle are a function of the mixture fraction for an equilibrium mixture. Here, the kinetic expressions for the rate of removal of carbon from a surface are evaluated for each species which reacts with the carbon. Note that different species are important in different regions of the flame.

The kinetic limit occurs when the chemical reaction at the surface is the slower process. In this limit, the rate of burning of the particle can be found by assuming that the oxidant concentration at the surface is equal to its value in the bulk fluid, and then evaluating the kinetic expression for the surface reaction rate. The previous section described how to find these rates.

If the kinetic rates are made faster and faster, eventually the oxidant will be consumed at the particle surface faster than it can diffuse to the surface from far away. This situation describes the diffusion limit of particle burning. The reaction rate is found by assuming that the oxidant concentration at the surface is zero, and that at infinity the oxidant concentration is equal to its value for the bulk fluid. For a spherical particle, the rate of diffusion of the oxidant from infinity to the surface is found by solving the diffusion equation in spherical coordinates. The reaction rate of the particle is found by evaluating the diffusive flux of oxidant to the surface. Thus, the burning rate of the particle is found in the diffusion limit.

Evaluating the diffusion limited rate requires one additional piece of information, the diffusion coefficient of the oxidant relative to the gas mixture. First, an approximate formula given by Kuo (1986) was used to find the binary diffusion coefficient for each pair of species in the mixture, and then an approximate formula given by Welty, et al. (1969) was used to find the diffusion coefficient of the oxidant in the mixture.

Thus, one can evaluate a kinetically limited and a diffusion limited reaction rate for the particle with each reacting gas species. The smaller of the two rates controls the overall reaction rate. For these calculations, a formula given by Kuo (1986) was used. The reciprocal of the kinetically limited rate was added to the reciprocal of the diffusion limited rate, and the reciprocal was taken of the sum.

Finally, the overall rate of carbon loss by the particle was found by performing the above calculation for each reactant, and adding the results. Thus, a total rate of carbon loss is found for a particle of a given diameter in a surrounding gas of given composition and temperature. By applying a mass balance to the carbon particle, the rate of carbon loss can be converted to rate of decrease of diameter. Thus, if the surrounding gas properties are taken as constant, the result is a differential

equation for the diameter of the particle as a function of time. This equation was solved numerically using a Runge-Kutta solver found in Press, et al. (1986). The time required for the particle diameter to vanish defines the particle lifetime.

b. Again using the NASA equilibrium code and the mixture fraction X to define the surrounding gas properties, the above procedure was used to find the lifetimes of particles of different initial diameters for several different values of X. The results are shown in Figure 2.

Two points can be made. First, some numerical experimentation (not shown here) shows that a particle would have to be 10 microns or so in diameter for the diffusion limit to be important. Thus, if the particles in this plume are of submicron size, the reactions will be kinetically limited. Secondly, Figure 2 shows that even small particles can have a lifetime of several milliseconds, even in the most reactive region of the plume. Taking 200 feet/second as a representative gas velocity, a one micron particle would travel about a foot in the time the particle requires to burn. Thus, it would be desirable to include the finite reaction rate of the carbon particles in the flare model.

V. PARTICLE TEMPERATURE CALCULATION:

a. The chemical reactions at the particle surface should generate heat, which will elevate the particle temperature above that of the surrounding gas. The particle temperature can be found from an energy balance, equating the heat released by the reactions to that transferred by conduction from the particle to the surrounding fluid.

There is one main difficulty in this procedure. The species that react with the carbon are known; the products of the reactions are not. Experimentalists have measured the rates at which certain species attack the carbon surface, but they do not necessarily know what reaction occurs. Even if the products of the reaction could be measured, one would have to distinguish between the products formed directly at the surface as a result of the surface reaction and products formed by subsequent gas phase reactions.

Lifetime of Carbon Particles
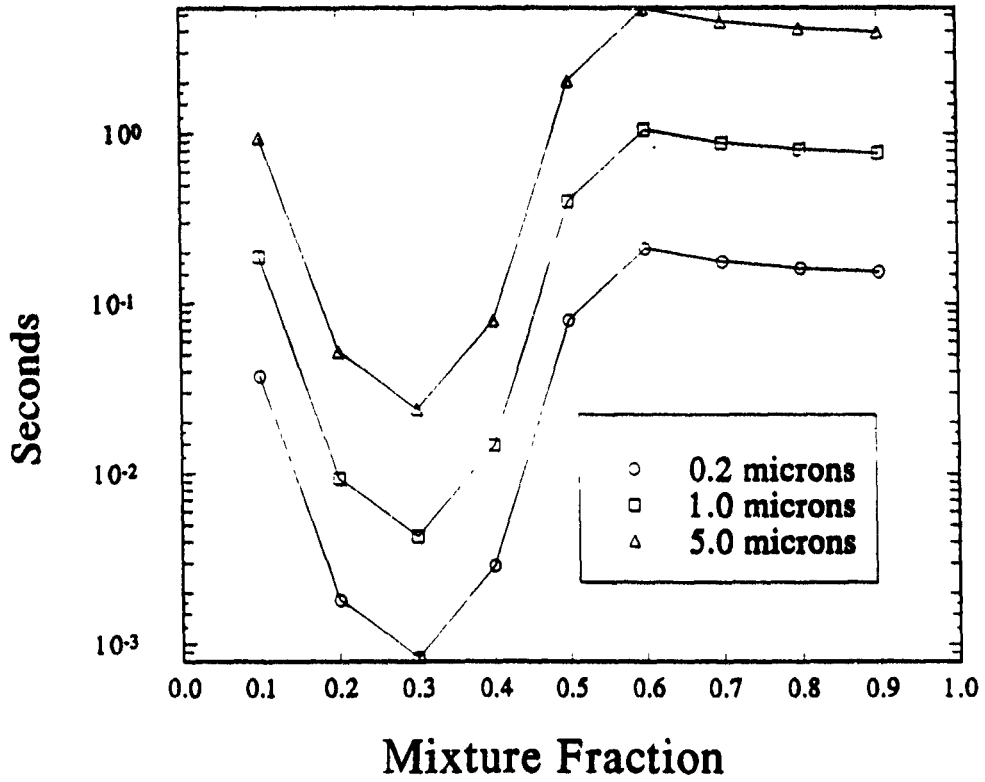
Figure 2

As a function of mixture fraction, the time required to burn up a particle is shown for particles with initial diameters of 5.0, 1.0, and 0.2 microns.

The following table shows the products which were assumed for the reactions of the plume gases with solid carbon. The enthalpy change, ΔH, of each reaction is the negative of the heat released, and was found from thermodynamic tables in the combustion text by Strehlow (1984) at a temperature of 2000 K. Note that the products of some reactions are radicals which will doubtlessly react further.

Reaction	ΔH Joules/gram of carbon
$C + O_2 \rightarrow CO_2$	-33034.
$C + CO_2 \rightarrow 2CO$	+13234.
$C + H_2O \rightarrow CO + H_2$	+11054.
$C + OH \rightarrow CO + H$	+5937.
$C + O \rightarrow CO$	-31155.
$C + H \rightarrow CH$	+30207.

Thus, for each reactant, the heat release rate is given per gram of carbon removed. Using the results of the previous section, the rate of carbon removal is known, thus the heat release rate can be found. An approximate formula from Kuo (1986) was used to find the thermal conductivity of the gas mixture, so the conductive heat loss to the gas was found. Equating the two yields an implicit equation for particle temperature. (Implicit because the surface reaction rates are evaluated at the particle temperature.) A root finder based on Brent's method from Press, et al. (1986) was used to solve the implicit equation and find the particle temperature.

b. The temperature difference between the various size particles and the surrounding gas as a function of the mixture fraction X is shown in Figure 3. One might conclude from this result that if the carbon particles in the plume are of submicron size, then the temperature difference between the particle and the gas will not be important.

Temperature Difference between Particle and Gas
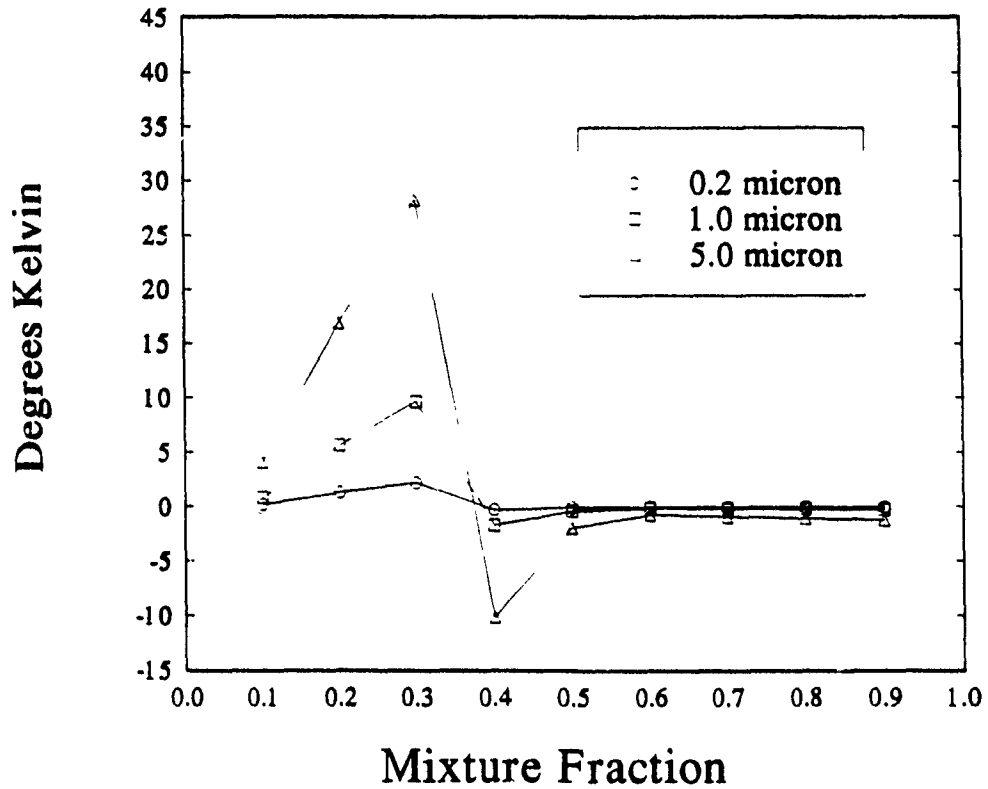
Figure 3

As a function of mixture fraction, the temperature difference between the particle and the gas is shown for 5.0, 1.0, and 0.2 micron particles. In the region of the plume where the reaction rates are greatest, the particles are hotter than the gas. Note that the effect vanishes as the particle size becomes smaller.

VI. RECOMMENDATIONS:

a. The flare model could be modified to include particle burning effects. The current program treats the solid carbon as if it were a gas. That is, the program computes an average carbon concentration (mass/volume) and ignores the fact that the mass is in the form of particles. The program needs kinetic expressions for the reaction of the carbon with other species in terms of this average carbon concentration. If an average particle diameter were known, then the particle surface area could be found from the average carbon concentration, and this could be used to find the kinetically limited reaction rate.

Further, if one assumes a particle size distribution function, the size distribution is completely determined by a few parameters of the distribution. For example, the log-normal distribution is determined by three parameters, the particle number density, some mean diameter, and the standard deviation. In a complex flow where the size distribution varies from point to point, one could allow these parameters to be functions of location and derive equations for their variation. The solution of these equations over the flowfield would specify the distribution parameters, and thus the distribution, at each point.

Thus, the existing model could be modified to include reacting particles.

b. The present results do not indicate any significant temperature difference between the particles and the gas. The paper by Bradley, et al. (1984) makes particularly interesting reading in this respect. Bradley, et al. compute the reaction rate of fine graphite particles in a hydrocarbon-air flame. They found that their computed particle temperatures did not differ much from the gas temperature. However, their experimental measurements showed that the actual temperature was significantly higher. The computed particle burning rates agreed well with the measurements, so they felt that their kinetic expressions were approximately correct. Bradley, et al. concluded by speculating that the carbon surface catalyzes the recombination of OH in the flame, and that this process is responsible for the anomalous temperature rise. This suggests that the present work should be extended to include recombination reactions.

c. The actual size of the carbon particles in the plume is unknown. Some experimental measurements would help the modeling effort.

REFERENCES

1. Blyholder, G., J. S. Binford, Jr., and H. Eyring, "Kinetic Theory for the Oxidation of Carbonized Filaments", Journal of Physical Chemistry, 1958, Vol. 62, pp. 263-267.

2. Bradley, D., G. Dixon-Lewis, S. El-Din Habik, and E. M. J. Mushi, "The Oxidation of Graphite Powder in Flame Reaction Zones", Twentieth Symposium (International) on Combustion, 1984, pp. 931-940.

3. Fenimore, C. P. and G. W. Jones, "Oxidation of Soot by Hydroxyl Radicals", Journal of Physical Chemistry, 1967, Vol. 71, pp. 593-597.

4. Feugier, A., "Soot Oxidation in Laminar Hydrocarbon Flames", Combustion and Flame, 1970, Vol. 19, pp 249-256.

5. Glassman, Irvin, Combustion, New York, Academic Press, 1977.

6. Gordon, S. and B. J. McBride, Computer Program for Calculation of Complex Chemical Equilibrium Compositions, Rocket Performance, Incident and Reflected Shocks, and Chapman-Jouguet Detonations, NASA/Lewis Research Center, NASA SP-273, 1976.

7. Haynes, B. S. and H. Gg. Wagner, "Soot Formation", Progress in Energy and Combustion Science, 1981, Vol. 7, pp 229-273.

8. Kuo, Kenneth K., Principles of Combustion, New York, John Wiley and Sons, 1986.

9. Lee, K. B., M. W. Thring, and J. M. Beer, "On the Rate of Combustion of Soot in a Laminar Soot Flame", Combustion and Flame, 1962, Vol. 6, pp. 137-145.

10. Neoh, K. G., J. B. Howard, and A. F. Sarofim, "Soot Extinction in Flames", in Particulate Carbon: Formation during Combustion, edited by Donald C. Siegla and George W. Smith, pp. 261-282, New York, Plenum Press, 1981.

11. Park, Chul and John P. Appleton, "Shock Tube Measurements of Soot Oxidation Rates", <u>Combustion and Flame</u>, 1973, Vol. 20, pp. 363-379.

12. Press, William H., Brian P. Flannery, Saul A. Teukolsky, and William T. Vetterling, <u>Numerical Recipes: the Art of Scientific Computing</u>, Cambridge, Cambridge University Press, 1986.

13. Radcliffe, Samuel W. and John P. Appleton, "Soot Oxidation Rates in Gas Turbine Engines", <u>Combustion Science and Technology</u>, 1971, Vol. 4, pp. 171-175.

14. Rosner, Daniel E. and H. Donald Allendorf, "High-Temperature Kinetics of Graphite Oxidation by Dissociated Oxygen", <u>AIAA Journal</u>, 1965, Vol. 3, pp 1522-1523.

15. Rosner, Daniel E. and H. Donald Allendorf, "Comparative Studies of the Attack of Pyrolytic and Isotropic Graphite by Atomic and Molecular Oxygen at High Temperature", <u>AIAA Journal</u>, 1968, Vol. 6, pp. 650-654.

16. Rosner, Daniel E. and H. D. Allendorf, "Kinetics of the Attack of Refractory Materials by Dissociated Gases", <u>International Conference in Metallurgy and Materials Science</u>, 1970, New York, Plenum Press, pp. 231-251.

17. Strehlow, Roger A., <u>Combustion Fundamentals</u>, New York, McGraw-Hill, 1984.

18. Welty, James R., Charles E. Wicks, and Robert E. Wilson, <u>Fundamentals of Momentum, Heat and Mass Transfer</u>, New York, John Wiley and Sons, 1969.

19. Wright, Franklin J.,"The Oxidation of Soot by O Atoms", <u>Fifteenth Symposium (International) on Combustion</u>, 1974, pp. 1449-1460.

20. Williams, Forman A., <u>Combustion Theory</u>, second edition, Menlo Park, California, Benjamin/Cummings, 1985.

1990 USAF-UES SUMMER FACULTY RESEARCH PROGRAM
GRADUATE STUDENT RESEARCH PROGRAM

Sponsored by the

AIR FORCE OFFICE OF SCIENTIFIC RESEARCH

Conducted by the

Universal Energy Systems, Inc.

FINAL REPORT

Noise Reduction in Rocket Test Videos using Mathematical Morphology

Prepared by:	Richard Alan Peters II, Ph. D.
Academic Rank:	Assistant Professor
Department and University:	Department of Electrical Engineering Vanderbilt University
Research Location:	Arnold Engineering and Development Center Arnold AFB, TN 37389
USAF Researcher:	J.A. Nichols
Date:	31 Aug 90
Contract No:	F49620-88-C-0053

Noise Reduction in Rocket Test Videos using Mathematical Morphology

by

Richard Alan Peters II

ABSTRACT

Video images of rocket tests are noisy. Thermal processes in the image sensor, imperfections in the recording medium, atmospheric distortion, and various environmental factors degrade the imagery. Blurring (lowpass filtering) individual frames of a video reduces high-frequency noise. However, it also degrades features such as edges that have high frequency components. Image noise and image features are not separable with linear filters if their frequency components overlap, and they usually do. Since most meaningful image features have shape and many types of noise do not, shape sensitive operators possibly could separate features from noise. Moreover, noise that is not correlated between frames could, in principle be detected and eliminated through a multiframe analysis.

Mathematical morphology includes shape-dependent, nonlinear filters that are effective noise reducers for two-dimensional imagery. We extended these filters into the time-domain for multiframe noise reduction of video imagery. We examine the opening transform, the open-close transform, the rolling-ball transform, and the rank filter (all are morphological operators) as spacetime operators. We show that these transforms reduce image noise effectively without degrading other features substantially.

Acknowledgements

I. INTRODUCTION

Engineers at Arnold Engineering and Development Center routinely make videotapes of rockets firing. The videos include x-rays of rocket engines burning and visible-light or infrared videos of rocket plumes from either stationary or flying rockets. They are used for performance evaluation and diagnostics. The utility of the videos is limited, sometimes greatly, by noise contamination.

Noise is introduced into video imagery in a number of ways. Thermal noise is ever-present in image sensors. It appears as a relatively low amplitude uniform or quasi-gaussian noise field. In low light conditions this is exacerbated by a low signal to noise ratio, since the amplitude of the thermal noise remains constant while that of the scene is low. Photo-multipliers may introduce shot noise that appears as bright spots in an image. Sometimes there is electromagnetic interference with adjacent test equipment. This may cause periodic patterns in individual image frames or flashing (amplitude modulation) across several frames or both. Atmospheric turbulence and haze distort images of distant rocket plumes. Vibration or nonperiodic motion of the camera or rocket test platform introduces motion blur and interframe jitter into the video. The scattering of x-rays also causes noise.

In the past, to reduce noise in rocket test videos, engineers have used linear filters on single frames. These effectively reduce some types of noise. If the noise and image features exist in different spatial frequency bands, (e.g., high frequency noise added to an inherently fuzzy image) then a linear filter can be designed that will completely remove the noise. If the image is broadband in spatial frequency and the noise spectrum overlaps it but is narrowband, then a band-reject filter can eliminate the noise without severely degrading the image. This situation sometimes occurs with electromagnetic interference or mechanical vibration. In most situations, however, the spatial frequency ranges of both the true image and the noise are broad and overlap one another; a linear filter that suppresses the noise degrades the image.

We examine the reduction of noise in time-sequences of video images. We restrict our examination to sensor noise and noise caused by atmospheric turbulence. We make two assumptions. Firstly, we assume that the noise in the sequence is uncorrelated in space or over time. That is, we assume that the pseudo features caused by noise are not contiguous over many pixels in spacetime. An

equivalent assumption is that true (non-noise) image features have contiguous support of multiple pixels in space-time. (By support, we mean the specific pixel locations which a feature occupies; by contiguous support we mean that the feature occupies a set of pixels that are connected together). In other words, a true feature exists on several adjacent pixels in a single frame and it persists across a few frames. This is not to assume that the feature is stationary, but only that the time sequence of spatial support neighborhoods overlap from frame to frame for a few frames. Secondly, we assume that the true features in the image can be approximated morphologically. These assumptions support the use of morphological operators for noise reduction.

Morphological operators, introduced by Matheron [6] and Serra [8], [9], [10] in the 1960's, are an extension of Minkowsky's set theory applied to image analysis. There are, in the general literature, a number of good tutorials on image morphology [1], [2], [3], [4], [5], [9]. We refer the novice to any of these papers for the fundamentals.

Morphological operators can be used for noise reduction because of the following property: When applied to an image, a morphological operator returns a quantitative measure of the image's geometrical structure. This measure can be used to construct a synthetic image containing regular approximations of the features in the original. A "regular" feature, in this sense, is a feature that can be reconstructed uniquely by the operator. The synthetic image is a smoothed version of the original image. But, the smoothing is nonlinear. Unlike a linearly smooth image, the morphologically smooth image contains sharp edges. The residual, i.e. the difference between the original image and the smoothed version, contains all "irregular" features such as noise and edges that could not be approximated by the operator. With a few assumptions about the differences between noise and edges, one can remove much of the noise from the residual image. Adding the "cleaned-up" residual back to the regular features yields a relatively noise free image with many edges intact and unblurred.

In the residual from a single image, one can discern between noise and edges on the basis of relative amplitude and support. One assumes true edges have greater amplitude and larger, contiguous spatial extent in the residual than does noise. To reduce the noise in a time-sequence of images, we extend morphological operators – and this assumption – into three dimensions (2 spatial dimensions and time).

We use three dimensional morphological operators to extract the regular spacetime structures from the image sequence. This smoothed sequence can be used directly as a noise reduced image sequence or the residual sequence can be modified and recombined with it. We examine both of these approaches using the following operators extended into spacetime: the opening transform, the open-close transform, the rolling-ball transform, and the rank filter. We show that these operators produce image sequences that are noticeably cleaner (i.e. contain less noise) than the original.

II. OBJECTIVES OF THE RESEARCH EFFORT

The analysis of a video of a rocket test is often hampered by the extremely noisy quality of the images. Current methods of noise reduction usually degrade non-noise image features. My goal as a participant in the 1990 Summer Faculty Research Program was to devise a new method for video image-sequence noise reduction that would leave important image features intact. I wanted the technique to be robust in the sense that many different people should be able to use it without understanding all the details. I wanted it to be relatively insensitive to the control parameters so that others could apply it to diverse data sets and achieve good results without much experimentation. I also wanted to write software to implement the procedure for a Unix workstation without special hardware. As this report will demonstrate, I believe that I met these objectives.

III. VIDEO IMAGE SEQUENCE NOISE REDUCTION

The video image sequences that we analyze are a series of digital images either 640 or 512 pixels horizontally by 482 pixels vertically. Pixels are 8 bits monochrome with 256 shades of gray. Zero represents black; 255 is white. For visible or infrared light the image sensor is a video camera using either a CCD array or a vidicon tube. In some cases the incoming light is amplified with a photomultiplier.

In vidicon tubes and many CCD cameras objects are photographed every 1/60th of a second in alternate frames. The frames are interlaced by row to form a single image. Each single image consists of 2 frames taken 1/60th of a second apart. Thus, the image of an object moving rapidly in the horizontal direction (with respect to the camera's focal plane) will be distorted; in a single image the object will appear in two places, pulled apart and interlaced on alternate scanlines. If the object's image is not moving very rapidly, this distortion will not be noticeable.

Apart from interlace, distortion, noise is introduced into video imagery in a number of ways. Our work focused on reducing sensor noise and reducing noise due to atmospheric disturbances.

Thermal noise in image sensors appears as a relatively low amplitude uniform or quasi-gaussian noise field that is added to the image of the scene. It is the result of quantum effects in the sensor. In low light conditions the image of the scene is dim and the thermal noise is exacerbated since the signal to noise ratio is small. That is, the amplitude of the noise remains constant while that of the scene is low. Typically, in a single pixel, thermal noise varies within a time interval much shorter than 1/60th of a second. The result is that the noise in successive frames is completely uncorrelated. Photo-multipliers introduce shot noise that appears as bright spots in an image.

Videos of flying rockets are made from a distance of many kilometers. Thus, atmospheric turbulence and haze distort the images. Atmospheric turbulence makes stars appear to "twinkle." The same process affects the image of a distant rocket plume. Individual points in the plume become darker or lighter over time, if not randomly, then with a process too complicated to model. Since both camera and rocket are moving, these points traverse a number of pixels across successive frames. Atmospheric haze will distort an image sequence. It can attenuate an image uniformly, across all its pixels, or it can attenuate some regions more than others. Such attenuation, whether uniform or

patterned, is dynamic over time.

In trying to reduce noise, one makes implicit assumptions about its characteristics. Then one proceeds to remove everything from the image with those characteristics. This may or may not be correct; some features may be removed, some true noise may be left. (It has been said that one person's noise is another person's feature.) We assume that the noise is uncorrelated, both spatially and over time. That is, any pattern that appears due to noise in a single frame does not exist near-by in an adjacent frame nor does it have the support of many contiguous pixels.

IV. TWO-DIMENSIONAL MORPHOLOGICAL NOISE REDUCTION

Morphological operators are a class of transforms defined on a complete lattice [7] (which is, essentially, a finite-dimensional euclidean space together with a partial order relation in which every nonempty subset has a supremum and in infimum). On a complete lattice, any operator that satisfies

1. Shift invariance – The results of the following must be identical: (i) translate a set in space and apply the operator. (ii) apply the operator and translate the result in space.

2. Size invariance – The results of the following must be identical: (i) expand (or contract) a set in space then apply the operator. (ii) apply the operator then expand (or contract) the result.

3. Local knowledge – The support of the operator is finite. If an operator is applied to two sets that are identical within a given region and different outside of the region, the results of the operator must be identical sufficiently deep inside the region. (A sufficient distance is the length of the longest line segment that can fit in the support of the operator. It could be smaller than that.)

4. Upper semicontinuity. – If a given infinite sequence of sets, I_n, converges to a specific set I through inclusion (i.e $I_0 \subseteq I_1 \subseteq \cdots \subseteq I_\infty \equiv I$), then the operator applied to the sequence, $\mathcal{M}(I_n)$ must converge (also through inclusion) to $\mathcal{M}(I)$.

is a morphological operator. This definition is broad; it includes shift invariant linear filters. We are interested in a nonlinear subclass of these transforms that includes openings, closings, and rank

filters. Our complete lattice is either $\mathcal{E} = \Re^2$ or $\mathcal{E} = \Re^3$ together with an order relation defined by set inclusion $(A \subset B)$ defined on $\mathcal{P}\{\mathcal{E}\}$, the power set (set of all sets in) $\mathcal{E}$.

Morphological operators are defined in terms of set inclusion. Both the image and the operator are defined as sets An image can be represented as a surface in a three dimensional space. Two of the dimensions correspond to the spatial dimensions of the image; the third corresponds to gray-level. That is, an image defines a surface above a plane. The altitude of the surface over a point (x, y) on the plane is given by the gray-level of the pixel p(x,y) from the image. The region space bounded by the surface (and the plane) comprises the image set. This region is called the "umbra" of the image [[11]]. (In rigorous definitions, the plane is considered to be an infinite distance below the image surface. The region of space bounded by the image, therefore extends to $-\infty$.)

The morphological operator is defined by another image surface (and umbra) in 3-space called a "structuring element". A useful structuring element (SE) is small relative to the image. In general, an SE can be of any shape or connectivity. The most useful SE's for our purpose are compact and simply connected. Examples include right circular cylinders with a flat or hemispherical tops.

Consider an image (umbra), I, and a structuring element, S. One point in S is designated as the origin of S. Let S_p represent the translation of S so that its origin coincides with point p in 3-space.

The opening of I by S, $I \circ S$, is the union of all translates, S_p, such that S_p is contained in I. That is

$$I \circ S = \bigcup_{S_p \subseteq I} S_p. \tag{1}$$

It is the best approximation of the image that can be made by translating and merging SE's subject to the constraint that the approximation is a subset of the original. The opening transform of an image is a smooth version of the image. Smooth, that is, with respect to the structuring element. But, unlike a linear smoothing, the opening will retain any edge that can be created by overlaying SEs. This includes the edges between uniform regions with support larger than that of the SE. Some of the details, however, will be missing. Features that are brighter than their immediate backgrounds and have smaller support than the SE will be eliminated from the transformed image. If only the noise in an image has this characteristic, then the opening is a good noise reduction transform. One must exercise care to select a structuring element that is small enough to approximate important features yet large enough to exclude most noise.

The difference between I and its opening, $I \circ S$, is called either a "tophat transform" or a "rolling ball" transform. (The former is used if the SE has a constant graylevel, the latter, if the SE has more than one graylevel.) That is

$$\text{tophat}[I] = I - (I \circ S) \qquad (2)$$

The tophat transform contains every bright feature (actual or noise) that cannot be approximated by unions of translations of the SE. This includes any bright area whose support is smaller than that of the SE, such as bright thin lines, curves, and corners.

The opening and tophat transforms can be used together to reduce noise in an image while retaining edges and thin bright areas. Consider the following statements: (1) Spatially uncorrelated (white) noise will tend to form spikes – very small regions that are brighter than their immediate surroundings – in an image. Therefore, much of it will be in the tophat transform as small isolated regions. (2) If the noise has a gaussian amplitude distribution, most of it will have lower amplitudes in the tophat transform. (3) True features can have any amplitude in the tophat transform. The most important of these have support of more than a few pixels, since features with low amplitude and small support will be indistinguishable from noise in the image.

If these three statements are true, then the tophat transform can be processed to separate features from noise. Statement 2 implies that much of the noise can be eliminated from the tophat image simply by thresholding it. Statements 1 and 3 suggest that eliminating small isolated regions in the tophat transform will discard noise and retain important features. We have found that the following is quite effective at isolating the most important features: Threshold the transform at a level that visibly excludes most of the noise pixels. (This sounds quite subjective, and the exact choice of threshold is. But, in most cases the correct range of thresholds is quite obvious.) Perform a binary opening on the support of the nonzero values in the thresholded image. This removes isolated regions and leaves those with more extensive support. Typically, a 3x3 square or plus, or a 5x5 quasi-disk is an appropriate SE. Subtract the threshold from the nonzero pixels that remain and add the result back to the opened image. The result is a relatively noise-free image with sharp edges intact.

As before, let I represent an image umbra and S, a structuring element. Let I^C represent the

complement of the umbra. That is

$$I^C = \left\{ p \in \Re^3 \mid p \notin I \right\} \tag{3}$$

The symmetric set, $\check{S}$, of S is S reflected in its origin. That is

$$\check{S} = \left\{ -p \in \Re^3 \mid p \in S \right\}. \tag{4}$$

The closing of I by S, $I \bullet S$, is the union of all translates, $\check{S}_p$, such that $\check{S}_p$ is contained in I^C. That is

$$I \bullet S = \bigcup_{\check{S}_p \subseteq I^c} \check{S}_p. \tag{5}$$

The closing is the dual with respect to complementation of the opening. It is the opening of I^C in euclidean 3-space by the symmetric SE, $\check{S}$. It is the best approximation of the image that can be made by translating and merging symmetric SE's subject to the constraint that the original image is a subset of the approximation. Like the opening, the closing is a smooth version of the image, with respect to the structuring element. Unlike the opening, the closing discards features that are darker than their immediate backgrounds and have smaller support than the symmetric SE.

The difference between the closing of I $I \bullet S$, and I is called either an inverted tophat transform or a inverted rolling ball transform. That is

$$\text{inverted tophat}[I] = (I \bullet S) - I \tag{6}$$

The inverted tophat transform contains everything that cannot be approximated by unions of translations of symmetric SE's. This includes any dark area whose support is smaller than that of the SE, such as dark thin lines, curves, and corners.

An opening alone smooths out only bright small areas. To smooth away both bright and dark areas requires an opening followed by a closing. This is called an openclose transform and is defined

$$\text{openclose}[I] = (I \circ S) \bullet S \tag{7}$$

The openclose transform can be used with the tophat and inverted tophat transforms to eliminate most bright and dark noise from an image as follows:

2D NOISE REDUCTION ALGORITHM

1. Select a structuring element, S, somewhat larger than the smallest important image features. To be most general it should be either a flat or hemispherically topped circular cylinder. We have gotten the best results from shallow hemispheres where the gray-level at the center is from 6 to 12 gray-levels larger than at the edges.

2. Perform an openclose on the image, I, using S. Call the result OC.

3. Compute a tophat transform, $TH = I - OC$. Set any negative pixels to zero.

4. Compute an inverted tophat, $IT = OC - I$. Set any negative pixels to zero.

5. Threshold TH at b to eliminate most bright noise. Call this $TH1$.

6. Open the support of $TH1$ with a 3x3 square or plus, or a 5x5 quasi disk SE to eliminate small bright regions. Call this $TH2$.

7. Subtract b from all nonzero pixels in $TH2$. Call this $TH3$.

8. Threshold IT at d to eliminate most dark noise. Note that IT is a "negative" image. A bright spot in IT represents a dark spot in I that could not be approximated by S. Thus, when thresholding IT we retain values greater than the threshold, just as with TH. Call this $IT1$.

9. Open the support of $IT1$ with a 3x3 square or plus, or a 5x5 quasi disk SE to eliminate small dark regions. Call this $IT2$.

10. Subtract d from all nonzero pixels of $IT2$. Call this $IT3$.

11. Add $TH3$ to OC.

12. Subtract $IT3$ from $OC + TH3$

The result of all this is a smooth image with crisp details. In practice the result can be quite dramatic.

Another morphological transform used for noise reduction is the rank-filter. In an nth-order rank filter, all the pixels in a neighborhood are sorted into descending order. The nth largest value is output. If there are N pixels in the neighborhood where N is an odd number, and $n = \lceil N/2 \rceil$, then the operator is a median filter. Median filters will remove isolated noise pixels from an image. They are especially good for removing salt and pepper noise without affecting step edges. When the noise is fairly dense gaussian or uniform white noise, however, the median filter tends to blur the image somewhat. We have found the 2D algorithm given above to be more effective at preserving edges than the median filter.

V. THREE-DIMENSIONAL SPACETIME MORPHOLOGICAL NOISE REDUCTION

The definitions of the morphological operators given in section IV apply to n dimensions. There we took $n = 2$ as a special case; here we take $n = 3$.

A time sequence of images, if stacked in time order, form a three-dimensional set. Two of the dimensions correspond to the two spatial dimensions of the images. The third dimension of the space corresponds to time. Each point in the 3D space has an intensity value associated with it that is the gray-level of the pixel.

Our goal is to reduce noise and leave true features unaltered. If we assume that true features are coherent over (at least short) time periods, then they form trajectories in spacetime. The shape of the trajectory depends on the motion of the feature. (In the following, we refer to motion with respect to the image plane.) A stationary particle forms a line parallel to the time axis. A particle moving with constant velocity forms a straight line not parallel to the time axis. The angle between the particle line and the time axis is proportional to the velocity of the particle. A particle moving with constant acceleration traces a parabolic curve. A particle with rotational motion in the image plane forms a spiral in spacetime. A particle with rotational motion orthogonal to the image plane forms a sinusoidal trajectory in spacetime. Objects (connected, rigid groups of particles) form generalized cylinders whose axes parallel the trajectories of the constituent particles.

As discussed in sections I and III, we assume that noise is uncorrelated over time and in space. Whereas true features form coherent trajectories in spacetime, noise does not. We use this lack of

coherence to eliminate the noise a much as possible

In our experiments, we used the following as spacetime operators: 3D median filter. 3D opening, 3D closing, 3D openclose. 3D tophat. A median filter in spacetime acts much like the 2D median. It will eliminate sparse salt-and-pepper noise while preserving step edges In spacetime, however, the edges include event boundaries – the sudden appearance or disappearance of objects. If the spatial support of the object is larger than the structuring element, if it has sharp edges and if it appears or disappears quickly, then the median filter will preserve the object.

To construct an intensity distribution, a 3D opening translates a structuring element to each point of spacetime and adjusts the intensity of the SE so that no pixel in the SE is brighter than its corresponding spacetime pixel. This obliterates any bright events whose spacetime support is smaller than the SE. A closing is similar to the opening except that it adjusts the intensity of the SE so that no pixel in the SE is darker than its corresponding spacetime pixel. This removes any dark areas with spacetime support smaller than the SE. To remove both light and dark noise requires either an openclose or a closeopen.

A tophat or rolling ball transform is the pointwise difference between the original image sequence and the opening. It, of course, contains all bright events with small support, i.e. noise and thin features. An inverted tophat or inverted rolling ball transform is the pointwise difference between the closing and the original image sequence: it contains all dark events with small support Through a process analogous to the 2D algorithm, we use the openclose and the tophat for noise reduction

3D SPACETIME NOISE REDUCTION ALGORITHM

1. Select a structuring element, S, somewhat larger in maximum 2D spatial extent than the smallest important image features. The time extent of the SE should be at least three frames. Select this minimum if there is much rapid motion of features. Select a larger time dimension is the features are moving less slowly. For noise reduction, the SE should be either a constant gray-level spheroid or a spheroid that is brighter in the middle than at the edges. We have gotten the best results from oblate spheroids (a sphere squashed in the time dimension) with a gray-level at the center that is from 6 to 12 gray-levels larger than at the edges.

2. Perform an openclose on the image sequence, I, using S Call the result OC

3 Compute a tophat transform. $TH = I - OC$. Set any negative pixels to zero.

4 Compute an inverted tophat, $IT = OC - I$. Set any negative pixels to zero

5 Threshold TH at b to eliminate most bright noise. Call this $TH1$

6 Open the support of $TH1$ with a 3x3x3 cube, a cube without corners (a 3D plus), or a 5x5x5 quasi disk SE to eliminate small bright regions. Call this $TH2$

7. Subtract b from all nonzero pixels in $TH2$. Call this $TH3$.

8 Threshold IT at d to eliminate most dark noise. Note that IT is a "negative" image. A bright spot in IT represents a dark spot in I that could not be approximated by S Thus, when thresholding IT we retain values greater than the threshold, just as with TH Call this $IT1$

9 Open the support of $IT1$ with a 3x3x3 cube, a cube without corners (a 3D plus), or a 5x5x5 quasi disk SE to eliminate small bright regions Call this $IT2$

10 Subtract d from all nonzero pixels of $IT2$ Call this $IT3$

11 Add $TH3$ to OC

12 Subtract $IT3$ from $OC + TH3$

We have tested various 3D spacetime morphological operators on a very noisy image sequence of a rocket firing. We used oblate spheroids as SE's. Those we tried included:

1. 5x5x5 median

2. 7x7x5 opening

3. 7x7x5 tophat enhanced opening

4. 7x7x5 median

5. 7x7x5 openclose

6. 15x15x5 median

7. 15x15x5 openclose

8. 15x15x5 tophat enhanced openclose

9. 15x15x5 tophat

10. 15x15 openclose on each frame individually

On the image sequence we used, we got the best results from the 15x15x5 tophat enhanced openclose. The 15x15x5 openclose without enhancement did a very good job as well. The noise was mostly eliminated; that was obvious by inspection. Examination of the tophat transform showed that it contained mostly noise; there was little or no indication of the coherent image features within it. The cleaned-up time sequence was very smooth both in space and time. Interestingly, the 15x15 openclose applied frame by frame with no time dependence resulted in imagery that was smoother spatially than the original. But, the time sequence was "jumpy" or "jittery". As a result, the sequence still looked quite noisy. The 15x15x5 median filter removed noise but also tended to blur the image more than the enhanced openclose. The smaller filters did noticeably clean up noise, but did not smooth the sequence as well as the larger operators.

VI   RECOMMENDATIONS

Three dimensional spacetime morphological operators are very useful for the noise reduction of time-sequence video images of rocket tests. The tophat enhanced openclose operator with an oblate spheroidal structuring element is especially adept. Median filters also clean noise well but tend to blur features more than the enhanced openclose. In some cases the openclose without enhancement works quite well

This report only scratches the surface of 3D morphological operators for time-sequence image enhancement and analysis. In particular, more study done on structuring element shape. Time axis cylinders, and solid and hollow paraboloids, hyperboloids, and hourglasses would make excellent velocity-tuned or acceleration-tuned filters that would permit the extraction of particles moving in particular directions or with particular velocities. This could be of great assistance in the analysis of fluid flow

Also new morphological operators that take advantage of a third dimension can be devised and should be explored. For example, an minmax operator that takes the minimum over a time interval of the maxima from the spatial neighborhoods in each time slice of the interval. Such an operator would track bright and dark moving particles. Coupled with the velocity-tuned structuring elements, these filters could be quite sensitive and highly selective

VII   REFERENCES

[1] Giardina, C. R and E. R. Dougherty, *Morphological Methods in Image and Signal Processing*, Prentice-Hall Englewood Cliffs New Jersey 1988

[2] Haralick, R. M, S. R. Sternberg, and X. Zhuang, "Image analysis using mathematical morphology" *IEEE Trans. Pattern Anal Machine Intell.*, vol. PAMI-9, No 4, pp. 532-550, 1987.

[3] Maragos, P and R W Schafer, "Morphological filters – part I their set theoretic analysis and relations to linear shift invariant filters," *IEEE Trans. Acoust., Speech, Signal Process.*, vol ASSP-35, No. 8, pp. 1153-1169, 1987.

[4] Maragos, P. and R W. Schafer, "Morphological filters - part II. their relations to median, order-statistic, and stack filters," *IEEE Trans. Acoust. Speech, Signal Process*, vol. ASSP-35, No 8, pp 1153-1169, 1987

[5] Maragos, P and R W Schafer, "Morphological Systems for multidimensional signal processing *Proc IEEE*, vol 78 No 4, pp 690-710, 1990

[6] Matheron, G., *Random Sets and Integral Geometry*, Wiley, New York, 1975

[7] Ronse, C , *Why Mathematical Morphology Needs Complete Lattices*, Manuscript M-270, Philips Research Laboratory Brussels, Avenue Van Becelaere 2, Box 8, B-1170 Brussels, Belgium, November, 1988.

[8] Serra, J., *Image Analysis and Mathematical Morphology*, Academic Press, London, 1982

[9] Serra, J , "Introduction to mathematical morphology," *Comp Vision. Graph., Image Process*, vol. 35, pp 283-305, 1986

[10] Serra, J ed, *Image Analysis and Mathematical Morphology, Vol 2 Theoretical Advances* Academic Press, New York, 1988

[11] Sternberg, S R , "Grayscale morphology," vol. 35, *Comp Vision Graph, Image Process*, pp 333-355, 1986

VIII. APPENDIX: COMPUTER PROGRAM MORPH3D

To carry out this research, I wrote two computer programs to perform morphological image processing. One was for 2D morphology of single still images. The other was for 3D morphology of image sequences. The following is a "man page" description of the 3D program.

morph3d   <FileList [>LogFile] -m e|d|o|c|r [-i g|b] [-s g|b] [-o s|f] [-t nnn [mmm]] [-r med|nnn] [-z]
           [-f slope inter] [-l] -k SEFile | 3x3x3 | 5x5x5 | plus | auto xxx yyy zzz [vvv]

where:

- FileList is an ascii file containing the filenames of the individual frames of the image sequence. Each frame must be a sun rasterfile of identical format. (Type <FileList so the file is read in through stdin.)

- Out is the pathname of a file for a log the program's activity. If this is omitted, the log is displayed in the csh window. (Type >LogFile so the file is output through stdout.)

- The letter following -m indicates the morphological operation:

    e - erode

    d - dilate

    o - open

    c - close

    r - rank filter

    t - top hat transform (image minus opening)

    b - top hat transform (closing minus image)

  one of these letters must be specified; there is no default.

- Switch -i indicates that the next letter tells the image type: either g for a gray-level image or b for a binary image. If -i is not included, the default is gray-level.

- Switch -s indicates that the next letter tells the structuring element type: either b for a binary SE or g for a gray-level SE. If -s is not included, the default is binary.

- The letter following -o, either s or f, indicates that the operation is either a set operation or a function operation. (See reference.) If -sf is not included, the default is set operation.

- -t nnn [mmm] indicates that a threshold of value nnn from below (and mmm from above; if unspecified mmm == 255) will be used on the input if the following 2 criteria are true: the input is a gray-level image AND the operation is a set operation. If the two criteria are true and -t nnn [mmm] is not included, the operation is treated as a function and set processing (FSP) operation (See ref.). If the criteria are not true and -t nnn is specified anyway, it is ignored.

- Switch -r is meaningful only if -m r is specified. Then the field following -r indicates the order of the filter. If the letters "med" are in the field, a median filter is used. If the field contains a number, nnn, then that value is used. If -m r is specified and -r med—nnn is not, the rank filter defaults to a median filter.

- The presence of switch -z tells the program NOT to zero-pad the boundary of the image. With this option, the output image has a border of zeros inside it the width and height of the SE. That is, the transformed area of the output image is smaller than the actual image dimensions. This is, in a sense, a more accurate result than the zero padded default. To zero pad the input permits the program to transform the border region, but it does this on the assumption that the original scene was black outside the image. This, of course, is almost never true. Thus, the border region is inaccurately transformed. Use this switch if accuracy is more important than having an image that is "colored in" out to the boundary.

- Switch -f tells the program to scale the output of the operation by multiplying each output pixel by slope and adding inter. Instead of the words "slope" and "inter", the user supplies two floating point numbers (or integers).

- Switch -l tells the program to display the log file info in the stderr window as it computes in addition to dumping it to stdout.

- Switch -k indicates that the next field is one of 5 things:

  1. "3x3x3" – specifies the structuring element to be a 3 by 3 by 3 cube of white pixels. (Don't use the quotes "" on the actual command line.)

  2. "plus" – specifies the SE to be a 3 by 3 by 3 "+" shaped set of white pixels.

  3. "5x5x5" – specifies the SE to be a 5x5 quasi sphere (cube without corners) of white pixels.

  4. "auto xxx yyy zzz [vvv]" – the program makes an SE. The self-made SE is a sphere with support covering xxx pixels horizontally, yyy pixels vertically, and zzz pixels across frames. xxx, yyy, and zzz must be odd. If specified, vvv is the gray level of the center pixel. If is not given, the level defaults to WHITE (255). If "auto" is specified the SE type is set to gray. The -o switch can be used to indicate a function operation (for full generality) or a set operation (in which case only the support of the disk is important – the gray-levels are ignored).

  5. If the field following -k is not one of the above, then the string, called SEFILE in the usage example, is taken as the pathname of a structuring element file. If the user has an environment variable called SEPATH, the program appends SEFILE to it for the complete pathname.

A structuring element file is an ASCII file of integers separated by spaces. The first three numbers, x, y, z, are the horizontal, vertical, and frame dimensions in pixels of the smallest box that will cover the structuring element. x, y and z must be > 0. The next three numbers, i, j, k are the horizontal, vertical, and frame coordinates, respectively, of the SE origin. The origin is expected to be in the covering box. The front upper left hand corner of the box has coordinates (0,0,0); the back lower right is $(x - 1, y - 1, z - 1)$. Following the first six integers are $x \times y \times z$ integers separated by spaces. These numbers are the SE elements. Their interpretation depends on the morphological operation being performed.

Negative SE elements are ALWAYS treated as logical DON'T CAREs. That is, when the operation is in progress, image pixels under negative SE elements are ignored. Thus, the support of the SE is limited to those elments that are nonnegative. This permits the creation of odd-shaped and multiply connected SE's.

If the input sequence is flagged binary, -i b, (i.e. pixels grouped as zero and not zero), and the SE is flaged binary, -s b, then the SE is used to perform a hit-or-miss transform. In this case, zero SE elements cover the "miss" support and nonzero (positive) elements cover the "hit" support. The gray-levels other than this are ignored.

If the input sequence is flagged -i b and the SE is flagged gray (-s g) then the nonnegative (both zero and greater than zero) SE elements determine the support of a "hit-only" transform. That is, the nonnegative suport is used as a standard "set"-type SE for set (binary) morphology. (Of course, the other gray-level info is ignored.)

Note: If the input is flagged -i b, then the flag [-o s—f] is ignored.

Here are the possible gray-level image sequence flags and the resulting interpretation of the SE elements:

-i g -s b -o s Function-set morphology on support of strictly greater than zero SE elements.

-i g -s b -o f Same as above.

-i g -s g -o s Function-set morphology on support of nonnegative (greater than or equal to zero) SE elements.

-i g -s g -o f Function-function morphology on support of nonnegative SE elements.

1990 USAF-UES SUMMER FACULTY RESEARCH PROGRAM

GRADUATE STUDENT RESEARCH PROGRAM

Sponsored by the

AIR FORCE OFFICE OF SCIENTIFIC RESEARCH

Conducted by the

Universal Energy Systems, Inc.

<u>FINAL REPORT</u>

<u>On the Hazard of Combustion Chamber Oscillations in a Large Freejet Test Cell</u>

Prepared by: John M. Russell, Sc.D. and Grant M. Watson, B.S.

Academic rank: Associate Professor and Graduate Student, resp.

Department and   Mechanical and Aerospace Engineering

 University: Florida Institute of Technology

Research Location: USAF/AEDC
                        Arnold AFB
                        Tennessee 37389

USAF Researcher: Clyde H. Kunz

Date: 24 Aug 90

Contract No: F49620-88-C-0053

On the Hazard of Combustion Chamber Oscillations in a Large Freejet Test Cell

by

John M. Russell and Grant M. Watson

ABSTRACT

The Aeropropulsion Systems Test Facility (ASTF) at the Arnold Engineering Development Center (AEDC) is to be used to test the powerplant for the National Aerospace Plane (NASP). The NASP powerplant is an airbreathing hydrogen fueled engine and is to be tested in a 'freejet' mode, i.e. not all of the inlet air in the test cell is to be ingested by the engine. Some of that air—the 'freejet spillage'—will flow past the engine to simulate the environment in which the engine will operate. Unplanned releases of hydrogen into the test cell (which may result from a flameout or leak in the fuel line) will allow it to mix with freejet spillage air and, if not disposed of, expose the facility to any of several potentially destructive combustion phenomena. One concept for a hydrogen disposition system (HDS) involves burning the hydrogen at an array of flameholders installed in the test facility for that purpose.

The present report focuses specifically on the hazard of combustion chamber oscillations in the region downstream of such an array of flameholders. Combustors in rocket engines and ramjets and afterburners in turbojets commonly experience such oscillations during development and, if not controlled, can destroy the device in which they arise. The physical proccesses involved in combustion chamber oscillations and theories for modeling them are reviewed. The usual trial-and-error approach for the development of combustion chambers for engines is not feasible when the device at risk is the ASTF. Technologies for suppressing such oscillations (e.g. the use of acoustic liners, baffles, and water spray) are reviewed. One conclusion of the report is that an HDS concept based on afterburning without any artifices for the suppression of resonant combustion introduces a credible threat to the ASTF and that further study of oscillation suppression devices in this geometry is called for.

Acknowledgements

I. INTRODUCTION

The present concept for the National Aerospace Plane (NASP) features an airbreathing powerplant fueled by hydrogen. The reliability of such a powerplant is a strong function of the kind of testing it is subject to during its development. Testing of the powerplant under conditions that simulate the high altitudes and supersonic speeds in which it is designed to operate is essential to such development. Of the various engine testing facilities in the free world, the one that comes closest to fitting the needs of the NASP engine development program is the Aeropropulsion Systems Test Facility (ASTF) at the Arnold Engineering Development Center (AEDC) at Arnold Air Force Base in Tennessee.

The ASTF features two test cells. The one in which the NASP engine is to be tested will be a "free jet" cell as distinguished from a "direct connection" cell. In a direct connection cell, all the air that enters the cell passes through the engine. In a free jet facility, air passes both through and around the engine. The air that flows around the engine in a free jet facility is sometimes called "freejet spillage", and we will apply that term in this document.

If during testing of the NASP powerplant, unburned hydrogen is discharged into the engine exhaust or the free jet spillage air, following perhaps, a flameout or a rupture of a fuel line, the resulting mixture of combustible gases may be explosive. Now the ASTF facility cost on the order of $640. million to build. The engineers who plan the testing of the NASP engine in the ASTF must therefore design a Hydrogen Disposition System (HDS) to render the gases down cream of the test engine nonexplosive under all credible contingencies.

Three broad classes of HDS concepts have been considered by personnel at AEDC (cf. STEPHENS & JORDAN (1988)), namely Inerting, Plant Bypass, and Afterburning. Inerting the explosive gases by injection of nitrogen or carbon dioxide can be effective, but the cost of procuring these gases in the amounts required is great as is the cost of installing suitable pumping apparatus. Inerting by steam would eliminate much of the cost of procuring inert gases but the inerting action of the steam may be defeated by the dehumidifying action of the machinery in the ASTF exhaust plant. A reversion of the exhaust gas from an inert form to an explosive form in the exhaust plant would expose the machinery there to an unacceptable risk. The concept of Plant Bypass involves installation of a scoop downstream of the test engine to collect the most hazardous gases and exhaust them separately from the free jet spillage. This option is also prohibitively expensive.

Afterburning is an HDS concept in which piloted flameholders, torches, or other incendiary devices are installed downstream of the engine to burn off the combustibles in a controlled fashion. In this concept, a portion of the test cell between the test engine and the exhaust plant operates like the afterburner of a jet engine (or, possibly, the combustor of a ramjet). STEPHENS & JORDAN

(1988), for example, favor afterburning over other HDS concepts on the grounds that it requires the least radical facility modifications to install and available technology inspires confidence that the combustible gases in the test cell can indeed be ignited and made to burn thoroughly.

The hazard of a single catastrophic detonation is, perhaps, the most obvious destructive combustion phenomenon to consider, but it does not exhaust the class of destructive combustion related hazards to which the ASTF may be exposed, even with a burnoff system installed. To see how other destructive combustion related hazards may arise even with a hydrogen burnoff system installed, we refer to an article by OLSON (1960) in a contribution to the Princeton Series on High Speed Aerodynamics and Jet Propulsion, Volume XI (titled Design and Performance of Gas Turbine Powerplants)

> "A particular class of vibration known generally as combustion oscillations should be mentioned here. Combustion oscillations are essentially periodic fluctuations in combustor pressure that are maintained by the combustion process.
>
> These oscillations may occur occasionally and unexpectedly in ducted burners of various kinds, although they are most often encountered in rockets..., ramjets..., and afterburners.... They are to be distinguished from rough burning, or intermittent explosions sometimes resulting from improper fuel-air mixtures.
>
> The amplitudes of combustion oscillations are often quite high, equal to or greater than the operating pressure of the system. Frequencies, too, are often quite high, from hundreds to thousands of cycles per second, giving rise to terminology such as 'chugging', 'howling', 'screaming', 'screeching', and so forth. These high amplitudes and high frequencies together with enhanced combustion temperatures and heat transfer rates, usually produce catastrophic failure of the combustion device."

(Ibid., p 344). In a paper titled "Driving Standing Waves by Heat Addition", BLACKSHEAR (1952) writes:

> "In most cases, a given combustor that exhibits one or more of these instabilities can be modified by a number of trial and error methods and the instabilities eliminated within the design range of operating conditions. For example, chugging rockets are quieted by increasing the pressure drop across the injectors; squealing in afterburners is subdued by increasing the velocity past the flame holders.
>
> The art of combustor design in its present state allows the designer in most cases to 'cure' a specific burner of instabilities when they arise but can in no way guarantee that a new design will be free of them.

(Ibid., p 2). Many quotations of similar gist may be found in papers and review articles by other authors. Particularly noteworthy in this regard are the reviews by ROSS & DATNER (1954), PUTNAM (1964), the reference book edited by HARRJE & REARDON (1972), and CULICK (1989).

The case for devoting some resources to the analysis of combustion chamber oscillations in designing the apparatus for the planned testing of the NASP engine in the ASTF may be summarized

as follows. When the only hardware exposed to the risk of combustion chamber instablity is a jet or rocket engine, the trial-and-error approach to combustion chamber development is feasible. When the hardware at risk is a facility as expensive as the ASTF however, the trial-and-error approach is out of the question. A satisfactory design must inspire confidence that the hazard of destructive combustion chamber phenomena in general, and combustion chamber oscillations in particular, has been reduced to a reasonable minimum before testing of the NASP engine in the ASTF commences.

Three points emerge from our study of the literature on this subject:

(i) Acoustic waves of large amplitude can be destructive to combustion chambers:

(ii) Acoustic waves can propagate through any gas, including burnt gas downstream of an array of flameholders in a hydrogen burnoff system.

(iii) Like any other gas filled container, a combustion chamber downstream of an array of flameholders is an acoustic resonator. An array of flameholders forms part of the internal boundary of that resonator. Unlike a smooth rigid wall, however, the flameholders (and the flames attached to them) may reflect acoustic waves so as to increase their energy (cf. section VII below). In the absence of effective damping mechanisms, these energy increases can be cumulative and lead, after sufficiently many cycles, to a large amplitude potentially destructive oscillation.

These points indicate that combustion chamber instability is due as much to the boundary conditions of the resonator in which it arises as to the combustibility of the gas as such.

The avoidance of destructive combustion chamber instabilty is a requirement that an acceptable design of a hydrogen burnoff system for the ASTF must satisfy. The rest of this document is meant to support efforts to meet this requirement.

II. OBJECTIVES

The objectives of our research effort this summer were:

1. Study the literature on destructive phenomena analogous to that of an afterburning hydrogen disposition system for the C-1 test cell of the ASTF and describe in broad outline their physical mechanisms.

2. Classify the various hazardous phenomena that can occur and assess their relative credibilities as a threat to the ASTF.

3. Recommend measures to mitigate the hazards to the ASTF from destructive combustion phenomena.

III. APPROACHES TAKEN AND NATURE OF THE RESULTS

There are many similarities between the action of a combustor or afterburner in a jet engine and the action of a Hydrogen Disposition System for the ASTF based on the afterburning concept. Both systems involve injection of combustible material into a moving airstream in a duct, deliberate ignition of the combustibles, and anchoring of the resulting flame at bluff body flameholders. Ramjet combustors and afterburners on turbojet engines normally feature subsonic flow in the interior of the chamber and a choked nozzle at the outlet. In this respect, the flow in cell C-1 of the ASTF differs from jet engine flows, since in the ASTF there is not supposed to be choked flow at the outlet. Besides the difference associated with the choked nozzle, jet engine flows are also of smaller scale and typically of lower Reynolds number than is the intended flow in the ASTF.

Despite these limitations in the analogy, we assumed that the class of internal flows in jet propulsion devices more nearly represents the flow likely to occur in cell C-1 in the ASTF than does any other class of flows for which a mature literature is available.

We began our reading this summer by consulting several of the twelve volumes of the Princeton-Series on High Speed Aerodyamics and Jet Propulsion, published by the Princeton University Press in the late fifties and the early sixties. Besides providing lucid expositions of the relevant fluid dynamics, we found citations of many useful primary sources, especially those published by the National Advisory Committee for Aeronautics. Once we had learned the customary terminology in the field, we were able to look up more recent contributions in the indexes, especially the International Aerospace Abstracts. The reference lists in the documents we found led us to still more sources in the usual way. The technical library at the Arnold Engineering Development Center has an excellent collection of documents published by agencies of the U.S. government and the NATO Advisory Group for Aeronautical Research and Development. In the few cases where a document we needed was not in the library collection, the staff obtained it through interlibrary loan.

In view of the objectives stated above, we have not tried to generate any results in the nature of calculations or measurements of our own. An attempt to produce such results before fully mining the rich literature that is available on the subject would have been premature. Our approach stemmed from a recognition that, in developing the necessary technology for the Hydrogen Disposition System for the ASTF, our hosts at AEDC must continually update their assessment of which phenomena pose the greatest threat to the safe operation of the facility. Our contribution (or "result") is an argument that combustion instabilities belong in the class of phenomena that deserve serious attention.

IV. CLASSIFICATION OF COMBUSTION CHAMBER OSCILLATIONS

Consider a container in the form of a right circular cylinder. If the container is filled with gas,

then many possible modes of vibration of the gas are possible. If the particle motions associated with one mode are all parallel to the axis of the cylinder, then that mode is called <u>longitudinal</u>. Longitudinal modes are often called <u>organ-pipe</u> modes. If, alternatively, the particle motions associated with a mode are all perpendicular to the cylinder axis, then that mode is called <u>lateral</u>. Lateral modes may be divided into various classes. Thus, lateral modes may be axisymmetric with no swirl. In such modes, the particle motions are radial and the instantaneous surfaces of constant pressure are coaxial cylinders interior to the vessel. Such lateral modes are called <u>radial</u>. In another class of lateral mode, the instantaneous pressure on any circle centered on the cylinder axis and lying in a cross sectional plane varies sinusoidally with respect to the azimuth angle. The simplest such nonradial lateral mode is one in which the pattern of disturbance pressure can be made stationary by viewing it relative to a suitably spinning reference frame. Such a feature of the motion suggests the term <u>spinning mode</u> and this term is common. In using the term "spinning mode", however, one must not surmise that there is any mean swirl necessarily associated with it.

A given spinning mode may be used to define a second spinning mode by reflecting the first through a plane of symmetry that passes through the cylinder axis. The superposition of such a pair of spinning modes is sometimes called a <u>transverse</u> or <u>sloshing</u> mode. The literature on combustion chamber instability imputes considerable destructive potential to the first transverse mode (see chapter V below). For a given combustion chamber geometry, the fundamental longitudinal mode is typically of much lower frequency than the first transverse mode. Such differences in frequencies gives rise to differences in nomenclature. Thus, an experimental study of combustor <u>screech</u> would typically apply to a transverse oscillation and one on <u>rumble</u> in an afterburner would typically apply to a longitudinal oscillation.

Some acoustic modes in cylindrical geometry are neither longitudinal nor lateral. The locus of points where the instantaneous pressure is a maximum may, for example, have the shape of a coil spring or <u>helix</u>. For present purposes, we will call such modes <u>helicoidal</u>.

The scientific literature on the coupling of heat addition with acoustic phenomena is old and a review of nineteenth century work on the subject may be found in a chapter titled "Theory of Resonators" in volume II of RAYLEIGH's <u>Theory of sound</u> (1896). Thus, for example, RIJKE (1859) reported an experiment in which organ pipe waves were generated by heat addition at a wire gauze situated at a cross section of the pipe. If a mean axial draft is maintained in the pipe and if the gauze is situated about one fourth of the length of the pipe inside the inlet, then the pipe will radiate sound spontaneously. The RIJKE tube phenomenon is not sensitive to the precise manner in which heat is added to the moving gas at the gauze. Thus, sound is produced if heat is added during the transient cool down of an initially hot gauze (<u>cf.</u> RAYLEIGH (1896, p 232)), or if the

pipe is a combustion chamber and the gauze is its flameholder (BAILEY (1957)). Sound can also be produced if the gauze is heated electrically. According to RAYLEIGH "...by keeping the gauze hot by the current from a powerful galvanic battery, RIJKE was able to obtain the prolongation of the sound for an indefinite period" (ibid.). RAYLEIGH (1896, pp 226–227) quotes a passage from an 1878 article by him in Volume XVIII, p 319 of Nature, in which he proposed that an acoustic wave may gain energy each cycle if the time dependent addition of heat is in phase with the passage of the high density portion of the wave. Many subsequent authors refer to the above criterion for sound generation as Rayleigh's criterion.

.Combustion chamber oscillations of the organ pipe type can be modeled by theories that involve only one space dimension, namely the axial coordinate. Such theories are less complicated than are theories of lateral oscillations. The reminder of this report will contain discussion of both types of oscillation.

V. ON THE SELECTIVE AMPLIFICATION OF LATERAL OSCILLATIONS TO DESTRUC-TIVE AMPLITUDES

Several authors have reviewed the literature on combustion chamber oscillations in general and lateral oscillations in particular. As we mentioned in chapter I above, we have found the reviews by ROSS & DATNER (1953) and PUTNAM (1964) to be especially useful as is the introduction to the reference book Liquid Propellant Rocket Combustion Instability, edited by HARRJE & REARDON (HARRJE & REARDON (1972)). Subsection 1.2.2 of that work was written by T.A. COULTAS and is titled "Classification". COULTAS divides combustion chamber instabilities into three broad classes, namely "low frequency, chug", "high frequency" instability or "resonant combustion", and "inter-mediate frequency, buzz". COULTAS describes the high frequency kind as "the most destructive" (ibid., p 17). Section 1.3 of the same chapter is called "Historical survey" and is written by D.T. HARRJE. HARRJE writes that "...resonant combustion is perhaps the most dramatic way to destroy an engine (burnout in a matter of milliseconds)..." (ibid., p 34).

In a paper titled "On Strong Transverse Waves Without Shocks in a Circular Cylinder", MASLEN & MOORE (1956) supply a theoretical argument in support of the hypothesis that transverse oscil-lations typically reach higher amplitudes than do longitudinal ones. On page 583 of this paper, they point out that

> "In a plane wave, the mechanism by which a pressure pulse steepens into a shock is well known—the high pressure portion of the pulse has an elevated speed of sound, and hence overtakes the low pressure portion ahead of it. A pulse moving transversely in a cylinder is also subject to the steepening effect; however, steepening is complicated by the scattering effect of a continuous reflection at a curved wall."

The ultimate result of such wave steepening in one dimension is, of course, the formation of a shock.

Now compresssible flows may be irrotational and isentropic. The velocity fields of those that are may be represented as the gradient of a velocity potential φ. If one refrains from making any small amplitude assumptions, φ satisfies a nonlinear partial differential equation called "the full potential equation". The full potential equation reduces to the (linear) acoustic wave equation in the limit of infinitesimal amplitude signals propagating through a gas nominally at rest. MASLEN & MOORE (1956) define an amplitude parameter ϵ for the disturbances and seek a solution of the full potential equation in the form of a perturbation series, i.e.

$$\varphi = \epsilon \varphi^{(1)} + \epsilon^2 \varphi^{(2)} + \epsilon^3 \varphi^{(3)} + \ldots , \tag{1}$$

in which $\varphi^{(1)}, \varphi^{(2)}, \ldots$ are new unknown functions that are independent of ϵ. Since MASLEN & MOORE were interested in modeling transverse modes, they also took the $\varphi^{(n)}$, $n \in \{1,2,3,\ldots\}$ to be independent of the axial coordinate x. If one substitutes the series (1) in place of φ in the (nonlinear) full potential equation and appeals to the linear independence of distinct powers of ϵ, then one may conclude that the coefficients of like powers of ϵ on the two sides of the resulting equation must balance separately. In this way MASLEN & MOORE decomposed the original nonlinear equation for φ into a sequence of linear equations for the $\varphi^{(n)}$, $n \in \{1,2,3,\ldots\}$. This technique, in which one substitutes a trial solution in the form of a series in powers of a small parameter ϵ into an exact equation and balances coefficients of like powers of ϵ, is the unifying theme of what mathematicians nowadays call perturbation theory. This aspect of the technique applied by MASLEN & MOORE is orthodox.

The equation for $\varphi^{(1)}$ is the (homogeneous) acoustic wave equation. The equation for each higher order solution $\varphi^{(n)}$, $n \in \{1,2,3,\ldots\}$ is an inhomogeneous equation whose homogeneous operator is the acoustic wave operator and whose inhomogenous part involves the functions $\varphi^{(n-1)}, \varphi^{(n-2)}, \ldots,$ $\varphi^{(1)}$ and their derivatives. By appropriate allowance for amplitude dependence of the frequency of a disturbance, MASLEN & MOORE found that shock free solutions of finite amplitude (i.e. of order ϵ^2 or higher) could indeed be found. Thus, they write (ibid., p 590)

> "The cylindrical mode can not be regarded as a train of distinct pulses, but is rather an interference pattern, in which the scattering effect of the wall overcomes any tendency for components to steepen into shocks such as occur in a plane mode of oscillation."

(emphasis ours). The significance of this result in the context of jet engines is summarized by the following passage (ibid., p 586)

> "So far as the internal aerodynamics of a jet engine are concerned, the possible permanence of strong isentropic waves is likely to be important in the following sense: if the combustion proccess is able to provide energy to drive an oscillation in any mode, then large amplitudes will tend to

be associated with modes having small inherent damping. Thus, perhaps, transverse oscillations may commonly be more severe than longitudinal, the latter being subject to shock losses."

This argument of MASLEN & MOORE is persuasive as long as the passage of a shock does not initiate combustion of the shocked gas. If it does, the possibility arises that a strong shock can initiate rapid enough combustion of the gas behind it for the energy released by the combustion to drive the shock in the manner of a detonation wave. CLAYTON, ROGERO, & SOTTER (1968) reported tests of a liquid fueled rocket combustion chamber in which "a steep fronted high amplitude pressure wave" swept "about the combustion chamber axis during a destructive liquid rocket resonant combustion mode...". The ratio of the pressure on the hot side of the wave to the pressure on the cold side was as large as twenty, a value typical of one dimensional detonation waves in gases. The nominal chamber pressure was 300 psi, so the inside wall of the combustion chamber near the injector plate was subject to transient pressures on the order of three tons per square inch.

In the controlled experiments reported by CLAYTON, ROGERO, & SOTTER (1968), the flow in an initially smooth running engine is disturbed by "an electrically initiated bomb pulse", which "precipitated the resonant combustion mode" (ibid., p 1253). According to these authors, "it was later demonstrated, with a different but similar engine that was spontaneously resonant, that the violent sustained oscillatory mode observed was not forced by the character of the initiating technique itself" (ibid., p 1253). CLAYTON, et al. report results obtained in a variety of chamber geometries. In one geometry, which these authors call a "stepped chamber", an annular groove is cut into the cylinder wall just downstream of the injector plate. On page 1258 of their paper, CLAYTON, et al. report that

> "The stepped chamber results indicate, however, that shocks are not always present for the spinning mode. In this case, an as yet ill defined propellant wall relationship was apparently varied which then did not allow the development of a severe steep fronted wave. For the sake of distinguishing the latter phenomena from the destructive mode exhibited by the standard chamber, we call the stepped-chamber mode nondestructive—even though it may still be an undesirable oscillation from an operational viewpoint."

The groove, in what CLAYTON, et al. call the "stepped chamber" is similar to "acoustic slots" described by T.A. COULTAS, C.L. OBERG, & J.M. SENNEF in HARRJE & REARDON (1972, §8.3.6). Section 8.3 of this reference book is thirty-one page long and is titled "Acoustic Liners". Article 8.3.6 "Further Acoustic Absorber Applications" begins on page 426. COULTAS, et al. repeatedly cite a report by OBERG titled "Final Report–Lunar Module Ascent Engine Acoustic Cavity Study" (Rocketdyne Report number R-7935, August 1969) as a case history of the successful use of acoustic slots to suppress combustion chamber instability. It appears that acoustic liners in general and acoustic slots in particular are artifices that often suppress combustion chamber oscillations when

they arise unexpectedly in development programs.

To summarize the point of this chapter, one interpretation of the results of MASLEN & MOORE (1956) and CLAYTON. et al. (1968) is that the energy of an unstable combustion chamber oscillation may be selectively accumulated in an isentropic lateral mode up to an amplitude at which the high temperatures associated with isentropic compression in the wave begin to induce significant enthapy release by combustion. Such additional enthalpy release may result in wave steepening and shock formation such that losses associated with irreversible processes in the shock are more than compensated for by the associated enthalpy released by combustion. The result may be a high amplitude detonation-like wave. An essential ingredient for the formation of such a wave, namely, the selective accumulation of wave energy in a transverse mode, may be removed and the instability suppressed if some kind of acoustic absorber is present to dissipate wave energy in the core region of the combustion chamber.

VI. EXCITATION OF LATERAL OSCILLATIONS IN COMBUSTION CHAMBERS BOUNDED UPSTREAM BY AN ARRAY OF FLAMEHOLDERS

ROGERS & MARBLE (1955,1956) report the results of a very perceptive study of the phenomenon of screeching combustion in the region of hot gas downstream of a premixed flame attached to a flameholder in a rectangular duct. These authors measured the time dependent pressures at various places on the chamber wall with electrical transducers. They also took high speed motion pictures of the natural plume illumination and made still pictures by the spark schlieren technique. The duct had a cross section four inches in height and one inch in span. The flameholder was two dimensional and spanned the duct. It was symmetrical about the duct centerline and had the cross sectional shape of an isosceles triangle (with apex angle $2\theta = 43°$ and apex pointing upstream). The axial length of the flameholder was $h = 3.5$ in. Its base b was therefore $2h \tan\theta \approx 2.757$ in. so the portion of the duct cross sectional area blocked by the flameholder in front view was 68.93%. The combustible gas was a mixture of vaporized industrial paint thinner and air. With the aid of this apparatus, ROGERS & MARBLE correlated screech limits with parameters such as equivalence ratio o (fuel to air ratio for the actual mixture divided by fuel to air ratio of a stochiometric mixture), the combustor inlet total temperature, the combustor mass flow rate, and the combustion chamber inlet MACH number. ROGERS & MARBLE point out that "the most direct indication of screech is the [time averaged] total pressure loss across the combustion chamber". They illustrated the transition into and out of the screech region by plotting the combustion chamber total pressure loss ratio as a function of o and found a hysteresis effect: the lean screech limit for increasing o was higher than the lean screech limit for decreasing o. The lean screech limit for decreasing o was, in turn, lower than the lean blowoff limit of the flame. ROGERS & MARBLE also found that the difference in o

between the lean blowoff limit and the lean screech limits decreased if the temperature of the fresh gas was increased.

As interesting as these measurements of the t'me averaged flow are, they reveal less about the mechanism of combustion chamber instability than do the results of high speed photography and measurement of time dependent wall pressures. The flow about a flameholder, like the flow about any other bluff body with salient edges, exhibits a low speed region of recirculating fluid in its wake. This low speed fluid consists mostly of hot burnt gas and is sandwiched between regions of fast moving fresh gas. There is a turbulent mixing layer between these regions which, like most mixing layers, exhibits what are now called "organized vortices" (cf. BROWN & ROSHKO (1974)). ROGERS & MARBLE observed that the size of these organized vortices was much greater in screeching flow than in smooth flow. In screeching flow, the organized vortices shed at the lips of the flameholder were shed asymmetrically about the duct centerline and the shedding frequency measured by analysis of the motion picture films matched the frequency of the dominant oscillation of the wall pressure (measured by transducers). In the abstract of the second paper, ROGERS & MARBLE wrote:

> "The following mechanism of exciting the oscillation is suggested. A mode of transverse os-
> cilation is excited as the result of periodic transport of combustible material, associated with the
> vortices, into the hot wake of the flameholder. The vortices, in turn, are generated at the flame-
> holder lips by the fluctuating transverse velocity. When the ignition time delay lies in the proper
> range, the phase relationship between oscillations in transverse velocity and combustion intensity
> is such that the oscillation is amplified."

A review of combustion chamber oscillations by PUTNAM (1964) includes a sympathetic discussion of ROGERS & MARBLE's proposed mechanism. We have not found any literature published in the intervening thirty-four years which challenges it. Its chief limitation seems to be its qualitative nature: it does not, for example, supply any quantitative method for the engineering prediction of screech.

The work of ROGERS & MARBLE (1955,1956) offers more insights into the mechanism of exciting lateral oscillation than do other reports we have consulted. One would do well to note, however, that other investigations have confirmed that transverse oscillations of significant amplitude arise spontaneously in ducts through which premixed streams of combustible gas flow and in which the gas is burned in flames anchored to flameholders. Among the most frequently cited investigations of this phenomenon are BLACKSHEAR, RAYLE, & TOWER (1955) and KASK \N & NOREEN (1955). A paper by TRUMAN & NEWTON (1955) reports results of a variety of tests of screech of the sort under discussion and notes that a sensitive parameter in correlating the onset of screech with geometric features of the combustor is the ratio, A_h/A_d, of the area of the flameholder array (A_h) to that of the duct (A_d). Specifically, TRUMAN & NEWTON report that screech always occurred if $A_h/A_d > 0.8$

and never occurred if $A_h/A_d < 0.3$. In a one-page article in the Canadian Aeronautical Journal, WISNIOWSKY (1957) reports results of some development work on screeching combustion in jet engine afterburners. WISNIOWSKY reports that an engine with a screeching afterburner may produce slightly higher thrust than one with smooth burning. The passage which follows echos the observations of both ROGERS & MARBLE and TRUMAN & NEWTON:

> "The experiments showed further that the reheat flame holder or stabilizer plays a most important part in exciting transverse gas oscillations. Its size was found to be critical. In other words, screech can be excited only when the stabilizer blocks a sufficiently high percentage of the tail pipe cross sectional area. The shape of the stabilizer is also very important since some configurations are more prone to screech than others with the same blockage area. The transverse gas oscillations which cause screech were found to originate close to the stabilizer trailing edge. It is assumed that vortex shedding from this edge is the origin of these oscillations. The discovery of the important role of the reheat flame stabilizer opened the way for successful work on the second objective of the investigation—the prevention of screech."

For other references prior to 1964, the reader is referred to the review by PUTNAM (1964).

VII. REFLECTION OF INCIDENT ACOUSTIC WAVES BY AN ANCHORED FLAME

Consider a nominally steady two dimensional flow of a premixed stream of combustible gases in a duct. Suppose that some initial ignition source is provided, that a stationary bluff body is situated on the centerline of the duct, and that the transverse size of the body is small compared to the duct width. Then for some values of the equivalence ratio φ, a stationary flame front attached to both the body and the side walls will form. Such a flame front has the shape of a "V" with apex pointing upstream. The results of an extensive series of experiments on flames of this kind were reported by SCURLOCK (1948), who also formulated a theoretical model for predicting the flame shape and the changes of thermodynamic properties of the gases across the flame. A synopsis of SCURLOCK's theory may be found in EMMONS (1958, §G.8). A modification to allow for certain compressibility effects neglected by SCURLOCK was published by TSIEN (1951).

MARBLE & CANDEL (1978) and MARBLE, MALLADI, & CANDEL (1980) have formulated a theory of the response of a SCURLOCK-type flame to an acoustic wave that propagates one dimensionally along the duct axis and impinges on the flame. The mathematical formalism of these works is similar to that of SCURLOCK (as summarized by EMMONS), but with the time dependent terms retained. Of considerable interest are computations of the coefficients of reflection and transmission for the acoustic waves. If, specifically, P^+ and P^- represent the complex amplitudes of travelling acoustic wave disturbances propagating in the direction from the cold fluid to the hot fluid and from the hot to the cold fluid, respectively, and if the subscripts "1" and "2" denote propagation in the regions of cold gas and in hot gas, then the reflection coefficient R of a acoustic wave incident

on the flame from the hot side may be defined by $R = P_2^+/P_2^-$. MARBLE, MALLADI, & CANDEL (1980) present curves of the magnitude and phase of R versus nondimensional frequency and find that for a particular set of parameters the $|R|$ curve has a peak value of between seven and eight. Evidently, a wave originating in the hot gas downstream of the flame and reflected back into it may be significantly stronger after the reflection. In this way the flame acts as an energy boosting reflector. One feature of the theory of MARBLE, MALLADI, & CANDEL (1980) that is especially worth noting is that the energy boosting action of the flame is effective even if the blockage ratio (the ratio of the frontal area of the flameholder to the total duct cross sectional area) is arbitrarily small. An experimental confirmation of some of the features of the theory of MARBLE, MALLADI, & CANDEL (1980) was published by POINSOT, et al. (1986).

VIII. ON LONGITUDINAL OSCILLATIONS

The contrast between longitudinal and transverse combustion chamber oscillations is summarized well by a quotation from CULICK's 1989 paper "Combustion Instabilities in Liquid Fueled Propulsion Systems—an Overview":

> "Perforated liners effectively attenuate the high frequency oscillations related to radial and tangential acoustic modes. Low frequency instabilities, often called 'rumble', tend to be more troublesome. Liners are ineffective at low frequencies and the problem of rumble is solved or reduced in practice by careful control and coordination of the distribution of injected fuel and the nozzle opening. It is a costly process to develop the system [afterburner], inevitably requiring several designs of the injection system and the flameholders, and expensive full-scale tests in altitude simulation test facilities."

This quotation exemplifies two facts that the designers of the HDS need to be aware of:

1. Two methods of suppresion may be needed. one to eliminate screech (a lateral instability) and the other to eliminate rumble (a longitudinal one);

2. Full-scale testing is an integral part of the development of a combustion chamber.

The second statement shows how the development of an HDS must differ from the development of an afterburner: while an afterburner can be tested at full scale before it is installed on an airplane. the HDS can only be tested at full scale by installing it in the ASTF.

Now longitudinal oscillations are not known for their destructive ability (see chapter V), and the prospect of flameholder destruction resulting from rumble may be low. Through our study of the literature. however, we have discovered nondestructive failures that may result during rumble that do not result from screech, and longitudinal oscillations may cause other problems that can be considered a failure in the HDS. For example, PUTNAM & DENNIS (1956) performed a set of experiments that resulted in the conclusion that longitudinal combustion instablities may cause

premature blowout of the flame. Longitudinal wave motion n y also result in intermittent blowout and reignition of the flame, as observed by BLACKSHEAR (1956):

> "As the lean blowout [low fuel-to-air ratio] was approached, the flame emitted a low-frequency noise at 87 cps. The average heat-release rate dropped abruptly. A survey taken with the photomultiplier probe showed the flame to be intermittently extinguished for all positions greater than 7/8 in. downstream of the flameholders."

In an article titled "Reheat Buzz: an Acoustically Coupled Combustion Instability. Part I. Experiment", LANGHORNE (1988) observed two regimes of oscillatory flow. In the first, called "weak buzz", hots spots associated with burning retain their identity over a relatively long axial portion of the duct and the amplitudes of the pressure oscillations are relatively low. This regime corresponds to an equivalence ratio of $\varphi < 0.65$. In the second regime, called "established buzz", hot spots retain their identity over a relatively short axial distance, the pressure oscillations were of relatively larger amplitude, and the coupling with the acoustic modes in the duct was direct. This regime corresponds to $\varphi > 0.65$. According to LANGHORNE (1988) (ibid., p 427) "Cine film of this shows that the flame alternately fills the duct then contracts, leaving only a kernel of flame on the gutter." Later, (ibid., pp 430–431), LANGHORNE remarks that in his configuration 4, "a significant increase in φ [above 0.65] caused sporadic, large amplitude events which caused blowoff."

In summary, longitudinal combustion chamber oscillations are a real threat to the safe handling of hydrogen gas in test cell C-1. While rumble may not cause destruction of the flameholders or exhaust duct, blowout of the flame is a real possibility. If this does occur, a combustible mixture of hydrogen and air may enter the exhaust plant. Therfore, the development of an HDS must include some certification that it is free of rumble.

IX. GLOBAL MODELING OF COMBUSTION CHAMBER OSCILLATIONS

A clear exposition of the basic theory of combustion chamber oscillations may be found in article 3.5.1 (written by W.A. SIRIGNANO) of HARRJE & REARDON (1972) and references cited therein. CULICK (1989) offers a more recent account whose scope includes not just liquid fuel rock ts (a restriction of HARRJE & REARDON (1972)) but also thrust augmentors and ramjets. This seventy-three page article contains fifteen pages of references* and is the most attractive presentation of the subject we have consulted so far. The reader is referred to this work (especially chapter 2) for a discussion of how both the field equations and the boundary conditions for acoustic waves in a chamber are modified by contributions from phenomena associated directly and indirectly with combustion. One passage especially bears repetition in the present context:

---

* The references are classified into four catagories: liquid rockets, thrust augmentors, ramjet engines, and passive and active control of combustion instabilities.

"Combustion instabilities may be regarded as the unsteady motions of a dynamical system capable of sustaining oscillations over a broad range of frequencies. The term 'combustion instability' is usefully descriptive but slightly misleading. In most instances the combustion processes themselves are stable–uncontrolled explosions or other intrinsic instabilities are not usually at work. The presence of an instability in a combustion chamber is established by observing either the gas pressure or accelerations of the enclosure. Excitation and sustenance of an oscillation occurs, [sic] because of coupling between the combustion processes and the gas dynamical motions, both of which alone may be stable. If the fluctuation of energy release responding to a pressure disturbance causes a further change of pressure in phase with the initial disturbance, then the result may be an instability. Thus one may view the behavior as that of a stable open-loop system (the gasdynamics) made unstable by a positive feedback loop, the gain being associated with the combustion processes.

Owing to the internal coupling between combustion processes and unsteady motions, an observer perceives an unstable motion as 'self-excited'. The amplitude of the motion grows out of the noise without the need for an external influence. Two fundamental reasons explain the prevalence of instabilities in combustion systems:

i.) An exceedingly small part of the available energy is sufficient to produce unacceptably large unsteady motions;

ii.) The processes tending to attenuate unsteady motions are weak, chiefly because combustion chambers are nearly closed.

These two characteristics are common to all combustion systems and imply that the possibility of instabilities occurring during development of a new device must be recognized and anticipated. Treating combustion instabilities is part of the necessary price to be paid for high performance chemical propulsion systems."

X. SOME METHODS OF SUPPRESSING COMBUSTION CHAMBER OSCILLATIONS

According to the introductory chapter of HARRJE & REARDON (1972) there are several design approaches for suppressing combustion instabilities in the case of liquid fueled rockets. Thus, if baffles (i.e. rigid surfaces parallel to the mean stream velocity) are placed on the injector plate of a liquid rocket combustion chamber, the resulting modification of the boundary conditions often suppresses the lower modes of lateral oscillations including the first transverse mode.

A second approach to suppressing oscillations involves the use of a liner in the combustion chamber to increase the portion of the energy of an incident acoustic wave that is absorbed during reflection. One standard concept for an acoustic liner amounts to an array of HELMHOLTZ resonators (cf. RAYLEIGH (1896, chapter XVI), INGARD (1953), BLACKMAN (1960), TANG & SIRIGNANO (1973), TANG. et al. (1973), and section 8.3 of HARRJE & REARDON (1973)*). These authors describe what appears to be a mature technology for the design of acoustic liners. As an early example

---

* The authors of section 8.3, titled "Acoustic liners", were: B.T. ZINN (Georgia Tech), T. TONON

of the successful use of an acoustic liner, a jet engine afterburner that had been prone to screech (apparently a combustion chamber oscillation in the transverse mode) was improved by installation of an acoustic liner of the above type (see, for example, the review by PUTNAM (1964, §H.1.2) of work done in the fifties by members of the Lewis Laboratory Staff).

A third method for the suppression of combustion oscillations is water injection. Although this method is not used in jet engine afterburners, it is a proven acoustic suppression technique, used at AEDC and elsewhere. MARBLE & CANDEL (1975) argued that, for evaporating droplets, the magnitude of the attenuation is related to the liquid volatility and the frequencies suppressed are related to the liquid mass fraction. The droplet radius may also play an important role in acoustic attenuation (MARBLE & CANDEL (ibid.)). Two additional references on acoustic attenuation are: MARBLE (1969) and MARBLE & WOOTEN (1970). Water injection appears to be a very viable method for the suppression of rumble in test cell C-1.

The references we have consulted support the view that combustion chamber oscillations are a common phenomenon that may well occur in a combustion chamber with smooth walls and no baffles. The task of predicting the successful suppression of combustion chamber oscillations by damping devices seems to be easier than is the task of predicting the spontaneous occurence of oscillations in the absence of those devices.

XI. CONCLUSIONS AND RECOMMENDATIONS

Our study of combustion instabilities this summer has led to the following conclusions:

C1. The history of combustion instabilities in development programs for jet and rocket engines indicates that a prototype device will be bedevilled by such instabilities unless means to suppress them are incorporated in its design ab initio.

C2. The discharge of flammable gases from a test engine into the air stream of the ASTF cell C-1 (in the configuration that has been proposed for testing of the NASP powerplant) raises a credible threat of destructive combustion instabilities in the region downstream of the sudden expansion.

C3. Hydrogen disposition systems based on the concept of afterburning do not, in themselves, alleviate the threat stated in C2, even if they achieve complete burning of the excess hydrogen. The threat will remain as long as acoustic waves in the chamber are weakly damped and there is a mechanism to couple acoustic oscillations with time dependent energy release by burning.

These conclusions lead to the following recommendations:

R1. In planning the program to develop the HDS system for NASP engine testing in the ASTF, allocate sufficient resources (and allow sufficient time) to come to grips with the problem of combustion instabilities.

R2. In carrying out the analysis for the HDS, plan from the start to incorporate at least one design feature either to reduce the excitation, or to increase the damping, of transverse acoustic waves and other acoustic waves that have historically bedevilled designs of rocket and jet engines.

REFERENCES

BAILEY, J.J. 1957 A Type of Flame-Excited Oscillation in a Tube. Journal of Applied Mechanics, 24, pp 233-239.

BLACKMAN, A.W. 1960 Effect of Nonlinear Losses on the Design of Absorbers for Combustion Chamber Instabilities. ARS Journal, 30, pp 1022-1028.

BLACKSHEAR, P.L. 1952 Driving Standing Waves by Heat Addition. NACA TN 2772.

BLACKSHEAR, P.L., RAYLE, W.D., & TOWER, L.K. 1955 Study of Screeching Combustion in a 6-inch Simulated Afterburner. NACA TN 3567

BLACKSHEAR, P.L. 1956 The Growth of Disturbances in a Flame-Generated Shear Region. Sixth Symposium (International) on Combustion, The Combustion Institute. pp 512-522.

BROWN, G.L. & ROSHKO, A. 1974 On Density Effects and Large Structure in Turbulent Mixing Layers. J. Fluid Mech., 64, pp 775-816.

CLAYTON, R.M., ROGERO, R.S., & SOTTER, J.G. 1968 An Experimental Description of Destructive Liquid Rocket Resonant Combustion. AIAA Journal, 6, pp 1252-1259.

CULICK, F.E.C. 1989 Combustion Instabilities in Liquid Fueled Propulsion Systems—an Overview. In Combustion Instabilities in Liquid Fuelled (sic) Propulsion Systems. Advisory Group for Aeronautical Research and Development, AGARD CP 450.

EMMONS, H.W. 1958 Flow Discontinuities Associated with Combustion. Fundamentals of Gas Dynamics. Volume III of High Speed Aerodynamics and Jet Propulsion. Princeton University Press.

HARRJE, D.T. & REARDON, F.H. (editors) 1972 Liquid Propellant Rocket Combustion Instability. National Aeronautics and Space Administration, NASA SP-194.

INGARD, U. 1953 On the Theory and Design of Helmholtz Resonators. The Journal of the Acoustical Society of America 25, pp 1037-1061.

KASKAN, W.E. & NOREEN, A.E. 1955 High Frequency Oscillations of a Flame Held by a Bluff Body. Transactions of the A.S.M.E., 77, pp 885-895.

LANGHORNE, P.J. 1988 Reheat Buzz: an Acoustically Coupled Combustion Instability. Part 1. Experiment. J. Fluid Mech.,193, pp 417-443.

MARBLE, F.E. 1969 Some Gasdynamic Problems in the Flow of Condensing Vapors. Astronautica Acta, 14, pp 585-614.

MARBLE, F.E. & CANDEL, S.M. 1975 Acoustic Attenuation in Fans and Ducts by Vaporization of Liquid Droplets. AIAA Journal, 13, pp 634-639.

MARBLE, F.E. & CANDEL, S.M. 1978 An Analytical Study of the Non-steady Behavior of Large Combustors. Seventeenth Symposium (international) on Combustion. The Combustion Institute. pp 761-769

MARBLE, F.E., MALLADI, M.V., & CANDEL, S.M. 1980 Analysis of Low-Frequency Disturbances in Afterburners. In Combustor Modelling, (AGARD Conference Proceeding CP-275)

MARBLE, F.E. & WOOTEN D.C. 1970 Sound Attenuation in a Condensing Vapor. The Physics of Fluids. 13. pp 2657-2664.

MASLEN. S.H., & MOORE, F.K. 1956 On Strong Transverse Waves Without Shocks in a Circular Cylinder. J. Aero. Sci., 23. pp 583-593. (See also MOORE, F.K. & MASLEN, S.H. Transverse Oscillations in a Cylindrical Combustion Chamber. NACA TN 3152 October 1954)

OLSON, W.T. 1960 Combustion Chamber Development. Section H of Design and Performance of Gas Turbine Powerplants. (Edited by W.R. HAWTHORNE and W.T. OLSON). High Speed Aerodynamics and Jet Propulsion, Volume XI, Princeton University Press.

POINSOT, T., LE CHATLIER, C., CANDEL, S.M., & ESPOSITO, E. 1986 Experimental Determination of the Reflection Coefficient of a Premixed Flame in a Duct. Journal of Sound and Vibration, 107, pp 265-278.

PUTNAM, A.A. & DENNIS, W.R. 1956 Some Stability Test on an Axially Symmetric Combustor. Sixth Symposium (International) on Combustion, The Combustion Institute. pp 439-500.

PUTNAM, A.A. 1964 Chapters F, G, and H: General Considerations of Autonomous Combustion Instablity, Experimental and Theoretical Studies of Combustion Oscillations, and Practical Considerations of Combustion Oscillations. In Nonsteady Flame Propagation (edited by G.H. MARKSTEIN). Advisory Group for Aeronautical Research and Development, AGARDograph No. 75, Pergamon Press, pp 183-314.

RAYLEIGH, J.W.S. 1896 The Theory of Sound. Second edition, Volume 2. Macmillan. (Reprinted by Dover Publications in 1945 and at various times since then).

RIJKE, P.J. 1859 Notice of a New Method of Causing the Vibration of the Air Contained in a Tube Open at Both Ends. Philosophical Magazine, Series 4, 17. pp 419-422.

ROGERS, D.E. & MARBLE, F.E. 1956 A Mechanism for High Frequency Oscillation in Ramjet Combustors and Afterburners. Jet Propulsion, 26. pp 456-462. (See also: A Mechanism for High Frequency Oscillation in Ramjet Combustors and Afterburners. Proceedings of the 1955 Heat Transfer and Fluid Mechanics Institute, UCLA, June 23-25, 1955)

ROSS, C.C. & DATNER, P.P. 1954 Combustion Instability in Liquid-Propellant Rocket Motors— a Survey. In Selected Combustion Problems, Fundamentals and Aeronautical Applications. Combustion Colloquium, Advisory Group for Aeronautical Research and Development, Butterworths Scientific Publications, pp 352-380.

SCURLOCK, A.C. 1948 Flame Stabilization and Propagation in High Velocity Gas Streams. Meteor Report No. 19, M.I.T. Fuels Research Laboratory.

STEPHENS, S.E., & JORDAN, J.L. 1988 Hydrogen-Rich Exhaust Gas Handling at AEDC. AIAA Paper 88-3019.

TANG, P.K. & SIRIGNANO, W.A. 1973 Theory of a Generalized Helmholtz Resonator. Journal of Sound and Vibration, 26, pp 247-262.

TANG, P.K., HARRJE, D.T., & SIRIGNANO, W.A. 1973 Experimental Verification of the Energy Dissipation Mechanism in Acoustic Dampers. Journal of Sound and Vibration, 26, pp 263-267.

TRUMAN, J.C. & NEWTON, R.T. 1955 Why do High Thrust Engines Screech? Aviation Age, 23, pp 136-144.

TSIEN, H.S. 1951 Influence of Flame Front on the Flow Field. Journal of Applied Mechanics, 18, pp 188-194.

WISNIOWSKY 1957 Screeching Combustion. Canadian Aeronautical Journal, 3, p 36.

1990 USAF-UES SUMMER FACULTY RESEARCH PROGRAM

GRADUATE STUDENT RESEARCH PROGRAM

Sponsored by the

AIR FORCE OFFICE OF SCIENTIFIC RESEARCH

Conducted by the

Universal Energy Systems, Inc.

FINAL REPORT

Laser-Induced Fluorescence of Nitric Oxide

Prepared by: Chun Fu Su, Ph.D.

Academic Rank: Associate Professor

Department and   Physics Department

University: Mississippi State University

Research Location: AEDC
                       Tullahoma TN   37389

USAF Researchers: M. Smith and D. Williams

Date: 22 August 90

Contract Number: F49620-88-C-0053

Laser-Induced Fluorescence of Nitric Oxide

by

Chun Fu Su

ABSTRACT

Preliminary computational models of the laser-induced
fluorescence spectrum of nitric oxide have been developed for two
different electronic transitions:

$B^2\Pi$ $(\nu'=7)-X^2\Pi$ $(\nu''=0)$ and $D^2\Sigma$ $(\nu'=0)-X^2\Pi$ $(\nu''=1)$.

Laser-induced fluorescence spectra of nitric oxide at room
temperature and at high temperature (up to 623°K) with various
pressures have been recorded. Comparison of the experimental
results with predicted spectra will be presented herein.

Acknowledgements

I wish to express my appreciation and gratitude to the Air Force System Command, the Air Force Office of Scientific Research, and the Arnold Engineering Development Center for sponsorship of this research. Sincere thanks are extended to the Universal Energy System for their concern and help in all aspects of this program. I greatly appreciated the collection of the observed LIF spectra by Mike Smith and the operation assistance of Billy McClure and Linwood Price. Finally, I deeply thank Donnie Williams, Section Head, for his support and encouragement of this project.

I. INTRODUCTION:

The NO molecule is a stable, free radical diatomic molecule. It is a key molecule in the chemistry of the upper atmosphere and a dangerous pollutant. It has also been detected in interstellar molecular clouds. In addition, this molecule is a natural constituent in combustion systems and arc-heated flow fields. No doubt, the NO molecule is important and interesting for both basic research and diagnostic applications.

The development and application of laser-induced fluorescence as a diagnostic technique has been underway for approximately twenty years. This experimental method can be used to make non-intrusive measurements in combustion systems and arc-heated flow fields. These measurements can be used to determine the species density and temperature as well as to assign the transitions. Assignments and determinations can best be obtained by measuring a component, such as O_2, N_2, NO, OH.., inside the combustion system or arc-heated flows.

Study of laser-induced fluorescence of nitric oxide was therefore decided on as the subject of the research project. Single photon excitation rather than multiphoton excitation was used. The ArF excimer laser system, Lambda Physik EMG 150 MSC, installed at AEDC was used for this project.

II. OBJECTS OF THE RESEARCH EFFORT:

For the overall research project, several individual tasks were done. In particular, they were:

1. Development of computational models of electronic transitions;

2. Observation of rotationally resolved laser excitation spectra at different temperatures and at various pressures;

3. Observation of vibrationally resolved laser excitation spectra at different temperatures and at various pressures.

III. RESULTS

1 Computational models

According to calculations of relative intensity, the $B^2\Pi$ $(\nu'=7)-X^2\Pi$ $(\nu''=0)$ transitions dominate at room temperature and the $D^2\Sigma$ $(\nu'=0)-X^2\Pi$ $(\nu''=1)$ transitions will be important at high temperature. The transitions of the former are $\Delta\Lambda = 0$ while those of the latter are $\Delta\Lambda = 1$. Therefore the calculations of energy levels, transition frequencies, and relative intensities for the two cases will be different. The rotational transitions of the former are P11, Q11, R11, P22, Q22, and R22, whereas those of the latter are P11, Q11, R11, P22, Q22, R22, S21, Q12, R21, P12, O12, and Q21. For line strengths, Honl-London factors(1) are used for the former and the formulas of Dieke and Crosswhite(2) are used for the latter. Consequently two different codes are needed for these models. They are PPTEST. and DPTEST. Both are stored at AEDC. The outputs of these

two codes were used to help make rotational assignments at room and high temperatures. The procedures for these two codes will be explained in detail in a mini-grant report.

2. Laser Excitation Spectra

a. **Rotationally resolved laser excitation spectrum at room temperature**

In order to understand the effect of pressure on the spectrum, various pressures were used. The laser was scanned from 192.8nm to 193.8nm to generate the electronic rotational transitions. A spectrometer set at 208nm and also a PMT with a band pass filter were used to record the rotational spectra. The spectra at pressures of 0.5 torr and 10.0 torr recorded by the PMT are shown in Figures 1 and 2, respectively. It is easy to find that the four groups of transitions were only slightly affected by pressure, and the transitions marked with (*) were significantly affected by pressure. The four groups are due to the $B^2\Pi$ $(\nu'=7)-X^2\Pi$ $(\nu''=0)$ transitions. The predicted spectrum with Voigt line shape is shown in Figure 3. Comparison of these three figures indicates that the observed and predicted spectra are consistent. The spectrum in the same region has been reported previously by Wodtke et al(3). For convenience, the predicted transitions with wavelengths are listed in Table I. The line

strengths of the Q-branch transitions are inversely
proportional to the rotational quantum numbers;
these lines, therefore, are weak in this wavelength
region.

The spectroscopic constants previously determined(4)
were used without any change for our models. They
are listed in Table II.

b. **Rotationally resolved laser excitation spectrum at
high temperature**

Mixtures of NO and N_2 were sent through an electri-
cally heated tube to the cell. The NO in the
mixture was approximately 5% or less. Various
temperatures were reached, and the rotationally
resolved laser excitation spectra at different
temperatures were recorded. The recorded spectrum
at the highest temperature 623°K is shown in
Figure 4.

Comparing Figure 4 with Figures 1 and 2, indicates
that the four groups aforementioned were slightly
changed whereas those with mark (*) were changed
more. In order to understand more about the
observed spectra, the predicted spectra with Voigt
line shape were calculated for the $D^2\Sigma$ $(\nu'=0)$-$X^2\Pi$
$(\nu''=1)$ transition. According to the predicted
spectrum shown in Figure 5, most of the transitions
with mark (*) shown in Figure 2 were due to this
electronic transition. For this electronic

transition, in addition to the P11, Q11, R11, P22, Q22, and R22 transitions reported by Andresen et al(5), the P12, Q12, Q21, S21, R21, and O12 transitions are also important s indicated by Scheingraber and Vidal(6). Th assumed spectroscopic constants for these two electronic states are listed in Table II, and the predicted transitions with wavelengths are listed in Table III.

c. **Vibrationally resolved fluorescence transitions at room temperature**

For fluorescence spectra, besides the rotational transitions, the vibrational transitions between two electronic states are also important. In order to understand the effects of pressure and temperature on the vibrational transitions, va.ious pressures and temperatures were used in this research. The laser wavelength was fixed at any of the observed lines listed in Table I. The spectrometer was scanned slowly from the laser wavelength to 330nm to record the vibrational transitions. A rotational transition at the fixed input laser wavelength was excited, producing the vibrational fluorescence spectrum. The vibrational spectra at pressures of 1.0 torr, and 10.0 torr at laser wavelength set at 193.30nm are shown in Figures 6 and 7, respectively. Of the transitions listed in Table I, one or more of

four transitions R_{11} (29 29½ → 30 30½),
P_{11} (26 26½ → 25 25½), K_{22} (28 27½ → 29 28½), and
P_{22} (25 24½ → 24 23½) were excited. The
vibrational fluorescence spectrum shown in Figure 6
is consistent with the previously reported one(7);
however, some expected vibrational transitions are
still weak in Figure 6 due to pressure effect. The
high pressure vibrational spectrum shown in Figure 7
shows more vibrational transitions and stronger
intensities. This is not surprising, because
increasing the pressure increases the molecular
density, and hence the intensities.

d. **Vibrationally resolved fluorescence transitions at**
high temperature
The process used to heat the cell is the same as
mentioned previously. The vibrational laser induced
fluorescence spectra at different temperatures were
recorded. The one at 623°K with laser wavelength
fixed at 193.30nm is shown in Figure 8. It is
obvious that the spectrum has even more transitions
and even stronger intensities than that at room
temperature. Because the rotational quantum numbers
shown in Table I are moderately high, the population
in these rotational energy levels should not be
large at room temperature. When the temperature is
increased, however, the population in these high
energy levels will be increased. Moreover, the

17-9

population in the rotational energy levels of the other vibrational state ($\nu''=1$) would be increased at high temperature. Consequently the transitions intensities will be increased.

IV. RECOMMENDATIONS:

Comparison of the experimental results recently obtained at AEDC with published reports (3,5,7) shows that the laser system works properly. Several experimental projects can be finished at AEDC in the near future using this laser system.

1. **Fluorescence spectra of rotational and vibrational transitions at higher temperatures.** So that the basic experimental results can be extended to temperature regions of interest to DoD. Those results will provide useful information for basic scientific research.

2. **Fluorescence spectra of arc-heated flows at AEDC.** Determination of temperature and molecular density is of importance for the mission of AEDC. Fluorescence spectra can be used for determination of temperature and molecular density. When finished, these experimental results will provide useful information for both basic research and diagnostic applications.

3. **Besides nitric oxide, the laser system can be used to investigate the spectra of other molecules, such as OH, that AEDC is interested in.**

REFERENCES

1. Herzberg, G., "Spectra of Diatomic Molecules," Van Nostrand, NY, 1950.

2. Dieke, C.H. and Crosswhite, H.M., "The Ultraviolet Bands of OH," J. Quant. Spectrosc. Radiation Transfer, 2, 97-199 (1962).

3. Wodtke, A.M., Huwel, L., Schluter, H., Meijer, G., Andresen, P., and Voges, H., "High-Sensitivity Detection of NO in a Flame Using a Tunable ArF Laser," Opt. Lett. 13, 910-912 (1988).

4. Engleman, R. Jr. and Rouse P.E., "The β and γ Bands of Nitric Oxide Observed during the Flash Photolysis of Nitrosyl Chloride," J. Mol. Spectrosc., 37, 240-251 (1971).

5. Andresen, P., Meijer, G., Schluter, H., Voges, H., Koch, A., Hentschel, W., Oppermann, W., and Rothe, E., "Fluorescence Image inside an Internal Combustion Engine Using Tunable Excimer Lasers," Appl. Opt., 29, 2392-2404 (1990).

6. Scheingraber, H. and Vidal, C.R., "Fluorescence Spectroscopy and Franck-Condon-Factor Measurements of Low-Lying NO Rydberg State," J. Opt. Soc. Am. B 2, 343-354 (1985).

7. Shibuya, K. and Stuhl, F., "Single Vibronic Emission from NO $B^2\Pi$ (ν'=7) and O_2 $B^2\Sigma_u^{-1}$ (ν'=4) Excited by 193 nm ArF Laser," J. Chem. Phys., 76, 1184-1186 (1982).

8. Huber, K.P. and Herzberg, G., "Molecular Spectra Molecular Structure IV: Constants of Diatomic Molecules," Van Nostrand, NY, 1979.
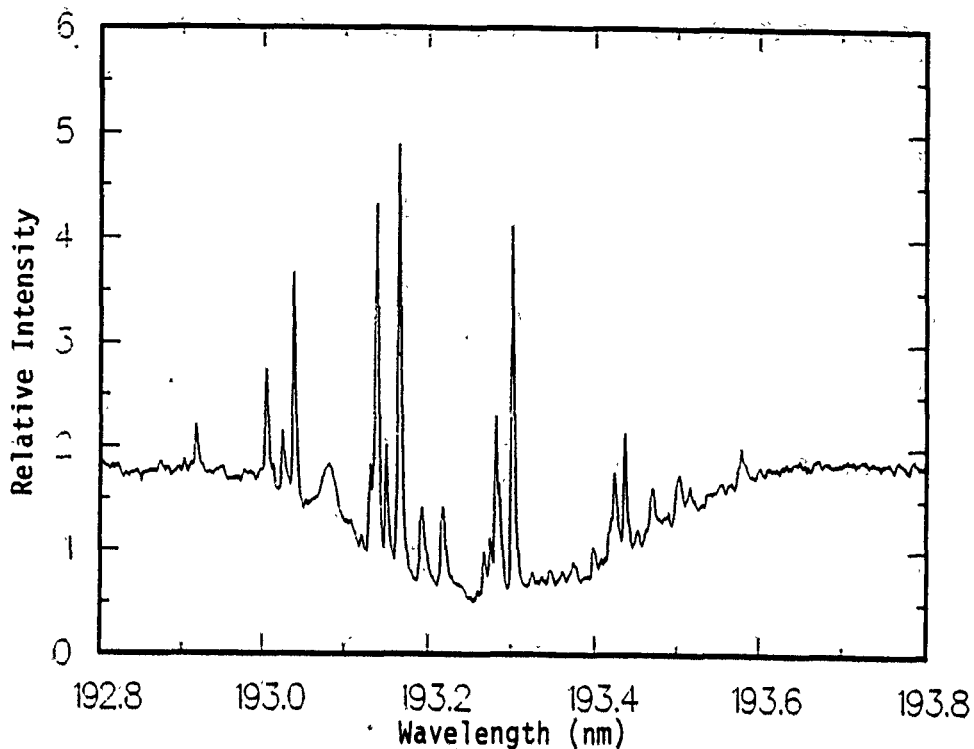
Figure 1. Observed rotationally resolved laser excitation spectrum of NO at room temperature and a pressure of 0.5 torr.
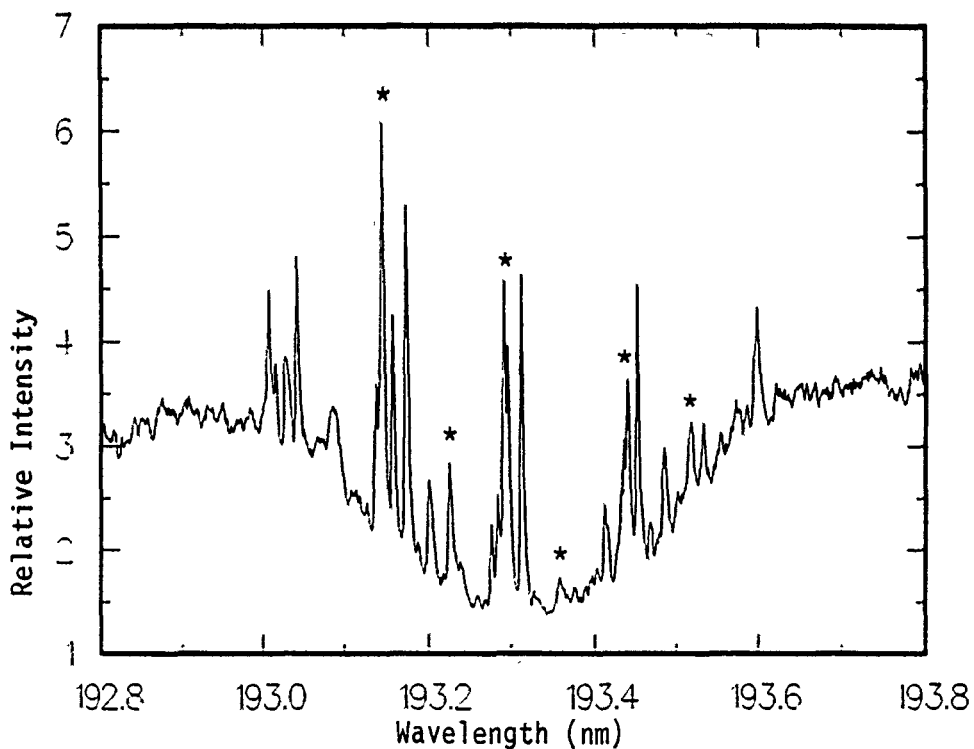
Figure 2. Observed rotationally resolved laser excitation spectrum of NO at room temperature and a pressure of 10.0 torr.
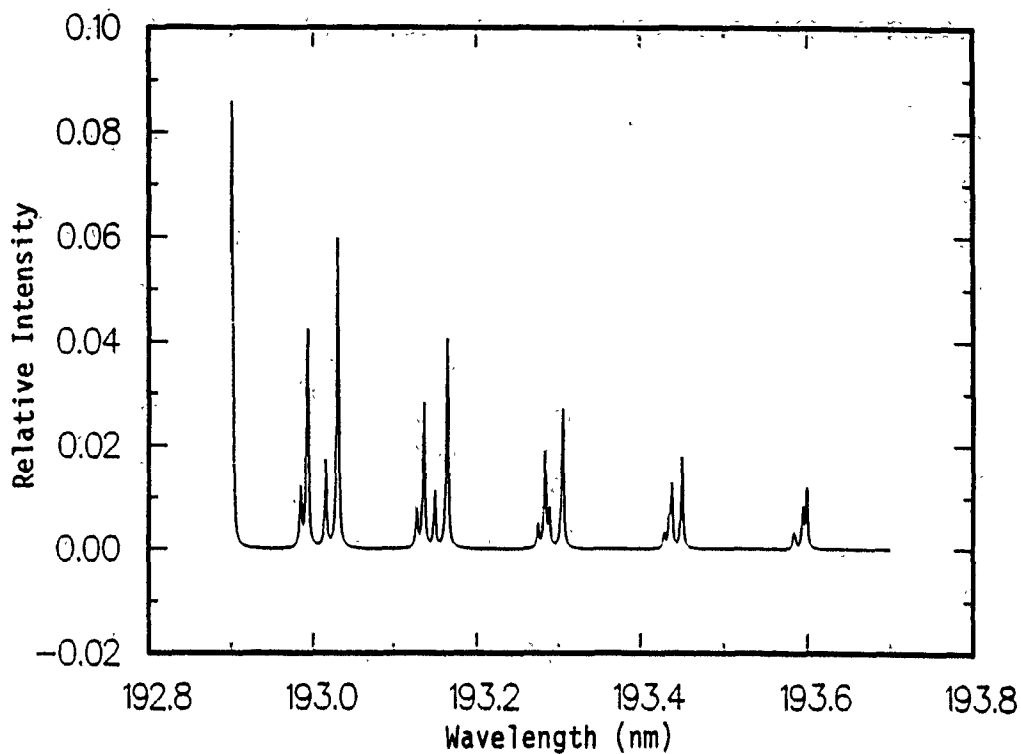
Figure 3. Predicted rotational spectrum of NO at room temperature for the $B^2\Pi(v'=7) - X^2\Pi(v''=0)$ transition.
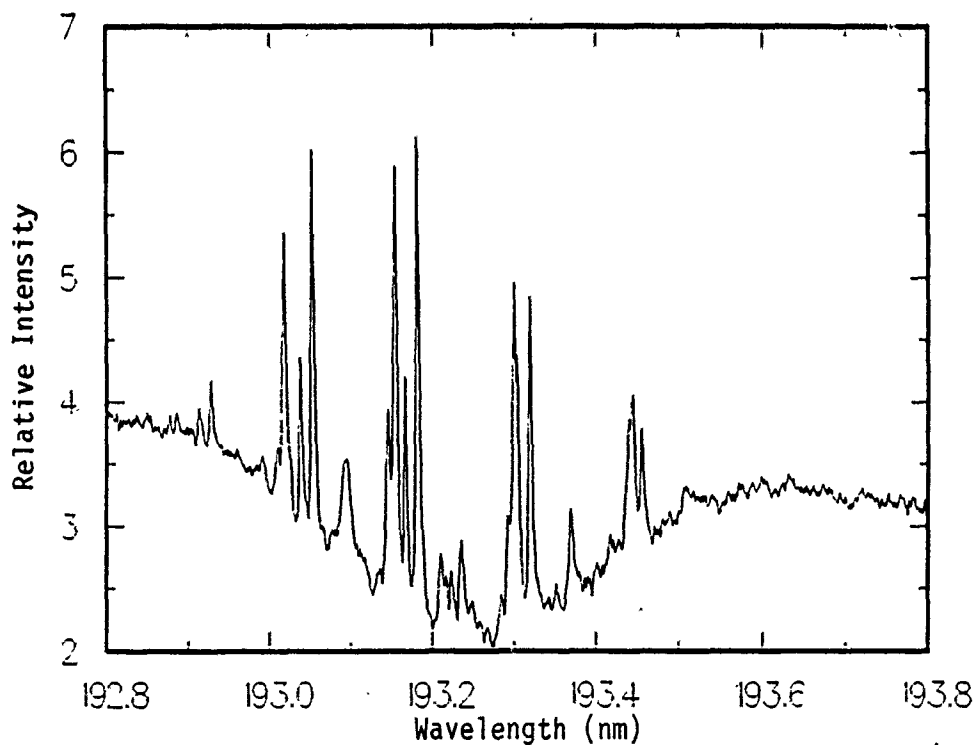
Figure 4. Observed rotationally resolved laser excitation of NO at temperature of 623°K.
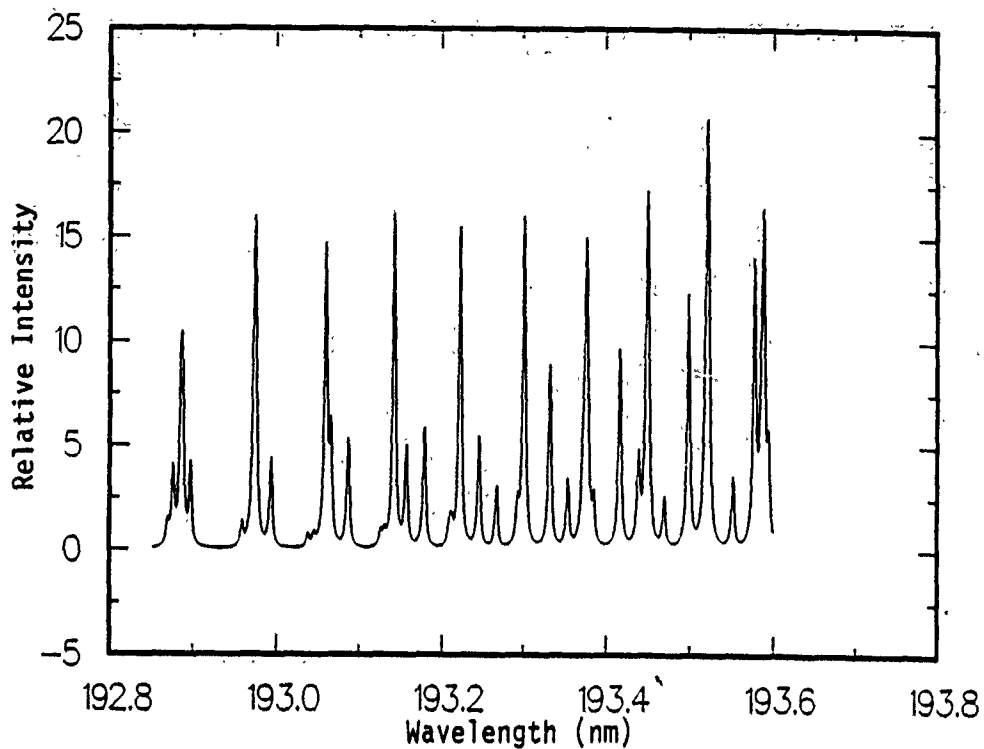
Figure 5. Predicted rotational spectrum of NO at 1200°K for the $D^2\Sigma(v'=0) - X^2\Pi(v''=1)$ transition.
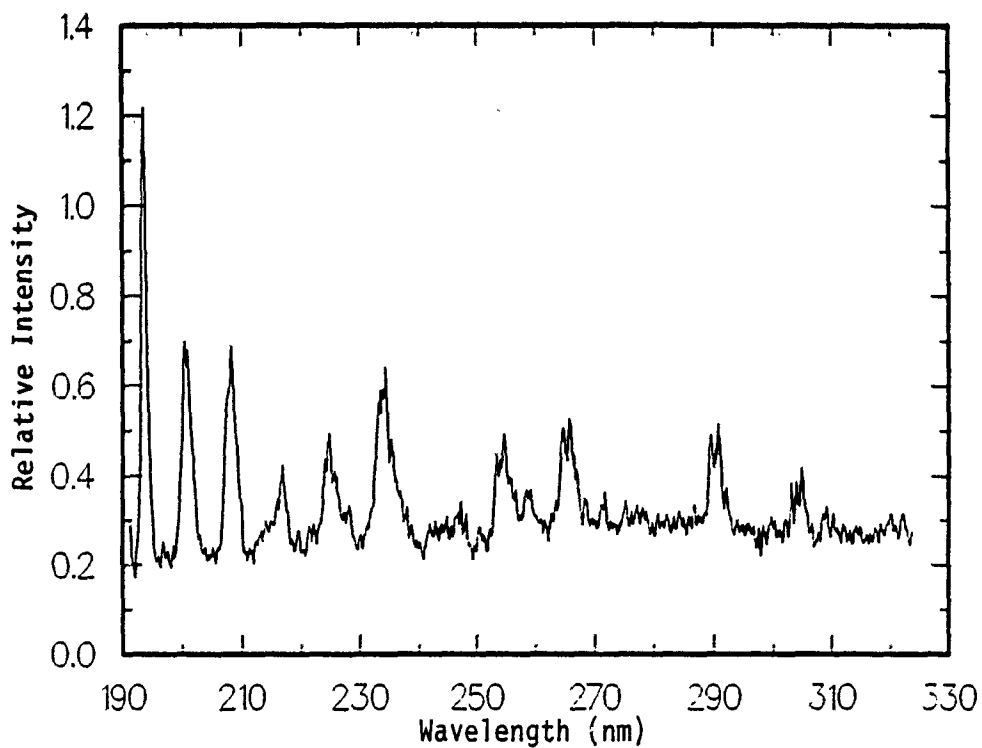
Figure 6. Observed vibrationally resolved fluorescence spectrum of NO at room temperature and a pressure of 1.0 torr with $\lambda = 193.30$nm.
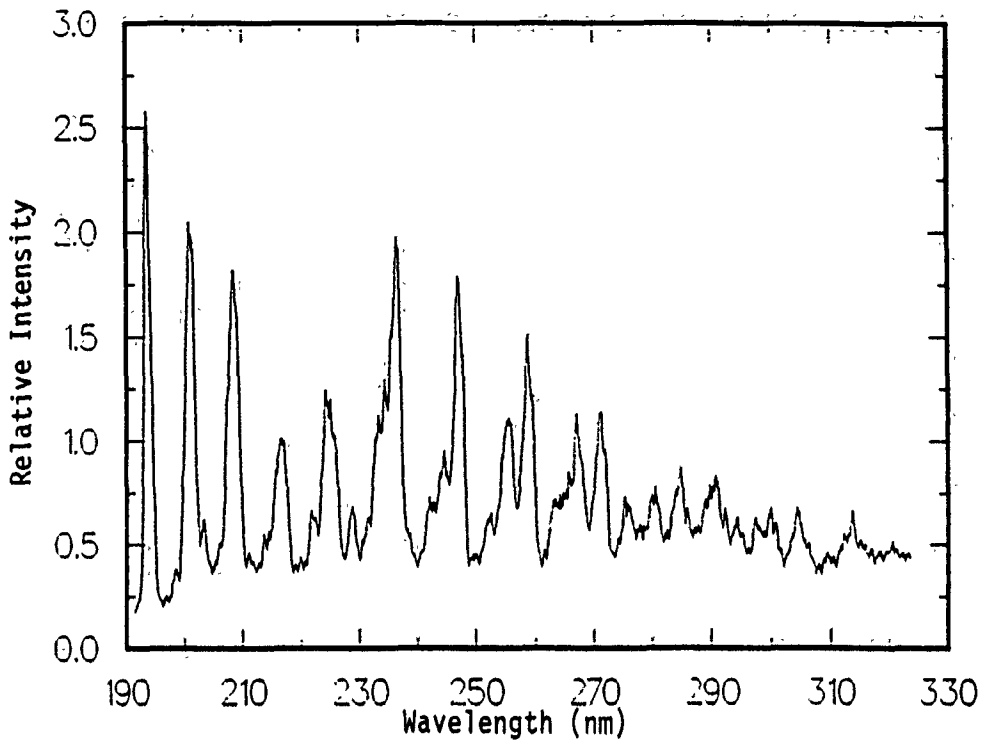
Figure 7.   Observed vibrationally resolved fluorescence
spectrum of NO at room temperature and a
pressure of 10.0 torr with λ = 193.30nm.
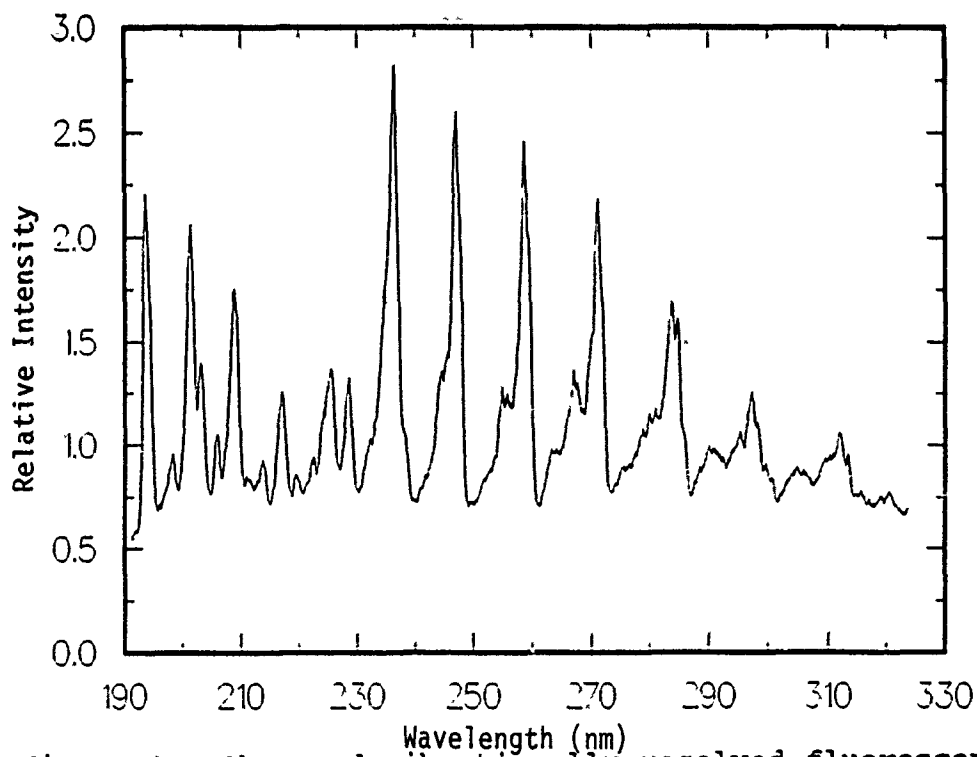
Figure 8.   Observed vibrationally resolved fluorescence
spectrum of NO at temperature of $623°K$ and
λ = 193.30nm.

Table I. Predicted Rotational Spectrum for the $B^2\Pi$ ($\nu' = 7$)–$X^2\Pi$ ($\nu'' = 0$) transitions of Nitric Oxide between 192.8 and 193.8 nm.

lower rotational energy level	wavelength (nm)
R11(29 29 1/2)	192.985
P11(26 26 1/2)	192.993
R22(28 27 1/2)	193.015
P22(25 24 1/2)	193.031
R11(30 30 1/2)	193.128
P11(27 27 1/2)	193.136
R22(29 28 1/2)	193.151
P22(26 25 1/2)	193.165
R11(31 31 1/2)	193.273
P22(28 28 1/2)	193.284
R22(30 29 1/2)	193.289
P22(27 26 1/2)	193.305
R11(32 32 1/2)	193.428
R22(31 30 1/2)	193.434
P11(29 29 1/2)	193.437
P22(28 27 1/2)	193.451
R22(32 31 1/2)	193.584
R11(33 33 1/2)	193.586
P11(30 30 1/2)	193.595
P11(30 30 1/2)	193.601

Table II. Assumed Spectroscopic Constants of Nitric Oxide.
Units are in cm^{-1}.

$B^2\Pi(\nu' = 7)$ state
  Te: 45868.53
  We: 1037.45
  WeXe: 7.47
  WeYe: 0.073
  Be: 1.031
  De: 4.9×10^{-6}

$D^2\Sigma(\nu' = 0)$ state
  Te: 53030.00
  We: 2323.90
  WeXe: 22.90
  WeYe: 0
  Be: 1.987
  De: 5.8×10^{-6}

$X^2\Pi(\nu'' = 0)$ state
  Te: 123.16
  We: 1904.4
  WeXe: 14.19
  WeYe: 0.024
  Be: 1.696
  De: 5.3×10^{-6}

$X^2\Pi(\nu'' = 1)$ state
  Te: 122.95
  We: 1904.4
  WeXe: 14.19
  WeYe: 0.024
  Be: 1.686
  De: 5.3×10^{-6}

Table III. Predicted Rotational Spectrum for the $D^2\Sigma(\nu' = 0)-X^2\Pi(\nu'' = 1)$ transitions of Nitric Oxide between 192.8 and 193.8 nm.

lower rotational energy level	wavelength (nm)
Q11(35 35 1/2)+Q21(35 35 1/2)	193.142
Q22(37 36 1/2)+Q12(37 36 1/2)	193.157
R22(31 30 1/2)	193.179
P22(43 42 1/2)+P12(43 42 1/2)	193.209
P11(41 41 1/2)	193.211
S21(23 23 1/2)	193.213
R11(28 28 1/2)+R21(28 28 1/2)	193.222
Q11(34 34 1/2)+Q21(34 34 1/2)	193.223
Q22(36 35 1/2)+Q12(36 35 1/2)	193.246
R22(30 29 1/2)	193.268
P11(40 40 1/2)	193.293
S21(22 22 1/2)	193.293
P22(42 41 1/2)+P12(42 41 1/2)	193.298
R11(27 27 1/2)+R21(27 27 1/2)	193.300
Q11(33 33 1/2)+Q21(33 33 1/2)	193.301
Q22(35 34 1/2)+Q12(35 34 1/2)	193.332
R22(29 28 1/2)	193.354
S21(21 21 1/2)	193.370
P11(39 39 1/2)	193.372
R11(26 26 1/2)+R21(26 26 1/2)	193.375
Q11(32 32 1/2)+Q21(32 32 1/2)	193.378
P22(41 40 1/2)+P12(41 40 1/2)	193.385
Q22(34 33 1/2)+Q12(34 33 1/2)	193.417
R22(28 27 1/2)	193.439
S21(20 20 1/2)	193.445
R11(25 25 1/2)+R21(25 25 1/2)	193.447
P11(38 38 1/2)	193.449
Q11(31 31 1/2)+Q21(31 31 1/2)	193.450
P22(40 39 1/2)+P12(40 39 1/2)	193.469
Q22(33 32 1/2)+Q12(33 32 1/2)	193.498
R11(24 24 1/2)+R21(24 24 1/2)	193.517
S21(19 19 1/2)	193.518
Q11(30 30 1/2)+Q21(30 30 1/2)	193.520
R22(27 26 1/2)	193.521
P11(37 37 1/2)	193.523

17-18

1990 USAF-UES SUMMER FACULTY RESEARCH PROGRAM/
GRADUATE STUDENT RESEARCH PROGRAM

Sponsored by the

AIR FORCE OFFICE OF SCIENTIFIC RESEARCH

Conducted by the

Universal Energy Systems, Inc.

<u>FINAL REPORT</u>

<u>An Algorithm for Defining the Shape
of a Plume Exhausting from a Rectangular Nozzle</u>

Prepared by: Kevin W. Whitaker, Ph.D.

Academic Rank: Assistant Professor

Department and   Aerospace Engineering

 University: The University of Alabama

Research Location: AEDC/DOT
                      Arnold Engineering Development Center
                      Arnold Air Force Base, TN   37389

USAF Researcher: Brian M. Wettlaufer, Sverdrup/AEDC Group

Date: August 10, 1990

Contract No.:   F49620-88-C-0053

An Algorithm for Defining the Shape
of a Plume Exhausting from a Rectangular Nozzle

by

Kevin W. Whitaker

ABSTRACT

Investigations into facility modifications required to
support future propulsion system testing are currently being
conducted at the Arnold Engineering Development Center.
These investigations have identified a need for tools which
will assist in the analysis of facility components. With
regards to new diffuser designs, there is a need to describe
the shape of a plume issuing from a rectangular nozzle. In
this report a simple modeling technique is derived for
rectangular nozzle plumes under static conditions. The
model is based on detailed flow fields of round nozzle
plumes. Subsequently, an attempt is made to extend the
method to cover nonzero flight speeds at which the external
stream affects the mixing rates and the shape of the plume.
Detailed construction of a plume model for rectangular
nozzles is described in terms of scaling an axisymmetric
plume, application of conservation of mass, and a spreading
procedure to simulate static and nonzero flight speeds. It
has been shown that a single calculation of an axisymmetric
plume can provide the basic solution for the plume issuing
from a rectangular nozzle. Further work needs to be
conducted on generalizing the algorithm and developing a
computer program utilizing the algorithm.

ACKNOWLEDGEMENTS

I would like to thank the U. S. Air Force along with Universal Energy Systems, Inc., for sponsoring the Summer Faculty Research Program. I have found the program to be not only beneficial but extremely enjoyable. Without question the program has played an important role in my professional development.

Sincere appreciation is due Brian M. Wettlaufer whose interest in the Summer Faculty Research Program provided me with what turned out to be a very interesting and timely research project. I also appreciated the valuable assistance provided by Carlos Tirres throughout the course of the program.

I. INTRODUCTION

Currently, studies are under way at the Arnold
Engineering Development Center (AEDC) to determine the test
facility modifications required to support future propulsion
system testing. Motivation for these studies is the desire
to conduct experiments in high supersonic flight regimes on
components such as inlets, exhaust nozzles, combustors, or
even entire engines. The studies are addressing many
modification concerns and, due to the complexity involved,
it is anticipated that some degree of subscale facility
modeling will be required prior to specifying and initiating
full-scale facility modifications.

One area of concern is the design of a diffuser section
appropriate for the testing of high speed propulsion
devices. The diffuser is a critical component in the test
facility and thus will require a concerted design effort.
The diffuser must capture the exhaust flow to protect the
test cell walls but do it in such a way so as to prevent
recirculation. Recirculating exhaust flow could allow
unburned fuel and oxidizer to accumulate in the test cell
resulting in a potentially explosive situation. To insure a
wide range of testing conditions, the diffuser must also
provide some degree of pumping. This pumping will dictate
the test cell pressure and, due to facility layout, must be
controlled from downstream. The downstream control
requirement imposes an additional condition that the
diffuser cannot choke.

Since a diffuser must capture the exhaust plume in a
manner described above, certain parameters of the plume flow
must be known for the design process. The spreading rate
and shape of the plume at any downstream location are two

important parameters. Typically, for round exhaust nozzles
these parameters can be determined from readily available,
empirically derived formulae. However, the exhaust nozzle
geometries of future propulsion systems are very likely to
be non-traditional, perhaps having rectangular, triangular,
or trapezoidal exit planes. Simple shape prediction
formulae do not exist for these nozzle geometries like they
do for axisymmetric geometries.

In order to describe the flow fields produced by these
potentially new nozzle geometries, high-level computational
fluid dynamics (CFD) analyses must be performed. This
typically dictates a need for a considerable amount of
super-computer time. However, at this point in the facility
modification studies it is neither desirous nor prudent to
expend large amounts of money on such super-computer
simulations. This is especially true in conjunction with
the design of any subscale testing facility. Thus a need
has developed for first-cut plume analysis tools which can
be used in the preliminary stages of diffuser design.

This need for a simple tool to define the shape of a
non-axisymmetric plume resulted in the author being selected
for the 1990 U. S. Air Force Summer Faculty Research
Program. The author's professional interests are in
compressible aerodynamics and experimental techniques. He
has had industrial experience with exhaust nozzle design and
his academic research has been oriented towards developing
user-friendly design tools for propulsion systems.

II. OBJECTIVE OF THE RESEARCH EFFORT

The objective of this research effort was to develop an algorithm capable of describing the shape of a plume issuing from a rectangular nozzle. The motivation behind this effort was the urgent need for design tools which can be used in the preliminary phases of test facility modifications. It appears that prior to initiating full-scale modifications, a subscale facility will be constructed at AEDC to perform preliminary tests and tools are needed to support its construction. Specifically, this research effort addressed the need for tools to assist in the design of a subscale facility diffuser.

Any tools developed to support the construction of a subscale facility must satisfy some specific requirements. The design tools must provide quick solutions with reasonable accuracy, be easy implemented, and possess the capability to handle a wide range of flow field geometries. To avoid the costs associated with super-computer simulations, it was decided to make sure any tools developed would be amenable to implementation on a personal computer.

III. ALGORITHM DEVELOPMENT

Two facts can be stated in regards to plumes. First, characteristics of plumes issuing from round nozzles are well documented. The second fact is that plumes from non-axisymmetric nozzles are not well documented. Therefore, the approach taken for this research effort was to derive a transformation to map a non-axisymmetric plume into an axisymmetric plume. This transformation could then be incorporated into an algorithm which would allow existing plume information to be used to describe non-axisymmetric plumes.

Paralleling the infrared plume signature work performed by Chu and Der [1], a procedure to accomplish this objective was developed for the summer work effort. The first step was to derive a transformation algorithm and validate it with a simple geometry. The simple geometry selected was a rectangular nozzle with no external flow and will be referred to as Case #1. The second step was to extend the algorithm developed for Case #1 by including external flow. The third step was to investigate the feasibility of generalizing this algorithm further, incorporating an inclined exit plane or unsymmetric external flow - both of which are possible in future propulsion systems.

• CASE #1

Extensive experimental investigations have verified that the plume issuing from a rectangular nozzle becomes axisymmetric at some point downstream from the nozzle exit. In fact, it becomes similar to a plume issuing from a round nozzle with the same exit momentum. Beyond this point, the plume can be treated as axisymmetric and available,

empirically-based shape description formulae apply. It is in the region between the nozzle exit and the location where the plume becomes axisymmetric that a new shape description algorithm must be derived.

Consistent with this phenomenon, a plume model was constructed for a rectangular nozzle and is illustrated in Figure 1. The rectangular nozzle plume was synthesized from two semicircular sides attached to a rectangular section in between. Justification for this was obtained from experimental observations of rectangular nozzle plumes at static conditions [2-6]. In the model the width of the rectangular section decreases and the diameter of the semicircular sections increase as the plume develops axially so that the transformation to an axisymmetric plume is correctly reproduced.

The problem at hand is to determine the flow properties in the rectangular and semicircular sections of the plume model. Plenty of data exist on round plumes so it is advantageous for the algorithm to make use of this information. It was hypothesized that the flow properties in the semicircular sections could be obtained from a round nozzle plume if they were properly adjusted through a transformation, or scaling factor, that allows for the difference in mixing rates between the axisymmetric and non-axisymmetric plumes. If the flow properties in the rectangular midsection of the plume are assumed to be constant along straight lines connecting the two sides, then the width of the midsection could then be determined from conservation of mass. Thus, the three essential elements of the shape description algorithm which must be derived are the distance at which the plume becomes axisymmetric, the scaling factor as a function of the downstream distance, and
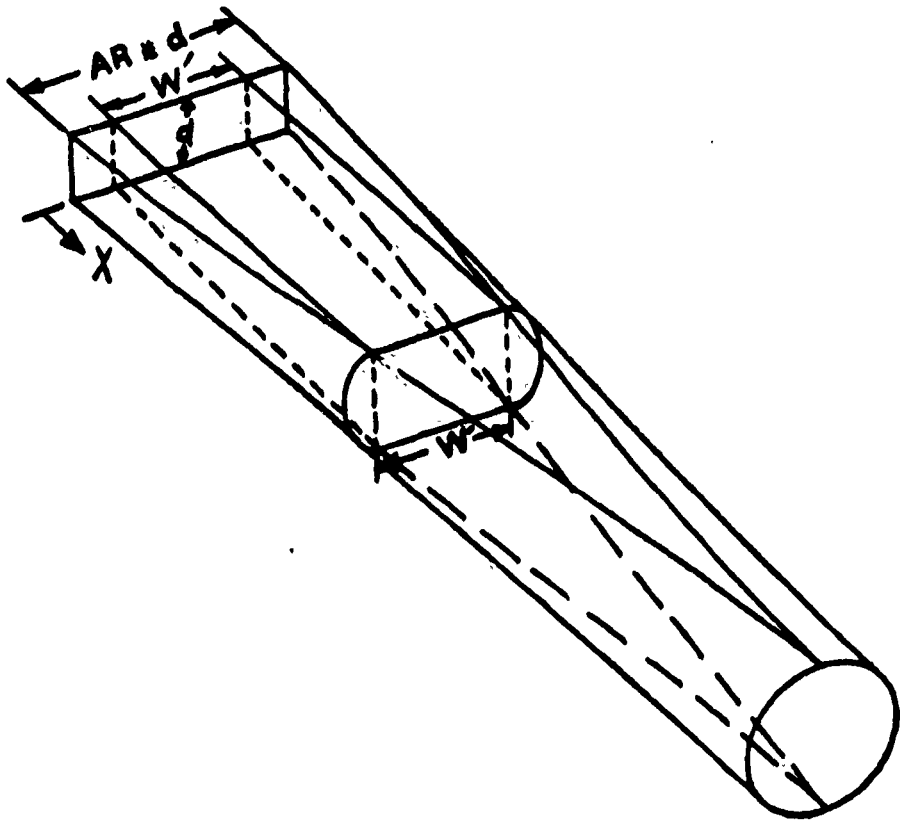
Figure 1.   Rectangular Nozzle Without External Flow

the width of the rectangular midsection. The derivation of each of these will be subsequently discussed.

It must be noted that due to the simplicity of the plume model it does not apply at the nozzle exit unless the exit has truly semicircular sides. This seemingly would result in a discontinuity at the exit. However, two approaches may be taken to solve this problem. The first is to alter the exit geometry to fit the model, keeping the same exit area. This is obviously not desirable since the physics of the problem are altered from the outset. The second approach is to compute the first station slightly downstream of the exit and then interpolate back to the nozzle. This approach is very easy and has found to be more than adequate.

As mention above, the plume from a rectangular nozzle becomes axisymmetric at some point downstream of the exit. A simple formula for determining this location can be derived utilizing an inductive approach. Consider a nozzle of height "d" and width "w". Let the width be fixed and let the height vary through $0 < d \le w$ to change the aspect ratio (AR $= w/d$). It seems reasonable to assume that the location where the plume becomes axisymmetric (designated X_a) varies with the nozzle height. For example, as the height approaches the width (driving the aspect ratio to unity) the location moves towards the nozzle exit. A simple expression for X_a is:

$$X_a = CF \qquad (1)$$

where C is a constant and F is a function of the rectangular nozzle height and width. Such a function should decrease monotonically with increasing nozzle height and must also be bounded. The simplest nondimensional expression for F is

w/(w+d) which decreases from unity to one-half as d increases from 0 to w. Thus a simple formula for X_a, after normalizing it with respect to the nozzle width, is:

$$X_a/w = C(w/(w+d)) \qquad (2)$$

or in terms of aspect ratio:

$$X_a/d = C(AR^2/(1+AR)) \qquad (3)$$

Based on experimental data presented in References 2 and 5, the constant C is best set to 12. Notice that the constant C in Equation (3) is the only empirically determined quantity for this modeling technique. It is also interesting to note that from another point of view, Equation (3) can be obtained by assuming that the distance at which the non-axisymmetric plume becomes axisymmetric is linearly proportional to the product of the nozzle's hydraulic diameter and aspect ratio.

The next step is to derive the scaling factor (transformation) which will allow the semicircular side sections to be described using a basic round nozzle plume. For convenience the basic plume to be used will have an exit diameter equal to the height of the rectangular nozzle (d). Flow properties of the basic plume can be obtained either experimentally or computationally using formulae found in Abramovich [7] or Pai [8]. The scaling factor can be defined as the multiplier which, when applied to the radial and axial coordinates of a data point on the basic round nozzle plume, gives the corresponding location on a non-axisymmetric plume.

To derive the scaling factor, a specific plume location

will be considered and then the process will be generalized. For simplicity, the location where the non-axisymmetric plume becomes axisymmetric will be selected because it is at this point where only the semicircular sections are involved (the rectangular midsection has vanished). At X_a given by Equation (3), the plume from a rectangular nozzle becomes round and is identical to the plume from a "phantom" round nozzle of unknown diameter but possessing the same exit momentum. Assuming the same average momentum per unit area, the phantom round nozzle must have the same exit area as the rectangular nozzle and thus an exit diameter (D) of:

$$D = Kd \qquad (4)$$

where $K = 2(AR/\pi)^{0.5}$. But since the basic round nozzle plume has a diameter of d, the phantom round nozzle plume can simply be obtained from the basic plume through similarity, i. e., multiplying the radial and axial coordinates of each data point of the basic plume by a factor of K.

However, what really needs to be determined is the diameter of the rectangular nozzle plume semicircular sections at X_a. Since the rectangular nozzle plume and phantom round nozzle plume become the same at X_a, all that is required is the diameter of the phantom plume at X_a. This is obtained from the basic plume. By taking X_a and dividing it by K, the corresponding axial location on the basic plume is obtained. The diameter of the basic plume at this axial location is then multiplied by K to obtain the diameter of the phantom plume and hence the diameter of the rectangular nozzle plume semicircular sections. This same scaling factor can also be used to determine flow properties of the non-axisymmetric plume knowing the flow properties of

the basic plume.

What has been derived at this point is only the value of the scaling factor at X_a. The procedure must be extended now to cover the entire range between the nozzle exit and X_a. In other words, the scaling factor as a function of the axial location, X, is needed. This can be determined using experimental data (References 2-6) and known boundary conditions.

The rate of change of the scaling factor with respect to the axial distance must vanish at X_a. This is because after X_a the plume is axisymmetric and the scaling factor is constant. At the nozzle exit the scaling factor is unity and its rate of change depends on the initial behavior of the plume. The initial rate of change of the scaling factor at the nozzle exit was approximated by the tangent of the nozzle wall angle, which was assumed to be zero. The scaling factor is derived from a cubic spline passing through the two end points and the two end slopes. The generalized scaling factor G as a function of the axial distance X is:

$$G = 1 + [3(X/X_a)^2 - 2(X/X_a)^3](K-1) \qquad (5)$$

All four conditions which define the spline are based on geometric and physical considerations of the flow. The only empirical quantity, X_a, is adjusted through the constant C. This approach lets the basic round nozzle plume take care of the turbulent mixing while using the scaling factor to describe the inviscid plume development. The physical meaning of the scaling factor is that at some downstream station X with scaling factor G, the semicircular side sections of the non-axisymmetric plume from a nozzle of

height d can be viewed as having the diameter of a cross section of an axisymmetric plume issuing from a phantom round nozzle with exit diameter Gd. As discussed, this is obviously true at X_a.

With a method derived to obtain the diameter of the semicircular side sections, a technique to determine the width of the rectangular midsection is now required. This will be accomplished using the conservation of mass principle. Assume that the portion of the plume in the midsection expands truly two-dimensionally, i. e., the mass inside the dividing stream surface per unit width of midsection remains constant from station to station although the height of the plume increases. Meanwhile, mass is continuously being transferred from the two edges of the midsection to the semicircular sides as the width of the midsection gradually deceases to zero. At X_a all the mass has been transferred to the two semicircular sections.

Now consider the width of the rectangular section (W') at a certain station where the scaling factor is G. It has been shown that the diameter of the semicircular side sections is similar to an axisymmetric plume originating from a phantom round nozzle with exit diameter Gd. Assuming that the mass flow per unit area in the exit planes of the phantom and rectangular nozzles is uniformly distributed, the mass flows originating from these nozzles are then proportional to their exit areas. It follows then that the mass flow in the two semicircular sections is proportional to the exit area of the phantom round nozzle and that the total mass flow is proportional to the exit area of the rectangular nozzle. Since the total mass flow is conserved within the dividing stream surface of the plume, the mass flow that still remains in the midsection is proportional to

$(AR-\pi G^2/4)d^2$. Since the midsection expands two dimensionally, this mass flow is the same as the mass flow contained in a segment of width W'd. Equating these two expressions and solving for the width of the rectangular midsection:

$$W'/d = AR - \pi G^2/4 \qquad \qquad (6)$$

This now completes the algorithm to define the shape of a plume issuing from a rectangular nozzle with no external flow. Equations (3), (5), and (6), along with a basic plume having a diameter equal to the height of the rectangular nozzle, form a closed set of equations.

● CASE #2

The next case to be considered involves a rectangular nozzle with external flow. This was selected to be representative of a plume issuing from a nozzle at a nonzero flight speed. An example of the geometry considered is shown in Figure 2. It is assumed in this discussion that the core flow is at a higher velocity than the surrounding external flow. This assumption makes sense intuitively because the magnitude of engine exhaust velocity is always larger than the magnitude of the vehicle velocity.

Physically, once the flows pass the exit of the nozzle the lower-velocity surrounding fluid will mix with the higher-velocity core flow. The end result will be a lower average momentum at any given cross section (at least compared to the situation with no external flow). If an average momentum is assumed over any cross section, no distinction will exist between the two flows. Thus, the procedure outlined in Case #1 will apply. The only
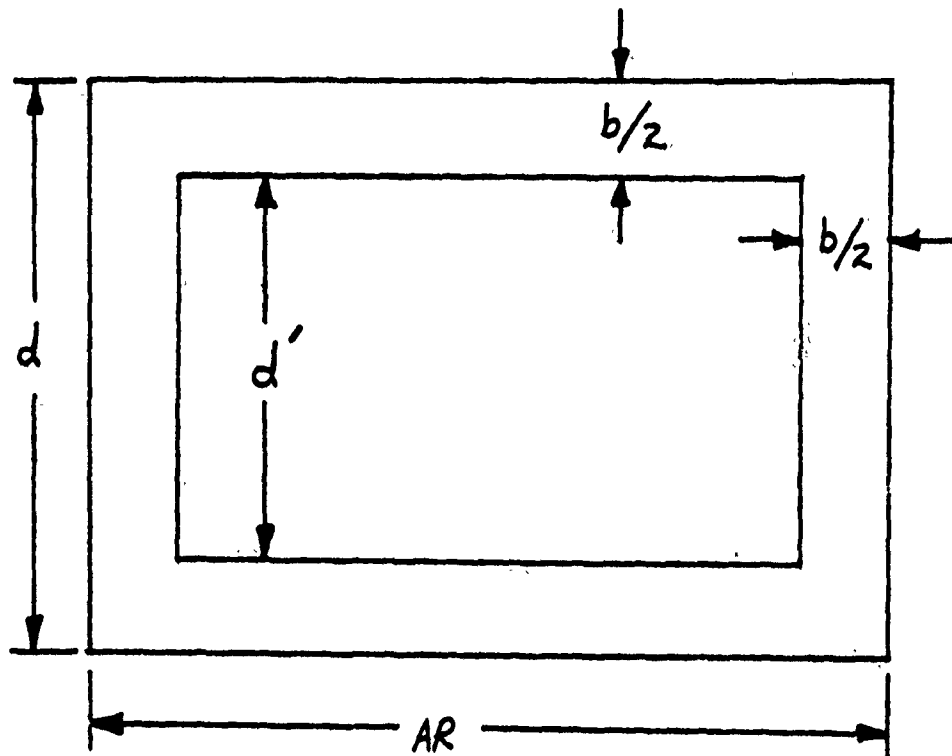
Figure 2. Rectangular Nozzle With External Flow

modification which must be made is in the scaling factor. A change in momentum per unit area must be accounted for.

The scaling factor in this case is still a function of aspect ratio and axial distance, as seen before, but also must include the ratio between the external and core mass flows. For simplicity, the exit area of the core flow and the exit area of the surrounding external flow were assumed to be equal. Following the procedure for defining a scaling factor in Case #1, the following modified scaling factor was obtained:

$$H = 1 + [0.1(X/X_a)^2 - 4.3(X/X_a)^3](K-1)(b/2d)^2 \qquad (7)$$

The algorithm procedure is now identical to Case #1 if Equation (7) is used in the place of Equation (5). The Equations (3), (6) and (7), along with a basic plume of diameter d form the closed set to be used. (Notice that the basic plume diameter is based on d and not d'.)

● CASE #3

An attempt was made to extend this approach for defining a shape description algorithm to non-axisymmetric plumes where the core was not surrounded by a symmetric uniform flow or where the exit plane was inclined. This was not successful primarily due to the time constraints of the summer program. It was also found that there was insufficient experimental data needed to validate some of the constants which result when defining a scaling factor. It is believed, however, that solutions can be obtained for these more complex geometries.

IV. RECOMMENDATIONS

Further generalization of the algorithm beyond what is presented in this report is obviously necessary. Only simplistic geometries and flow conditions have been addressed. The algorithm needs to be much more robust in order to accommodate the many possibilities posed by future propulsion systems. For example, one item not even addressed was the temperature of the plume for both static and nonzero flight speeds.

An aspect hindering further development is the lack of experimental data for the various nozzle geometries to be considered. A considerable effort needs to be directed towards collecting data so that algorithms can be validated. If the necessary experimental data are not available in the published literature, simple experiments will need to be conducted.

The algorithms developed to date need to be incorporated into a user-friendly computer program. Such a program could be easily developed for a personal computer. It would need to be modular, however, in order to allow for the easy change-out of algorithms as new ones are developed.

It is suggested that further algorithm development continue, addressing these as well as other items under the auspices of an AFOSR Research Initiation Grant (an integral part of the Summer Faculty Research Program).

REFERENCES

1. Chu, C. W. and Der, J., "ADEN Plume Flow Properties for Infrared Analysis", AIAA Paper No. 82-406, 1982.

2. Sfeir, A. A., "Investigation of Three-Dimensional Turbulent Rectangular Jets", AIAA Journal, Vol. 17, No. 10, pp. 1055-1060, 1979.

3. Trentacoste, N. and Sforza, P. M., "Further Experimental Results for Three-Dimensional Free Jets", AIAA Journal, Vol. 5, No. 5, pp. 885-891, 1967.

4. Sforza, P. M., Steiger, M. H., and Trentacoste, N., "Studies on Three-Dimensional Viscous Jets", AIAA Journal, Vol. 4, No. 5, pp. 800-806, 1966.

5. Sfeir, A. A., "The Velocity and Temperature Fields of Rectangular Jets", International Journal of Heat and Mass Transfer, Vol. 19, pp. 1289-1297, 1976.

6. Saheli, F. P., "Experimental and Analytical Evaluation of Three-Dimensional Exhaust Plumes", AIAA Paper No. 80-1399, 1980.

7. Abramovich, G. N., The Theory of Turbulent Jets, M.I.T. Press, 1963.

8. Pai, S. I., Fluid Dynamics of Jets, Van Nostrand Publishing, 1954.

FINAL REPORT

Strain Enhancing Binder Blends
For Use in Rocket Propellants

Prepared by:	Daniel Lee Fuller, Ph.D.
Academic Rank:	Professor
Department and	Chemistry Department
University:	Nicholls State University
Research Location:	AL/RKP Edwards AFB Lancaster, CA 93523
USAF Researcher:	Claude Merrill, Ph.D.
Date:	5 August 90
Contract No.	F49620-88-0053

Strain Enhancing Binder Blends
For Use in Rocket Propellants

by

Daniel Lee Fuller

ABSTRACT

Rocket propellants were prepared by polymerization of the
hydroxy terminated polybutadiene (HTPB) with isocyanates and
copolymers of HTPB and amine terminated polypropylene glycol
(ATPPG) isocyanate. The binder composition was modified both by
varying the isocyanate to hydroxyl ratio and by varying the
percent of ATPPG. Mechanical properties were determined using an
"Instron." We reported the maximum stress, maximum strain,
initial modulus, stress at rupture, and elongation at rupture for
these propellant systems.

Acknowledgement

I wish to thank the Air Force Systems Command and the Air Force Office of Scientific Research for sponsoring this research. Universal Energy Systems should be recognized for their willingness to help me in all of the various administrative aspects and, in particular, for their willing guidance and direction at the beginning of the program. Their help was especially appreciated.

My experience was rewarding and enriching because of so many different people. Claude Merrill is most significant because he shared willingly of his knowledge of his field. Additionally, he provided me with support, encouragement, and a truly enjoyable working atmosphere. The help of Sgt. Dave Foxx and Ms. Jeri Van Dyke was also invaluable in overcoming technical problems. The valuable and enlightening discussions with Shirl Breitling and John O'Drobinak were greatly appreciated. Most of all, the in-depth conversation and patience of Dr. Merrill clearly added to every aspect of this project.

I. INTRODUCTION

Most catastrophic failures of rockets using solid propellants occur within seconds after ignition. One of the principal causes is due to cracks that have developed in the propellant grain. These cracks increase the surface area of the propellant thereby increasing the burning rate of the fuel. The gas cannot escape rapidly enough through the nozzle resulting in an increase in the pressure within the rocket chamber. A characteristic of a solid propellant is that the burn rate increases as the pressure increases. The higher pressure resulting from increased combustion causes the propellant to burn faster and faster. The pressure rapidly builds to the point at which it exceeds the strength of the chamber containing the propellant resulting in failure of the rocket.

The Rocket Propulsion Division of the Astronautics Laboratory (AL) at Edwards Air Force Base is particularly concerned with the prevention of crack development in propellants. Today, solid propellants use an elastomeric binder in order to impart elasticity to the propellant. Presently, most binder systems have mechanical properties, specified by stress-strain measurements, that only meet the minimum required performance criteria for satisfactory use in a rocket propulsion system.

My interest has been in the area of property-structure relationships of polymers and the modification of physical and

chemical properties of polymer systems by the use of additives. My experience as a consultant working on novel problems and my overall knowledge of chemistry, especially polymer science, contributed to my assignment to the binder formulation unit of the Rocket Propulsion Division.

II. OBJECTIVES OF THE RESEARCH EFFORT

The objective of this project was to improve the mechanical properties of the HTPB/isocyanate propellants through strain crystallization. Polymers of hydroxy terminated polybutadiene (HTPB) which have been chain extended with isocyanates are commonly used as binders in solid rocket propellants. HTPB propellants normally have strain capabilities only slightly better than requirements. The irregular appearance of markedly reduced strain capability with HTPB propellants causes motor failures as well as increases costs for both motor development and motor manufacture. Irregular sharp reductions in HTPB propellant failure strains may partly be due to the fact that HTPB\isocyanate binders have strain characteristics which are quite sensitive to surface conditions. Certain surface conditions can cause the elongation capability to decrease by 50% or more. With decreased rupture strain cracking problems begin to occur. The decreased strain capability seems related to the ease of transverse crack propagation that is a characteristic failure mode for HTPB/isocyanate propellants under tension. Thus, if propellant cracks become more easily initiated under low stress

conditions, rupture failures occur at low stress values primarily because of facile transverse crack propagation rather than by change in bulk propellant properties. This dilemma could be attributed to the absence of significant strain crystallization character in HTPB elastomers. Without substantial strain crystallization traits HTPB chain extended with isocyanates should display strain capabilities governed by rather capricious surface effects that would vary the ease of crack initiation. This would follow since the energies required to propagate cracks is low in HTPB binder systems. The propellant system we proposed to examine consisted of a polybutadiene matrix with the inclusion of various proportions of polypropylene glycol (PPG). It was hoped that the PPG segments would add strain crystallizing character to the binder system. It was also conceivable that separate microphases of butadiene and PPG could result in elastomers where crack-tips might be deflected in crossing from one microphase regime to another. In this way crack propagation might be inhibited.

My assignment, as a participant in the 1990 Summer Faculty Research Program (SFRP), was to determine whether incorporation of amine terminated polypropylene glycol (ATPPG) into the HTPB/isocyanate system would improve the mechanical properties of the propellant. Several prepolymer blends were evaluated over a range of cure ratios based upon systems stress-strain behavior. The mechanical properties were measured by an Instron tensile test machine to measure the tensile modulus, percent elongation,

and tensile strength. Test samples were in the configuration known as Class C dogbones.

ATPPG was chosen, rather than hydroxyl terminated PPG, because of the isocyanates greater reactivity with amines than with hydroxyl groups. This difference in reactivity allowed the amine terminated polyethers to chemically react with isocyanate groups using the HTPB as a solvent. The isocyanate terminated polyethers then cured slowly with the HTPB resulting in random copolymers.

Variation of the isocyanate to the total -OH and -NH$_2$ functionality influences final tensile strength, modulus, and rupture strain properties of the propellant by controlling the overall extent of polymerization. Throughout the remainder of this report the total -OH and -NH$_2$ functionality will be simply referred to as the -OH functionality. Since propellant physical properties are a composite of rubber binder characteristics, modified by polar and nonpolar interaction with the ionic (ammonium perchlorate) and metallic (aluminum) solid fillers, optimum -NCO/-OH ratios were searched for by varying -NCO/-OH ratios in four values ranging from 1.0 to .775. The desired values of physical properties were roughly 100 psi tensile strength, 500 psi modulus, and rupture strains as great as possible, but, hopefully greater than 30 %.

Both difunctional and trifunctional ATPPG were formulated into propellant and tested. As the proportion of polyether was

varied, the mechanical properties of the simple AP and Al propellant processing and physical properties were observed to change. Early chemical processes were considered to range from diisocyanate end capping of the amine terminated PPG (D-4000 and -5000) followed by chain extension through the HTPB prepolymer hydroxyl groups. The organic system at this stage should have been larger prepolymer molecules containing both HTPB and PPG segments. Once solids were added and the final isocyanate curative incorporated, diisocyanate cure provided rubbery propellants. An excess of HTPB was utilized resulting in a random copolymer containing domains of PPG embedded in a polybutadiene (PB) matrix. Optimum mechanical properties were searched for by utilizing 0, 10, 20 % proportions of D-4000 or T-5000 in the formulations at cure ratios (-NCO/ -OH + -NH$_2$) of 0.775, 0.85, 0.925, and 1.0. The trifunctional amine terminated PPG (T-5000) not only should influence the system in a similar manner to D-4000, but in addition should be capable of bringing about chemical cross-linking. The cross-linking of elastomers is a critical factor in controlling the mechanical properties of polymers. We, for this reason, chose to examined T-5000's influence on mechanical properties of solid rocket propellant systems by varying the composition of the T-5000 in the formulation by 0%, 10%, and 20%.

III. Method

To achieve our objectives, the procedure used was based on

the following techniques. Screening the propellant systems would be based on propellant formulations rather than gumstocks. The necessity of working with the less time efficient composite propellant rather than gumstock has been demonstrated previously at Aerojet Tactical Systems Co. A brief portion of their study is given in Table 1. The study shows that addition of 90% solids (AP plus Al) changes the mechanical properties of the binder significantly but, unfortunately, unpredictably.

Table. 1.

Comparison of Mechanical Properties of HTPB/TDI Gumstock and Propellant at 25° C.

Solids, Wt, %	Plasticizer	σ_m, psi	ε_m, %	ε_b, %	E_o psi
0	DOA	18	454	463	10
70% AP 20% Al	DOA	123	23	24	768

At Edwards Air Force Bases's AL, previous studies have delineated the essential components for solid rocket propellants. In this investigation, the formulation employed was a result of their experiences. The components of the formulation and the function of each component is given in Table 2.

To determine the optimum ratios of -NCO/-OH and of R-45M/ATPPG, in order to obtain improved mechanical properties, a number of propellant systems were studied. The ratios examined are given in Figure 1.

Figure 1.

Compositions of Solid Rocket Propellants Prepared in This Investigation.

Equivalent Ratio: -NCO to -OH					
1.00	o	o	o	o	o
0.925	o	o	o	o	o
0.85	o	o	o	o	o
0.775	o	o	o	o	o
	20 D	10 D	0	10 T	20 T

Percent Amine Terminated PPG
(D: D-4000   T: T-5000)
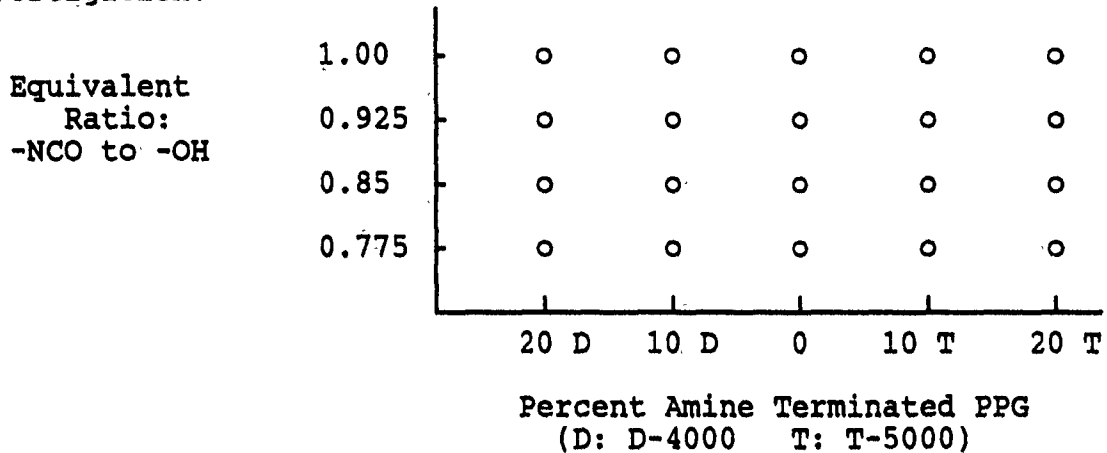
IV. RESULTS AND OBSERVATIONS

At any given % ATPPG, the values of E_o, σ_m, σ_r, F_m increase with greater values of -NCO/-OH ratios ; whereas, the maximum elongation and elongation at rupture decay with increasing values of -NCO/-OH (Tables 3, 4 and 5). Inspection of the data in Tables 3, 4, and 5 shows a general trend that the values of E_o, σ_m, σ_r, F_m obtain a maximum at 0 % ATPPG regardless of the -NCO/-OH ratio. The ε_m and ε_r for the 0% ATPPG are less than 10% ATPPG regardless of the curative ratio.

A possible explanation for these trends in the tensile properties could be that in the preparation of the propellant half of the isocyanate curative needed to obtain the -NCO/-OH ratio is being used. In these recent experiments at least a fourfold excess of isocyanate was present for reaction with the ATPPG. As a consequence, the ATPPG would have an average repeat unit of one and

Table 2.

Baseline Formulation for Solid Rocket Propellants Prepared in this Study.

Ingredient	Function	%Wt.	Structure/Formula
BINDER SEGMENT			
R-45M	Prepolymer	Variable	Hydroxy-terminated Polybutadiene
D-4000	Prepolymer	Variable	Linear Amine-terminated Polypropylene glycol
T-5000	Prepolymer	Variable	Branched Amine-Polypropylene Glycol
TDI	Curing Agent	Variable	Toluene Diisocyanate
IPDI	Curing Agent	Variable	Isophorone Diisocyanate
Flexzone-6H	Antiozodant	0.2	N,N'-Diphenyl-phenylene Diamine
DTBH	Antioxidant	0.06	Ditertiary Butyl Hydroquinone
DOA	Plasticizer	2.0	Dioctyl Adipate
HX-752	Bonding Agent	0.2	Diaziridine Derivative Isophthalic Acid
PRIMARY FUEL SEGMENT			
AP, 200μ	Oxidizing Agent	46%	Ammonium Perchlorate Ave. 200 Micron Size
AP, 10μ	Oxidizing Agent	21%	Ammonium Perchlorate Ave. 10 Micron Size
Al, 6μ	Reducing Agent	20%	Aluminum Ave. 6 Micron Size

be endcapped with the isocyanate rather than be chain extended into an ATPPG/isocyanate polymers with a large number of repeating ATPPG units. As binder cure proceeded, the much less reactive hydroxyl groups of the excess R-45M would react and the endcapped ATPPG would be randomly incorporated into the R-45M matrix. Compared to a homopolymer of R-45M, which would have a

relatively uniform structure, the random copolymer of R-45M and ATPPG would have substantially less order. This might cause the ATPPG to function as an internal plasticizer with resulting lower values for propellant tensile stress. If this concept is correct, the properties of these propellants might be improved by reducing the quantity of dioctyl adipate plasticizer. This could have two advantages. The first is that the quantity of rubber binder network could be increased by 2 percent. The second advantage could be that plasticizer migration from the binder into liner and /or insulation interfaces would be eliminated.

Another consequence of the early isocyanate addition as described above is that the viscosity of the organic binder increases. When overdone this can result in difficulties in blending the solids, AP and Al, into the uncured organic binder, hence, requiring longer stirring cycles with the danger of shearing and damaging the polymer binder molecular structure.

Table 3

Summary of Mechanical Properties of Propellants Formulated with a -NCO to -OH Ratio of 1.00 and Various % ATPPG.

ATPPG %	Maximum Force, lbs.	Maximum Strain, in./in.	Initial Modulus, p.s.i.	Stress at Rupture, p.s.i.	Elongation at Rupture, in./in.
20 D-4000	14.75	0.231	679.7	56.38	0.32
10 D-4000	21.56	0.247	942.7	90.86	0.32
0 ATPPG	35.73	0.222	1435.5	109.14	0.23
10 T-5000	24.27	0.194	1232.7	125.27	0.257
20 T-5000	23.37	0.194	1186.7	114.7	0.214

Since unacceptably soft propellant cures were achieved, mechanical properties were not obtained for ATPPG solid

propellants with an -NCO/-OH ratio of 0.775 or 20% D-4000 with a
-NCO/-OH ratio of 0.85 (See Table 5). Too low a proportion of

Table 4

Summary of Mechanical Properties of Propellants
Formulated with a -NCO to -OH Ratio of 0.925 and Various %
ATPPG.

ATPPG %	Maximum Force, lbs.	Maximum Strain, in./in.	Initial Modulus, p.s.i.	Stress at Rupture, p.s.i.	Elongation at Rupture, in./in.
20 D-4000	4.78	0.517	78.8	19.65	0.741
10 D-4000	14.67	0.270	548.7	52.33	0.403
0 ATPPG	23.46	0.35	1038.0	119.49	0.398
10 T-5000	14.27	0.369	375.6	67.31	0.434
20 T-5000	8.44	0.343	247.0	37.89	0.421

curative could be the cause for the soft propellants. Data in
Table 6 for baseline (no ATPPG) propellants showed the IPDi
curative yielded solid propellant having somewhat greater rupture
strain (73.5 % versus 66.9 %) and maximum stress (98 psi versus 83
psi) as compared to solid propellant formulated with half TDI and
half IPDI curative. As observed earlier these propellants
exhibit exceptionally good strain capabilities that are likely
due to the new processing method that was used.

Table 5
Summary of Mechanical Properties of Propellants
Formulated with a -NCO to -OH Ratio of 0.85 and Various % ATPPG.

ATPPG %	Maximum Force, lbs.	Maximum Strain, in./in.	Initial Modulus, p.s.i.	Stress at Rupture, p.s.i.	Elongation at Rupture, in./in.
20 D-4000			"To Soft To Machine"		
10 D-4000	5.13	0.787	31.3	29.36	0.788
0 ATPPG	16.09	0.575	440.9	82.74	0.670
10 T-5000	8.61	0.781	101.5	45.27	0.865
20 T-5000	4.25	0.319	49.6	24.41	0.589

Table 6

Summary of Mechanical Properties of Propellants Formulated with a -NCO to -OH Ratio of 0.85 Using Different Isocyanate Curatives.

Isocyanate	Maximum Force, lbs.	Maximum Strain, in./in.	Initial Modulus, p.s.i.	Stress at Rupture, p.s.i.	Elongation at Rupture, in./in.
IPDI	18.24	0.711	440	98.2	0.735
TDI/IPDI	16.09	0.575	349	82.7	0.669

IV. RECOMMENDATIONS

An important goal for the Astronautics Laboratory is to obtain a R-45M solid propellants having superior strain capabilities. Such solid propellant would provide significantly fewer motor failures resulting in savings of money and, probably, some human lives. Obtaining superior strain capability is a severe technical challenge since the physical properties of HTPB solid rocket propellants are dependent on control of a multitude of variables.

Abrasive mixing of the oxidizing agent, AP, into liquid HTPB prepolymer, which contains allylic hydroxyl groups, might lead to oxidation of the hydroxyl groups needed to chain extend the HTPB. Loss of even one percent of the hydroxyl groups would significantly reduce the ability to achieve high molecular weight HTPB polymers, thereby resulting in a loss of desired physical properties. The manner of addition of the oxidizing agent, AP, appeared to influence the physical properties of the solid propellant especially when conditions led to a mixture that became "dry-gritty" in texture. This raises the question of the

optimum approach to attain mix time and the manner of AP addition for obtaining the preferred mechanical properties.

The reason for the current approach came out of an old advertising brochure by Atlantic Richfield Company (ARCO) during the period that they owned the R-45M prepolymer production facility. In their brochure they provided an account of gumstock studies with both pure R-45M and a 50-50 R-45M a... PG 3000 mixture cured by TDI at a 140° F temperature. An -NCO/-OH ratio of one was employed. The mixed R-45M and PPG gumstock had both maximum tensile strength and rupture strain at least three times greater than for the pure R-45M gumstock. If this magnitude of change could be made for solid propellant, all industry problems with low strain capability for workhorse propellants (primarily for large booster applications) would be solved. With a very large margin of surplus strain capability even relatively large errors in formulation, processing, and quality control might routinely yield propellant having adequate strain capability.

However, substantial problems loomed for translating the ARCO results to solid propellant. First, cure at 140° F did not seem feasible for reasons of manufacturing safety, the likely prospect of having poor long term propellant aging qualities, and high motor grain stresses derived from thermal grain shrinkage by cool down to normal operational and storage temperatures. Further, R-45M propellants due to high -OH functionalities of about 2.3 employ -NCO/-OH ratios less than one to avoid an

overpopulation of crosslinks. With the chemical reactivity of the R-45M -OH groups less than about one tenth that of the PPG -OH groups the low -NCO/-OH ratios would leave some of the PPG as plasticizer rather than as rubber network contributing to binder strength and strain capability. Another factor discovered during the effort reported here was that the PPG's viscous interactions with propellant solids, AP and Al, produce greatly higher processing viscosities that lessened propellant castability.

Chain extension, increasing prepolymer molecular weight by reaction of a fraction of the propellant curative prior to solids addition during propellant processing, is a process often proven to provide substantial propellant strain capability enhancement. The availability of difunctional and trifunctional amine terminated PPG's D-4000 and T-5000, provided the appearance of a solution to the envisioned chemical and propellant processing difficulties. Addition of half of the desired quantity of diisocyanate curative to a mixture of R-45M and ATPPG in -NCO/-NH$_2$ ratios large enough to ensure that most of the ATPPG would quickly become isocyanate terminated (due to high -NH$_2$ group reactivity with -NCO groups) followed by a slower chain extension reaction with the remaining excess of R-45M -OH groups would ensure incorporation of short PPG segments in random fashion into the R-45M binder network. Several questions could be asked about such a process. Primary among these questions is, " Will the random short block PPG incorporation provide similar enhanced strain and strength as with gumstock?" In the mixed

gumstock almost pure R-45M binder network would likely be terminated by long blocks of PPG due to the differential -OH group chemical reactivities of the two prepolymers. Other questions could be about the strength and direction of binder to solid filler interactions and how important processing methods are to propellant strain capabilities. Thus, the approach reported here contained the hope that incorporation of PPG into the R-45M binder network was the important influence rather than the block sizes and/or block order of polybutadiene and PPG polymer segments.

After the work reported here the random short segments of PPG incorporation into a R-45M binder network did not enhance propellant capabilities, further efforts should be directed at investigating both internal and terminal PPG long block segments chemically attached to the R-45M binder networks. Techniques not conceived of prior to this effort make such binder chemical structures now seem feasible in a propellant processing environment.

1990 USAF-UES SUMMER FACULTY RESEARCH PROGRAM/
GRADUATE STUDENT RESEARCH PROGRAM

Sponsored by the
AIRFORCE OFFICE OF SCIENTIFIC RESEARCH
Conducted by the
Universal Energy Systems, Inc.

FINAL REPORT

A Development of Molecular Modeling Techniques to Study Intermolecular Forces Found Between Solid Rocket Oxidizers and Their Binding Agents

Prepared by: Shannon G. Lieb

Academic Rank: Associate Professor

Department and   Chemistry
University: Butler University
                    Indianapolis, IN 46208

Research Location: Astronautics Laboratory/LSX
                    Edwards AFB, California 93532

USAF Researcher: John Rusek

Date: August 10, 1990

Contract No: F49620-88-C-0053

A Development of Molecular Modeling Techniques to Study Intermolecular Forces Found Between Solid Rocket Oxidizers and Their Binding Agents

by

Shannon G. Lieb

ABSTRACT

In light of the many failures of solid rocket motors due to improper adhesion of the oxidizer to the binding agent, this study was embarked upon with the idea of modeling the nature of binding to a solid ionic surface at the molecular level. This approach should yield ways of improving the method of mixing the oxidizer and propellant and should give a better understanding of the concept of binding itself. With this general goal in mind, the specific system of ammonium perchlorate (oxidizer) and hydroxy-terminated polybutadiene (binder) are made the model system to study. These materials are commonly used in these roles and are well characterized in terms of their thermodynamic and spectroscopic properties. These ingredients are essential to modeling the inter- and intramolecular forces needed to carry out molecular mechanics calculations of this system. Appropriately small prototype systems must first be studied to test the parametrization scheme to be used in the large scale problem. Once the essential interactions are characterized, the scaling up to the complex system of long chain binders adhering to a solid surface requires a partitioning of efforts into two parts. One part is the study of the lattice statistics of a long chain aldene adhering to the ammonium perchlorate surface. The second is the investigation of the most energetically stable interactions between the binder and oxidizer. Together these approaches yield a molecular description of the oxidizer/binder interaction.

ACKNOWLEDGMENTS

I.   INTRODUCTION

In the past decade the development of semiclassical quantum mechanical calculations refered to as molecular mechanics has been developed to deal with large scale molecular systems (i.e., 50-3000 atoms or more). These systems can not be approached by ab initio calculations with present computer technology; therefore, molecular mechanics has been developed to confront these large scale problems. This approach can be characterized as an appropriate mixture of highly accurate ab initio calculations on prototype systems, experimentally established parameters of inter- and intramolecular force fields and chemical intuition. This approach has been used extensively in the areas of biochemistry (protein structure and reactivity) and pharmaceutical industry (drug design and interaction) in an attempt to understand fundamental molecular mechanisms. In a little more than a decade ago, the advent of the application of molecular dynamics to protein structures was viewed as intractably complex by many chemists and not a development that would contribute significantly to the knowledge of protein chemistry by many biologists. Since that time the literature has exploded with dynamic simulations which have greatly enhanced our understanding of protein function. Conformational changes in proteins account for its binding activity, information transmission and other important functions. The development of protein dynamics is not the thrust of this research but only an example of the utility of the application of properly guided chemical intuition to the solution of large scale molecular problems via a dynamics presentation (albeit Newtonian mechanics). A good overview of protein dynamics, structure and thermodynamics is given in a review volume by Charles Brooks, et. al. (1) bearing that title.

The problem at hand is one of elucidating the meaning of the term adhesion at the molecular level. Organic binders have been formulated in the past along with oxidizing agents to make solid rocket propellants. In order to get a more efficient motor, one needs to bind these two ingredients together. Presently there is no molecular level description of the intrapropellant binding process. In order to understand adhesion defects and circumvent problems relating to them, an in depth understanding of the binding phenomenon is desirable. Beyond that, if the action of adhesion at the molecular level is understood, possibly new propellants could be developed that no longer require bonding agents. With the development of large scale molecular dynamics programs like CHARMM, AMBER and BIOGRAPH, the appropriate time for this type of investigation seems ripe. These programs have

been developed for the study of protein dynamics but are general in the sense that they have large internal libraries defining the parameter files that describe the fundamental interaction potentials between atoms. My own experience is with the program CHARMM developed by Martin Karplus of Harvard University (hence the name Chemistry HArvard Molecular Mechanics). The data library can be accessed and modified to include new atoms and their associated parameters (to be described later) so that the program can attack new problems with the same fundamental algorithms for solving Newton's equations of motion.

The objective of this introduction is to state the problem of adhesion and to point to the present tools at hand for possible solution to that problem - molecular mechanics and dynamics. With that in mind, the following sections will develop more of the detail in plan of attack, the results at present and what needs to be done.

II. OBJECTIVES

Studies of hydroxy-terminated polybutadiene (HTPB) in relation to their binding properties have been carried out using various experimental measurements including thermodynamic (2,3), rheologic (4,5) and spectrophotometric (4,6). The recurring hypothesis is that binding is due primarily to hydrogen-bonding at the ionic surface with the hydroxy terminal group of HTPB. Hydrogen-bonding is indicated as the major source of binding for carboxyl-terminated polybutadiene (5) as well. Using this hypothesis as a starting point, the development of methods to understand the interactions available to the binder with ammonium perchlorate (AP) have been put in place. There are many possible attractive interactions possible and the goal is to list and prioritize these interactions and then build a model that either confirms or suggests alternate possibilities.

In general, there appears to be two paths to follow so as to clarify the issues at hand. One path is the examination of the various conformational interactions of HTPB with AP through a statistical model. This is a "static" model in which different conformational energetics are examined and appropriately weighted via Boltzmann statistics. The description of the interaction of the two dimensional lattice provided by the AP with the various states available to the HTPB is based on the generalization of the two dimensional Ising model refered to as Potts models (7).

The second path is a "dynamic" model which investigates the time evolution of a molecular system. This approach can be investigated with the use of the program CHARMM. Incorporated in this program are the parameters which describe the interaction terms of each individual atom's intramolecular and intermolecular forces. Those interactions which are missing because of a novel system can be added to the library of parameters. This program carries out not only a (local) minimization of the structure which is presented but also carries out an "annealing" process; whereby, the molecular system is subjected to large, random kinetic energy inputs which force the molecular geometry into other conformations which maybe near to the proposed local energy minimum, but separated by a large conformational energy barrier. This allows for a search of the global minimum of the proposed structure. Because the intermolecular forces are approximated as harmonic oscillators there is no dissociation of the molecule by inputting kinetic energies that correspond to 1000 Kelvins. In order to simplify the study of the dynamics of the system, there is a molecular dynamics simulation with stochastic boundary conditions. This method allows the partitioning of the molecular system into several regions based on their spatial disposition with respect to a primary area of interest. There is a reaction region and a reservoir region. Further there is a buffer region which forms the interface between the reaction zone and reservoir. The reservoir supplies the stochastic forces to be applied to the reaction zone through the buffer region atoms. The buffer region atoms are tied to the reaction region boundary, but are connected through a harmonic potential. One can then apply the simplified Langevin dissipative and random forces to simulate the dynamics of the condensed phase with a small fluctuation around the mean temperature.

Up to this point the objectives have been stated as a definition of the problem in terms of what constitutes the "model" molecular system for solid rocket propellant (i.e., HTPB and AP) and a brief account of methodologies that can be applied in an attempt to answer the question of "What is the nature of adhesion at the molecular level?". Now we must turn to the question of what are the essential input parameters to explore the statistics and dynamics of our model system. Since the studies that are suggested are interested in the molecular motion of the nuclear framework of the molecules in question, the approach of molecular dynamics is one of classical dynamics and the understanding of classical potentials and/or forces. That does not preclude the use of quantum mechanical calculations to aid in the determination of the parameterization, but it means that the quantum mechanical effects have to be incorporated into a classical mechanics regime. In particular, the

forces between atoms within a molecular unit (intermolecular) are represented as harmonic stretching and bending motions and as torsional motions. These three internal mode motions thereby need their motions characterized by harmonic force constants as derived from normal coordinate analysis of fundamental frequencies via infrared spectroscopy. The torsional mode parameters can be estimated from semi-empirical computational packages like MOPAC (available at the Kirkland AFB supercomputer on the CRAY2) or from ab initio calculations (e.g., CADPAC also available at the aforementioned supercomputer) of smaller prototype systems containing appropriate chemical aspects of the larger molecular system. The forces between molecular units (intramolecular forces) are typically characterized by electrostatic (Coulombic) forces plus London dispersion forces generally either in the form of the Lennard-Jones 6-12 potential or the exp-σ potential in which the repulsive portion of the potential (i.e., r^{-12}) is replaced by a somewhat less steep exponential term. These dispersion potentials require two parameters to describe the well depth and an effective interaction distance (8). These parameters are evaluated for all atom pairs and are only effective for interactions that are more than four bonded neighbors away or non-bonded, but spacially neighboring atoms. The Coulomb potential has two parameters as well. The first is the dielectric of the media and the other the partial charge associated with each atom. The partial charge can be obtained by a Mulliken population analysis of an ab initio quantum mechanical calculation of the molecule in question or of an appropriate prototype.

Finally, I would like to note that there is available in the molecular dynamics simulations the availability of solvent interactions. These could be useful in determining the detrimental or useful aspects of leaving behind solvent molecules when a binder is applied to the oxidizer. Also, some have conjectured that humidity has played a role in the deterioration of proper binding. If water molecules are entered into the "reaction" zone of the dynamics simulation, its positive or negative (or neutral) effects can be evaluated.

III.   METHODOLOGY AND DEVELOPMENT

The computing facilitities available to me now (at the Edward's AFB Astronautics Laboratory and Kirkland AFB) do not have a copy of CHARMM or its equivalent for the dynamics calculation, but there is the latest version of molecular mechanics authored by N.L. Allinger, et.al. (12) called MM2. The intermolecular potential terms are the harmonic stretching and bending vibrational modes , their

coupling and torsional modes. The explicit representation of these potential terms is as follows. The stretching mode potential has the form:

$$E_s = 143.88 \frac{k_s}{2} (1 - 1_0)^2 [1 + c_s(1 - 1_0)]$$ (1)

where k_s is the harmonic stretching force constant, 1_0 represents the equilibrium (minimum energy) internuclear separation and c_s represents the cubic stretching term whose value is presently set at -2.00. The lengths are in Angstroms and k_s has the units of mdynes/Angstrom. The bending potential has the form:

$$E_\theta = k_\theta (\theta - \theta_0)^2 [1 + 7.0 \times 10^{-8} (\theta - \theta_0)^2]$$ (2)

where k_θ is the harmonic bending constant in units of mdynes/Angstrom-radians^2 and θ_0 is the equilibrium bond angle in radians. Finally, the torsional potential which includes terms up to three fold bond rotational terms:

$$E_\omega = \frac{V_1}{2} (1 + \cos \omega) + \frac{V_2}{2} (1 - \cos 2\omega) + \frac{V_3}{2} (1 + \cos 3\omega)$$ (3)

where the V_i 's are the parameters that are either set to zero or evaluated relative to the rotational energy barrier about a bond. This energy is expressed in kcal/mole. As for the intramolecular energy terms, the van der Waals forces are those forces between atoms that are either more than 3 bonds distant or spacially near one another without the benifit of a bonding interaction. The van der Waals force in this case is mimicked by an exp-6 potential of the form:

if P<3.311

$$E_{vdw} = \varepsilon * \left[2.9 \times 10^5 \exp(-\frac{12.5}{P}) - 2.25 \, P^6 \right]$$ (4a)

if P>3.311

$$E_{vdw} = \varepsilon * 336.176 \, P^2$$ (4b)

where P is the inverse of the reduced internuclear distance; i.e., P = r*/R. The value of R is the instantaneous internuclear separation and r* is the interaction range parameter refered to earlier. The other parameter, $\varepsilon*$, is the van der Waals well depth. These parameters for all pair-wise interactions are assessed by an atom-atom interaction potential which uses simple combination rules to evaluate two different atoms approaching one another. Specifically, r* equals the sum of the

individual van der Waals atomic radii and ε^* is the geometric mean of the atomic "hardness" parameters. The coulombic interaction term is simply:

$$E_c = \frac{q_1 q_2}{\kappa r_{12}} \tag{5}$$

where q_i is the charge of the i-th atom and κ is the appropriate dielectric constant. There are many specific, attendant details which are addressed in reference 12.

In order to parameterize MM2, experimental data and quantum mechanically calculated values must be gathered together. To this end I have prepared Table I which contains crystallographic, thermodynamic and spectroscopic values for ammonium perchlorate. The Schoenflies symmetry symbols used to identify the vibrational frequencies come from the normal mode analysis in which the 9 vibrational modes are reduced to a nondegenerate, A_1, and triply degenerate, T_2, set of stretching modes and a doubly degenerate, E, and triply degenerate, T_2, set of bending vibrational modes. Because the stretching and bending T_2 modes are of the same symmetry there is a mixing of these two modes in the normal coordinate mode analysis. The best normal mode coordinate force constants are determined by minimizing the square of the residual of the calculated versus experimental fundamental frequencies. After the determination of the best normal mode force constants, the normal mode coordinate force constant matrix was back transformed to give the internal coordinate force constants. These resultant force constants are found to be k_s = 6.658 mdynes/Angstrom, k_θ = 3.469 mdynes/Angstrom-radian^2 and $k_{r\theta}$ = 1.610 mdynes/Angstrom-radian for the perchlorate anion and k_s = 3.481 mdynes/Angstrom, k_θ = 1.441 mdynes/Angstrom-radian^2 and $k_{r\theta}$ = 0.532 mdynes/Angstrom-radian for the ammonium cation.

The theoretical evaluation of the harmonic frequencies throught the CADPAC package at Kirkland AFB supercomputing facility has yielded the results on Table II. Unfortunately at this moment, the second order Moller-Plessant (MP2) calculations do not work properly on the CRAY2 at Kirkland. However, the present results are due to a geometry optimized SCF calculation which utilizies the polarized 631G* basis functions provided by the library contained in the CADPAC program. To that basis was added an f-orbital basis to the Cl atom as suggested by E.D. Simandiras, et. al. (16) to improve the harmonic frequency analysis of the bending modes. This simple addition changed the bending frequencies from 100% too low to 7% too high for the E mode and 9% too high for the T_2 "bending" mode. The best results for prediction of harmonic frequencies (16,17) have been obtained by further refing the

SCF calculation by invoking MP2 corrections. Although the frequencies found by this method are above the observed fundamental frequencies, that is to be expected because one needs the first overtone frequencies to correctly extract the harmonic frequencies from the fundamental. As noted in Table II, the Mulliken population analysis shows that the Cl charge is 1.589 and the oxygen charge is -0.647. According to the analysis of reference 13, the total charge on the perchlorate anion should be -0.34 which is one third the value of the charge used in the SCF calculation. This can be corrected by placing an ammonium ion at an average N-- Cl crystal distance and allowing the charge to redistribute among all the atoms of the neutral formula unit. Several orientations of the ammonium ion relative to the perchlorate anion will be applied. This procedure is ready to be put in place as soon as the implementation of MP2 is properly installed.

The other half of this study is the development of a model of the hydroxy-terminated polybutadiene which will interact with the ammonium perchlorate surface. Another facility of the CADPAC program is the setting up of a point charge lattice and allowing the user to evaluate the interaction of a molecule with a point electrostatic field. Some model systems that seem appropriate prototypes are the comparisons of ethanol to methane interacting with lattice point charges or ethylene to methane and even 1-hydroxy 2-propene compared to methane interactions with a point charged lattice. These comparisons should give some insight into the relative bonding strengths and thereby the relative configurational energies of interaction between the binder and the lattice. One can extend this to the HTPB system using the semi-empirical package MOPAC (available at the Kirkland supercomputing center) which has the same point charge lattice option available to it, refered to as "sparkles".

To understand the most probable conformation of HTPB, one can apply the same considerations as is used in the Ising model (7) to develop a statistical distribution understanding of conformational energies and associated geometry. This has been done by Paul Flory (20). His methodology is one of picking the energetically accessible energy minima to characterize the entire potential surface available to the torsional states of a polymer. The approximation of nearest neighbor interactions along the polymer chain is in direct analogy with the one dimensional Ising model. The number and relative energies of the torsional potential minima (rotational isomeric approximation) determine the dimension and statistically weighted values of the matrix representing the partition function of the monomer unit of a polymer. Once the partition function is created, all thermodynamic

values are accessible as well as average length of the polymer and its spacial distribution (hence the configuration). Through experimental methods of light scattering and viscosity, one can infer the second moment of the chain length (i.e., $<r^2>$, the average squared end-to-end length of the polymer). From this one has some bench mark calculations to perform to see if the approximation scheme has validity. With this sort of conformational analysis along with the information as to interactions between the polymer with itself and with the AP surface, the range of expected binding configurations should be more limited.

IV.   RECOMMENDATIONS

The basic outline of attack is laid out. There exists a problem both of technical interest as well as theoretical interest. The accomplishments of this summer lie in the generation of enthusiasm over the solution to this problem of adhesion. The tools of computational chemistry are available for use in this novel problem and we have begun to use them. Specifically, I would recommend the pursuit of the analysis of the prototype systems in order to gauge the important aspects of the large molecular problems posed by the HTPB interface with the AP crystal. The development of the "static" statistical mechanical picture in conjunction with the classical dynamics picture that CHARMM (for instance) can provide will undoubtedly provide insights into the query of "What is adhesion?". The purchase of a graphics workstation along with the molecular modeling software that aids in "seeing" the results of the dymanics simulation will provide a powerful tool in the elucidation of this problem. There are experiments that probe the surface interactions of the binder with the oxidant. These must be investigated as well. Experiment and theory must develop together if proper grounding of theory in experiment and guidance of experiments through theory are to emerge.

Table I

Experimental data summary of NH_4ClO_4

Crystallographic data[a]

Madelung constant	3.3134	
Electrostatic energy	149.4 kcal/mole	
Total lattice energy	143.8 kcal/mole	
Average Cl--O radius	1.86 Angstroms	

	Goldschmidt radius	Polarizabilities
NH_4^+	1.43 Angstroms	2.00 Angstroms^3
ClO_4^-	2.36 Angstroms	5.09 Angstroms^3
ClO_4 charge	-0.34	

Thermodynamic data[b]:

$\Delta H^o_{f,298}$	-70.6 kcal/mole
$\Delta S^o_{f,298}$	-165.93 cal/mole-K
$C_{p,298}$	30.61 cal/mole-K

Infrared and Raman Spectroscopic Data[c]:

mode symmetry	NH_4^+	ClO_4^-
A_1	3213 cm^{-1}	937 cm^{-1}
E	1685 cm^{-1}	463 cm^{-1}
T_2	3268 cm^{-1}	1078 cm^{-1}
T_2	1410 cm^{-1}	633 cm^{-1}

Rotational Barrier of NH_4^+ in NH_4ClO_4[d]:   0.4 kcal/mole

(a) see reference 13
(b) see reference 14
(c) see reference 15
(d) see reference 15 and 19

Table II

Summary of CADPAC SCF geometry optimization calculation of ClO_4^- using 631G* basis plus an f orbital basis on Cl

Atomic Populations

		charge
Cl	15.41143	+1.58857
O	8.64714	-0.64714
O	8.64714	-0.64714
O	8.64714	-0.64714
O	8.64714	-0.64714

Molecular Geometry (Angstroms)

atom pair	calculated	experimental[a]
Cl--O	1.439	1.445
O--O	2.350	2.360

Harmonic Frequencies

mode	calculated frequency (cm^{-1})	experimental[b] frequency (cm^{-1})
A_1	1033	935
E	494	462
T_2	1247	1102
T_2	692	628

(a) the averaged Cl--O and O--O bond distances in reference 18
(b) see reference 15

REFERENCES

(1) Charles L. Brooks III, Martin Karplus and B. Montgomery Pettitt, <u>Proteins:</u> <u>A Theoretical Perspective of Dynamics, Structure, and Thermodymanics,</u> Advances in Chemical Physics, Volume LXXI, New York, New York, John Wiley and Sons, 1988.

(2) R. L Shoemaker, J.A. Stark and R.E. Taylor, "Thermophysical Properties of Propellants", <u>High Temperatures-High Pressures,</u> 1985, Volume 17(4), pp. 429-35.

(3) K. Kishore, S. Sankaralingam, A.S. Begum, "Changes in the Calorimetric Value and Ignition Temperature of Composite Solid Propellants During Aging", <u>Deflagration Science Journal,</u> 1986, Volume 36(4), pp. 425-8.

(4) K. Hori, A. Iwama and T. Fukuda, "On Adhesion Between Hydroxyl-Terminated Polybutadiene Fuel Binder and Ammonium Perchlorate". <u>Propellants, Explosives and Pyrotechnics,</u> 1985, Volume 10(6), pp. 176-80.

(5) R. Sanden, "Rheological Properties of Composite Powder With Hydroxyl-Terminated Polybutadiene as Bonding Material", <u>Science and Technology Aerospace Report,</u> 1979, Volume 17(9), pp. 1-82

(6) K. Hori, T. Fukuda and A. Iwama, "Interfacial Chemistry Between Ammonium Perchlorate and Hydroxyl-Terminated Polybutadiene Fuel Binder", <u>Kogyo Kayaku,</u> 1987, Volume 48(2), pp. 65-70.

(7) D. Chandler, <u>Introduction to Modern Statistical Mechanics,</u> Chapter 5, Oxford University Press, New York, New York, 1987.

(8) C.E. Dykstra, "Stuctures and Frequencies of Small Water Complexes From Electrical Molecular Mechanics", <u>Journal of Chemical Physics,</u> 1989, Volume 91(10), pp. 6472-76.

(9) A.G. Csaszar, G. Fogarasi and J.E. Boggs, "Theoretical Prediction of the Vibrational Spectrum, Geometry and Scaled Quantum Mechanical Force Field for Phenylacetylene", <u>Journal of Physical Chemistry,</u> 1989, Volume 93, pp. 7644-51.

(10) K.B. Wiberg and K.E. Laidig, "Barriers to Rotation Adjacent to Double Bonds. 3. The Barrier in Formic Acid, Methyl Formate, Acetic Acid and Methyl Acetate. The Origin of Ester and Amide Resonance", Journal of the American Chemical Society, 1987, Volume 109, pp. 5935-43.

(11) G.C. Maitland, M. Rigby, E.B. Smith and W.A. Wakeham, Intermolecular Forces, Oxford University Press, New York, New York, 1981.

(12) N.L. Allinger, S. H.-M. Cheng, D.H. Glaser and H. Honig, "An Improved Molecular Mechanics Force Field for Alcohols and Ethers", Israel Journal of Chemistry, 1980, Volume 20, pp.51-56.

(13) H.D.B. Jenkins and K.F. Pratt, "Single Ion Properties by Lattice Energy Minimization", Journal of the Chemical Society Faraday II, 1977, Volume 73, pp. 968-81.

(14) E.F. Westrum, Jr. and B.H. Justice, "Molecular Freedom of the Ammonium Ion. Heat Capacity and Thermodynamic Properties of Ammonium Perchlorate From 5 - 350 K", Journal of Chemical Physics, 1969, Volume 50, pp. 5083-87.

(15) T. Chakraborty, S.S. Khatri and A.L. Verma, "Temperature-Dependent Raman Study of Ammonium Perchlorate Single Crystals: The Orientational Dynamics of the NH_4^+ Ions and Phase Transitions", Journal of Chemical Physics, 1986, Volume 84(12), pp. 7018-27.

(16) E.D. Simandiras, J.E. Rice, T.J. Lee, R.D. Amos and N.C. Handy, "On the Necessity of f Basis Functions for Bending Frequencies", Journal of Chemical Physics, 1988, Volume 88(5), pp. 3187-95.

(17) N.C. Handy, J.F. Gaw and E.D. Simandiras, "Accurate Ab Initio Prediction of Molecular Geometries and Spectroscopic Constants, Using SCF and MP2 Energy Derivatives", Journal of the Chemical Society, Faraday Transactions 2, 1987, Volume 83(9), pp. 1577-93.

(18) H.G. Smith and H.A. Levy, "Neutron Diffraction Study of Ammonium Perchlorate", Acta Crystallography, 1962, Volume 15, pp. 1201-4.

(19) P.S. Leung, T.I. Taylor and W.W. Havens, Jr., "Studies of Phase Transitions in Ammonium Salts and Barriers to Rotation of Ammonium Ions by Neutron Scattering Cross-Sections as a Function of Temperature", Journal of Chemical Physics, 1968, Volume 48(11), pp. 4912-18.

(20) P. Flory, Statistical Mechanics of Chain Molecules, John Wiley Interscience Publishers, New York, New York, 1969.

1990 USAF-UES SUMMER FACULTY RESEARCH PROGRAM

GRADUATE STUDENT RESEARCH PROGRAM

Sponsored by the

AIR FORCE OF SCIENTIFIC RESEARCH

Conducted by the

Universal Energy Systems, Inc.

FINAL REPORT

Design and Analysis

of Reaction Wheel Actuators for ASTREX

Prepared by:	Tom C. Pollock and Johnny E. Hurtado
Academic Rank:	Assoc. Professor and Graduate Student
Department and	Aerospace Engineering Department
University:	Texas A & M University
Research Location:	Astronautics Laboratory
	Edwards AFB, CA 93523
USAF Researcher:	Alok Das, Ph.D.
Date:	September 21, 1990
Contract No:	F49620-85-C-0013

Design and Analysis

of Reaction Wheel Actuators for ASTREX

by

Tom C. Pollock and Johnny E. Hurtado

ABSTRACT

Reaction wheel actuators have been designed for the ASTREX experimental article. The reaction wheel torquers are PMI servodisc motors outfitted with reaction wheels. The type JR25 series will be employed to provide controlled fine point maneuvering while a JR16 series will be used to actively suppress vibration of the structure. Software has been written that aid in the design and analysis of reaction wheel torquers. *Designer* helps to design and size the reaction wheel. *Analyst* helps to analyze the response of the motor and wheel pair in the time domain. *Myfrf* is a Matrix$_x$ executable function which analyzes the response of the motor and wheel pair in the frequency domain. User guides have been written which explain the input to the codes and their algorithms. In addition, the necessary mounting brackets have been designed and documentation regarding the assembly of the reaction wheel actuators has been provided.

Acknowledgements

We wish to thank the Air force Systems Command, the Air Force Office of Scientific Research, and the VSSS of the Astronautical Laboratory at Edwards AFB for sponsorship of this research. Universal Energy Systems must be mentioned for their help to us in all administration aspects of this program.

Our experience was rewarding and enriching because of many different influences. Dr. Alok Das provided us with support and an enjoyable working atmosphere. The help of Angel Cruz in overcoming many technical roadblocks is appreciated.

I. INTRODUCTION

Recently, there has been a continued growing interest in the control of Large Space Structures (LSS). Often, control is meant to include enabling these structures to perform fine point maneuvering and active vibration suppression. Two types of actuators used in providing control are cold gas thrusters and reaction wheel torquers.

The Astronautics Laboratory of Air Force Systems Command (AFSC) has recently completed construction of the Advanced Space Structures Technology Research Experiments (ASTREX) facility. ASTREX is to serve as a testbed for validating and integrating emerging space structure technology in fine point maneuvering and vibration suppression. The facility is unique as the nation's testbed for large-angle slewing and real-time vibration suppression of realistic space models because of several key features. These key features of ASTREX include its size, its spherical air bearing system, an advance real-time control computer, and a 3-mirror Space Based Laser (SBL) beam expander structure.

This report will begin with a statement of the objectives of this research effort. Next, sections discussing the approaches taken in realizing each of the listed objectives and their results follow. Finally, recommendations to this research effort will be given.

II. OBJECTIVES OF THE RESEARCH EFFORT

As suggested earlier, future mission performance of many LSS require that they be able to execute fine point maneuvering. And because these structures typically exhibit light structural damping, are very large and highly flexible, active control to suppress vibration following a maneuver will likely be required.

The primary goal of this research effort was to design reaction wheel torquers to provide fine point maneuvering and vibration suppression for the ASTREX experimental article. The design was to be complete. That is, appropriate DC motors and driving amplifiers were to be selected, reaction wheels were to be sized and designed, the response of the motor and wheel pair—the motor and wheel pair constitute a reaction wheel torquer—was to be analyzed, and any neccessary mounting brackets were to be designed.

The approach taken to completing each design stage listed above and the results of that approach is presented in the following sections.

III. COMPONENT SELECTION

a. The selection of adequate DC motors was largely based upon the rated torque that a motor was able to provide. It was estimated that for ASTREX to execute fine point maneuvering, 20 ft-lbs of torque about each axis would be necessary. For vibration suppression, an estimate of 2-3 ft-lbs of torque about each axis would be necessary. Also, motors which did not have any cogging associated with their performance were regarded as being more desirable. The amplifiers used to drive the motors would be based upon the motors themselves.

b. The PMI JR25 series and PMI JR16 series motors were selected for this research effort. The JR25 is able to provide roughly 10 ft-lbs of rated torque at 33 amps and 3000 rpm. Two of these motors in series would be able to provide the torque neccessary to execute fine point maneuvering. The JR16 is rated at 2.7 ft-lbs of torque at 9.55 amps and 3000 rpm. This motor would be able to provide the torque neccessary for actively suppressing vibration. Moreover, motors by PMI boast to be zero cogging because of their servodisc design. The suggested driving amplifier for the JR25 series motor is a model RXA 180-50-70 by PMI. A transformer (model T-125-10) and choke (model CH-35-70) accompany this model amplifier. For

the JR16 series motor, an AXA-180-10-30, also by PMI, is the suggested driving amplifier. This amplifier comes equipped with an internal transformer and choke (660 μ - Henry inductance).

With the motors and amplifiers selected, focus was then shifted to designing and sizing the reaction wheels. The motors would then be outfitted with these wheels resulting in a reaction wheel torquer.

IV. DESIGN OPTIMIZATION

a. In this section, we consider the approach taken to designing the wheels for the reaction wheel torquers. The software *Designer* was written to aid in this design. The power of *Designer* lies in its ability to conceive many wheels of different dimensions and then compare and contrast them in one sweep. The approach taken by *Designer* is outlined below. A user's guide to this software, which contains a more detailed algorithm, has been left with the VSSS at the Astronautics Laboratory.

With a motor selection having been made, there are certain motor constants and parameters which become important in designing the reaction wheels. A listing of constants and parameters (along with their units) is given below.

K_t : torque constant (oz in / amp)

K_b : back emf constant (volts / krpm)

R_t : terminal resistance (ohms)

K_d : viscous damping constant (oz in / krpm)

L_a : armature inductance (Henrys)

Irotor : inertia of the rotor (oz in sec^2)

maxacc : maximum no load acceleration (krad / sec^2)

shlen : motor shaft length (in)

shdia : motor shaft diameter (in)

diamh : diameter of the motor housing (in)

The particular constants and parameters which are important to this part of the design stage is a subset of this list.

To begin the design, a material for the wheel is chosen. Three equations are used in sizing the wheels. The first equation estimates a designing frequency while the other two equations compute the volume and inertia of a wheel 'piece'. I say 'piece' because the wheel is broken into components and the volumes and inertias of the components are calculated and summed.

For a DC motor modeled as a first order system, the time constant is given by

$$T = \frac{R_t J}{K_t K_b} \tag{1}$$

where J is the inertia of the wheel and rotor (oz in sec^2), and K_b has dimension volts / rad / sec. The cut-off frequency (or designing frequency) is then

$$\omega_{co} = \frac{1}{T} \ (rad/sec). \tag{2}$$

This frequency sets a particular moment of inertia (J) of the wheel and rotor.

By treating each component of a wheel as a ring, the volume and inertia of each component is calculated by

$$\text{Vol} = \pi t \left(R_2{}^2 - R_1{}^2 \right), \tag{3}$$

$$J = \frac{1}{2} \, mass \left(R_2{}^2 + R_1{}^2 \right) \tag{4}$$

where t is the thickness (in), R_2 is the outer radius (in) and R_1 is the inner radius (in). Mass is simply the product of the density and volume. Two basic wheel geometries are offered in *Designer*. These are a rimmed and a disk wheel. The disk wheel consists of a hub and disk, while the rimmed wheel consists of a hub, web, and rim. The two wheel geometries are shown below

21-7
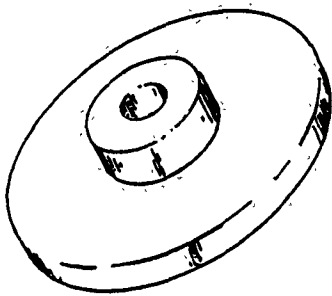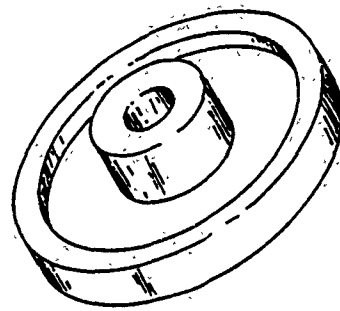
Fig.1a Disk Wheel   Fig.1b Rimmed Wheel

The approach taken is to consider the maximum and minimum values of particular dimensions which describe the wheels, and the number of perturbances desired. The inertias of the different wheels resulting from all the possible permutations of dimensions used to describe the wheels are then computed. After this, the list of possible wheels is reduced by throwing out those wheels whose inertias are smaller than that set by the design frequency. Following this reduction, the four wheels with the smallest inertias are retained, for they will result in frequencies closest to, but not greater than, the design frequency.

In the case that there is a 'better' wheel residing close to the four wheels remaining after the above pass, the program *Designer* investigates solutions in the range near each previous solution. A 'better' wheel is defined as one with an inertia closer to that as defined by the designing frequency. With this second pass we hope to locate any local mimima which might describe a more desirable wheel.

Only the 'best' wheel, as defined above, of each second pass is retained for the final output of the program. The output contains enough information so that a wheel selection can be made.

b. The results of executing *Designer* to design wheels for the two motors is presented here.

For the JR25 series motor, a design frequency of 8 Hz was used. The inertia of the resulting wheel for this frequency is 1.99 oz in sec^2. The designed wheel is a rimmed wheel of the following dimensions—all dimensions in inches.

Hub	inner dia	1.236	Web	inner dia	3.7
	outer dia	3.7		outer dia	11.6
	thickness	2.472		thickness	0.125
Rim	inner dia	11.6			
	outer dia	12.0			
	thickness	0.75			

For the JR16 series motor, a design frequency of 9.8 Hz was used. The inertia of the resulting wheel for this frequency is 0.25 oz in sec^2. The designed wheel is a disk wheel of the following dimensions—all dimensions in inches.

Hub	inner dia	.625	Disk	inner dia	1.875
	outer dia	1.875		outer dia	.475
	thickness	1.25		thickness	6

With the motor and wheel now known, we may discuss the response of the reaction wheel torquer to various commanded input.

V. DYNAMIC ANALYSIS of TORQUER RESPONSE

a. In this section, we consider the approach taken to analyzing the time response of the reaction wheel torquers to various commanded input. The software *Analyst* was written to perform this analysis. Because it is desirable to be able to drive a reaction wheel torquer in either voltage or current command, this software was written to accomodate the two modes. The approach taken by *Analyst* is outlined below. A user's guide to this software, which contains a more detailed algorithm, has been left with the VSSS at the Astronautics Laboratory.

The approach taken begins with noting that, as with *Designer*, certain motor parameters and constants become important when analyzing the time response of the torquer. Those that are important in this discussion are a subset of those parameters and constants already listed. The mathematical model of the wheel and motor pair is a coupled set of first order ordinary differential equations. The first equation relates the applied voltage to the armature current and motor shaft speed. This equation reads,

$$V = iR_t + L\dot{i} + K_b\omega \tag{5}$$

where V is the applied voltage (volts), L is the inductance of the armature and any choke in series with the motor (Henrys), i is the current through the armature (amps), and ω is the shaft speed (rad / sec). The second differential equation relates the torque produced to the shaft speed and reads

$$\text{Torque} = J\dot{\omega} + K_d\omega \tag{6}$$

where J is the inertia of the wheel and rotor (oz in sec^2). But the torque is related to the armature current by

$$\text{Torque} = K_t i, \tag{7}$$

thus

$$K_t i = J\dot{\omega} + K_d\omega. \tag{8}$$

Casting equations (5) and (8) into a state spaced form yields

$$\left\{ \begin{array}{c} \dot{i} \\ \dot{\omega} \end{array} \right\} = \left[\begin{array}{cc} -R_t/L & -K_b/L \\ K_t/J & -K_d/J \end{array} \right] \left\{ \begin{array}{c} i \\ \omega \end{array} \right\} - \left[\begin{array}{c} V/L \\ 0 \end{array} \right]. \tag{9}$$

Equations (9) represent those used when driving the motor in a voltage command mode. They may be integrated forward in time for a given applied voltage as a function of time to observe the time response of the current and wheel speed. For

analyzing the response due to an applied current as a function of time, we investigate Eq's (5) and (8). Equation (8) requires some rearranging to become

$$\dot{\omega} = \frac{K_i i - K_d \omega}{J}.$$ (10)

Equations (5) and (10) are those to be used for analyzing the response due to an applied current.

Note that when in voltage mode, the lead and lag characteristics of the motor and wheel pair may be obtained from analyzing the response to a sinusoidal input. The value by which the current leads or lags the commanded voltage is determined by noting the time at which these functions cross the zero axis. The bandwidth and system damping may be obtained from analyzing the response to a step input. The rise time of the motor and wheel is first determined. The rise time is determined by noting the time at which di / dt is zero. The bandwidth is then given by

$$B \, T_r = 0.3$$ (11)

where B is the bandwidth (Hz), and T_r is the rise time (sec). This equation is valid for systems in which the percent overshoot ($P.O.$) is small (less than 10%). In addition to the bandwidth calculation, the system damping is computed. First, the square of the natural frequency of the second order system is obtained from

$$\omega_n{}^2 = \frac{K_d R_t + K_t K_b}{J L}.$$ (12)

The damping coefficient is then computed from

$$C_f = \frac{K_d L + J R_t}{J L}.$$ (13)

The system damping factor is then

$$\zeta = \frac{C_f}{2\omega_n}.$$ (14)

Note that when in current mode, the lead and lag characteristics of the motor and wheel pair—with respect to a commanded currrent—may be obtained from analyzing the response to a sinusoidal input. The value by which the voltage leads or lags the commanded current is determined in two ways. The first method investigates the zero crossings of the functions. A second method is necessary because the voltage signal may be biased and thus a 'zero crossing' is no longer valid. The second method compares the times at which the signals reach a minimum value.

The rise time and bandwidth calculation is not performed if the commanded current is a step. Analyzing the response of the motor and wheel pair subject to this type of input is done mostly to observe $V(t)$ and $\omega(t)$ for a 'bang-bang' type of commanded torque.

b. The time response of the JR25 and JR16 series motors outfitted with their respective designed wheels is discussed below.

As mentioned earlier, the JR25 series motor was selected to enable the AS-TREX structure to perform fine point maneuvering. Recall that the designed wheel for this motor is a rimmed wheel with a inertia of 1.99 oz in sec^2. The results from *Analyst* suggest that the bandwidth of this reaction wheel torquer is 19 hertz. Also, the apparent operating range is from 5 to 21 hertz. We define the operating range as the range of frequencies for which the lead or lag angle is less than 45 degrees. This operating range and bandwidth seem suitable for enabling ASTREX to perform fine point maneuvering. The system damping for this second order model is 0.7052. For a typical second order model, the suggested damping factor os 0.7071.

Recall that the JR16 series motor was selected to actively suppress vibration of the ASTREX test article. The designed wheel for this motor is a disk wheel with an inertia of 0.25 oz in sec^2. For this reaction wheel torquer, the results from *Analyst* suggest that the bandwidth is 125 hertz. The apparent operating range is from 9.5 to 206 hertz. This range and bandwidth seem suitable for suppressing many high

frequency vibrations following a maneuver. This system is over damped, for the system damping factor is 2.39.

Shown below are graphs reflecting the output of *Analyst* for the two reaction wheel torquers. Figure 2a shows the response of the JR25 series motor and wheel pair when subjected to a sinusoiudal *voltage* commanded input of 10 hertz. Note that the current leads the voltage at this frequency by 10.7 degrees. Figure 2b shows the response of the JR16 series motor and wheel pair when subjected to a sinusoiudal *current* commanded input of 100 hertz. At this frequency, the current lags the voltage by 16.9 degrees. These two figures are typical output of the software *Analyst*.
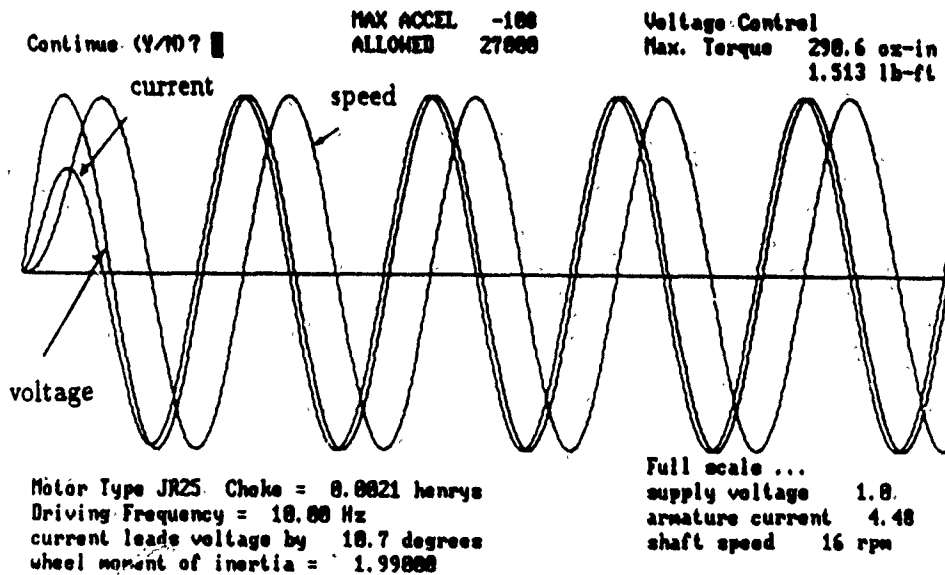

Fig.2a Time Response (JR25)
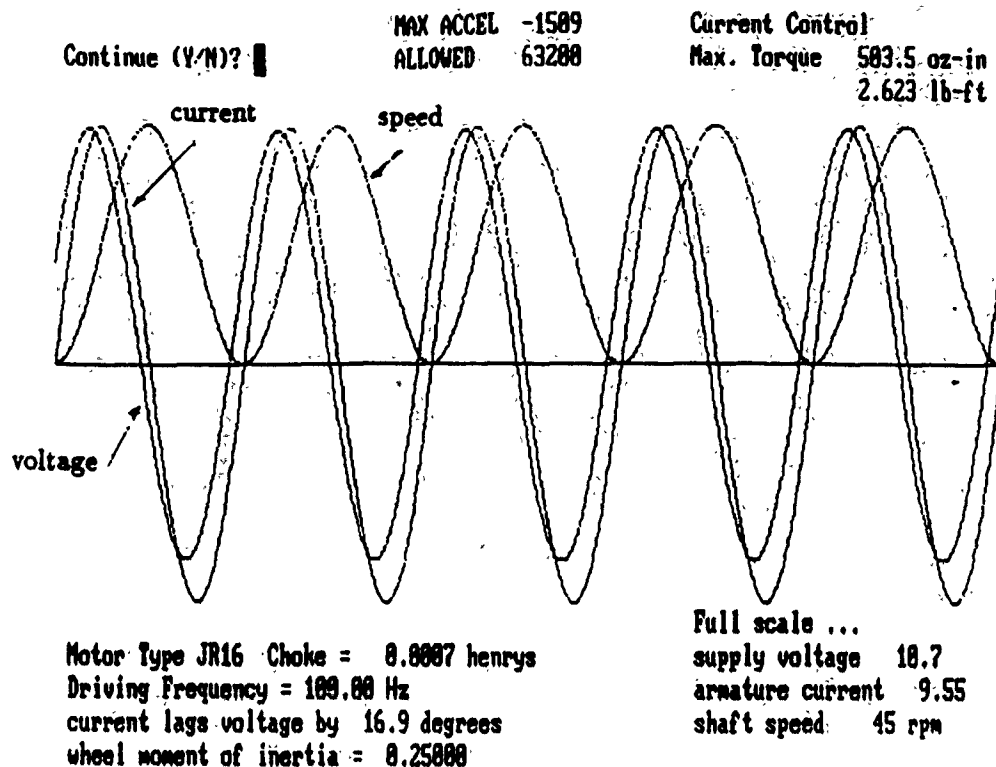
Fig.2b Time Response (JR16)

In the next section, we introduce the frequency domain analysis of the reaction wheel torquers.

VI. RESPONSE in the FREQUENCY DOMAIN

a. In this section we consider the approach taken to analyzing the frequency response of the reaction wheel torquers. The Matrix$_x$ executable function *Myfrf* was written to analyze the frequency response in a voltage commanded mode. The approach taken by *Myfrf* is outlined below. A user's guide to the function, which contains a more detailed algorithm and explaination, has been left with the VSSS of Astronautics Laboratory.

As with *Analysis* and *Designer*, certain motor constants and parameters are important in discussing this analysis. Again, the list of important constants and parameters is a subset of the list previously given. The state space model used in

21-14

this function is one in which the armature current and shaft wheel speed are the states, the applied voltage is the input, and the current is the output. That is,

$$\left\{ \begin{matrix} \dot{i} \\ \dot{\omega} \end{matrix} \right\} = \left[\begin{matrix} -R_t/L & -K_b/L \\ K_t/J & -K_d/J \end{matrix} \right] \left\{ \begin{matrix} i \\ \omega \end{matrix} \right\} + \left[\begin{matrix} V/L \\ 0 \end{matrix} \right], \qquad (15)$$

$$i = \begin{bmatrix} 1 & 0 \end{bmatrix} \left\{ \begin{matrix} i \\ \omega \end{matrix} \right\}. \qquad (16)$$

Here, i is the current through the armature (amps), ω is the shaft speed (rad / sec), J is the inertia of the reaction wheel and rotor (oz in sec^2), L is the inductance of the armature and any choke in series with the motor (Henrys), and V is the applied voltage (volts). Note that in Eq.(15), K_b and K_d are expressed in terms of radians per second and not in krpm. Basically, *Myfrf* takes the state spaced model and computes the frequency response over a user specified range of frequencies. The input to the function includes the inertia of the reaction wheel, the inductance of any choke in series with the motor, the maximum frequency (Hz) of the desired range, and a 6 × 1 vector containing certain motor constants. The output of the function includes plots and data of the absolute value of the response, the gain (db), and the phase (degrees) as functions of frequency. The series of commands issued to execute the function *Myfrf* are given in the user's guide.

Shown below are graphs reflecting the output of *Myfrf* for the two reaction wheel torquers. Figure 3a shows the phase portrait of the JR25 series motor and wheel pair. These phase portraits are useful because the bandwidth of the reaction wheel torquers are readily obtained. Note that the operating range of the JR25 series motor and wheel pair agrees with the results obtained in *Analyst*. Similarly, figure 3b shows the phase portrait of the JR16 series motor and wheel pair. Again, note that the operating range of the JR216 series motor and wheel pair agrees with the results obtained in *Analyst*. These two figures are typical output of the function *Myfrf*.
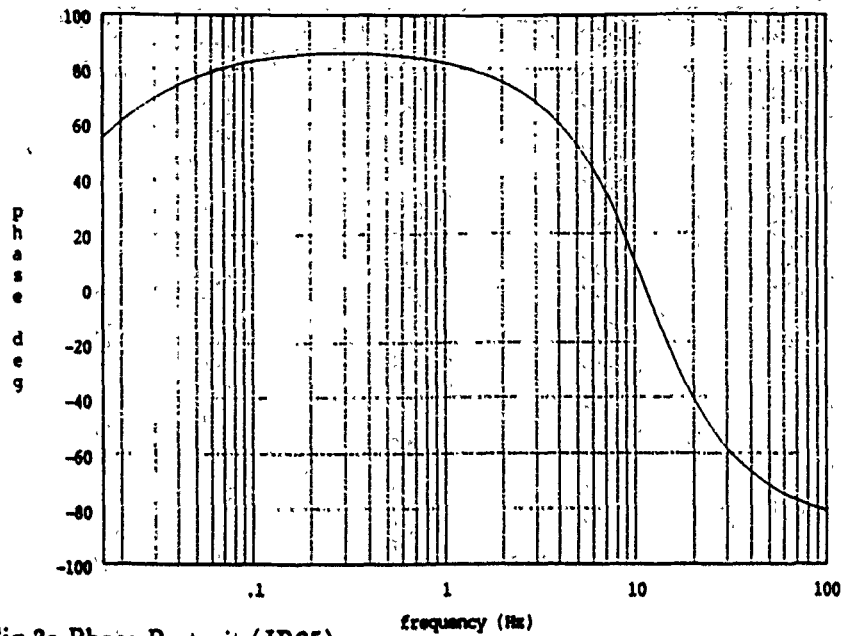
Fig.3a Phase Portrait (JR25)

frequency (Hz)
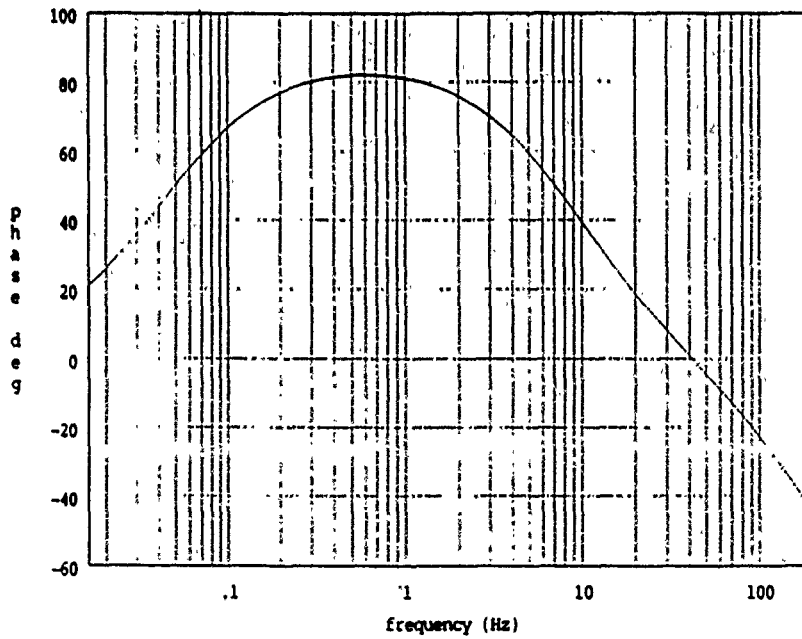
Fig.3b Phase Portrait (JR16)

In the next section we discuss the final design stage of the reaction wheel torquers.

VII. FINAL DESIGN of TORQUERS

In this section we present a brief description of the final designed reaction wheel

torquers. We include drawings of the final wheels and necessary mounting brackets. Detailed drawings of all parts and a *thorough* discussion of the assembly procedure is outlined in a design document left with the VSSS at the Astronautics Laboratory.

The final designed wheels for the reaction wheel torquers are shown below. Note that these figures show mounting hubs and plates designed to attach the wheel to the the motor shaft.
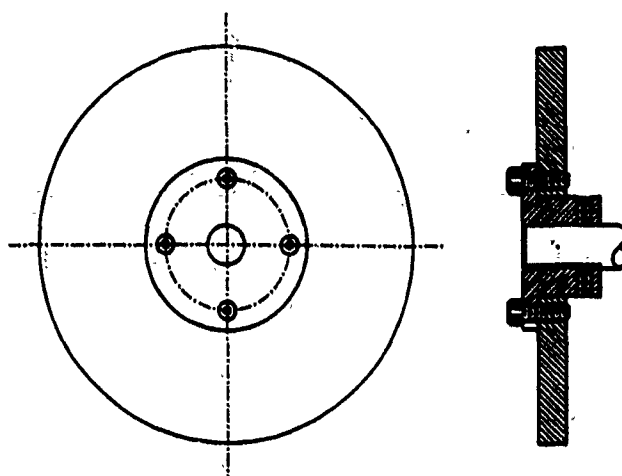
Fig.4a Small Wheel (JR16)
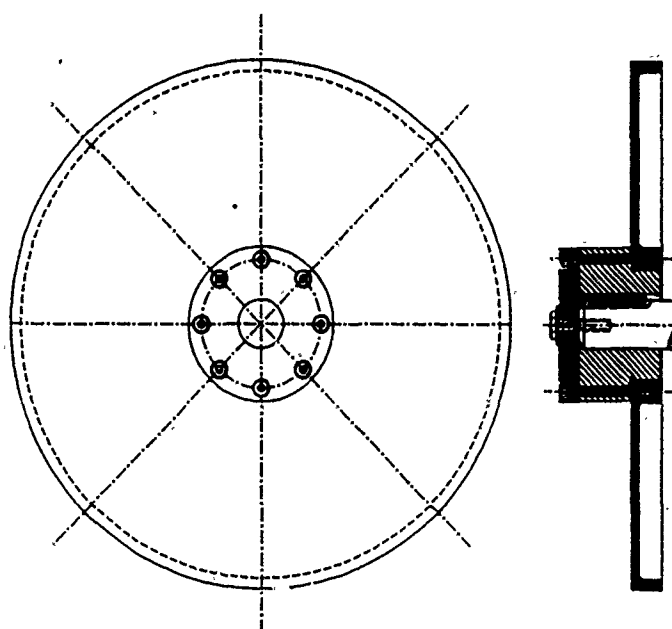
Fig.4b Large Wheel (JR25)

The figures below show a typical mounting base and the designed small torquer assembly mounted on the secondary mirror of ASTREX.
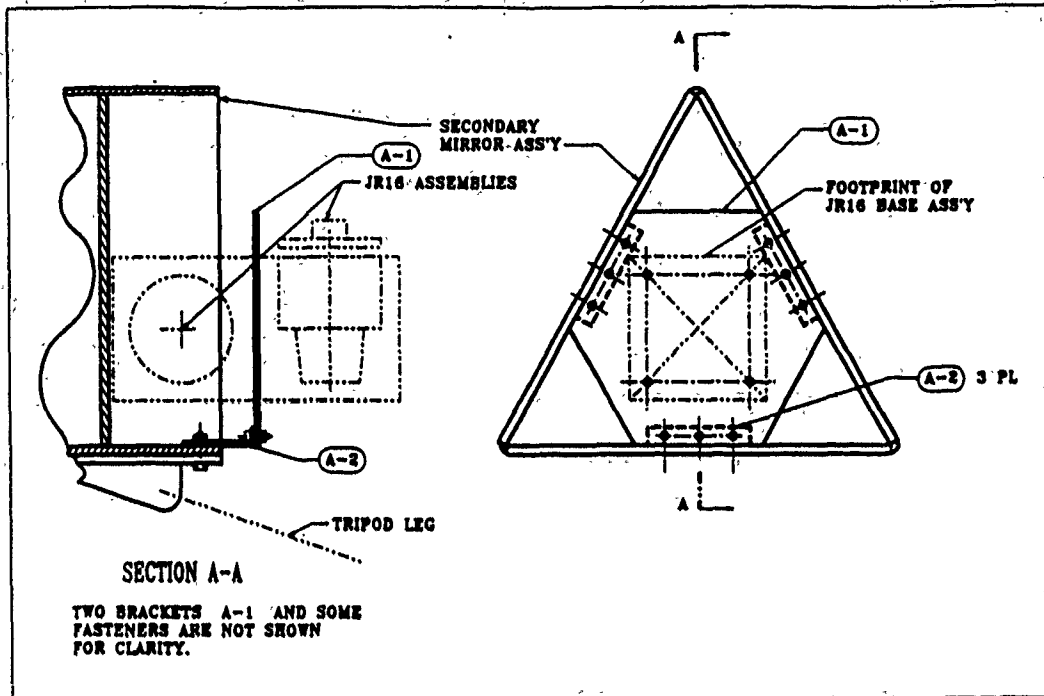

Fig.5a Small Torquer Assembly Mounted on Secondary Mirror
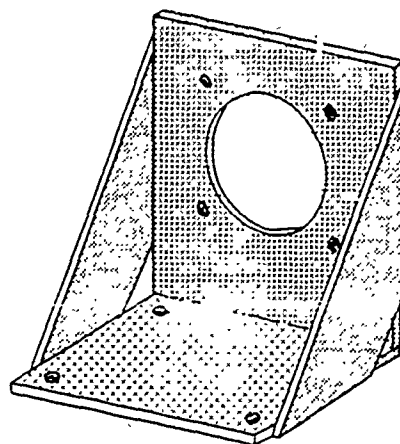
Fig.5b Typical Base

VIII. SUMMARY

A complete design of reaction wheel torquers for the ASTREX experimental article has been performed. The reaction wheel torquers were designed to enable ASTREX to perform fine point maneuvers and actively suppress vibration. Software was written to aid in the design and analysis of the torquers. Complete documentation of the software and assembly procedure has been left with the VSSS at the Astronautics Laboratory, Edwards AFB.

IX. REFERENCES

[1]Van de Vegte, J., *Feedback Control System*, Prentice-Hall, Inc., Englewood Cliffs, N.J., 1990.

[2]Bogart, T.F., *Laplace Transforms and Control Systems Theory for Technology*, John Wiley & Sons, New York, 1982.

1990 USAF-UES SUMMER FACULTY RESEARCH PROGRAM

GRADUATE STUDENT RESEARCH PROGRAM

Sponsored by the

AIR FORCE OFFICE OF SCIENTIFIC RESEARCH

Conducted by the

Universal Energy Systems, Inc.

FINAL REPORT

Component Design for the Multi-Body

Dynamics Experiment

Prepared by:	Roger C. Thompson, Ph.D.
Academic Rank:	Assistant Professor
Department and	Aerospace Engineering
University:	The Pennsylvania State University
Research Location:	Astronautics Laboratory/VSSS Edwards AFB Edwards, CA 93523
USAF Researcher:	Alok Das, Ph.D.
Date:	30 October 1990
Contract No:	F49620-88-C-0053

Component Design for the Multi-Body

Dynamics Experiment

by

Roger C. Thompson

ABSTRACT

An experimental facility is currently under development for the study of the behavior of multi-body systems. In the initial phase of the project, the operational characteristics were established and the parameters for the design of the components were determined. Conceptual outlines for the structure, interconnections of the components, and the complete design and specification of the elements were to be achieved during this phase of the project. A detailed layout of the experiment was produced such that individual components could be sized for the final design and fabrication. Several problems were encountered in finding suitable components due to the high performance requirements set for the facility. The drive units have been specified for the shoulder and elbow joints, and the mounting system for the shoulder motor was completed. Additional tests were performed on the air cushion flotation system because the mass of the elbow structure will be substantially higher than predicted by the initial estimates. An analysis of the performance of the structure with larger mass elements was completed; from the results, it was determined that the frequencies of the structural vibrations would be shifted in range, but the frequency spread would not change significantly. The flexible elements can be scaled such that the first mode frequency remains the same (0.5 Hz).

Acknowledgements

I wish to thank the Air Force Office of Scientific Research/Air Force Systems Command for sponsoring the Summer Faculty Research Program under which this research was performed. The summer program is extraordinarily beneficial to faculty because it promotes technical exchange with Air Force researchers and provides exceptional facilities for conducting ground-based experiments. In addition, I wish to thank Universal Energy Systems for managing this program and for their direction and assistance.

I wish to acknowledge the guidance and support provided by Dr. Alok Das who served as my Technical Focal Point. His advice and assistance are greatly appreciated. I also wish to acknowledge the assistance provided by Mr. Waid Schleagel in the computational analyses completed as part of this project. Finally, I wish to thank Ms. Sandra Scrivener for her assistance in completing this report.

I.   INTRODUCTION:

The principal mission of the Astronautics Laboratory is to investigate and verify concepts that will be employed in future space vehicles. Therefore, the Vehicle Systems branch of the Astronautics Laboratory is acutely aware of the need for a thorough analysis of the behavior, modeling, and control methodologies to be applied to large flexible spacecraft. Consequently, the Astronautics Laboratory is developing a wide variety of experimental research facilities for testing concepts and components that will be an integral part of the future technology for spacecraft in general and large space structures in particular. Among these facilities is an experiment in dynamic interaction of multiple bodies connected by flexible components. The simplest structure that displays the behavior associated with multi-body dynamics is a two-link flexible manipulator, and this is what has been chosen for the new facility.

Because the environment of space cannot be duplicated on the Earth's surface, experiments have been designed to examine very specific subsystems or simplified motions. Typical test articles have typically consisted of simple structures such as a rigid central body with flexible elements attached, not multi-body structures. Examples of these simpler experiments supported by the Astronautics Laboratory include the Draper/RPL experiment and the JPL Antenna experiment. The Multi-Body Dynamics Experiment is the latest entry in a steady progression of research efforts aimed at developing new technology in predicting and controlling flexible vehicles. Other recent experiments (Refs. 1-3) in flexible manipulators are true multi-body structures, but the purpose of the experiments is to control the flexibility of manipulators alone. The facility

at the Astronautics Laboratory will be used to investigate the fundamental behavior of multi-body spacecraft.

The initial phase of the experiment design has been completed (Refs. 4-5); the conceptual configuration of the apparatus is known, and the baseline operational parameters have been determined. The second phase of the project is to design the structural components such that the projected characteristics of the experiment can be achieved. The nature of the multi-body behavior is that the motions of each component interact with all of the other elements in a complex, and difficult to predict, fashion. Consequently, the design of the experimental structure must be accomplished in parallel; each component cannot be specified separately because it will affect and be affected by the design of the other components. This iterative process is the second phase of the project, and the assembly of the research facility is the final phase.

My research interests are in dynamics and control of large flexible structures. Although most of my research is analytical in nature, I am very interested in developing an active program of experimental research in dynamics and control. My background, which includes industrial experience in machine design and fabrication was a contributing factor in my assignment to this project. The association with related Air Force research facilities and personnel will assist the formation of experimental research capabilities at the Pennsylvania State University. The objective is to provide an experimental program that will complement similar research programs at the Astronautics Laboratory.

II. OBJECTIVES:

The objective of the Astronautics Laboratory is to produce a suitable mechanism for various studies in multi-body dynamics. The simplest apparatus that exhibits the dynamic behavior common to multi-body structures is a two-link flexible manipulator. It is a structure on which many different experiments (with different goals) can be accomplished. The long-term goal for the project is to test all aspects of multi-body behavior. Individual topics to be examined will include, but not be limited to, coupled motions, sensor/actuator dynamics, control/structure interaction, and time-optimal control technology.

The objective of the 1990 Summer Faculty Research Program (SFRP) was to develop the specifications and detailed design of the components that make up the Multi-Body Dynamics Experiment. Because the overall dynamic behavior of the structure is dependent upon the interactions between each element, the baseline structure design must be iteratively refined until complete specifications are achieved. A more typical approach, in which each component is developed separately would not be as effective as the parallel process that was adopted.

The estimated date for completion of the experiment extends beyond the ten week period allotted to the SFRP. Therefore, the design process will be completed at the Pennsylvania State University, and the experiment should be operational by the end of 1990.

III. BASELINE CONFIGURATION:

The Jet Propulsion Laboratory determined estimates of the global operational characteristics of the Multi-Body Dynamics Experiment based upon the criteria established by the Astronautics Laboratory (Ref. 4). In the preliminary design report, the authors proposed that the structure be supported on a cushion of air above a highly polished, extremely flat and level granite table (Fig. 1). The air cushion will reduce frictional forces to a minimum and simulate the free motion in a plane. A summary of the original system performance criteria are:

Flexible arm length:	1 m	Beam mass:	0.5 kg
First mode frequency:	0.5 Hz	Shoulder motor torque:	31.4 Nm
Elbow motor torque:	6.2 Nm	Angular velocity:	3 rad/s
Angular displacement:	135°		

The baseline configuration was immediately altered to improve the capability of the apparatus. The angular displacement limit an the shoulder joint was discarded because it would hamper investigations of the coupled behavior of motions at high angular rates. The remainder of the design recommendations were accepted as the design criteria for the project.

IV.   COMPONENT DESIGN:

A. Shoulder/Elbow Joints

The majority of activity during the 1990 SFRP was in developing the shoulder and elbow joints. The operation of the experiment depends almost entirely upon the motorized hubs of the two-link manipulator. Each hub must rotate smoothly, with a prescribed torque, throughout the range of motions that are available. In addition, the mass of each joint must remain within assigned limits in order to maintain the dynamic characteristics of the experiment.

The combined constraints of low mass, small size, and high torque were difficult to achieve. The original concept for the structure included direct drive, frameless DC motors with hollow shafts. It was anticipated that the frameless, hollow-shaft style of motor would have substantially less mass and rotor inertia than is found in their framed, solid-shaft counterparts. After examining several manufacturer's catalogs, it was obvious that a motor with the required characteristics could not be found.

To achieve high torque at low speed, the magnetic field strength of a motor must be increased; more magnets must be used and/or the magnets must be larger and heavier. Consequently, the mass of the motor increases substantially for a modest increase in torque. A second disadvantage of the higher field strength is that the motor exhibits a motion at low speed known as "cogging." The ferrous rotor tends to align itself with the closest magnet and to resist being displaced from that alignment. Rather than rotating smoothly at a constant speed, for a constant voltage, the rotor slows as it leaves alignment with one magnet and speeds up as it approaches alignment with the next magnet. When

the motor voltage is reduced to zero, the rotor slows until it is again in alignment with a magnet; this motion may include a short reversal of direction as the rotor speed approaches zero.

Obviously, these characteristics are completely unacceptable for this experiment. The high mass of the motors alone (up to 20 kg) precludes their use in this experiment. Because the investigations to be performed with this structure will rarely require more than one revolution from a direct drive motor, cogging torques will be a significant problem; the flexible modes will be disturbed and precise positioning of the beams will not be possible. To reduce the mass and to achieve the desired torque, a gear reduction unit must be included. After an extensive search of manufacturer's literature on high reduction, low mass, and low backlash (freeplay) gear drives, only one acceptable model was found for each hub. Both motor units have zero cogging, and the continuous stall torque is equal to the maximum torque required for the experiment.

The mass of each motor is, however, higher than estimated in the original design criteria. It was then necessary to determine how the increased mass would affect the dynamic performance of the structure. A simple analysis, via the NASTRAN structural analysis program was performed; from the results, it is clear that the natural frequency spread was not widened for the 0.5 Hz design, but the modal frequencies for higher modes of the 1 Hz design were pushed intolerably high. Because the 0.5 Hz design was chosen as the target structure, the increased mass was deemed acceptable. Consequently, the two drive units were placed on order in July, 1990.

Selection of the motors solved most of the problems associated with the operation of the hubs; however, the size and shape of the gear reduction units presented an

additional problem. The gear reduction units are "harmonic" drives which are very accurate, have zero backlash, and they have low inertia. The diameter of the drives are within the size constraints for the test-bed, but the length is very disproportionate. If the shoulder motor were to be mounted "conventionally" on the surface of the table, as shown in Fig. 1, the shoulder hub would be very large with a large inertia, and the experiment would be subject to twisting torques from having the center of mass so far above the table. It became apparent that the shoulder motor must be mounted below the surface of the table. However, this required that a large center hole be cut into the table, and there was great concern that the granite table might be irreparably damaged by the heat and vibration from the drill. Nonetheless, the design requirements demanded that the motor be mounted below the table's surface, and this operation was performed successfully in late July, 1990. With this change in design, the center of mass of the components could be lowered nearer to the surface of the table and the shoulder hub size could be minimized. A diagram of the revised structure is shown in Fig. 2 indicating the individual elements of the structure and their relative connections.

B.   Air Flotation System

The increased mass of the elbow motor could present a problem for the air cushion flotation system; the largest mass lifted in the pad design test was 3.6 kg. The lifting capacity of the original test article was checked again for higher mass loadings, and the tests were carried out on the granite table to be used for the Multi-Body Dynamics Experiment. A 5.4 kg mass was successfully lifted without any modification to the pad design; larger mass loadings were not attempted because the 5 kg load should be larger

than the total mass of the elbow hub. It was observed that the pressure must be regulated carefully because too high a flow rate will initiate chatter in the plate. Miniature, in-line flow regulators can be placed in the air lines immediately before each pad to maintain a proper flow rate.

Although it was not necessary to modify the plate design to increase lifting capacity, the flotation pads could be altered to reduce their mass. The pressure required to lift 5.4 kg is less than 3 psi, so the flotation pads will not be subject to a measurable mechanical stress due to the pressure. Consequently, the modified pad design consists of a thin aluminum backplate, for stiffness and flatness, with an acrylic distribution plate bonded to the aluminum (Fig. 3).

C.   Miscellaneous Components

The remainder of the components to be specified are the hub elements that connect the flexible beams to the motors. At the close of the SFRP, preliminary sketches of these elements had been completed, but the work could not be finished until a method of attaching the hubs to the flotation pads could be found. The type of attachment would determine the height above the table for the hubs which, in turn, would dictate the dimensions of the hub elements. Ideally, the pads should be allowed to swivel relative to the hubs to maintain a uniform "contact" with the granite table in the event that the hubs were to "twist" out of plane due to the flexible torsion/bending coupling induced by the applied torques. Any tilt of the flotation pads would cause a loss of the air film, and the resulting friction would disturb the experiment. A spherical joint was needed that would swivel with low friction and allow the unrestricted passage of air. A suitable

swivel joint was not found before the end of the SFRP; however, the design work was continued at the Pennsylvania State University, and an acceptable ball joint was acquired in late September, 1990. As of the writing of this report, the design of the hub elements, being continued at Penn State, is nearing completion.

V.   RECOMMENDATIONS:

The Multi-Body Dynamics project is proceeding into the final stages. Many of the components have been designed and ordered; a few key components remain to be completed. The 1990 SFRP was very productive with regard to solving many of the potential problems associat d with meeting the performance demands of the experiment. Principal among these was the motor specifications, shoulder motor mounting configuration, dynamic response with higher mass values, and the flotation system scaling. The hub design is nearing completion through a continuation of the summer work at the Pennsylvania State University, and these components should be finished by mid-November, 1990. The completed specifications will be sent to the Astronautics Laboratory for fabrication. Final assembly should begin near the end of the year.

One element of the structure that has not been fully addressed is the rotary coupling. During the summer, the size of the coupling (number of terminals) needed for the experiment was determined and a product with excellent performance characteristics was found, but the cost of the rotary coupling was prohibitive. By reducing the performance of the device, the price may be brought within the range appropriate for this facility. An alternative to using a rotary coupling is to provide enough length in the sensor and elbow motor wiring to allow the structure to rotate a small number of times

(3-5) about the shoulder without binding or perturbing the experiment. At the end of each test, the structure would have to be "unwound." This alternative is not as attractive as using a rotary coupling, but the inconvenience would be partially offset by the cost reduction. At the very least, the wind/unwind approach could be used for a short period of time until a better solution is found.

At the conclusion of this project, the existence of the facility and its performance characteristics will be announced through the publication of paper(s) that describe the structure and the results of the initial experiments.

GRANITE TABLE

SHOULDER JOINT

TIP MASS

FLEXIBLE ARM

ELBOW JOINT
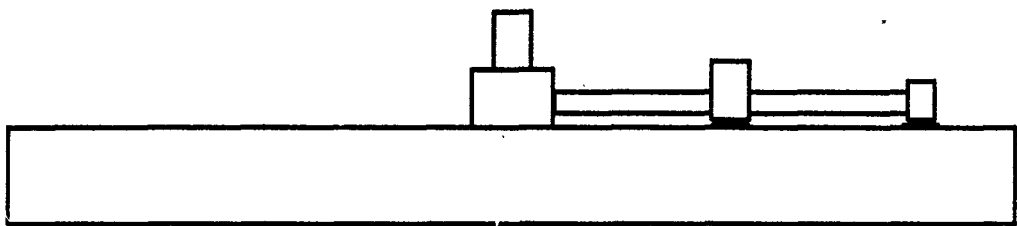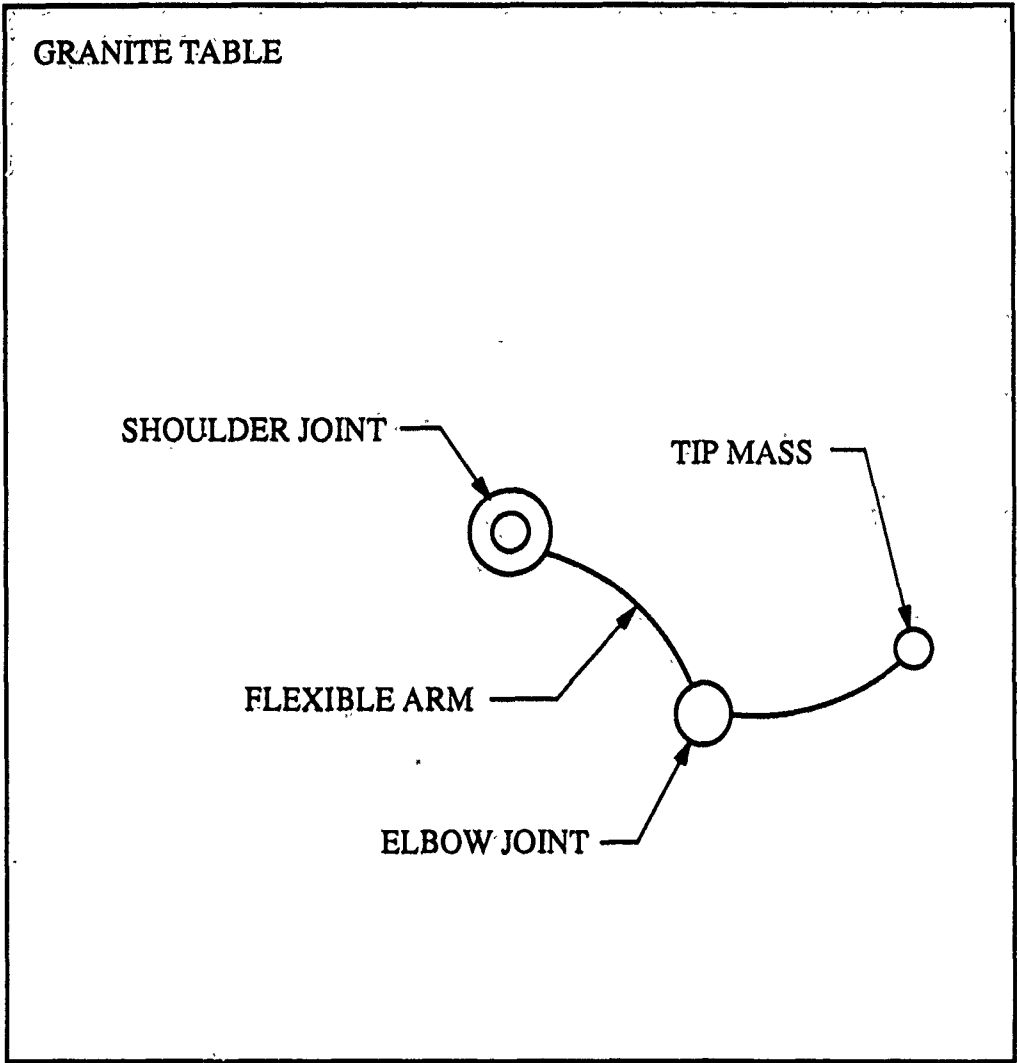
Figure 1   Baseline Configuration
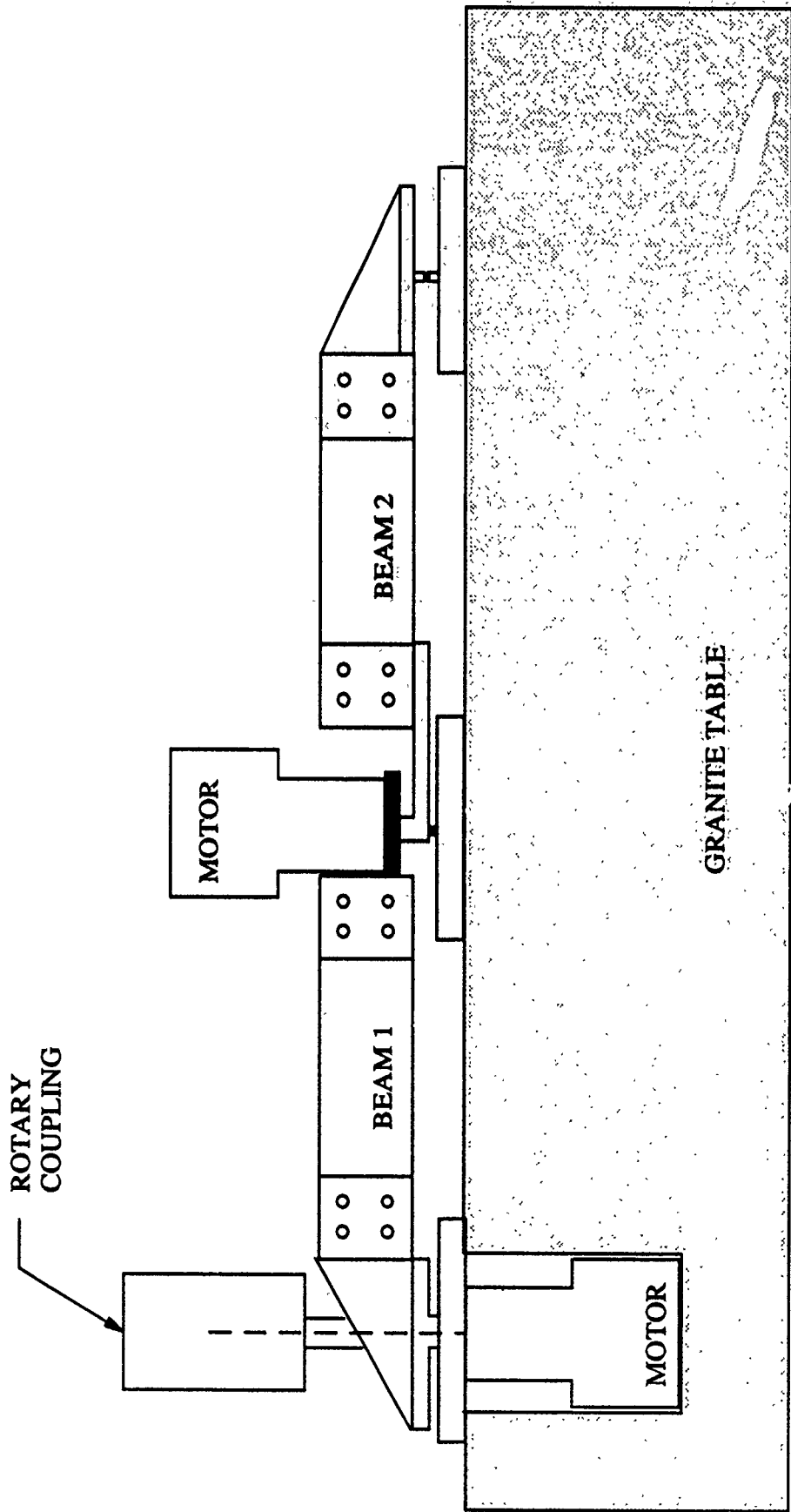
Figure 2 Current Configuration

Aluminum Baseplate

Acrylic Distribution Plate

12 Vent Holes

24 Vent Holes
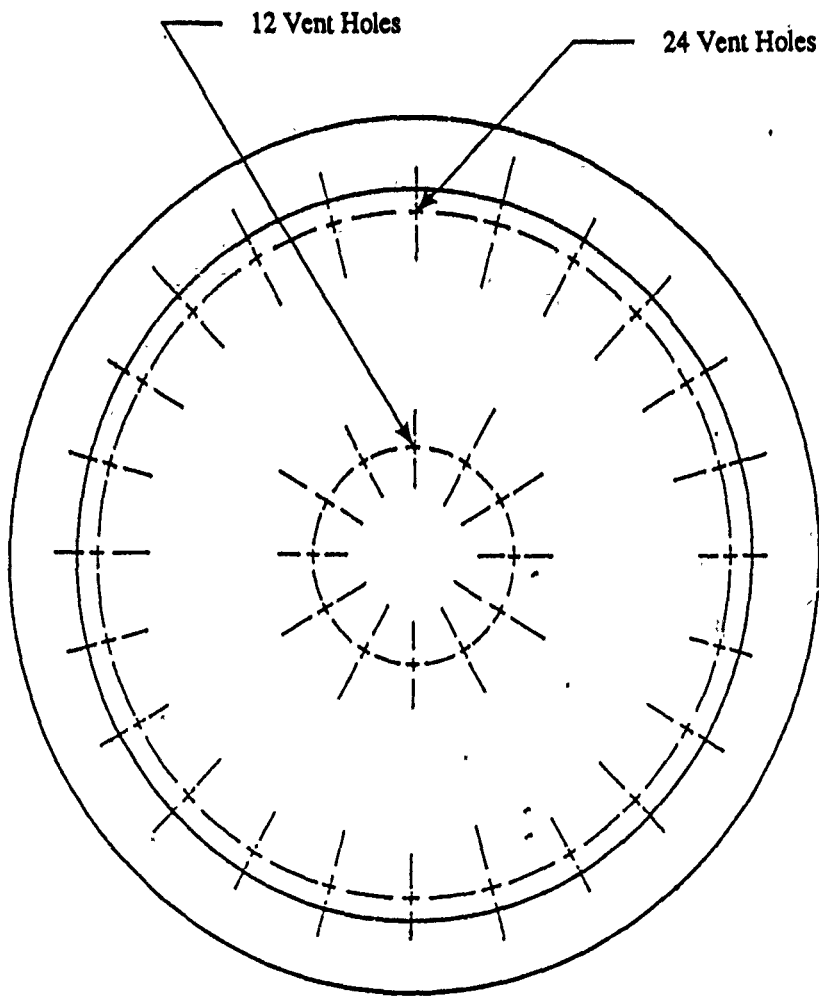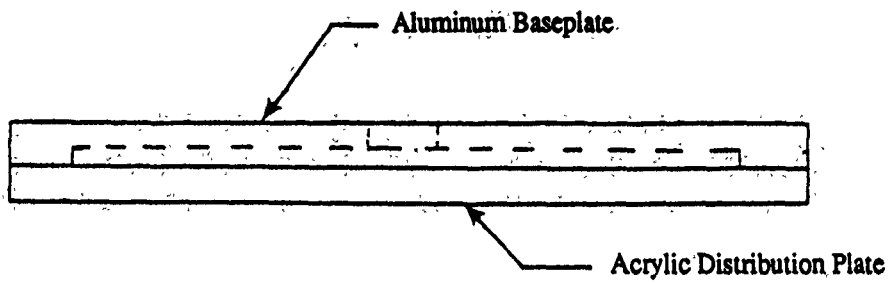
Figure 3 Flotation Pad

REFERENCES

1. Oakley, C. M. and Cannon, R. H., "Initial Experiments on the Control of a Two-Link Manipulator with a Very Flexible Forearm," Proceedings of the 1988 IEEE Robotics and Automation Conference, pp. 996-1002.

2. Buchan, K. S., Carusone, J., and D'Eleuterio, G. M. T., "RADIUS - A Laboratory Facility for the Study of the Dynamics and Control of Elastic Manipulators," Presented at the Seventh VPI&SU/AIAA Symposium on Dynamics and Control of Large Structures, Blacksburg, VA, May 8-10, 1989.

3. Schmitz, E. and Ramey, M., "A Simplified Dynamic Model for an Experimental Planar Manipulator with an Elastic Forearm," Presented at the American Control Conference, Pittsburgh, PA, June 21-23, 1989.

4. Scheid, R. E. and Schliesmann, R. G., "Multibody Dynamics Experiment: Requirements Definition and Preliminary Design," JPL Report No. JPL D-6472, May 30, 1989.

5. Thompson, R. C., "Design and Development of a Flexible Multi-Body Dynamics Experiment," Final Report to Universal Energy Systems, Contract No. F49620-88-C-0053, September, 1989.

1990 USAF-UES SUMMER FACULTY RESEARCH PROGRAM

GRADUATE STUDENT RESEARCH PROGRAM

Sponsored by the

AIR FORCE OFFICE OF SCIENTIFIC RESEARCH

Conducted by the

Universal Energy Systems, Inc.

FINAL REPORT

CONTROL DESIGN OF ASTREX TEST ARTICLE

Prepared by: Hung V. Vu, Ph.D., Assistant Professor

                    Joseph P. Baldonado, Graduate Student

                    Hung M. Nguyen, Graduate Student

Department and   Mechanical Engineering

 University: California State University, Long Beach, CA 90840

Research Location: Astronautics Laboratory / VSSS

                    Edwards AFB, CA 93523

USAF Researcher: Alok Das, Ph.D.

Date: September 20, 1990

Contract No: F49620-88-C-0053

CONTROL DESIGN OF ASTREX TEST ARTICLE

by

Hung V. Vu

Joseph P. Baldonado

Hung M. Nguyen

ABSTRACT

A scaled-down control system of ASTREX (Advanced Space Structures Technology Research Experiments) test article was successfully designed. The control system consisted of a scaled-down ASTREX test article, a PID (proportional-plus-integral-plus-derivative) controller, electrolytic tilt sensors, and stepper motors. MATRIX$_x$/SystemBuild and MAX_100 (products of Integrated Systems, Inc.) were used for real-time control. The results were satisfactory. It was found that in order to control the stepper motors effectively, the real-time controller must have sufficiently high sampling rate.

ACKNOWLEDGEMENTS

I. INTRODUCTION

Many flexible structures, such as flexible spacecraft and large space structures (LSS), have been designed using passive and active vibration control [1-2]. Active control, in particular, provides new powerful tool for the vibration engineer. Control-structure interaction (CSI), also called by various names, such as flexible structure control or structural control [1-6] is becoming increasingly important as the lightly damped structures require more precise and less tolerant to vibrations.

The Astronautics Laboratory of Air Force Systems Command (AFSC) at Edwards Air Force Base has recently completed construction of the ASTREX (Advanced Space Structures Technology Research Experiments) facility, which is a testbed for validating and integrating CSI technology [7].

The authors' research interests have been in the area of theory and application of CSI technology. As a result, there is a good match with the Astronautics Laboratory. The first author has been conducting research in CSI and teaching in the areas of structural dynamics and control, and the second and third authors are graduate students working towards their master's degrees in the above-mentioned fields.

II. OBJECTIVES OF THE RESEARCH EFFORT

An ASTREX test article (Fig. 1) has been constructed recently at the Astronautics Laboratory. The test article is supported near its center of gravity by a spherical air bearing. The air bearing, which provides full 3-axis rotational freedom to the test article, sits at the top of a test-article support system (Fig. 2). This system includes a double gimbal cable follower unit which is actively controlled to follow attitude motions of the test article.

Legend

1. Secondary mirror support
2. Tertiary mirror support
3. Primary mirror support
4. Rod assembly
5. Hub
6. Tracker
7. Propeller
8. Non-structural dead mass
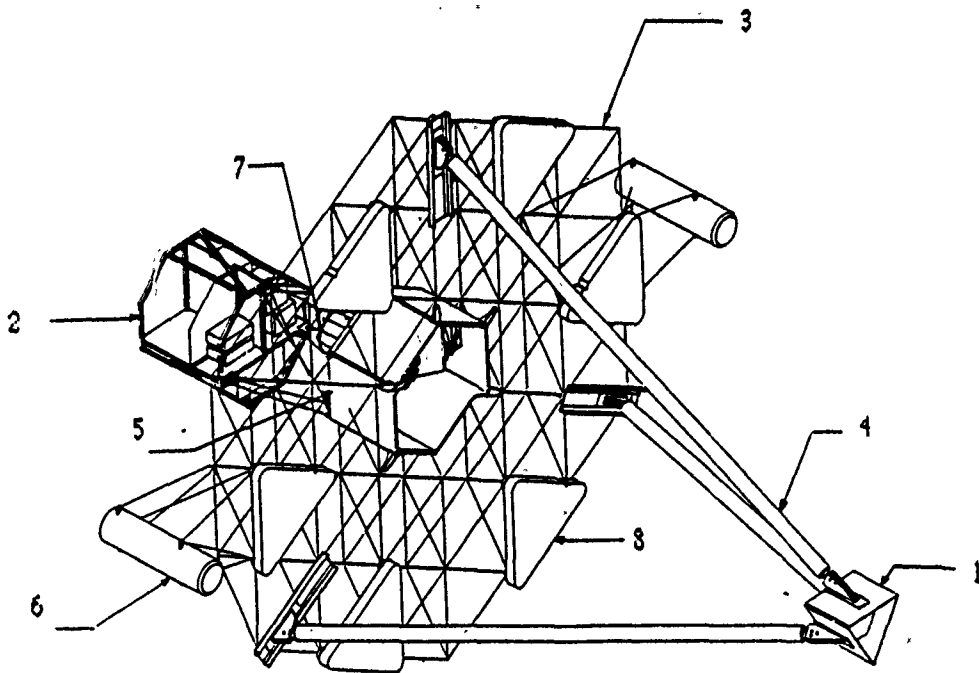
Fig. 1 ASTREX test article
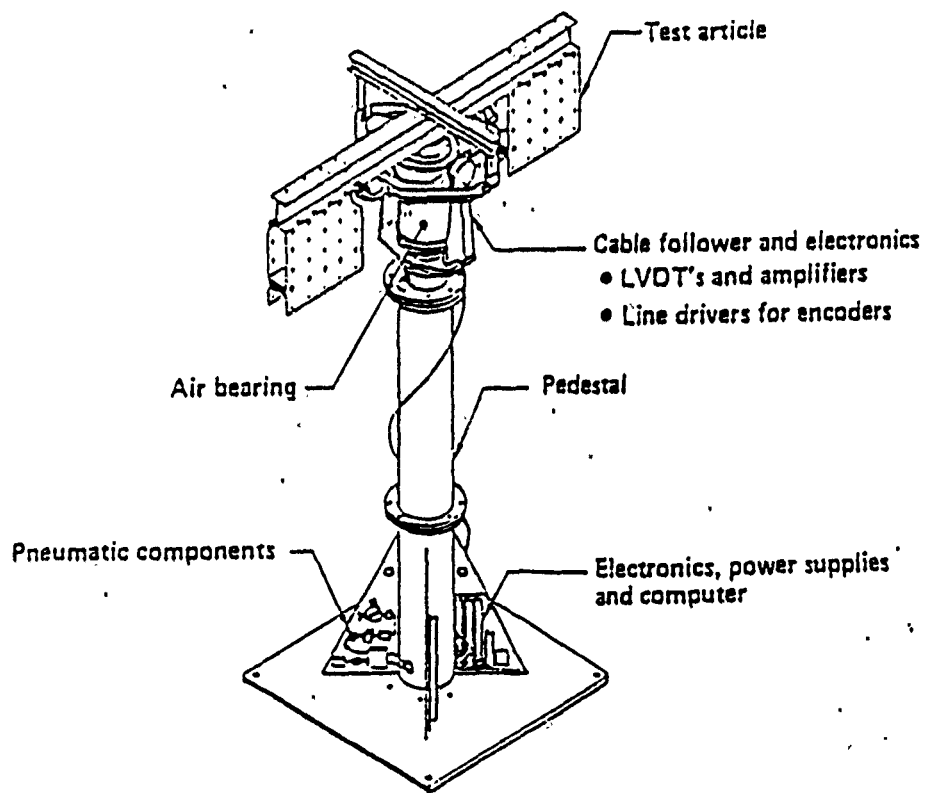
Fig. 2 ASTREX test-article support system

The original ASTREX test article (without actuators and sensors) is quasi-balanced, but when it is subject to a disturbance in the form of mass loading of actuators and sensors, it requires a feedback control system or an automatic balancing system to maintain the desired configuration. The design requirement is that the control system will have to perform the fine tuning (the coarse tuning can be done by dead mass).

In order to have a well design control system for the relatively complex and huge ASTREX test article, it was decided that a scaled-down model of the article and the corresponding control system should be built first because the scaled-down model would be easier to work with. Moreover, the scaled-down model is advantageous for presentation purposes since it is portable.

The primary objective of this research project is, therefore, to design a functional control system which consists of a scaled-down ASTREX test article, actuators, sensors, controller.

III. <u>CONTROL-SYSTEM DESIGN</u>

Electrolytic tilt sensors are selected because of their relatively lower cost (compared to gyro sensors), and stepper motors are chosen as actuators because they provide precise positioning. Since the mathematical models (or the dynamics) of the plant, actuators, and sensors are not known, PID (proportional-plus-integral-plus-derivative) controller, using the second method of Ziegler-Nichols tuning rules [8], is the best candidate. The controller was designed and physically implemented using $MATRIX_x$/SystemBuild and MAX_100 (products of Integrated Systems, Inc.)

Since the axis that is parallel with the gravity needs not be controlled, only two axes must be controlled. The control system uses two sets of independent controllers, actuators, and sensors as two parallel sub-systems (Figs. 3 and 4). It consists of the Max_100, a

stepper motors driver, a function generator, two stepper motors, and two sensors. The reference angles and PID controllers are created inside MATRIX$_x$/SystemBuild (Figs. 5 and 6). For each motor, the error signal (output of the summing junction) controls the rotation direction of the motor, and the PID-controller output either enables or disables the motor. The speed of the motor is determined by the clock rate (frequency of the pulse train) which is generated by the function generator.

Using MATRIX$_x$ /SystemBuild, on the VAX system, the block diagrams are first created, then saved in a real-time file, then converted to a FORTRAN file, then downloaded into the MAX_100, and finally converted into a machine-language file. Real-time operations is then subsequently implemented.

The angle signals, measured by the tilt sensors, are fed into the MAX_100 where they are compared to the reference signals by means of summing junctions (Figs. 3 and 5). The outputs of the MAX_100 are two sets of similar but independent signals. Each set consists of one enable/disable signal and one direction signal. A high enable/disable signal enables the stepper motor and a low disables it; a high direction signal rotates the motor in one direction and a low reverses it.
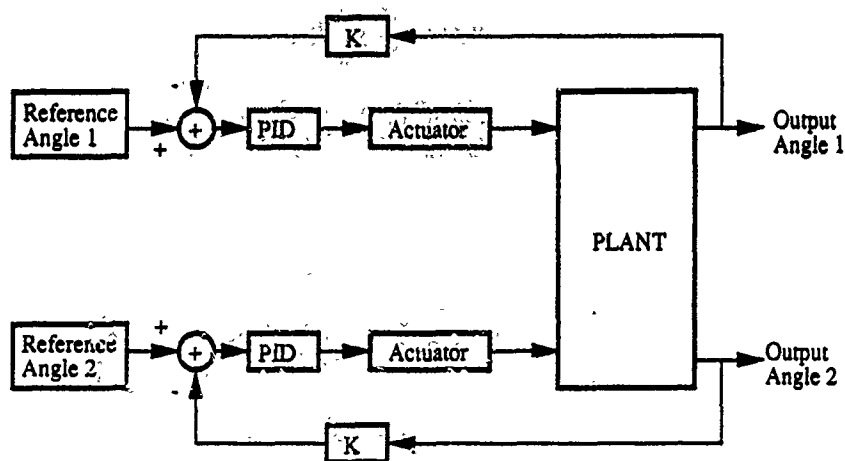
Fig. 3 System block diagram.
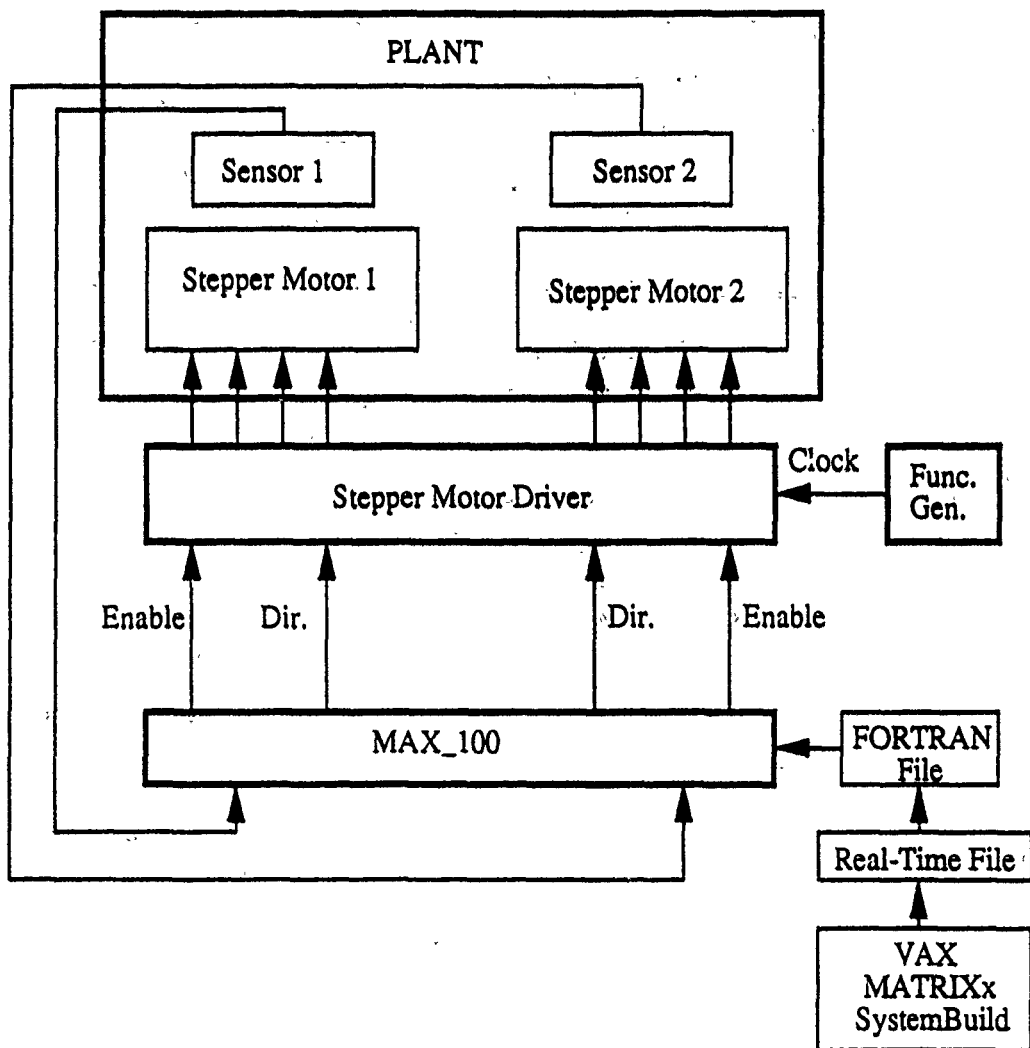
Fig. 4   System block diagram with the MAX_100.
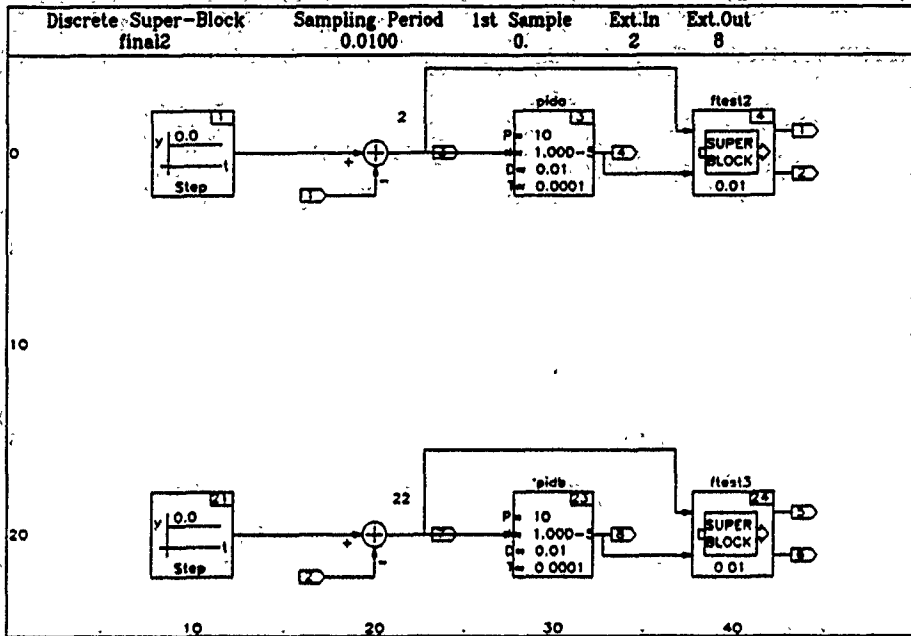
Fig. 5 References, PIDs, enable/disable and direction outputs.
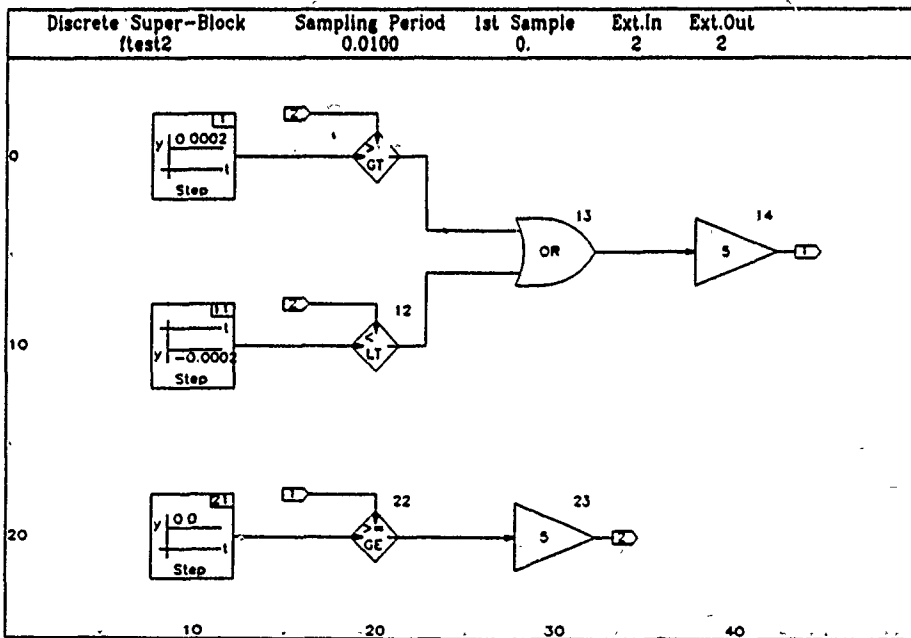

Fig. 6 Details of Super Block ftest2

For simulation, let us assume that the signals from the sensors are decaying sinusoids as shown in Fig. 7. The simulated sensor signals have different frequencies (0.5 Hz and 1 Hz), and one decays faster than the other. A zero reference is chosen for both sub-systems. The two PID controllers and the two super blocks, ftest2 and ftest3, are identical, respectively. The simulation results are shown on Fig. 8. The first motor is disabled at about 24.5 sec. while the second at about 41 sec. In both cases, the signals that control the rotation directions of the motors are not zero after the disabling times, but this is of no concern since the motors are already been disabled. (The results from real-time control were observed to be close to that of simulation.)
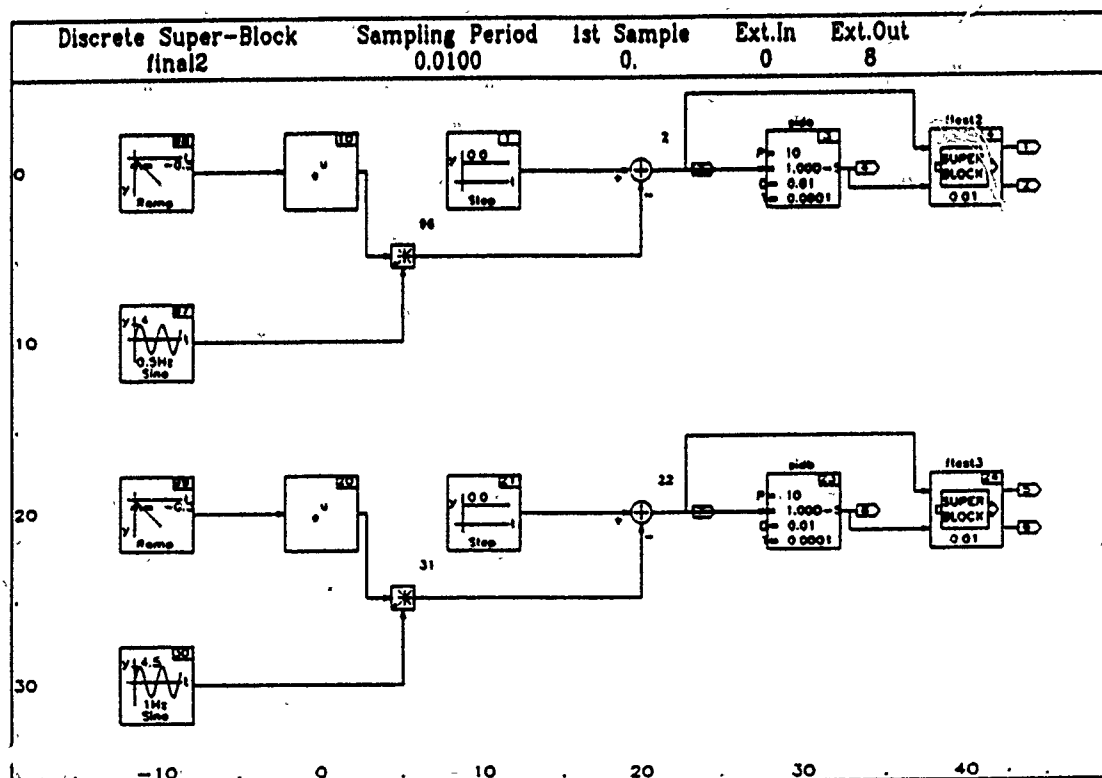
Fig. 7 Simulated sensor signals
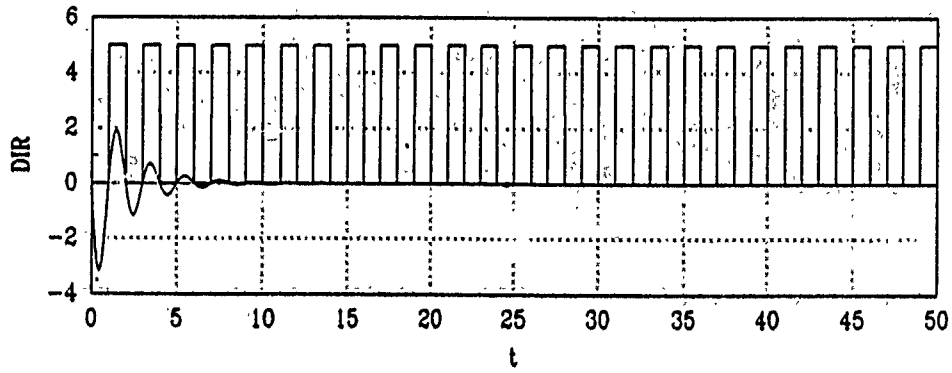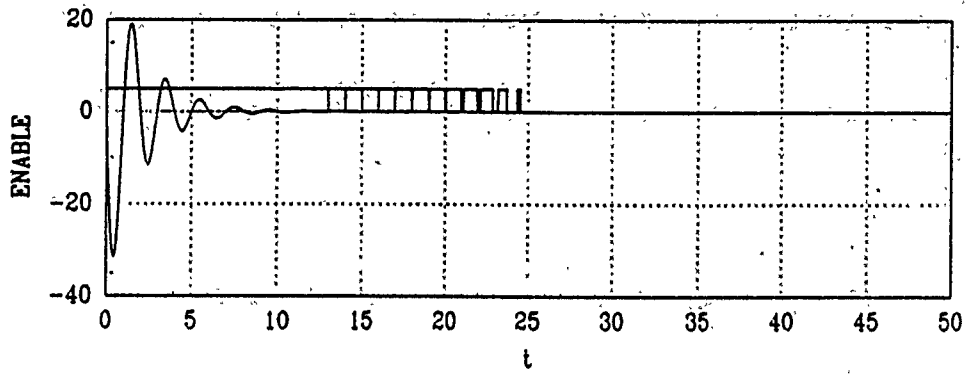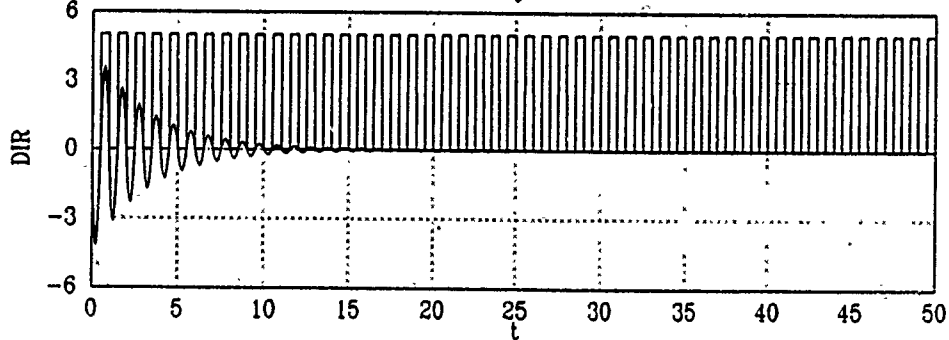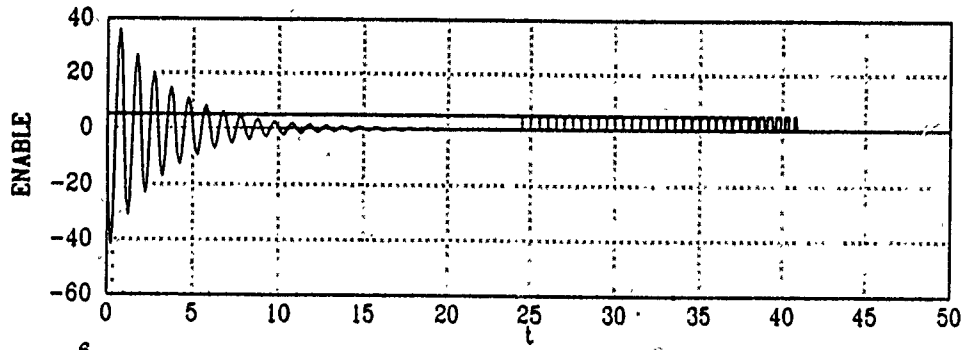
Fig. 8 Enable/disable and direction signals: (a) first motor, (b) second motor

IV. CONCLUSIONS

The scaled-down control system of ASTREX test article was successfully designed. The PID controller, electrolytic tilt sensors, and stepper motors provided satisfactory results. It was found that a significant limitation of the MAX_100 in controlling the stepper motors is its slow sampling frequency. This problem can be solved by using a real-time controller with higher sampling frequency, such as the AC-100.

V. RECOMMENDATIONS

As a recommendation for the follow-on basic research, which is a continuation of the 1990 summer research, the following tasks are proposed to be investigated, using the scaled-down controlled system of ASTREX test article:

1) To obtain a good mathematical model of the plant, actuators, and sensors, which includes the full 3-axis rotational freedom to the test article and the control-structure interaction aspects

2) To replace the PID control law by an optimal control law, considering Luenberger observer (deterministic) and Kalman-Bucy filter (stochastic)

3) To determine the optimal locations for actuators and sensors

After having a better understanding of this proposed fundamental system, the knowledge and results gained can then be applied directly to more complex systems, such as the full-scale control system of ASTREX test article.

REFERENCES

1. Shaw, O. G. and H. V. Vu, "Modal Analysis and Active Vibration Control of a System of a Cantilever Beam and a Reaction-Mass Actuator," *Proceedings of the AIAA Guidance, Navigation, and Control Conference*, 1990, pp. 73-78.

2. Duke, J. P., S. Webb, and H. V. Vu, "Optimal Passive Control of Multi-Degree of Freedom Systems Using a Vibration Absorber," *Proceedings of the AIAA Guidance, Navigation, and Control Conference*, 1990, pp. 1657-1663.

3. Meirovitch, L., *Dynamics and Control of Structures*. New York: John Wiley & Sons, 1990.

4. Atluri, S. N. and A. K. Amos (Editors), *Large Space Structures: Dynamics and Control*. Berlin: Springer-Verlag, 1988.

5. Inman, D. J. and J. C. Simonis (Editors), *Vibration Control and Active Vibration Suppression*. New York: The American Society of Mechanical Engineers, 1987.

6. Leipholz, H. H. E., *Structural Control*. Amsterdam: North-Holland Publishing Co., 1979.

7. Norris, G. A., "The ASTREX Testbed for Large/Precision Space Structures: Initial Capability and Near-Term Research," Presented at the Workshop on Computational Techniques in Identification and Control of Flexible Flight Structures, Lake Arrowhead, CA, Nov. 2-4, 1989.

8. Ogata, K., *Modern Control Engineering*. Englewood Cliffs, NJ: Prentice-Hall, Inc., 1990 (2nd Edition).

1990 USAF-UES SUMMER FACULTY RESEARCH PROGRAM

GRADUATE STUDENT RESEARCH PROGRAM

Sponsored by the

AIR FORCE OFFICE OF SCIENTIFIC RESEARCH

Conducted by the

Universal Energy Systems, Inc.

<u>FINAL REPORT</u>

<u>IDENTIFICATION AND CONTROL OF FLEXIBLE SPACECRAFT</u>

Prepared by: Dr. Trevor Williams

Academic Rank: Assistant Professor

Department and   Aerospace Engineering

 University: University of Cincinnati

Research Location: AF Astronautics Laboratory
                    Edwards AFB
                    Edwards, CA 93523

USAF Researcher: Dr. Alok Das

Date: 23 Sept 90

Contract No: F49620-88-C-0053

IDENTIFICATION AND CONTROL OF FLEXIBLE SPACECRAFT

by

Trevor Williams

ABSTRACT

The first objective of this research was to investigate how to identify the structural

parameters of flexible spacecraft from vibration test time-response data. A study carried

out on the ASTREX testbed structure revealed that natural frequencies could be estimated

quite accurately. Care needs to be taken, though, to prevent numerical sensitivity issues

from leading to overestimates for damping levels.

A second topic of research was that of sensor/actuator placement for flexible spacecraft. A

new simple technique was developed for solving this important problem and tested, in

prototype form, on a model of the Astronautics Laboratory grid structure. The new method

appears to be readily generalizable for application to any sensor/actuator combination

envisaged for the ASTREX structure.

Finally, the performance of various widely used control schemes was investigated and

compared, and certain very simple generic properties discovered when these are applied to

flexible structures. The conclusions obtained have important implications for vibration

suppression control system design.

ACKNOWLEDGEMENTS

I. INTRODUCTION

Many important practical difficulties arise in the dynamics and control of large flexible spacecraft. In particular, such structures typically have a great number of lightly-damped, closely-spaced natural frequencies. This makes it difficult to correctly identify a mathematical model for the dynamics of such a vehicle from vibration test data. Additionally, questions such as where sensors and actuators should be positioned in order to give the best performance, and what control laws should be used for slewing and vibration suppression, are very difficult to solve.

The Air Force Astronautics Laboratory at Edwards AFB has been very active in carrying out research into such questions. Notably, the ASTREX test article which has recently been completed there is one of the best laboratory testbeds available for conducting investigations into the practical problems that arise in the identification and control of flexible spacecraft.

My research work at Kingston Polytechnic, NASA Langley Research Center and the University of Cincinnati has applied my background in Electrical Engineering to the problems of identification and control of large flexible spacecraft. It was therefore felt that my assignment to the Astronautics Laboratory would be beneficial both to me, in that it would provide exposure to practical experimental problems, and to the Laboratory, in that my background would complement the Mechanical Engineering background of the other researchers.

II. OBJECTIVES OF THE RESEARCH EFFORT

The first objective of this work was that originally stated, namely to investigate how to identify the structural dynamics of flexible spacecraft from vibration test time-response data. The purpose of this research was to compare the results obtained in this way with those given by more well-established frequency-domain methods, for instance fast Fourier

transforms (FFT) and the Eigensystem Realization Algorithm (ERA). The ASTREX testbed structure was to be used for the study, as FFT and ERA results had already been obtained from it, allowing meaningful comparative studies to be carried out.

An additional topic which was decided upon for research in the latter part of the tenure was that of sensor/actuator placement on flexible spacecraft. In particular, it would be very useful to have a relatively simple, yet reliable, technique for deciding which of several possible locations should be used in order to give good closed-loop response.

Finally, a question concerning the performance of linear optimal regulators under comparatively high gains arose as a result of discussions with Astronautics Laboratory personnel on experiments involving the grid structure there. As this question may have great significance for future practical implementation of optimal control laws, it was deemed worthy of study also.

III.   TIME-DOMAIN IDENTIFICATION

Most well-established techniques for identifying the dynamics of flexible structures are based in some way on the frequency-response of the system. In particular, fast Fourier transforms are inherently frequency-domain quantities, while the Eigensystem Realization Algorithm operates on the given data to give impulse responses, which are equivalent to frequency-domain transfer functions. These established methods have already been applied to the ASTREX structure to estimate its natural frequencies and damping ratios, so it was decided that it would be of interest to try a time-domain method for comparative purposes.

The technique chosen was that of Kalman filtering, which is mathematically equivalent [1] to least squares estimation on the input and output time histories. (Another method that was originally intended for application, that of [2], was not compatible with the single-

24-5

input ASTREX test data available.) The implementation of this estimation technique that was written during the tenure (program FLEXID, Appendix 1) was based on iterative use of Matrix-X function RLS; the iteration terminated when no further significant improvement was achieved in the squared residual errors. This least squares procedure produced estimated coefficients for the numerator and denominator polynomials of the discrete-time transfer function between input and output. The roots of the denominator were then converted from discrete to continuous time to give the desired natural frequency and damping ratio estimates.

It was observed that using time-domain data for a complicated structure with as many vibrational modes as ASTREX presented difficulties not experienced in the frequency domain. For instance, if the data were used raw, the identified model invariably contained an unstable, and so physically impossible, structural mode. Filtering the data over a finite range of frequencies (see Figure 1 for raw and typical filtered ASTREX data) overcame this problem and led to quite satisfactory frequency estimates. The damping ratio estimates produced were somewhat high though, typically being a few percent instead of the true few tenths of a percent. This appears to be a result of the numerical sensitivity that can often occur in the roots of a polynomial when these all lie just inside the unit circle, as arises for a discrete-time model of a lightly-damped flexible structure. Similar conclusions were given in the Jet Propulsion Laboratory report [3] on time-domain identification of the flexible antenna testbed structure under study there. It should be noted that time and equipment constraints prevented the collection of ASTREX data with input forcing functions optimized for the least squares identification technique. It is probable that this refinement could lead to significant improvement in the damping estimates.

IV. SENSOR/ACTUATOR PLACEMENT

A question that has received a great deal of attention is that of deciding where on a given flexible structure control sensors and actuators should be placed. This problem is particularly important for complex structures such as ASTREX, as physical intuition is no longer adequate for the task. The type of approach that has been taken by many authors is to place sensors so as to make structural modes as observable as possible, and actuators so as to make them as controllable as possible. However, close consideration of the properties of control systems shows that this technique does not necessarily lead to good closed-loop performance. For instance, if the control objective is to minimize vibrational effects on the line-of-sight of a spacecraft antenna, placing sensors and actuators in the way just described does not reflect this control objective, and so will not necessarily help to achieve it.

A new placement method that overcomes this problem has recently been developed by the author [4]. The approach taken is to choose those sensor and actuator positions which make the resulting transmission zeros of the system as highly damped as possible. These zeros closely reflect the performance achievable by the closed-loop system, so this method places sensors and actuators in such a way as to improve the closed-loop response (for instance, line-of-sight) as much as possible. The new algorithm is very efficient computationally, involving only calculation of a set of vector or matrix norms. It outputs a 'figure of merit' for each possible sensor/actuator location, allowing these to be ranked in order of utility. The algorithm as presently developed (program PLACENC, Appendix 2) is specifically for high-authority/low-authority applications; however, the modification to placement of arbitrary sensors and actuators appears to be quite straightforward.

Figure 2 shows the root loci that result for the Astronautics Laboratory grid structure from placing a low-authority sensor/actuator pair at the optimum position as determined by the

new algorithm. It can be seen that all portions of the root loci have been shifted away from the imaginary axis: this stability augmentation is the property which leads to the desired good closed-loop performance.

V. LINEAR OPTIMAL REGULATORS

This work was motivated by experimental results obtained by Astronautics Laboratory personnel on their flexible grid structure. The experiment consisted of applying state feedback so as to minimize the effects of structural vibrations on the line-of-sight of a laser reflector mounted on the grid, and worked very successfully. The observation that motivated the present research was that all peaks of the Bode plot of frequency response amplitude of the closed-loop system had very nearly equal heights. Given the fact that this data was from a real experiment, this suggested that the idealized optimal frequency response of a flexible structure should have peaks of exactly equal amplitude. This question was therefore investigated, by carrying out simulations of the effect of a linear quadratic regulator (LQR) [5] on various flexible structures. It is interesting to note that the general properties of LQRs acting on flexible structures have not been studied extensively; [6] by the author is one of the few references on the subject. Furthermore, when LQRs are studied they are usually analyzed in state-space rather than frequency-response terms. Thus, the question studied here appears not to have been investigated to date.

The result of this investigation was that an LQR applied to a flexible structure does indeed produce equal frequency-response peaks as control gains are increased, at least for the case of collocated sensors and actuators. Figure 3 shows typical results for a uniform beam example. It seems likely that this result has a physically meaningful energy interpretation. Furthermore, it is very reminiscent of H_∞ control techniques, and so should lead to further connections between these two disparate but very widely-used approaches to control system design. It is also interesting to contrast the LQR results with what is observed

24-8

(Figure 4) when the Uniform Damping Control approach of [7] is applied to the same example. Increasing the gain in this approach leads to increasingly different peak amplitudes and, it appears likely, increasingly inefficient use of control energy. This observation has important implications for the choice of control strategy in practical vibration suppression applications.

VI. RECOMMENDATIONS

a.   The time-domain structural identification and sensor/actuator placement techniques discussed in Sections III and IV have been implemented, and fully documented, as Matrix-X user-defined functions FLEXID and PLACENC, respectively. They are therefore available for immediate use in a fully machine-portable form.

. b.   The new low-authority control sensor/actuator placement algorithm is numerically stable, very efficient computationally, and gives results which make good physical sense. A future development that would be of great interest would be to generalize it to allow arbitrary types of sensors and actuators. It would then be well suited to the difficult problem of deciding where on the ASTREX structure sensors and actuators should be placed. This question must be resolved before control experiments can be carried out on the structure.

Further work is also merited on the implications for control law generation of the LQR frequency-response properties discussed in Section V. In particular, these results highlight the strong connections between traditional optimal control and the more modern H_{∞} control techniques, both of which have been used extensively. Additional study of the experimental results previously obtained for the Astronautics Laboratory grid structure, as well as of the energy interpretation of the theoretical results reported here, should be of great importance in designing good vibration control strategies for the ASTREX structure.

REFERENCES

1. Middleton, R.H. and G.C. Goodwin, <u>Digital Control and Estimation: A Unified Approach</u>, Englewood Cliffs, New Jersey, Prentice-Hall, 1990.

2. Williams, T.W.C., "Identification of Large Space Structures: A Factorization Approach", <u>Journal of Guidance, Control, and Dynamics</u>, 1987, Vol. 10, pp. 466-473.

3. Vivian, H.C. et al., "Flexible Structure Control Laboratory Development and Technology Demonstration", AFAL-TR-88-093, Jan. 1989.

4. Williams, T.W.C., "Transmission Zeros and High-Authority/Low-Authority Control of Flexible Space Structures", <u>Proc. AIAA/AAS Astrodynamics Conference</u>, Portland, Oregon, Aug. 1990.

5. Kwakernaak, H. and R. Sivan, <u>Linear Optimal Control Systems</u>, New York, Wiley-Interscience, 1972.

6. Williams, T.W.C., "Optimal Root Loci of Flexible Space Structures", to appear, <u>IEEE Transactions on Automatic Control</u>.

7. Silverberg, L.M., "Uniform Damping Control of Spacecraft", <u>Journal of Guidance, Control, and Dynamics</u>, 1986, Vol. 9, pp. 221-227.
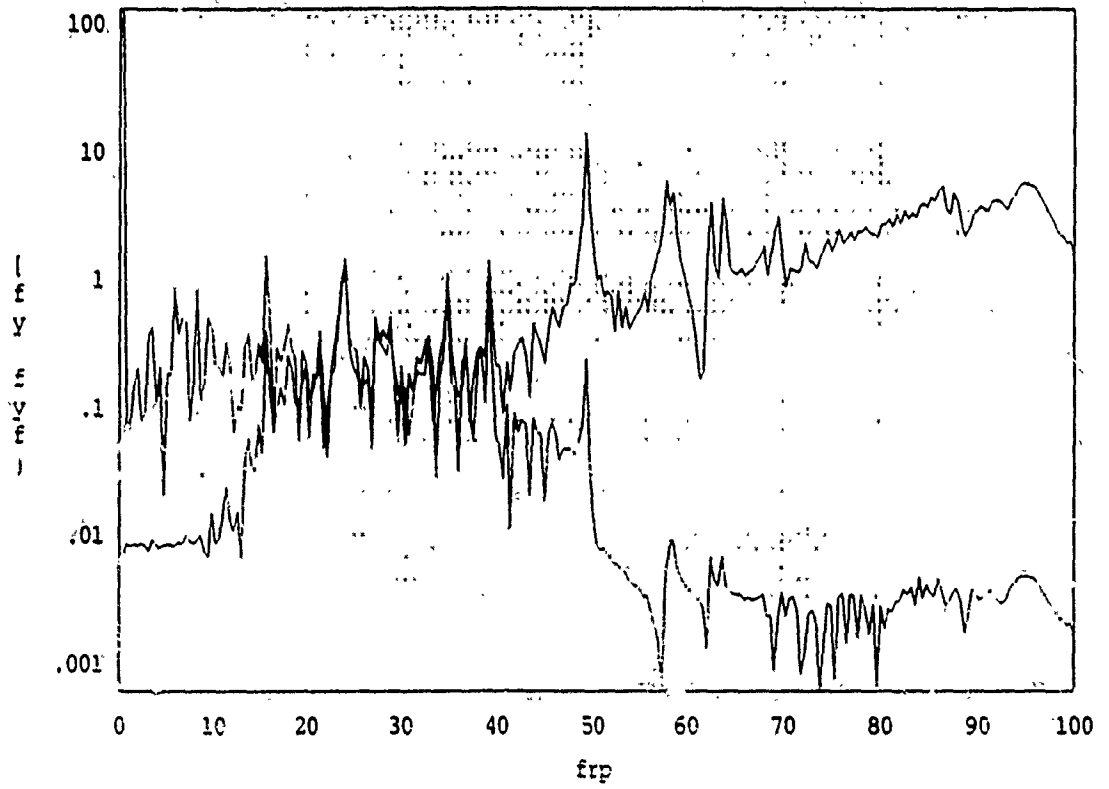
ASTREX colloc case 3; 20-40 Hz filter

Figure 1
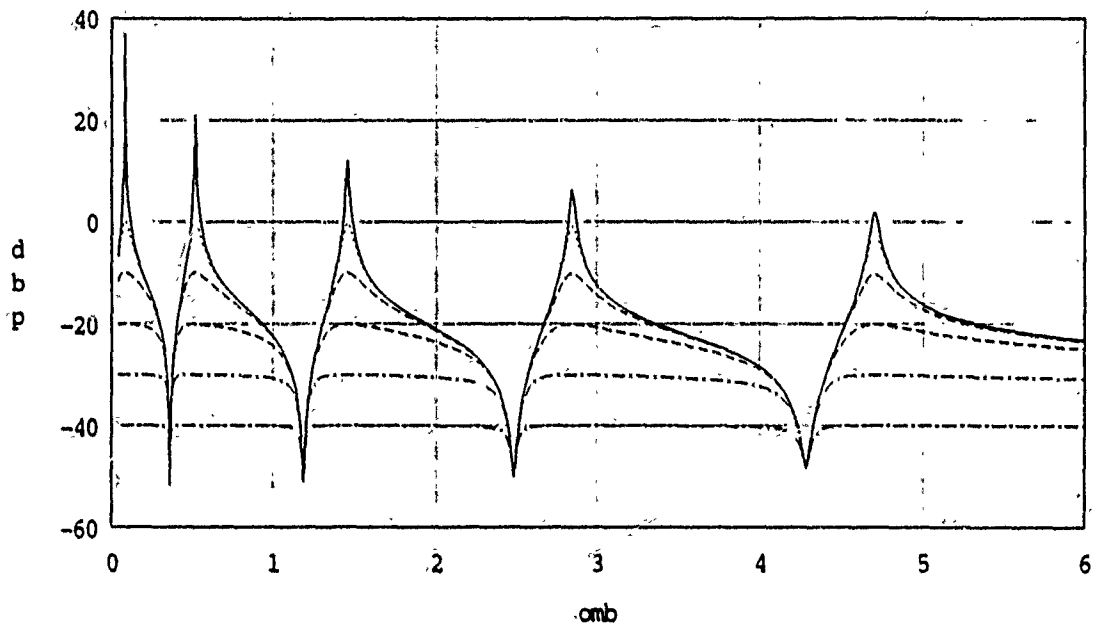
Figure 2

Beam open- & closed-loop (ro 100 to 1e-4)

Figure 3
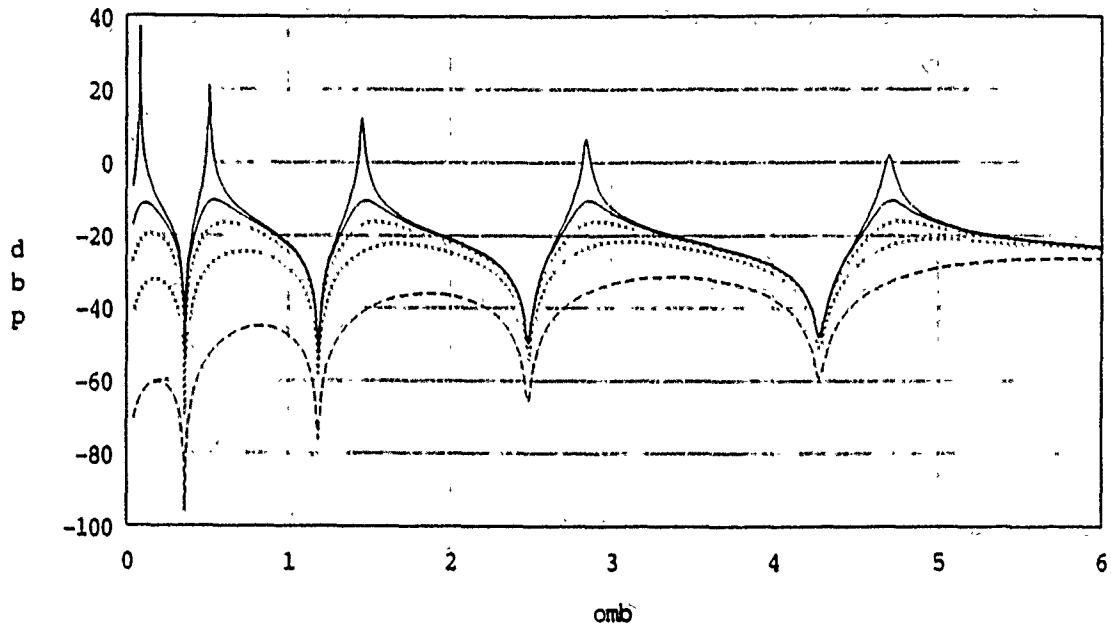
Beam open- & closed-loop (Silv, t=10, 5, 2.5, 1)

Figure 4

```
// [yf,frnat,zeta,infco,var]=flexid(y,u,nmode,fsamp,fmin,fmax)
//
// DESCRIPTION:
//
// FLEXID identifies the natural frequencies, damping ratios and
// influence coefficients of a flexible structure from sampled-data
// single-channel input and output time histories.
//
// The method used is to iterate over the Matrix-X function RLS
// (recursive least squares), at each step estimating the coefficients
// of a discrete-time transfer function to fit the measured data.
// These coefficients are then used as the starting data for the next
// iteration; convergence is tested by examining the decrease in the
// squared measurement residuals from one step to the next.
//
// The results obtained by this algorithm are strongly influenced by
// the filtering applied to the output data. (In particular, ASTREX data
// was found to give rise to extreme difficulties if not filtered at all).
// Careful consideration should be given to the values selected for
// nmode, fmin and fmax.
//
// INPUTS:
//
// y:      Measured output time history of system
//
// u:      Applied input time history
//
// nmode:  Desired number of modes in identified model
//         (Note that nmode is an UPPER LIMIT on the number
//         of valid modes that will be obtained, as spurious
//         non-conjugate-pair poles are sometimes produced.)
//
// fsamp:  Sampling rate of measured data
//
// fmin:   Lowest frequency in filtering range of interest
//
// fmax:   Highest frequency in filtering range of interest
//         (Note that this should be no greater than fsamp/2)
//         Entering a value of 0 for fmax prevents filtering
//
// OUTPUTS:
//
// yf:     Filtered (and detrended) system output
//
// frnat:  Natural frequencies of all valid estimated modes
//
// zeta:   Damping ratios of all valid estimated modes
//
// infco:  Approximate influence coefficients of all valid modes
//
// var:    Estimated variance of measurement residuals
//
//=================================================================
//
    clear yf frnat zeta infco var
//
// Detrend input and output
//
    ud=detrend(u);
    yd=detrend(y);
//
// Filter output, if desired, in specified range of frequencies
//
    yf=y;
//
    if fmax > 0 then b1=fmin/fsamp; b2=fmax/fsamp; bands=[b1 b2 1]; ...
```

24-15

```
        ir=fwin(bands,32); s=diag(ones(31,1),1); s(32,:)=ir(32:-1:1); ...
        yf=filp(s,yd);
//
//  Set up parameters for iterative use of recursive least squares
//
        n0=ones(1, 2*nmode+1); d0=n0; e0=0; de=1;
//
//  Iterate over RLS until estimates are converged (tested by residuals)
//
        for idum = 1:20; while abs(de) > 0.01*e0; ...
            [n,d,e]=rls(yf,ud,n0,d0); ...
            de=e0-e; n0=n; d0=d; e0=e;
//
//  Save estimated variance of measurement residuals
//
        nsamp=size(yf); nsamp=nsamp(1); var=e/nsamp;
//
//  Convert discrete-time poles into natural frequencies & damping ratios
//
        pd=roots(d); pc=fsamp*log(pd);
        omega=abs(pc); fr=omega/(2*pi);
        ze=real(-pc)./omega;
//
//  Compute (discrete-time) influence coefficient for each mode
//
        for i=1:(2*nmode); polei=pd(i); ...
            num=0; for jcoeff=1:(2*nmode); num=(num+n(jcoeff))*polei; ...
            den=1; for jpole=1:(2*nmode); if jpole <> i then ...
            den=den*(polei-pd(jpole)); ...
            ic(i)=2*abs(num/den);
//
        ind=sort(fr); fr=fr(ind); ze=ze(ind); ic=ic(ind);
//
//  Save only one set of data for each valid conjugate pair
//
        ipick=1; jsave=1;
        while ipick < (2*nmode); if abs(fr(ipick)-fr(ipick+1)) < 1e-10 ...
            then frnat(jsave)=fr(ipick); zeta(jsave)=ze(ipick); ...
            infco(jsave)=ic(ipick); ...
            ipick=ipick+2; jsave=jsave+1; ...
            else ipick=ipick+1;
//
        retf
```

```
// [weight,irank,dpoles,dzeros,chat]=placenc(omega,zeta,bhi,chi,blo,damp);
//
// DESCRIPTION:
//                                                                    Appendix 2
// PLACENC addresses the question of damper placement for flexible
// structures.  Given a set of possible damper locations on the
// structure considered, the routine computes a numerical measure
// of how effective a damper placed at each would be in improving
// closed-loop system performance.  This ranking is then used to
// actually place the required dampers, and the resulting poles,
// zeros and damping matrix computed.
//
// The basic approach used is to make the zeros of the damping-
// augmented system as damped as possible.  This also indirectly
// guarantees that the poles of the system are quite well damped,
// so the entire root loci of (structure + dampers) are shifted
// into the left half-plane.  The aim is to ensure good performance
// and spillover protection when a high-authority outer loop is
// applied to the damping-augmented system.
//
// For further details, see Williams, 1990 Astrodynamics Conference.
//
// Warning: PLACENC has not yet been fully tested and developed.
// Note also that the high-authority sensors are assumed for simplicity
// to measure only displacements.
//
// INPUTS:
//
// omega: Natural frequencies (rad/s) of given structure
//
// zeta:  Damping ratios of given structure
//
// bhi:   Control influence matrix (in a mass-normalized modal model) for
//        the specified high-authority actuator stations
//
// chi:   Measurement influence matrix for the specified high-authority
//        sensor stations
//
// blo:   Influence matrix for all possible low-authority damper locations
//
// damp:  Set of damper strengths (in e.g. Ns/m) to be actually used.
//
// OUTPUTS:
//
// weight: Weighting of all possible damper locations.  The size of this
//         parameter is a guide to how useful the corresponding damper
//         location is for improving overall closed-loop performance
//
// irank:  Ranking of all possible damper locations, based on the weighting
//         parameter described above
//
// dpoles: Poles of the structure augmented with optimally-placed dampers
//
// dzeros: "Zeros" of the structure augmented with optimally-placed dampers
//         Note that these are not actually the transmission zeros of the
//         system (indeed, there are generically none for a non-square system),
//         but rather the left-half plane finite optimal root loci terminii.
//         These can be shown to be the zeros of a squared-down system.
//
// chat:   Damping matrix of the structure plus optimally-placed dampers
//
//======================================================================
//
    clear weight irank dpoles dzeros chat
//
// Determine the numbers of structural modes and HAC sensors and actuators
```

```
//
    nm=size(bhi); n=nm(1); m=nm(2);
    p=size(chi); p=p(1);
//
//  Similarly, find the number of possible damper locations to be studied
//
    mlac=size(blo); mlac=mlac(2);
//
//  Compute QR decomposition of HAC B; hence find its orthogonal complement
//
    [q r]=qr(bhi); qb2=q(:,m+1:n);
//
//  Similarly for HAC C matrix
//
    [q r]=qr(chi'); qc2=q(:,p+1:n);
//
//  For each possible damper location, estimate its closed-loop effectiveness
//
    for i=1:mlac, xi=qc2'*blo(:,i)*blo(:,i)'*qb2; ...
        weight(i)=sqrt(norm(xi,'fro'));
//
//  Find ranking (1 best, ...) for all candidate LAC damper positions
//
    ind=sort(-weight); irank=sort(ind);
//
//  Sort specified damper strengths into descending order
//
    dsort=sortv(-damp); blsort=blo(:,ind);
    mdamp=size(damp); mdamp=max(mdamp);
//
//  Set up damping matrix resulting from placing the given dampers optimally
//
    chat=diag(2*zeta.*omega);
//
    for i=1:mdamp, chat=chat+dsort(i)*blsort(:,i)*blsort(:,i)';
//
//  Construct a state space model for damped structure
//
    a=[-chat -diag(omega)**2; eye(n) 0*eye(n)];
    b=[bhi; 0*bhi]; c=[0*chi chi];
//
//  Form the appropriate composite squared-down system
//
    if p<m then as=[a -b*b';0*a -a']; bs=[0*c'; -c']; cs=[c 0*c]; ...
    else as=[a 0*a;-c'*c -a']; bs=[b; 0*b]; cs=[0*b' -b'];
//
    ds=0*eye(min(p,m));
    ss=[as bs;cs ds];
//
//  Compute the poles and zeros of this damped system
//
    dpoles=-sortv(-eig(a),'magn');
//
    dzeros=sortv(zeros(ss,4*n));
    nzeros=size(dzeros); nzeros=nzeros/2;
    dzeros=dzeros(1:nzeros); dzeros=-sortv(-dzeros,'magn');
//
    retf
```

1990 USAF-UES SUMMER FACULTY RESEARCH PROGRAM/

GRADUATE STUDENT RESEARCH PROGRAM

Sponsored by the

AIR FORCE OFFICE OF SCIENTIFIC RESEARCH

Conducted by the

Universal Energy Systems, Inc.

FINAL REPORT

INVESTIGATING THE LOADING RATE EFFECT ON THE CRACK GROWTH

BEHAVIOR IN A COMPOSITE SOLID PROPELLANT

Prepared by: HSIEN-YANG YEH, PH.D., MINH D. LE

Academic Rank: ASSOCIATE PROFESSOR

Department and   MECHANICAL ENGINEERING DEPARTMENT

 University: CALIFORNIA STATE UNIVERSITY, LONG BEACH

Research Location: ASTRONAUTICS LABORATORY
                    EDWARDS AIR FORCE BASE, CA   93523-5000

USAF Researcher: C.T. LIU, PH.D.

Date: JULY 16, 1990

Contract No: F49620-88-C-0053

INVESTIGATING THE LOADING RATE EFFECT ON THE CRACK GROWTH BEHAVIOR IN A COMPOSITE SOLID PROPELLANT

by

Hsien-Yang Yeh

Minh D. Le

ABSTRACT

The crack growth behavior in a highly filled composite solid propellant was studied through the use of a centrally cracked strip biaxial specimen. The specimen was tested under a constant crosshead speed at room temperature. In this study, three different crosshead speeds and two different crack lengths were considered. During the experiment, a video camera was used to monitor the crack growth and a tape-recorder was used to record the load as a function of time. The raw experimental data (crack length, load, time) together with a response surface equation (relating the normalized stress intensity factor to the two half crack lengths) were used to calculate the instantaneous crack growth rate and the associated stress intensity factor. The experimental data were analyzed to investigate the effect of crosshead speed on the crack growth behavior in the material.

ACKNOWLEDGMENTS

I. INTRODUCTION:

When cracks occur in rocket motor grains, they may significantly alter the subsequent motor performance. Consequently, as performance requirements are advanced, it becomes critical to incorporate fracture mechanics concepts into the evaluation of the structural integrity of motor grains.

Over the past decade, attempts have been made to develop mathematical models for predicting fracture behavior in rocket motors but model validation has been inhibited by lack of an extensive data base for validating general crack effects. In particular, the near tip behavior of cracks in solid propellant material during opening and extension of the crack needs to be quantified experimentally. Based on the above consideration, it is clear that the concepts and procedures for crack growth study are of fundamental importance. Thus, we choose the subject "investigation of the loading rate effect on the crack growth behavior in a composite solid propellant" for this ten-week summer faculty research program.

My research interests have been in the area of application of linear elastic fracture mechanics to study the failure phenomena about composite materials and ceramic insulators. My work on the structural integrity of composite materials and ceramic insulators contributed to my assignment to the fracture study about the composite solid propellant of the propulsion division.

II. OBJECTIVES OF THE RESEARCH EFFORT:

In the past decade, many experimental studies were directed primarily toward the characterization of crack growth behavior in solid propellant (Refs. 1-3). Based on linear

elastic fracture mechanics, these experiments have examined the functional relationships between the crack growth rate and the stress intensity factor.

My assignment as a participant in the 1990 Summer Faculty Research Program (SFRP) was to investigate the loading rate effect on the crack growth behavior in a composite solid propellant.

III. <u>APPROACHES AND RESULTS</u>:

A. Approaches

In this study, the crack growth behavior in a highly filled composite propellant was investigated through the use of a centrally cracked strip biaxial specimen. The length of the specimen was 8.0 in., the width was 2.0 in., and the thickness was 0.2 in. The geometry of the specimen is shown in Fig. 1. A razor blade was used to pre-crack the specimen. Two crack lengths of 1.0 in. and 2.0 in. were used. The crack was centered and located on the horizontal centerline of the specimen. Prior to the experiment, the specimen was conditioned at room temperature for at least one hour. It was then placed in an Instron testing machine and pulled at a constant crosshead speed of 0.1 in./min. until the specimen fractured. Following these procedures, three different crosshead speeds (0.1 in./min., 1 in./min., and 10 in./min.) and two different crack lengths (1.0 in. and 2.0 in.) were considered. Each case was repeated three times and a total of 18 specimens were tested. During the experiment, a video camera was used to monitor the crack growth and a tape recorder was used to record the crack growth data on a tape for future data reduction. In addition, a strip chart recorder was used to record the load and the time during the test. After the test, the

data recorded on the tape was played back and shown on a television screen to measure the crack growth as a function of time. The raw data obtained from the test were the two half crack lengths, a_r and a_l, which were measured from the center of the specimen, the time t, and the loading rate. These data were used to calculate the crack growth rate da/dt, by two different methods, known as the secant method and the total polynomial method. In the secant method, the crack growth rate was computed by calculating the slope of a straight line connecting two adjacent "a" versus "t" data points and assigning the average crack growth rate at a point midway between each pair of data points. The total polynomial method involved fitting a high order polynomial to a set of data and the coefficients of the polynomial function were estimated by the method of least squares. The structural mechanics test reduction program MECH 500 was used to perform the above calculations.

To determine the stress intensity factor at the crack tip it is necessary to relate the load on the specimen to crack and specimen dimensions. A three-dimensional finite element computer code, TEXGAP-3D (Ref. 4), was used to determine the stress intensity factors as a function of the crack lengths for a given load applied at the boundary of the specimen. The calculated mode I stress intensity factors, K_{Ir} and K_{Il}, at the right side and the left side tips were normalized with respect to the applied load. A nonlinear regression analysis program was conducted to generate two response surface equations, relating the dependent variables, K_{Ir} and K_{Il}, to the independent variables a_r and a_l. On top of that, the leftover composite solid propellant was used to run several dogbone uniaxial tests under three different loading rates, with and without side notch. These raw experimental data were

directly input to the IBM personal computer and the corresponding stress-strain curves were plotted by using the least square curve fitting technique.

B. Results

The comparison of the various stress-strain curves under different loading rates is shown in Fig. 2, it indicates clearly that the composite solid propellant material is getting stiffer under the higher loading rate. Fig. 3 shows that with side notch, the fracture strains are independent of the various loading rates. The stress intensity factor of the composite solid propellant material under various loading rates are calculated and listed in Table I. Fig. 4 shows clearly that crack initiation load is increased with the increased loading rate but decreased with the increased crack length.

Crack growth rate determination requires analysis of discrete data relating the instantaneous time, t, to the corresponding crack length, a. The general problem encountered in determining crack growth rate is evaluating the derivative of a function, a = f (t), which is known only at certain data points. In addition, the inherent non-homogeneous nature of a highly filled composite solid propellant will inevitable cause a considerably higher scatter in the measured data. Therefore, ti is anticipated that a smooth and steadily increasing relationship between the crack growth rate da/dt, and the time, t, is difficult to obtain and that different methods of da/dt calculation and different time increments for measuring the crack length may result in different solutions.

The results of the data analysis, plotted as the stress intensity factor K_I, versus the crack extension Δa, under different loading rates, are shown in Fig. 5. This figure

shows a similarity to the R-curve observed from metallic and composite materials. These experimental data show that at the beginning of the test the crack tip radius continually increased with increasing applied load and no crack extension took place. When the applied load reached a critical value, a stable crack growth under an increasing load was observed. The amount of the increasing load was related to the positive slope of the R-curve. As the stable crack grew continually, the relationship between the crack extension and the K_I changed successively. This was indicated by the continually changed slope of the R-curve. At some value of the crack length, the transition from stable crack growth to unstable crack growth was observed. The unstable crack growth region was characterized by a continual decrease in the applied load with a continual increase in the crack length and a relatively constant value fo the stress intensity factor K_I. However, in this region, the crack was not driven at constant velocity, instead it propagated at an accelerating rate.

The plot of the crack growth resistance data K_I and Δa on a Log-Log scale under different loading rates is shown in Fig. 6. The data indicate that an acceptable correlation exists between $LogK_I$ and $Log \Delta a$. The straight line relationship between $LogK_I$ and $Log \Delta a$ implies that a power law relationship exists between these two parameters. Based on these experimental data, it is observed that a shifting factor may be used to relate the straight lines from $LogK_I$ vs $Log \Delta a$ plots for different loading rates. This shifting phenomenon is similar to the shifting of the mechanical properties data in the temperature-time plots of viscoelastic materials. In Fig. 7, the data exhibit a relatively large scatter, especially in the early stage of crack growth. There are many factors that may contribute to the scatter of

experimental data. When a highly filled composite propellant material is strained, the different size and distribution of the filler particles, the variation in the bond strength between the particles and the binder, and the different cross-like density of polymer chains can all produce a highly non-homogeneous local stress field. Since crack growth behavior is controlled by the combination of local stress and local strength in varying combinations, it is expected that the crack growth data obtained from a number of tests will show a considerably larger scatter even though the testing conditions remained identical.

Finally, the functional relationship between the stress intensity factor K_I and the crack growth length rate $\dot{a}$ were determined by using a linear regression analysis. The results show that a power law relationship exists between K_I and $\dot{a}$ which is consistent with the theoretical results obtained by Schapery (Ref. 8) and Knauss (Ref. 9) in their study of fracture of linear viscoelastic materials. Mathematically, it can be written as

$$\frac{da}{dt} = C_1 K^{C2} \tag{1}$$

where C_1 and C_2 are empirically determined constants. It is expected that their values will vary from test to test as well as from one $\dot{a}$ calculation method to another. In addition, the test data obtained from individual tests were analyzed to determine the values of the exponent and the intercept of Equation (1). The constants C_1 and C_2 are not independent but are mutually dependent and related through the equation

$$\text{Log}C_1 = A + BC_2 \tag{2}$$

where $A = -\text{Log}\dot{a}$ and $B = \text{Log}K_I$.

IV. CONCLUSIONS:

The principal conclusion which may be derived from the results of this work, under the conditions considered in this study, are

(a) for notched specimen, the composite solid propellant material shows stiffer property under the higher loading rate; however, the fracture strains are independent of the various loading rates.

(b) the crack initiation load is increased under higher loading rate but decreased with larger existing crack length.

(c) by shifting the higher rate "curve" toward the right side, a master "curve" in the $LogK_I$ vs. $Log \Delta a$ plot may be obtained; this implies that the crack growth resistance concept developed for rate insensitive materials could be used to study the fracture behavior of the rate sensitive materials.

(d) a power law functional relationship exists between the stress intensity factor K_I and the crack growth rate $\dot{a}$, as shown in equation (1). where C_1 and C_2 are mutually dependent constants and can be determined from experimental data.

V. RECOMMENDATIONS:

(a) This experimental study provides useful information in the mechanical design of the composite solid rocket propellant. However, the higher loading rate will stiffen various composite propellants to a different level. The mutually dependent constants C_1 and C_2 are materials related, thus, for the composite solid propellant with different ingredients, the constant C_1(or C_2) can only be determined by

experiments.

(b) There are many factors that may contribute to the scatter of experimental data. However, through this experimental study of the crack initiation and growth behavior in a solid propellant, it was observed that the proper and precise determination of crack initiation plays an extremely important role in the biaxial fracture tests. The uncertainty of determining the exact location of crack initiation would provide a large scatter experimental data. Even though the theory of fracture mechanics has been studied and developed by many excellent scientists and engineers for several decades, the studies of the criterion for crack propagation are far from matured. Being one of the fundamental problems in the theory of fracture and damage mechanics, the determination of a precise fracture initiation and growth criterion for general cracks is one of the key subjects that need to be settled as soon as possible. From 1963 to the present, there are criteria of maximum tangential stress, maximum strain energy release rate, S-theory, T-theory, J-integral, etc., and some empirical criteria obtained from experimental results. As different hypotheses are used in the formulation of each of these criteria, the results for a given problem can be somewhat different depending upon the criteria used. This also leads to limitations on their applicability.

It is thus suggested that to advance the fundamental research of the crack growth behavior in a composite solid propellant, it is imperative to modify and improve these criterion for crack initiation and propagation through analysis and comparison.

(c) The advanced fiber reinforced laminated composite materials show great potential in developing the weight sensitive engineering structures such as aircraft and space vehicles, etc. However, one of the common strength reduction and failure problems of the filamentary laminated composite material is due to delamination. This experimental research technique can be used to observe and study the delamination growth in filamentary laminated composite materials.

REFERENCES

1. Liu, C.T., "Crack Propagation in an HTPB Propellant," 1980 JANNAF Structures and Mechanical Behavior Subcommittee Meeting, CPIA Publication 311, Vol. I, March 1980, pp. 193-205.

2. Liu, C.T., "Variability in Crack Propagation in a Composite Propellant," AIAA Paper No. 83-1015, AIAA/ASME/AHS 24th Structure, Structural Dynamics, and Materials Conference, May 1983.

3. Liu, C.T., "Crack Growth Behavior in a Composite Propellant with Strain Gradients - Part I," AIAA Paper No. 84-1294, AIAA/ASME/SAE 20th Joint Propulsion Conference, June 1984.

4. Kathiresan, K., and Atluri, S.N., Three-Dimensional Homogeneous and Bi-Material Fracture Analysis for Solid Rocket Motor Grains by a Hybrid Displacement Finite Element Method, AFRPL-TR-78-65, 1978.

5. Schapery, R.A., On a Theory of Crack Growth in Viscoelastic Media, Report MM 2763-73-1, Texas A & M University, March 1973.

6. Knauss, W.G., "Delayed Failure - The Griffith Problem for Linearly Viscoelastic Materials," International Journal of Fracture Mechanics, Vol. 6, March 1970, pp. 7-20.
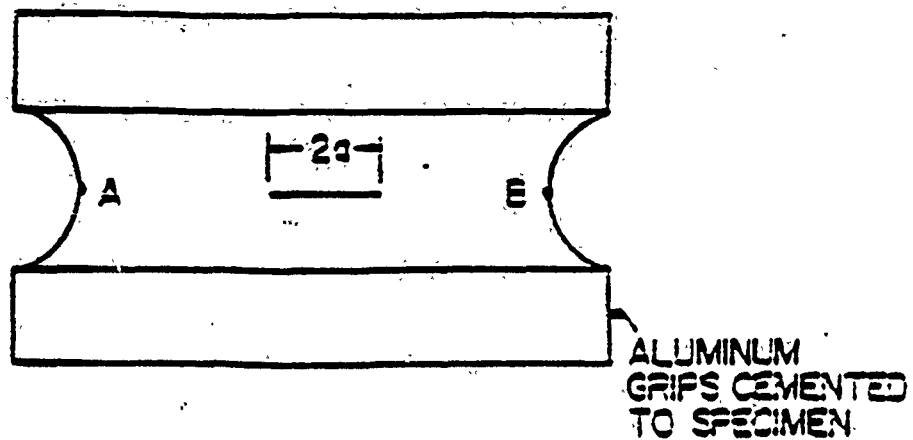
Fig. 1. Testing Specimen

Table I. Stress Intensity Factor for Notched Uniaxial Tests

Test	Loading Rate (in/min)	Tensile Stress at Crack Initiation (PSI)	K_I	Average Percent Increase
001	0.1	15	25.05	–
002	0.1	15.4	25.72	
003	1.0	20	33.40	21.7
004	1.0	17	28.39	
005	10.	32	53.44	97.36
006	10.	28	46.76	

Fig. 2. Effect of Loading Rate on
Elasticity of Propellant 2302M1G2

STRESS (PSI)

Loading Rate (in/min)
———— .1
—+— 1.
—◇— 10.
—△— 20.

146 psi
133 psi
106 psi
86 psi

STRAIN
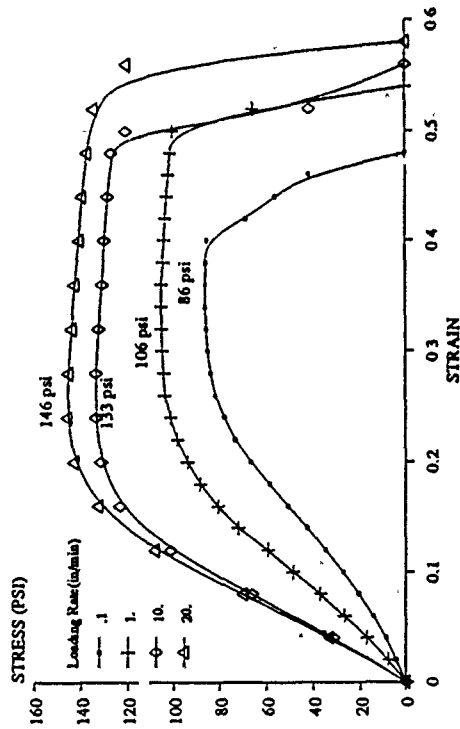
Fig 3. Effect of Loading Rate on
Elasticity, 1/8" Side Notch

STRESS (PSI)

Loading Rate
———— .1 (in/min)
—△— 1. (in/min)
—◇— 10. (in/min)

92 psi
63 psi
48 psi

STRAIN
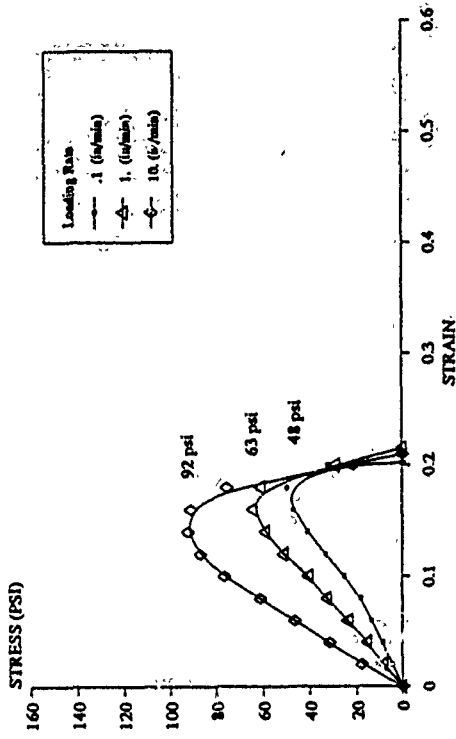
Fig. 4a. Crack Initiation Load vs.
Loading Rate

Crack Init. Load (lb)

Crack Length
—☐— 1 in.
—*— 2 in.

Loading Rate (in./min)
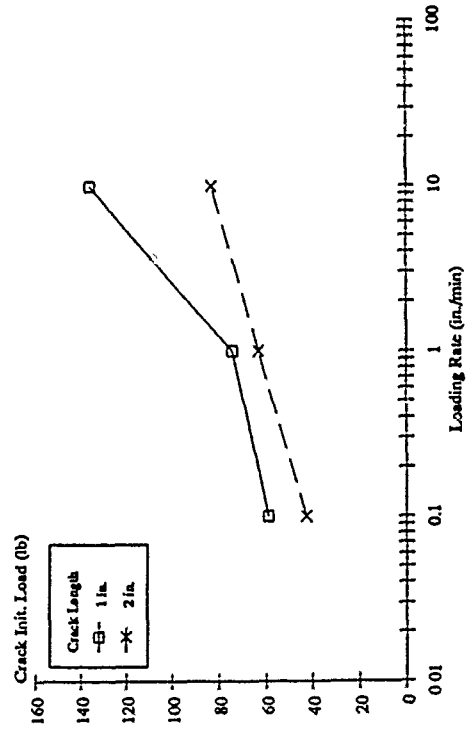
Fig. 4b. Crack Initiation Load vs.
Crack Length

Crack Init. Load (lb)

Loading Rate
—☐— .1 in/min
—X— 1. in/min
—◇— 10. in/min

Crack Length (in.)

25-15
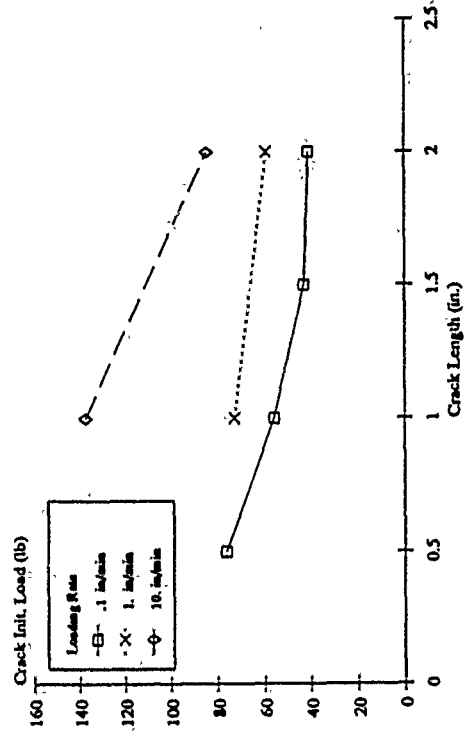
Fig. 5

RUN 409, 410, 411
METHOD 5 0.1 IN/MIN
DELTA A vs SIF
LOG/LOG
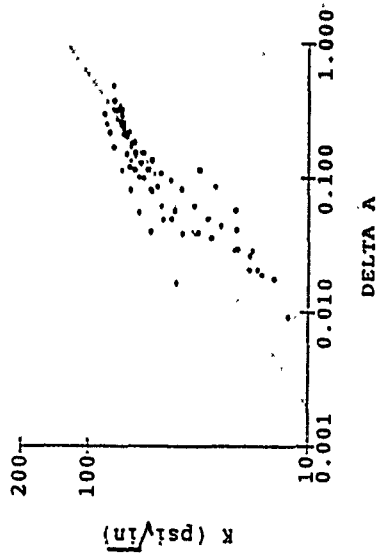
RUN 412, 414, 415
METHOD 5 1.0 IN/MIN
DELTA A vs SIF
LOG/LOG
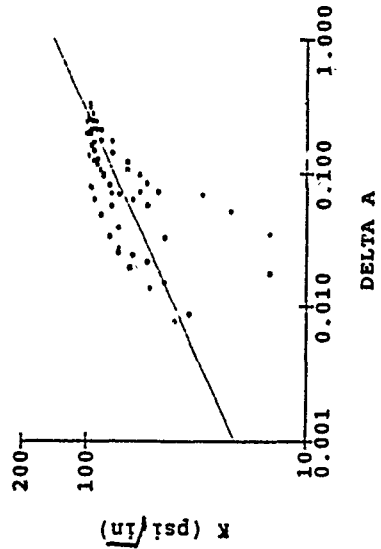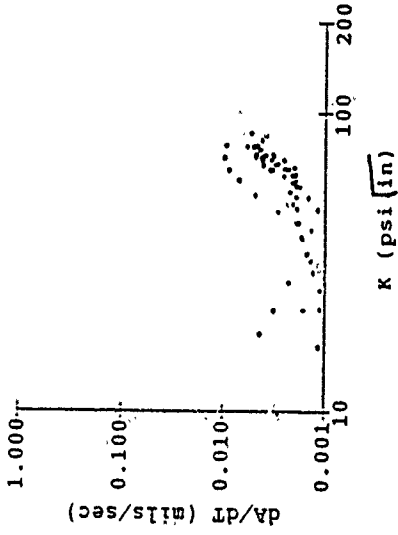
RUN 416, 417, 418
METHOD 5 10.0 IN/MIN
DELTA A vs SIF
LOG/LOG

Fig. 6
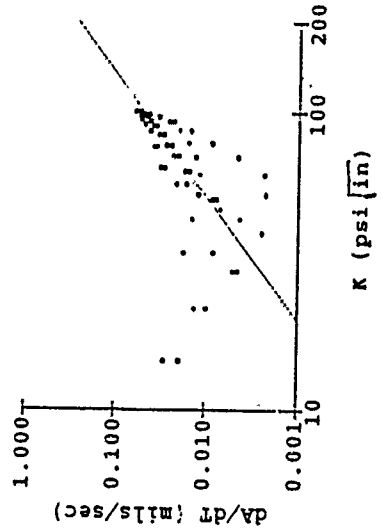
Fig. 7

1990 USAF-UES Summer Faculty Research Fellow
Graduate Student Research Program

Sponsored by the
AIR FORCE OFFICE OF SCIENTIFIC RESEARCH

Conducted by
the Universal Energy Systems, Inc.

FINAL REPORT
WALSH FUNCTION ANALYSIS OF IMPULSE RADAR

Prepared by: Chih-fan CHEN, Ph.D.

Academic Rank: Professor
Department: Applied Science
University: Boston University

Research Location: AFSC Electronic Systems Division
Hanscom AFB MA 01731-5000
USAF Researcher: Lt Colonel James D. Taylor, P.E.

Date: October 1., 1990
Contract No: F49620-88-C-0053

WALSH FUNCTION ANALYSIS OF IMPULSE RADAR

by

CHIH - FAN CHEN

ABSTRACT

A conventional radar is with extremely narrowband, while an impulse radar is with ultrawideband; The impulse radar has a potential to achieve the goals such as resolution, risetime and bandwidth. As experts in this field indicated: we have to think about ways of increasing range resolution or widen the bandwidth of the signal. However the tools for analyzing impulse radars are not quite ready. It is known that the mathematical tools for conventional radars are based on Fourier theory which is not very suitable for impulse radars, because it can not cope with a short time situation and it always has Gibb's phenomenon and it is comparatively slow in processing. Following Harmuth's suggestion, instead of using Fourier theory, we apply Walsh functions for impulse radar studies. An operational matrix is used for integration; by use of which ordinary differential equations and simple partial differential equations are solved by Walsh analysis . The final goal is to attack the Maxwell equations in order to solve impulse radar problems.

Acknowledgememts

The author would like to thank Lt. Colonel James D. Taylor of Hanscom for suggesting the topic, bringing to his attention the related references and offering a general vision on impulse radars, to Dean A. Hershfield and Professor R.Skvarcius of Metropolitan college of Boston University for encouragement and helpful discussions, to the Air Force Office of Scientific Research for sponsorship of this research and to Universal Energy Systems for their concern and administrative help.

Intruduction

The difference between a conventional radar and an impulse radar is the relative bandwidth . The former is with extremely narrowband , while the latter, ultrawideband. What the conventional radar needs to be improved is resolution, rise time and bandwidth. The impulse radar has a potential to achieve those goals. As experts in this field indicated: we have to think about ways of increasing range resolution or widen the bandwidth of the signal[1,2,3].

The objective for using impulse radar is for improving target identification based on target echo characteristics; however, it is known that the mathematical tools for conventional radars are based on. Fourier analysis which is powerful in many aspects[3]. However, Fourier methods are not very suitable for impulse radars. The reasons are as follows:

* Fourier analysis is a steady state oriented approach: it, therefore, can not cope with a short rise time situation;

* No matter how many term of Fourier series being taken, there is always the well known Gibb's phenomenon involved;

* Although the fast Fourier algorithm is available, it is still too slow for on line operations.

Therefore, pioneers, for example, Harmuth[4], suggested that Fourier oriented approaches should be modified or even abandoned in studying impulse radars. Instead, Walsh functions, block pulse functions or other square-shaped orthogonal functions should be explored for impulse radar studies.

1   Objective of this Research Effort

The objective of this research is to solve Maxwell equations via Walch functions for applying to the impulse radar problems. Before reaching that goal, some preparation works should be done.

* Solution of time-invariant systems via Walsh functions is established. An operational matrix is formulated and tested. The principal investigator's earlier work

is generalized. Not only problems of state equations with higher dimensions are solved, but also solutions for higher order systems with multi-input-output problems are formulated.

- Solution of simple partial differential equations via Walsh functions by using double Walsh series is given. This implies that the technique can be extended naturally to solving transmission line problems via Walsh functions. The ultimate objective of the research is to solve Maxwell equations via orthogonal functions in general and by Walsh functions in particular. This report is the preliminary studies.

2   Walsh Functions in Dynamic Systems Studies

Rademacher developed a set of square functions of unit high with periods equal to 1, 1/2, ..., 1/8 etc, the number of cycles of the square wave of $r_k(t)$ is 2. Obviously it is a set of odd functions about t= 1/2. Of course, Radamacher function is imcomplete. A year later, that was 1923, Walsh developed a complete set known as Walsh functions[6,7].

Walsh functions for communication analysis can be traced back to 1969. Harmuth's paper in Spectrum and his book "Transmission of information by Orthogonal Functions [5] were well known.However, not too much progress has been made since that time. On the other hand, Chen and Hsiao[8,9] initiated a series studies of the Walsh function in its dyadic order to organize an operational matrix for integration. Let us start the investigation with the dyadic ordered Walsh function.[10]

A function f(t) that is absolutely integrable in [0,1) may be expanded as a Walsh series

$$f(t) = c_0 \phi_0(t) + c_1 \phi_1(t) + ... + c_n \phi_n(t) + ... \tag{1}$$

where c_n are called coefficients of Walsh series, while $\phi_n(t)$ are called Walsh functions which are derivable from Rademacher functions $r_r(t)$ i.e.,

$$\phi_n(t) = (r_q(t))^a (r_{q-1}(t))^b (r_{q-2}(t))^c ... \tag{2}$$

in which abc is the binary expression of n and $q = (log_2 n) + 1$ which (.) means taking the greatest integer of ".". For example,

$$\phi_9(t) = (r_4(t))^1 (r_3(t))^0 (r_2(t))^0 (r_1(t))^1 \tag{3}$$
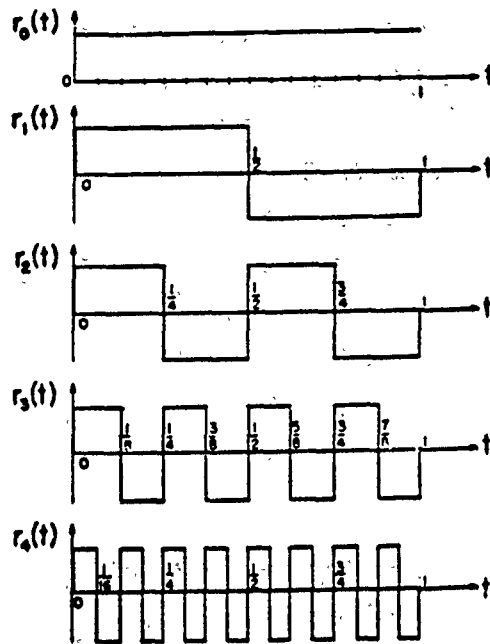
Fig.1. Rademacher functions
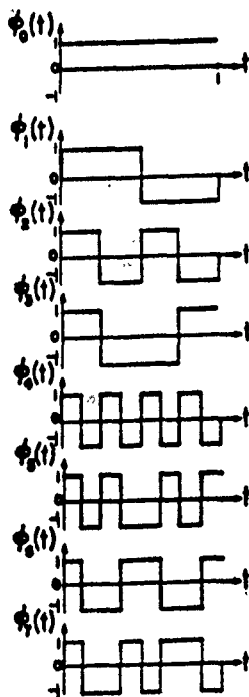
Fig.2. Walsh functions

now we find the Walsh coefficients for a sine wave:

$$f(t) = sin(\pi t) \cong \sum_{n=0}^{\eta} c_n \Phi_n(t) \qquad (4)$$

in which c_n can be evaluated by

$$c_n = \int_0^1 \Phi_q(t) f(t) dt \qquad (5)$$

and we obtain the following

$$c_0 = 0.637, \quad c_1 = c_2 = 0, \quad c_3 = -0.263$$

$$c_4 = 0, \quad c_5 = -0.126, \quad c_6 = -0.0573$$

Fig.3 shows the Walsh approximation of the sine wave.

If we take the integration of $\phi_i(t)$ curves, what will happen? Simply apply Eq.(5) to each $\phi_i(t)$ or by inspection and easily obtain a set of triangular curves as shown in Fig.4. Then we can find the Walsh coefficients for each triangular curve and get:

$$\int \phi_0 dt = (\frac{1}{2})\phi_0 + (-\frac{1}{4})\phi_1 + (-\frac{1}{8})\phi_2 + (-\frac{1}{16})\phi_4$$

$$\int \phi_1 dt = (\frac{1}{4})\phi_0 + (-\frac{1}{8})\phi_3 + (\frac{1}{16})\phi_5$$

$$\cdots\cdots$$

$$\cdots\cdots$$

$$\int \phi_7 dt = (\frac{1}{16})\phi_3 \qquad (6)$$

we can rearrange (5) into a matrix form as follows:

$$
\begin{pmatrix} \int \phi_0 dt \\ \int \phi_1 dt \\ \int \phi_2 dt \\ \int \phi_3 dt \\ \int \phi_4 dt \\ \int \phi_5 dt \\ \int \phi_6 dt \\ \int \phi_7 dt \end{pmatrix}
=
\begin{pmatrix}
\frac{1}{2} & (-\frac{1}{4}) & (-\frac{1}{8}) & 0 & (-\frac{1}{16}) & 0 & 0 & 0 \\
\frac{1}{4} & 0 & 0 & (-\frac{1}{8}) & 0 & (-\frac{1}{16}) & 0 & 0 \\
\frac{1}{8} & 0 & 0 & 0 & 0 & 0 & (-\frac{1}{16}) & 0 \\
0 & \frac{1}{8} & 0 & 0 & 0 & 0 & 0 & (-\frac{1}{16}) \\
\frac{1}{16} & 0 & 0 & 0 & 0 & 0 & 0 & 0 \\
0 & \frac{1}{16} & 0 & 0 & 0 & 0 & 0 & 0 \\
0 & 0 & \frac{1}{16} & 0 & 0 & 0 & 0 & 0 \\
0 & 0 & 0 & \frac{1}{16} & 0 & 0 & 0 & 0
\end{pmatrix}
\begin{pmatrix} \phi_0 \\ \phi_1 \\ \phi_2 \\ \phi_3 \\ \phi_4 \\ \phi_5 \\ \phi_6 \\ \phi_7 \end{pmatrix}
$$

$$(7)$$

In a compact form

$$\Phi_{(8)} = P_{(8)} \Phi_{(8)} \qquad (8)$$
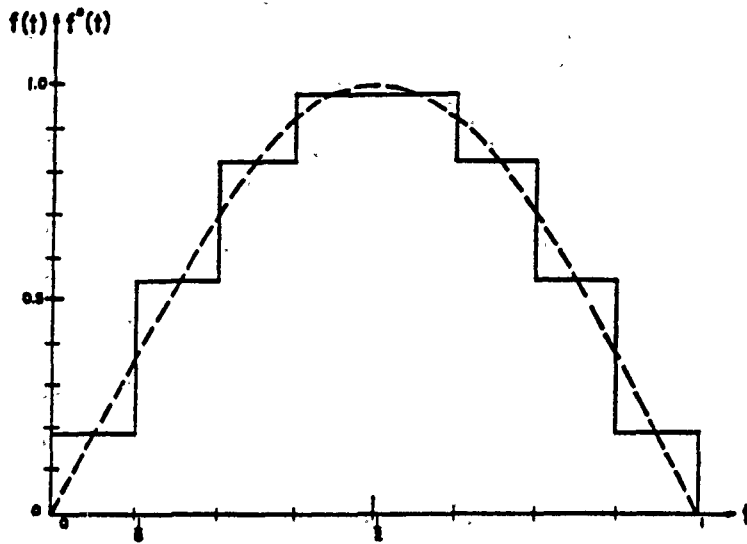
Fig.3. Sine function and its Walsh series approximation
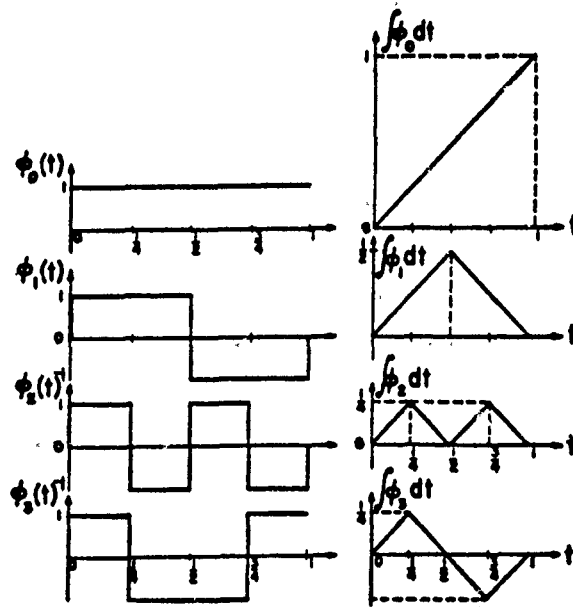
Fig.4. Walsh funtions and Integration of Walsh.

It can be easily verified that the upper left conner of $P_{8\times 8}$ is $P_{4\times 4}$ and $P_{8\times 8}$ would become the upper left corner of $P_{16\times 16}$ etc. In (6a); $P_{8\times 8}$ is called the operational matrix for 8 terms taken. In general, if we take m terms, the corresponding matrix would be written as follows

$$
P_{m\times m} = \begin{pmatrix}
\frac{1}{2} & \frac{-1}{m}I_{\frac{m}{2}} & & & \\
& & \frac{-1}{m}I_{\frac{m}{4}} & & \\
\frac{1}{m}I_{\frac{m}{2}} & O_{\frac{m}{2}} & & & \\
& & & & \frac{-1}{2m}I_{\frac{m}{2}} \\
\frac{-1}{m}I_{\frac{m}{4}} & & O_{\frac{m}{4}} & & \\
& \frac{-1}{2m}I_{\frac{m}{2}} & & & O_{\frac{m}{4}}
\end{pmatrix}
\tag{9}
$$

where $m = 2^z$ and z is an integer number. We can use Eq.(9) to solve a time invariant differential equation, considering the following simple one:

$$
\dot{x} = -4x, \quad x(0) = 1
\tag{10}
$$

we would like to solve Eq.(10) by using the Walsh operational matrix Eq.(9)

First of all, we assume $\dot{x}$ has a Walsh expansion with m=4 undetermined coefficients:

$$
\dot{x} = \sum_{n=0}^{4} c_n \phi_n = C'\Phi
\tag{11}
$$

The Walsh series expansion of x is obtained through integration

$$
\begin{aligned}
x(t) &= c' \int \phi(t)d(t) + x_0 \\
&= C'P\Phi + x(0)
\end{aligned}
\tag{12}
$$

Substituting (9) and (10) into (8), we have

$$
\begin{aligned}
C &= [I + 4P']^{-1} \begin{pmatrix} -4 \\ 0 \\ 0 \\ 0 \end{pmatrix} \\
&= \begin{pmatrix} 3 & 1 & \frac{1}{2} & 0 \\ -1 & 1 & 0 & \frac{1}{2} \\ -\frac{1}{2} & 0 & 1 & 0 \\ 0 & -\frac{1}{2} & 0 & 1 \end{pmatrix}^{-1} \begin{pmatrix} -4 \\ 0 \\ 0 \\ 0 \end{pmatrix}
\end{aligned}
\tag{13}
$$

Finally we obtain the solution,

$$
\begin{aligned}
\dot{x} &= C'\Phi(t) \\
&= -\frac{80}{81}\phi_0(t) - \frac{64}{81}\phi_1(t) - \frac{40}{81}\phi_2(t) - \frac{32}{81}\phi_3(t)
\end{aligned}
\tag{14}
$$

$$x = c'P\Phi(t)$$
$$= -\frac{20}{81}\phi_0(t) - \frac{16}{81}\phi_1(t) - \frac{10}{81}\phi_2(t) - \frac{8}{81}\phi_3(t) \tag{15}$$

The exact and Walsh solution curves are shown in Fig.5.

3 Double Walsh Series for Solving Partial Differential Equations

Before our trying to solve Maxwell equations vis Walsh functions, we start from the investigation with a simplest partial differential equation. To solve a partial differential equation should be a natural extension of the solution for ordinary differential equation via Walsh functions.

Let us consider the following simplest partial differential equation with constant coefficients.

$$\frac{\partial y}{\partial t} + \frac{\partial y}{\partial x} = ay + bu \tag{16}$$

$$when \quad x = 0, \quad y(0,t) = f(t)$$

and

$$when \quad t = 0, \quad y(x,0) = g(x)$$

where y(x,0) means

$$y(x,0) = [\frac{\partial y}{\partial t}(x,t)]_{t=0} \tag{17}$$

The transform method for approaching this problem is quite straightforward; for example, the Laplace transform method is used: we take the t domain Laplace transform for Eq.(13):

$$\mathcal{L}_t \frac{\partial y}{\partial t} + \mathcal{L}_t \frac{\partial y}{\partial x} = \mathcal{L}_t ay + \mathcal{L}_t bu \tag{18}$$

Evaluation and considering x as constant yields

$$s\frac{dY(x.s)}{dx} + \frac{dY(x.s)}{dx} - aY(x,s) = y(x,0) + bU(x,s) \tag{19}$$

wheres s can be considered as a parameter and the above equation become an ordinary differential equation. We can solve it either by transforming it with respect to x and an algebra equation will be obtained; or by using the classical method, i.e. finding its complementary function and particular integral respectively; and then taking the inverse Laplace transform with respect to t to get the final solution.
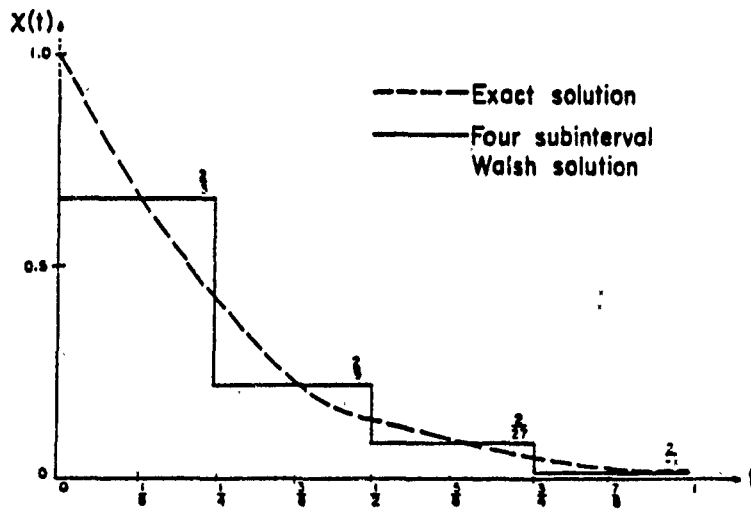
Fig.5. Walsh series solution of a free system

The reasoning and thinking of the Walsh approach is assumed to be similar to that of the Laplace transform approach. That means to use the Walsh series twice or double Walsh series to deal with the partial differential equation problem.

A function y(x,t) can be represented by a Walsh series with respect to t as follows:

$$y(x,t) = \sum_0^\infty y_i(t)\phi_i(t) \tag{20}$$

where $\phi_i(t)$ is the i-th order Walsh function. If we truncate Eq.(20) to the first n terms, we have:

$$y(x,t) = \sum_0^{n-1} y_i(t)\phi_i(t) \tag{21}$$

The coefficient functions $y_i(x)$ of equation Eq.(10) become

$$y_i(x) = \int_0^1 y(x,t)\phi_i(t)dt \tag{22}$$

Likewise, a Walsh series approximation of $y_i(x)$ gives

$$y_i(x) = \sum_0^{m-1} \phi_i(x)y_{ji} \tag{23}$$

where $\phi_i(t)$ are Walsh functions with respect to x, and y_{ji} are coefficients obtained by the following:

$$y_{ji} = \int_0^1 \phi(x)y_i(x)dx = \int_0^1\int_0^1 \phi_j(x)y(x,t)\phi_i(t)dxdt \tag{24}$$

Combining equations Eq.(10) and Eq.(12) gives

$$y(x,t) = \sum_0^{n-1}\sum_0^{m-1} \phi_j(x)y_{ji}\phi_i(t) \tag{25}$$

This equation can be written into the following matrix form:

$$y(x,t) = \Phi_{(m)}^T(x)Y\Phi_{(n)}(t) \tag{26}$$

where

$$\Phi_{(n)}(t) = [\phi_0(t), \phi_1(t), .., \phi_{n-1}(t)]^T \tag{27}$$

$$\Phi_{(m)}(t) = [\phi_0(x), \phi_1(x), ..., \phi_{n-1}(x)]^T \tag{28}$$

and coefficient matrix $y_{m \times n}$ is as follows:

$$\begin{pmatrix} y_{00} & y_{01} & \cdots & y_{0,n-1} \\ y_{10} & y_{11} & \cdots & y_{1,n-1} \\ & \cdots & \cdots & \\ & \cdots & \cdots & \\ y_{m-1,0} & y_{m-1,1} & & y_{m-1,n-1} \end{pmatrix} \qquad (29)$$

Equation Eq.(26) is the double Walsh series approximation of $y(x,t)$. $\phi_{(m)}$ and $\phi_{(n)}$ can be integrated from 0 to 1 and we arrive at:

$$\int_0^1 \Phi_{(n)}(t')dt' = P_{(n \times n)}\Phi_{(n)}(t) \qquad (30)$$

$$\int_0^x \Phi_{(m)}(x')dx' = P_{(m \times m)}\Phi_{(m)}(x) \qquad (31)$$

where $P_{(m \times m)}$ and $P_{(n \times n)}$ are operational matrices of integration. The general form of the operational matrix is Eq.(9), while m=4 , the matrix become:

$$P_{(4 \times 4)} = \begin{pmatrix} \frac{1}{2} & -\frac{1}{4} & -\frac{1}{8} & 0 \\ \frac{1}{4} & 0 & 0 & -\frac{1}{8} \\ \frac{1}{8} & 0 & 0 & 0 \\ 0 & \frac{1}{8} & 0 & 0 \end{pmatrix} \qquad (32)$$

which is the upper left corner of Eq.(9).

We will apply Eq.(26) with Eq.(30) and Eq.(31) to solve partial differential equations.

4 Recommendation

Our ultimate goal is to solve Maxwell equations via Walsh analysis . Before doing that, we have to solve simple time varying differential equation and simple integral equation first. We expect that various operational matrices can be derived and should be investigated.

Recently, Lewis[12] established a method replacing the solution of a two -variable partial differential equation with the solution of a solution of a linear algebraic generaized 2-D sylvester equation . That is an natural extension of Chen and Hsiao' Walsh function analysis and it is possible to generalize the technique to higher dimension domain in order to solve the Maxwell equations.

Harmuth [5,11] also strongly recommended another set of orthogonal functions-block pulse functions and the auther develops them for irrational functions of the s variable[11]. This implies that the partial differential equations can be solved by the block pulse functions approach.

5 References

[1] Ross, D. *Mr. Dooley, Prof. Harmuth and Impulse Radar*, Los Alamos National Laboratory.

[2] Taylor, J. D. *1990 Military electronics systems evaluation and ultrawideband technology AFSC Electronics*, Division, Hanscom.

[3] Kong, J.A.,(ed) *1989 Progress in Electromagnetics Research Symposium Proceedings*, Boston, Massachusetts.

[4] Harmuth, H.F., *1969 IEEE SPECTRUM*, vol.6. no.11.

[5] Harmuth, H.F., *1969 Transmission of Information by Orthogonal Functions*, Springer-Verlag, New York

[6] Butzer, P.L., *1972 Application of Walsh Functions Symposium*, Naval Research Laboratory.

[7] Tzagestas, S.G., *1985 Walsh Functions in Signal and Systems Analysis and Design* van Nostrand Reinhold Co.

[8] Chen C.F. and C.H. Hsiao, *1975 Walsh series analysis in optimal control* vol. 21. no.6. 1975

[9] Chen C.F. and C.H. Hsiao, *1975 System identification via Walsh Functions.* Proceedings of Institute of Electrical Engineers, vol. 122, p.565.

[10] Chen C.F. and W.K. Leung *1985 Algorithms for converting sequency, dyadic-and Hadamard-ordered Walsh functions*, Mathematics and Computers in Simulation. vol. 27.

[11] Chen C.F., T.Tsay and T.T. Wu, *1977 Walsh operational matrices for fractional calculus and their applications to distributed systems*, Journal of Frandlin Institute, vol. 303. no.3.

[12] Lewis, F. L., W. Marsgalek and B.G. Mertzios, *1990 Walsh function analysis of 2-D generalized continuous systems* IEEE Transactions on Automatic Control. vol AC-35, no. 6, pp.1140-1144

1990 USAF-UES SUMMER FACULTY RESEARCH PROGRAM

Sponsored by the

AIR FORCE OFFICE OF SCIENTIFIC RESEARCH

Conducted by the

Universal Energy Systems, Inc.

FINAL REPORT

HIGH OXYGEN/CARBON RATIO FUEL CANDIDATES FOR CLEAN AIR

FIRE FIGHTING FACILITY PROJECT

Prepared by:	William W. Bannister, PhD
Academic Rank:	Professor
Department and	Chemistry
University:	University of Lowell Lowell, MA 01854
Research Location:	AFESC/RDCF Tyndall AFB, FL 32403-6001
USAF Researchers:	Mr. Charles Risinger Mr. Joseph Walker
Date:	25 September 1990
Contract No.:	F49620-88-C-0053

HIGH OXYGEN/CARBON RATIO FUEL CANDIDATES FOR CLEAN AIR FIRE FIGHTING FACILITY PROJECT

William W. Bannister

Abstract

This project will evaluate performance and burn characteristics of isobutyl acetate [IBA] and ethoxyethyl propionate [EEP] as high oxygen/carbon ratio [high O/C] low smoke candidates for replacement of JP-4 and other hydrocarbon fuels in firefighting training facilities. The tests will compare the following characteristics of IBA and EEP with JP-4: relative fire safety of the test candidates; extinguishabilities by 3% Aqueous Film Forming Foam (AFFF), and other extinguishing agents; qualitative and quantitative analyses of smoke generation; and qualitative and quantitative analyses of air and fire pit water pollutants.

ACKNOWLEDGMENTS

I am very grateful to the Air Force Systems Command and the Air Force Office of Scientific Research for sponsorship of this project, and to Universal Energy Systems, Inc. for administration and supervision of the work. I am also indebted for the ongoing help and friendship extended to me by military and civilian staff members at the Fire Protection and Crash Rescue Systems Branch [RDCF] at Tyndall Air Force Base: Mr. Joseph Walker (Head), Mr. Richard Vickers, Mr. Charles Risinger, CAPT John Floden (USAF), CWO4 Bobby Barrow (USAF), Mr. Hugh Pike, Mr. Douglas Schwartz, and Mr. Lew Scott; Dr. John Storm, Mr. Mike Wilson, Mr. Billy Dees, and Mr. Donald Lewis of ARA Corporation at Tyndall AFB; and Mr. Perry Sullivan (USAF-USE SFRP coordinator at Tyndall AFB, AFESC) and Mr. Andrew Poulis (Chief Librarian at Tyndall AFB AFESC). I express my great appreciation to all of these experts who have contributed greatly to these efforts.

BURN CHARACTERISTICS TESTS OF HIGH OXYGEN/CARBON RATIO FUEL

CANDIDATES FOR CLEAN AIR FIRE FIGHTING FACILITY PROJECT;

PHASE I. PRELIMINARY SMALL SCALE TESTS [TEST PLAN]

SECTION I

INTRODUCTION

A. SCOPE.   This project will evaluate performance and burn
characteristics of isobutyl acetate [IBA] and ethoxyethyl
propionate [EEP] as high oxygen/carbon ratio [high O/C] low
smoke candidates for replacement of JP-4 and other
hydrocarbon fuels in fire fighting training facilities. The
tests will compare the following characteristics of IBA and
EEP with comparision to JP-4: relative fire safety of the
test candidates; extinguishabilities by 3% Aqueous Film
Forming Foam (AFFF), and other extinguishing agents;
qualitative and quantitative analyses of smoke generation;
and qualitative and quantitative analyses of air and fire
pit water pollutants.

The tests at the Sky X Fire Research Facility at Tyndall
AFB (TAFB) will consist of five (5) small scale four foot
diameter pan burn tests which shall investigate the fire
safety, extinguishability, and relative smoke emission
aspects of IBA and EEP, alone and in mixture with JP-4. (A
sixth small test fire will be conducted by a contractor who
shall undertake to determine components of smoke and vapor
emissions from burning IBA for subsequent use in qualitative
and quantitative analyses of large scale IBA burn tests.)

B. BACKGROUND. In current DOD (and civilian) fire training exercises, large (500 gallons) volumes of JP-4 or other hydrocarbon fuels are ignited in large (8,000 ft^2) open fire pit facilities. For extinguishment AFFF is mixed with water to 3% or 6% concentrations and applied to the fire using the Air Force's front line P-19 firefighting or other vehicle, or with simpler handline equipment; or with powder, water fog, or halon extinguishing agents.

Such fire training exercises are quite realistic, matching conditions routinely encountered in large scale, three dimensional fires with heavy thermal and smoke outputs. Severe environmental problems exist, however, especially in terms of air pollution from billowing smoke plumes. Increased pressures to curtail such training may therefore be encountered in the form of local, state and federal statutes and guidelines.

A variety of simulated training devices and structures have been designed to provide smoke-free fire training capabilities, including computerized games; computerized propane burner facilities with controls by which training staff can input evaluations of the level of fire fighting effectiveness and thereby reduce intensities of the propane flames; and smoke abatement buildings (with scrubbing devices to wash smoke from the air, but with limited scale fires by comparison with open field facilities). All of these are expensive; none provide adequate realism and

flexibility for important fire fighting training exercises required by the Air Force (e.g., for running fuel fires fires in large hanger or other open structures or areas).

(Environmental problems also exist in terms of possible pollution of ground water by discharges of water remaining in the fire pits with suspended residues of unburnt JP-4, combustion products, and AFFF agent.)

At TAFB the AF Engineering and Services Center [AFESC] Airbase Fire Protection and Crash Rescue Systems Branch [RDCF] has found that carboxylic esters with high O/C ratios are clean fire training fuels. Such esters have lower toxicities than JP hydrocarbon fuels; many are food additives with FDA approval and no requirement for personnel protection. Unlike JP-4, esters are biodegradable with no ground water environmental problem for fire training exercises. The simple, low molecular weight esters form much fewer pyrolytic degradation products and thus much lower contamination problems for air emissions than larger hydrocarbon molecules comprising JP fuels. Moreover, the high oxygen contents of the esters provide more thorough combustion, again with fewer contamination products. Various esters can be selected to match volatilities and flash points of any fuels (JP-4,JP-5, JP-8, Jet A-1, and AV GAS) used by military and civilian aircraft.

Though esters cost more than JP, this is more than offset by obviating large capital and maintenance outlays

for high-tech smoke scrubbing structures or other simulated training devices. Moreover, these clean air fuels will continue to provide excellent flexibility and realism in conventional fire pit and three dimensional training facilities, with acceptable smoke emission levels. It may also be feasible to mix ester and JP fuels and still provide acceptable smoke emissions but at much lower cost.

There are potential drawbacks. Candidates of most interest (IBA and EEP) are more polar than conventional hydrocarbon fuels. Fires involving these fuels may resemble highly polar alcohol fires requiring alcohol type AFFF agents; this would inacceptable for fire training facilities. Preliminary small scale fire tests did indicate that conventional 3% AFFF was an effective extinguishing agent for small IBA fires; but large scale tests need to be performed to demonstrate large scale 3% AFFF extinguishing capabilities for such esters, or for mixtures of hydrocarbon fuels with the esters. Such hydrocarbon/ester mixes have very greatly reduced polarities; thus, 3% AFFF should have increased effectiveness against such mixtures.

The flash points of the candidate ester fuels are significantly higher than JP-4:

flash point, $^\circ$ F

JP-4	16	
IBA	64	Note: mixtures of IBA or EEP with
EEP	132	JP-4 have same flash point as JP-4

On the other hand, IBA and EEP have high oxygen contents and thus are anticipated to burn hotter, and more rapidly once fully developed fire conditions have been achieved. Thus, preliminary medium scale test burns should be conducted with these fuels to ensure that unanticipated safety problems involving its flammability do not exist.

Due to increased polarity, IBA and EEP are somewhat (though not greatly) more soluble in water than JP fuels. (However, IBA and EEP do not form suspensions in water as do JP fuels; and these are much more easily biodegradable than are hydrocarbon fuels. Moreover, due to the very greatly decreased polarity of ester and hydrocarbons mixtures, IBA or EEP mixtures with JP have very low water solubilities.) Large scale tests need to be performed to demonstrate the extent, or lack of extent of ground water pollution problems which may exist for IBA and similar esters, and for decomposition products arising from combustion. And, even though it is anticipated that these esters will produce much fewer and much less toxic airborne combustion products than is the case for hydrocarbon fuels, the actual contaminants and the levels of concentrations of such materials need to be determined for large scale fires.

C. AUTHORITY

HQ USAF Program Management Directive (PMD) 63723F (2104), March 1985, provides authority for this test, which will be conducted as directed in PMD and AFR 80-14.

D. PURPOSE

Test objectives are to evaluate performance and burn characteristics of isobutyl acetate [IBA] and ethoxyethyl propionate [EEP] as high O/C low smoke candidates for replacement of hydrocarbon fuels in fire fighting training facilities; investigate extinguishabilities by 3% AFFF, Purple K, water fog, and halon extinguishing agents; and perform qualitative analyses of smoke emissions.

SECTION II

TEST OBJECTIVES AND TESTING MEASURES OF MERIT

A. TEST OBJECTIVES

Performance and burn characteristics of IBA and EEP as high O/C low smoke candidates will be studies for replacement of hydrocarbon fuels in fire fighting training facilities; extinguishabilities by 3% AFFF, Purple K, water fog, and halon extinguishing agents will be studied; and qualitative analyses of smoke emissions will be performed.

Tests at TAFB will consist of five 4 ft pan burns, with specific objectives to verify that IBA alone (and EEP solution in JP-4 solution) present no increased safety hazard relative to use of JP-4 when used alone as a fire training fuel; verify that 3% AFFF, Purple K, water fog, and halon satisfactorily extinguish fires when applied to burning IBA or EEP/JP4; and verify that significant smoke reductions occur in combustion of IBA and EEP agents, relative to smoke emissions of JP-4.

o Neither IBA or EEP/JP4 shall ignite or accelerate to
   fully developed burn state faster than JP-4 alone.

o Both IBA and EEP/JP4 shall be ignited electrically,
   easily, with no requirement for accelerator fuels.

o Both IBA and EEP/JP-4 shall be extinguished by 3% AFFF;
   Purple K; water fog; and halon, using no more than 25%
   additional agent nor more than 25% additional time than
   needed by for extinguishment of comparable JP-4 fires.

(A sixth test shall be conducted separately by the
contractor to determine components of smoke and vapor
emissions from burning IBA for subsequent use in qualitative
and quantitative analyses of larger scale IBA burn tests.)

B. MEASURES OF MERIT

1. IBA and EEP/JP-4 fuels shall ignite readily, but no
more vigorously than JP-4 pools of comparable size.

2. 3% AFFF; Purple K; water fog; and halon shall be
capable of extinguishing IBA and EEP/JP-4 fires,
using no more than 25% of volumes or time than needed for
JP-4 fires of comparable size.

3. Smoke emissions from IBA and JP-4 fires shall not
exceed more than 40% of levels from comparable JP-4 fires.

4. Non-gaseous vapors in emitted smoke plumes, and non-
degradable water-borne contaminants (other than AFFF) shall
not exceed more than 30% of comparable JP-4 fires levels.

SECTION III

MANAGEMENT AND ORGANIZATIONAL RESPONSIBILITIES

A. MANAGEMENT

Overall test responsibility rests with the AFESC/RDCF Test Director. The Test Director will delegate authority, as necessary. Specific responsibilities for safety, security, communication, photography, and engineering support are contained in the test plan annexes.

B. ORGANIZATIONAL RESPONSIBILITIES

1. AFESC: responsible for overall test management.

2. AFESC/RDCF:

a. Develop, coordinate, and publish a test plan.

b. Provide the test director.

c. Prepare test report; test preparation and protocol.

3. AFESC/WE (Staff Meteorologist): provide daily weather forecasts and briefings to the test director. If the AFESC Staff Meteorologist is unavailable, weather briefings will be provided by TAFB Weather Station.

4. AFESC/PA (Public Affairs Office):

Notification and media inquiry response of the test.

5. Contractor: provide analytical laboratory and technical staff to identify significant pollutants in smoke plumes resulting from test burns of JP-4 and IBA. Prepare a complete protocol for testing as cited in 5.a. above for submission to RDCF. This will become Annex 4 of this Plan when accepted by RDCF.

SECTION IV

TEST EXECUTION

A. INTRODUCTION

This test phase at TAFB is comprised of five (5) small scale 4 ft. pan burn tests, mainly to investigate fire safety and extinguishability aspects. These tests are described in the following paragraphs. (Contractor tests to perform qualitative analyses of smoke emissions will be described separately in this Test Plan in Annex 4.)

B. TEST SITE

Tests will be conducted at the AFESC Sky X Fire Research Facility approximately 10 miles southeast of the main gate and about one mile east of U.S. Highway 98. TAFB is located on the Gulf Coast of Florida, about 10 miles southeast of Panama City, on US Highway 98. The local soil is characteristic of the coastal lowlands of Western Florida, where fine gray/white beach sands are underlaid at variable depths by the Atronelle Formation. This material is very permeable and free- draining. The subgrade is a poorly graded sand. The water table in the area varies with the season, from 4 feet to just below ground surface, usually occuring about 2.5 feet below the surface. Surface drainage is normally in a southerly direction into a swampy area.

C. TEST SCHEDULE

The TAFB test period is planned for 1 - 2 November 1990. A detailed test schedule is contained in Annex 1.

D. SUPPORT REQUIREMENTS

AFESC/RDCF will plan, coordinate and execute the test. Fuel requirements and methods of extinguishment for each test are provided in Table I, below. It can be assumed that no more than one pound of soot; one half pound of CO; 2.5 pounds of organics; or 0.04 pound of NOx will be emitted in each of these tests. (This is a maximized accounting based on calculations taken from A Generalized Air Quality Assessment Model for Air Force Operations, AFWL TR-74-304, Feb. 1975.) The hanger area shall be well ventilated during and after each test in which the hanger us utilized. AFESC Sky X Fire Research Facility, with an electrical fire ignition system, will be the test site for these fires. Suitable small-scale extinghishing equipment shall be provided for application of each of the extinguishing agents onto the fires. Video and still photography of each fire test will be provided by AFESC/RDCF. Detailed support requirements are contained in Annex 2.

E. DATA COLLECTION

1. Genèral. Prior to testing each day, all project participants will be briefed by the test director on data collection and recording requirements. The test director, or his designated representative, will complete the test readiness/data collection checklist contained in Annex 6, as testing progresses, and ensure that all necessary data and photographic and video records are collected/taken.

2. Video Recording. Video recordings of all tests will be made. The video cameras will be configured to record real time on the video tape to facilitate data reduction.

3. Meteorological Data. Meteorological data from TAFB Weather Station will be recorded for each test day by AFESC/WE and forwarded to the AFESC/RDCF Test Director.

F. PRELIMINARY SMALL SCALE BURN TESTS

Major objectives of this test series arc to investigate fire safety and extinguishability aspects. A secondary objective will be to verify the capability of the test agents to burn with greatly reduced smoke emissions.

The tests will include five 4-foot pan fires as per Table 1 which indicates fuel compositions and method of extinguishment for each fire:

TABLE 1

Test No.	Gallons of Fuel In Each Test			Method of Extinguishment
	JP-4	IBA	EEP	
1	1.0			3% AFF
2	1.0			3% AFFF
3	0.2	0.8		Powder
4	0.2		0.8	Halon
5	0.2	0.5	0.3	Water fog

1. Test Procedure - General

A total of five individual fires are planned, all within the hanger space available in the Fire Research Sky X facility. With no significant wind effects, it is

anticipated that the flame column and smoke from each test burn will be maintained in a relatively vertical position. Initial plans are to conduct all five tests the first day, with backup work, if any, to be performed the next day. Pretest briefings will be conducted before each test, to discuss results of previous tests, verify that all systems are functional, and plan subseuqent testing. All personnel will be at their assigned locations a minimum of one hour before commencement of the series. All test materials and equipment will be set up and ready for the test a minimum of 1 hour before the scheduled ignition time. At T-30 minutes (30 minutes before ignition time) a pretest checklist, as contained in Annex 6, will be completed to ascertain the readiness of all functions. These functions will include, but are not limited to, safety, weather, test pit readiness, and data collections readiness. When all functions are ready, the fire will be ignited. The order to ignite the fuel will be given by the AFESC Test Director.

2. Test Procedures - Specific

When the test director confirms that all systems are go he will verbally direct ignition. After ignition, the fire will be allowed to burn for 30 seconds, and the extinguishing agent then aggressively extinguish the fire. Record time and amount of extinguishing agent required to extinguish the fire. A detailed Fire Operations Test Checklist is contained in Annex 6.

SECTION V

SAFETY

A. GENERAL

Safety is an integral part of the test. The test director is responsible for accident prevention. Personnel and equipment safety will take precedence over test execution at all times. Special emphasis will be placed on providing thorough supervision and guidance throughout all test phases. Premission briefings will be conducted daily by the test director detailing the test procedures for the day and emphasizing safety in all test phases.

The AFESC Test Director will function as the safety officer and will monitor all test phases. He will suspend the test any time a safety hazard is observed. Identification of a potential safety hazard will result in test suspension until the hazard can be evaluated and corrected to the satisfaction of all responsible agencies.

Emergency medical personnel will be notified by telephone (ext 911 or 283-2333) before each test that a controlled fuel fire will be conducted at AFESC Sky X Research Facility at Farmdale Road, approximately 1.0 miles east of Highway 98 and 10 miles east of Tyndall AFB.

B. IDENTIFIED HAZARD

All open fires of any dimension are hazardous. All fires planned for these tests will be 4 feet in diameter and will burn for approximately 2 minutes. The approved test

area has been thoroughly examined for safety distance from surrounding objects and found to be well within safe distance limits. Primary and backup firefighting equipment will be on hand at the test site during all fires.

C. SAFETY REPORTING

Accidents, incidents, and serious hazards will be reported in accordance with AFR 127-4 through AFESC/SEG and HQ USAFADWC/SEG. The appointed on-site safety officer is responsible for accident/incident reporting.

The Test Director will ensure that all safety procedures are followed throughout all testing. Testing will be suspended if an event occurs compromising safety. Additional safety procedures are contained in Annex 3.

SECTION VI

ENVIRONMENTAL IMPACT

In accordance with AFR 19-2, Air Force Form 813 has been completed and approved, and it is determined that these tests qualify for Categorical Exclusion 2y. As stated in Form 813, it is anticipated that all evidence of visible smoke will disperse within one hour. Air Quality Assessment Model (AQAM) calculations were made for these one gallon test fires for levels of particulate matter, hydrocarbons, carbon monoxide, and nitrogen oxides.

These calculations presume the burning of JP-4 hydrocarbon fuel. For tests involving IBA, the following additional factors have been entered into the calculation:

JP-4: average constituent, C9H20;

average molecular weight = 128

% carbon = 84.3%

density = 0.8

1 gallon of JP-4 weighs 6.7 pounds.

carbon content in 1 gallons = 5.3 lbs

IBA: C6H12O2;

molecular weight = 116

% carbon = 62%

density = 0.9

1 gallon of IBA weighs 3750 pounds

carbon content in 1 gallon = 4.65 pounds

Carbon based emissions from IBA fires:

approximately 4.65/5.3 = 88% of JP-4

emissions

Lower levels of pollutants will result from burning EEP, since it has a lower carbon percentage (58%) in its formula [C7H14O3]. Table 2 presents results of calculations.

Any major fuel spills or other unplanned event that may affect the environment will immediately be reported to the AFESC and Tyndall AFB environmental offices.

Table 2. AIR EMISSION ESTIMATES FOR LARGE HYDROCARBON FIRES

Note: Unlike JP-4, which has no oxygen content, IBA has a high oxygen/carbon ratio and burns with much less smoke and unburnt fuel emissions. Calculations for combustion emissions for IBA as presented below are based on data available for JP-4; therefore this data is probably a gross overestimate of values which will actually be encountered.

Since combustion is more complete for IBA and EEP, higher combustion temperatures and therefore higher NOx concentrations will be likely. An increase of 25% in NOx is arbitrarily assumed on this basis. EEP values are assumed to approximate those of IBA. In fact, the EEP values should be anticipated to be lower, due its higher oxygen content and lower carbon content.

	FIRE SIZE (each test)							AIR POLLUTANTS* (each test)				
TEST	GAL. JP-4	LBS JP-4	GAL. IBA	LBS IBA	GAL. EEP	LBS EEP	TYPE OF EEP EXTING.	LBS PM	LBS CO	LBS ORGANICS	LBS NOx	TOTAL LBS
1	1.0	6.5					AFFF	0.84	0.37	2.1	0.028	3.34
2			1.0	7.5			AFFF	0.73	0.32	1.8	0.036	2.89[1,2]
3	0.2	1.3	0.8	6.0			POWDER	0.75	0.30	1.9	0.034	2.98[1,2]
4	0.2	1.3			0.8	6.0	HALON	0.75	0.30	1.9	0.034	2.98[1,2]
5	0.2	1.3	0.5	3.8	0.3	2.0	FOG	0.75	0.30	1.9	0.034	2.98[1,2]
Total	1.6	10.2	2.3	17.3	1.1	8.0		3.8	1.6	9.6	0.17	15.2[1,2]

* PM = Particulate Matter   CO = Carbon Monoxide
  HC = Hydrocarbons   NOx = Oxides of Nitrogen

Notes: (1) As noted above, these are maximum values; actual values predicted much lower.
(2) As noted above, NOx values are estimated to be 25% higher than for JP-4.

Reference: A Generalized Air Quality Assessment Model for Air Force Operations, AFML-TR-74-304, February 1975.

1990 USAF-UES SUMMER FACULTY RESEARCH PROGRAM/

GRADUATE STUDENT RESEARCH PROGRAM

Sponsored by the

AIR FORCE OFFICE OF SCIENTIFIC RESEARCH

Conducted by the

Universal Energy Systems, Inc.

FINAL REPORT

RATE-LIMITED MASS TRANSFER AND SOLUTE TRANSPORT

Prepared by:	Mark L. Brusseau
Academic Rank:	Assistant Professor
Department and	Soil and Water Science
University:	University of Arizona
Research Location:	AFESC/RDVC Tyndall AFB, FL
USAF Researcher:	Dave Burris
Date:	2 August 1990
Contract No.:	F49620-88-C-0053

RATE-LIMITED MASS TRANSFER AND SOLUTE TRANSPORT

by

Mark L. Brusseau

ABSTRACT

Mass transfer processes such as sorption/desorption and immiscible liquid-aqueous phase transfer can have significant impact on solute transport and remediation of contaminated groundwater, especially when local equilibrium is defied. The objective of the work reported herein was to investigate nonequilibrium sorption of representative organic chemicals by aquifer materials comprised of low organic carbon. The miscible displacement technique was employed for this purpose. Results suggest that the first-order reverse sorption rate constant is log-log linearly related to the sorption equilibrium constant. Furthermore, it appears that nonequilibrium sorption is similar for all five aquifer materials investigated. Thus, the empirical relationship obtained from these data may serve as a means to obtain estimates of sorption rate constants. It is important to note, however, that a time scale effect was observed, such that the sorption rate constant varied with pore-water velocity.

I. INTRODUCTION:

Nonequilibrium sorption can have a significant impact on the transport and fate of contaminants in the subsurface. In addition, remediation of contaminated soils and aquifers can also be constrained by nonequilibrium. In recognition of this importance, the sorption kinetics of organic chemicals has recently become an active area of research. In the investigation and modeling of sorption dynamics it has generally been assumed in the past that the sorption "reaction" was sufficiently fast such that the local equilibrium assumption (LEA) was valid. Recent experimental and theoretical investigations have, however, caused the validity of the LEA to be re-evaluated. Most of the experimental work that has been reported, however, has concerned soils and sediments with relatively high organic carbon contents. Conversely, there has been little work reported on the nonequilibrium sorption of organic chemicals by aquifer materials comprised of low organic carbon (c.f., Lee et al., 1988; Brusseau et al., 1990a; 1990b; 1990c). The objective of the work reported herein was to investigate nonequilibrium sorption of representative organic chemicals by aquifer materials comprised of low organic carbon.

II. OBJECTIVES OF THE RESEARCH EFFORT:

The major objective of the research effort was to investigate the nonequilibrium sorption of organic chemicals by low organic-carbon aquifer materials.

III. MATERIALS AND METHODS:

Experimental apparatus

The techniques employed for the miscible displacement experiments were similar to those utilized by Brusseau et al (1990b). The column apparatus was an Alltech preparative chromatography column made of precision-bore stainless steel, with an internal diameter of 2.25 cm and a length of 7 cm. Bed supports on both ends were stainless steel diffusion mesh of pore size 60 μm. The diffusion mesh enhanced radial distribution of influent solution and also minimized dispersion at the effluent end. The column apparatus was designed to have a minimum void volume in the end plates. Two dual-piston HPLC pumps (Waters 510) were connected to the column with a Rheodyne switching valve to facilitate switching between solutions with and without the solute of interest. The system was designed so that the solute contacted only stainless steel.

Effluent from the column was directed through a flow-through, variable wave-length UV detector (Waters 450) to allow continuous monitoring of the solution-phase concentration of the solute, which was recorded on a strip chart recorder (Soltec 1242). The wavelength to be used for each experiment was determined by selecting for maximum response. Previous miscible displacement studies have usually employed collection of effluent fractions, which were then analyzed by GC or HPLC. For volatile chemicals, this method suffers from the potential for loss by volatization during the fraction collection and analysis steps. The use of the flow-through detection method eliminates this problem. It also

significantly simplifies the analytical process. However, this method is limited to the use of detectors that are suitable for flow-through operation. This constraint will obviously restrict the chemicals that may be used to detector-specific set.

Materials

The following chemicals were employed for the miscible displacement experiments: 1,4-dichlorobenzene, tetrachloroethene, p-xylene, and naphthalene; pentafluorobenzoic acid was employed as a nonsorbing tracer. The following five aquifer materials were used for these experiments: Lula, Borden, Tinker, Columbus, and Barksdale. Properties of these materials are reported by Stauffer (1987).

Experimental procedure

The column was packed in incremental steps with the dry material to establish uniform bulk density. After completion of packing, electrolyte solution (0.005 M $CaSO_4$, 0.02% NaN_3) was pumped through the column until steady-state water saturation was established; this generally required approximately two days. The constancy of column masses (i.e., maintenance of saturated conditions) was monitored periodically throughout the experiments. The measured dead volumes were used to determine the corrected pore volume of the column. The matrix for all solutions was that described above. Saturated stock solutions for each solute were prepared by placing quantities in excess of their solubility limit in contact with the electrolyte solution and stirring the solution for at least 48 hours. Solutions were filter sterilized with 0.45 μm filters prior to use. Aliquots of the stock solution were

diluted with electrolyte solution until the desired concentration was achieved. The concentration values (C_0) of the solutions used for the MDC experiments were generally 10% to 25% of the aqueous solubility.

A typical experiment involved the continuous injection of a pulse of the selected solute, the pulse size being large enough such that the point of $C/C_0 = 1$ was reached. The solute pulse was then displaced with 0.005 M $CaSO_4$ solution until the point of $C/C_0 = 0$. Constancy of flow was periodically checked by collecting effluent fractions. These measured flow rates were checked against the average flow rate determined by collecting and measuring all effluent over the injection period; they compared well in all cases. The flow rates used for the experiments were 2, 1, and 0.1 ml/min (average pore-water velocity = approx. 80, 40, and 5 cm/hr, repectively).

To check for the existence of nonidealities other than nonequilibrium sorption (e.g., nonlinearity), comparisons of the frontal and distal portions of the breakthrough curves were made. The presence of nonlinearity, for example, would result in non-coincident frontal and distal curves. The comparisons showed the two portions to be coincident (see Figure 1 for an example). To check the reproducibility of the method, repeat experiments were occasionaly performed. An example of such is presented in Figure 2. These results suggest a high degree of reproducibility.

Data anlysis

The results of the miscible displacement experiments were analyzed with a first-order bicontinuum model. Models of this

type, where sorption is assumed to be instantaneous for some portion of the porous medium and rate-limited for the remainder, have been presented by Selim et al. (1976) and Cameron and Klute (1977). Sorption is described as follows:

$$S_1 = F\,K_p\,C \qquad (1a)$$
$$dS_2/dt = k_1\,S_1 - k_2\,S_2 \qquad (1b)$$

where C is the solute concentration in the water-phase (M/L^3), S_1 is the sorbed-phase concentration in the equilibrium domain (M/M), S_2 is the sorbed-phase concentration in the kinetic-controlled domain (M/M), K_p is the sorption equilibrium constant, F is the fraction of sorbent for which sorption is instantaneous, and k_1 and k_2 are the forward and reverse sorption rate constants (T^{-1}), respectively. These models can represent each of the three processes, namely physical nonequilibrium, chemical nonequilibrium, and intrasorbent diffusion, responsible for nonequilibrium sorption (Brusseau and Rao, 1989a).

To simulate solute transport, the following two nondimensional equations are employed:

$$\partial c^*/\partial p + (\beta R-1)\,\partial c^*/\partial p + (1-\beta)R\,\partial s^*/\partial p = (1/P)\,\partial^2 c^*/\partial x^2 - \partial c^*/\partial x \quad (2)$$
$$(1-\beta)R\,\partial s^*/\partial p = \omega\,(c^* - s^*) \qquad (3)$$

where

$$c^* = C/C_0 \qquad (4a) \qquad\qquad P = vL/D \qquad (4b)$$
$$s^* = S_2/(1-F)K_p \qquad (4c) \qquad\qquad R = 1 + (\rho/\theta)K_p \quad (4d)$$

$$p = vt/L \quad (4e) \qquad\qquad \beta = (1 + F(\rho/\theta)K_p)/R \quad (4f)$$

$$X = x/L \quad (4g) \qquad\qquad \omega = k_2(1-\beta)RL/v \quad (4h)$$

and where D is the dispersion coefficient (L^2/T), v is the average pore-water velocity (L/T), x is distance (L), L is column length (L), ρ is bulk density (M/L^3), and θ is volumetric soil-water content. To run the model, knowledge of the following parameters is required: the Peclet number P, which represents the dispersive-flux contribution to transport; the retardation factor R, which represents the effect of sorption on transport; the fraction of instantaneous retardation, β; the Damkohler number ω, which is a ratio of hydrodynamic residence time to characteristic time of the sorption "reaction"; and T_0, the size in pore volumes of the input pulse. The value for P was obtained from the BTC of a nonsorbing solute. The value for R was obtained by moment analysis, i.e., the first, normalized, absolute temporal moment of a dirac pulse (Brusseau et al., 1990b, or from area above the breakthrough curve (Nkedi-Kizza et al., 1987). The value of T_0 is known from measurement. The two unkown parameters are thus β and ω. The nonlinear, least-squares optimization program CFITIM (van Genuchten, 1981) was used under flux boundary conditions to determine values for the two unknowns.

IV. RESULTS AND DISCUSSION:

Pentafluorobenzoic acid breakthrough curves were obtained for the columns to establish their hydrodynamic character and to determine values for P. These BTCs were symmetrical and sigmoidal

in shape and were invariant with pore-water velocity, which suggests the absence of physical nonequilibrium (Brusseau and Rao, 1989a). BTCs for the organic chemicals were, in contrast, asymmetrical (see Figures 1 and 2). This, in conjunction with the symmetrical BTCs obtained for a nonsorbing tracer, is highly suggestive of a sorption-related nonequilibrium process (Brusseau and Rao, 1989a).

The relationship between k_2, values of which were determined by optimization, and K_p was evaluated using the linear-free-energy-relationship technique, in the manner of Brusseau and Rao (1989b). The results for the 2 ml/min velocity experiments are shown in Figure 3, where the regression equation reported by Brusseau and Rao (1989b) is included for comparison. An inverse correlation between k_2 and K_p is evident. In addition, it appears that all five aquifer materials exhibit similar nonequilibrium behavior. This observation that sorbent appears to play only a secondary role on the nature of nonequilibrium sorption was also reported by Brusseau et al. (1990b; 1990c).

The effect of velocity on rate-constant values was investigated by comparing data obtained at the fast velocities to that obtained at 0.1 ml/min. Inspection of Figure 4 reveals that the rate constants appear to vary with velocity. Inspection of Figure 4 also shows that the K_p values did not change significantly with velocity. This suggests that additional sorption is not taking place at the slower velocity and, therefore, that the velocity effect is related to the nature of the first-order model approximation. This time scale effect is important to consider

when determining appropriate rate-constant values for a given situation.

V. RECOMMENDATIONS:

a) The empirical relationship obtained from these da a may serve as a means to obtain estimates of sorption rate cor tants. These would be useful for input to models that may then be used to investigate the relative importance of nonequilibrium sorption on the transport and fate of organic contaminants in the subsurface.

b) One suggested topic of follow-on research is to compare the effect of heterogeneous aquifer properties (e.g., hydraulic conductivity, sorption capacity) to that of nonequilibriunm sorption on the transport of organic chemicals. Another topic would be an investigation of mass transfer of organic contaminants between residual immiscible liquids and water.

ACKNOWLEDGMENTS

I would like to thank Dave Burris and Tom Stauffer for their assistance, as well as that of the RDV staff. I would also like to thank Mary Reid for her help in performing the experiments reported herein.

REFERENCES

Brusseau, M. L. and Rao, P. S. C, Sorption nonideality during

organic contaminant transport in porous media, CRC Critical Reviews in Environ. Control, 19, 33, 1989a.

Brusseau, M. L. and Rao, P. S. C., Evidence for diffusional mass transfer within sorbent organic matter as a cause for sorption nonequilibrium, Chemosphere, 18, 1691, 1989b.

Brusseau, M.L., Larsen, T., and Christensen, T.H., Rate-limited sorption and nonequilibrium transport of organic chemicals in low organic carbon aquifer materials, Water Resour. Res. (in review), 1990a.

Brusseau, M.L., Jessup, R.E., and Rao, P.S.C., Sorption kinetics of organic chemicals: Evaluation of gas-purge and miscible-displacement techniques, Environ. Science Technol., 24, 727, 1990b.

Brusseau, M.L., Jessup, R.E., and Rao, P.S.C., Nonequilibrium sorption of organic chemicals: Elucidation of rate-limiting processes, Environ. Science Technol., (in press), 1990c.

Cameron, D. R., and Klute, A., Convective-dispersive solute transport with a combined equilibrium and kinetic adsorption model, Water Resour. Res., 13, 183, 1977.

Lee, L. S., Rao, P. S. C., Brusseau, M. L., and Ogwada, R. A., Nonequilibrium sorption of organic contaminants during flow

through columns of aquifer materials, Environ. Tox. Chem., 7, 779, 1988.

Nkedi-Kizza, P., Rao, P. S. C., and Hornsby, A. G., The influence of organic cosolvents on leaching of hydrophobic organic chemicals through soils, Environ. Sci. Technol., 21, 1107, 1987.

Selim, H. M., Davidson, J. M., and Mansell, R. S., Evaluation of a two-site adsorption-desorption model for describing solute transport in soils, Proc. Summer Computer Simulation Conf., Washington, D.C., 1976.

Stauffer, T..B., Sorption of nonpolar organics on minerals and aquifer materials, Ph.D. dissertation, College of William and Mary, 1987.

Van Genuchten, M. Th., Non-equilibrium transport parameters from miscible displacement experiments, USDA, US Salinity Lab, Research Report No. 119, 1981.

Figure 1   Symmetry

P-xylene / Lula

Pore Volumes
□   From

Relative Concentration

28-13
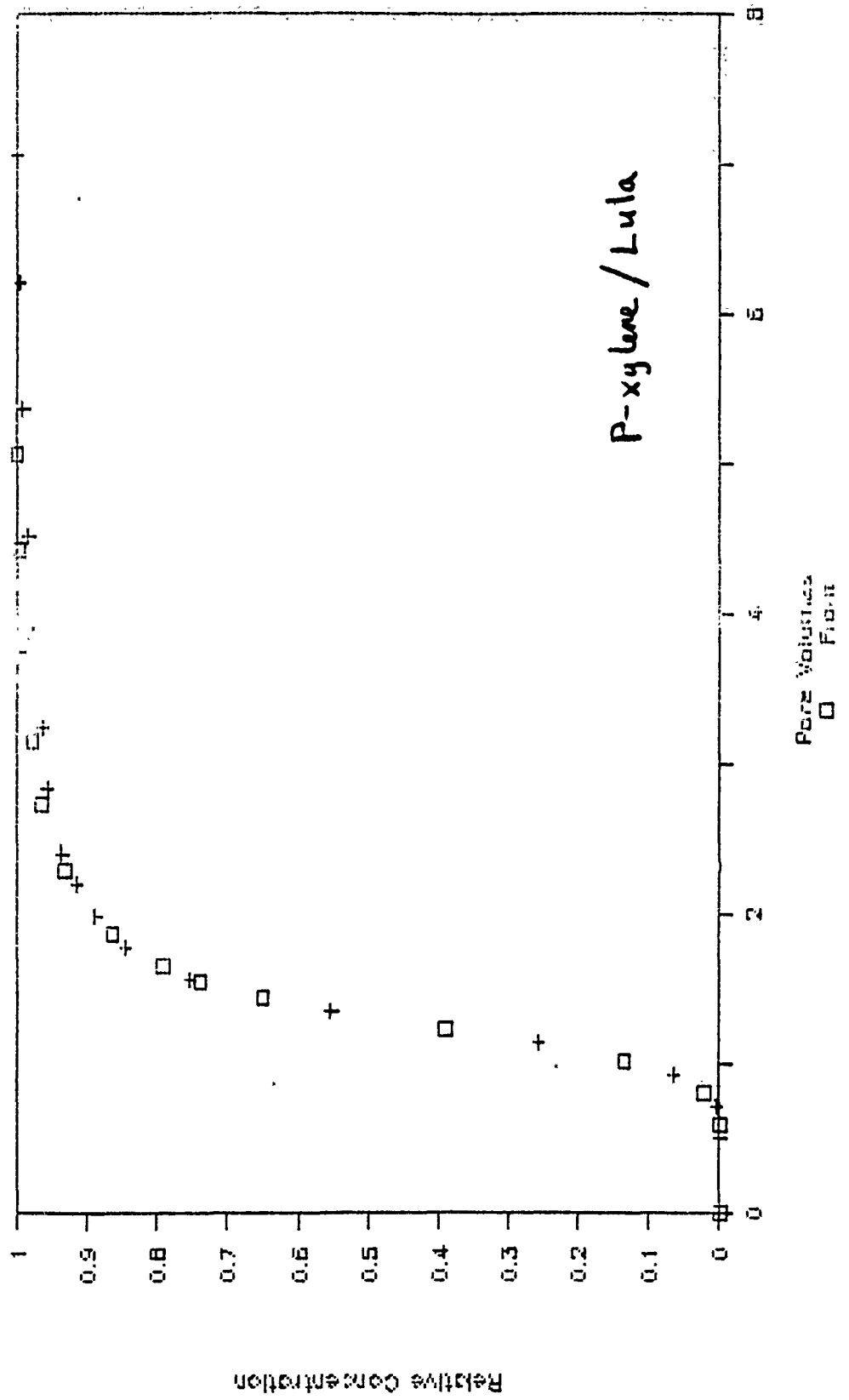
Figure 2 Reproducibility

P-xylene/Lula

Pore Volumes
□ First   + 23 days later

Relative Concentration

28-14
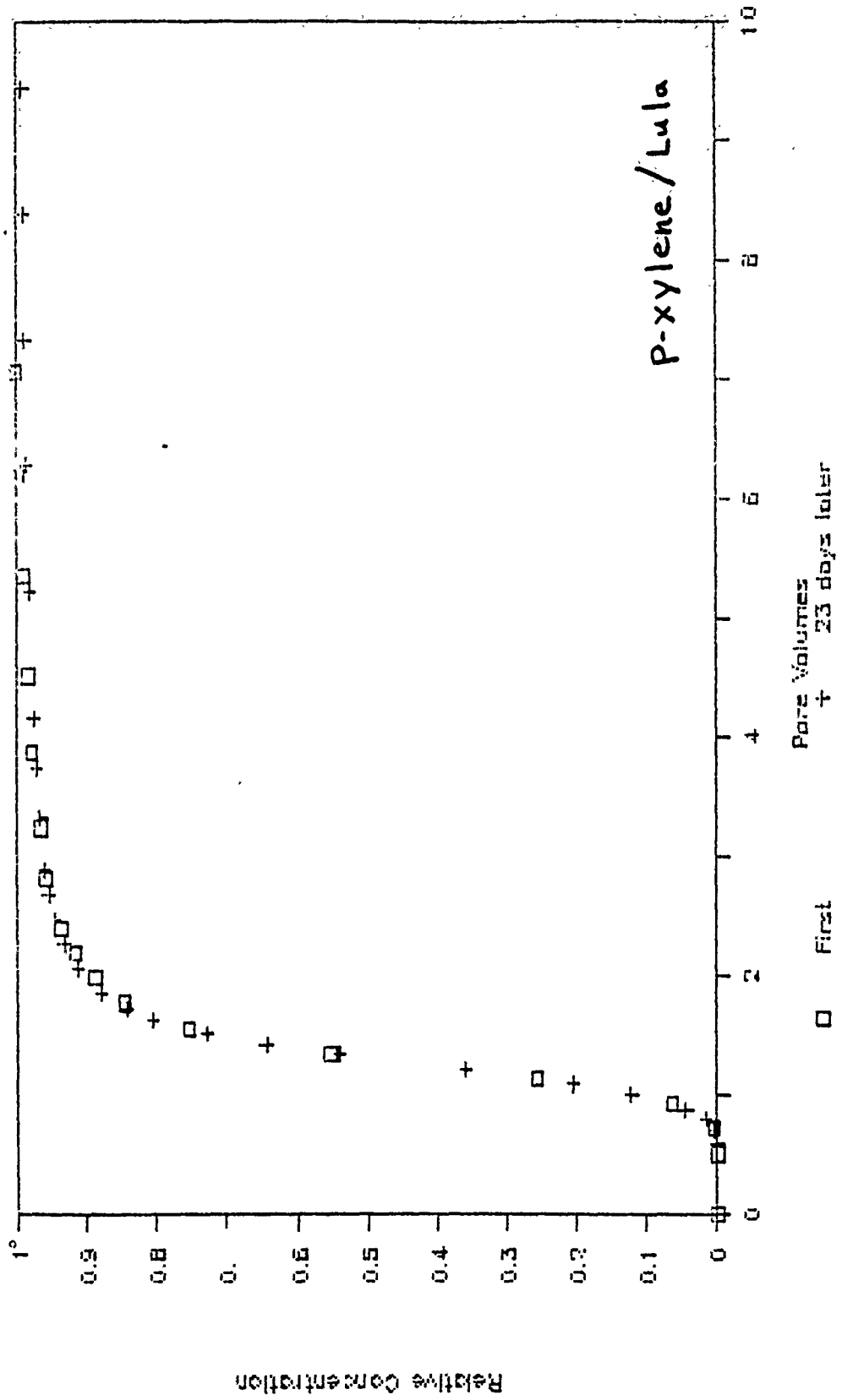
Figure 3.

Relationship: K2 vs. Kp

$\log k_2 = 0.20 - 0.67 \log k_P$

log Kp

log K2

□ Lula   + Borden   ◇ Tinker   △ Colum.   × Burks.
                      Borden   Tinker
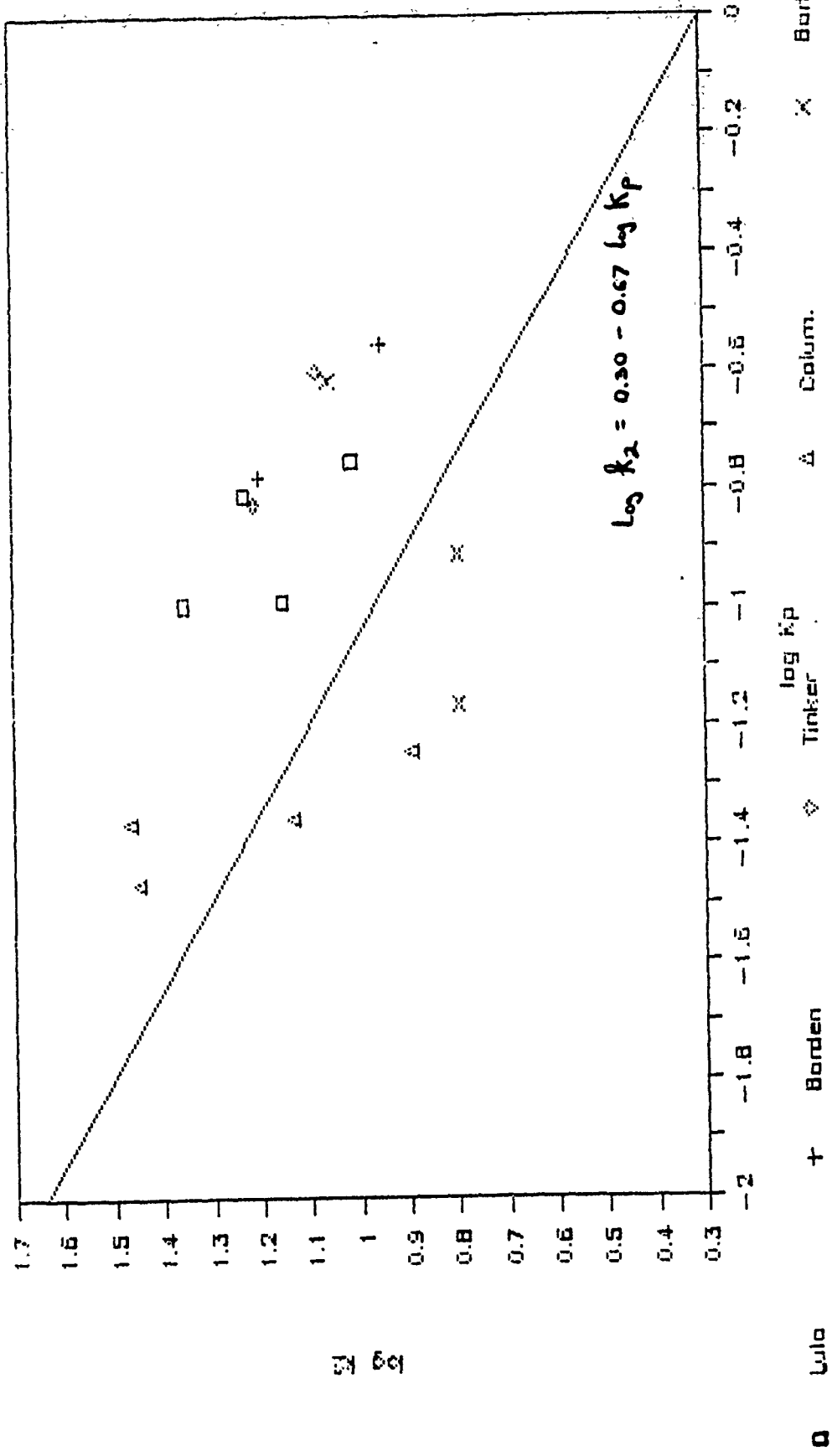
Figure 4.   Effect of Velocity
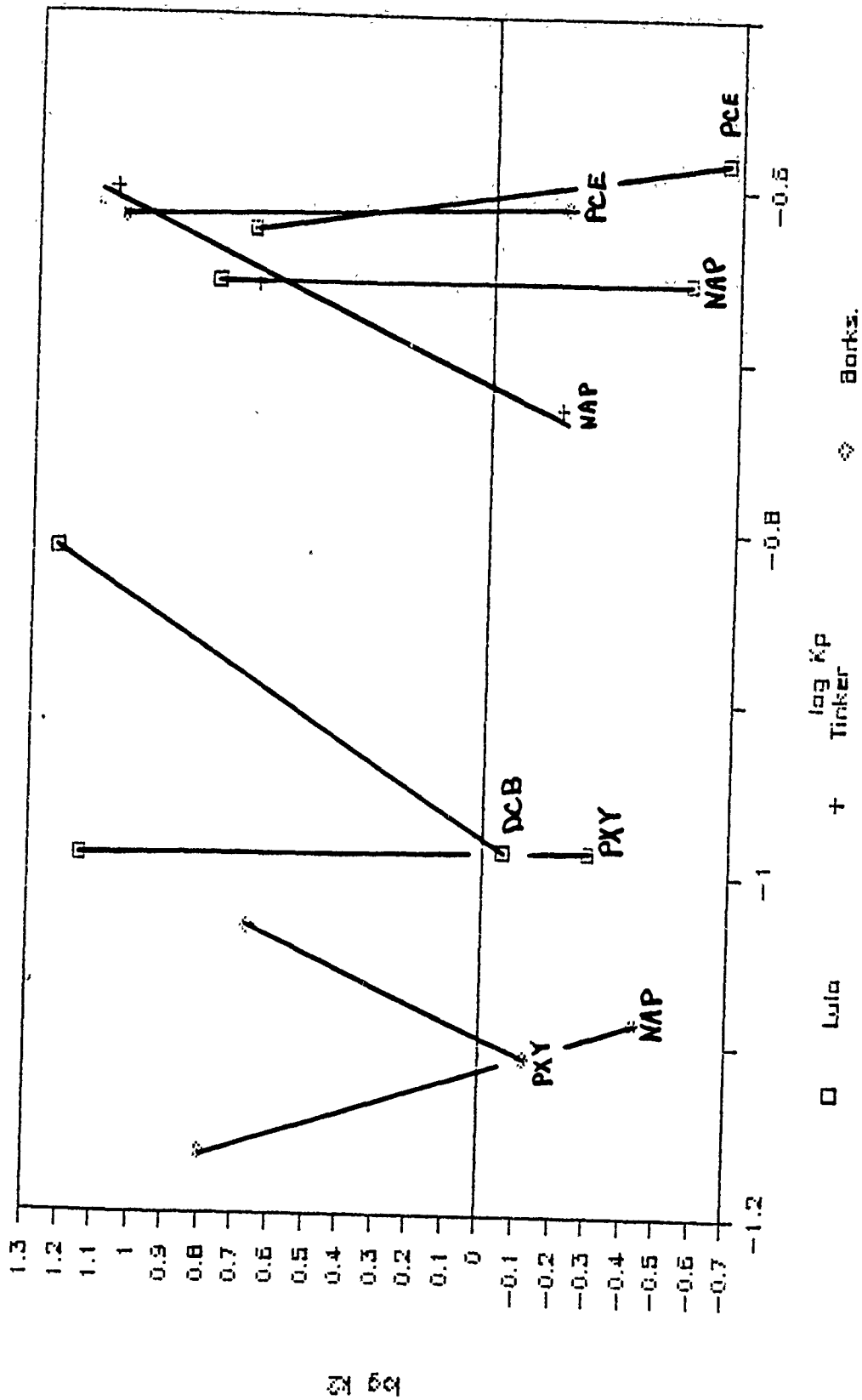
APPENDIX: DATA

Kp	k2		log Kp	log K2
0.081	17.5	TCE/o	-1.09151	1.243038
0.16	14.4	PXYL/o	-0.79588	1.158362
0.101	22.6	PCE/2-2	-0.99567	1.354108
0.154	17	DCB/2-2	-0.81247	1.230448
0.103	0.89	DCB/2-01	-0.98716	-0.05060
0.176	10.3	NAP/2-2	-0.75448	1.012837
0.102	14.2	PXYL/2-2	-0.99139	1.152288
0.118	7.14	PXYLr/2-2	-0.92811	0.853698
0.164	6.31	PXYL/2-1	-0.78515	0.800029
0.103	0.51	PXYL/2-01	-0.98716	-0.29242
0.222	0.277	NAP/2-01	-0.65364	-0.55752
0.221	6.13	NAP/2-1	-0.65560	0.787460
0.354	1.2	NAP/2a-1	-0.45099	0.079181
0.317	0.146	NAP/2a-01	-0.49894	-0.83564
0.237	4.9	PCE/2-1	-0.62525	0.690196
0.261	0.22	PCE/2-01	-0.58335	-0.65757
0.123	2.1	PCE/5-01	-0.91009	
0.276	9	PCE/5-2	-0.55909	
0.165	15.8	NAP/5-2	-0.78251	
0.128	8.75	PCE/3-1	-0.89279	
0.149	16.2	DCB/3-2	-0.82681	
0.071	12.2	PXYL/3-1	-1.14874	
0.22	4.71	NAP/3-1	-0.65757	
0.25	12.1	NAP/3-2	-0.60205	
0.187	0.637	NAP/3-01	-0.72815	
0.043	29.2	DCB/1	-1.36653	
0.057	7.8	NAP/1	-1.24412	
0.034	28	PCE/1	-1.46852	
0.044	13.6	PXYL/1	-1.35654	
0.241	11.45	PCE/4-2	-0.61798	
0.245	0.63	PCE/4-01	-0.61083	
0.19	15.45	PCE/4-1	-0.72124	
0.0135	6.5	NAPr/4-1	-1.86966	
0.036	3.9	NAP/4-1	-1.44369	
0.082	0.37	NAP/4-01	-1.08618	
0.228	3.4	NAP/P4-1	-0.64206	
0.0684	6.26	NAP/4-2	-1.16494	
0.0023	7.1	DCB/4-2	-2.63827	
0.139	2.12	DCB/P4-2	-0.85698	
0.234	0.17	PXY/P4-01	-0.63078	
0.078	0.76	PXY/4-01	-1.10790	
0.093	4.69	PXY/4-1	-1.03151	
0.123	6.26	PXY/4-2	-0.91009	

1990 USAF-UES SUMMER FACULTY RESEARCH PROGRAM/

GRADUATE STUDENT RESEARCH PROGRAM

Sponsored by the

AIR FORCE OFFICE OF SCIENTIFIC RESEARCH

Conducted by the

Universal Energy Systems, Inc.

<u>FINAL REPORT</u>

<u>Centrifuge Modeling of Explosive Induced</u>

<u>Stress Waves in Unsaturated Sand</u>

Prepared by: Wayne A. Charlie (1) and Andrew J. Walsh (2)

Academic Rank: (1) Professor and (2) Graduate Student

Department and   Department of Civil Engineering

 University: Colorado State University

Research Location: HQ AFESC/RDCM
                      Tyndall AFB FL

USAF Researcher: Capt Steven T. Kuennen and Dr C. Allen Ross

Date: September 28, 1990

Contract No: F4962-88-C-0053

Centrifuge Modeling of Explosive Induced
Stress Waves in Unsaturated Sand

by

Wayne A. Charlie and Andrew J. Walsh

ABSTRACT

Influence of moisture content on explosive induced stress wave propagation in compacted sand is reported. A series of 0.87 gram explosive charges were detonated on the centrifuge at 15 and 30 times earth's gravitational field (15 and 30 g's) to model prototype explosive charges of 3 and 27 kilograms respectively. Stress wave velocity, peak stress and stress transmission increased from 0 to 20 percent saturation and then decreased from 60 to 80 percent saturation. Results follow trends obtained from Split-Hopkinson Pressure Bar tests.

Acknowledgments

I. INTRODUCTION:

Prediction of stress transmission in unsaturated sands is important to the Air Force because strategic structures utilize compacted soil for backfill. Of particular importance are contained bombs which penetrate and detonate in compacted soil surrounding structural walls and in compacted soil located between burster slabs and structural roofs. Ross et al. (1989), Pierce et al. (1989) and Charlie and Pierce (1988) report that the moisture content during compaction of sands influences stress wave velocity and stress transmission in Split-Hopkinson Pressure Bar (SHPB) tests. This report presents the results of explosive tests conducted on unsaturated compacted sand. A series of 0.87 gram explosive charges were detonated on a centrifuge at 15 and 30 times earth's gravitational field to model a prototype explosive charge of 3 and 27 kilograms respectively.

II. OBJECTIVES OF THE RESEARCH EFFORT:

Major objectives of the research are 1) to determine the effects of moisture content on blast-induced stress wave velocity and stress transmission in compacted sand, 2) compare the results with previous results obtained on the Split-Hopkinson Pressure Bar, and 3) evaluate the potential of using centrifuge tests to predict field performance.

III. PARTIALLY SATURATED SANDS

Current design practice assumes that capillarity does not influence the behavior of cohesionless soils. Ross et al. (1989) observed unexpected stress wave velocity and stress transmission trends for sand compacted at various water contents to the same dry density (Figure 1). Currently, there are no theoretical models to explain the results obtained by Ross et al. (1989). The theory of effective stress for partially saturated sands proposed by Bishop and Blight (1963) predicts similar trends but the theory has been shown to not be theoretically correct. Fredlund's (1986) theory, although theoretically correct, does not predict the trends observed. Research conducted by Foster (1962) and Broms and Forssblad (1969) show that the dry density obtained for a given compaction energy is affected by moisture content. This is thought to be due to capillarity but again no theory is available relating dry density to compaction energy and moisture content.

IV. THEORY OF CENTRIFUGE MODELING

The use of physical models, often termed the observational method, is one of the most useful tools in the practice of geotechnical and explosive engineering. This method ranges from measuring field behavior of full scale models to measuring the behavior of scaled models. However, although scale models are relatively inexpensive, most earth materials are stress dependent and non-linear. As a result, modeling at one g does not result in good model-prototype similitude.
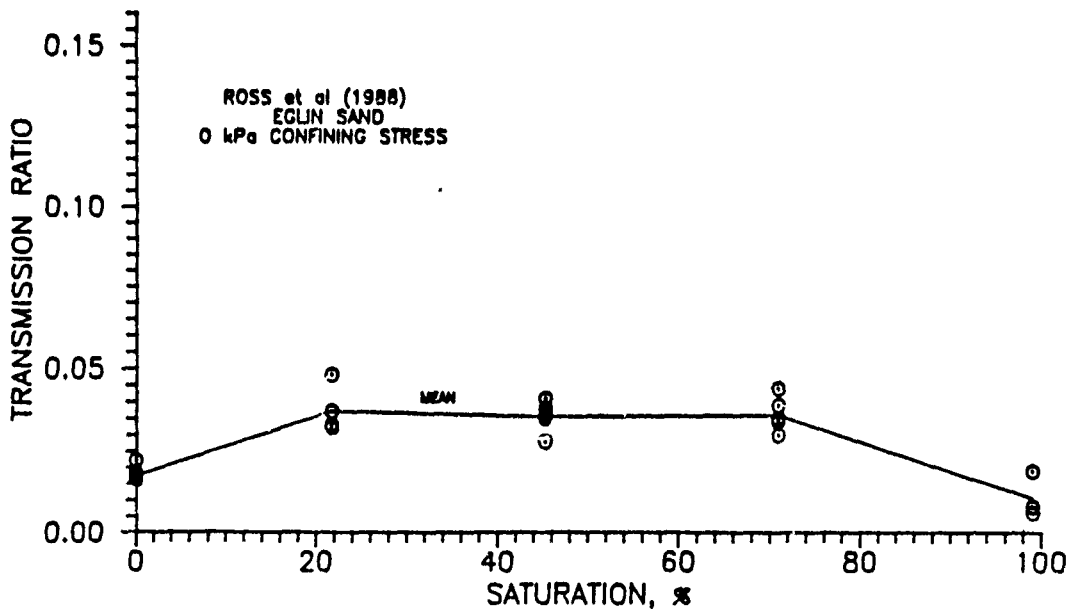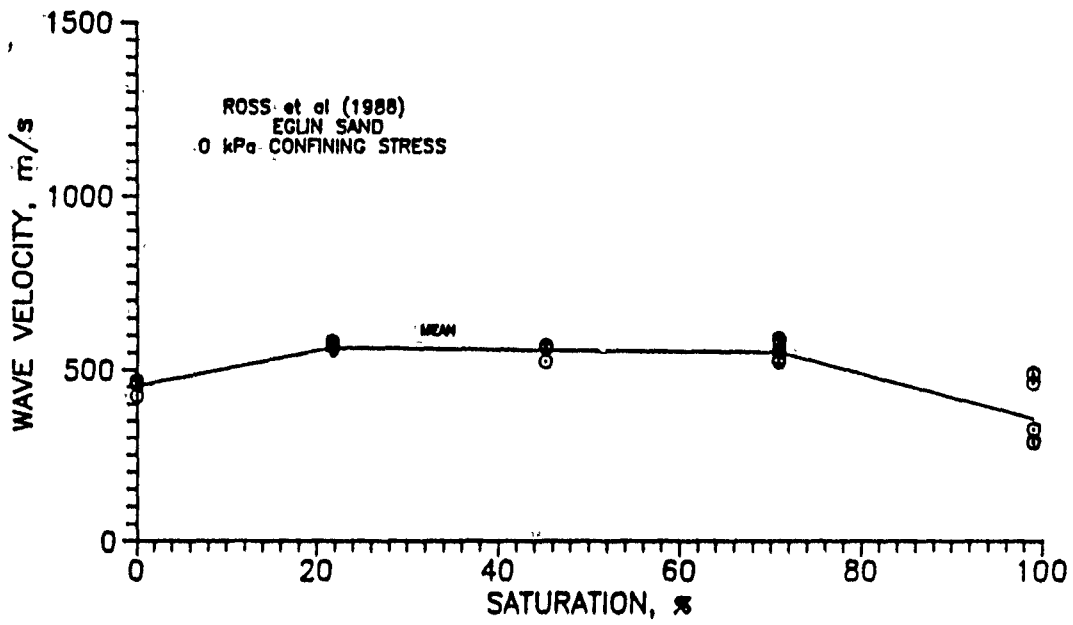
Figure 1   Stress Wave Velocity and Stress Transmission versus
Saturation for Eglin Sand (Ross et al., 1989).

Centrifuge modeling of earth structures was introduced in America by Bucky in 1931 and independently in Russia by Pokrovsky and Davidenkou in 1933 (Cheney and Fragaszy, 1989). The centrifuge provides a unique means to test small scale soil models at prototype stress levels. The basic theory of centrifuge modeling is that 1) stresses at the same geometric points in the prototype at one g and the model at N g's should be the same and 2) strains in the model and prototype made with materials having identical mechanical properties will also be identical. Unfortunately (or fortunately for explosives), other characteristics of response depend upon conditions other than stress resulting in scaling relations for each quantity. Some scaling laws, determined by using the principles of dimensional analysis, are presented in TABLE 1 (Scott and Morgan, 1977; Schmidt, 1977; Tabatabai et al., 1988; Nielson, 1983; and Townsend et al.,1985).

Centrifuge modeling of explosive events in soils offers the advantage that the explosive size required on the centrifuge to model a full scale field event scales with N^3 provided identical explosives are used. For example, a field explosive of 1000 kg of PETN can be simulated in the centrifuge with one gram of PETN at a centrifugal acceleration of 100 g. Scaling relationships are derived on the assumption that the material properties in the model and prototype are the same. Methods to design and construct small scale structures utilizing micro-concrete are discussed in detail by Cunningham et al. (1986); Gill (1985); Thompson and Kim (1988); Krawinkder and Moncart (1973); and Sabnis et al. (1983). TABLE 2 lists some of the explosives research conducted on the centrifuge.

TABLE 1. SCALING RELATIONS

Quantity	Full Scale (Prototype)	Centrifuge Model at n g's
Linear Dimension	1	$1/n$
Area	1	$1/n^2$
Volume	1	$1/n^3$
Time		
In Dynamic Terms	1	$1/n$
In Diffusion Cases	1	$1/n^2$
In Viscous Flow Cases	1	1
Velocity (Distance/Time)	1	1
Acceleration (Distance/Time^2)	1	n
Mass	1	$1/n^3$
Force	1	$1/n^2$
Energy	1	$1/n^3$
Stress (Force/Area)	1	1
Strain (Displacement/Unit Length)	1	1
Density	1	1
Energy Density	1	1
Frequency		
In Dynamic Problems	1	n

TABLE 2. CENTRIFUGE MODELING OF EXPLOSIVE EVENTS IN SOIL

Authors	Event Modeled	Scaling Factor
James (1978)	Pore Pressure	
Schmidt (1978)	500 Ton Nuclear Crater	
Schmidt and Holsapple (1980)	Craters in Dry Sand	Yield of explosive scaled N^3
Fragaszy et al. (1983)	Liquefaction	
Nielson (1983)	Soil-Structures Interaction	Yield of explosive scaled N^3
Gill (1985)	Buried Structures in Soil	
Kutter et al. (1985)	Free Field Blast Parameters	
Goodings et al. (1988)	Craters	Yield of explosive scaled N^3
Serrano et al. (1988)	Craters	Yield of explosive scaled N^3
Felice et al. (1988)	Crater and Pile Response	
Townsend et al. (1985)	Buried Structures in Soil	
Schmidt (1988)	Craters	Yield of explosive scaled N^3

29-8

V. SOIL, EXPLOSIVES, STRESS GAGES, AND DATA ACQUISITION

Soil - Tyndall AFB beach sand, utilized for this research, is a uniform, quartz sand having sub angular grains with a mean grain size, D_{50}, of 0.25mm. Maximum and minimum dry relative densities are 1630 and 1450kg/m^3. Desaturation-resaturation curves obtained by the porous plate method are given in Figure 2. The sand is compacted in four 2.54 cm layers in a thick walled (1.27cm thick) stainless steel mold. Each layer is compacted to a dry density of 1600 kg/m^3 at a moisture content to give the required saturation after compaction. Piezo-resistive miniature carbon stress gages are placed between lifts one and two and between lifts three and four (5.08 cm apart).

Explosives - The explosive charges utilized are instantaneous electrical detonators (Reynolds Model RP-83). The detonators dimensions and charge mass are given in Figure 3. The detonators are placed on and perpendicular to the soil's surface.

Stress Gages - The research utilizes carbon stress gages which are 1/8 watt 1000 ohm (+5%) carbon resistors manufactured by Allen Bradley. The gages are 4.00 mm long by 1.58 mm in diameter. The gages utilize the resistance-pressure characteristics of carbon (Holloway et al., 1985; Krehl, 1978). The gages are utilized as a quarter bridge and stress-voltage relationships are experimentally determined by means of quasi-static loading the resistors and recording their respective voltage. Static load calibration of the resistors resulted in a linear stress-voltage relationship. Figure 4 presents a typical stress-voltage
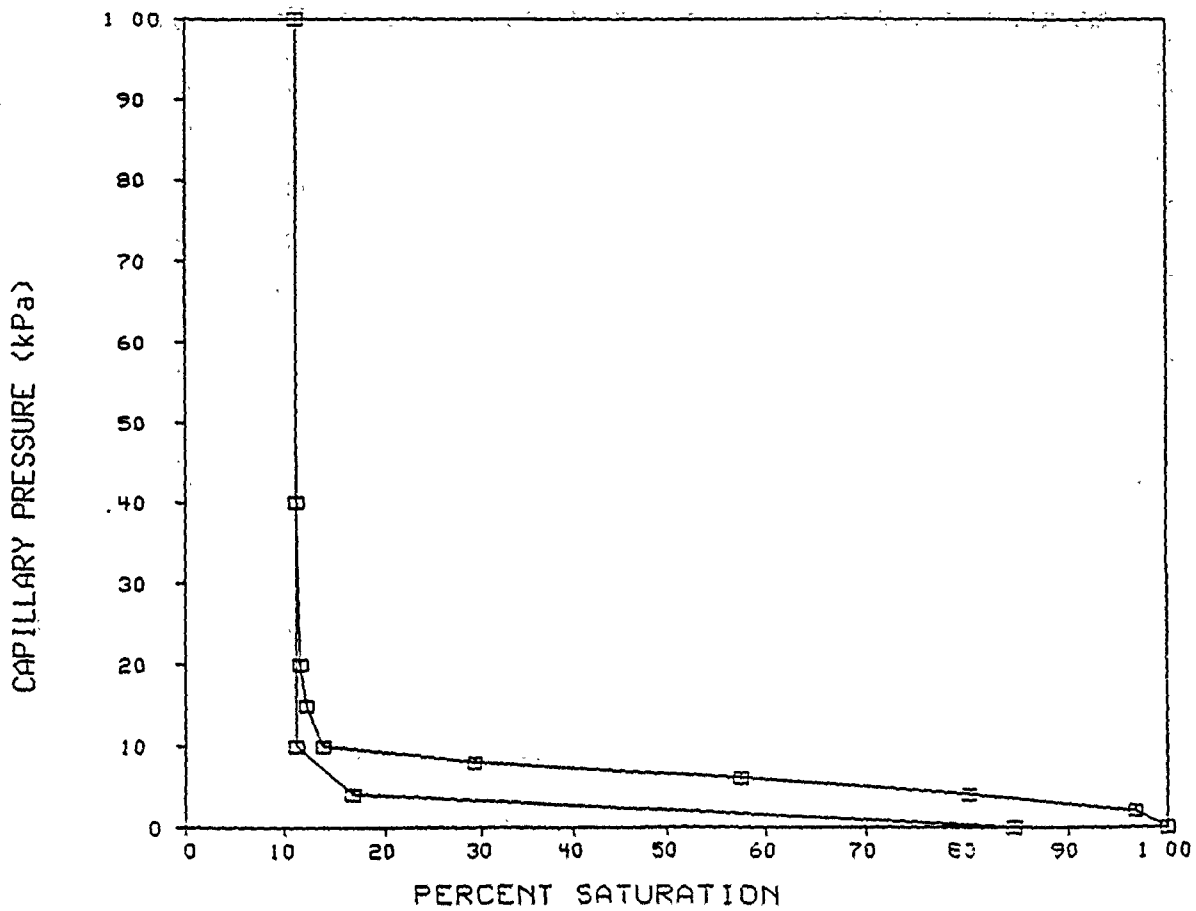
Figure 2   Desaturation curve for Tyndall Beach Sand.

RP-83 DETONATOR P/N 167-8676
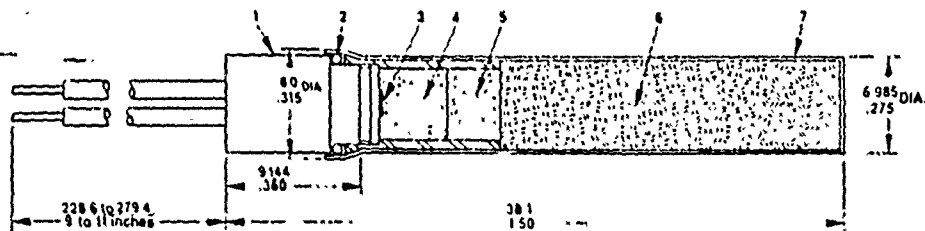
PARTS DESCRIPTION

1. PLASTIC HEADER
2. "O" RING
3. BRIDGEWIRE, GOLD, .0015 DIA, .040 LONG
4. INITIAL EXPLOSIVE PRESSING, PETN, .080 gm

5. PELLET RDX, 0.125 gm
6. OUTPUT CHARGE RDX, 0.87 gm
    (13.5 grains) @ 1.55-1.70 gm/cc density
7. CUP, .007 Thick Aluminum

OUTPUT CAPABLE OF DETONATING COMPRESSED TNT, COMPRESSED NITROSTARCH, COMP C-3, & COMP C-4.

Figure 3   Detonator dimension and charge mass.

REGRESSION EQUATION f(x)=1762.8x
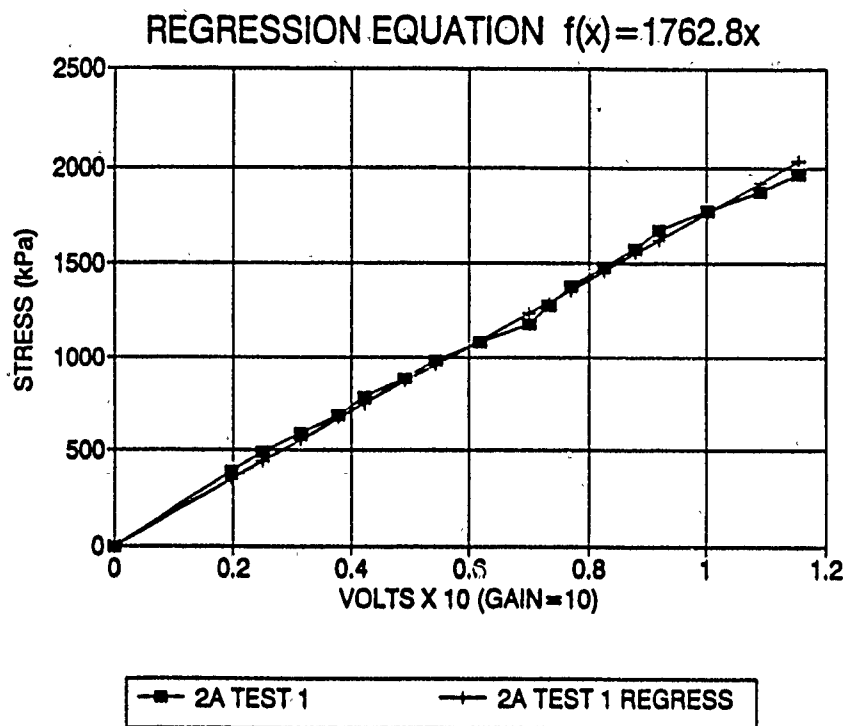
Figure 4   Quasi-Static calibration of carbon pressure gage.

relationship. A linear regression is utilized to convert from voltage to stress. The stress-voltage relationship remains linear over the stress range experienced during the explosive tests.

Data-Acquisition - Voltage-time history outputs from the carbon pressure gages are amplified and recorded by a transient 12 bit transient resolution data recorder (Pacific Model 5700) mounted on the centrifuge arm. A digitizing rate of one million samples per second (1,000,000 Hz) is utilized for the full 256 kilobytes of memory per channel. A signal from the firing apparatus is utilized to trigger all 6 channels utilized in this research. An onboard video camera and VCR is used to record the events.

VI. AFESC CENTRIFUGE FACILITY

The HQ AFESC Centrifuge facility is located at Tyndall AFB, Florida. Originally used at Kirtland AFB, New Mexico, for testing electronic and mechanical packages, it was modified in 1981 and moved to Tyndall AFB in 1986 (Thompson and Kim, 1988). The hydraulic centrifuge (Genisco Inc. of California, model E-185, SN 11) can apply controlled centrifugal accelerations of up to 100 g's with payloads up to 200 kg. Maximum effective radius to the swinging platform is 183 cm and the maximum centrifuge capacity is 13 g-tons.

VII. RESULTS

Stress waves are recorded by means of carbon stress gages located in the compacted soil. Pressure Gage A is located 2.54 cm below the sands surface and pressure Gage B is located 5.04 cm below pressure Gage A. Results are given in Tables 3 and 4 and plotted on Figures 5 and 6.

Stress Wave Velocity - Centrifuge explosive tests conducted at 15 g display wave velocities verses saturation trends similar to Split Hopkinson Pressure Bar tests shown in Figure 1a (Ross et al., 1989). A significant increase in wave velocity occurs from 0 to 20 percent saturation, remains relatively constant from 20 to 60 percent, then abruptly decreases from 60 to 80 percent saturation (Figure 5). These results indicate a "locked-in" stress effect in the range of 20 to 60 percent saturation at constant dry densities. The centrifuge tests conducted at 30 g's indicate similar trends, however, an increase in velocity from 0 to 20 percent saturation does not occur (Figure 5).

Stress Transmissions - Figure 6 gives the ratio of the peak stress recorded by pressure Gage B divided by the peak stress recorded by pressure Gage A. This stress ratio increases from less than 60% at 20% saturation to about 100% at 40% saturation and then decreases with increasing saturation.
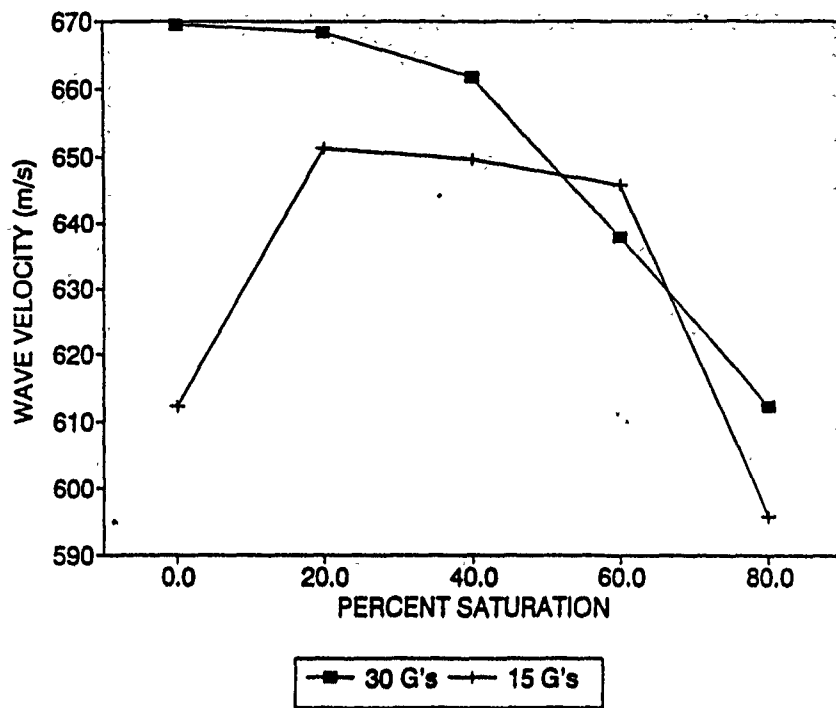
Figure 5   Wave Velocity versus Saturation for Tyndall Beach Sand
tested at 15 and 30 g's.
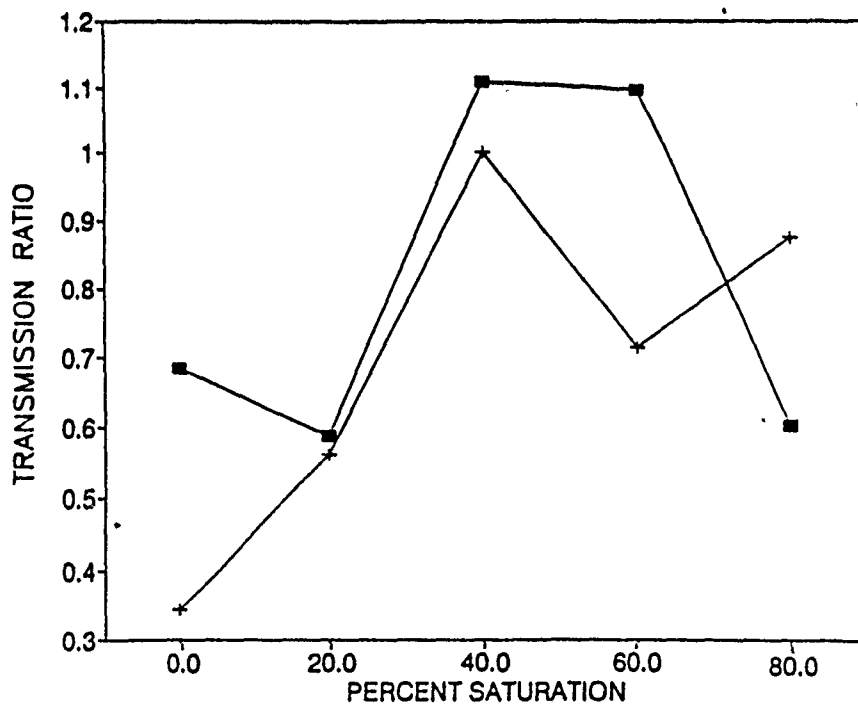
Figure 6   Stress transmission versus saturation for Tyndall Beach Sand
tested at 15 and 30 g's.

Table 3 Wave velocity and stress transmission ratio for the 15 g tests.

15'g CENTRIFUGE TEST RESULTS 8/8/90
CARBON PRESSURE GAGE (PEAK VOLT-50GAIN)

TEST	CYL	1st ARR (mic sec) (TRIGER @ TIME=0)	2nd ARR (mic sec)	VEL. (m/s)	1st PEAK VOLT A	1st PEAK VOLT B	ATTENU. VB/VA
15-0-1	c1	30.0	112.0	619.5	0.9	0.4	0.49
	c2	27.0	113.0	590.7	1.7	0.1	0.05
	c3	33.0	114.0	627.2	1.1	0.5	0.49
15-20-1	c1	33.0	111.0	651.3	1.9	1.0	0.54
	c2	37.0	115.0	651.3	1.8	1.0	0.57
	c3	36.0	114.0	651.3	2.1	1.2	0.57
15-40-1	NO DATA						
15-40-2	c1	36.0	111.0	677.3	1.8	1.4	0.77
	c2	38.0	115.0	659.7	1.8	2.3	1.27
	c2	35.0	118.0	612.0	2.4	2.3	0.96
15-60-1	c1	32.0	111.0	643.0	2.1	1.7	0.81
	c2	34.0	112.0	651.3	2.7	1.8	0.66
	c3	35.0	114.0	643.0	2.9	1.9	0.67
15-80-1	c1	39.0	121.0	619.5	1.5	1.3	0.84
	c2	38.0	125.0	583.9	1.7	2.2	1.31
	c3	40.0	127.0	583.9	3.8	1.8	0.47

Table 4 Wave relation and stress transmission ratio for the 30 g tests.

30'g CENTRIFUGE TEST RESULTS 8/8/90
CARBON PRESSURE GAGE (PEAK VOLTS-50GAIN)

TEST	CYL	1st ARR. (mic sec) (TRIGER @ TIME=0)	2nd ARR. (mic sec)	VEL. (m/s)	1st PEAK VOLT A	1st PEAK VOLT B	VB/VA
30-0-1	c1	33.0	110.0	659.7	1.3	1.0	0.80
	c2	41.0	118.0	659.7	1.2	1.0	0.80
	c3	43.0	124.0	627.2	1.2	0.9	0.79
30-0-2	c1	31.0	109.0	651.3	1.4	1.3	0.89
	c2	34.0	106.0	705.6	1.4	1.4	0.96
	c3	30.0	100.0	725.7	1.8	1.2	0.70
30-0-3	NO DATA						
30-0-4	c1	19.0	102.0	612.0	3.1	1.3	0.41
	c2	32.0	108.0	668.4	1.7	1.2	0.69
	c3	30.0	109.0	643.0	1.9	1.2	0.64
30-0-5	c1	26.0	107.0	627.2	1.9	1.3	0.69
	c2	32.0	104.0	705.6	1.5	1.0	0.67
	c3	34.0	108.0	686.5	1.8	0.9	0.51
30-20-1	POOR DATA						
30-40-1	c1	34.0	108.0	686.5	2.1	1.2	0.57
	c2	37.0	112.0	677.3	1.8	1.3	0.70
	c3	36.0	117.0	627.2	2.1	3.9	1.90
30-60-1	c1	36.0	116.0	635.0	2.0	1.5	0.78
	c2	36.0	117.0	627.2	2.1	3.3	1.54
	c3	36.0	114.0	651.3	2.4	2.3	0.97
30-80-1	c1	41.0	125.0	604.8	1.7	1.3	0.78
	c2	40.0	125.0	597.6	1.7	1.1	0.66
	c3	43.0	123.0	635.0	2.7	1.0	0.37
30-20-2	NO DATA						
30-20-3	c1	35.0	112.0	659.7	1.9	1.1	0.59
	c2	36.0	112.0	668.4	1.9	1.2	0.60
	c3	37.0	112.0	677.3	2.2	1.3	0.58
30-30-1	c1	40.0	119.0	643.0	2.0	1.2	0.62
	c2	36.0	112.0	668.4	1.7	1.4	0.82
	c3	39.0	118.0	643.0	1.9	1.4	0.73
30-40-2	c1	34.0	111.0	659.7	1.9	2.0	1.08
	c2	35.0	110.0	677.3	2.0	1.6	0.76
	c3	37.0	116.0	6.3.0	2.1	3.5	1.64

VIII. CONCLUSIONS

The moisture content of Tyndall AFB sand during compaction influences stress wave velocity, peak stress, and stress transmission. The highest wave velocity and largest stress transmission occurs between 20 to 60 percent saturation. The trends are similar to those obtained by Split-Hopkinson Pressure Bar tests reported by Ross et al. (1989) and Charlie and Pierce (1988). The results indicate that unsaturated soils can be tested on the centrifuge. However, the peak g's that the soil can be tested at may be limited by the desaturation characteristics of the soil.

IX. RECOMMENDATIONS

Full scale explosive tests at 1 g are needed to verify scaling parameters and to determine if centrifuge tests can be used to model 1 g events in partially saturated soil. In addition, theoretical methods to model the behavior of partially saturated compacted sand are needed.

X. REFERENCES

Bishop, A. W. and Blight, G. E. (1963), "Some Aspects of Effective Stress in Saturated and Partially Saturated Soils," Geotechnique, Vol. 13, No. 3, Sept., pp. 177-179.

Broms, B. B. and Forssblad, L. (1969), "Vibratory Compaction of Cohesionless Soils," Proc. of the 7th International Conf. on Soil Mechanics and Foundation Engr., ISSMFE, Mexico City, Mexico, August, Specialty Session 2, pp. 101-118.

Charlie, W. A. and Pierce, S. J. (1988), "High Intensity Stress Wave Propagation in Partially Saturated Sand," Final Report to AFOSR, 1988 USAF-UES SFRP Contract No. F49620-87-0004, Department of Civil Engineering, Colorado State University, Sept.

Cheney, J. A. and Fragaszy, R. J. (1989), "The Centrifuge as a Research Tool," Geotechnical Testing Journal, GTJoDJ, Vol. 7, No. 4, Dec., pp. 182-187.

Cunningham, C. H., Townsend, F. C., and Fagundo, F. E. (1986), "The Development of Micro-Concrete for Scale Model Testing of Buried Structure," ESL-TR-85-49, Air Force Engineering and Services Center, Tyndall Air Force Base, Florida, Jan.

Felice, C. W., Steedman, R. S., Gaffrey, E. S. (1988), "Centrifuge Models of Pile Response in a Blast and Shock Environment," Centrifuge 88, Editor J. F. Corte, Proc. of the International Conf. on Geotechnical Centrifuge Modeling, Paris, France, April, pp. 67-72.

Foster, C. R. (1962), "Field Problems: Compaction," Chapter 12 of Foundation Engineering, Edited by Leonards, G. A., McGraw Hill, New York, New York, pp. 1000-1029.

Fragaszy, R. J., Voss, M. E., Schmidt, R. M. and Holsapple, K. A. (1983), "Laboratory and Centrifuge Modeling of Blast-Induced Liquefaction," Proc. 8th Int. Symp. on Military Applications on Blast Simulation, Spiez, Switzerland, Vol. II, pp. III.5-1 to III.5-20.

Fredlund, D. G. (1986), "Soil Mechanics Principles that Embrace Unsaturated Soils," Proc. of the Eleventh Int. Conf. on Soil Mechanics and Foundation Engr., SSMFE, San Francisco, pp. 465-472.

Gill, J. J. (1985), "Centrifugal Modeling of Subterranean Structure Subjected to Blast Loading," Master's Report, Dept. of Civil Engr., University of Florida, Gainesville, Florida, Dec.

Goodings, D. G., Fourney, W. C., and Dick, R. D. (1988), "Geotechnical Centrifuge Modeling of Explosion Induced Craters - A Check for Scalding Effects," Final Report to AFOSR, Project AFOSR-86-0095, Dept. of Civil Engineering, University of Maryland, College Park, Maryland.

Holloway, D. C., Wilson, W. H., and Bjarnholt, G. (1985), "Use of Ordinary Carbon Resistors as Piezoresistive Transducers to Dynamically Measure Borehole Pressures," Proc. of the 1985 Society for Experimental Mechanics, Grenelefe, Florida, Nov.

James, R. G. (1978), "Cratering Experiments on the Centrifuge (2nd Series)," Cambridge University, Dept. of Engineering, Cambridge, U.K.

Krawinker, H. and Moncart, P. D. (1973), "Similitude Requirements for Dynamic Models," ACI Special Publication SP 73-1.

Krehl, P. (1978), "Measurements of Low Shock pressures with Piezoresistive Carbon Gages," The Review of Scientific Instruments, V. 49, No. 10, Oct., pp. 1477-1484.

Kutter, B. L., O'Leary, L. M., and Thompson, P. Y. (1985), "Centrifugal Modeling of the Effects of Blast Loading on Tunnels," Proc. of Second Symp. on the Interaction of Non-Nuclear Munitions with Structures, Panama City Beach, Florida, April 15-18.

Nielsen, J. P. (1983), "The Centrifugal Simulation of Blast Parameters," ESL-TR-83-12, Air Force Engineering and Services Center, Tyndall Air Force Base, Florida, Dec.

Pierce, S. J., Charlie, W. A., and Ross, C. A. (1989), "High Amplitude Stress Wave Propagation in Moist Sand," Proc. of the Fourth Symp. on the Interaction of Non-Nuclear Mutations with Structures, Panama City Beach, Florida, April.

Ross, C. A., Thompson, P. Y., Charlie, W. A., and Doehring, D. O. (1989), "Transmission of Pressure Waves in Partially Saturated Soils," J. of Experimental Mechanics, Soc. for Experimental Mechanics, Vol. 29, No. 1, March 1989, pp. 80-83.

Sabnis, G. M., Harris, H. G., White, R. N., and Mirza, M. A. (1983), "Structural Modeling and Experimental Techniques," Prentice - Hall, Englewood Cliffs, N. J.

Schmidt, R. M. (1978), "Centrifuge Simulation of the Johnie Boy 500 Ton Cratering Event," Proc. 9th Lunar and Planet Sci. Conf., pp. 3877-3889.

Schmidt, R. M. and Holsapple, K. A. (1980), "Theory and Experiments on Centrifuge Cratering," J. of Geophysical Research, Vol. 85, No. B1, Jan., pp. 235-251.

Schmidt, R. M. (1977), "A Centrifuge Cratering Experiment: Development of a Gravity-Scaled Yield Parameter," In Impact and Explosion Cratering, Roddy, D. J., Pepin, R. O., and Merrill, R. B., editors, Pergamon Press, New York, pp. 1261-1278

Schmidt, R. M. (1988), "Centrifuge Contributions to Cratering Technology," Chap. in Centrifuges in Soil Mechanics, Craig, W. H., and James R. G., and Schofield, A. N., editors, A. A. Balkema, Rotterdam, pp. 199-202.

Scott, R. F. and Morgan, N. R. (1977), "Feasibility and Desirability of Constructing a Very Large Centrifuge for Geotechnical Studies, Report 760-170, NSF, Washington, D. C.

Serrano, C. H., Dick, R. D., Goodings, D. J., and Fourney, W. L. (1988), "Centrifuge Modeling of Explosion Induced Craters," Centrifuge 88, Editor J. F. Corte, Proc. of the International Conf. on Geotechnical Centrifuge Modeling, Paris, France, April, pp. 445-450.

Tabatabai, H., Bloomquist, D., McVay, M. C., Gill, J. J., and Townsend, F. C. (1988), "Centrifugal Modeling of Underground Structures Subjected to Blast Loading," ESL-TR-87-62, Final Report to Air Force Engineering and Services Center, Tyndall Air Force Base, Florida, March.

Thompson, P. Y. and Kim, Y. S. (1988), "The Development of a Geotechnical Centrifuge Facility at Tyndall Air Force Base," Centrifuge 88, Editor J. F. Corte, Proc. of the International Conf. on Geotechnical Centrifuge Modeling, Paris, France, April,

Townsend, F. C., McVay, M. C., Bradley, D. M., Cunningham, C. H. and Yovaish, D. J. (1985), "Numerical and Centrifugal Modeling of Buried Structure Response to Near Blast," Proc. of 2nd Symp. on the Interaction of Non-Nuclear Munitions with Structure," Panama City Beach, Florida, pp. 982-987.

1990 USAF-UES SUMMER FACULTY RESEARCH PROGRAM/

GRADUATE STUDENT RESEARCH PROGRAM

Sponsored by the

AIR FORCE OFFICE OF SCIENTIFIC RESEARCH

Conducted by the

Universal Energy Systems, Inc.

FINAL REPORT

Pathways of 4-Nitrophenol Degradation

Prepared by: Joseph H. Dreisbach, PhD

Academic Rank: Professor

Department and   Chemistry Department

 University: University of Scranton

Research Location: USAF Engineering and Services Center

                      (USAFESC/RDVW)

                      Tyndall AFB, FL   32403-6001

USAF Researcher: Jim C. Spain

Date: 25 September 1990

Contract No: F49620-88-C-0053

Pathways of 4-Nitrophenol Degradation

by

Joseph H. Dreisbach

ABSTRACT

Three soil bacteria isolates, designated 402, 428, and 443, were used in this investigation to determine the pathway of 4-nitrophenol oxidative degradation. Pathways were studied using respirometry with whole cells and cell free extracts, O-18 incorporation studies, and gas chromatography-mass spectrometry analysis of extracts of the reaction media. A mutant of 402 which accumulates 1,2,4-benzenetriol and hydroxybenzoquinone was obtained. Results support the proposed pathway which involves two oxygenase reactions to yield 1,2,4-benzenetriol from 4-nitrophenol. Benzenetriol is then converted through 3-hydroxymuconic acid to maleylacetate by an ortho ring fission reaction.

Acknowledgements

The summer research experience at Tyndall Air Force Base was exciting and rewarding. I thank the Air Force Office of Scientific Research for making the program available. Thanks also to Universal Energy Systems, Inc for their expert administration of the program.

Performing research in Dr. Jim Spain's microbiology laboratory is a chance of a lifetime. Jim provided me with much technical and moral assistance, especially during the first few weeks of the project. He taught me much more than he realizes. It was enjoyable to watch his style of management and direction. Shirley Nishina provided more support and guidance than I could ever have expected. Shirley's interest, knowledge, and expertise cannot be quantified. I hope she realizes that it was never taken for granted. I cannot say enough about her patience.

Jim Spain's research group provided enormous amounts of insight and experience as well as social escapes from the lab. Thanks to Billy Haigler, Chuck Pettigrew, and Bill Seffens for all they did. Mike Henley and Howard Mayfield are expert with the GC-MS. I thank them for staying overtime to do some of the analyses. Sergeant Don Volnoff, Lucy Barnes, and Bob Donne provided information and assistance which made the day-to-day operations much smoother. Conversations with Captain Catherine Vogel, Hubert Attaway, and Mike MacFarland also contributed to a wonderful ten week experience. I also thank Perry Sullivan for providing me with much perspective on the objectives of the Engineering and Services Center and especially for the many fascinating ideas which he proposed.

I. INTRODUCTION:

Nitroaromatic compounds are used in the manufacture of a
wide variety of products including explosives, many pesticides,
dyes, pharmaceuticals, and industrial solvents. Accumulation of
these compounds in the environment is a substantial problem being
addressed by military, industrial, and agricultural institutions.

One way of addressing the environmental damage caused by
these and other chemical agents involves the use of
bioremediation. Bioremediation incorporates biological agents,
most often microbes, in approaches to reclaim polluted soil or
water. The ability to obtain microbes with diverse metabolic
capabilites, as well as the potential to use these systems on
on site, renders bioremediation techniques widely applicable and
cost effective.

The microbiolgy laboratory at Tyndall Air Force Base,
Florida is involved in studying the use of microbes in the
degradation of chlorinated aromatics and nitroaromatics as well
as other substances. One major effort involves elucidation of
the pathways of degradation for various compounds by different
microbial isolates. Identifying the intermediates present on the
degradation pathways is critical in order to confidently utilize
the microbes in field applications.

The author has significant research experience in microbial
biochemistry including isolation and purification of microbial
extracellular enzymes. His background in bioanalytical chemistry
and high performance liquid chromatography methods development
allowed him to contribute to the research efforts of the

microbiology laboratory at Tyndall Air Force Base.

II. OBJECTIVES OF THE RESEARCH EFFORT:

The widespread use and diverse applications of
nitroaromatic-based compounds, especially in explosives and
pesticides, and the occurrence of these compounds and their
derivatives in the environment, make them major targets for
biremediation applications. The compound 4-nitrophenol (para-
nitrophenol, PNP) is of particular interest since it is derived
from hydrolysis of parathion. Even more important, from a
military application, is the fact that PNP is an excellent model
compound for investigations of biodegradation of nitrotoluenes -
major components of explosives.

A number of studies have shown that some pseudomonads
convert PNP to hydroquinone with concomitant release of nitrite
(1,2,3). Investigations of PNP catabolism with other pseudomonad
isolates indicate that 4-nitrocatechol is an intermediate in some
pathways (4,5). A number of bacterial isolates which are able to
utilize PNP as the sole carbon source were isolated by Jim Spain
and his research group at Tyndall Air Force Base. The objective
of this research project was to elucidate the pathway of PNP
degradation by three of these bacterial isolates.

III. ISOLATION OF A MUTANT WHICH ACCUMULATES HYDROXYQUINONE:

Three bacterial isolates were used in this project.
Isolates are designated 402, 428, and 443. One of the mutants,
labelled as 402M6N, obtained after ethylmethanesulfonate (EMS)

treatment of 402, was shown to accumulate a red colored metabolite during growth with PNP. The red colored metabolite was identified as hydroxyl-1,4-benzoquinone (HBQ).

HBQ is an oxidation product of 1,2,4-benzenetriol (7). Research from this project shows that HBQ is formed rapidly and nonenzymatically from 1,2,4-benzenetriol in pH 7.0 buffer. The reaction rate is accelerated in the presence of a metal ion mixture. These observations support the hypothesis that 1,2,4-benzenetriol is an intermediate in PNP degradation by 402.

IV. <u>OXIDATION</u> <u>OF</u> <u>SUBSTRATES</u> <u>BY</u> <u>PNP-GROWN</u> <u>CELLS</u>:

Cells grown in the presence of PNP were examined for their ability to oxidize possible intermediates on the pathway. Results are shown in Table 1. Oxidation of the substrate was determined by measuring O_2 utilization by whole cells in the presence of the substrate.

TABLE 1.

OXYGEN CONSUMPTION BY WASHED CELLS

(nanomoles O_2/min mg protein)

	PNP	4-nitrocatechol	benzenetriol	hydroquinone
402	130	100	130	0
428	210	180	97	2
443	110	90	110	0
402M6N	47	32	0	-

PNP grown cells are capable of oxidizing PNP,
4-nitrocatechol, and benzenetriol at rates required to support
growth. Hydroquinone is not oxidized at biologically significant
rates. The mutant 402M6N displays no activity with benzenetriol.

V. OXIDATION OF BENZENETRIOL BY CELL FREE EXTRACTS:

Cell free extracts were prepared by disrupting late log
phase cells using a French pressure cell. The particulate
fraction obtained after centrifugation to remove unbroken cells
and cell debris was used in the experiments. Results are
provided in Table 2.

TABLE 2
OXYGEN CONSUMPTION BY CELL FREE EXTRACTS
USING 1,2,4-BENZENETRIOL SUBSTRATE
(nanomoles O_2/min mg protein)

Growth medium[a]	YE	YE + PNP	PNP
Cells			
402	28	130	340
428	28	140	1060
443	21	210	870

[a] YE: grown on yeast extract; YE + PNP: grown on yeast
extract and induced with PNP; PNP: grown on PNP containing
medium.

PNP addition to YE grown cells results in substantial
increases in benzenetriol oxidase activity. Spectral analysis of

the reaction of benzenetriol reveals the formation of a nonaromatic compound with an ultraviolet absorbance maximum at 242 nm. These properties are consistent with the formation of maleylacetate, an ortho ring fission product of 1,2,4-benzenetriol (7). No significant cell free activity is observed using PNP, 4-nitrocatechol or hydroquinone.

VI. STOICHIOMETRY OF O_2 USE BY WHOLE CELLS:

Stoiciometric relationships of total O_2 consumed versus moles of substrate oxidized were determined using PNP and 4-nitrocatechol substrates. Moles of nitrite released were also compared to amount of substrate oxidized. Results are listed in Table 3.

TABLE 3

STOICHIOMETRY OF O_2 CONSUMPTION AND NITRITE RELEASE

USING PNP AND 4-NITROCATECHOL SUBSTRATES

(Molar ratios)

	O_2/PNP	NO_2^-/PNP	O_2/Ncatechol	NO_2^-/Ncatechol
402	5.3	1.0	4.5	0.95
428	5.4	1.0	4.2	1.0
443	5.4	1.1	3.8	1.0

In each case O_2/substrate ratios are greater for PNP than for 4-nitrocatechol under the same conditions. These data indicate that oxidative degradation of PNP requires an additional

mole of O_2 compared to 4-nitrocatechol catabolism. The data also indicate that the release of nitrite is stoichiometrically equivalent to the moles of substrate oxidized.

VII. IDENTIFICATION OF INTERMEDIATES USING C-14 LABELLED PNP:

An experiment was designed in which 443 cells, grown on PNP medium, were washed and incubated with C-14 PNP. Just prior to addition of C-14 PNP, unlabelled benzenetriol, hydroquinone, and 4-nitrocatechol were added to the reaction mixture. Final concentrations of PNP were 0.033 mM and the unlabelled compounds were 0.30 mM. Aliquots of the reaction mixture were removed and analyzed using reversed phase high performance liquid chromatography (HPLC). Fractions from the HPLC were collected and measured for presence of C-14. The large concentration of unlabelled compounds should allow for the accumulation of radiolabel if that compound is actually on the reaction pathway.

Results indicate that the majority of the radiolabel (>95% of the reacted label from PNP) accumulates as benzenetriol. A small amount of radiolabel (< 1%) accumulates as hydroquinone. No label is found in the 4-nitrocatechol peak. Concentrations of the unlabelled compounds did not change substantially over the three minute reaction time.

VIII. INCORPORATION OF O-18 IN 1,2,4-BENZENETRIOL:

In order to determine if the conversion of PNP to 1,2,4-benzenetriol involves monooxygenase or dioxygenase activity, an O-18 incorporation experiment was performed. Active 402M6N cells
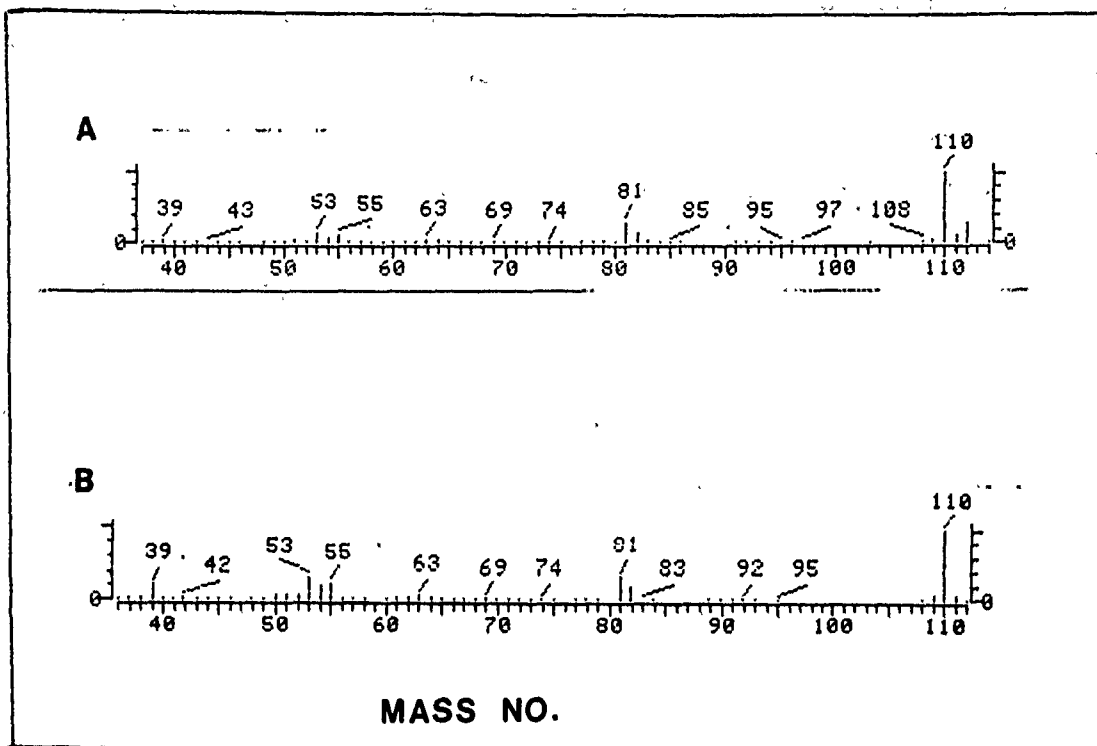
FIGURE 2. Mass spectra of 1,4-hydroquinone from a reaction extract. A. $^{18}O_2$ experiment. B. No $^{18}O_2$ present in the reaction vessel.

Spectra for both 1,2,4-benzenetriol and 1,4-hydroquinone reveal a molecular weight +2 peak in the O-18 experiments. No such peak is present when the reaction is performed in the absence of O-18. These results eliminate the possibility that both atoms of oxygen are added from one molecule of O_2 since this situation would result in some benzenetriol with mass 130 (MW + 4) and no benzenetriol with mass 128 (MW + 2). The small

were induced with PNP, washed, and incubated with PNP in the presence of $^{18}O_2$ (both oxygen atoms = 18) in a sealed container. A red intermediate accumulated during the reaction. The supernatant was extracted with ethyl acetate and, after evaporation, the residue was examined using gas chromatography - mass spectrometry. Mass spectra of the compounds with retention times identical to 1,2,4-benzenetriol and hydroquinone are provided in Figures 1 and 2.
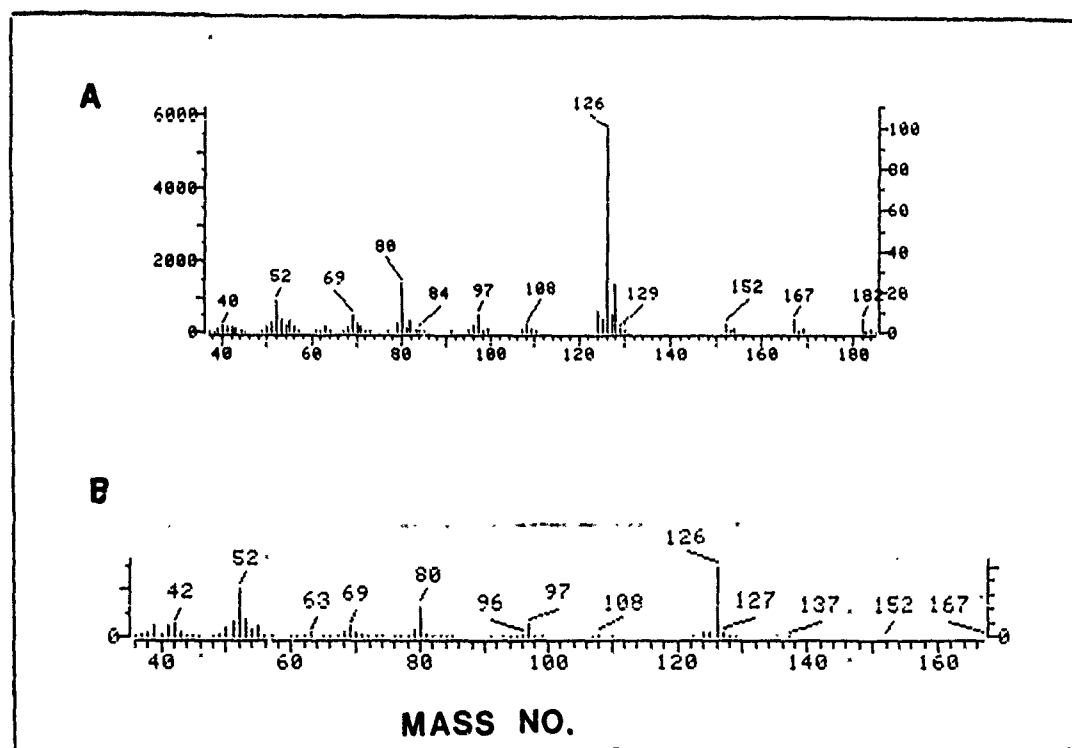

FIGURE 1. Mass spectra of 1,2,4-benzenetriol from the reaction extract. A. $^{18}O_2$ experiment. B. No $^{18}O_2$ present in the reaction vessel.

peak at mass 130 most likely results from the addition of two O-18
atoms during separate reactions.

IX. DISCUSSION:

A number of groups have reported that PNP is converted to
hydroquinone during oxidative catabolism by certain soil
pseudomonads (1,2,3) while 4-nitrocatechol has been identified in
other PNP degradation pathways of soil microbes (4,5). Results
of the studies reported here support the hypothesis that 1,2,4-
benzenetriol is a catabolic intermediate in PNP by the soil
isolates 402,428, and 443.

Hydroquinone has also been identified in the reaction
extracts and is found to possess an O-18 label when oxidation of
PNP is performed in an atmosphere containing $^{18}O_2$. The low rate
of hydroquinone oxidation by the isolates and the negligible
accumulation of radiolabel in hydroquinone when C-14 PNP is used
as substrate indicates that hydroquinone is not a major
intermediate in the pathway. No 4-nitrocatechol production was
observed in these studies.

Experiments with O-18 incorporation yield mass spectra with
a molecular weight increase of 2 amu for 1,2,4-benzenetriol.
These results lead us to propose that conversion of 4-nitrophenol
of 1,2,4-benzenetriol involves two monooxygenase reactions.
Stoichiometric data which indicate that oxidation of 4-
nitrophenol requires an additional mole of O_2 compared to the
oxidation of 4-nitrocatechol support this hypothesis. A proposed
pathway is presented in Figure 3.

4-nitrophenol (PNP)
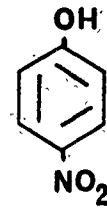
[4-nitroresorcinol]
proposed intermediate
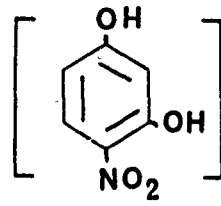
1,2,4-benzenetriol
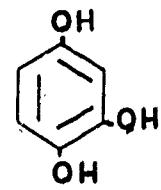
3-hydroxymuconic acid
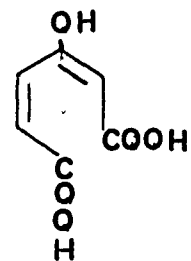
FIGURE 3. Proposed pathway for the degradation of
4-nitrophenol by isolates 402, 428, 443.

The proposed pathway includes the tentative intermediate 4-nitroresorcinol. Additional experiments need to be performed in order to identify the intermediate and to examine the use of 4-nitroresorcinol by the isolates.

X. RECOMMENDATIONS:

A pathway for the oxidative degradation of PNP by bacterial isolates 402,428, and 443 has been proposed. The route is different from the reaction pathways which have been proposed with other organisms. Results from this study support the pathway of conversion of PNP to benzenetriol through two oxygenase reactions. The identity of the intermediate produced during the first reaction remains to be determined.

Identification of all intermediates is important to allow for the full understanding of how these pathways may influence other organisms in mixed culture conditions. These mass balance studies must be performed prior to any field application of these bioremediation system.

REFERENCES

1. Munneke, D. M., D. P. H. Hsieh. (1974) Microbial Decontamination of Parathion and p-Nitrophenol in Aqueous Media. <u>Appl. Microbiol.</u> <u>28</u>: 212-217.

2. Simpson, J. R. and W. C. Evans. (1953) The Metabolism of Nitrophenols by Certain Bacteria. <u>Biochem. J.</u> <u>55</u>: xxiv.

3. Spain, J. C., O. Wyss, and D. T. Gibson. (1979) Enzymatic Oxidation of p-Nitrophenol. <u>Biochem. Biophys. Res. Commun.</u> <u>88</u>: 634-641.

4. Raymond, D. G. M. and M. Alexander. (1971) Microbial Metabolism and Cometabolism of Nitrophenols. <u>Pesticide Biochem. Physiol.</u> <u>1</u>: 123-130.

5. Sudhakar-Barik, R. Siddaramappa, P. A. Wahid, and N. Sethunathan. (1978) Conversion of p-Nitrophenol to 4-Nitro-catechol by a <u>Pseudomonas</u> sp.. <u>Antonie von Leeuwenhoek</u> <u>44</u>: 171-176.

6. Carlton, B. C. and B. J. Brown. "Gene Metabolism", in <u>Manual of Methods for General Bacteriology</u> (P. Gerhardt, ed), American Society for Microbiology, Washington, DC, 1981, pp 222-242.

7. Chapman, P. J. and D. W. Ribbons. (1976) Metabolism of Resorcinylic Compounds by Bacteria: Alternative Pathways for Resorcinol Catabolism in <u>Pseudomonas putida</u>. <u>J. Bacteriol.</u> <u>125</u>: 985-998.

1990 USAF-UES SUMMER FACULTY RESEARCH PROGRAM

Sponsored by the

AIR FORCE OFFICE OF SCIENTIFIC RESEARCH

Conducted by the

Univeral Energy Systems, Inc.

FINAL REPORT

Permanent Deformations in Airfield Pavement Systems with Thick Granular Layers

Prepared by:	David J. Kirkner
Academic Rank:	Associate Professor
Department and	Civil Engineering
University:	University of Notre Dame
Research Location:	Engineering and Services Center
	Tyndall AFB, FL 32403-6001
USAF Researcher:	James Murfee
Date:	26 Sept 90
Contract No.:	F49620-88-C-0053

Permanent Deformations in Airfield Pavement Systems with Thick Granular Layers

by

David J. Kirkner

ABSTRACT

A finite element code was developed to analyze airfield pavement systems allowing an elasto-plastic material law to be employed to describe the mechanical behavior of the pavement layer as well as the granular base and sub-base layers. The principal material law utilized in this report was based on linear elastic behavior below yield and during unloading and a Drucker-Prager failure line with an elliptic cap yield surface. Subsequently, using measured physical constants for the material in the pavement test bed at Tyndall Air force Base and some reasonable values for the cap parameters not measured, simulations were conducted for the Tyndall test site. It was found that this model could reasonalbly capture the peak deformation which occurred during loading and also predicted reasonalble results for the permanent deformation occurring after unloading.

Acknowledgements

1.0 INTRODUCTION:

Most analysis and design of airfield pavement systems is done assuming an elastic response governing the behavior of the pavement and of the granular base and sub-base layers. Current methodology uses a nonlinear elastic stress-strain law employing the modulus of resilience. There are a great many ways to generalize the linear elastic stress-strain relationships for use in nonlinear elastic regimes. One class of constitutive laws called variable modulus laws (Desai and Siriwardane, 1984) simply uses a stress-strain relationship of the same form as the linear one but assumes that the material constants are stress state dependent. A popular constitutive law, used for pavement subsytems in particular, employs the resilient modulus. In the stress-strain relationahip the modulus of elasticity is simply replaced with the resilient modulus which is often defined as the ratio of repeated deviatoric stress to the recoverable part of the axial strain in a conventional triaxial test.

However the consideration of greatly increased tires pressures raises the concern over long term permanent deformations, i.e. rutting, occurring in existing pavements and brings into question current design techniques for future airfields. Modeling of this type of behavior requires the ability to predict inelastic or permanent deformations in the mechanical response of the pavement system.

In order to evaluate some of the effects of increased tire pressures and to provide a data base for modeling efforts on this problem, the Air Force constructed a test bed at Tyndall Air Force Base and conducted a series of instrumented tests using two basic mix designs for the asphalt concrete; a Marshall design and a Gyratory design. Many passes of the test vehicle were made over the test pavement and the long term permanent deformation monitored. It was deemed worthwhile to develop the modeling capability to simulate permanent deformations in pavement systems using a mechanistically based constitutive law, i.e.

not in simply modifying results from a simulation where the underlying consititutive law cannot actually predict any permanent deformation.

My background and research interests are in the area of finite element techniques applied to problems of interest in several areas of science and engineering. My experience in developing nonlinear finite element codes and my background in teaching advanced courses in solid mechanics allowed me to perform preliminary feasibility studies to determine the utility of standard elasto-plastic constitutive laws for this problem.

2.0 OBJECTIVES OF THE RESEARCH EFFORT:

Current modeling techniques used by the Air Force (Crockford et al, 1990) use a variable modulus type constitutive law incapable of predicting permanent deformations in pavement systems.Since much of the strength data from standard triaxial compression tests were available for the Tyndall test bed it was deemed useful to investigate the applicability of elasto-plastic constitutive laws in conjunction with a finite element code to attempt to simulate not only peak deformation under static loading but also permanent deformation reulting from removal of the load. In the long term it is felt that the ability to predict the permanent deormation after one or a small number of cycles plus a growth law which requires parameters from standard tests would provide a mechanistically based analysis methodology to assess the potential for long term rutting.

My objectives were to develop a finite element computer program capable of performing a nonlinear, axisymmetric static analysis and to use the available data from the Tyndall test site along with a fairly simple elasto-plastic material law to simulate the deflection basins after loading and unloading.

3.0 FINITE ELEMENT MODELING WITH AN ELASTO-PLASTIC MATERIAL CONSTITUTIVE LAW:

Herein we give a brief review of the concepts involved in performing a finite element analysis employing an elasto-plastic constitutive law. The basic discretized equations to be solved in a finite element analysis using an incremental-iterative solution scheme may be written

$$K\Delta u = p ,$$
<div align="right">(EQ 1)</div>

where the stiffness matrix, K , and the residual, or load vector, p, are in general updated each iteration. The principal computational task in this update is the calculation of the current stress state given the stress state at the previous iteration and the increment in the strains between the current state and the previous one. For a discussion of the algorithmic considerations involved in this calculation the reader is referred to Prevost (1987). Herein the constitutive law governing the material response is based on elastic response below yielding and during unloading and plastic flow when the stress state is on the yield surface. The consitutive law we employ is the isotropic, rate independent cap model of DiMaggio and Sandler (1971); also see Sandler and Rubin (1979). For the cap model the loading function, which determines when plastic flow takes place, is assumed to be isotropic and to consist of two parts; an ultimate failure envelope which limits the maximum shearing stress and a strain-hardening yield surface or cap. In this work we have taken the failure envelope to be described by a Drucker-Prager relationship,

$$f = k - \alpha I_1 = 0$$
<div align="right">(EQ 2)</div>

where k, α are material paramaters and I_1 is the first invariant of the stress tensor. The yield surface or cap isdefined by

$$f = \frac{1}{R}\sqrt{\{ [X(\kappa) - L(\kappa)]^2 - [I_1 - L(\kappa)]^2 \}} = 0$$
<div align="right">(EQ 3)</div>

where R is a material constant. The functions X and L are defined in figure 1. The hardening parameter κ is implicitly defined as a function of the plastic volumetric strain. Herein the relationship used is

$$\bar{\varepsilon}^p_v = W\{exp\,[DX(\kappa)] - 1\} \qquad (EQ\ 4)$$

where $\bar{\varepsilon}^p_v$ is history dependent functional of the plastic volumetric strain and W and D are material parameters. See Sandler and Rubin (1979) for the complete definition of the cap model and for a discussion of the algorithm used to calculate the current stress state. Finally it should be noted that the five material constants required for a complete defintion of the cap model may all be obtained from a standard triaxial test. The strength parameters κ and α were determined for the materials used in the Tyndall test pavement and subgrade. Below we will assume some reasonable values for the remaining parameters to get a sense of the utility of this type of model for application to pavement systems
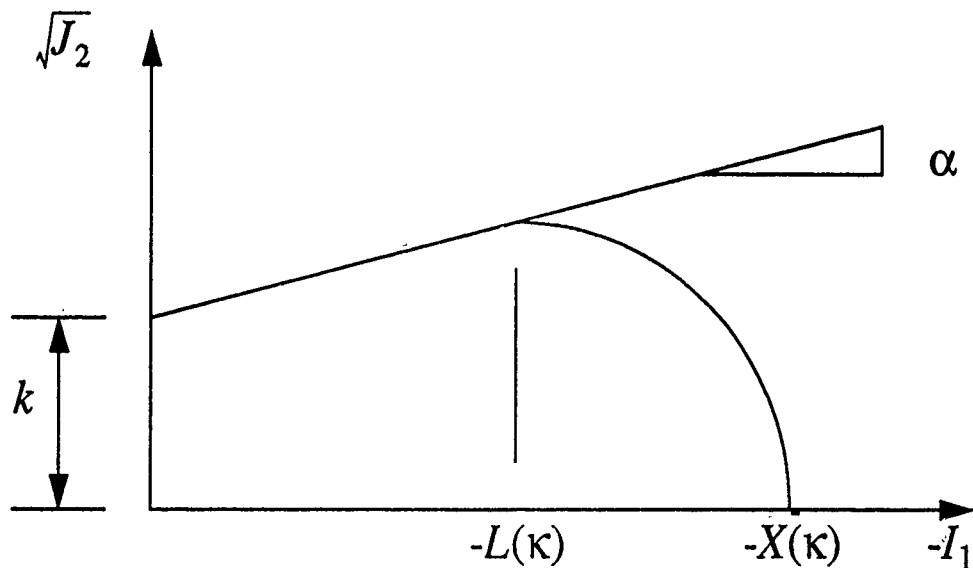

FIGURE 1. Failure and Yield Surface in Cap Model

4.0 SIMULATIONS:

In this section we present the results of some simulations for the Tyndall test pavement. The elastic and strength properties are taken from Crockford et al (1990). Hereafter this will be referred to as the TTI report. Given below are pertinant data, i.e. physical dimensions and material properties. In the TTI report a nonlinear elastic model was used. The moduli of elasticity given below are the minimum moduli used in their simulations. The cap paramaters were assumed as no experimental results were available. The values chosen are reasonable for the materials used (see Desai and Siriwardane, 1984). However it should be noted that they were adjusted somewhat to see if the model would reasonably replicate the field data. Following the TTI report all simulations were performed with the asphalt concrete remaining linear elastic.

TABLE 1. Material Properties for Tyndall Test Pavement

Property	Asphalt Concrete	Base	Subgrade-1	Subgrade-2
Modulus of Elasticity	177,000	36,316	22000	26000
Poisson's ratio	0.47	0.40	0.40	0.42
Thickness(in)	6	12	16	526
Cohesion,c,psi	0	28	0	0
Angle of Friction φ, degrees	0	62	45	45
D		0.75	0.0005	0.0005
R		2.5	2.0	2.0
W		0.075	0.01	0.01

To calculate the strength parameters α, and k, from the cohesion and angle of internal friction the following relationships were employed.

$$\alpha = \frac{2\sin\varphi}{\sqrt{3}\,(3 - \sin\varphi)} \qquad \text{(EQ 5)}$$

$$k = \frac{6c \times \cos\varphi}{\sqrt{3}\,(3 - \sin\varphi)} \qquad \text{(EQ 6)}$$

It is assumesd that the surface of the pavement is loaded over a circular area five inches in radius. The mesh that we used for the simulations consisted of fifty-four eight-noded qua-

dratic isoparametric elements containing one hundred ninety three nodes in total. A number of verification runs, both elastic and elasto-plastic were made with this mesh.

Results will be presented below for two loading cases from the Tyndall tests; 174 psi tire pressure and 244 psi tire pressure. The field deflection measurements are taken from figures 63, 64, 67, 68, 71, 72, 75, 76 of the TTI report. It should be noted that there is not a great deal of permanent deformation occuring in one cycle of loading. This can be seen by comparing the peak deflection from the field tests against an analysis where all layers are assumed to be linear and elastic. Figure 2 shows this result for the surface deflection basin and figure 3 shows the deflection versus depth at a distance of eight inches from the center of the load. Note MDD stands for multi-depth deflectometer, the apparatus used to take the deflection measurements.Figure 4 shows the surface deflection basin plot for the 174 psi load case using the cap model and parameters from table 1. Note that upon unloading the surface in the vicinity of the laod is left with a permanent deflection of approximately 2 mils. Since these results are somewhat contrived because the cap parameters were not obtained from experiments, the model was run using the same paramaters for the 244 psi load case. The surface deflection basin for this case is given in figure 5. After unloading in this case a permanent deflection of aprroximately 3.5 mils remains. The permanent deflections calculated here are of the order of the permanent deflections reported in the TTI report. Finally we note that the cap parameters can be varied quite a bit without substantially affecting the deflection results presented above.

5.0 RECOMMENDATIONS:

The results of the previous section are simply meant to show the applicability of the elasto-plastic constitutive law employed herein to the prediction of permanent deformations in pavement systems. This study is meant to be demonstrative and not necessarily to provide accurate quantitative predictions of the rutting which occurred in the Tyndall test pavement. To obtain useable rutting predictions several tasks need to be accomplished. First,
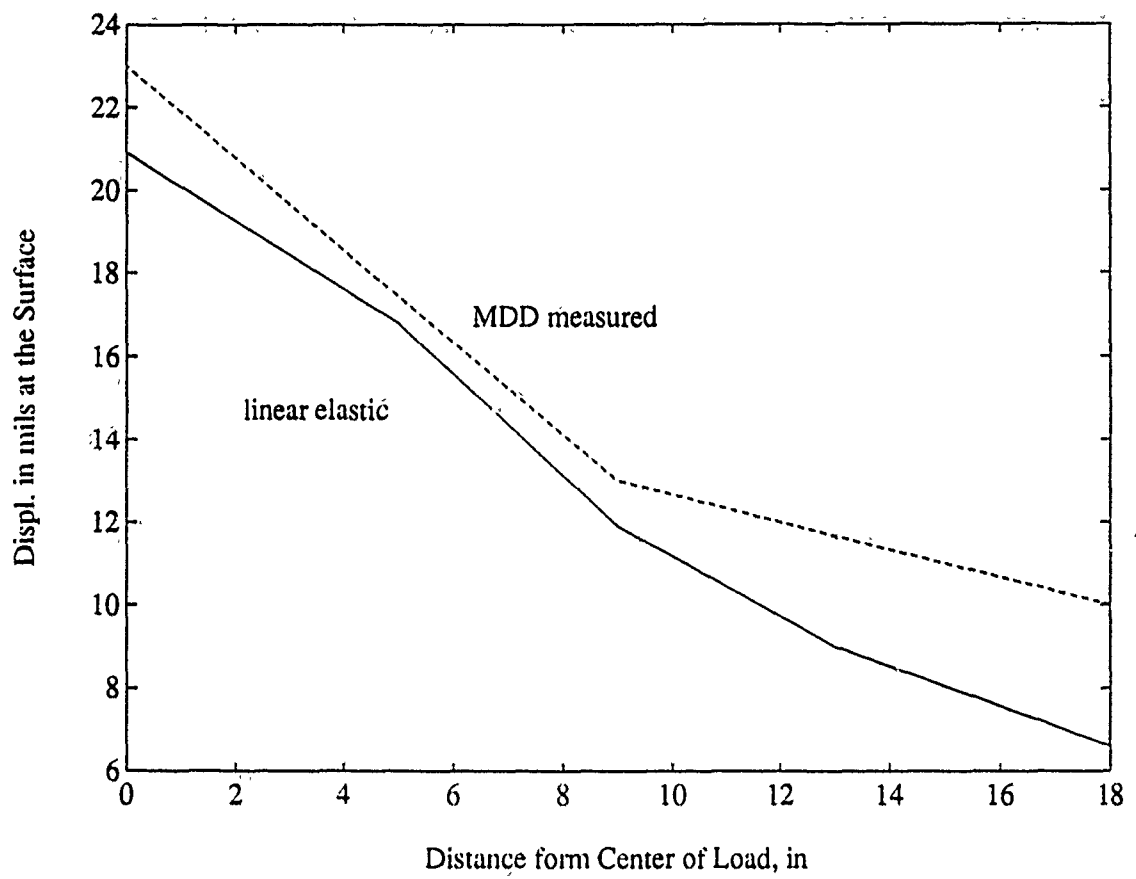
Figure 2. Surface Deflection Basin; Linear Elastic Model vs Field Measurements
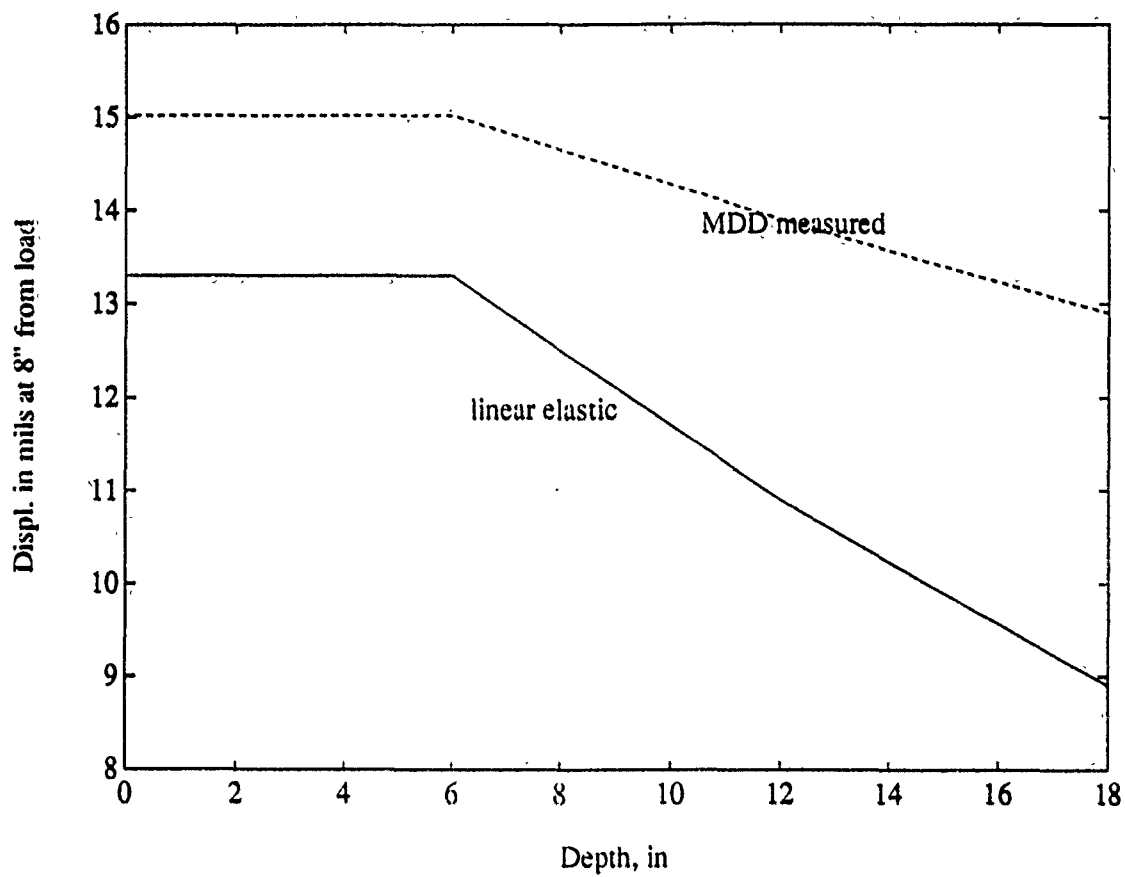
Figure 3. Linear Elastic Model vs Field Measurements
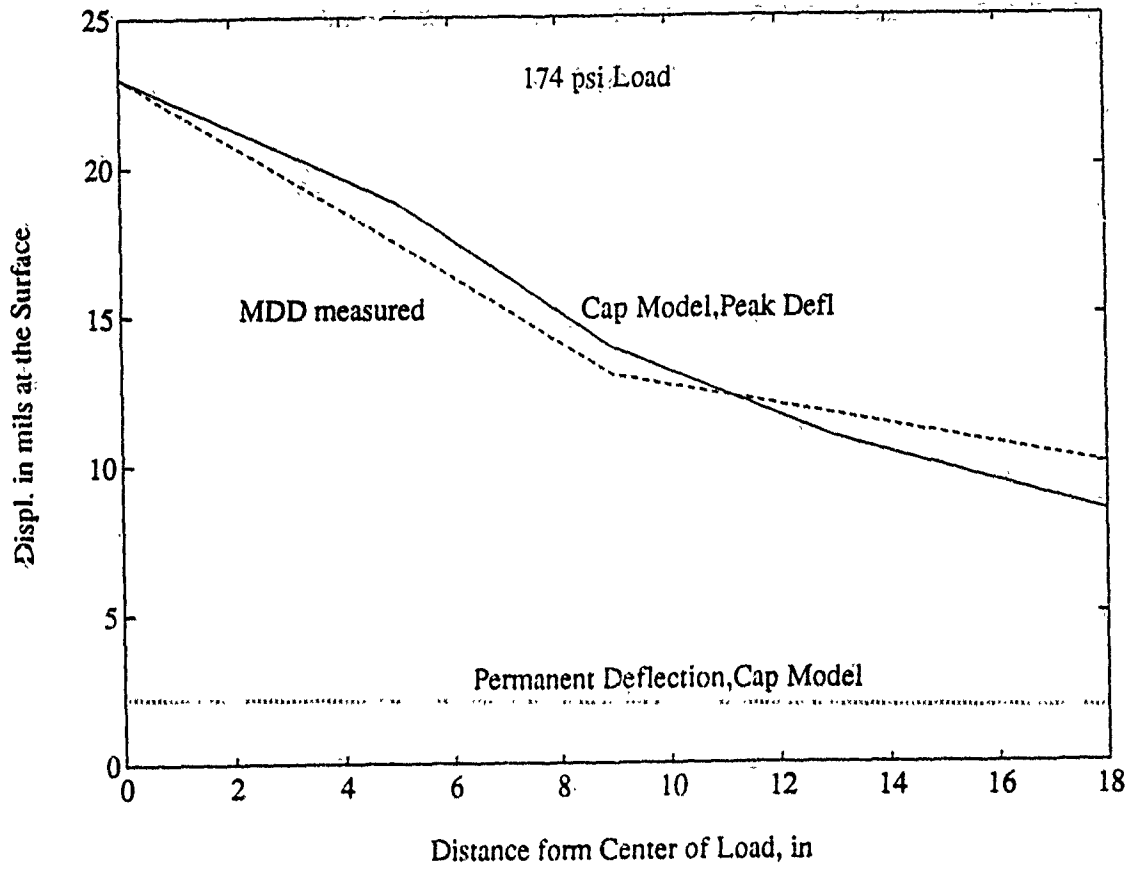
Figure 4. Surface Deflection Basin; Cap Model; 174 psi
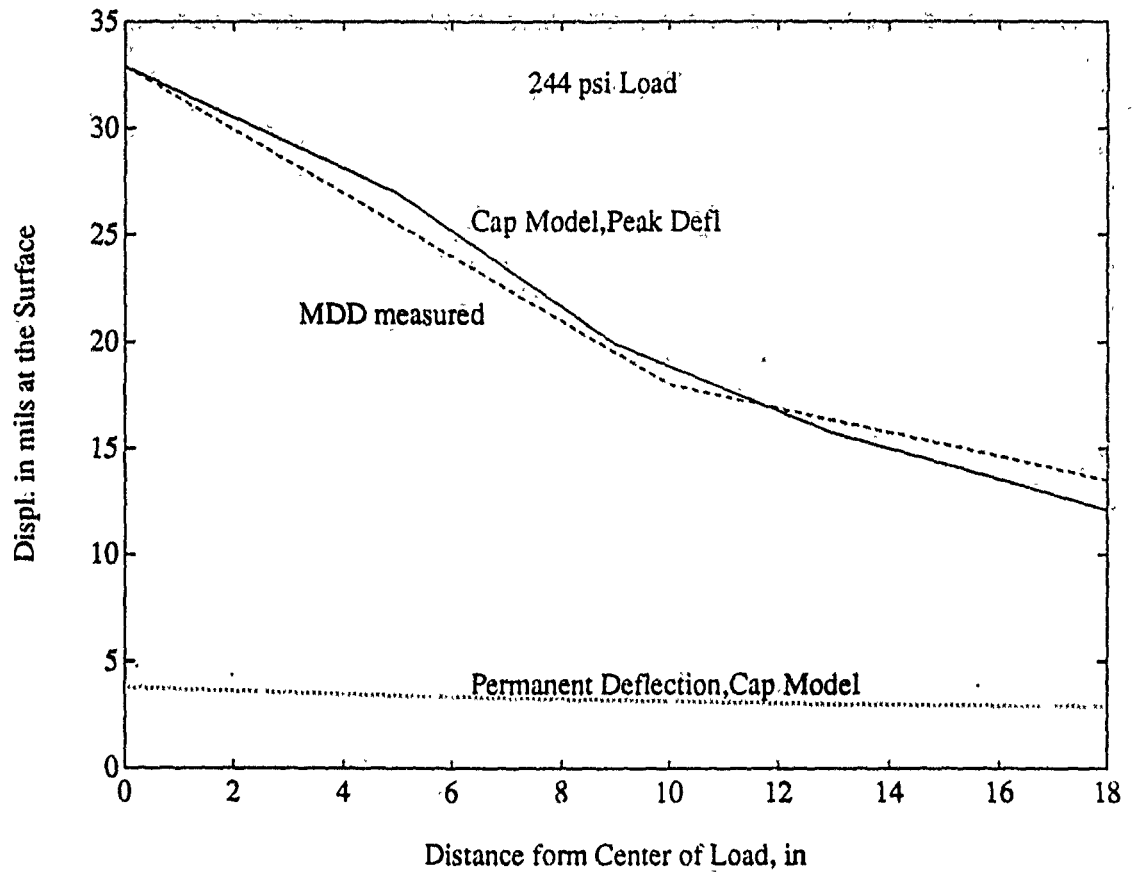
Figure 5. Surface Deflection Basin; Cap Model; 244 psi

whether the cap model used herein or a more elaborate model is used, all of the appropriate material constantsshould be accurately determined from experiment. Constitutive laws are considered most useful if all the requited data can be determined from tests such as the standard triaxial test

There are clearly aspects of the pavement loading problem which cannot be captured with the axisymmetric assumption used here and in previous Air Force work (Crockford et al, 1990). The rolling tire causes a stress path at each point in the pavement and the base material which may be quite complicated. This is often referred to as the problem of rotation of the pricipal planes. To capture this effect a fully three dimensional analysis is required.

REFERENCES

Crockford, W. W., L. J. Bendana, W. S. Yang, S. K. Rhee, S. P. Senadheera, "Modeling Stress and Strain States in Pavement Structures Incorporating Thick Granular Layers", Final Report, United States Air Force Contract No. F08635-87-C-0039, Tyndall Air Base, 1990.

Desai, C. S., H. J. Siriwardane, Constitutive Laws for Engineering Materials, Englewood Cliffs, New Jersey, Prentice-Hall, Inc., 1984.

DiMaggio, F. L., I. S. Sandler, "Material Model for Granular Soils", Proc. Am. Soc. Civ. Eng., 1971, pp. 935-950.

Prevost, J. H., "Modeling the Behavior of Geomaterials", in Geotechnical Modeling and Applications, Houston, Texas, Gulf Publishing Co., 1987, pp. 76-146.

Sandler, I. S., D. Rubin, "An Algorithm and a Modular Subroutine for the Cap Model", International Journal for Numerical Methods in Engineering, vol. 3, 1979, pp. 173-186.

1990 USAF-UES SUMMER FACULTY RESEARCH PROGRAM/

GRADUATE STUDENT RESEARCH PROGRAM

Sponsored by the

AIR FORCE OFFICE OF SCIENTIFIC RESEARCH

Conducted by the

Universal Energy Systems, Inc.

FINAL REPORT

The High-Speed Separation and Identification of Jet Fuel

Prepared by: Paul R. Kromann, Ph.D.

Academic Rank: Associate Professor

Department and Chemistry Department

University: Fort Valley State College

Research Location: HQ USAFESC/RDVC
Tyndall AFB
Panama City, FL

USAF Researcher: Howard T. Mayfield, Ph.D.

Date: 17 Sept 90

Contract No: F49620-88-C-0053

The High-Speed Separation and Identification of Jet Fuel

by

Paul R. Kromann

ABSTRACT

Gas chromatography and pattern recognition were used to effect the high-speed separation and identification of aviation fuels. A 0.10-mm diameter capillary column was used and the chromatographic conditions were found which allowed chromatographic analysis to be carried out five times faster than before. Use of a flame ionization detector lowered the cost of the equipment considerably.

In addition to faster analysis using less-expensive equipment, the system used here gave better identification accuracy compared with the earlier work. The SIMCA pattern recognition system classified all available aviation fuels (154 samples distributed among seven different fuel types) with 100% accuracy. The SIMCA system correctly classified 16 out of the 18 available weathered samples.

Acknowledgements

I wish to thank the Air Force Systems Command and the Air Force
Office of Scientific Research for providing the Summer Faculty Research
Program and for sponsoring this research. Thanks also to Universal
Energy Systems for handling the organizational aspects of the program.

Dr. Howard T. Mayfield, my mentor, was involved in every aspect of
this project. His expertise in chromatography was inspiring and his
patience was comforting. Despite his own demanding schedule, he was
always available with advice and assistance. Howard was the major
factor in my great enjoyment of the SFRP. He also carried out all
the pattern recognition calculations. Mike Henley helped me a lot
in the lab, especially with the data system. Bruce J. Nielsen
supplied environmental information and much help in obtaining the
samples of contaminated soil.

The Environics Division of the Air Force Engineering and Services
Center provided excellent scientific equipment and an encouraging
atmosphere. It was a pleasure to work under those stimulating
conditions.

I. INTRODUCTION:

Gas chromatography is said to be the world's most widely-used analytical technique. (1) High resolution gas chromatography offers: (a) the best method for separating volatile mixtures, (b) relatively short analysis time, and (c) good sensitivity.(2) Because of these advantages, gas chromatography is particularly well-suited for the high-speed separation and identification of jet fuel and aviation gasoline.

The reasons for USAF interest in this area have been detailed in earlier work by Mayfield and Henley.(3) These authors (3) used high resolution gas chromatography/mass spectrometry (GC/MS) to separate the fuels into their individual components. Then, using a pattern recognition system, they were able to obtain classification accuracies of about 90% on various types of jet fuels.

It would be desirable, however, to obtain these same good results without the high cost of the GC/MS equipment and the relatively long analysis time (70 minutes for each chromatogram). Mayfield (4) suggested that the analysis time could be shortened considerably by use of a newly-available 0.10-mm diameter capillary column; and that the flame ionization detector could be an adequate and much less expensive detector than the mass selective detector.

My interests have been in the area of high resolution gas chromatography, especially the analysis of commercial automobile gasolines. Thus, my interests tied in well with this project on the analysis of aviation fuels.

II. OBJECTIVES OF THE RESEARCH EFFORT:

The desirability of a faster analysis using less-costly equipment for the characterization of jet fuel was pointed out by Mayfield (4). My goal, as a participant in the 1990 USAF-UES Summer Faculty Research Program, was to develop a method involving less-expensive equipment for the high-speed separation and identification of jet fuel.

The objectives in support of this goal are:

1. to see if a 0.10-mm diameter capillary column with flame ionization detection can accomplish the high-speed separation;
2. to find the appropriate chromatographic conditions for obtaining the high-speed separation;
3. to determine the chromatographic profiles of all available jet fuels to train the pattern recognition system;
4. to compare these pattern recognition results with those of Mayfield and Henley (3);
5. to determine the chromatographic profiles of all available real-world fuel-in-the-environment samples;
6. to see if the fuel-in-the-environment samples can be identified by the pattern recognition system;
7. to investigate the extent of fuel-contaminated areas by taking samples from a grid of points.

III. THEORY:

Gas chromatography (GC), like the older fractional distillation, is a separation method, so it was natural for GC to use some distillation terminology. Height Equivalent to a Theoretical Plate (HETP) describes the efficiency of a distillation column. The corresponding term for a chromatographic column is h. The smaller the numerical value of h, the greater the separation efficiency of the column.

The Golay (5) equation, a form of the van Deempter (6) equation, relates h to other chromatographic parameters, all of which are inter-related. Jennings (1) has simplified this to show how h_{min}, the minimum possible value of h, is related to column radius, r, and partition ratio, k.

$$h_{min} = r[(11 \ k^2 \ + \ 6 \ k \ + \ 1)/3(1 \ + \ k)^2]^{1/2}$$

Figure 1, from Jennings (2), shows the variation of h_{min} (column efficiency) with column radius. Note that the column used in this research has only half the radius of the best example in Figure 1, and therefore will be even more efficient.
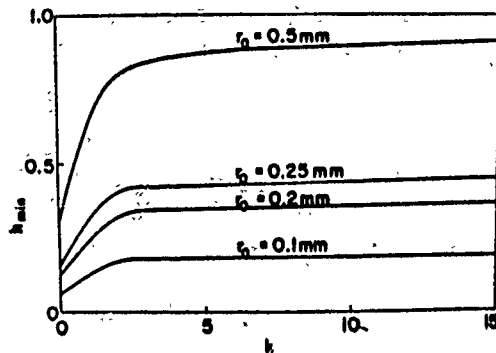

FIGURE 1. Relationship between the minimum height equivalent to a theoretical plate, h_{min}, and the partition ratio k of the test compounds for columns of several radii.

IV. EXPERIMENTAL:

A. Equipment

Hewlett Packard 589CA gas chromatograph with flame ionization detector

10 m x 0.10 mm fused silica capillary column with 0.34 μm HP-5 coating (Hewlett Packard Co.)

Hewlett Packard 7673A automatic sampler, set for 1-μL injection

Hewlett Packard 18652A A/D Converter

Helium carrier gas

Acquired data were stored on disk until needed for the pattern recognition calculations

B. Procedure

Preparation of samples for analysis:

Prior to analysis, 100.0μL of a fuel were added to 900μL of CH_2Cl_2 spiked with D_{10}-anthracene as an internal standard. This diluted fuel was then injected for analysis.

Table 1 — Gas chromatographic conditions for all fuel samples

Initial Temperature:	60° C
Initial Time:	0.34 min
Temperature Program Rate:	18° C/min
Final Temperature:	270° C
Final Time:	0 min
Injector Temperature:	250° C
Detector Temperature:	270° C
Carrier Gas Head Pressure:	30 psig
Split Flow:	30 mL/min

Extraction of soil samples:

Three mL of CH_2Cl_2, spiked with D_{10}-anthracene as an internal standard, were added to 3 grams of soil and the mixture was agitated vigorously for 5 minutes. The mixture was then centrifuged (2000 rpm for 5 minutes) and allowed to stand overnight. The supernatant was decanted and centrifuged again (2000 rpm for 5 minutes). Samples of this extract were diluted, as above, for analysis.

C. Fuels:

The fuels studied in this project are listed here, with their main users.

Jet-A	U. S. commercial jet-liners
JP-4	U. S. Air Force
JP-5	U. S. Navy
JP-7	high altitude flights
JPTS	high altitude flights
JP-8	NATO countries
AVGAS	propeller-driven aircraft

These fuels were collected previously by Dr. H. T. Mayfield of the Environics Division. As soon as received, the fuel samples (in sealed containers) were placed into storage at -20° C.

V. RESULTS AND DISCUSSION:

Varying the conditions to minimize the analysis time while still maintaining adequate resolution led to the conditions listed in IV., above. These conditions provided adequate resolution in only 12 minutes, thus fulfilling the first and second objectives.

The GC oven required about 3 minutes to cool down and become ready for the next sample, giving a total GC analysis time of 15 minutes. Assuming a similar cool-down time needed in the earlier work (3) means that the present conditions allow GC analysis about 5 times faster than before.

All chromatograms are plotted as detector response versus time in minutes. Figure 2 shows the chromatogram of the methylene chloride with its trace of cyclohexene preservative (retention time between 1.6 and 1.7 minutes) and the added D_{10}-anthracene internal standard (retention time about 11.4 minutes).

A reference solution containing the n-alkanes from 7 carbons to 16 carbons was prepared in the same manner as the fuel samples. A sample of the reference solution was run along with every batch of 10-15 fuel samples. The simple chromatogram of the reference solution, Figure 3, provided a check on the continued proper functioning of the chromatographic equipment.

Independent samples (from different sources and at different times) of the fuels listed in IV., C. had been obtained earlier by Dr. H. T. Mayfield. The chromatographic profile was run for each available fuel sample, 154 samples in all, and the results were used to train the pattern recognition system. This fulfilled the third objective.

Representative chromatograms of the fuels studied are shown in Figure 4.

The increase in chromatographic speed resulting from use of the
0.10-mm column can be seen by comparing Figure 5, a chromatogram of
JP-4 from Reference 3, with Figure 6, a chromatogram of JP-4
from this research. Two chromatograms of JP-4 from this research are
plotted on a different scale in Figure 7, showing that the resolution
here is adequate even though the analysis time is short.

From the similarity in profile of all the fuels except JP-4 and
aviation gasoline, it is seen that the pattern recognition system has a
difficult task in distinguishing among these similar patterns. Another
difficult task for the pattern recognition system is recognizing such
widely-differing profiles, as shown in Figure 7, as the same f·.;l, JP-4.

Data were collected and stored with a HP-3357 Laboratory Automation
System (Hewlett-Packard Company). The data from the chromatographic,
integration reports were transduced into the data vectors using the
SETUP chromatographic transducing program, developed by Mayfield. Data
vectors produced by SETUP were subjected to various feature selection
and pattern recognition procedures using the ARTHUR pattern recognition
package (ARTHUR Version 4.1, Infometrix, Inc,. Seattle, WA).

The collected chromatograms included 154 chromatograms of known
fuel samples, 11 chromatograms of recovered fuel product, and 7
chromatograms from soil extracts. Where fuel chromatograms exhibited
"humps" of unresolved materials above the baselines, valley-to-valley
peak integrations were used. In the initial data treatments, peak areas
were divided by the peak area of the internal standard peak for each run
to obtain a response value for each peak.

In the initial treatment, SETUP located 242 peaks which were exhibited by one or more of the chromatograms. The retention times for these peaks were placed in a "reference list" and used by the program to locate the peaks in the database of chromatograms. Thus a 242-dimensional data vector was obtained for each chromatogram in the database. The data vectors were used to represent the chromatograms in the subsequent pattern recognition analysis. The raw 242-dimensional data set was transferred to a Cyber 830 mainframe computer for pattern recognition analysis.

In order to remove the influence of the solvent and the internal standard from the pattern recognition analysis, the two peaks due to the methylene chloride and the peak due to the internal standard were removed from the data vectors prior to further analysis, giving 239 remaining features.

Classifications were made using the k-nearest neighbor classification technique. In an attempt to improve accuracy and reliability of the classifications, the 239 features were weighted with their Fisher weights. The best k-nearest neighbor classification obtained from this data set was based on the 4-nearest neighbors. The overall classification accuracies obtained using the 4-nearest neighbors with Fisher weighted raw data averaged 91.6%, with all the AVGAS and all the JPTS samples being classified correctly.

In order to permit soil extracts to be included in the data set, it was decided to base a new set of data vectors on peak area normalized to the total chromatogram area rather than on the peak area normalized to an internal standard. In transducing a new data set based on normalized

peak areas, we used the same 239- feature list.

The raw 239-dimensional training set was best classified by the k-nearest neighbor system with a committee size of 4, using 10 features selected on the basis of their Fisher weights and made orthogonal, giving a classification accuracy of 92.3%. Here, all the JP-4, JP-7, and JPTS samples were classified correctly.

Yet another transducing into data vectors was performed, this time with the requirement that the reference list features be present in 40% or more of the chromatograms. The resulting reference list contained retention times of 132 features. The training set consisted of chromatograms of the 154 known fuel samples. The test set consisted of 4 samples of floating product recovered from a Naval Air Station and strongly presumed to be JP-5, 7 samples of floating product recovered from monitoring well T9W on Tyndall AFB and strongly presumed to be JP-4, and extracts of 7 soil samples obtained at various depths from a 7-foot soil coring taken near the T9W monitoring well.

The raw data from the 132-dimensional area percent data were auto-scaled and submitted to the SIMCA classification system. The theory of the SIMCA system has been given by Wold (7) and Sjostrom (8). This system classified all 154 training set chromatograms without error, i. e., classification accuracy of 100%. This compares with classification accuracy of about 90% by Mayfield and Henley (3), thus accomplishing the fourth objective.

We were greatly interested in whether the pattern recognition system could identify correctly the fuel samples, from leaks or spills, which had been out in the environment. Mayfield had already obtained

the four samples of floating product from a Naval Air Station. The SIMCA classification system correctly identified two of these samples as JP-5 but misclassified the other two samples as Jet-A. This is not too surprising, considering the similarity in the profiles of these two fuels.

The T9W monitoring well is located in an area that was formerly an aviation fuel tank farm near building 504, south-east of the flight line of Tyndall AFB. The fuel tanks had been removed some years earlier. We lowered a sampling device down the well and skimmed 7 samples from the surface of the material in the well. The light tan clear liquid samples were obtained from about a 6-foot depth. The SIMCA system correctly classified all 7 of these samples as JP-4. The area that was formerly the aviation fuel tank farm is shown in Figure 1 of Reference 9. H. T. Mayfield, B. J. Nielsen, and I augered a hole 7 feet into the ground at sampling point No. 25 (see Figure 1 of Reference 9), and I took 7 soil samples from various depths. The samples were quickly placed into sealed containers for storage in the freezer until time for extraction and analysis.

The chromatograms of the soil extracts looked very much like those of JP-4. However, SIMCA classified four of the soil extracts as aviation gasoline and three as JP-4. At this point, we began to doubt the value of SIMCA until we learned that aviation gasoline had also been stored at this tank farm. Closer examination of the initial portion of the chromatograms showed the similarity between the soil extracts and aviation gasoline.

Because the soil was no doubt contaminated by both JP-4 and

aviation gasoline, SIMCA will be credited with correct classification of the 7 soil extracts. These plus the 7 JP-4 samples plus the two JP-5 samples give 16 correct classifications and two understandable misclassifications out of the 18 available fuel-in-the-environment samples. This accomplishes the fifth and sixth objectives.

In order to determine the concentration of fuel contamination in the soil samples, fuel samples were prepared containing different amounts of JP-4 and were chromatographed by the usual method. Total detector response was plotted versus fuel volume, as a calibration curve. Using the calibration curve, total detector response for each soil extract was converted to fuel volume which was then, using fuel density, converted to fuel weight. This, with the 3-g soil sample weight, then could be converted to parts per thousand (ppt) of fuel in the soil. Figure 8 shows ppt of fuel in the soil plotted versus depth.

Sampling point No. 25 was chosen for the soil coring because an earlier measurement of fuel at a certain depth in the soil had been carried out there (9). This particular soil sample had been treated by supercritical fluid extraction, then the extract had been chromatographed. This point was also plotted in Figure 8, and is seen to be compatible with the data in this report.

The seventh objective could not be accomplished because the procedures involved (obtaining a soil sample and then extracting it) are so time-consuming for a single sample. A whole grid of points would be impossible in a 10-week Summer.

VI. RECOMMENDATIONS:

"Weathering" of fuel is the change in composition of the fuel resulting from evaporation, oxidation, and/or bacterial action which occur after release of the fuel into the environment.

A. Cnly 18 samples of weathered fuel were available for this research. To extend this work, many more weathered fuel samples should be run. This effort should concentrate on samples which have a known history, so that the success of the pattern recognition system can be measured against extent of weathering of the fuels.

B. Soil extraction was a slow step in the analysis of some of the weathered samples in this work. A high-speed extraction technique (i.e., supercritical fluid extraction) should be developed to go along with the high-speed chromatographic profiling demonstrated in this work.

C. The soil extracts in this work appeared to be a mixture of aviation gasoline and JP-4. However, the SIMCA system could only choose one or the other. It would be desirable to have a pattern recognition system that could identify the components of a mixture and also determine the relative amounts of each, such as the system being developed by Dr. Barry Levine of Clarkson University. Known mixtures of different fuels should be run to test such a pattern recognition system.

REFERENCES

(1) Jennings, Walter, Advances in Capillary Chromatography, J.G. Nikelly (ed.), New York, NY, Huethig, 1986.

(2) Jennings, Walter, Gas Chromatography with Glass Capillary Columns, 2nd Ed., New York, NY, Academic Press, 1980.

(3) Mayfield, H.T. & M.V. Henley, "Classification of Jet Fuels using High Resolution Gas Chromatography and Pattern Recognition", accepted for publication in Monitoring Water in the 1990s: Meeting New Challenges, ASTM STP 1102, J.R. Hall & G.D. Glysson (eds.), American Society for Testing and Materials, Philadelphia, PA, 1991.

(4) Mayfield, H.T. private communication.

(5) Golay, M.J.E., in Gas Chromatography, Coates, V.J., et al (eds.), pp. 1-13. New York, NY, Academic Press, 1958.

(6) van Deempter, J.J., F.J. Zuiderweg, & A. Klinkenberg, Chem. Soc., 1956, Vol. 5, p. 271.

(7) Wold, S. & M. Sjostrom, "SIMCA: A Method for Analyzing Data in Terms of Similarity and Analogy", in Chemometrics: Theory and Approach, B.R. Kowalski (ed.), ACS Symposium Series 52, Washington, DC, 1977.

(8) Sjostrom, M. & B.R. Kowalski, Anal. Chim. Acta, 1977, Vol 112, p. 11.

(9) "Soil-Gas Survey: Tyndall AFB, Panama City, FL" This work was done by Lockheed Engineering & Sciences Co., Las Vegas, NV, under an interagency agreement between the U.S. EPA and the Air Force Engineering & Services Center, under EPA project number 21590J04, contract number 68-03-3245.
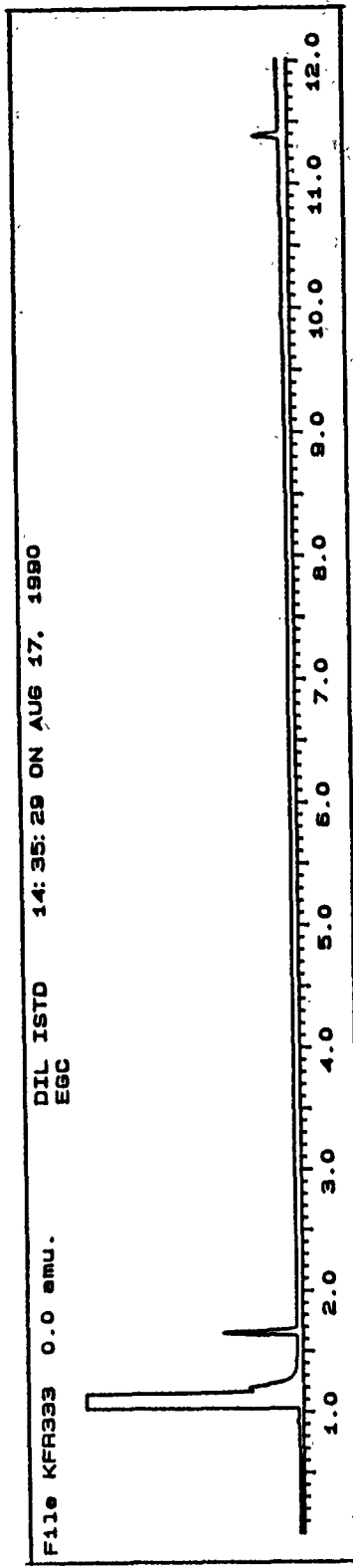
Figure 2 Methylene chloride with internal standard.
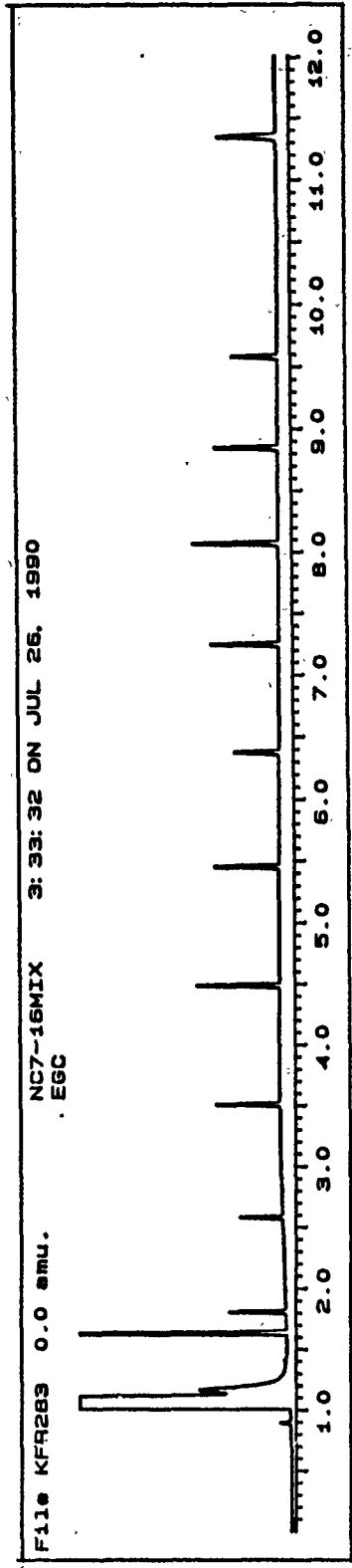
Figure 3 Reference solution.
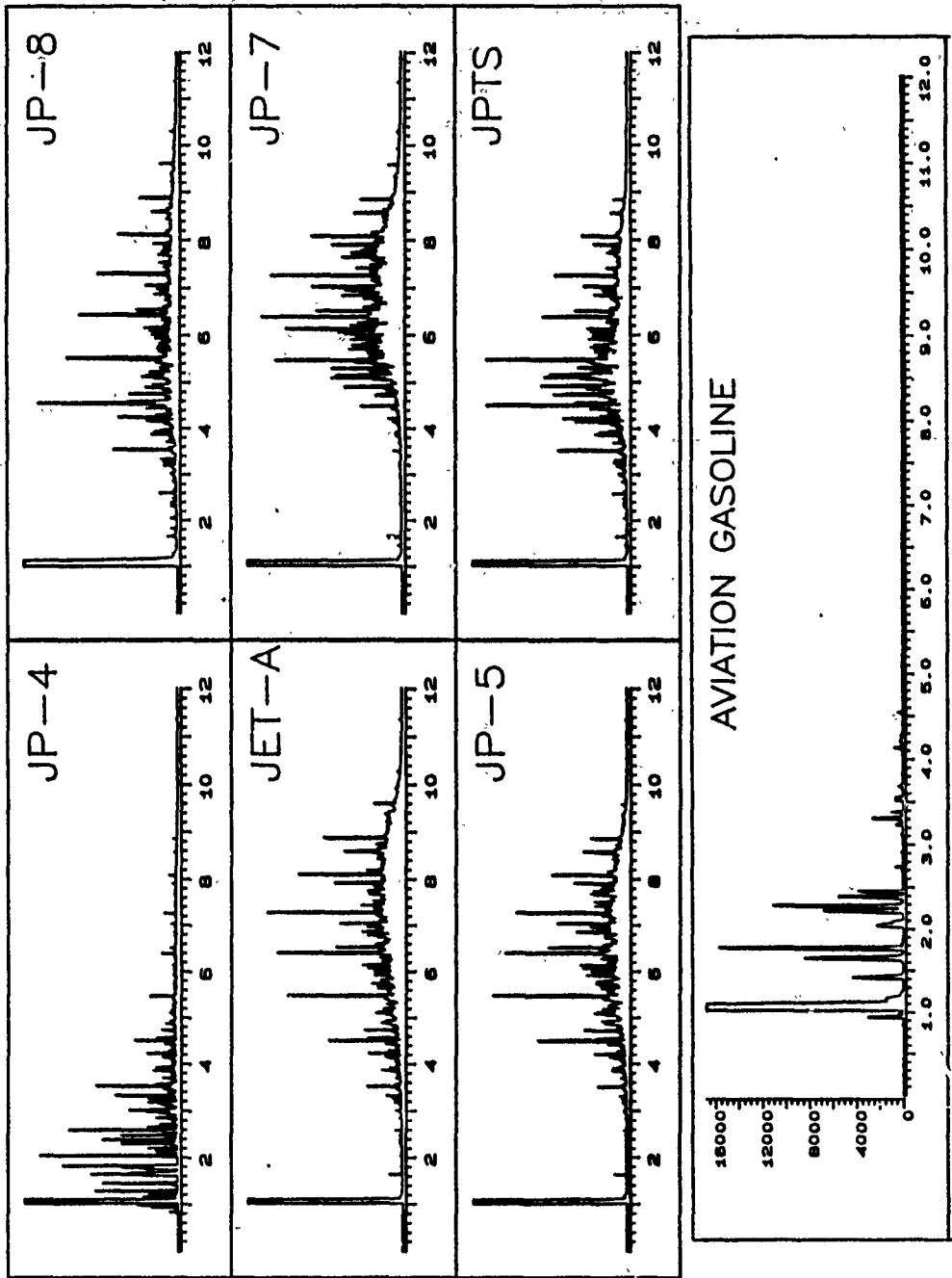
Figure 4 Representative chromatograms of fuels studied.
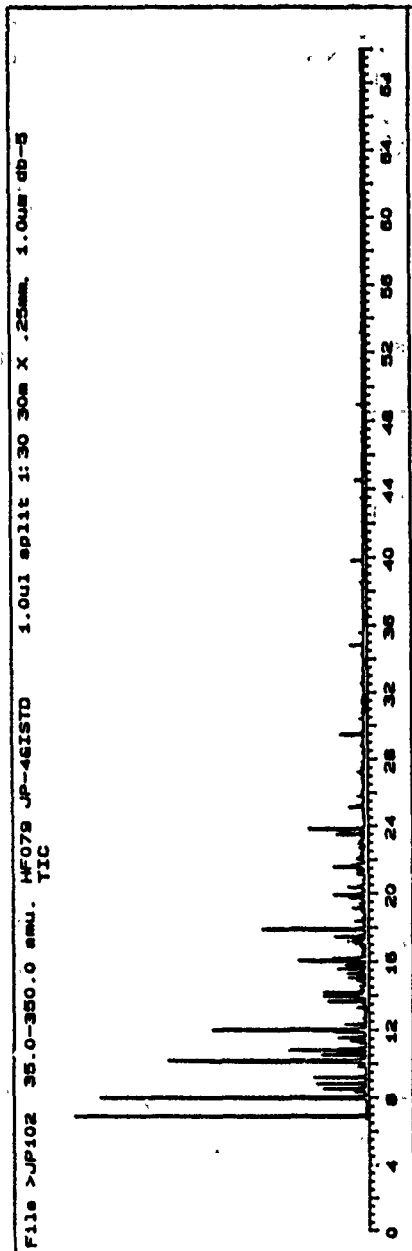
Figure 5 Chromatogram of JP-4 from Reference 3.
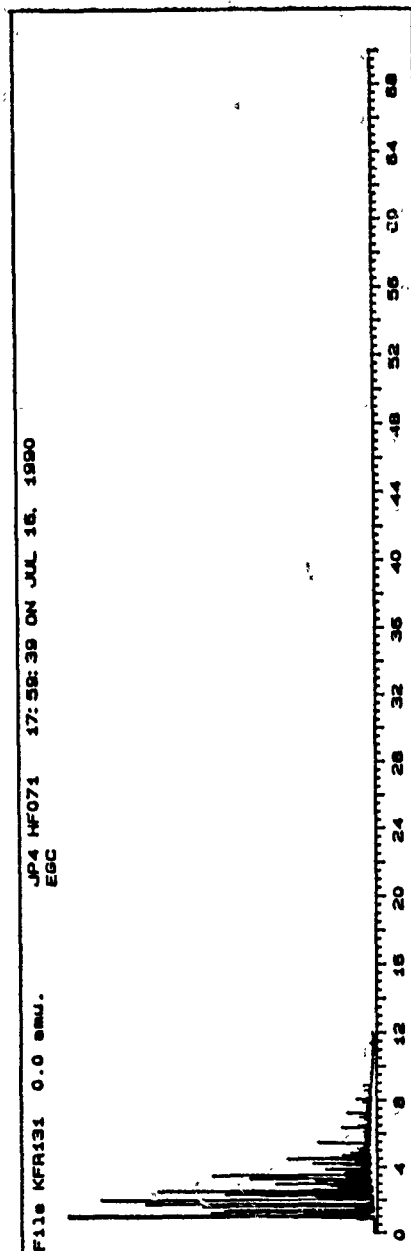
Figure 6 Chromatogram of JP-4 from this research.
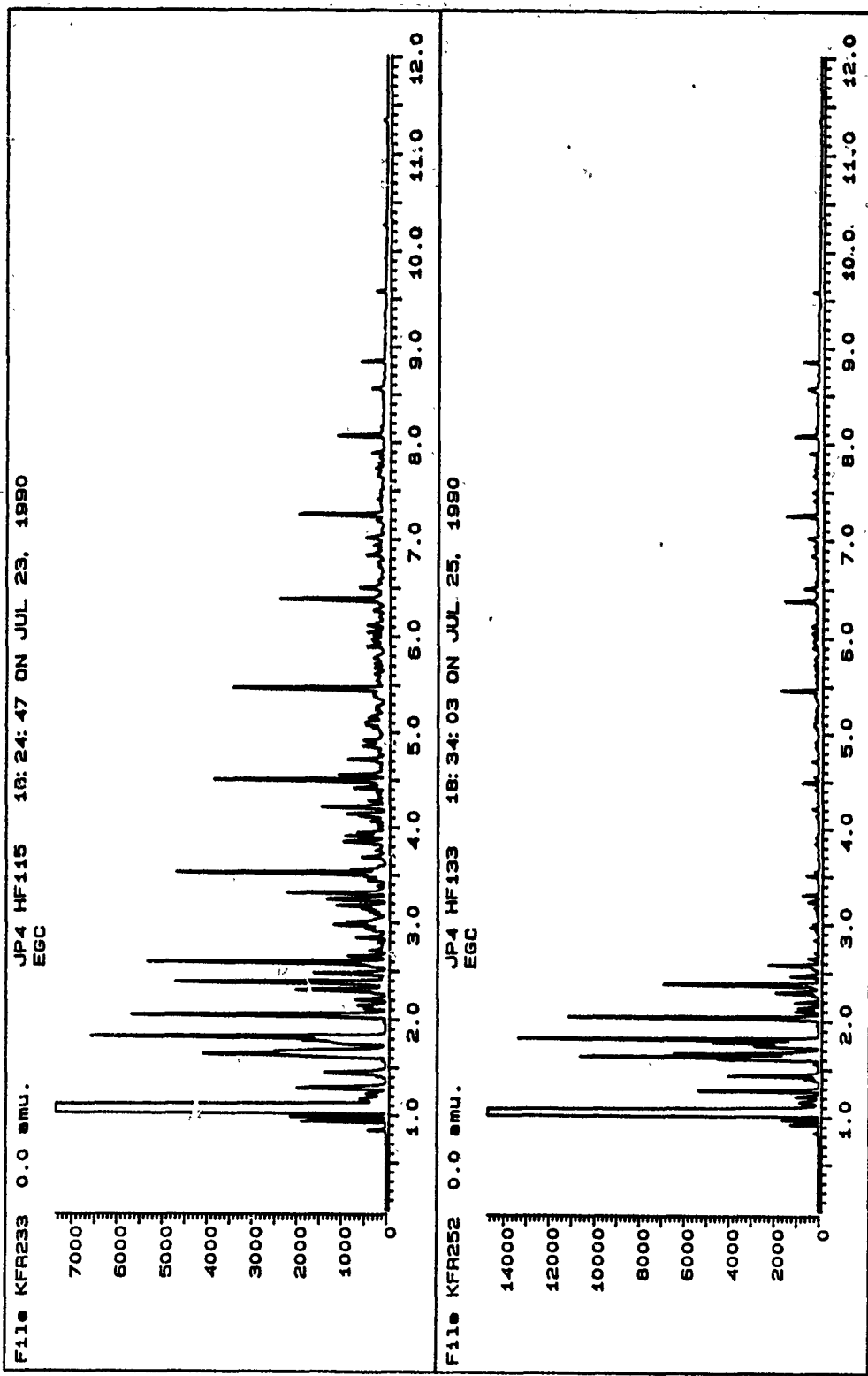
Figure 7   Chromatograms of JP-4.
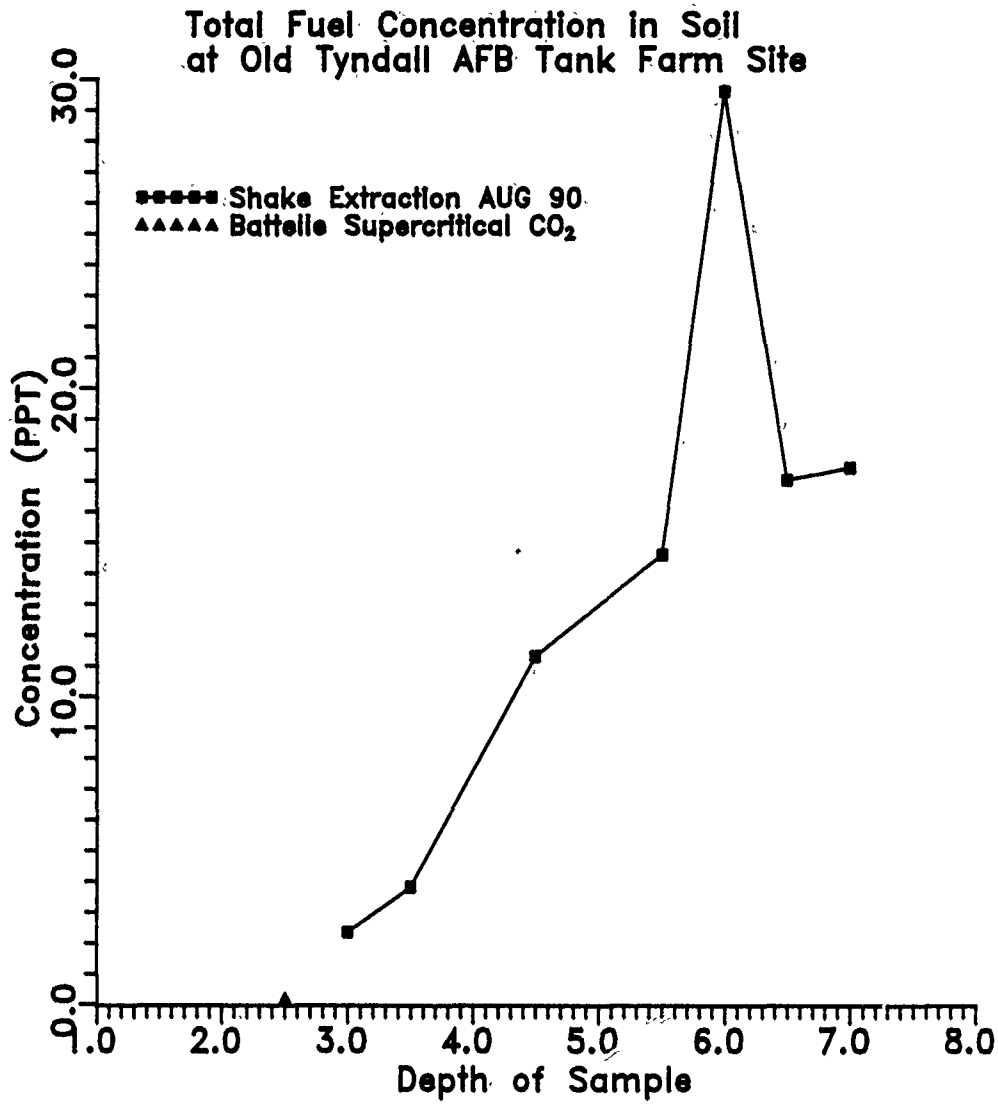
Figure 8   Fuel concentration in soil.

1990 USAF-UES SUMMER FACULTY RESEARCH PROGRAM

GRADUATE STUDENT RESEARCH PROGRAM

Sponsored by the

AIR FORCE OFFICE OF SCIENTIFIC RESEARCH

Conducted by the

Universal Energy Systems, Inc.

FINAL REPORT

UTILIZATION OF ION EXCHANGE RESINS FOR THE PURIFICATION OF PLATING BATHS

Prepared by: Kyung C. Kwon

Academic Rank: Associate Professor

Department and   Chemical Engineering Department

 University: Tuskegee University

Research Location: Environics Division, Engineering & Services
                      Laboratory, HQ AFESC/RDVC,
                      Tyndall Air Force Base,
                      Florida 32403-6001

USAF Researcher: Capt. Helen Jermyn and Dr. Howard Mayfiell

Date: 7/16/1990

Contract No: F49620-88-C-0053

UTILIZATION OF ION EXCHANGE RESINS FOR THE PURIFICATION OF PLATING BATHS

by

Kyung C. Kwon

ABSTRACT

Experiments were performed for the removal of Cr^{+6}, Fe^{+2}, Cu^{+2} and Ni^{+2} with Dowex XFS 4195.02 ion exchange resin as an adsorbent at 25°C. No removal of Fe^{+2} was observed in the presence of the Dowex resin. A mathematical model on the removal of both Cr^{+6} and Cu^{+2} from aqueous solutions was developed in the presence of the Dowex resin, assuming that intraparticle diffusion is a controlling step for the adsorption of the heavy metal ions on the resin. The intraparticle diffusivities of Cr^{+6} and Cu^{+2} through the resin were obtained to be 0.5 and 0.03 - 0.05 cm^2/min, respectively, by applying experimental data to the developed mathematical model.

Experiments on isotherm equilibrium adsorption of Cu^{+2} on the Dowex ion exchange resin were performed at pH 1.5 and 25°C. A mathematical equation on the isotherm equilibrium adsorption of Cu^{+2} on the resin was developed, using the Freundlich equation.

A series of experiments on the regeneration of Cu^{+2}-saturated Dowex XFS-4195.02 ion exchange resin were conducted at 25°C, using 0.5-2N NH_4OH aqueous solution as a regeneration reagent. A mathematical model on the regeneration of exhausted Dowex XFS 4195.02 ion exchange resin was developed, using experimental data of regeneration.

ACKNOWLEDGMENTS

I. INTRODUCTION:

The U.S. Air Force currently performs most of its industrial plating operations at five Air Logistics Centers throughout the United States. During the plating operation, plating baths and rinsewaters are contaminated with excess heavy metals such as chromium, copper, iron, aluminum, lead, nickel, zinc and others. These contaminant metals in plating baths reduce the efficiency of plating operations. Contaminated plating solutions are currently replaced and, disposed according to the Federal environmental regulations restricting hazardous waste discharges.

Contaminated plating bath solutions contain expensive heavy metals such as chromium and nickel, and other valuable chemicals such as sodium hydroxide, sodium bicarbonate, hydrochloric acid, sulfuric acid, boric acid, ammonium chloride, sodium citrate and sodium hypophosphite. Replacing and disposing contaminated bath solutions are costly to the Air Force. The Air Force sponsored the previous research projects in order to restore efficiencies of metal-contaminated bath solutions with chelating ion exchange resins such as Amberite IRC-718, Duolite ES-467, Dowex XFS-43084, Dowex XFS-4195, Unicellex UR-10 and Sumichelate CR-2 (Gold, 1985).

According to the previous research report, the resins proved effective in the removal of metals from the plating solutions when they are fresh resins or have been effectively regenerated. The Duolite ES-467 was very effective in the removal of zinc from electroless nickel bath solution and eassily regenerated. Dowex XFS-4195 was effective in the removal of contaminant metals when it was fresh. Laboratory-scale tests were recommended on the effective regeneration of the Dowex XFS-

4195 in order to prevent contamination of baths during subsequent treatments by the previous researcher (Folsom, 1989).

In this research project, Dowex XFS-4195.02 was selected as a representative of chelating ion exchange resins for the removal of heavy metals. Copper, Chromium, Nickel and Iron were chosen representatives of contaminant heavy metals in plating bath solutions. Ammonium hydroxide was used as a regenerant for the Cu-saturated Dowex resin. Emphases on this research were given to identifying kinetics on the removal of Cu^{+2} from aqueous solutions by the fresh Dowex ion exchange resin, and understanding kinetics on the regeneration of Cu-saturated Dowex ion exchange resins.

II. CBJECTIVES OF THE RESEARCH EFFORT:

Heavy metal wastes generated from plating operations can be removed with ion exchange resins, which selectively remove contaminant metals from plating baths. Metals collected on ion exchange resins during treatment are removed from used resins during regeneration of used resins. Ion exchange resins were reported to be effective in removal of heavy metals such as Ni, Cd, Cr, Pb, Cv, Fe and Zn from the plating solutions when they are used as fresh resins or have been effectively regenerated.

The main objectives of this research are (1) to identify optimum conditions of regeneration for the used Dowex XFS-4195.02 ion exchange resin by treating the used resin in the presence of NH_4OH aqueous solution as a regeneration reagent at various concentrations of NH_4OH aqueous solution and at various durations of regeneration, (2) to study kinetics on the regeneration of the Dowex XFS-4195.02 ion

exchange resin loaded with heavy metals at various regeneration conditions, and (3) to study kinetics on the removal of heavy metals from aqueous solutions in the presence of the Dowex XFS-4195.02 ion exchange resin at various treatment conditions.

III. EXPERIMENTS:

Dowex XFS-4195.02 (Grinstead, 1984) was selected as a representative of chelating ion exchange resins. Copper, chromium, nickel and iron were chosen as contaminant heavy metals. Experimental runs on both the removal of heavy metals from aqueous solutions and the regeneration of the exhausted resin were performed in a 100 cm³ glass batch containers (Gritton, 1987), which are relatively inert to both aqueous metal solutions and regenerating solutions.

The contactor was charged with 20-120 cm³ 40-120 ppm aqueous metal solutions and 0.1-0.6 g Dowex resin for the removal of heavy metals from aqueous solutions at 25°C. A Teflon-coated magnetic stirrer was introduced in the aqueous heavy metal solution in the contactor to keep the concentration of heavy metal ions in the contactor homogeneous during the removal of heavy metals from the aqueous solution. Samples of aqueous metal solutions were drawn from the contactor at various time intervals to be analyzed with an atomic adsorption spectrometer.

The contactor also was charged with 0.2-0.8 g used Dowex resin and 80 cm³ 0.5-2.0N NH₄OH aqueous solution for the regeneration of the exhausted Dowex resin at 25°C. A magnetic stirrer is introduced into the contactor to keep concentrations of the NH₄OH aqueous solution in the contactor homgeneous. Samples of aqueous metal solutions were drawn

from the contactor at various time intervals to ᵤe analyzed with the atomic adsorption spectrometer.

IV MATHEMATICAL MODELS:

Several mathematical models for the removal of heavy metals from aqueous solutions and the regeneration of used Dowex XFS-4195.02 resin were developed under several assumptions. Intraparticle diffusion (Yoshita, 1985) is assumed to be a controlling step for the removal of heavy metals from aqueous solutions and reaction rate (Levenspiel, 1972) is assumed to be a controlling step for the regeneration of the used Dowex resin in the conjunction with a mass balance (Himmelblau, 1982) of heavy metal ions in the batch reactor.

A mathematical model on the removal of heavy metals from aqueous solutions was developed in the presence of Dowex XFS-4195.02 ion exchange resin, as shown in equation 1.

$$-\frac{4\pi D_e A R t}{V} = \ln\left[\frac{Y^2 + AY + A^2}{1 + A + A^2}\right]^{-0.5} + \ln(1-x_A)^{-A} + \ln\left[\frac{Y - A}{1 - A}\right]$$

$$+ \sqrt{3}\left[\tan^{-1}\left[\frac{2Y + A}{\sqrt{3}A}\right] - \tan^{-1}\left[\frac{2 + A}{\sqrt{3}A}\right]\right] \qquad (1)$$

where $\qquad A = \left[1 - \frac{C_{Ao}Vb}{W}\right]^{1/3}$.

$\qquad\qquad Y^3 = 1 - (1 - A^3)x_A$

V: volume of aqueous metal solution.
W: amounts of resins.
L_B: density of dry ion exchange resin.
R: radius of a spherical resin.

33-7

B: adsorption capacity of resin, gmole metal ion/g-resin.
t: adsorption time.
D_e: effective intraparticle diffusion of heavy ion metals through resins.
x_A: removal fraction of heavy metal ions by ion exchange resins.
CAo: initial concentration of metal ions.

A mathematical model for the regeneration of Cu^{+2}-saturated Dowex XFS-4195.02 ion exchange resin was developed, assuming that reaction rate is a controlling step for the regeneration of the Cu^{+2}-saturated Dowex resin in the presence of NH^4OH aqueous solution, as shown in equation 2.

$$-\ln\left[\frac{(x_e - x)}{(x_e - x_o)}\right] = kt \tag{2}$$

where

x: regeneration fraction.
t: regeneration time, min.
x_o: instantaneous regeneration fraction.
x_e: equilibrium regeneration fraction.
k: regeneration rate constant, min^{-1}.

A mathematical model for the regeneration of the Cu^{+2}-saturated Dowex XFS-4195.02 ion exchange resin was developed, assuiming that intraparticle diffusion of Cu^{+2} through the resin is a controlling step in the presence of NH_4OH aqueous solution as a regenerant, as shown in equation 3.

$$1 - Y^{-1} - \ln Y = \frac{4\pi D_e R}{3V} t \tag{3}$$

$$Y^3 = 1 - \frac{VC_A}{WB}$$

where

t: regeneration time, min.
V: volume of aqueous regeneration solution.

W: amounts of resins.

R: radius of a spherical resin.

B: adsorption capacity of resin, gmole-metal-ion/g-resin.

D_e: effective intraparticle diffusivity of heavy metal ion through resin.

C_A: concentration of metal ion in aqueous regeneration solution.

V. RESULTS AND DISCUSSION

An experiment on adsorption of Fe^{+2} on Dowex XFS 4195.02 ion exchange resin was conducted at 25°C. A 86 ppm Fe^{+2} aqueous solution was prepared, adding ferrous sulfate ($FeSO_4.7H_2O$) and H_2SO_4 to distilled/deionized water. Iron aqueous solution of 82 g and 0.1 g resin were introduced in the the glass container equipped with a stirrer. No removal of Fe was observed.

Experiments on isotherm equilibrium adsorption of Cu^{+2} on the Dowex XFS-4195.02 ion exchange resin were performed at pH 1.5 and 25°C. A mathematical equation on the isotherm equilibrium adsorption of Cu^{+2} on the resin was developed, using the Freundlich equation (see Figure 1).

Experiments on the adsorption of Cu^{+2} on Dowex XFS-4195.02 ion exchange resin were performed in a 100 cm^3 glass container at pH 1.5 and 25°C. Concentrations of Cu are dectected at various time intervals with the atomic adsorption spectrometer.

A series of experiments were conducted, varying amounts of the resin (0.1-0.3 g) in the 80-g 80 ppm Cu^{+2} aqueous solution in order to identify effects of resin amounts on removal rates of Cu with holding initial concentrations of Cu^{+2} constant (see Figure 2). Removal fractions of Cu^{+2} from aqueous solutions increase with amounts of the resin. The mathematical model on the removal of Cu^{+2} from its aqueous solution was applied to these data in order to compute intraparticle diffusivities of Cu^{+2} through the resin during the removal of Cu^{+2} from

its aqueous solution. The solid lines in Figure 2 are predicted fractional removal of Cu^{+2}, which are calculated with the Equation 1 and the calculated intraparticle diffusivity values . Intraparticle diffusivities increase with amounts of the resin

Another series of experiments were conducted with 0.2 g Dowex XFS-4195.02 ion exchange resin and 80-g aqueous solution, varying 40 to 120 ppm in the initial Cu^{+2} concentration in order to identify effects of the initial Cu^{+2} concentration on the removal of Cu^{+2} from its aqueous solution. Experimental data were applied to the removal model of metals to identify the right-side values of the removal model (see Figure 3). The solid line in Figure 2 was obtained by applying the right-side values of the removal model and the corresponding time data to the least squares method.

The intraparticle diffusivities of Cu^{+2} through the resin, as shown in Figure 3, were obtained from the slope of the solid line. Intraparticle diffusivities increase with initial concentrations of Cu^{+2}, with holding amounts of the resin and aqueous solutions constant. The solid lines in Figure 4 are the data, which are predicted from the removal model. Removal fractions increase with decreased initial concentrations of Cu^{+2} in aqueous solutions, as shown in Figure 4. These observation may indicate that a controlling step for the removal of Cu^{+2} from aqueous solutions is diffusion of Cu^{+2} through the resin.

Another series of experiments on the removal of Cu^{+2} from the 80 ppm (initial concentration) Cu^{+2} aqueous solution were conducted with 0.2 g Dowex XFS-4195.02 ion exchange resin at 25°C, varying amounts of the 80-ppm Cu^{+2} aqueous solution. The removal-fraction-vs-removal-

duration data were applied to the removal model in order to identify effects of solution amounts on the removal of Cu^{+2} from the aqueous solution. The intraparticle diffusivities of Cu^{+2} through the resin increase with the amounts of the aqueous solution, as shown in Figure 5. These data may indicate that increased mass ratios of solution to resin result in increased removal of Cu^{+2} from the aqueous solution.

Aqueous solutions containing both Cu^{+2} and Ni^{+2} were prepared as simulated artificial plating bath solutions. Experiments on the removal of Cu^{+2} were carried out in the presence of Dowex XFS 4195.02 ion exchange resin as a adsorbent to identify the validity of the developed mathematical model on the removal of Cu^{+2} in the presence of other heavy metal ions, and to find effects of Ni^{+2} on the removal of Cu^{+2} from the aqueous solutions containing Cu^{+2} and Ni^{+2}. The removal of Cu^{+2} from the aqueous solutions is slightly retarded in the presence of Ni^{+2}, and independent of the concentrations of Ni^{+2} in the aqueous solutions, as shown in Figure 6.

An experiment on the removal of Cr^{+6} from the 80-ppm (initial concentration) 80-g Cr^{+6} aqueous solution was performed in the presence of the Dowex resin in order to examine applicability of the developed removal model to various metals and compare intraparticle diffusivities of Cr^{+6}, Cu^{+2} and Co^{+2} (Gritton, 1987), as shown in Figure 7. These data may reveal that the removal model is applicable to the removal of most metals from their aqueous solution, using Dowex XFS-4195.02 as an adsorbent. Cu-saturated Dowex XFS-4195.02 resin at various NH_4OH concentrations and 25°C. Copper-saturated Dowex resin of various amounts was submerged in 80-g NH_4OH aqueous solutions with various NH_4OH concentrations to

obtain equilibrium concentrations of Cu^{+2} in aqueous NH_4OH solutions (see Figure 8). Equilibrium concentrations of Cu^{+2} in aqueous NH_4OH solution decrease with increased amounts of Cu-saturated Dowex XFS-4195.02 resin, and independent of NH_4OH concentrations.

A series of experiments on the regeneration of Cu^{+2}-saturated Dowex XFS-4195.02 ion exchange resin were conducted at 25°C, using 0.5-2N NH_4OH aqueous solution as a regeneration reagent. Two mathematical models on the regeneration of Cu^{+2}-saturated Dowex XFS-4195.02 ion exchange were developed, using experimental data of regeneration (see Equations 2 and 3). Instantaneous regeneration fractions and regeneration rate constants of Cu^{+2} were obtained from intercepts and slopes of straight lines, which were obtained by applying experimental data to the reaction-controlling model for the removal of Cu^{+2}. Intraparticle diffusivities of Cu^{+2} through the Cu^{+2}-saturated Dowex resin and time delays were obtained from the intraparticle-diffusion controlling model (see Figures 9 and 10).

Regeneration rate constants of Cu^{+2}-saturated Dowex resin in the presence of NH_4OH aqueous solution are independent of resin amounts and, dependent on NH_4OH concentrations. Instantaneous regeneration fractions of the Cu^{+2}-saturated resin are independent of resin amounts and NH_4OH concentrations in the case of the reaction rate control for the removal of Cu^{+2} from the exhausted resin (see Figure 9). The reaction-rate-controlling model for the removal of Cu^+ from Cu^{+2}-saturated resin is applicable to 1-2N NH_4OH aqueous solution as a regenerant.

Controlling step for the regeneration of Cu^{+2}-saturated Dowex resin

in 0.5N NH₄OH aqueous solution is dependent on resin amounts. The regeneration data follows the reaction-controlling model (Equation 2) in the presence of 0.2 g resin in 80-g NH₄OH aqueous solution, and the intraparticle-diffusion-controlling model (Equation 3) in the presence of 0.3-0.6 g resin in 80-g NH₄OH aqueous solution (see Figure 10). This observation may suggest that controlling step for the removal of Cu^{+2} from Cu^{+2}-saturated Dowex XFS-4195.02 resin is dependent on mass ratios of resin to NH₄OH aqueous solution, using 0.5N NH₄OH aqueous solution as a regenerant.

VI. <u>CONCLUSIONS</u>:

The following conclusions were drawn on the basis of experimental data for the removal of heavy metals from aqueous solutions in the presence of Dowex XFS-4195.02 ion exchange resin and the regeneration of exhausted Dowex XFS-4195.02 resin in the presence of NH₄OH aqueous solution as a regenerant.

1. The removal of Cu^{+2} is controlled by the intraparticle diffusion of Cu^{+2} through the resin. Removal rates of Cu^{+2} increase with initial concentrations of Cu^{+2} and amounts of resins, and are independent of solution quantities.

2. Removal rates of Cu^{+2} decrease slightly in the presence of Ni^{+2}, and are independent of Ni^{+2} concentrations.

3. Regeneration rates of resins are dependent on NH₄OH concentrations, independent of mass ratios of solution to resin at high NH₄OH concentrations, and dependent on mass ratios at low NH₄OH concentrations.

4. Instantaneous regeneration fractions of resins are independent

of mass ratios and NH_4OH concentrations. Regeneration rate constants are independent of mass ratios and dependent on NH_4OH concentrations.

VII. RECOMMENDATIONS

Experiments on the removal of heavy metals from aqueous solutions are recommended to be carried out by feeding continuously aqueous solutions to fixed beds of ion exchange resins, using various ion exchange resins and actual plating bath solutions. Main objectives of continuous removal experiments are (1) to find applicabilities of the removal model (obtained from the batch experiment) to the continous removal system, (2) to develop a removal model equation for a continuous removal process with experimental data at various continuous operation conditions, and (3) to identify optimum removal conditions for a scale-up continuous removal process.

Experiments on the regeneration of exhausted ion exchange resins are recommended to be conducted by feeding continuously regenerating solutions to fixed beds of exhausted resins, using various regenerating conditions such as temperatures, flow rates and concentrations of regenerants. Main objectives of continuous regeneration experiments are (1) to find applicabilities of the regeneration model equations (obtained from the batch regeneration experiment) to the continuous regeneration system, (2) to develop a regeneration model equation for a continuous regeneration system with experimental data at various continuous regeneration operations, and (3) to identify optimum regeneration conditions for a scale-up continuous regeneration process.
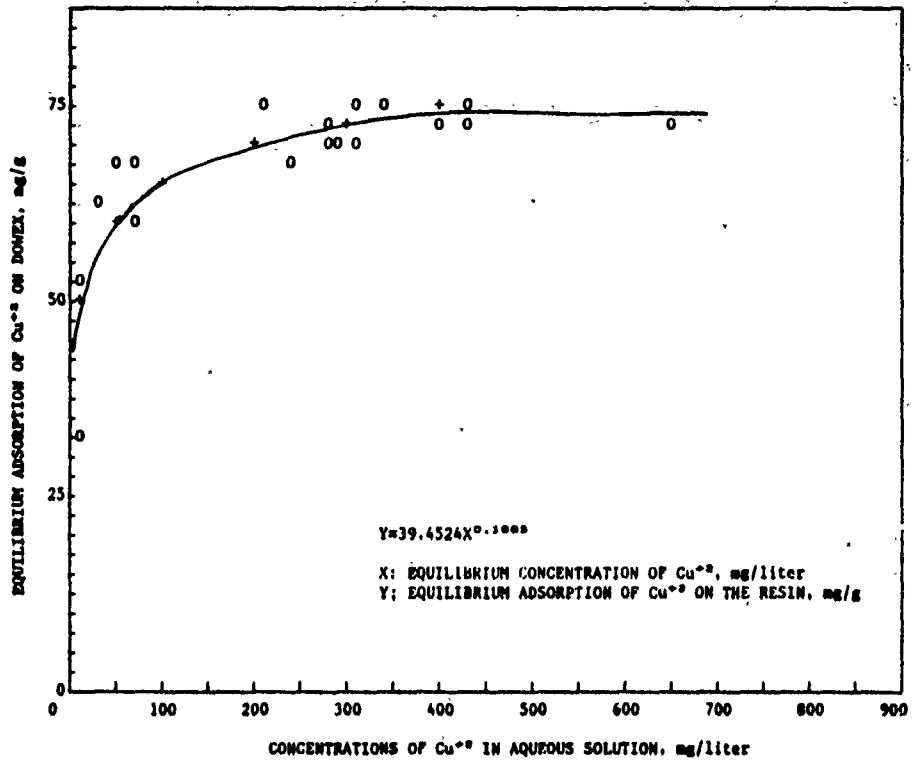
Figure 1. Isotherm equilibrium adsorption of Cu[+2] on Dowex XFS-4195.02 ion exchange resin at 25°C.
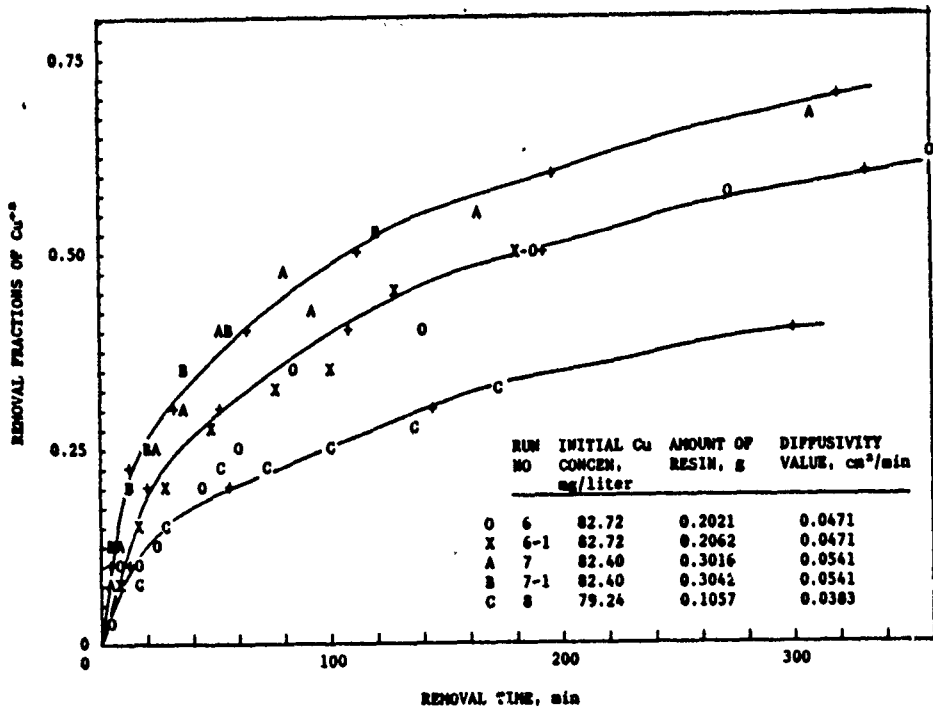

Figure 2. Removal fractions of Cu[+2] from 80-g 80-ppm aqueous solution in the presence of Dowex XFS-4195.02 ion exchange resin at 25°C and pH 1.5.

33-15
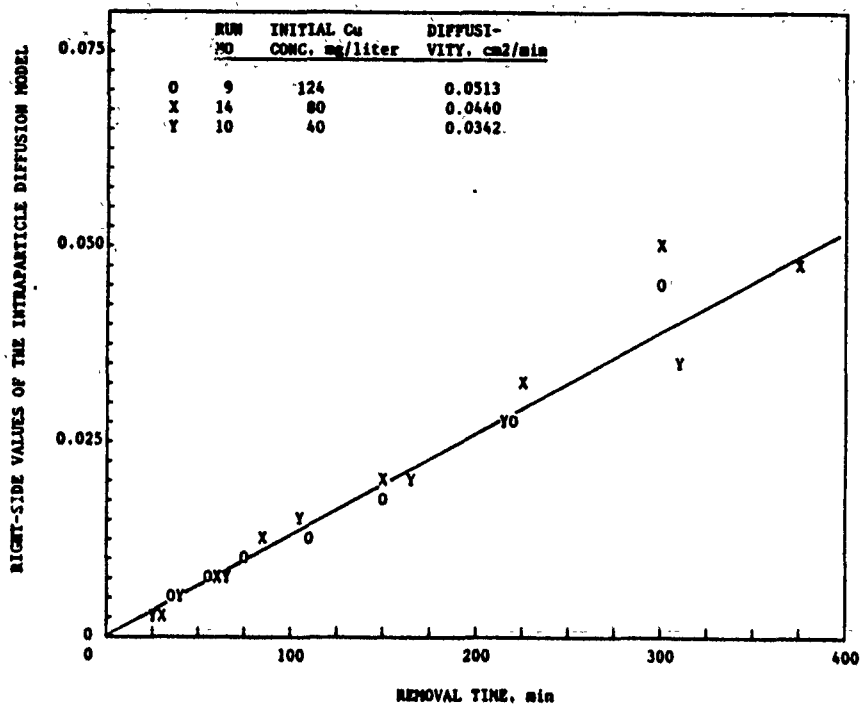
Figure 3. Effects of Cu⁺² concentrations on removal fractions of Cu⁺² from 80 g aqueous
solution in the presence of 0.2 g Dowex XFS 4195.02 ion exchange resin
at 25°C and pH 1.5.
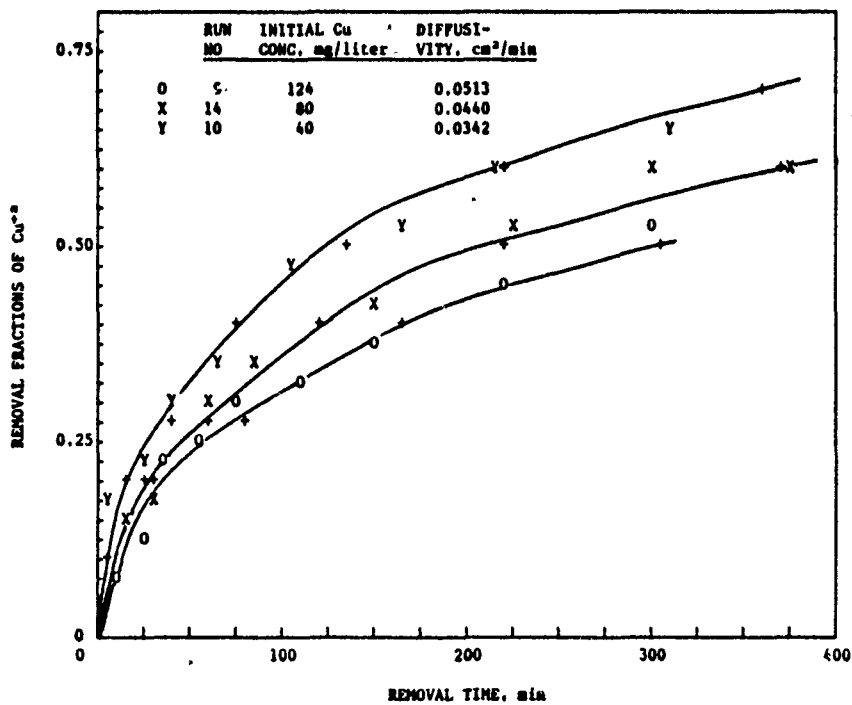
Figure 4. Effects of Cu⁺² concentrations on removal fractions of Cu⁺² from its 80 g
aqueous solution in the presence of 0.2 g Dowex XFS 4195.02 ion exchange resin
at 25°C and pH 1.5.
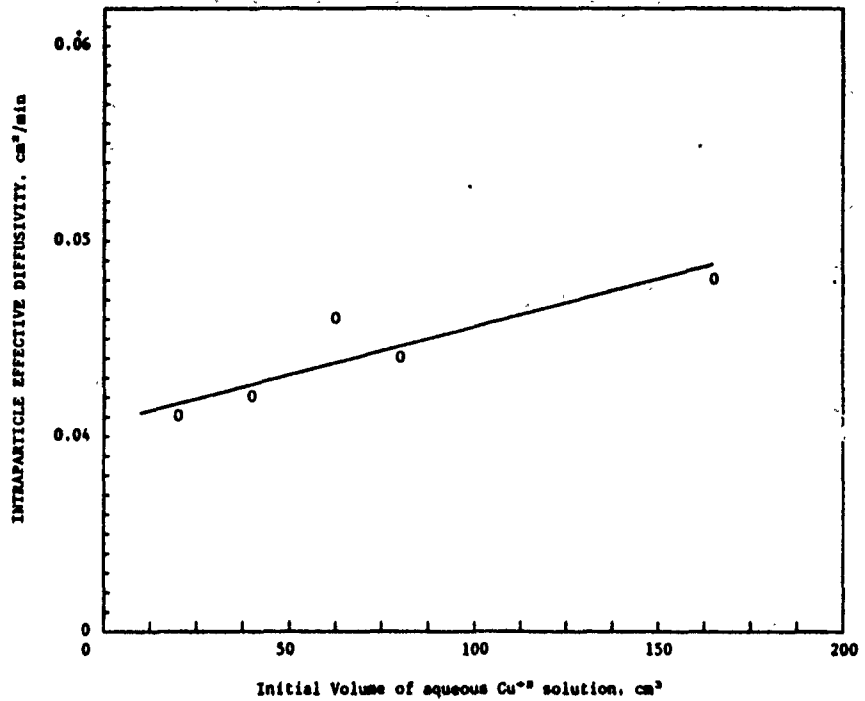
Figure 5. Effects of initial volume on intraparticle diffusivity of Cu^{+2} through 16-50 mesh 0.2-g Dowex XFS 4195.02 ion exchange resin at pH 1.5, initial concentration of Cu^{+2} (81.01 mg/liter) and 25°C.

|	RUN NO	INIT CON. mg/liter Cu	Ni	AMOUNT, g SOLUTION	RESIN	DIFFUSIVITY, cm²/min
O	11	81.91	82.00	81.14	0.1992	0.0415
X	17	81.06	161.75	82.23	0.2001	0.0394
Y	18	81.95	242.78	81.98	0.2046	0.0412
A	6	82.72	0	78.53	0.2042	0.0473
B	14	81.02	0	81.16	0.2026	0.0441
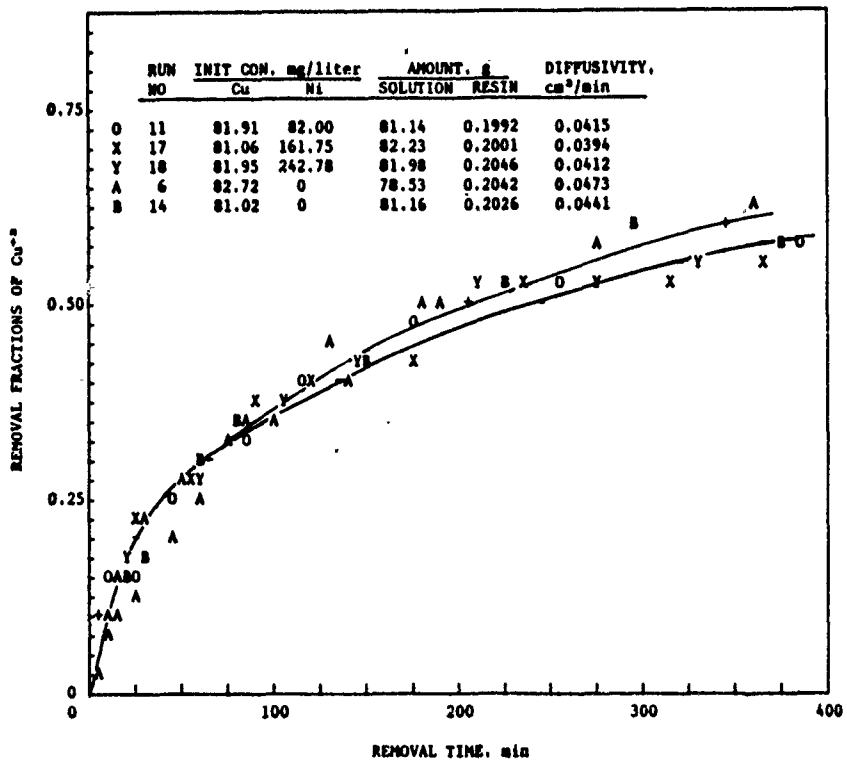
Figure 6. Effects of Ni^{+2} on the removal of Cu^{+2} from its aqueous solution in the presence of Dowex XFS 4195.02 ion exchange resin at 25°C and pH 1.5.

33-17
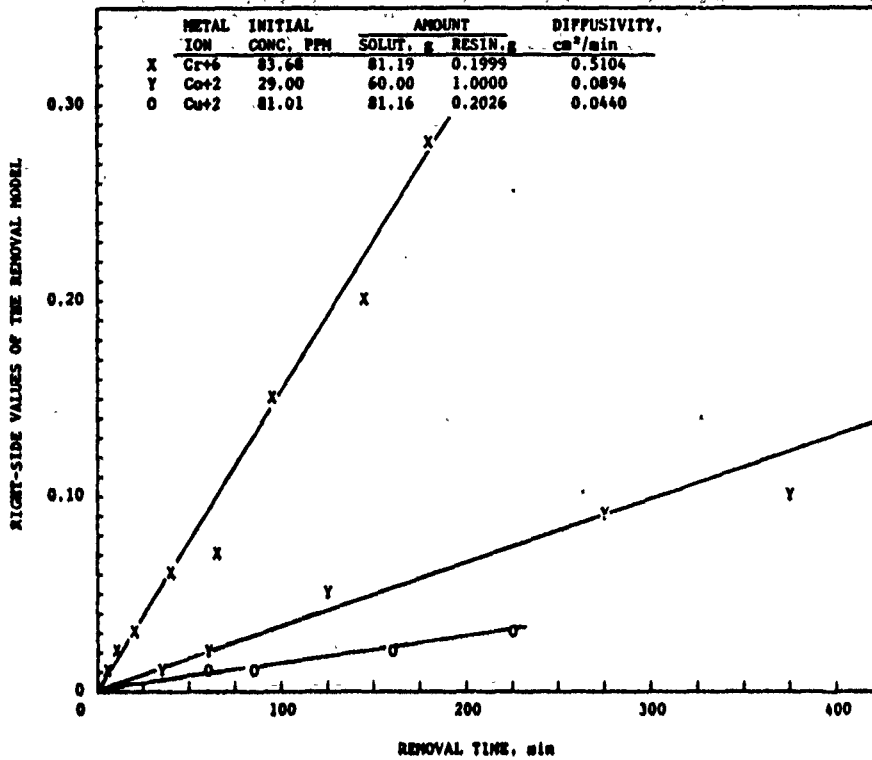
Figure 7. Comparison of intraparticle diffusivities of heavy metal ions through Dowex XFS-4195.02 ion exchange resin.
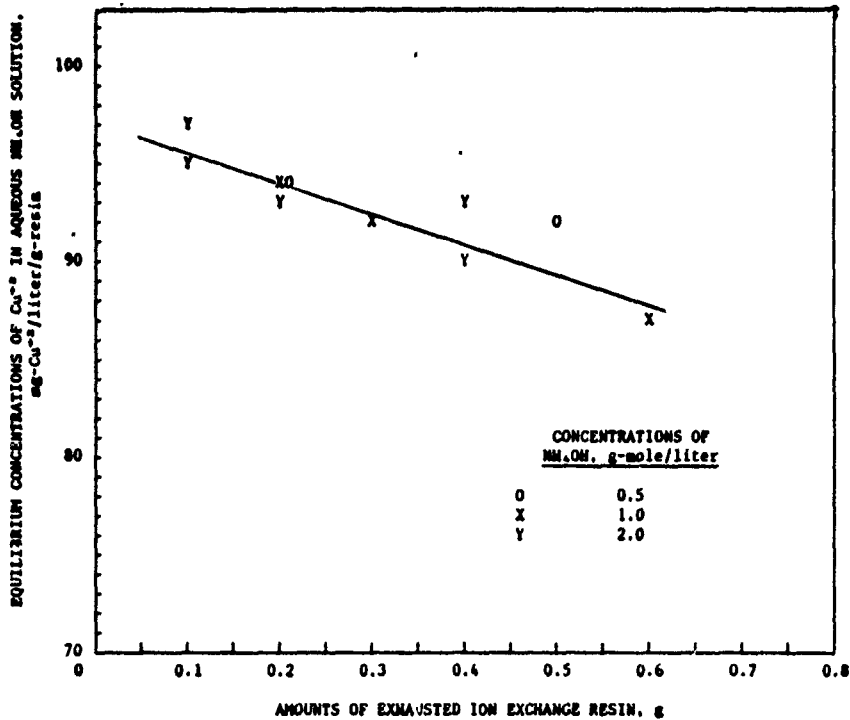

Figure 8. Equilibrium concentrations of Cu^{+2} in 80 g aqueous NH$_4$OH solution as a reagent of regenerating exhausted Dowex XFS 4195.02 ion exchange resin at 25°C.
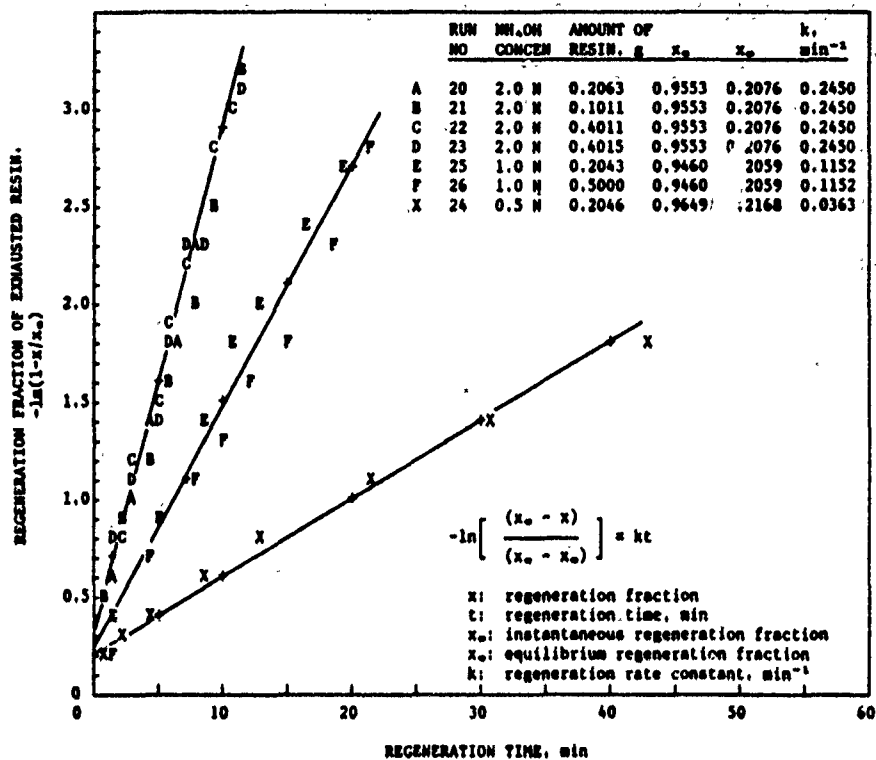
Figure 9. Regeneration of Cu^{+2}-saturated Dowex XFS 4195.02 ion exchange resin in the presence of 80 g NH$_4$OH aqueous solution at 25°C.
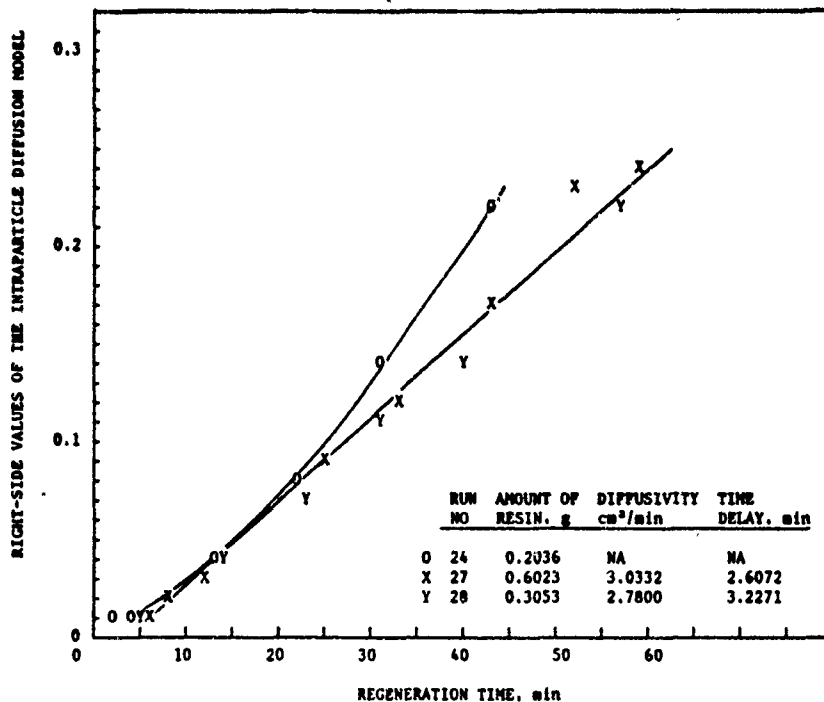

Figure 10. Effects of amounts of Cu-saturated Dowex XFS 4195.02 ion exchange resin on the regeneration mechanism in the presence of 80-g 0.5-N-NH$_4$OH aqueous solution at 25°C.

REFERENCES

1. Folsom, D. W. and Langham, Anne, "Selective Ion Exchange Pilot Plant Demonstration", Final Report to Headquarters, Air Force Engineering and Services Center, Tyndall AFB, Florida, Battelle Columbus Division, January 1989.

2. Gold, H., Czupryna, G., Robinson, J. M. and Levy, R. D., "Purifying Air Force Plating Baths by Chelate Ion Exchange", Final Report to Headquarters, Air Force Engineering and Service Center, Tyndall AFB, Florida, Foster-Miller, Inc., July 1985.

3. Grinstead, R. R., "New Developments in the Chemistry of XF4195 and XFS 43084 Chelating Ion Exchange Resins", Ion Exchange Technology, 1984, pp 509-518.

4. Gritton, K. S. and Jeffers, T. H., "Numerical Prediction of Cobalt Sorption in a Continuous Ion exchange Column", Bureau of Mines Report of Investigations RI 9120, 1987.

5. Himmelblau, D. A., Basic Principles and Calculations in Chemical Engineering, 4th ed., Prentice-HALL, 1982.

6. Levenspiel, Octave, Chemical Reaction Engineering, 2nd ed.,John Wiley & Sons, 1972.

7. Yoshita, H., Kataoka, T. and Ikeda, S., "Intraparticle Mass Transfer in Bidispersed Porous Ion Exchanger, Part I: Isotopic Ion Exchange", Canadian J. of Chemical Engineering, Vol. 63, June 1985.

1990 USAF-UES SUMMER FACULTY RESEARCH PROGRAM/

GRADUATE STUDENT RESEARCH PROGRAM

Sponsored by the

AIR FORCE OFFICE OF SCIENTIFIC RESEARCH

Conducted by the

Universal Energy Systems, Inc.

FINAL REPORT

Methanotrophic Cometabolism of Trichloroethylene (TCE) in a Two Stage Bioreactor System

Prepared by:	Michael J. McFarland, Ph.D.
Academic Rank:	Assistant Professor
Department and	Civil and Environmental Engineering
University:	Utah State University
Research Location:	Engineering & Services Laboratory HQ AFESC/RDVW Tyndall AFB, FL 32403-6001
USAF Researcher:	Catherine M. Vogel
Date:	20 September 90
Contract No:	F49620-88-C-0053

Methanotrophic Cometabolism of Trichloroethylene in a Two Stage Bioreactor System

by

Michael J. McFarland

ABSTRACT

A two stage bioreactor system inoculated with a locally obtained mixed methanotrophic culture was found to be effective in biodegrading trichlorethylene (TCE) when supplied with sodium formate as reducing power. During methane additions, a maximum TCE removal rate of 21.1 mg TCE per gram volatile solids per day was found when the influent formate concentration was 20 mM. Termination of methane while maintaining the same formate loading resulted in a TCE removal rate of 25.5 mg TCE per gram volatile solids per day suggesting that methane may competitively inhibit TCE removal. Under formate limiting conditions, TCE removal occurred mainly by adsorption to microbial flocs.

Acknowledgements

I wish to thank the Engineering& Services laboratory and the Air Force Office of Scientific Research for sponsorship of this research. I would also like to thank Universal Energy Systems (UES) for their efforts in coordinating the summer faculty research program.

My experience was rewarding and enriching because of the interdisciplinary research environment provided me at RDVW. I would like to thank Captain Cathy Vogel for her support and helpful discussions during the entire experimental program. I would also like to thank Dr. Jim Spain whose suggestions and comments proved invaluable to the outcome of this work. Others from the biological research team who provided me with support include Drs. William Haigler, Chuck Pettigrew, and William Seffens.

I would also like to mention the support from the chemical research team without whose help progress would have been very difficult. I would like to thank Drs. Tom Stauffer, David Burris, and Howard Mayfield for their helpful discussion concerning the chemical behavior of trichloroethylene. I would also like to acknowledge the assistance of Mr. Mike Henley in developing some of the analytical procedures.

Appreciation is also extended to Mr. Perry Sullivan and Ms. Mary Reynolds for their administrative assistance and support during the summer program.

Finally, I would like to thank Colonel Gallagher for his keen interest in my research and the application of biological systems for environmental remediation in general.

I   INTRODUCTION:

Many aquifers underlying Department of Defense (DOD) facilities are contaminated by chlorinated solvents such as Trichloroethylene (TCE). Due to its potential health threat, methods to permanently remove TCE from groundwaters remains a priority for DOD.

The least cost alternative for permanent removal of TCE is biological degradation. Although there is much activity in *in situ* bioremediation research, above ground bioreactors are a preferred approach since they offer better process control together with more effective containment of toxic degradation products.

TCE does not serve as a primary growth substrate for microorganisms and is biodegraded under aerobic conditions only through the process known as cometabolism or cooxidation (Folsom *et al.*, 1990; Little *et al.*, 1988; Roberts *et al.*, 1989). Although much is known about the biochemical fundamentals of cometabolic metabolism, very little progress has been made regarding the engineering application of cometabolic systems to remediate TCE contaminated groundwaters.

One group of microorganisms that has the ability to cometabolize trichloroethylene are methanotrophic bacteria. These organisms meet their energy requirements through the oxidation of methane under aerobic conditions. The enzyme system responsible for both methane and TCE oxidation has been identified as methane monooxygenase (MMO) (Little *et al.*, 1988). Although the prime catabolic function of MMO is to catalyze the conversion of methane to methanol, its low substrate specificity enables it to mediate TCE oxidation. Figure 1 outlines the biological pathway by which methanotrophic bacteria generate both energy for growth and precursors to biomass formation.
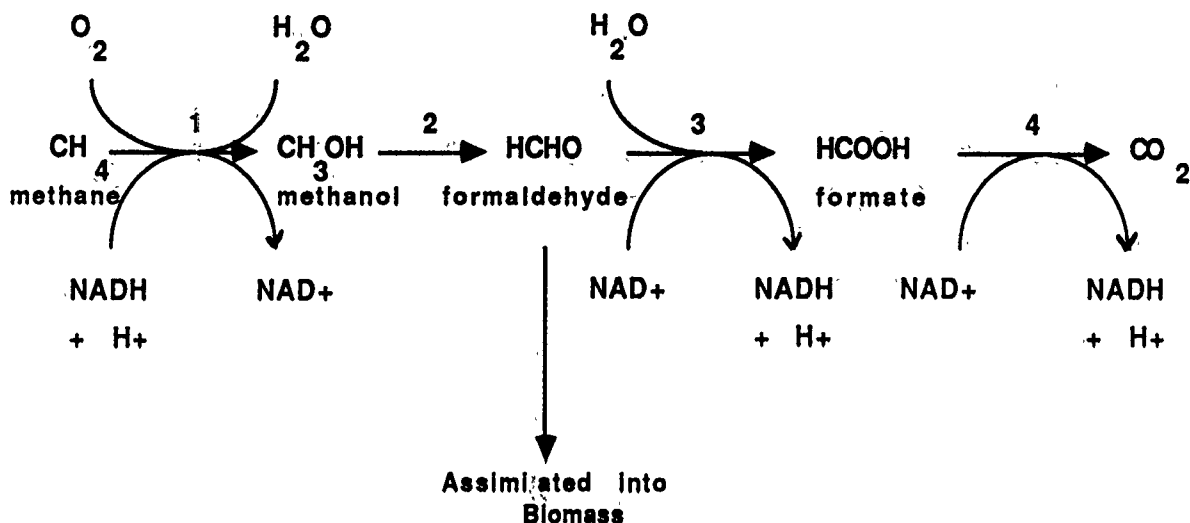
Fig 1.   Methanotrophic oxidation of methane. Enzymes of interest include;
         1) methane monooxygenase, 2) methanol dehydrogenase, 3) formaldehyde
         dehydrogenase, 4) formate dehydrogenase. Adapted from Dalton and
         Stirling, 1982.

Figure 1 indicates that the reduction of methane monooxygenase enzyme by nicotinamide adenine dinucleotide (NADH) is required for methane oxidation to occur. This reduction (or energy requirement) of MMO provides a unique engineering approach to regulating MMO activity. Under normal methanotrophic growth conditions, this reducing power is generated internally by the oxidation of the chemical intermediates formaldehyde and formate. For biotreatment purposes, MMO activation may be maintained by reducing agent additions.

Particulate and Soluble Methane Monooxygenase (MMO) Enzyme

Methane monooxygenase (MMO) enzyme may exist in one of two active forms, soluble and particulate. Both forms catalyze the oxidation of methane to methanol (Figure 1). Interest in the form of MMO enzyme present in biological waste treatment systems stems from their difference in biocatalytic properties and susceptability to inhibitors. Thus far, it has only been the soluble form of MMO that has been found to mediate TCE oxidation (Oldenhuis *et al.*, 1989). Under methane and/or copper limitations, many

methanotrophs have the ability to increase their intracellular level of soluble MMO (Scott *et al.*, 1981; Stanley *et al.*, 1983).

Operation of Methanotrophic Bioreactor for TCE Removal

Although some studies have reported biodegradation of TCE in actively growing methanotrophic cultures, it has recently been observed that active methanotrophic growth may actually reduce TCE removal rates (Oldenhuis *et al.*, 1989; Tsien *et al.*, 1989). This is due to the fact that nonlimiting concentrations of methane can saturate the catalytic site of the MMO enzyme responsible for TCE oxidation. Comparison of the half velocity constant of soluble MMO enzyme from the methanotroph *Methylosinus trichosporium* OB3B for TCE (K_s - 200μm) to that of methane (K_s - 2 μm) illustrates the much stronger affinity of the enzyme for methane *viz a viz* trichloroethylene (Oldenhuis *et al.*, 1989).

Conversely, it has been reported that the addition of reducing power in the form of formate can enhance the rate of TCE degradation (Tien *et al.*, 1989). Formate is a source of reducing power for the enzyme which does not compete with TCE for the catalytic site of MMO. Formate enhanced biodegradation of TCE was investigated as part of the summer research program.

To reduce competitive inhibition of TCE by methane, a two stage system was proposed in the present study in which methanotrophic growth and TCE removal processes were physically separated. A schematic diagram of the two stage bioreactor is given in Figure 2. Details of reactor design and operation are contained in Materials and Methods section.
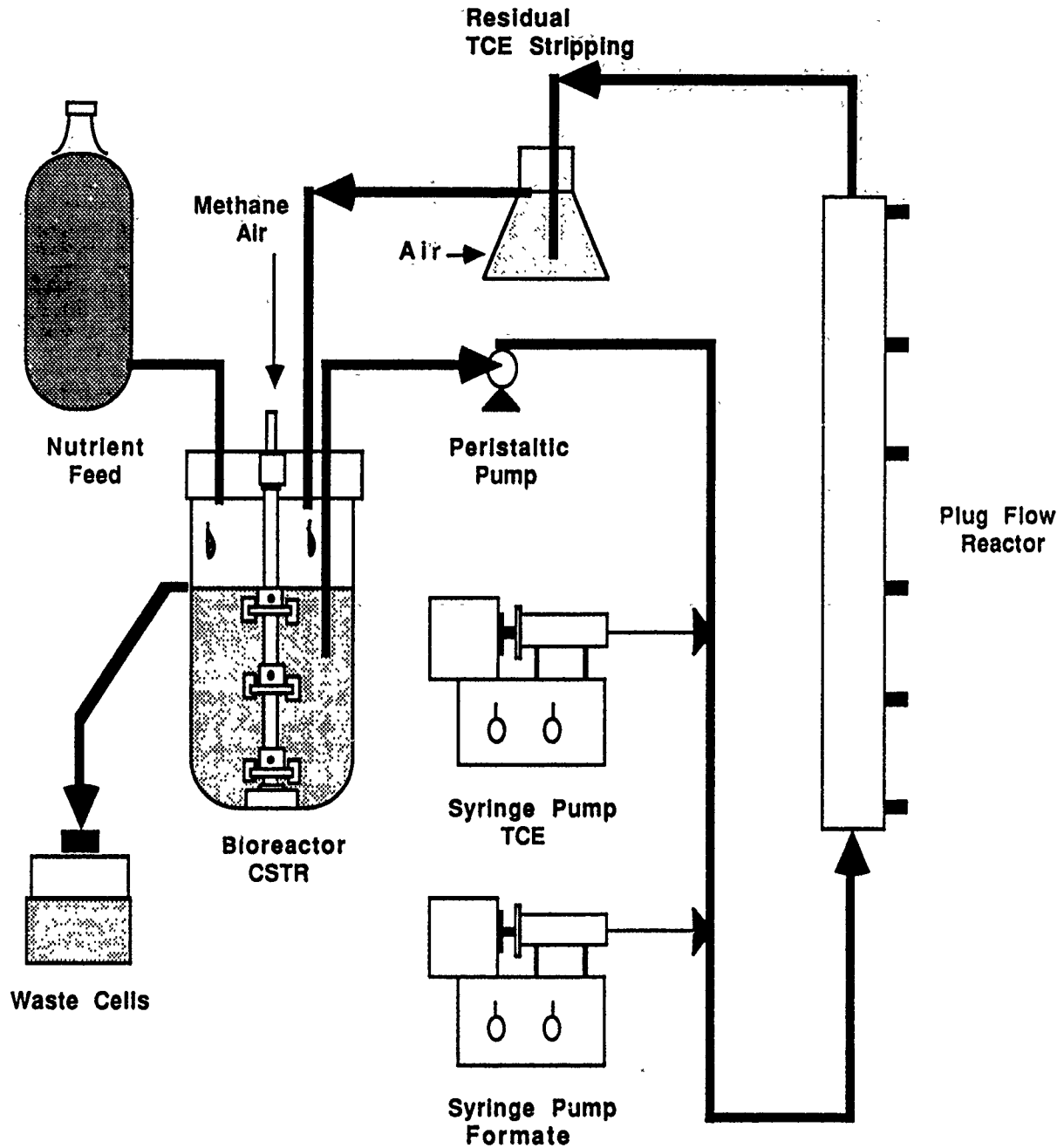
Fig. 2   Schematic Diagram of Two Stage Methanotrophic Reactor System for TCE Removal

II OBJECTIVES OF THE RESEARCH EFFORT

The goal of the summer faculty research project was to evaluate the technical feasibility of a two stage methanotrophic biological system to degrade trichloroethylene (TCE).

The specific research objectives include;

a. design, construction, and testing of a two stage bioreactor system

b. development of a mixed methanotrophic culture

c. monitoring of TCE removal in abiotic and biotic reactor systems

d. evaluation of the use of reducing power (*e.g.*, formate) to improve methanotrophic TCE removal rates

III MATERIALS AND METHODS

Reactor Design and Operation

The bioreactor system consisted of two stages; a methanotrophic growth unit and a TCE biodegradation unit. The methanotrophic growth unit consisted of a continuously stirred tank reactor (CSTR) or chemostat having a 1.4 liter working volume. The glass chemostat (New Brunswick Inc.) was equipped with a stainless steel impeller operated at 350 rpm. The hydraulic retention time for the biological reactor was maintained at 24 hours while the temperature was held at 28° C during the entire study.

Methane, oxygen, and nutrients were added continuously to promote growth of methanotrophic bacteria. Methane and air were added at flow rates of 0.1 and 0.4 liters per minute, respectively, while the nutrient flow rate was one milliliter per minute. Table 1 descibes the composition of the nutrient salts media fed to the methanotrophic growth unit.

Table 1

Nitrate Salts Medium Solution
(from Cornish *et al.*, 1984)

Nitrate Salts Medium Solution contained the following;

$NaNO_3$ - 0.85 g/l, KH_2PO_4 - 0.53 g/l, Na_2HPO_4 - 0.86 g/l, K_2SO_4 - 0.17 g/l, $MgSO_4.7H_2O$ - 0.037 g/l, $CaCl_2.2H_2O$ - 0.007 g/l.

Two milliliter of trace element solution was added per one liter of nitrate salts medium.

The trace element solution contained the following;

$ZnSO_4.7H_2O$ - 0.287 g/l, $MnSO_4.H_2O$ - 0.169 g/l, H_3BO_3 - 0.062 g/l, $NaMoO_4.2H_2O$ - 0.048 g/l, $CoCl_2.H_2O$ - 0.048 g/l, KI - 0.083 g/l, H_2SO_4 (1mM), $FeSO_4.7H_2O$ - 0.012 g/l.

The TCE biodegradation unit consisted of a 400 milliliter stainless steel plug flow reactor that was operated with zero reactor headspace. The plug flow reactor was equipped with stainless steel valves (Supelco, Bellefonte, Pa.) for TCE sampling. The contents of the biological growth reactor was pumped into the TCE removal unit at a flow rate of ten milliliters per minute resulting in an average hydraulic retention time (HRT) of 40 minutes for the second stage. The effluent from the plug flow reactor was aerated to remove any residual TCE before being recycled to the biological growth unit via a gravity feed line. The TCE stripping unit consisted of a 250 milliliter glass side arm flask in which a glass diffuser was used to supply air for volatilization of untreated TCE from the plug flow unit.

A short length of Tygon[TM] tubing was used for transfer of microbial cells from the bioreactor and for the pumping of the nutrient feed. The remainder of the fluid transfer lines were 1/8" I.D. stainless steel tubing. All stainless steel tubing was connected using

stainless steel Swagelock™ fittings. TCE and formate were introduced to the biotreatment system by a Harvard Apparatus Compact Syringe Pump (model 975).

Methanotrophic Inoculum

The mixed methanotrophic inoculum was obtained locally from the wastewater treatment lagoon located at Tyndall Air Force Base Florida. A ten milliliter sediment sample was diluted 1:50 with nitrate salts medium and placed in the methanotrophic growth reactor. Methane and air were added at flow rates of 0.1 and 0.4 liters per minute, respectively. After approximately four days, a dense biomass culture had developed. The culture had a orange-red color and existed mainly as large flocculant particles or dense microbial films associated with the chemostat wall and impeller.

TCE Analyses

Five milliliter liquid samples to be analyzed for TCE were withdrawn from the plug flow reactor using a Lurelock™ glass syringe (Becton Dickinson, Rutherford, N.J.). The samples were injected through a stainless steel tube into a ten milliliter amber colored glass vial (Pierce Co., Rockford, Illinois) containing a five milliliter solution of hexane. Samples were injected underneath the hexane solution to minimize TCE volatilization loss. The hexane solution contained tetrachloroethylene (PCE) at a concentration of 0.5 mg/liter as an internal standard.

After introduction of the sample, the vials were sealed using a Teflon™ lined silicone septa capped by a crimped aluminum lid. Solvent-solvent extraction of the TCE was accomplished by shaking the sample bottles for approximately thirty seconds followed by centrifugation for 3 minutes at 1200 rpm to insure complete separation of hexane/water phases (IEC Clinical Centrifuge - Damon/IEC division) .

For quantitation of TCE, a 1 μl sample was withdrawn from the hexane phase and injected on the gas chromatograph. A Hewlett Packard 5890 gas chromatograph equipped with an electron capture detector (ECD) interphased with a 18652A A/D converter was used

for TCE analyses. Separation of TCE and PCE peaks was accomplished using a ten foot packed column containing 10% SP-1000 80/100 Supelcoport packing.

Dissolved oxygen was measured in both reactor stages using a Clark type oxygen electrode (Model 5331 Yellow Springs Instrument Co., Yellow Springs, Ohio.) Reactor pH was measured by an Orion Research pH meter Model 601A/Digital Ionanalyzer. Biomass concentrations were estimated using volatile solids analyses according to procedure outlined in Standard Methods (17th edition-1989).

Reagent grade trichloroethylene (TCE) was purchased from MCI, Cincinnati, Ohio. Reagent grade tetrachloroethylene (PCE) was supplied by J.T. Baker Phillipsburg, N.J. Reagent grade hexane used was purchased from Fisher Scientific (OPTIMA).

Methane and nitrogen gases were obtained from stock supplies at Tyndall Air Force Base while air for the biotreatment system and stripping unit was supplied from an in-house compressor located at the Engineering and Services Center.

IV   EXPERIMENTAL APPROACH

The summer research program was divided into three phases. The first phase was an abiotic control study in which TCE laden distilled water was pumped through the plug flow reactor system. Results from this phase provided information regarding; 1) time for breakthough of TCE, and 2) steady state concentrations of TCE obtainable in the absence of microorganisms.

In the second phase, methanotrophic bacteria from the biological growth reactor were introduced into the TCE removal unit. Comparison of the effluent TCE concentrations in the presence of microorganisms to that obtained in the abiotic control experiments provided an estimate of methanotrophic degradation of TCE under methane limiting conditions.

In the third phase, sodium formate was added as reducing power for the MMO enzyme. Evaluation of TCE removal from this experimental phase provided insight into the effectiveness of enzyme activation on TCE biodegradation.

V   RESULTS

Liquid-liquid hexane extraction procedure yielded recovery efficiencies of 90.7% using standard TCE solutions. This recovery efficiency was comparable to TCE recoveries using similar internal standard methods (Oldenhuis *et al.*, 1989). All data reported are averages of duplicate analyses. The following sections summarize data obtained during the three phases of the experimental program.

Abiotic Control

The change in TCE concentration with time in the plug flow reactor system is shown in Figure 3. A steady state TCE concentration of 15 mg/liter was reached after approximately 50 bed volumes (*i.e.*, 33 hours).

Since a TCE concentration of 15 mg/liter is known to be nontoxic to methanotrophic organisms (Oldenhuis *et al.*, 1989), this concentration was used in the biological degradation study. After 80 bed volumes, methanotrophic bacteria were pumped into the plug flow reactor from the biological growth unit to begin the second phase of the experimental program.

Biotic Removal of TCE

Immediately after introduction of biomass to the plug flow unit, TCE concentrations were observed to decrease (Figure 4). Initial indications suggested that the methanotrophic bacteria were removing TCE. However, with time, the TCE concentrations began to increase. Visual inspection of the samples in the bottom and top of plug flow reactor indicated that much of the biomass had settled. In order to increase the total biomass in the system, the waste cells from the chemostat were recycled to the biotreatment system. This

led to a further reduction in the effluent TCE concentration initially, but, within 24 hours, the TCE concentration had increased. The TCE concentration at the bottom of the reactor eventually reached 30 mg/liter which was twice the abiotic steady state concentration suggesting that TCE adsorption to microbial cells was occuring. (It should be noted that no attempt was made to distinguish between adsorbed TCE and dissolved TCE. The TCE concentrations reported are for total TCE contained in sample).
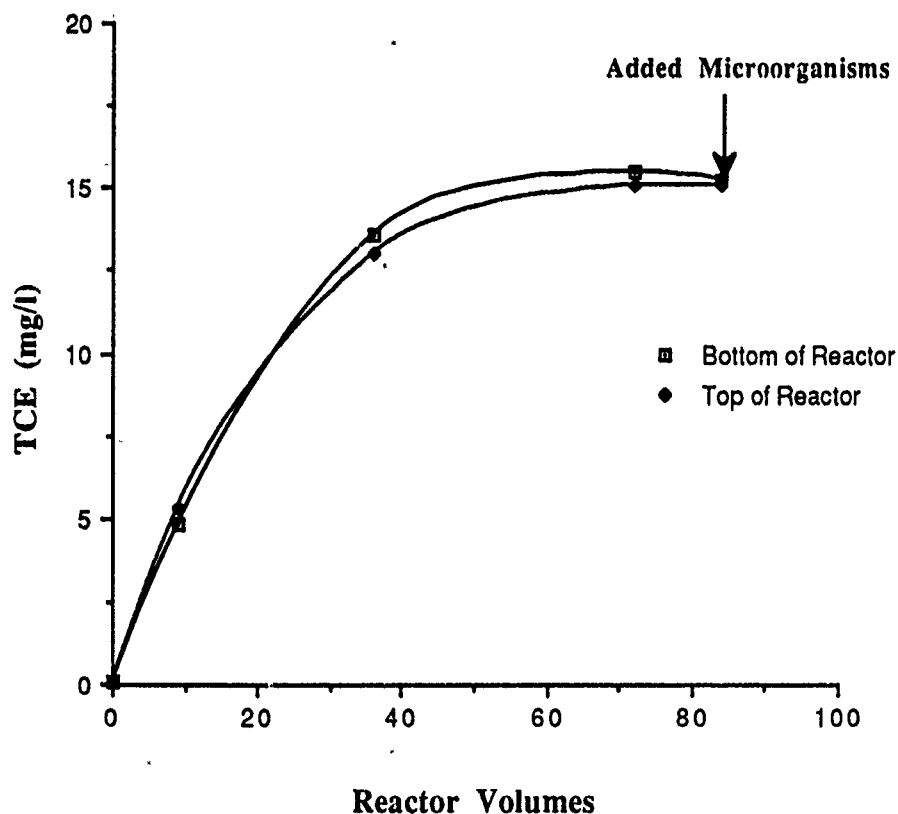

Fig. 3   Results of abiotic control TCE study. A steady state TCE concentration of 15 mg/liter was achieved after 50 bed volumes (*i.e.*, 33 hours).

The pH of the treatment system was measured to be 7.0 at the beginning and end of the study (duplicate samples). Dissolved oxygen levels in samples from the biological unit were estimated to be between 8.2 and 8.4 mg/liter while the dissolved oxygen level in the

plug flow reactor was approximately 1.5 mg/liter (duplicate samples). It should be noted that the method employed for measuring dissolved oxygen required the samples to be placed in a constant temperature water bath (ca. 20° C). Due to the difference in temperature between the bioreactor (28° C) and dissolved oxygen measurements (ca. 20° C), the actual dissolved oxygen levels existing in the treatment unit may have been lower than our reported values.

Although low dissolved oxygen in the plug flow reactor could explain the negligible TCE removal, only TCE adsorption to settled biological flocs could have resulted in TCE concentrations increasing above the abiotic steady state value.
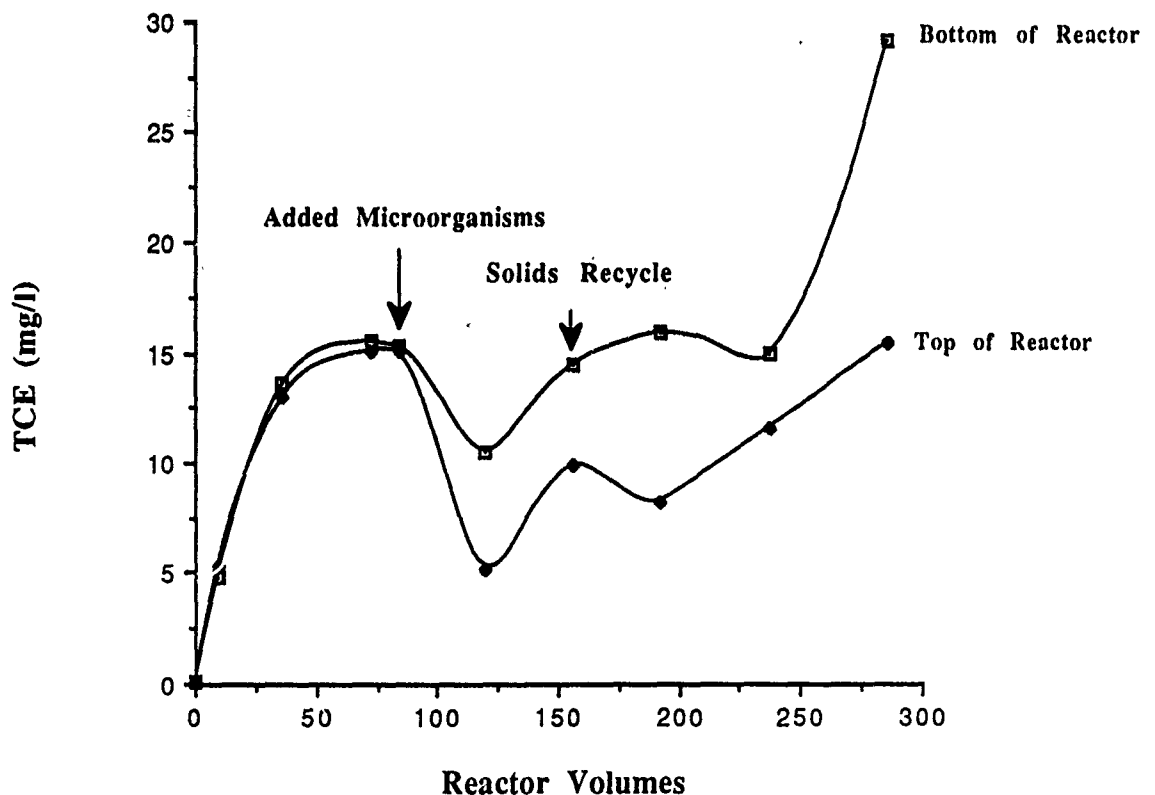

Fig. 4   Results of methanotrophic biomass addition sudy. Adsorption of TCE to biomass were consistent with observations made during this phase of the program.

Formate Enhanced Biodegradation of TCE

To estimate the effect of reducing power addition on TCE removal, formate was added continuously to the biotreatment system at a concentration of 20 mM. Results of formate addition are given in Figure 5. Formate addition resulted in rapid reduction in TCE concentration in the plug flow reactor. The concentration of TCE at the influent of the plug flow reactor decreased from 29.2 to 1.4 mg/liter TCE within 24 hours after formate addition.
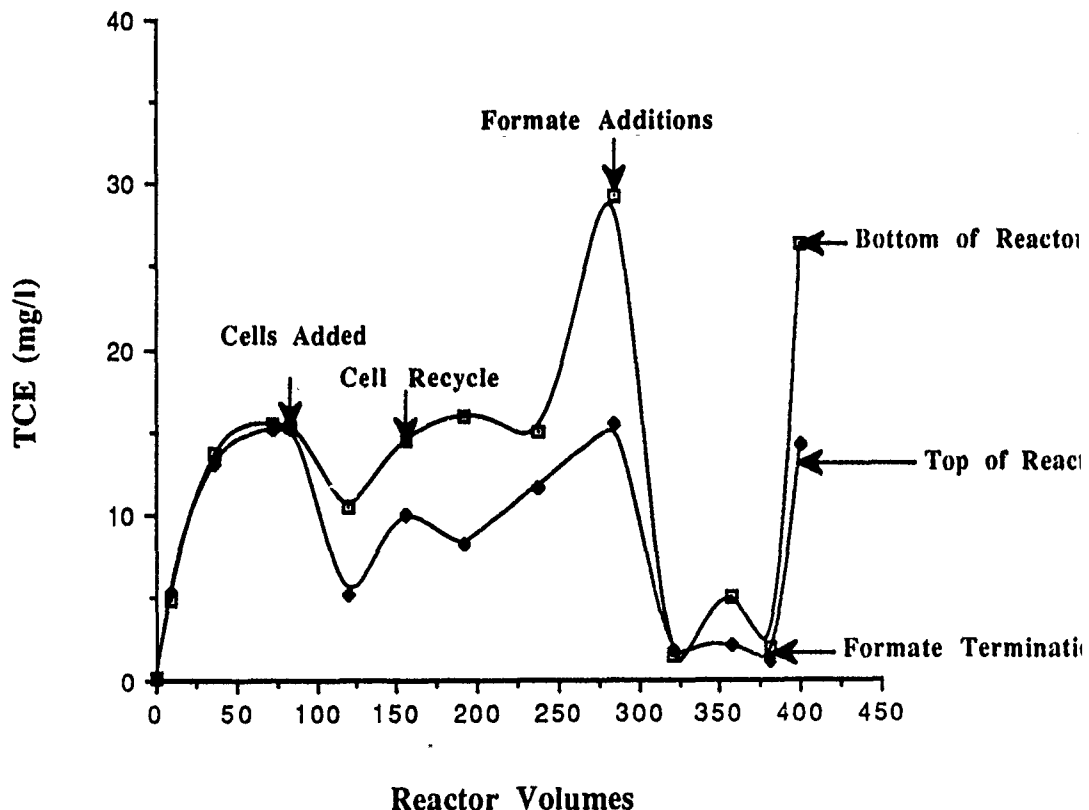

Fig. 5   Results of formate enhanced biodegradation of TCE. Formate additions led to rapid reduction in TCE concentration. Termination of formate additions led to increased TCE levels in plug flow reactor.

Volatile solids levels at the influent of plug flow reactor was estimated to be 1.3 grams volatile solids per liter. Assuming that the TCE removal occured mainly in the

influent portion of the reactor (*i.e.,* where biomass had settled), the maximum rate of TCE removal was estimated to be 21.1 mg TCE/gm VS-day.

After two days of continuous addition, the formate loading was discontinued. Termination of formate addition led to a rapid increase in TCE concentration suggesting that reducing power was limiting the TCE removal rate.

Due to the possible inhibition of TCE oxidation by residual methane entering the plug flow reactor, it was decided to evualuate the effects of adding formate in the absence of methane addition to the biological growth unit. Results of this study are provided in Figure 6. The concentration of TCE in the bottom of the reactor (*e.g.,* measured at the first side sampling port) decreased from 22.3 to 10.2 mg/liter TCE within seven hours. The volatile solids concentration was measured to be 1.6 grams VS/liter at this level of the reactor. This decrease in TCE is equivalent to an average TCE removal rate of 25.9 mg TCE/gm VS-day.

VI   DISCUSSION

Results form this preliminary study suggest that the methanotrophic two stage bioreactor system is effective in removing TCE from contaminated water. However, the mixed methantrophic culture was only effective in biodegrading TCE when it was supplemented with formate. In the absence of reducing power, the removal of TCE occured mainly by adsorption to biological flocs.

A maximum TCE removal rate of 21.1 mg TCE/gmVS-day was estimated during both formate and methane addition. This may be a very conservative estimate given the fact that 24 hours had elapsed before a TCE measurement was made. Actual maximum TCE removal rate may have been much greater. The TCE removal rate estimated in the present study is significantly greater than that reported recently by Phelps *et al.,* 1990 for a mixed methanotrophic culture (*i.e.,* 15 mg TCE/gmVS-day).
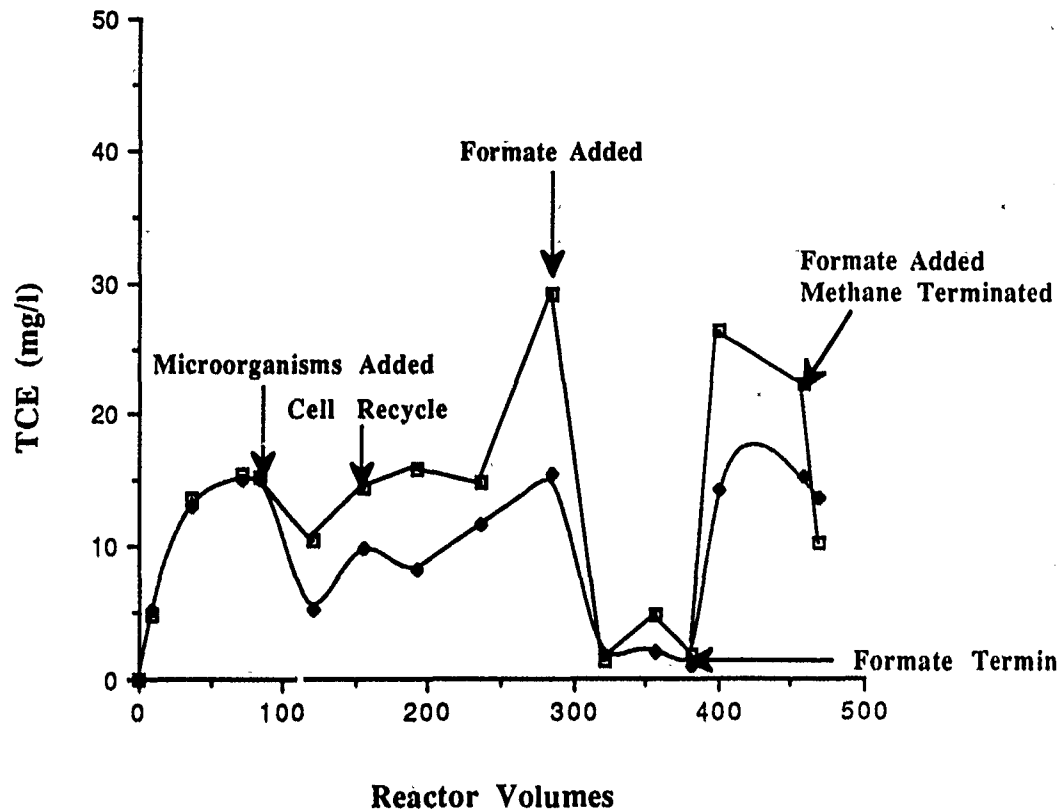
Fig. 6   Results of formate enhanced biodegradation of TCE with methane termination. Formate additions led to rapid reduction in TCE concentration.

When formate was added a second time with simultaneous termination of methane addition, the TCE removal rate increased to 25.9 mg TCE/gm VS-day. The increase of TCE removal in the absense of methane is consistent with results reported by others (Oldenhuis *et al.*, 1989; Tsien *et al.*, 1989). It is unknown whether or not methane levels were zero after seven hours but it seems clear that residual methane may limit TCE removal.

VII   RECOMMENDATIONS

Results from this summer research efforts indicate several lines of research that should be pursued in order to develop a commercial scale biological system for remediation

of sites contaminated with trichloroethylene. The following summarizes my observations and recommedations for expediting process development.

First, the kinetics of formate enhanced biodegradation of TCE must be clearly established. Mass balances on TCE will be essential to provide confidence in rate data. In the present study, rates of TCE removal were measured a time intervals of 7 to 24 hours which may have been too long to estimate actual maximum removal rates. Batch studies are required to estimate the maximum formate enhanced TCE degradation rates in the presence and absence of methane. Knowledge of maximum TCE removal rates and the effects of residual methane would be important for the engineering design criteria and, in particular, establishing the maximum TCE loading that can be treated in the bioreactor system.

Second, it is clear that a mixed methanotrophic culture is more effective in biodegrading TCE when supplied with suitable reducing power (*e.g.*, formate). However, the enzymes that are being activated will not retain their biological integrity indefinitely and will eventually be degraded. A simple solution to this problem is to create a TCE sludge blanket reactor that is to receive periodic additions of fresh methanotrophic cells. The TCE contaminated water and formate could be added continuously to such a system with periodic removal of inactive biomass.

Third, the concentration of TCE used in the present study was low compared to what may be encountered in actual field situations. Although TCE concentrations much above 25 mg/liter have been found to be toxic to growing populations of methanotrophic bacteria (Oldenhuis *et al.*, 1989), no one has reported the toxicity of TCE to nongrowing cultures. It is important to establish the toxic threshold of TCE on nongrowing methanotrophic biomass cultures if the two stage bioreactor system is to be used under field conditions.

Fourth, recent studies have reported that rates of TCE degradation are much greater using propanotrophic microorganisms (Wackett *et al.*, 1989). The effectiveness of mixed

propanotrophic cultures should be evaluated in the present biological reactor system and the results compared to those achievable by methanotrophic cultures. An advantage in using propanotrophs, from an engineering standpoint, is that propane is much more water soluble than methane and thus should result in larger biomass yields.

Finally, pure methanotrophic and propanotrophic cultures should be evaluated for their utility in biological waste treatment systems. It is well known that the methanotroph *Methylosinus trichosporium* OB3B is able to degrade TCE at rates nearly three orders of magnitude greater than that of mixed methanotrophic cultures. However, a pure culture's utility in waste treatment will ultimately depend on its ability to be selectively enriched in a heterogeneous environment. Much work needs to be done to determine the environmental conditions that will result in a selective enrichment of pure culture organisms.

REFERENCES

1. Cornish, A., Nicholls, K.M., Scott, D. Hunter, B.K., Ason, W.J., Higgins, I.J. and J.K.M. Sanders (1984)
    "In vivo ^{13}C NMR Investigations of Methaol Oxidation by the Obligate Methnotroph *Methylosinus trichosporium* OB3B"
    Journal of General Microbiology vol. 130, pp. 2565-2575

2. Dalton, H. and D.I. Stirling (1982)
    "Cometabolism"
    Phil. Trans. R. Conf. Lond. B vol. 297, pp. 481-496 pp. 481-496

3. Fliermans, C.B., T.J. Phelps, D. Ringelberg, A.T. Mikcll, and D.C. White (1988)
    "Mineralization of Trichloroethylene by Heterotrophic Enrichment Cultures"
    Appl. and Environ. Microbiol. 54, no. 7 pp. 1709-1714

4. Folsom, B.R., Chapman,P.J. and P.H. Pritchard (1990)
    "Phenol and Trichloroethylene Degradation by *Pseudomonas cepacia* G4: Kinetics and Interactions between Substrates"
    Appl. and Environ. Microbiol. vol. 56, No. 5 pp. 1279-1285

5. Little, C.D., A.V. Palumbo, S.E. Herbes, M.E. Lindstrom, R. L. Tyndall, and P. J. Gilmer (1988)
    "Trichloroethylene Biodegradation by a Methane Oxidizing Bacterium"
    Appl. and Environ. Microbiol. 54, no. 4 pp. 951-956

6. Oldenhuis, R., Vink L.J.M. R., Janssen, D.B. and B. Witholt (1989)
    "Degradation of Chlorinated Aliphatic Hydrocarbons by *Methylosinus trichosporium* OB3B Expressing Soluble Methane Monooygenase"
    Appl. and Environ. Microbiol. vol. 55, No. 11 pp. 2819-2826

7. Phelps, T.J., Niedielski, J.J., Schram, R.M., Herbes, S.E. and D.C. White (1990)
   "Biodegradation of Trichloroethylene in Continuous-Recylce Expanded-Bed
   Bioreactors"
   Appl. and Environ. Microbiol. vol. 56, No. 6 pp. 1702-1709

8. Roberts, P.V., L. Semprini, G.D. Hopkins, D. Grbic-Galic, P.L. McCarty and
   M. Reinhardt (1989) "In Situ Aquifer Restoration of Chlorinated Aliphatics by
   Methanotrophic Bacteria" EPA/600/2/89/033

9. Scott D., Brannan J., and I.J. Higgins (1981)
   "The Effect of Growth Conditions on Intracytoplasmic Membranes and Methane
   Mono-oxygenase Activities in *Methylosinus trichosporium* OB3B"
   Journal of General Microbiology vol. 125, pp. 63-72

10. Standard Methods for the Examination of Water and Wastewater (1989)
    Edited by L.S. Clesceri, A.E. Greenberg, R.R. Trussell (17th Edition)
    APHA, AWWA, WPCF

11. Stanley, S.H., Prior, S.D., Leak, D.J. and H. Dalton (1983)
    "Copper Stress Underlies the Fundamental Change in Intracellular Location of
    Methane Mono-oxygenase in Methane- Oxidizing Organisms:Studies in Batch and
    Continuous Cultures."
    Biotechnology Letters vol. 5, no. 7 pp. 487-492

12. Tsien, H.C., G.A. Brusseau, R.S. Hanson, and L.P. Wackett (1989)
    "Biodegradation of Trichloroethylene by *Methylosinus trichosporium* OB3b.
    Appl. and Environ. Microbiol. vol. 55 no. 12 pp. 3155-3161

13. Wackett, L.P., Brusseau, G.A., Householder, S.R. and R.S. Hanson (1989)
    "Survey of Microbial Oxygenases: Trichloroethylene Degradation by Propane-Oxidizing Bacteria"
    Appl. and Environ. Microbiol. vol. 55, No. 11 pp. 2960-2964

1990 USAF-UES SUMMER FACULTY RESEARCH PROGRAM

Sponsored by the

AIR FORCE OFFICE OF SCIENTIFIC RESEARCH

Conducted by the

Universal Energy Systems, Inc.

FINAL REPORT

SUBMICRON ANTENNAS FOR SOLAR ENERGY CONVERSION

Prepared by: Dr. Perry R. McNeill, P.E.

Academic rank: Professor

Department and   Industrial Technology

 University: University of North Texas

Research Location: USAF Engineering and Services Center
                    Air Base Energy Systems Branch
                    Tyndall AFB, FL 32403-6001

USAF Researcher: Thomas C. Hardy

Date: 20 Sep 90

Contract: F49620-88-C-0053

Submicron Antennas for Solar Energy Conversion

by

Dr. Perry R. McNeill, P.E.

ABSTRACT

This report deals with the synthesis and evaluation of
literature in the area of using submicron antennas to convert
solar energy to electrical power. A number of articles in
three areas are discussed; Solar Cells, Submicron Antennas,
and Related Work. The primary document analyzed is "Antenna
Solar Energy to Electricity Converter (ASETEC)", Dr. Erich A.
Farber, University of Florida. A secondary set of documents
included in the report were patents issued to Dr. Alvin M.
Marks for submicron antennas and fabrication techniques for
use in solar energy conversion.

Acknowledgments

I want to thank the Air Force Systems Command and the Office
of Scientific Research for providing this opportunity for me
to spend time away from the campus pursuing the very exciting
topic of alternative energy research. The Universal Energy
Systems corporation provided excellent logistic support in
this endeavor.

I was fortunate to work with some very competent individuals
at the Air Force Engineering and Services Center (AFESC).
Mr. Tom Hardy was very supportive of my efforts and provided
me with an abundance of technical assistance and support.
Mr. Ed Alexander must be mentioned for his administrative and
logistical support of the project. Ms. Julie Herrlinger
provided superb clerical and secretarial assistance.
Ms. Janet Davis of the AFESC library deserves exceptional
accolades for her tenacity in finding even the most obscure
technical journal and reference.

I. INTRODUCTION:

The USAF has a fundamental interest in discovering alternative energy sources for its base utilities program. Considerable work has been done in research laboratories, universities, and commercial companies on using solid state devices to convert solar energy to electrical energy. There are many existing commercial and military installations utilizing solar cells. Because of the low maximum efficiency of these devices, interest has been expressed in finding more efficient techniques for this power conversion.

The Air Base Energy Systems Branch of the Engineering Research Division of the Air Force Engineering & Services Center at Tyndall Air Force Base is concerned with finding alternative energy sources for the many main operating and remote air bases in the theaters. The direct conversion of solar energy utilizing absorbing antennas would be of great benefit in these efforts.

My research and teaching interests have been in the electronics and energy areas. My work with microwave tracking antennas at the Oklahoma State University Electronics R&D Laboratory and my work with the Electrical Power Industry on a National Science Foundation contract contributed to my assignment to work in the Energy Systems Branch.

II. OBJECTIVES OF THE RESEARCH EFFORT:

a. Statement of the Problem The maximum theoretical
efficiency of solar cells is limited to about 24%. The more
common commercial cells operate in the 10-15% region.
Converting solar electromagnetic radiation in the submicron
region directly into electrical energy with dielectric
antennas would theoretically improve this conversion
efficiency dramatically. Ideally one could recover 100% of
the energy striking the antenna.

b. Plan of Action My assignment as a Fellow in the 1990
Summer Faculty Research Program (SFRP) was to evaluate
literature and reports that had been collected by the Air
Base Energy Systems Branch and search for additional sources
of information on solar energy conversion using submicron
antennas. The primary document to be evaluated was a report
prepared under an Air Force contract with the Solar Energy
and Energy Conversion Laboratory of the University of
Florida. Based on this evaluation and search, I then made a
set of recommendations concerning additional work that should
be started to build a working model of the antenna concept.

III. REVIEW OF THE LITERATURE

The literature review for this report was accomplished with
the aid of the Library in the Air Force Engineering and

Services Center and the Gulf Coast Community College/Florida
State University Library in Panama City. The material has
been divided into three categories; Solar Cells, Submicron
Antennas, and Supporting Work.

a. Solar Cells Recovering energy from the sun has tremendous
potential for use in solving the world's dependency on fossil
fuels. The earth receives about 10^{18} kWh of solar energy
each year. In the mid 1980's the worldwide consumption of
energy was about $80X10^{12}$ kwh. This corresponds to less than
0.008% of the worlds needs (24). Machata (15) has produced
tables showing the reception of solar energy distribution
across the U.S. for all four seasons.

The major efforts in converting solar to electrical energy
have been with the use of solar cells. A number of public
utilities now have the capability to generate a portion of
their electrical load with the use of solar cells. Jewell
(10) and Ramakumar (11) documented difficulties that the
utilities have adjusted to as these systems are brought on
line.

The real difficulty of solar cells has been with the
conversion efficiency. The upper limit of these cells is
less than 24% due to the energy available in a photon of
light and the barrier potential of the PN junction. In spite
of this difficulty Nasbitt (19) predicts in his Megatrend

book that the cost will fall to $1.50 per watt by the year 2000 and become a $7.5 billion business supplying the majority of the energy for the 21st century.

Texas Instruments has decided to enter the market for solar cells according to a recent article in the Dallas Morning News (25). They plan on joining forces with California Edison in a $5 million development project this next year.

There have been several studies and proposals (2,8) made to collect the solar energy at a space station with solar cells. This energy would then be formed into a microwave beam for transmission to earth. It would then be received with a combination antenna and rectifier system called a "rectenna".

b. Submicron Antennas The primary work discussed in this report covers experimental work done on submicron antennas and an patent granted for a submicron antenna. Dr. Erich A. Farber (5) of the Solar Energy Laboratory, University of Florida performed a series of experiments at 0.2-0.3 GHz, 10 GHz, 100 GHz and concluded with the collection of data in the visible light region. This report was funded by AF C F08635-83-C-0136, Task 85-6. His objective in starting in the microwave region was to show that the same phenomena occurred as he moved upward in magnitude. His major conclusion is that one can use submicron antennas to collect solar energy and directly convert it to electrical energy. A more

complete analysis of his data and results is included in Section IV. The limitations of his experiment were compounded by not having an appropriate submicron antenna array. He used silicon carbon crystals found on common "sandpaper" as his submicron antennas.

A related area was a patent awarded to Dr. Alvin Marks for a "Device for Conversion of Light Power to Electrical Power" (17). He calls this device a LEPCON. This device would consist of a number of dipole antenna of length 0.18 microns arranged in an array with a diode bridge rectifier incorporated in the base. He also presented this concept to the Workshop on Solar Applications (16). The Boston Herald (12) reported in 1984 that Marks had licensed his technology to Phototherm, Nashua N.H., for production of LEPCON panels to produce electricity. A later newspaper report, 1988, (21) indicated that he could obtain at least 40% efficiency with his array.

While Farber proposed pyramid arrays as opposed to Mark's dipoles, their concepts are essentially the same. Both would build submicron antenna arrays with diode rectifiers in the base of the array.

c. Related Work Since neither Marks nor Farber have actually produced antennas in the submicron range, the question naturally arises as to whether or not such a fabrication can

be accomplished. There are a number of related articles included in the reference section indicating that considerable work in the submicron region is underway. There is also some information on concepts that support the work done by Farber and Marks.

Three organizations have indicated a desire to participate in the fabrication of the submicron silicon pyramid antennas; "American Matrix" (20), "I Squared R Element Co." (4), and Professor Whitton (26), Queen's University.

An article in Spectrum (9) discussed a new technique of building sensors and even dc motors on a solid state chip with a new micromechanics technique. Structures as small as 2 by 100 microns have been fabricated. Another article (20) indicates that infrared photodetectors have been fabricated on a silicon chip in the 1.3-1.55 micron range. An article in the "International Journal of Infrared and Millimeter Waves" (22) discusses the fabrication of antennas on a 1 micron thick membrane. Rutledge (23) reported on the construction of a submillimeter trapezoid antenna operating at 118 microns. Another report (3) details the microfabrication of devices for the 200-265 GHz range. Researchers at the Bell Labs (14) have succeeded in creating an infra-red photodetector on a silicon chip.

Another group of articles deals with improving the reception

of energy by changing the surface structure of antennas. A USSR patent (1) discusses an electromagnetic absorber. An Applied Physics Letter (6) discusses the use of submicron pillars on solar absorbers. A computer simulation (7) found that pyramids provided an improvement over diffuse surfaces.

## IV. APPRAISAL OF A SOLAR ENERGY ANTENNA PROPOSAL

It is the intent of this section to discuss the data, conclusions, and recommendations from the document, "Antenna Solar Energy to Electricity Converter" (5).

First consider the spectrum of energy radiated from the sun and striking the surface of the earth. The following graph (24) illustrates this radiation. It can be seen from this graph that the highest intensity of the solar spectrum occurs between about 0.5 microns and 0.8 microns. The graph of the electromagnetic spectrum (13) indicates that these wavelengths, λ, occur between the upper end of the infra-red, 3.75×10^{14} Hz, and the blue-green visible light frequency, 6.0×10^{14} Hz. The frequency is calculated from the following relationship:

$$f = \frac{3 \times 10^8 \ m/sec}{\lambda \ m} \qquad (1)$$

a. Microwave Energy It is apparent from equation (1) that moving into the visible light portion of the EM spectrum implies that one will be dealing with extremely small

35-10

configurations as compared to say microwave components.
Farber's conclusion that miniaturization would not affect the
power received is of course very pertinent and true if one
can fabricate the components.
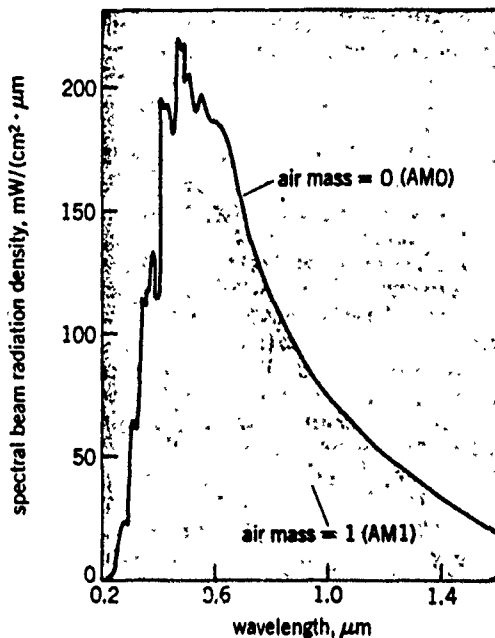
Spectral distribution of sunlight in space (AM0) and on sur-
face of Earth with the Sun at the zenith (AM1).

Figure 1 Solar Intensity versus Wavelength (24)

b. Solar and Light Energy Due to a shortage of funds,
Farber was not able to construct a submicron antenna array
from which to collect solar and light data.   His narrative
and photographs lead to the drawings on the following page
which clearly show how he collected the data on the
Carboroundum® array.   The decision to use Carboroundum®
sandpaper gave Farber a ready supply of an inexpensive source
of solid state crystals.   In order to collect energy from
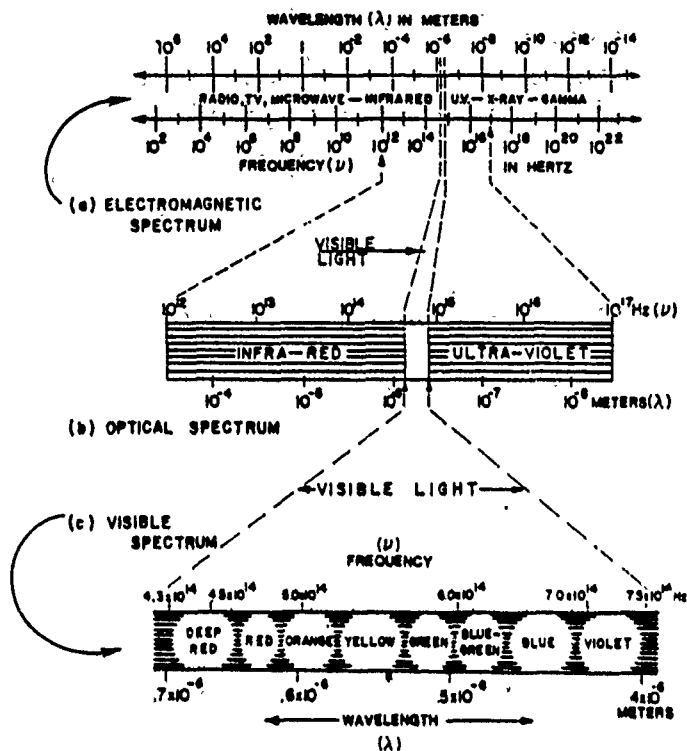
Figure 2 Electromagnetic Spectrum (13)

these crystals it was necessary to have a conductor in contact with them. He simply used a stranded wire with the insulation removed and spread out the strands over the top and bottom of the sandpaper as indicated in the cross section of his collector. He collected a great deal of data with the lamp and battery circuit which are shown as graphs in his report. He did expose the circuit to sunlight and indicated that he measured a voltage. He did not, however, report any of this solar data in either tables or in the form of graphs.

c. **Areas of Concern** The general observation concerning this report is that it is an excellent first start at investigating the collection of solar energy with submicron
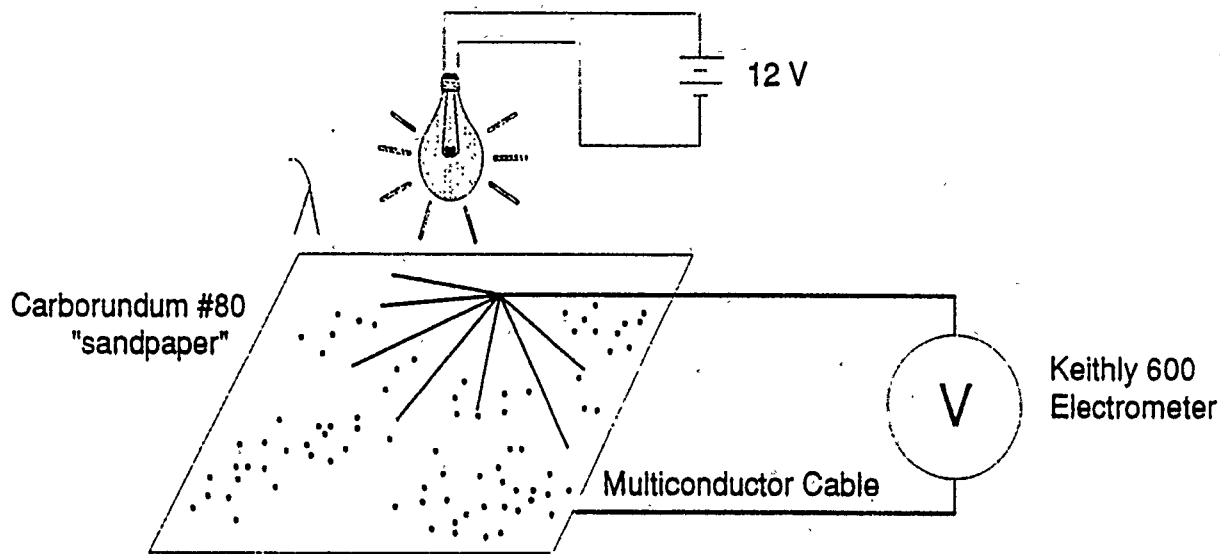
Figure 3 Farber's Solar/Light Energy Collecting Circuit
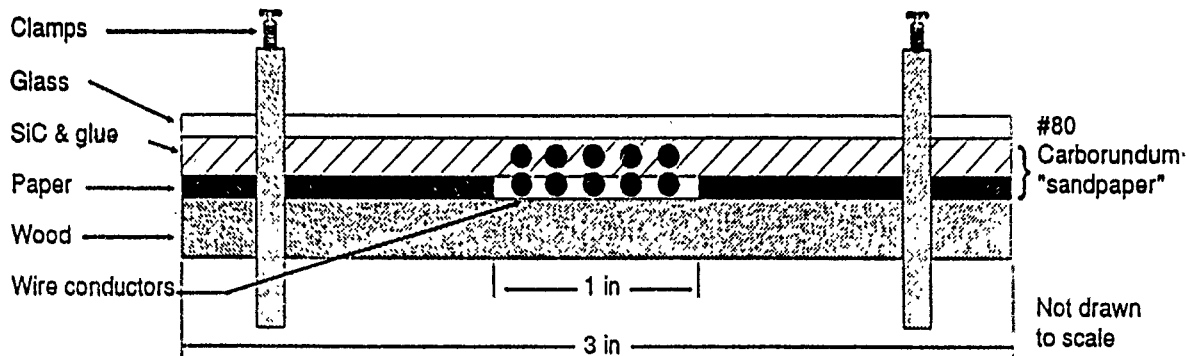
Figure 4 Solar/Light Converter-End View

antennas. The data does seem to support the contention that
crystals can function as antennas for solar energy
conversion. Ignoring the fact that he had to use a very
crude array, Carboroundum®, there are still some questions

to resolve before proceeding to a fabrication stage. Since no information was presented on the quantity of light radiating from the 150 watt lamp and impinging on the collector, no conclusions can be made concerning the efficiency of the collectors. Clearly the efficiency would not be very high due to the random orientation of the crystal on the sandpaper, but it should be investigated. As part of this efficiency measurement, one must raise the question as to what sort of detection scheme was occurring with the wires on the crystals and the Electrometer. The Keithly 600 meter will not respond properly to frequencies in the region of 10^{14}. With the metal wires pressed on the crystals, Farber may have created a point contact diode on the array. This should also be investigated in any subsequent work on this topic.

As Farber states in his report, the collection of data in the laboratory with the lamp is easier to control than with solar conditions. Since the ultimate goal is to use this device to collect solar data, the experiment should be replicated outside the laboratory with the sun as a source and using a light meter to record the array output versus solar intensity.

Broadband capabilities are the desired characteristics for this array as opposed to a single frequency or narrow band as is common in signal antennas. The experimental set up used

by Farber was composed of all crystals of the same size, but not necessarily of the same shape. A request to the manufacturer of Carboroundum® sandpaper to obtain crystals before they are crushed would allow one to create an array composed of several different sized crystals and aligned in the same orientation.

On page 143 of his report Farber discusses the directional characteristics of the Carboroundum® array. Since the crystals are oriented in a very random pattern, the directivity of the array would be affected. While he discusses this concept, there is no data or graphs to illustrate the phenomenon. He does, however, state that he obtained the classical pear shaped curve of a directional array.

VI. SUMMARY

This review of the literature supports the following :

a. Solar cells continue to be an important alternate source of energy conversion. The efficiency of these devices has not reached the theoretical maximum of 24%.

b. The use of submicron antennas to convert solar energy to electrical energy is not yet a proven technology. The literature search revealed only two locations where work had

been done on these devices, The University of Florida Solar Laboratory and Phototherm Inc. Amerst, NH. A major challenge with both concepts is in the fabrication of the antennas.

c. . A lot of work has been done on millimeter antennas that can be extended to these submicron antennas.

d. Fabrication technology in the micron region appears to be at a point where these antennas could be fabricated.

VII. RECOMMENDATIONS

Based on this survey of the literature, it seems that both Farber's and Marks' work indicate that there is a potential utilization of solar submicron antennas by the Air Force. The following recommendations are based on this review:

a. The Farber experiment using Silicon Carbon crystals should be replicated using more control to determine a measure of the efficiency of such an array. This experiment should attempt to obtain and use these crystals before they are crushed and placed on the Carboroundum® paper.

b. Additional dialog should be initiated with Dr. Marks' company, Phototherm, to ascertain if his concepts are as viable as they appear in the literature.

c. Conversations and visits should be initiated with U.S. semiconductor companies and research laboratories to determine the feasibility of fabricating an experimental model of both the Farber and Marks antennas.

REFERENCES

1. Alimin, B.F. and Suslov, L.M., "Electromagnetic Wave Absorber USSR Patent Nr. 698088 15 Nov. 1979", USAF Systems Command Foreign Technology Division, June 26, 1985.

2. Brown, William C., "Satellite Power Stations: A New Source of Energy?", IEEE Spectrum, March, 1973.

3. Corcoran, V.J., "State of the Art of Infrared and Submillimeter Wave System Application", International Conference on Infrared Physics Proceedings, Zurich, Switzerland, March 5-9, 1979.

4. Davis, J.R., Letter, I Squared R Element Co., Inc., Jul 20, 1987.

5. Farber, Erich A., "Antenna Solar Energy to Electricity Converter (ASETEC)", Solar Energy Conversion Laboratory, University of Florida and Tyndall AFB, Florida AFC F08635-83-C-0136 Task 85-6, November, 1988.

6. Gittleman, J.I.; Sichel, E.K.; Lehmann, H.W. and Widmer R., "Textured Silicon: A selective absorber for solar thermal conversion", Applied Physics Letters-American Institute of Physics, November 15, 1979.

7. Green, Martin A. and Campbell, Patrick, "Light Trapping Properties of Pyramidal Textured and Groved Surfaces", IEEE PHOTOVOLTAIC SPECIALIST CONFERENCE, 1987.

8. Gregory, Gordon R. and Woodcock, Gordon R. "Satellite Energy Systems for Earth Power", Systems for Earth Power Solar Energy Technology, McGraw Hill, 1977.

9. Howe, R.T.; Muller, R.S.; Kaigham, J.G. & Trimmer, W.S.N., "Silicon Micromechanics: Sensors on a Chip", IEEE Spectrum, July, 1990.

10. Jewell, W., "Electric Utility Experience with Solar Photovoltaic Generation", IEEE Transactions on Energy Conversion Vol. 4 No. 2, June, 1989.

11. Jewell, W. & Ramakumar, R., "The Effects of Moving Clouds on Electric Utilities with Dispersed Photovoltaic Generation", IEEE Transactions on Energy Conversion Vol. EC-2 No. 4, December, 1987.

12. Krasner, Jeff, "Scientist's idea for cheap electricity", The Boston Herald, December 26, 1984.

13. Laser and Optics Fundamentals. Engineering Technology Incorporated, Waco Texas, 1980.

14. Luryi, S. et. al., "Waveguide Infrared Photodetectors on a Silicon Chip", IEEE Electron Devices Letter Vol. EDL-7, February, 1986.

15. Machta, L., "Availability of Solar Energy at Ground Level", Vol 2. Ch. 2, Economics of Solar Energy and Conversation System.. CRC Press,, 1980.

16. Marks, A. and Bourke, E., "Lepcon: Light to Electrical Power Conversion", Workshop on Solar Applications of Energy Conversion Technology,, Solar Energy Research Institute, Golden Colorado, February 19, 1985.

17. Marks, Alvin M., "Device for Conversion of Light Power to Electrical Power, U.S. Patent Office, April 24, 1984.

18. Marks, Alvin M., "Femto Diode and Applications", U.S. Patent Office, January 19, 1988.

19. Naisbitt, John and Aburdene, Patricia, Megatrends 2000-

Ten New Directions for the 1990's. William Moorrow and Co. Inc., New York, 1990.

20. Nixdorf, R.D., Letter from V.P. for R&D, American Matrix, Inc. Knoxville, TN, July 20, 1987.

21. Overell, A. M., "Inventors Claim Tiny Antennae Can Solve the Energy Problem", New Technology Week, February 8, 1988.

22. Rebeiz, G.M.; et. al., "Submillimeter-Wave Antennas on Thin Membranes", International Journal of Infrared and Millimeter Waves, Vol. 8, No. 10, 1987.

23. Rutledge, D.B. et. al., "Progress in Submillimeter Antennas", IEEE Conference Digest 4th International Conference on Infrared Millimeter Waves, December 10-15, 1979.

24. Schueler, D.G., "Solar Energy", Encyclopedia of Science and Technology, McGraw-Hill, New York, 1987.

25. Steinert, Tom, "TI finds a place in the sun", The Dallas Morning News, July , 1990.

26. Whitton, J.L., Letter, Department of Physics, Queen's University, Kingston, Canada, Aug. 5, 1987.

1990 USAF-UES SUMMER FACULTY RESEARCH PROGRAM

GRADUATE STUDENT RESEARCH PROGRAM

Sponsored by the

AIR FORCE OFFICE OF SCIENTIFIC RESEARCH

Conducted by the

Universal Energy Systems, Inc.

FINAL REPORT

Dynamic Analysis of Impulse Loading on Laminated Composite Plates

Using Normal-Mode Techniques

Prepared by:	John L. Scharf, Ph.D.
Academic Rank:	Assistant Professor
Department and	Department of Mathematics, Engineering, Physics, and Computer Science
University:	Carroll College
Research Location:	USAFESC/RDCS Tyndall AFB, FL 32403-6001
USAF Researcher:	Jon Anderson
Date:	30 September 90
Contract No:	F49620-88-C-0053

Dynamic Analysis of Impulse Loading on Laminated Composite Plates Using Normal-Mode Techniques

by

John L. Scharf

ABSTRACT

The normal-mode technique has been applied by previous investigators to the dynamic analysis of impact loading on beams and plates. In this work, the method is applied to one-way, simply supported, laminated, composite plates under uniformly distributed, impulse loads. Governing equations are formulated based on kinematic assumptions that allow the transverse shear deformations to vary through the thickness of the laminated plate. A solution is obtained for a two-ply, $-\theta/+\theta$ laminate. This solution shows that immediately after the impulse is applied, sharp peaks in the transverse shear stresses occur at the two end supports. These shear stress peaks then propagate from the supports across the span at the shear wave speed for the material that comprises the laminated plate. This result is consistent with those obtained by the earlier investigators, and it leads to two recommendations. The first is that any numerical techniques applied to the analysis of laminated composite plates must accommodate the large strain gradients and high speeds of the transverse shear waves. The second is that design modifications should be investigated that will mitigate the effects of transverse shear stress peaks on laminated composite plates under impulse loads.

Acknowledgements

I am sincerely grateful to the Air Force Engineering and Services Center and to the Air Force Office of Scientific Research for supporting this work. I owe much gratitude to all the fine people at AFESC/RDCS, Tyndall AFB, Florida, for the time and effort that they expended to make my summer research experience very worthwhile. In particular, Dr. Jon Anderson was most helpful by giving me the latitude to pursue a project that was of special interest to me. Lt. Jim Underwood, Capt. Diane Miller, Capt. Rich Reid, Mr. Stan Strickland, Ms. Cathy Bishop, and Ms. Astoria Wilder all helped to provide a most enjoyable and comfortable working environment that was very conducive to productive research work. I am also very grateful to Dr. Michael G. Katona for his confidence and support in this endeavor. Finally, I would like to thank Universal Energy Systems for their efficient management of the Summer Faculty Research Program.

I. INTRODUCTION:

The United States Air Force through its Engineering and Services Center is planning to develop a new generation of air transportable, protective shelters that would be used in circumstances where expedient and rapid deployment are required. The purpose of these structures is to provide protection for personnel and for vital equipment and hardware.

In addition, the Engineering and Services Center is also developing concepts and theory for the application of aerospace composite materials in the design and construction of these protective shelters. These composite materials offer the advantages of high strength-to-weight ratios, allowing for expedient transportability of relatively strong shelters, and they are adaptable to meet specific application requirements.

Under combat conditions, it is expected that laminated composite plate structures could be subjected to large area blast loads of strong intensity and short duration. One way to model this condition is to consider an impulse load of uniform magnitude applied over the area of the laminated plate. The response of the plate is then determined by applying the normal-mode technique to solve the governing differential equations. This method was applied to simple Timoshenko beams by Karthaus and Leussink (1983), and was extended to apply to isotropic Mindlin plates by Mercx and Harmanny (1987). Mercx (1989) showed how the normal-mode technique can be useful in nonlinear and finite element analyses of beam and plate structures.

In this paper, the normal-mode technique will be applied to analyze simply supported, one-way, laminated, composite plates under a uniformly distributed impulse load as shown in Figure 1. Governing equations are formulated based on kinematic assumptions that allow transverse shear deformations to vary through the thickness of the laminated plate. A solution is obtained for a two-ply, $-\theta/+\theta$ laminate. This solution shows that immediately after the impulse load is applied, sharp peaks in the transverse shear stresses occur immediately at the supports. These stress peaks then propagate from the supports across the span at the shear wave speed for the material that comprises the laminated plate. This result for laminated, composite plates is similar to those that were obtained by the earlier investigators for plates made from isotropic materials.
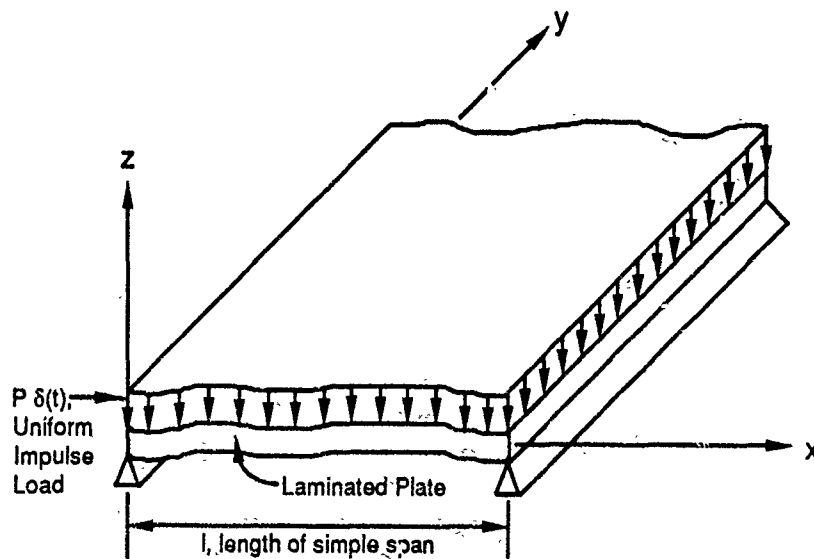

Figure 1   One-Way Simply Supported Plate Loaded
with a Uniform Impulse Load of Intensity, P,
at Time, t=0

II. OBJECTIVES OF THE RESEARCH EFFORT:

The objectives of this research effort are:

1. to apply the normal-mode technique to analyze laminated composite plates under impulse loads.

2. to provide insight into the behavior of laminated composite plates under impulse loads.

3. to provide a reasonable basis for the development of effective analysis, design, and construction methodologies for lightweight composite plate structures that are to be used in combat environments.

4. to show that care must be exercised in applying standard numerical methods (i.e., finite elements and finite differences) in analyzing laminated, composite plates under impulse loads.

5. to provide a basis for experimental verification of analysis results that are obtained.

III. THE NORMAL-MODE TECHNIQUE:

The normal-mode technique is explained in detail by Karthaus and Leussink (1980), by Mercx and Harmanny (1987), and by Mercx (1989). Essentially, the method is based upon a decomposition of the uniform load, P, into Fourier components, each of which has a wave length corresponding to one of the normal, vibrational mode shapes of the plate structure to which the load is applied. These Fourier components also satisfy the geometric boundary

conditions on the plate and they are mutually orthogonal. Consequently, the total response can be obtained by independently applying to the plate each of the Fourier components of the load, and then adding together all of the individual responses.

IV. KINEMATIC ASSUMPTIONS:

The thickness of the plate is divided into n layers, each layer having a uniform thickness over the area of the plate. Figure 2 shows the ith layer in a plate that has been divided into n layers.


(z is measured from the center of the laminate)
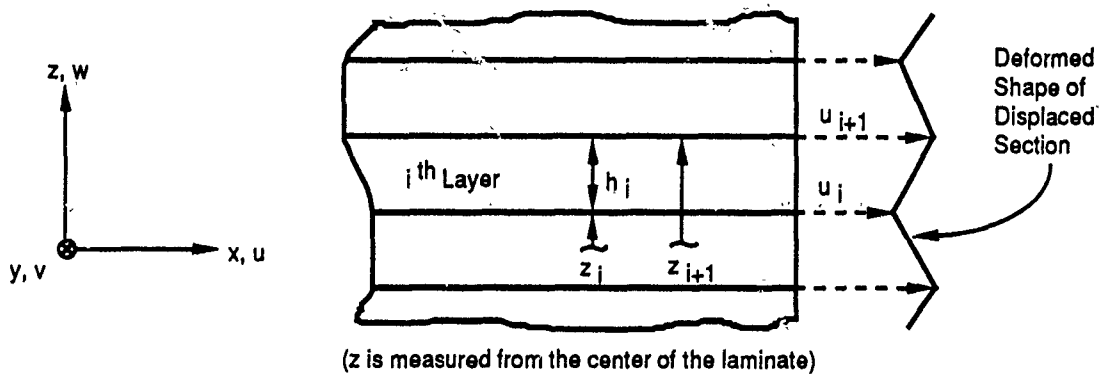
Figure 2   In-Plane Displacements, $u(x,y,z,t)$, of the ith Layer of a Plate with n Layers

Transverse shear deformations can be provided for by a displacement field that is described by the following displacement functions:

$$u(x,y,z,t) = \frac{u_i + u_{i+1}}{2} - \frac{u_i - u_{i+1}}{h_i} (z - \overline{z}_i) \qquad (1)$$

$$v(x,y,z,t) = \frac{v_i + v_{i+1}}{2} - \frac{v_i - v_{i+1}}{h_i} (z - \overline{z}_i) \qquad (2)$$

$$w(x,y,z,t) = w \qquad (3)$$

where u, v, and w are displacements in the x, y, and z directions, respectively, and $i = 1, 2, \ldots, n$. In each of the n layers, $z_i \leq z \leq z_{i+1}$, $\overline{z}_i = \frac{z_i + z_{i+1}}{2}$, and $h_i = z_{i+1} - z_i$. The functions, u_i, u_{i+1}, v_i, v_{i+1}, and w, on the right hand sides of equations (1), (2), and (3) are all functions of x, y, and t. The function u(x,y,z,t), that is described in equation (1) above, represents the displacements of the plate in the x-direction and is illustrated in Figure 2.

As a minimum, each lamination in a laminated plate should be represented by one layer in the displacement field described above. However, if one wishes, additional layers can be included to provide a higher order model to capture more accurately the distribution of transverse shear deformations and stresses through the thickness of the plate. These kinematic assumptions were used by Spilker, Chou, and Orringer (1977) in their finite element formulation for laminated plates.

V. GOVERNING EQUATIONS:

Engineering strains are obtained in the usual fashion from the displacement field described in Equations (1), (2), and (3). Each lamination of the composite plate is assumed to be comprised of a linearly elastic, orthotropic material under plane stress conditions, and the orientation of the orthotropic material in each lamination can be arbitrarily specified. Based upon these assumptions the stresses in the plate are determined.

The principle of virtual work is used to obtain the governing partial differential equations in the space variables, x and y, and the time variable, t. These include the equations of motion of the plate together with appropriate boundary conditions. The virtual work statement is:

$$\delta V = \int_V (\sigma^T \, \delta\varepsilon + \rho \ddot{u} \, \delta u) \, dV - \int_A \{ \, [P \, \delta(t)] \, \delta w \, \} \, dA = 0 \qquad (4)$$

where $\sigma^T = (\sigma_x, \sigma_y, \sigma_{xy}, \sigma_{yz}, \sigma_{zx})$, $\varepsilon^T = (\varepsilon_x, \varepsilon_y, \varepsilon_{xy}, \varepsilon_{yz}, \varepsilon_{zx})$, $u = (u, v, w)$, ρ is the mass density distribution, V is the volume, and A is the area of the laminate. If there are n layers, the variational statement in equation (4) will give 2n+3 partial differential equations in the same number of unknown displacement functions.

The simple span of the one-way plate is taken in the x-direction and the long axis is taken in the y-direction, as shown in Figure 1. The assumption of one-way bending requires that all strains must be constant with respect to y. This

reduces the governing partial differential equations to ordinary differential equations in x. These equations are solved using the normal-mode technique as described in the preceding articles.

VI. SOLUTION

To demonstrate the model, a solution is obtained for a two-ply, $-60°/+60°$ laminate having a simple span of 10 m and a thickness of 1 m (each lamination is 0.5 m thick). Each of the two laminations is of the same orthotropic material having the following properties in material coordinates: $\rho=2400$ kg/m^3, $E_1=40.5$ GPa, $E_2=8.38$ GPa, $\nu_{12}=0.05$, $G_{12}=4.14$ GPa, $G_{31}=4.14$ GPa, $G_{23}=3.03$ GPa. Solutions for the governing equations are obtained for the first 1000 Fourier components of the uniform impulse load and these are superimposed to obtain the total response of the laminate. For each wave number (i.e., for each component of the uniform load) there are 2n+3 natural frequencies of the laminated plate with corresponding vibrational mode shapes, where n is the number of laminations. In this example, n=2 and therefore the number of modes for each wave number is 7. In calculating the total response, only the lowest frequency and corresponding mode shape were retained from each group of seven, and the higher frequency modes were discarded. This is commonly done in applying the normal mode technique and is justified in the previous articles by Karthaus and Leussink (1983) and by Mercx (1989).

Figure 3 shows the transverse, interply shear strain, γ_{zx}, across the simple, one-way span at time intervals shortly after the unit impulse load is applied. Immediately after the impulse, peaks in these shear strains and the
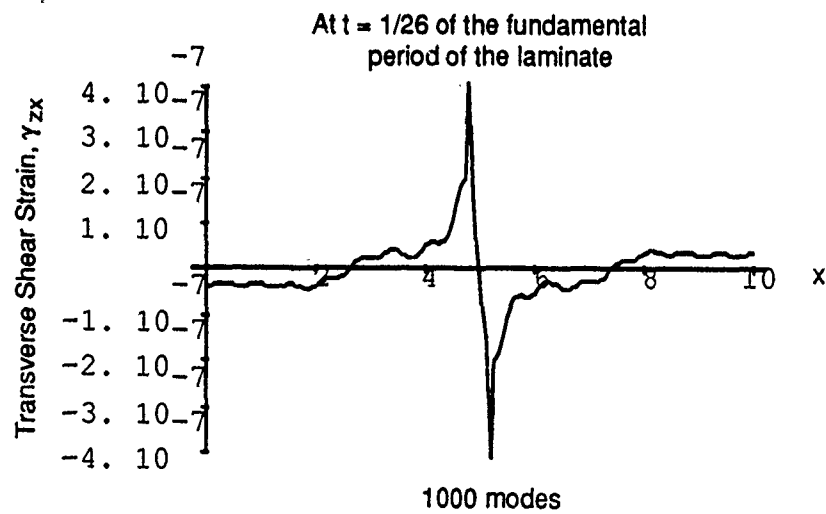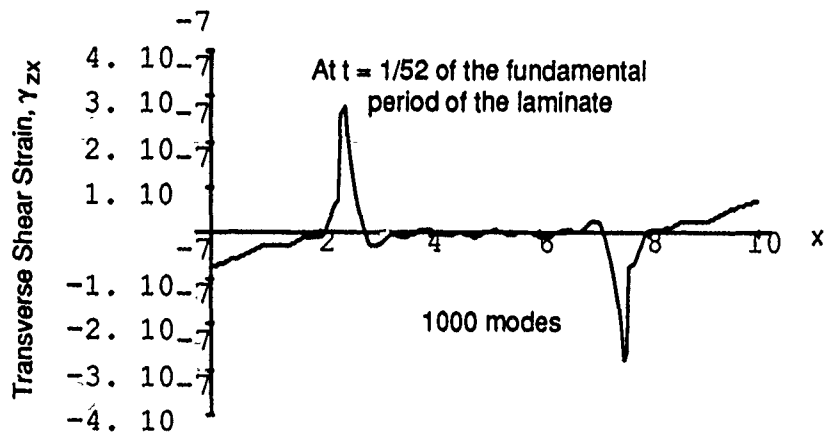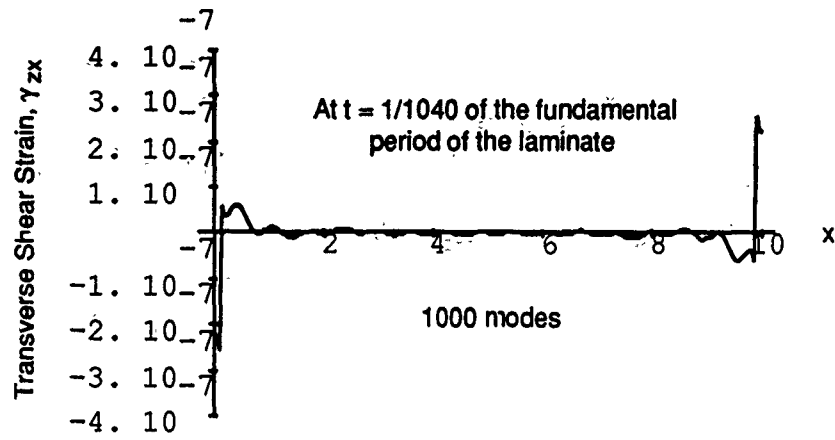
Figure 3   Distribution of Transverse, Interply Shear
Strains Across the Simple, One-Way Span
at Time Intervals Shortly After the Impulse
Load
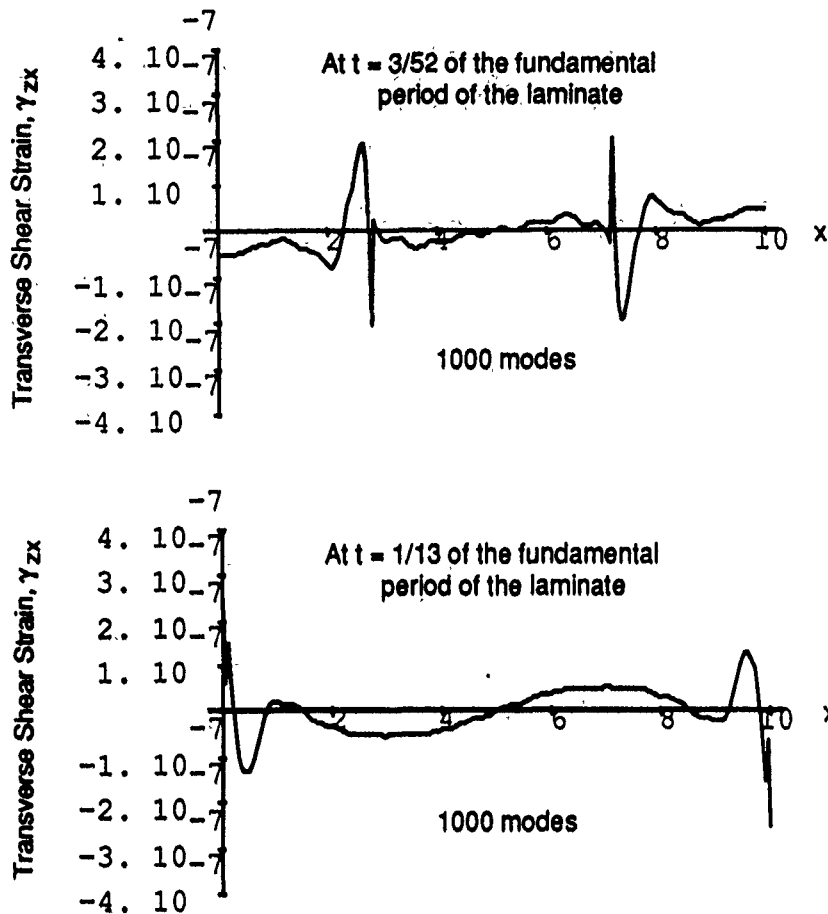
Figure 3 (Continued)
Distribution of Transverse, Interply Shear
Strains Across the Simple, One-Way Span
at Time Intervals Shortly After the Impulse
Load

corresponding shear stresses occur at the supports. These disturbances then travel across the span at a speed equal to the shear wave speed for the laminated plate. This wave speed is given by the formula, $v=\sqrt{G_{zx}/\rho}$. These results are consistent with those obtained by Karthaus and Leussink (1983).

VII. RECOMMENDATIONS:

Impulse loads on laminated plates present the analyst and/or designer with special challenges that are not encountered under static load conditions, or even under "slow" dynamic load conditions. The results of this study combined with those obtained by the earlier investigators indicate that special care must be exercised both in the analysis and in the design of laminated plate structures that are subjected to impulse or blast loads. In particular, the following recommendations are made:

1. The results in Figure 3 show that under impulse type loads, large shear strains and shear strain gradients occur in the plate. Consequently, whenever finite element methods are employed to analyze these structures, fine meshes and/or high order elements must be used to accurately capture this behavior.

2. The shear strain peaks, that occur at the supports immediately after the impulse, travel across the plate at a high speed equal to the shear wave speed of the laminated plate. As a result, any numerical technique that employs a finite-difference, time-marching scheme must use small time steps to capture these waves.

3. Transverse, interply shear strains cause laminated composite plates to fail by delamination. Therefore, design methods need to be developed that will mitigate the shear strain peaks that occur in laminated plates under blast load conditions.

a. At the material level, laminated composite plates can be designed by selecting appropriate materials, ply stacking sequence, and lamination thicknesses. The normal-mode technique provides a valuable tool for performing parametric studies on various material designs.

b. At the structural level, geometries, connections, and support structures must be developed and designed. More general numerical methods, such as finite elements and finite differences, will have to be used for the required analyses, however, the normal-mode technique can be used to guide the application of the more sophisticated techniques so that realistic and accurate results are obtained.

REFERENCES

Karthaus, W. and Leussink, J.W., "Dynamic Loading: More Than Just a Dynamic Load Factor", Proceedings of the Symposium of the Interaction of Non-Nuclear Munitions with Structures, U.S. Air Force Academy, Colorado, 1983.

Mercx, W.P.M., "The Normal Mode Technique: Applications for the Analysis of Transient Loaded Structures", Proceedings of the Fourth International Symposium on the Interaction of Non-Nuclear Munitions with Structures, Panama City Beach, Florida, 1989.

Mercx, W.P.M. and Harmanny, A., "The Normal Mode Technique: A Useful Tool to Investigate the Behavior of Structures Subjected to Local Impulsive Loading", Proceedings of the Symposium of the Interaction of Conventional Munitions with Protective Structures, Mannheim, Federal Republic of Germany, 1987.

Spilker, R.L., Chou, S.C., and Orringer, O., "Alternate Hybrid-Stress Elements for Analysis of Multilayer Composite Plates", Journal of Composite Materials, Vol. 11, January, 1977, p 51.

1990 USAF-UES SUMMER FACULTY RESEARCH PROGRAM/ GRADUATE RESEARCH PROGRAM

Sponsored by the

AIR FORCE OFFICE OF SCIENTIFIC RESEARCH

Conducted by the

Universal Energy Systems, Inc.

FINAL REPORT

A SPECIMEN PREPARATION TECHNIQUE FOR MICROSTRUCTRAL ANALYSIS OF UNSATURATED SOIL

Prepared by:	George E. Veyera, Ph.D., Assistant Professor Blaise J. Fitzpatrick, Graduate Student
Department:	Department of Civil and Environmental Engineering
University:	University of Rhode Island
Research Location:	USAF Engineering and Services Center HQ AFESC/RDCM Tyndall AFB Panama City, FL 32403-6001
USAF Researcher:	Dr. C. Allen Ross
Date:	30 September 90
Contract No.:	F49620-88-0053

A SPECIMEN PREPARATION TECHNIQUE FOR MICROSTRUCTRAL ANALYSIS OF UNSATURATED SOIL

by

~ra, Ph.D.

Blaise J. Fitzpatrick, Graduate Student

Department of Civil and Environmental Engineering
University of Rhode Island

ABSTRACT

Recent research has demonstrated that compacting moist sands at different saturations prior to dynamic testing can increase the stress transmission ratio by as much as a factor of two and can also lead to increased stress wave propagation velocities. Other research studies have also shown that the compaction method and the amount of moisture has a measurable influence on the both static and dynamic properties of sands. Experimental evidence suggests that the behavior can be attributed to variations in soil microstructure and compressibility as a result of conditions during compaction. However, a clear and concise explanation of the phenomenon is not currently available. Therefore, the need for further investigations to study the fundamental relationships between macroscopic behavior and microstructural features is evident. Considering this, the investigation outlined herein was conducted to develop a simple laboratory procedure to prepare specimens of compacted unsaturated soil for microstructural analysis. The technique involves preserving the structure formed during compaction for detailed study at the microscopic level. The method can be used to investigate and qualitatively describe the development of microstructure in compacted unsaturated soils and its effect on stress transmission from conventional weapons detonations. The results of such studies will lead to a better fundamental understanding of the role of microstructure as it affects the macroscopic engineering behavior of soils and has direct applications to groundshock prediction techniques including stress transmission to structures. The microstructural characterization of unsaturated soils will be a key element in establishing and developing an understanding of stress transmission in unsaturated soils. The research is important to the U.S. Air Force since there are currently no theoretical, empirical or numerical methods available for predicting large amplitude compressive stress wave velocity and stress transmission in unsaturated soils.

ACKNOWLEDGEMENTS

I. INTRODUCTION:

The prediction of ground motions from explosive detonations and their effects on structures requires information about the response of geologic materials to intense transient loadings. Both laboratory and field investigations have provided insight into the stress wave propagation characteristics of soils. Of particular interest is the ability of a soil to transmit applied dynamic stresses. Since soil is a multiphase media, in the general case (eg. solids, water and air), its static and dynamic behavior is very complex. The general nature of stress wave propagation in particulate media such as soils depends on a number of parameters, the interrelationship between which is not fully understood. Soil microstructure is affected by the degree of saturation (moisture condition), soil density, effective stress, applied stress intensity, stress history and the nature of the material itself (e.g. particle size, shape, distribution, mineralogical constituent(s), etc.).

The ability of a soil to transmit applied dynamic stresses (energy) is of particular interest to the U.S. Air Force with respect to military protective construction and survivability designs. Typical engineering analyses assume that little or no material property changes occur under dynamic loadings and in addition, analyses do not account for the effects of saturation (moisture conditions) on energy transmission in soils. This is primarily due to an incomplete understanding of the behavior of soils under transient loadings and uncertainties about field boundary conditions. Results from U.S Air Force field and laboratory tests with explosive detonations in soils have shown that material property changes do in fact occur and that variations in soil stiffness (or compressibility) significantly affect both dynamic and static stress transmission. However, there are currently no theoretical, empirical or numerical methods available for predicting large amplitude compressive stress wave velocity and stress transmission in unsaturated soils (Ross et al., 1986).

The ability of granular soils to transmit compressive stresses has been shown to be dependent upon the moisture content and boundary conditions present during compaction (Ross et al. 1986; Ross 1989; Veyera 1989). It is believed that the observed behavior can be attributed to variations in soil microstructure developed during compaction which remains intact at least until the soil is disturbed (ie., during testing). Considering this, the research outlined herein was performed as a part of the 1990 Summer Faculty Research Program (SFRP) and Graduate Student Summer Support Program (GSSSP) to develop a simple laboratory procedure to prepare specimens of compacted unsaturated soil for microstructural analysis. The technique can be used to examine the influence of selected parameters on the development of microstructure in unsaturated granular soils. The results of such studies will lead to a better fundamental understanding of the role of microstructure on stress transmission in soils and has direct applications to groundshock prediction techniques including stress transmission to structures. In addition, a theoretical model that accounts for microstructural effects could then be developed to predict the stress transmission and wave propagation velocity in unsaturated soils.

Dr. Veyera's primary research interests have been in the area of soil dynamics with particular emphasis on the behavior of soils subjected to high intensity dynamic compressive stress loadings such as those from explosive detonations. He has performed some preliminary investigations of stress transmission in unsaturated soils at AFESC/RDCM (Veyera 1989) and is very interested in microstructural analysis of soils particularly with regards to their ability to transmit (or absorb) applied dynamic energy and static loads. Dr. Veyera has also previously conducted research for the U.S. AFOSR on blast-induced liquefaction of saturated sand which involved the development of a state-of-the-art experimental laboratory facility. In addition, Dr. Veyera has performed research on the behavior of unsaturated soils to evaluate the engineering and hydraulic flow properties of dynamically compacted moist soil specimens.

Mr. Fitzpatrick is a graduate student in the Civil Engineering Department at the University of Rhode Island. His major area of concentration is Geotechnical Engineering with an emphasis on the dynamic behavior of unsaturated soils and soil microstructural analysis. The work performed during the summer research program at Tyndall AFB, AFESC/RDCM, forms an integral part of his master's thesis research.

II. RESEARCH OBJECTIVES:

The primary objective of the summer research effort was to develop a simple laboratory procedure to preparing specimens of compacted unsaturated soil that can be used in microstructural analysis. The technique involves preserving the structure formed during compaction so that detailed studies can be performed at the microscopic level. The method is based on standard petrographic procedures available in the open literature. Particular emphasis was directed at being able to examine the influence of moisture content (saturation) and boundary conditions on soil behavior during compaction. The long range objective for further research then is to use the procedure to investigate and qualitatively describe the development of microstructure in compacted unsaturated soils and its effect on stress transmission from conventional weapons detonations. The research is important to the U.S. Air Force since there are currently no theoretical, empirical or numerical methods available for predicting large amplitude compressive stress wave velocity and stress transmission in unsaturated soils (Ross et al., 1986).

III. BACKGROUND:

A. Previous Research

Recent research by Ross et al. (1986) and Ross (1989) has demonstrated that compacting moist sands at different degrees of saturation prior to dynamic testing can increase the stress transmission ratio by as much as a factor of two and can also lead to increased stress wave propagation velocities. Additional research by Charlie and Pierce (1988) to study the influences of capillary stresses on the behavior of the same soils tested by Ross further confirmed and extended those findings. Veyera (1989) studied four

different sands and found that the effects of microstructure may be significant in determining dynamic and static stress transmission characteristics of these soils. A number of other research studies have also shown that the compaction of moist sands has a measurable influence on both static and dynamic soil properties which can be attributed to variations in soil microstructure and compressibility. Mulillis et al. (1977) investigated 11 different packing methods and showed that the method of compaction, particularly the initial moisture conditions, strongly influences the cyclic liquefaction behavior of fine sands. Wu et al. (1984) performed resonant column tests on fine sands and observed that capillary pressures in specimens compacted moist at saturations in the range of from 5 to 20% produced a significant increase in the dynamic shearing modulus. Using mercury intrusion porosimetry techniques, Juang and Holtz (1986) were able to characterize the effects of compaction and compaction moisture content by a Pore Size Distribution (PSD) index. Nimmo and Akstin (1988) found that the permeability of sandy soils was highly dependent upon the compaction method, especially moist compaction. They attributed the variation in permeability to preferred grain orientations during compaction as a result of moisture being present as opposed to dry packing which should give a random orientation.

In addition, research has also been conducted in an attempt to characterize and relate soil structure at the microscopic level to the engineering properties of soils (macroscopic level). These studies have resulted in the development of techniques for microstructural studies of soils which involve thin sectioning of specimens and characterization by statistical analysis of directional grain and pore space orientations. LaFeber (1965) developed a technique for analyzing soil microstructure in terms of the spatial orientation of planar pore patterns. He indicates their significance by stating that these patterns "..can be expected to be an expression of the depositional and/or stress-strain history of the particular soils. As such, they should be of paramount importance in the study of the mutual relations between soil fabric and soil mechanical behavior." LaFeber (1972) further extended his work to the analysis of three-dimensional grain orientations and anisotropic fabrics by studying compound linear and planar fabric patterns and demonstrated the influence on soil fabric on the mechanical properties of several soils. Oda (1972a, 1972b) noted that particle arrangements in sands are determined by both the particle shape and the method of compaction and that initial fabric is important to mechanical properties. He also developed a method for characterizing fabric features in terms of a projected area ratio which can be used to estimate mechanical properties of sands. Mitchell et al. (1976) studied the effects of sand fabric and sample preparation method on the liquefaction behavior of sand. They performed cyclic triaxial tests and observed differences in behavior based on how specimens were prepared. Microstructural analyses of specimens showed measurable differences in grain orientations and resultant fabrics from the different compaction methods.

While the research performed to date has recognized the influence of moisture and compaction method on the behavior and properties of cohesionless soils, a clear and concise explanation of the phenomenon is

not currently available. Therefore, the need for further investigations to study the fundamental relationships between bulk behavior and properties (ie., macroscopic scale), and microstructural features (ie., microscopic scale) is evident.

B. Soil Response to Compressive Loading

Soil behavior is primarily controlled by the fundamental principal of effective stress Strictly speaking, the concept only applies to a dry or saturated soil, as originally developed, and is defined as:

$$\sigma' = \sigma - u_w \tag{1}$$

where, σ' is the effective stress, σ is the total stress and u_w is the porewater pressure ($u_w = 0$ for a dry soil). However, most naturally occurring soil deposits and compacted soils exist at intermediate levels of saturation (between 0% and 100%) where capillary pressures exist at air-water interfaces in the soil pores. Therefore, these pressures enter into the effective stress relationship. Several researchers have attempted to extend effective stress relationships to unsaturated soils. Bishop and Blight (1963) presented the following expression for the effective stress in a unsaturated soil:

$$\sigma' = (\sigma - u_a) + X(u_a - u_w) \tag{2}$$

For a dry soil, $X=1$ and for a saturated soil, $X=0$. Equation 2 accounts for the influence of soil suction on effective stress through the second term, however, compressibility effects are not directly accounted for.

Static and dynamic compressive loading of soil produces corresponding volume changes. In an unsaturated soil, the compressibility represents the combined effects of the soil skeleton, the pore water and pore air compressibilities. Unsaturated porous media will have continuously varying fluid compressibilities due to the multiphase (e.g. air, water, solid) nature of the bulk material. Based on the work of Bishop and Blight (1963), Fredlund (1985) proposed a constitutive relationship for the incremental volumetric strain, $d\varepsilon_v$, in a unsaturated soil:

$$d\varepsilon_v = C_t \, d(\sigma - u_a) + C_w \, d(u_a - u_w) \tag{3}$$

where, C_t is the soil skeleton compressibility with respect to a change in ($\sigma - u_a$), and C_w is the soil structure compressibility with respect to a change in capillary pressure, ($u_a - u_w$). Equation 3 includes compressibility effects which must be determined experimentally.

From elastic theory, it can be shown that the confined, uniaxial stress wave propagation velocity (wave speed), V_c, is given by:

$$V_c = \sqrt{\frac{M}{\rho}} \qquad (4)$$

where, M is the constrained modulus and ρ is the mass density. For a constant mass density, Equation 4 indicates that the wave propagation velocity (and correspondingly the stress transmission) is a function of stiffness modulus which in turn is a function of stress level and compressibility. Since volumetric strain (Equation 3), wave speed (Equation 4) and stress transmission are all dependent on compressibility, it should be possible to develop relationships among these parameters.

Charlie and Pierce (1988) developed capillary retention curves for Ottawa 20-30 and Eglin sands. They demonstrated that the influence of capillary pressures on effective stresses in sands is negligible, being on the order of about 7 kPa (1 psi) or less which is insignificant in comparison with high intensity transient dynamic loadings. Therefore, it appears that capillary pressures do not directly affect a granular soil's ability to transmit stresses. However, research performed by Ross et al. (1986), Ross (1989), Veyera (1989) and as a part of this study suggests that the influence of these capillary pressures on the soil microstructure developed during compaction (including soil placement and soil formation in the field) may significantly affect both the static and dynamic behavior of soil. The experimental evidence also suggests that soil microstructure is a common factor affecting wave speed, stress transmission and volumetric strain response. The microstructural characterization of unsaturated soils will be a key element in establishing and developing an understanding of stress transmission in unsaturated soils. In addition, it will also be an extremely important aspect of material model development for use in estimating the magnitude of stress transmitted through soils by conventional weapons effects.

IV.   EXPERIMENTAL INVESTIGATION:

A.   Introduction

To obtain information on the microstructure of a compacted soil, it is necessary to preserve the grain structure that results when the soil formed either naturally or by compaction in the laboratory. Therefore, a specimen preparation procedure using a suitable bonding agent is required. For the purposes of this study, it was of particular importance to be able to evaluate the effects of compaction moisture content, compaction energy, degree of saturation and boundary conditions on the resultant soil structure which could then be related to material properties and behavior.

B.   Description of Soil Tested

A commercially available granular soil designated as "Ottawa 20-30 sand" was used in all tests. Approximately 227 kg (500 lbs) of the sand was obtained from the Ottawa Silica Company for this study. Random samples were taken from the bulk quantity. The material is a uniformly graded, subrounded to rounded, medium sand with no fines. Physical properties of the sand are summarized in Table 1 and the grain size distribution is shown in Figure 1.

TABLE 1.   Physical Properties of Ottawa No. 20/30 Sand.

USCS Classification	SP
Specific Gravity	2.65
D_{50} particle size	0.70 mm
[a]C_u	1.40
[b]C_c	1.03
[c]Percent passing #100 sieve	<1 %
[d]Maximum dry density	1,763 kg/m^3
[d]Minimum dry density	1,587 kg/m^3
Maximum void ratio	0.669
Minimum void ratio	0.504

Note: [a]Coefficient of Uniformity   [c]U.S. Standard Sieve
         [b]Coefficient of Curvature   [d]Data from Ottawa Silica Sand Company

C. Description of Epoxy Used

A number of commercially available epoxies and bonding agents routinely are used in standard petrographic analyses of geologic materials. Many require special handling and sometimes involve complicated and lengthy preparation procedures. In this study, several criteria were set forth in selecting a suitable bonding agent, including the following requirements:

1)   strong bonding with soil grains and able to remain intact during cutting and polishing;

2)   relatively low viscosity material;

3)   straightforward and simple preparation procedure;
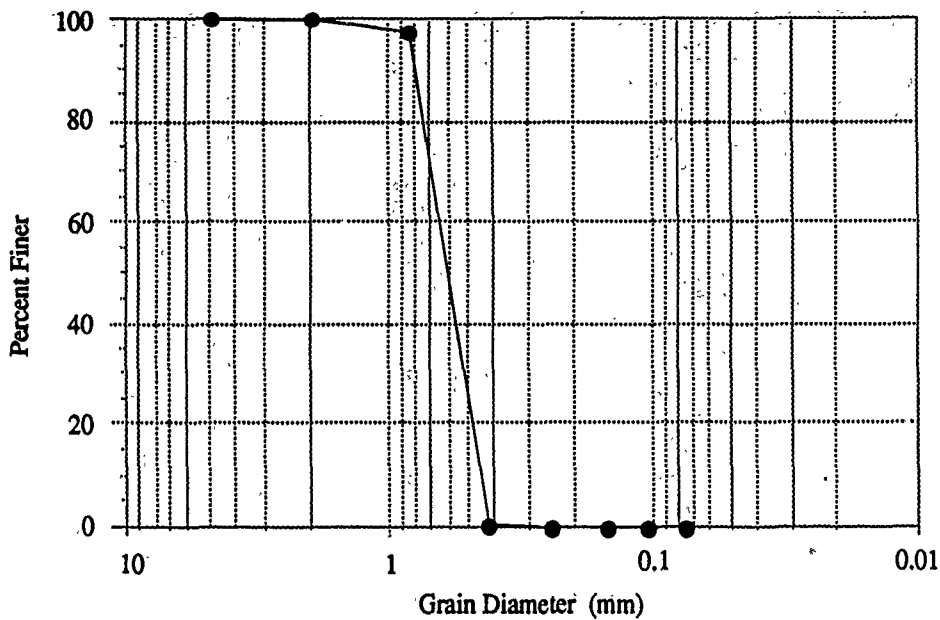
FIGURE 1. Grain Size Distribution for Ottawa 20-30 Sand.

4) no shrinkage during curing;

5) relatively rapid curing time under controlled conditions;

6) bonding agent can be easily colored or dyed (as necessary);

Several commercially available products were evaluated in the laboratory. Contact was made with various manufacturers and persons having first-hand experience with these epoxy bonding agents. After careful evaluation, "EPOTEK 301," an epoxy produced by Epoxy Technologies, Inc., of Billerica, Massachusetts was selected. EPOTEK 301 is a spectrally transparent, low viscosity (100 cps), two component epoxy. Curing time is about one hour in a dry, temperature controlled oven at 65 ± 2 ^{0}C (temperature fluctuations are undesirable since the epoxy will not completely cure regardless of oven time.). Specimens can also be cured at room temperature overnight. When fully cured, the epoxy is strongly bonded to the specimen grains and maintains the integrity of the soil structure during cutting and polishing operations. A commercially available dry lubricant, "TFL," manufactured by Remgrit Corp., of Connecticut was used as a mold release agent inside the specimen containers. Since the epoxy is clear, it was necessary to introduce color to provide adequate contrast between the pores and grains. Several coloring agents and dyes were investigated and the most acceptable results were obtained using commercially available biological stains in powdered form (Sudan IV - dark red; Sudan Black - dark blue to black).

D. Preparation of Compacted Specimens

Specimens of the Ottawa 20-30 sand were dynamically compacted to a constant dry density of 1.715 g/cm^3 (107.0 pcf) at varying degrees of saturation (different initial moisture contents) in three different stainless steel tubes. The stainless steel tubes were used to simulate different degrees of boundary stiffness that might typically be encountered in the field. Each tube was 7.62 cm (6.00 inches) long with an inside diameter of 5.08 cm (2.00 inches). Tube wall thicknesses were 2.54 cm (1.00 inches), 1.27 cm (0.50 inches) and 0.159 cm (0.0625 inches). An assembly drawing of a typical specimen container is shown in Figure 2.

A Standard Proctor hammer, ASTM D-698 (ASTM 1990), was used to consistently apply a controlled amount of compactive effort per impact to each soil specimen (7.5 Joules or 5.5 ft-lbs per impact). Prior to compaction, each specimen container and bottom steel wafer insert were sprayed with the release agent (TFL). All test specimens were formed using four individually compacted layers of equal weight such that a final specimen length of 10.16 cm (4.00 inches) would be obtained. Four individual lifts, each having a final thickness of 2.54 cm (1 inch), were used. Saturations were varied from near 0% (dry) to 80% for each soil. At saturations near 0%, each layer of dry soil was poured directly into the tube and compacted.

In preparing moist specimens, the required amount of water for a given degree of saturation (at final density when compacted) was added to the originally dry soil, thoroughly mixed in and then allowed to equilibrate before compacting. Although the dry density was constant for each specimen, the amount of compactive effort required varied with the amount of moisture (saturation). Since the specimens ranged in degree of saturation from about 0% to about 80%, the tests were conducted on unsaturated specimens. With respect to this study, the term "unsaturated" implies that both continuous air and water phases exist in the soil (eg. there are no isolated air or water pockets in the grain matrix). For most soils, this generally occurs at saturations less than about 85% (Corey, 1977).

E. Preparation of Epoxied Specimens

The procedure described herein was developed for epoxying compacted specimens of unsaturated granular soil. Since the epoxy used does not mix or cure in the presence of water, specimens of soil initially compacted moist at varying degrees of saturation in the steel specimen containers were dried in a temperature controlled oven at 110 ^{0}C for at least 12 hours. Specimens were then allowed to cool to room temperature before epoxying. Careful handling of the specimen container is essential during all phases of preparation to insure that the compacted soil structure is not be disturbed (ie., by vibration, jarring, etc.).

Material quantities shown were determined based on a calculation of the available pore space for a medium granular soil (Ottawa 20-30 sand) compacted to a void ratio of 0.545 and epoxied with EPOTEK 301 epoxy. Allowance has been made for additional material required to cover particles, minor losses in

FUNNEL

COMPACTED SOIL SPECIMEN

SPECIMEN CONTAINER

O-RING

APPROXIMATELY
10 DEGREES

STEEL WAFER

WEDGE

(NOT TO SCALE)
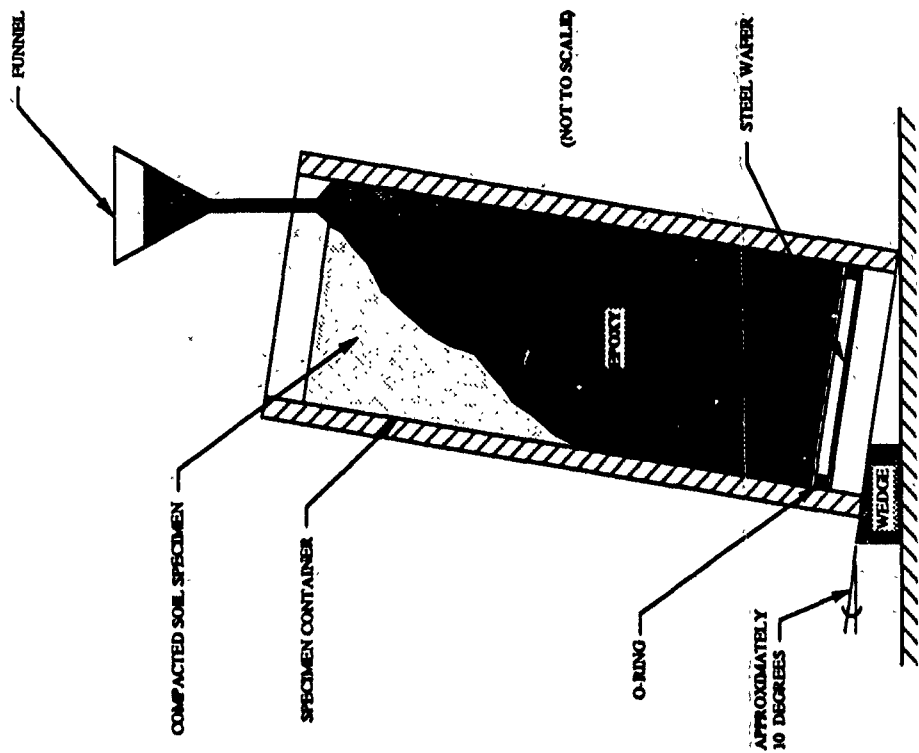
FIGURE 3. Typical Compacted Specimen Being Exposed for Microstructural Analysis.

THREADED ROD

TOP FLANGE
PLATE

SPECIMEN
CONTAINER

O-RING

STEEL WAFER

COMPACTED SOIL
SPECIMEN

PEDESTAL

(NOT TO SCALE)
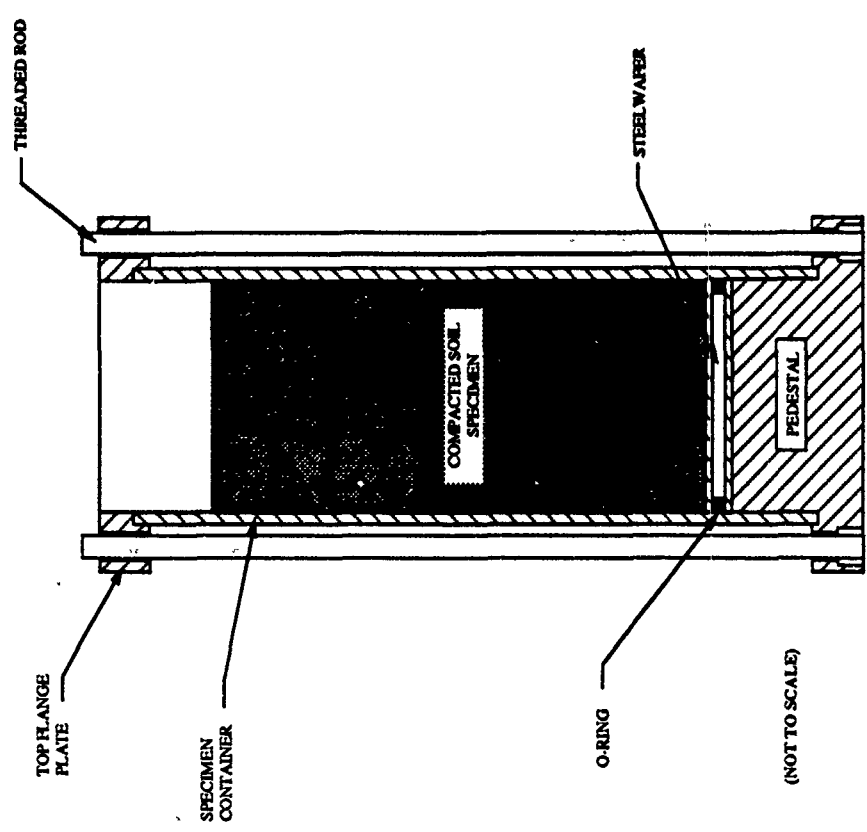
FIGURE 2. Typical Assembly Drawing for Specimen Container.

37-12

handling, etc., with a minimum of waste. The mixing ratio for the epoxy component parts is 4:1 (resin to hardener) as specified by the manufacturer. Disposable containers are recommended for preparing and mixing the components and wax lined paper cups worked quite well. A level, covered work area is recommended for epoxying the specimens. Figure 3 shows a typical specimen being epoxied. The general procedure is outlined as follows:

1) place the specimen container on the working surface and tilt it at an angle of about 10 degrees, ;

2) weigh out exactly 70 grams of resin in a container;

3) weigh out exactly 17.5 grams of hardener in a second container;

4) weigh out approximately 0.20 grams of biological stain (Sudan Black or Sudan IV);

5) pour the hardener and biological stain into the cup containing the resin and thoroughly mix using a glass rod until a uniform color is obtained;

6) slowly pour the epoxy mix into the specimen container using a small funnel; do not allow the epoxy to cover more than half of the exposed specimen surface at any time and pour close to the specimen surface to avoid disturbing the soil structure (see Figure 3);

7) allow the epoxy to slowly percolate down into the specimen until it eventually reaches the surface on the side opposite of where pouring is done; this aids in saturating the pores by forcing air out ahead of the epoxy; the epoxy has a pot life of about 35 minutes as mixed;

8) once the sample appears to be fully saturated with the epoxy mix, set the specimen container fully upright and observe for about 2-3 minutes; add additional epoxy if necessary;

9) for curing, place the specimen container in a dry temperature controlled oven at 65 ± 2 ^{0}C for at least one hour (longer time is required for the thick-walled containers); curing can also be done at room temperature in about 6-8 hours; curing is complete when the epoxy is hard to the touch.

F. Extruding Epoxied Specimens

After curing, the next step is to extrude each specimen from the steel specimen container. For oven cured specimens, the containers must be cooled before extrusion. The procedure uses a modified Marshall Testing machine for loading, and requires a loading piston, loading support blocks and a flange plate. The general procedure is outlined as follows:

1) place the specimen container on the flange plate with the steel wafer facing upwards;

2) place the specimen container and flange plate on the loading blocks;

2) insert a steel loading piston into the specimen container on the steel wafer and then lower the testing machine's reaction cross-member until it contacts the piston;

6) apply the quasi-static load until the specimen is fully extruded from the specimen container;

7) remove and thoroughly clean the steel specimen container, steel wafer and o-ring seal, removing any epoxy (fine sand paper and denatured alcohol worked well for cleaning);

G. Preparing Epoxied Specimens for Microstructural Analysis - Step I: Initial Rough Cutting

A water-cooled Buehler Metaseu Powermet I Automatic Abrasive Cutter (ACC) Unit with interchangeable cutting wheels was used for rough cutting of epoxied specimens. Also, a simple aluminum specimen alignment device for making uniform cuts was fabricated. The alignment device has dimensions of 7.62 x 7.62 x 7.94 x 12.70 cm long (3 x 3 x 0.125 by 5 inches). Once a specimen is properly aligned, the ACC automatically makes a complete cut through the specimen. Each cut section is clearly marked to record the original orientation. Figure 4 shows the location of the various cutting planes.

Initial Specimen Section Cuts

   a)   the first cut removes about 0.3125 cm (0.125 in) from each end of the specimen;

   b)   the second cut splits the specimen in half along its long axis (Fig. 4 (A-A) and Fig. 5);

   c)   the third cut splits one of the specimen halves along its diameter (Fig. 4 (B-B) and Fig. 6).

Final Specimen Section Cuts

   a)   a vertical cut about 0.3125 cm (0.125 in) in thickness is made along the long axis of one of the halves from the initial cuts, step b (Fig. 7);

   b)   a horizontal cut about 0.3125 cm (0.125 in) in thickness is made along the diameter of one of the halves from the initial cuts, step c (Fig. 8).

The general procedure for rough cutting epoxied specimens is outlined as follows:

   1)   turn on safety power switch and the water supply line;

   2)   set cutting force pressure to approximately 345 kPa (50 psi);

   3)   open the safety shield cover and place the specimen securely against the alignment device in the AAC machine chucks;

   4)   close the safety shield cover, turn on the internal lighting unit and bring the cutting wheel down until it just contacts the specimen using the "RAPID ADVANCE" control;

   5)   set the power switch to "ON" and activate the internal water pump;

   6)   engage the "AUTO" cutting mechanism and wait until the ACC unit comes to a complete stop; remove the specimen and realign the necessary portion for the next cut;

   7)   repeat steps 3 through 6 for each cut to be made; reorientation of the alignment device is necessary for the different cuts.

H. Preparing Epoxied Specimens for Microstructural Analysis - Step II: Grinding and Polishing

The final preparation procedure for the specimens prior to microstructural analysis involves several steps and uses a Buehler Datamet Micro-Processor Grinding and Polishing Unit. Also, the following items (available from Buehler), are required: a) a grooved cast iron polishing wheel with #600 Polishing Grit, b) a smooth cast iron polishing wheel , c) a polishing cloth, d) Metadi Fluid, e) diamond
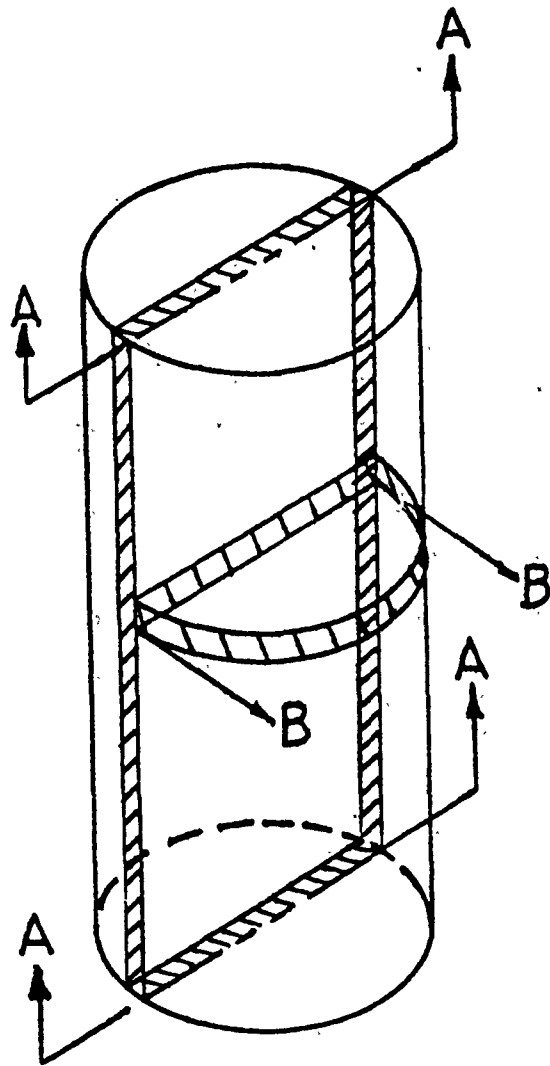
FIGURE 4. Location of Cutting Planes for Epoxied Specimen.
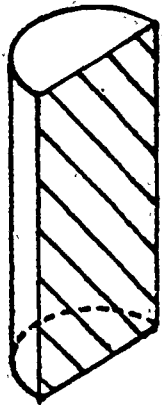
FIGURE 5. Initial Specimen Cut Along
the Long Axis (Section A-A).
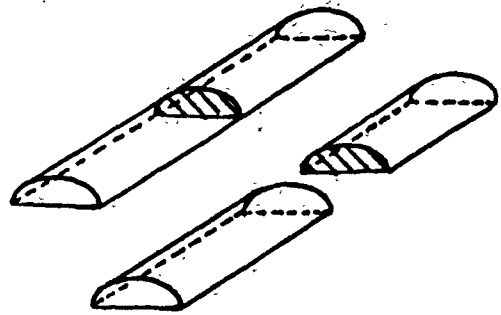
FIGURE 6. Initial Specimen Cut Along the
Diametral Axis (Section B-B).
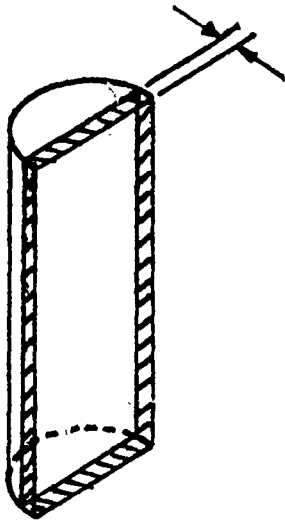
FIGURE 7. Final Cut of Specimen Section
Along the Long Axis.
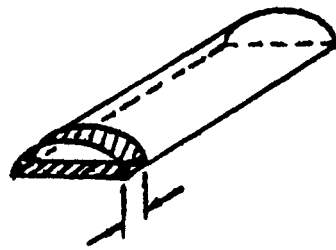
FIGURE 8. Final Cut of Specimen
Along the Diametral Axis.

paste, and, f) Micropolish "C". The procedure involves three separate sequential steps and is outlined as follows:

1) Initial Grinding - This step is used to true the planar surface obtained during the rough cutting process and to prepare the specimen surface for polishing.

    a) set the Datamet system controls as follows: Speed = 120 rpm, Time = 5 minutes, and Water Supply = "ON";

    b) place the grooved cast iron polishing wheel on the Datamet machine;

    c) evenly spread about one level teaspoonful of #600 Polishing Grit on the polishing wheel;

    d) if a template is available for holding the specimen section, set the machine to apply 133.5 Newtons (30 lbs) of force and begin grinding; if no template is available, hold the specimen section on the grinding wheel firmly in place by hand and begin grinding; in either case, wait until the machine automatically stops before removing the specimen.

2) Rough Polishing - This step is used to rough polish the specimen section surface prior to detailed finish polishing.

    a) set the Datamet system controls as follows: Speed=120 rpm, Time = 5 minutes, and Water Supply = "OFF";

    b) place the smooth polishing wheel with the polishing cloth on the Datamet machine;

    c) saturate the polishing cloth on the polishing wheel with the Metadi Fluid;

    d) extrude a small amount of diamond paste (about 0.635 cm or 0.125 inches in length) and thoroughly mix with the Metadi fluid to evenly cover the polishing cloth surface;

    e) if a template is available for holding the specimen section, set the machine to apply 133.5 Newtons (30 lbs) of force and begin polishing; if no template is available, hold the specimen section on the grinding wheel firmly in place by hand and begin polishing; in either case, wait until the machine automatically stops before removing the specimen.

    f) thoroughly clean the polishing cloth with water to remove all diamond paste and Metadi Fluid before polishing the next specimen section.

3) Fine Polishing - This step is used to develop a smooth, highly polished surface finish that provides adequate contrast between the specimen grains and the expoy-filled pores.

    a) set the Datamet system controls as follows: Speed = 120 rpm, Time = 5 minutes, and Water Supply = "ON";

    b) place the smooth polishing wheel with the polishing cloth on the Datamet machine;

    c) saturate the polishing cloth on the polishing wheel with water;

    d) spread about one level teaspoonful of Micropolish "C" on the polishing cloth, thoroughly mix with water and evenly cover the polishing cloth surface;

e) if a template is available for holding the specimen section, set the machine to apply 133.5 Newtons (30 lbs) of force and begin polishing; if no template is available, hold the specimen section on the grinding wheel firmly in place by hand and begin polishing; in either case, wait until the machine automatically stops before removing the specimen.

f) thoroughly clean the polishing cloth with water to remove all Micropolish "C" before polishing the next specimen section.

Once the final polishing has been completed, specimens are examined under a microscope to check if the surface has been properly prepared and if adequate contrast between pore spaces and individual grains has been developed. Properly prepared specimens can then be used in microstructural analysis studies.

V. RESULTS:

From this study, a suitable procedure has been developed to prepare specimens of Ottawa 20-30 sand for microstructural analysis. A number of trial specimens compacted at various moisture contents were successfully prepared using the method described herein. We are currently performing some preliminary examinations of the microstructure from some of the compacted specimens using photomicrographic techniques in preparation for a more detailed study. The initial findings are encouraging and suggest that variations in microstructure with moisture during compaction may exist. However, these findings represent general observations and are inconclusive at present. A more comprehensive study is required. In addition, the technique was applied to a limited number of Eglin sand specimens. Eglin sand is a well graded material, consisting of medium to fine sands. It appears that it may also be possible to preserve the microstructure of this sand following the method developed. However, some modifications to the procedure will be necessary due to the presence of fines and the color of the sand (light to medium brown).

VI. RECOMMENDATIONS:

The degree of saturation (moisture content) during compaction is an important factor affecting the development of microstructure in soils. The understanding of unsaturated soil behavior to applied loads is very limited at present and further studies, particularly those involving microstructure, are necessary. The results of such studies will be very important to the U.S. Air Force with respect to military protective construction design and survivability. Although the influence of moisture (saturation) and compaction method on the behavior and properties of cohesionless soils has been observed in previous research, a clear and concise explanation of the phenomenon is not currently available. Therefore, more extensive laboratory and field studies that specifically address the role of microstructure are needed. Several specific recommendations can be made:

1) A detailed microstructural analysis of granular soils compacted at varying degrees of saturation should be performed. The study should include measurements of preferred grain orientations, pore space configurations, packing structure, relative grain arrangements and local/global variations in these parameters. Due to the large number of grains and pores in a given soil specimen, a statistical analysis of the data will be required so that useful correlations can be derived.

2) The fundamental aspects of load transfer mechanisms and the effects of boundary conditions in unsaturated compacted soils should be examined for both static and dynamic loading conditions. Experimental studies should also be conducted to examine the limiting relationship between the degree of saturation and input energy applied during compaction with respect to soil stiffness and dynamic stress transmission. Based on the results, relationships that correlate soil microstructure with macroscopic behavior and soil properties such as compressibility, wave speed, transmission ratio, strength, etc., should be developed.

3) A series of fully instrumented, carefully controlled small scale field explosive tests should be conducted in close coordination with further laboratory studies. Test parameters should include variations in saturation (moisture content), compaction methods, boundary conditions and applied energy. Field instrumentation should provide measurements of input energy, transmitted energy, and soil deformation and stress (both vertically and horizontally) as a minimum. Results will be useful for relating laboratory and field measured soil behavior, providing valuable input for material model development.

REFERENCES

1. ASTM (1990) Annual Book of ASTM Standards - Volume 04.08 Soil and Rock: Dimension Stone: Geosynthetics, American Society for Testing and Materials, Philadelphia, PA, pp. 160-164.

2. Bishop, A. W. and Blight, G. E. (1963) "Some Aspects of Effective Stress in Unsaturated Soils." Geotechnique, Vol. 13, No. 3, September, pp. 177-179.

3. Charlie, W. A. and Pierce, S. J. (1988) "High Intensity Stress Wave Propagation in Unsaturated Sands." Final Report to US AFOSR/UES Under Contract Number F49620-87-0004, Engineering and Services Center, AFESC/RDCM, Tyndall AFB, FL, September, 20 p.

4. Corey, A.T. (1977) Mechanics of Heterogeneous Media, Water Resources Pub., Ft. Collins, CO.

5. Fredlund, D. G. (1985) "Soil Mechanics Principles that Embrace Unsaturated Soils." Proceedings of the 11th International Conference on Soil Mechanics and Foundation Engineering, ISSMFE, San Francisco, pp. 465-472.

6. Juang, C. H. and Holtz, R. D. (1986) "Fabric, Pore Size Distribution, and Permeability of Sandy Soils." Journal of the Geotechnical Engineering Division, ASCE, Vol. 112, No GT9, September, pp. 855-868.

6. Juang, C. H. and Holtz, R. D. (1986) "Fabric, Pore Size Distribution, and Permeability of Sandy Soils." Journal of the Geotechnical Engineering Division, ASCE, Vol. 112, No GT9, September, pp. 855-868.

7. LaFeber, D. (1965) "The Graphical Presentation of Planar Pore Patterns in Soils." Australian Journal of Soil Research, Vol. 3, August, Australia, pp. 143-164.

8. LaFeber, D. (1972) "Micromorphometric Techniques in Engineering Soil Fabric Analysis." 3rd International Working-Meeting on Soil Micromorphology, September, Wroclaw, Poland, pp. 669-687.

9. Mitchell, J.K., Chatoian, J.M. and Carpenter, G.C. (1976) "The Influences of Sand Fabric on Liquefaction Behavior." Contract Report S-76-5, US Army Corps of Engineers Waterways Experiment Station, Soils and Pavement Laboratory, Vicksburg, MS.

10. Mulillis, J. P., Seed, H. B., Chan, C. K., Mitchell, J. K. ard Arulanandan, K. (1977) "Effects of Sample Preparation on Sand Liquefaction." Journal of the Geotechnical Engineering Division, ASCE, Vol. 103, No GT2, February, pp. 91-108.

11. Nimmo, J. R. and Akstin, K. C. (1988) "Hydraulic Conductivity of a Sandy Soil at Low Water Content After Compaction by Various Methods." Journal of the Soil Science Society of America, Division S-1-Soil Physics, Vol. 52, No. 2, March/April, pp. 303-310.

12. Oda, M (1972) "Initial Fabrics and Their Relations to Mechanical Properties of Granular Materials." Soils and Foundations, Japanese Society of Soil Mechanics and Foundation Engineering, Vol. 12, No. 1, March, Tokyo, pp. 17-36.

13. Oda, M (1972) "The Mechanism of Fabric Changes During Compressional Deformation of Sand." Soils and Foundations, Japanese Society of Soil Mechanics and Foundation Engineering, Vol. 12, No. 2, June, Tokyo, pp. 1-18.

14. Ross, C. A. (1989) "Split-Hopkinson Pressure Bar Tests." Final Report No. ESL-TR-88-2, HQ AFESC/RDCM, Air Force Engineering and Services Center, Tyndall AFB, FL.

15. Ross, C. A., Nash, P. T. and Friesenhahn, C. J. (1986) "Pressure Waves in Soils Using a Split-Hopkinson Pressure Bar." Technical Report No. ESL-TR-86-29, USAF Engineering and Services Center, Tyndall AFB, FL, July.

16. Wu, S., Gray, D. H. and Richart, F. E. (1984) "Capillary Effects on Dynamic Modulus of Sands and Silts." Journal of the Geotechnical Engineering Division, ASCE, Vol. 110, No GT9, September, pp. 1188-1202.

17. Veyera, G. E. (1989) "Static and Dynamic Behavior of Compacted Unsaturated Sands." Final Report to US AFOSR/UES Under Contract Number F49620-87-0004, Engineering and Services Center, AFESC/RDCM, Tyndall AFB, FL, September.